Chemostratigraphical characterisation of lower Silurian black shales from the Formigoso Formation (southern Cantabrian Mountains, Spain)

Timothy Ferriday

PhD Thesis
(October 2014)

Volume I
Thesis

Keele University

Declaration Part 1. To be bound in the thesis

SUBMISSION OF THESIS FOR A RESEARCH DEGREE

Part I. DECLARATION by the candidate for a research degree. To be bound in the thesis

Degree for which thesis being submitted: **PhD**

Title of thesis: **Chemostratigraphical characterisation of lower Silurian black shales from the Formigoso Formation (southern Cantabrian Mountains, Spain)**

This thesis contains confidential information and is subject to the protocol set down for the submission and examination of such a thesis.

NO [please delete as appropriate; if YES the box in Part II should be completed]

Date of submission **30/01/2014** Original registration date **01/09/2009**
(Date of submission must comply with Regulation 2D)

Name of candidate: **Timothy Ferriday**

Research Institute: **EPSAM** Name of Lead Supervisor: **Dr Michael Montenari**

I certify that:

(a) The thesis being submitted for examination is my own account of my own research
(b) My research has been conducted ethically. Where relevant a letter from the approving body confirming that ethical approval has been given has been bound in the thesis as an Annex
(c) The data and results presented are the genuine data and results actually obtained by me during the conduct of the research
(d) Where I have drawn on the work, ideas and results of others this has been appropriately acknowledged in the thesis
(e) Where any collaboration has taken place with one or more other researchers, I have included within an 'Acknowledgments' section in the thesis a clear statement of their contributions, in line with the relevant statement in the Code of Practice (see Note overleaf).
(f) The greater portion of the work described in the thesis has been undertaken subsequent to my registration for the higher degree for which I am submitting for examination
(g) Where part of the work described in the thesis has previously been incorporated in another thesis submitted by me for a higher degree (if any), this has been identified and acknowledged in the thesis
(h) The thesis submitted is within the required word limit as specified in the Regulations

Total words in submitted thesis (including text and footnotes, but excluding references and appendices) **90,280 words**

Signature of candidate Timothy Ferriday …… Date 15/08/2014 ……

Note

Extract from Code of Practice: If the research degree is set within a broader programme of work involving a group of investigators – particularly if this programme of work predates the candidate's registration – the candidate should provide an explicit statement (in an 'Acknowledgments' section) of the respective roles of the candidate and these other individuals in relevant aspects of the work reported in the thesis. For example, it should make clear, where relevant, the candidate's role in designing the study, developing data collection instruments, collecting primary data, analysing such data, and formulating conclusions from the analysis. Others involved in these aspects of the research should be named, and their contributions relative to that of the candidate should be specified (*this does not apply to the ordinary supervision, only if the supervisor or supervisory team has had greater than usual involvement*).

This work is dedicated in loving memory of my late Father

Robert William Ferriday

30th September 1958 – 25th February 2012

Abstract

This thesis focuses on the development of the black shales belonging to the lower Silurian Formigoso Formation (Fm.) situated within the Cantabrian Fold Belt, Northern Spain. The geochemical data obtained by the use of an energy-dispersive Niton XL3t XRF analyser under controlled laboratory conditions is comparable to that of conventional wavelength dispersive XRF analysers. The *in-situ* field analysis resulted in similar geochemical signals and elemental concentrations to that of the laboratory analysed samples. The high-resolution geochemical database, consisting of 4148 readings of the Formigoso Fm. was used to characterise the shales of the Formigoso Fm. relative to a number of international shale standards. Following this geochemical characterisation, a number of palaeoenvironmental proxies for [1] anoxia reconstructions, [2] palaeosalinity, [3] palaeohumidity, [4] weathering indices, and finally [5] bioproductivity were utilised. The combined outcome of these proxies together with field-based sedimentological observations led to a detailed reconstruction of the environment that prevailed during the deposition of the Bernesga Mb. black shales. A generic model is developed for the formation of these organically enriched sediments. This model is subsequently compared to previously published Silurian, black 'hot' shale models. The major parameters controlling the development of the Cantabrian black shale deposits were mainly the presence of a pronounced palaeorelief, which was generated by a combination of tectonic pulses related to the widening of the Rheic Ocean to the north and glaciogenic processes of the Hirnantian ice masses to the south. Orbital parameters or 'deep time cycles', mainly Obliquity and Eccentricity in combination with tectonic pulses led to high resolution sea-level oscillations and consequent cyclic behaviour of the redox elements recorded within the 'hot' shale deposits of the southern Cantabrian Basin. Additionally, 209 measurements of 76 international and inter-laboratory standards were performed to formulate new equations for the precise calibration of major and trace elements.

Contents

Figures and tables:

Abbreviations

A

API American Petroleum Institute
AR Accumulation Rate

B

BMS Black Marine Shale
BSE Back Scatter Electron

C

Cal Calibrated
CGR Computed Gamma-Ray
CIA Chemical Index of Alteration
CIW Chemical Index of Weathering
CIZ Central Iberian Zone
CZ Cantabrian Zone

D

DBD Dry Bulk Density
DBS Depth Below Surface
D.L Detection Limits
DOP Degree of Pyritization

E

ED-XRF Energy Dispersive – X-Ray Fluorescence

EF Enrichment Factors

F

FFT Fast Fourier Transform

FM. Formation
Or **Fm.**

G

Gp. Group
GR Gamma Ray

H

HR High Resolution
HST Highstand Systems Tract

I

ICV Index of Compositional Variation

K

Kyr Thousands of years

L

LDPE Low Density Polyethylene
LST Lowstand Systems Tract

M

MAR Mass Accumulation Rate
Mb. Member
MFS Maximum Flooding Surface
Myr Millions of years

O

OM Organic Matter
OMZ Ossa Morena Zone

P

PIA Plagioclase Index of Alteration
PP Palaeobioproductivity
PP Primary Production
PPM Parts Per Million
PVP Polyvinylpyrrolidone

S

S.D Standard Deviation
SEM Scanning Electron Microscope
SGR Spectral Gamma-Ray
SP South Pole
SPZ Southern Portuguese Zone
SR Sedimentation Rate
Sst. Sandstone

T

TE's Trace Elements
TOC Total Organic Carbon
TS Total Sulphur
TS Transgressive Surface
TST Transgressive Systems Tract

W

WALZ West Asturian-Leonese Zone
Wt% Weight percentage

X

XRD X-Ray Diffraction
XRF X-Ray Fluorescence

Z

Z Atomic number

Acknowledgements

Firstly, I would like to thank my supervisors **Michael Montenari** and **Graham Williams** for sourcing the funds to allow the project to commence, a truly life changing event. My thanks go specifically to **Michael** for his endless support and knowledge towards the subject area. My appreciation goes to **Nigel Cassidy** and **Ann Billington** for being highly supportive during the passing of my Father. Huge thanks go to **David Emily** for contributing towards the calibration process and vital sample preparation techniques for the newly acquired Niton XL3t handheld XRF. '**Dutch' Pete** for the incredible conversations aiding in the development of this very project, the fine Cuban cigars and development work of his historical Cantabrian manor. Thanks to **Paul Wignall** for simply sending me a copy of his work titled 'Black Shales' (1994). Regards to the Cantabrian team **Stu Clarke**, **Helen Doherty**, **Steven Rogers** and **Michael Kelly** for the incredible Cantabrian times and to **Annabel** and **Horhay** of the 'Hostal San Emiliano'. Many thanks to **Tino**, the 'Sena de Luna Campsite manager' for providing the best hospitality during the vital field seasons. Much respect to my mother **Jane Ferriday**, for always being there. The incredible support of the soon to be in-laws **Keith** and **Judy Moore**, without which, the final stages of the research wouldn't have been possible. Many thanks to my step mother **Dianne Ferriday** for her support. A special thank you goes to my brothers, **John** and **Robert Ferriday** for simply being amazing. Lastly, most importantly, to my wonderful partner **Melissa Moore**, who literally got me over every hurdle I faced with the project and for that matter the past 10 years!

Chapter 1
Introduction

The main aim of this thesis is to characterise geochemically the lower Silurian black shale successions of the Bernesga Member (Mb.) within the Cantabrian Fold Belt (NW Spain). The Cantabrian Fold Belt (or Cantabrian Basin) is situated within the Cantabrian Mountains in northern Spain. The localities selected for analysis and detailed discussion within this thesis (Aralla, Caldas de Luna, La Majua, Sena de Luna and Villanueva) are all part of the southern Cantabrian Basin. Little is known about the processes which led to the formation of the Cantabrian black shales. This thesis aims to constrain the major parameters controlling the development of these organically enriched black shale deposits.

The lower Silurian period is characterised by the presence of wide-spread, anoxic graptolitic black shale sediments, mainly deposited along the northern rim of Gondwana. In the present day these deposits can be found mainly within North Africa, Jordan, Saudi Arabia and northern Spain (Iberia), although they have also been documented elsewhere. These black shales are attracting a considerable amount of scientific interest, as it is nowadays hypothesised that their genesis might be closely related to major changes within the palaeo-geographical configuration of continents, the oceanic circulation patterns but also drastic climatic perturbations. Furthermore, these black shale successions can be of highest economical significance, as some of them form major source rocks for oil reserves. For example, the lower Silurian black shales source ~80-90% of the hydrocarbons derived from the Palaeozoic in North Africa (Lüning *et al*., 2000; Lüning *et al*., 2005).

Previous work encompasses much debate as to the controls on the deposition of the Silurian shales within the peri-Gondwanan region. Various models for the formation of these organically enriched deposits have been postulated. Lüning *et al*. (2000) suggest that these black shales formed during the onset of the lower Silurian eustatic transgression, basically following the previously developed basal transgressive ‘puddle model’ of Wignall and Hallam (1991). Within this model, the patchy, discontinuous lateral distribution of the black shales is mainly controlled by the presence of palaeo-topographical features. However, in developing an alternative model, Armstrong *et al.* (2005) argue that the black shales were forming during the maximum extent of the Silurian marine transgression (drawing on the ‘expanding puddle model’ of Wignall and Hallam, 1991), and that the major factor controlling the formation of the lower Silurian black shales is not necessarily the presence or absence of a palaeo-relief on the continental shelfs, but a stratified shelfal water column generated by a prominent and partly persistent fresh-water cap.

The main objectives of this research are two-fold. The first aims to utilise high-resolution whole rock geochemical data obtained from the Silurian black shales of the Cantabrian Basin to reconstruct the palaeoenvironmental conditions that prevailed at the time of deposition. This palaeoenvironmental data and reconstructions are then used, together with the results of previously published studies, to develop a new generic depositional model for the black shale successions of the Cantabrian Basin. This model is compared and contrasted to the previously proposed models (see above). The high-resolution chemostratigraphical data generated for this research project were combined with detailed biostratigraphical data available from the published literature. Graptolites and palynomorphs such as acritarchs and chitinozoans, have been successfully used in the past as important biostratigraphic markers to precisely constrain the age of the Silurian 'hot' shales of northern Gondwana (e.g. Marshall, 2000; Butcher, 2009; Paris *et al.*, 2012, with further references therein). However, their use for biostratigraphic purposes during field-based exploration campaigns has proven to be problematic (e.g. Lüning *et al*., 2000), as the biostratigraphic potential of these fossils is often hampered by their poor preservation or even absence in surface or near-surface samples. The organic material from such samples is commonly oxidised and hence destroyed. Under such circumstances, the use of chemostratigraphical methods can provide complementary and sometimes even vital information, especially where biostratigraphical data are absent or scarce, thus potentially enabling larger scale intra- and inter-basinal correlations. For this purpose, the whole rock geochemical signatures of the Cantabrian black shales, with particular emphasis on redox sensitive but conservative elements, like uranium or vanadium, were analysed, interpreted and correlated.

The second aim had a predominantly methodological nature. The establishment of chemostratigraphic signatures and geochemical 'fingerprints' is nowadays a fundamental part of any field-based exploration campaign, especially within the hydrocarbon industry. Data have to be generated fast, at comparable low costs, in statistically relevant quantities and if possible *in-situ* at the site of a potential play. The recent development and continued advancement of portable XRF-analysers has offered a possibility to provide this type of data under the conditions described above. In order to test whether a state-of-the-art portable XRF-analyser can be used to achieve the goals and demands outlined above, a portable Niton XL3t XRF analyser was used to generate the data under both, controlled laboratory conditions and during *in-situ* field analysis. Furthermore, to advance the analytical precision and reproducibility and therefore the interpretative value of data generated by portable XRF analysers during stationary, laboratory measurements, but also during

field- and exploration campaigns, equations for the calibration of all major and trace elements were determined by the systematic and replicated analysis of 76 international and inter-laboratory standards. These equations are made available within this thesis.

Chapter 2
Geological Setting

Contents

2.1 Introduction to the geology of the Iberian Massif and the Cantabrian Zone

The Variscan Belt (or Hercynian Orogen) extends for over 3000 km from southern Iberia to northeastern Bohemia and is 700-800 km in width (Paris and Robardet, 1990; Weil *et al.,* 2001). The Variscan Belt formed during the late Palaeozoic (Late Devonian to Carboniferous, ~ 370 – 290 Ma ago) as the result of the convergence of two major continents, Laurasia and Gondwana, including a number of smaller microplates and fragments of magmatic arcs (Dias and Ribeiro, 1995; Weil *et al.,* 2001; Abalos *et al.,* 2002; Martínez Catalán *et al.,* 2009a). Within the Iberian Penninsula, Upper Proterozoic to Carboniferous rocks outcrop widely in its western part, in what is known as the Iberian or Hesperian Massif.

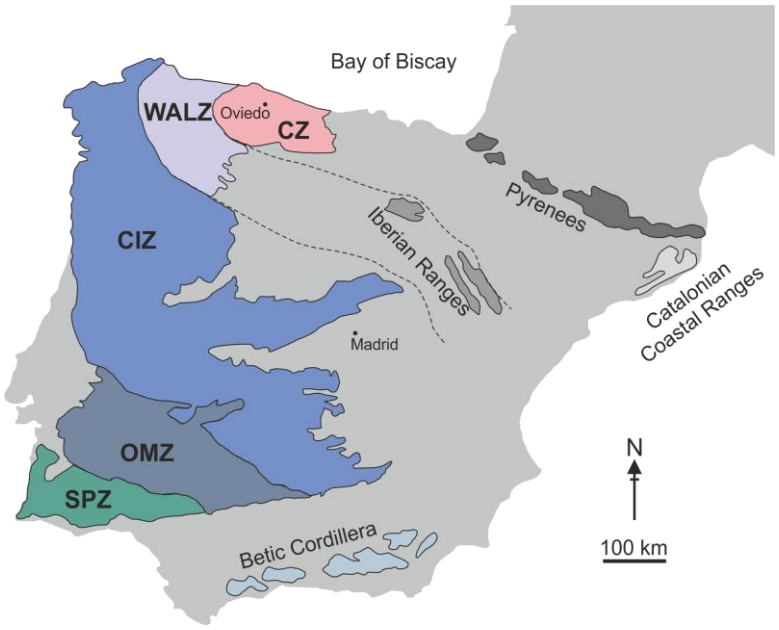

Figure 2.1; Major Variscan units of the Iberian Massif according to Lotze (1945) and Julivert (1971). **CZ**: Cantabrian Zone; **CIZ**: Central Iberian Zone; **OMZ**: Ossa Morena Zone; **SPZ**: Southern Portuguese Zone; **WALZ**: West Asturian-Leonese Zone. Modified after Garcia-Alcalde *et al.* (2002a).

The Iberian Massif provides the largest outcrops of Variscan and pre-Variscan rocks in Europe (Valladares *et al.,* 2002). It developed between the Upper Devonian and the Late Carboniferous (Fernández-Suárez *et al.,* 2000; Abalos *et al.,* 2002) and has been sub-divided into five different domains, based on sedimentological differences in the Lower Palaeozoic sedimentary successions (Julivert *et al.,* 1972; Abalos *et al.,* 2002): [1] The Cantabrian Zone (CZ), the [2] West Asturian-Leonese (WALZ) Zone, [3] Central Iberian Zone (CIZ), [4] Ossa-Morena Zone (OMZ) and [5] South Portuguese Zone (SPZ) (see **Figure 2.1**). The boundaries between these zones are major

Varsican thrusts and reverse faults, that were in some instances reactivated by extensional tectonics following the Variscan orogeny (Nance *et al.,* 2010).

The Cantabrian Mountains are located in northern Spain within the province of Castilla y Leon. These mountains form a part of the geologically distinct region known as the Cantabrian Zone (**CZ**) or Cantabrian Arc (**Figure 2.1)**. The **CZ** represents the most external zones of the Iberian Massif foreland (and the external zone of the Variscan belt), located near the core of the Cantabrian Orocline (Paris and Robardet, 1990; Garciá-López and Bastida, 2002; Aller *et al.,* 2005; García-López *et al.,* 2007; Pastor-Galán *et al.,* 2013). Oroclinal bending caused by east-west compression was responsible for the arc shaped nature; this arc is largely of Late Hercynian to post-Hercynian origin, latest Carboniferous (Weil *et al.,* 2000; Weil *et al.,* 2001; Keller *et al.,* 2008; Weil *et al.,* 2010; Gutiérrez-Alonso *et al.,* 2012). The distribution of distinct sedimentary facies together with palaeocurrent data provide evidence, that the Lower Palaeozoic passive margin faced northwards, away from the central core of the orocline (Shaw *et al.,* 2012 in: Gutiérrez-Alonso *et al.,* 2012).
The CZ is an area that comprises Palaeozic pre-orogenic sediments of relatively small thickness (Martínez Catalán *et al.,* 2009a), and is characterised by thin-skinned tectonics, which are the product of a combined Variscan and Alpine tectonic overprint. The thin-skinned general structural pattern of the **CZ** is dominated by a principle decollement, located within the Lower-Middle Cambrian limestones of the Lancara Fm. (Julivert, 1971; Aller *et al.,* 2005). The resulting tectonic shortening is approximately 50% to 75% (Keller *et al.,* 2008). The delicate relationship between the thrusts and the folds gives the Cantabrian Arc its distinctive shape (Julivert and Marcos, 1973; Pérez-Estaún *et al.,* 1988; Abalos *et al.,* 2002).

In the CZ, the Variscan deformation took place without any significant metamorphism. Very low to low grade metamorphic overprints only appear towards the north and north-western parts of the Zone, close to the boundary with the WALZ (Garciá-López and Bastida, 2002; Aller *et al.,* 2005; García-López *et al.,* 2007; Pastor-Galán *et al.,* 2013).

The CZ during the Cambro-Ordovician was one of many graben structures within the northern margins of the Gondwanan palaeocontinent; it has a comparable stratigraphical succession to other areas surrounding the Mediterranean, like the Anti-Atlas, southern Montagne Noire and south-west Sardinia (Aramburu-Zabala Higuera and García Ramos, 1993; Álvaro *et al*., 2000a; Álvaro *et al*., 2000b). The CZ can be regarded as a Cambrain to Devonian passive continental

shelf area, that progressively developed into a Carboniferous foreland basin, receiving sediments due to erosion from the internal zones of the Variscan Orogen (Garciá-López and Bastida, 2002).

Sedimentary, faunal and zircon populations in the Palaeozoic sediments show strong similarities to those found on the Saharan Craton and with zircons found in Libya. This is used as evidence to suggest that NW Iberia occupied a palaeoposition close to present-day northern Africa during this time interval (Keller *et al.,* 2008; Martínez Catalán *et al.,* 2009b).

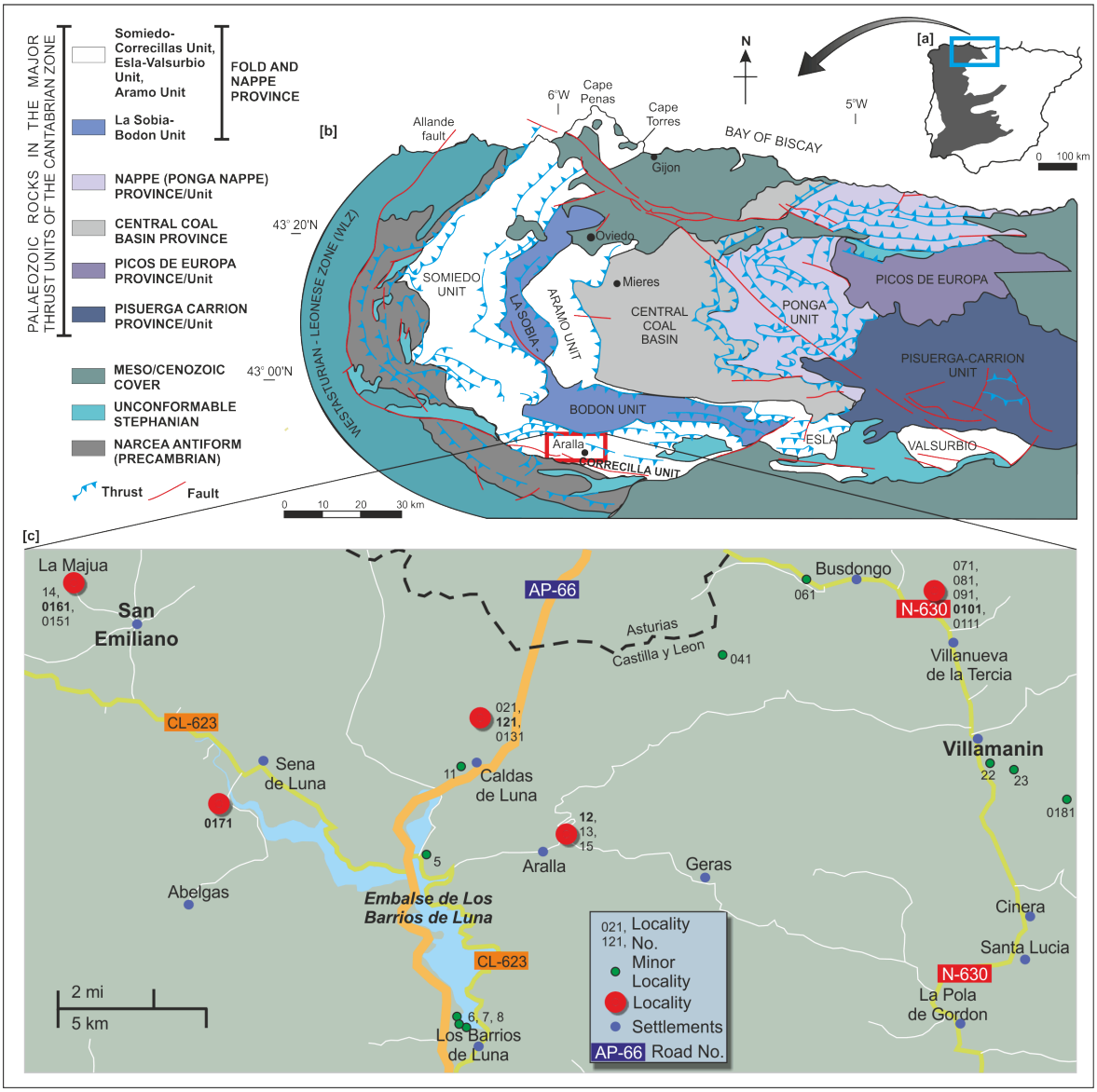

Figure 2.2: Overview, tectonostratigraphic units and sampled localities; [a] showing the Iberian Peninsula, the grey shaded area represents the Palaeozoic outcrops; [b] tectonostratigraphic units of the Cantabrian Zone, modified after Julivert (1971); Pérez-Estaún *et al.* (1988); Aller *et al.* (2005). [c] Investigated area: the locality numbers are listed next to points; the bold numbers represent the number assigned to a major locality.

Two tectonostratigraphic units are present within the **CZ** (Julivert, 1978; Marcos and Pulgar, 1982 in: García-López *et al.,* 2007). First, a pre-orogenic (pre-Variscan) unit formed by pre-Carboniferous successions (Abalos *et al.,* 2002; Aller *et al.,* 2005), in which all stratigraphic systems are represented, found in the western region of the **CZ** (Garciá-López and Bastida, 2002).

This succession consists of a siliciclastic Lower Palaeozoic series and a siliciclastic series with calcareous intercalations in the Devonian. The succession formed mainly in a shallow water marine environment, characteristic of a passive margin. Palaeocurrent data recorded in this lower Palaeozoic strata indicate, that its sediment source was located to the east, yet, the precise provenance area remains still controversial (Pastor-Galán *et al.,* 2013). This series forms a wedge, that thins towards the foreland (Garciá-López and Bastida, 2002). The pre-orogenic sequence rests unconformably on the Proterozoic rocks of the Narcea Antiform (see **Figure 2.2**), bounding and outcropping in the western CZ (Abalos *et al.,* 2002).

The second unit is syn-orogenic formed by Carboniferous rocks that appear throughout the **CZ** (Sarmiento *et al.,* 1994; García-López *et al.,* 2007). They were deposited in a foreland basin setting and can be sub-divided into several clastic wedges, that resulted from the filling of foredeep basins that formed in front of the major thrust units (Julivert, 1978; Aller *et al.,* 2005). The clastic input was prodvided from the internal zones towards the west and the south (Aramburu-Zabala Higuera and García Ramos, 1993). Late Variscan, unconformable Stephanian rocks with molassic facies, partially bounded by faults (see **Figure 2.2**), appear in several areas of the CZ (Garciá-López and Bastida, 2002).

The **CZ** can be further sub-divided into a number of smaller thrust fault units. Julivert (1971) and Pérez-Estaún *et al.* (1988) separated the CZ into five distinct units: [1] Folds and Nappes (typified by a near complete Palaeozoic succession), [2] Central Asturian coal-field (mainly formed by Carboniferous rocks that can reach a thickness up to 6000 m; a band of Cambrian-Ordovician rocks appears towards the eastern edge, near the basal thrust-system (Garciá-López and Bastida, 2002), [3] Ponga Nappe (depicted by the abscence or very small thickness of Silurian and Devonian rocks and the presence of several large thrust units, forming a strongly folded nappe), [4] Picos de Europa (an imbricate system of thrust sheets formed predominantly by Carboniferous rocks) and the, [5] Pisuerga-Carrion province (most of this unit is para-autochthonous in the CZ and consists predominantly of Carboniferous rocks, although Silurian and Devonian rocks are also present to a subordinate extent (Abalos *et al.,* 2002).

The Folds and Nappes province itself has been further subdivided based on differing distinctive stratigraphic successions (Julivert, 1971; Pérez-Estaún *et al.,* 1988 in: Abalos *et al.,* 2002): the Somiedo-Correcilla unit (the Somiedo part to the north and the Correcilla part to the south), the La Sobia-Bodon unit (the La Sobia part to the north and the Bodon part to the south), the Aramo unit,

the Esla nappe unit and finally the Valsurbio unit (or the last two combined to the Esla-Valsurbio unit as in (Garciá-López and Bastida, 2002; Abalos *et al.,* 2002). The Somiedo-Correcillas unit (**Figure 2.2**), located towards the centre of the Cantabrian Zone, is the area of interest (particually the southern Correcilla unit, red box, outlining study area), as it contains the most complete sucession spanning from the Cambrian to the Carboniferous. Most importantly, it includes well preserved complete successions of the Silurian black shales of the Formigoso Fm., as described in the following stratigraphy section.

2.1.1 Synoptic stratigraphy of the Cantabrian Zone

The overall stratigraphy of the Cantabrian Zone is summerised and described in the following **Figure 2.3** and **Table 2.1**:

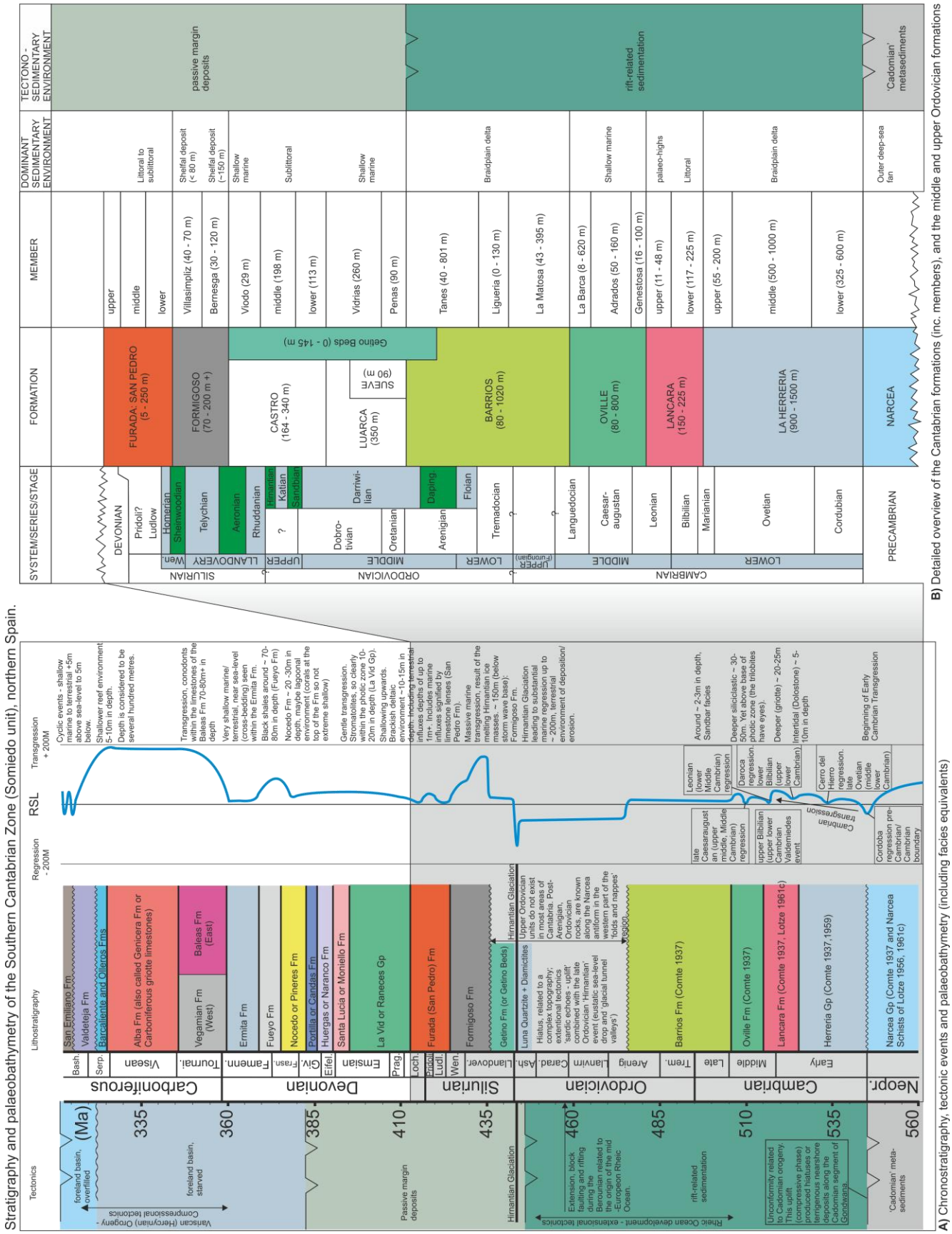

Figure 2.3: Chronostratigraphy and palaeobathymetry of the Cantabrian Zone northern Spain. A) An overview of all the Cantabrian formations including tectonic events and sea-level fluctuations, B) illustrates the Proterozoic and lower Palaeozoic, including all formations (and members): the Middle and Upper Ordovician formations (Luarca, Sueve and Castro) do not occur in the southern CZ, yet are included for comparison with the Getino Beds. Modified after Garciá-López and Bastida (2002) and Keller *et al.* (2008).

Name (Oldest to youngest)	Age and thickness	Lithology	Environment of deposition
Narcea Gp.	**Thickness:** 1000-2000 m (Pérez-Estaún 1973; Pérez-Estaún 1978) **Age of the Narcea Gp.:** at the eastern flank of the Narcea Antiform: age is constrained by the presence of cyanobacterial sphaeromorphs: *Sphaerocongregus variabilis* and *Palaeogomphosphaeria caurensis* both indicate an age of middle (?) -late Vendian age (Vidal *et al.* 1994; Narcea Schists of Lotze 1956; Valladares *et al.* 2002).	Alternating shales and sandstones. Pérez-Estaún (1973) and Pérez-Estaún (1978) defined three units: The lowest comprises interbedded porphyritic volcanic rocks, sandstones and shales; above these are turbiditic shales and greywackes; and the uppermost unit consists predominantly of shales with interbedded sandstones (Valladares *et al.* 2002).	The succession has been interpreted as a deep-sea fan (Valladares *et al.* 2002).
Herreria Gp.	**Thickness:** 900-1700 m **Age of Herreria Gp.:** The Herreria Gp. (Comte 1959) yields Early Cambrian ichnofossils and acritarchs from its lowest levels (Vidal *et al.* 1994). Trilobite assemblages suggest an Early Cambrian - late Ovetian age (Sdzuy 1971; Liñán *et al.* 1993; Comte 1937; Lotze 1961; Valladares *et al.* 2002; Liñán *et al.* 2002).	Conglomerate, quartzite, feldspathic sandstone, rare dolomitic levels and interbedded mudstones form the Herreria Gp. The contact between the underlying Narcea Gp. is an angular unconformity showing palaeoalteration due to subariel exposure. The angle of the angular discordance decreases from east to west (Comte 1937; Lotze 1961; Valladares *et al.* 2002; Liñán *et al.* 2002).	The Herreria Gp. has been interpreted as a transitional fluviatile-marine environment (braid plain delta) (Crimes *et al.* 1977; Truyols *et al.* 1990; Aramburu *et al.* 1992; Comte 1937; Lotze 1961; Valladares *et al.* 2002; Liñán *et al.* 2002).
Lancara Fm.	**Thickness:** 150-225 m **Age of the Lancara Fm.:** The lower member contains archaeocyathans of Bilbilian age and Lower Cambrian trilobites (Sdzuy 1995). The upper member (griotte) contains brachiopods, echinoderms, molluscs and porifera (Zamarreño and Julivert 1967). Diachronous boundaries for the griotte from Leonian to Caesaraugustan age (Mid Cambrian) based on trilobite records (Sdzuy 1968; Comte 1937; Lotze 1961; Liñán *et al.* 2002).	Dolomite, limestone and interbedded shale. Lower member: dolomite, grey limestones and oolitic limestones. The upper member: (griotte facies) red nodular limestones. (Liñán *et al.* 2002; Comte 1937; Lotze 1961).	The lower member suggests shallow sublittoral (Zamarreño 1972) and the upper member sublittoral. (Liñán *et al.* 2002; Comte 1937; Lotze 1961).
Oville Fm.	**Thickness:** 80-800 m **Age of the Oville Fm.:** Consists of three members, all with diachronous boundaries: the lowest contains; trilobites, brachiopods and echinoderms. The trilobites indicate an age of upper Leonian to upper Caesaraugustan (Zamarreño 1972). The following younger members contain Middle Cambrian-Tremadoc acritarchs (Fombella 1978; Liñán *et al.* 2002; Comte 1937; Lotze 1961).	Siliciclastic unit comprise glauconitic sandstone, green shale and some quartzite beds towards the top (Truyols *et al.* 1990; Liñán *et al.* 2002).	Shallow marine environment of deposition (Liñán *et al.* 2002).
Barrios Fm.	**Thickness:** 80-1020 m **Age of the Barrios Fm.:** Acritarchs indicate an age between highest Mid Cambrian and Early Ordovician (Aramburu *et al.* 1992). Ichnofossils indicate the presence of the Tremadoc and Arenigian (Crimes and Marcos 1976). In most areas younger Ordovician rocks do not exist and the Barrios Fm. is directly overlain by the Silurian Formigoso Fm. (Comte 1937; Lotze 1961; Gutierrez-Marco *et al.* 2002).	Light coloured quartzite with minor intercalations of siltstones and shales, and some conglomeratic levels. Some localities express 100 m of dark shales in the upper parts of the Barrios Fm. followed by 50 m of quartzites (Linan *et al.* 2002; Gutierrez-Marco *et al.* 2002). The transition from the underlying Oville Fm. is gradational (Aramburu *et al.* 1992). There are three members within the Barrios Fm. [1] the Matosa member (Mb.) containing white quartzites with volcanic intercalations, it has an erosive top. The [2] Ligueria Mb. (found in the eastern zone of Cantabria) containing conglomerates and sandstones. Finally the [3] Tanes Mb. containing white to pinkish quartzites. There is a long term hiatus between the Matosa and Tanes Mbs, yet this hiatus is difficult to observe due to the very similar facies development of both members.	The lowermost part of the Fm. may represent a lateral facies change from the upper part of the Oville Fm. The formation was deposited in a tidal environment– shallow maybe beach environment (Truyols *et al.* 1990; Aramburu *et al.* 1992). A braid to braid-plain delta environment with marine influence (Aramburu-Zabala Higuera and García Ramos 1993; Linan *et al.* 2002; Gutierrez-Marco *et al.* 2002). The Tanes Mb. represents fluvial to coastal and shallow marine deposits.

Luna Quartzite and Diamictites (glacial deposits)	**Thickness:** varies, dependent on the incised valleys cut by the Hirnantian Glaciation 200-250 m for the main fill deposits (diamictites) (Gutiérrez-Marco *et al.* 2010). **Age of the Luna Quartzite and diamictites:** Hirnantian age of the diamictites is given by a low diversity, typical *Hirnantia*-fauna brachiopods, eg, *Plectothyrella crassicosta chauveli* and *Arenorthis* sp. (Bernárdez Rodríguez *et al.* 2006; Gutiérrez-Marco *et al.* 2010).	The Luna quartzite: well-sorted, medium- to coarse-grained sandstone. Pebble- to cobble-sized rip-up clasts of mudstone are locally embedded. Beds are 0.2−1.5 m thick, horizontally to subhorizontally laminated, with subordinate cross-stratification. Upper horizons are bioturbated. *Hirnantia*-fauna occurs at the base of the Luna Quartzite (Bernárdez Rodríguez *et al.* 2006; Gutiérrez-Marco *et al.* 2010).	Deposited during the Hirnantian. During advance and/or retreat of the ice masses, palaeovalleys incised in the underlying Barrios Fm. (~ 250 m). The glacial fill (diamictites) filled these valleys during and after the Hirnantian Glaciation. Which in turn is capped by the Luna Quartzite in some areas; Gutiérrez-Marco *et al.* 2010).
Getino Fm. (or Getino Bed)	**Thickness:** ~ 10.5 m (Sarmiento *et al.* 1994) **Age of the Getino Fm.:** Late Ordovician to earliest Silurian age (Sarmiento *et al.* 1994; Aramburu *et al.* 1992). Gutiérrez-Marco *et al.* (2010) state that the Getino Beds are following the Luna Quartzite and diamictites and lies at the base of the Formigoso Fm. making it early Silurian in age.	Brecciated sandstones, glauconitic sandstones and red and green shales with limestone and dolostone intercalations towards the top (Sarmiento *et al.* 1994). Located above an erosive contact with the Barrios Fm. (Gutiérrez-Marco *et al.* 1996b; Evers 1967). The Getino Fm. has been described as “transitional beds” by Bosch (1969).	Deposited during the initial transgression after the Hirnantian Glaciation. Is usually found at the base of the Fomigoso Fm. (Gutiérrez-Marco *et al.* 2010). The presence of glauconite, ferruginous sediments and intense bioturbation indicates a shallow marine environment reaching coastal to inner ramp depths (Aramburu 1989; Gutiérrez-Marco *et al.* 1996b).
Formigoso Fm.	**Thickness:** 50-800 m+ (massive lateral variation in thickness. Maybe controlled by the underlying glacial relief of the Barrios Fm.) **Age of the Formigoso Fm.:** The Fm. yields an abundance of graptolites and palynomorphs as well as scarce brachiopods, bivalves, cephalopods and trilobites. It extends from the Aeronian-Telychian boundary into the lower Sheinwoodian as determined by graptolite assemblages (Truyols *et al.* 1974). These dates are confirmed by organic walled microfossils (chitinozoans) by Cramer and Diez (1978). Verniers *et al.* (1995) confined the lower chitinozoan assemblage to the *Conochitina alargada* Biozone corresponding to the middle Aeronian (Robardet and Gutierrez-marco 2002).	Black and grey siltstones and shales with sand intercalations towards the top of the Fm. that show ripple laminations, hummocky cross-stratifications and trace fossils. The Fm. shows a shallowing upwards sequence. The sand intercalations are getting coarser, thicker and more frequent towards the top of the Formigoso Fm. Kegel (1929) proposed two members: [1] the Bernesga Mb. and [2] Villasimpliz Mb.. The relationship between the pure black graptolitic shales at the base of the Fm. (Bernesga Mb.) and the sandstone containing Villasimpliz Mb. is seen clearly observable at locality no. 12. Locality no. 12 expressed 40 m+ of the Bernesga Mb. and 150 m+ of the Villasimpliz Mb. (Suárez de Centi *et al.* 1989; Robardet and Gutierrez-marco 2002; Ferriday and Montenari 2012).	Shallow marine shelf deposits or shelf margin deposits (Robardet and Gutierrez-marco 2002). The environment of deposition is related to a rapid marine transgression followed by a shallowing upwards sequence (represented by the sandstone beds) into the gradational boundary of the overlying San Pedro Fm. The lateral variation in the thickness of this Formation is very dramatic. Ranging from less than 50m to More than 800 m+. The thickness maybe controlled by the Hirnantian glacial palaeorelief as described by (Bernárdez Rodríguez *et al.* 2006; Gutiérrez-Marco *et al.* 2010; Ferriday and Montenari 2012).
Furada (San Pedro) Fm.	**Thickness:** 80-200 m **Age of the Furada (San Pedro) Fm.:** The Fm. contains upper Wenlock palynomorphs from its lowermost section and Ludlow and Pridoli brachiopods, graptolites and palynomorphs from its middle and upper sections. Truyols *et al.* (1974) and Aramburu *et al.* (1992) suggest the boundary between the Silurian and Devonian lies within the Upper part of the San Pedro Fm. (Robardet and Gutierrez-Marco 2002; Garcia-Alcalde *et al.* 2002b).	Grey and reddish ferruginous sandstones with shaley intercalations, thin oolitic ironstone beds and in the uppermost part some sandy limestone lenses (Robardet and Gutierrez-Marco 2002; Garcia-Alcalde *et al.* 2002b).	Terrestrial iron stained sandstone - River deposits. With intercalated shallow marine limestone lenses. Distal deltaic environment with terrestrial input (Robardet and Gutierrez-Marco 2002; Garcia-Alcalde *et al.* 2002b).

La Vid or Raneces Gp.	**Thickness:** 400-600 m **Age of the La Vid or Raneces Gp.:** Nieva Fm.: Contains Lochkovian to Pragian brachiopods. Banugues/Felmin Fm.: Lochkovian-earliest Emsian poor record of fossils. The Ladrona/Pedrosa/Valporquero Fm. (Emsian) contains brachiopods, crinoids and trilobites in the limestones and dacryoconarids and ostracods are common in the relatively distal dark shales. The Aguion/Coladilla Fm. (late Emsian) contains crinoids, brachiopods, corals and bryozoans (Garcia-Alcalde *et al.* 2002b).	Predominant calcareous series. The Nieva Fm. at the base, 200 m of thick-bedded sometimes dolomitized bioclastic limestones alternating with dark, argillaceous bioturbated limestones, thin shale layers and siltstone lenses. The Banugues/Felmin Fm. 150-200 m of dolostones, dolomitized bioclastic limestones and thick sandstone intercalations. The Ladrona/Pedrosa/Valporquero Fm. 130-140 m of fossiliferous, grey argillaceous limestones alternating with dark shales. The upper group consists of the Aguion/Coladilla Fm. 200 m of very fossiliferous, pink to red coloured crinoidal limestones, dark marls and grey to brown shales (Garcia-Alcalde *et al.* 2002b).	The calcareous sedimentation of the La Vid Gp. and the presence of small reef build-ups suggest a probably tropical setting for the sedimentary basin during the Early Devonian times (Garcia-Alcalde *et al.* 2002b).
Santa Lucia or Moniello Fm.	**Thickness:** 250-260 m **Age of the Santa Lucia or Moniello Fm.:** Upper Emsian; Corals, stromatoporoids, bryozoans and brachiopods are the dominant fossils within this Fm. (Garcia-Alcalde *et al.* 2002b)	Argillaceous limestones with thin intervening bioturbated shales at the base and the top of the Fm. (Garcia-Alcalde *et al.* 2002b).	Exhibits facies developed within a sublittoral shallow, open marine platform (Garcia-Alcalde *et al.* 2002b).
Huergas or Naranco Fm.	**Thickness:** 50-500 m **Age of the Huergas or Naranco Fm.:** The Fm. is early Eifelian to Givetian in age: The sandstones are dominated by brachiopods, molluscs and bryozoans. Dacryoconarids, ostracods and ammonoids dominate the distal black shales (Garcia-Alcalde *et al.* 2002b).	Siliciclastic sediments (Garcia-Alcalde *et al.* 2002b).	The wide range of facies types within the Fm. indicates varied marine and transitional environments of deposition linked to large south-sloping deltas (Garcia-Alcalde *et al.* 2002b).
Portilla or Candas Fm.	**Thickness:** 100-200 m **Age of the Portilla or Candas Fm.:** The Fm. is dated to be Givetian - early Frasnian. Reefal episodes with abundance of corals, stromatoporoids, crinoids and brachiopods (Garcia-Alcalde *et al.* 2002b).	Thick fossiliferous limestones as well as argillaceous and sandy limestones with minor shaley intercalations (Garcia-Alcalde *et al.* 2002b).	The facies types signify a shallow marine, sublittoral platform. Abundant storm deposits and hummocky cross-bedding probably record hurricanes (Garcia-Alcalde *et al.* 2002b).
Nocedo or Pineres Fm.	**Thickness:** 300 m **Age of the Nocedo or Pineres Fm.:** The Fm. is dated as Early Frasnian-Famennian by the abundance of brachiopods and crinoids (Garcia-Alcalde *et al.* 2002b).	Thick alterations in shales, siltstones, calcareous sandstones and limestones arranged in two regressive-transgressive sequences. The lower part is generally more calcareous then the upper and contains refal horizons (Garcia-Alcalde *et al.* 2002b).	Shallow marine shelf environment as indicated by the reefal horizons (Garcia-Alcalde *et al.* 2002b).
Fueyo Fm.	**Thickness:** 130 m **Age of the Fueyo Fm.:** (Famennian) Pelagic faunas, mostly nautiloids, bivalves and ostracods (Garcia-Alcalde *et al.* 2002b).	Black nodular shales with a thin polymict conglomerate in the lower part and alternations in shales and sandstone in the upper part (Garcia-Alcalde *et al.* 2002b).	Deeper marine environment represented by the shales. The conglomerate may indicate a storm event, possible distal deltaic fan environment (Garcia-Alcalde *et al.* 2002b).
Ermita Fm.	**Thickness:** 60 m **Age of the Ermita Fm.:** Famennian (Garcia-Alcalde *et al.* 2002b).	Cross-bedded sandstones and quartz sandstones, siltstones, thin shale horizons and sandy limestone lenses with abundant micro-conglomeratic sandstone layers. Most cases the Fm. grades both upwards and laterally into 1-15 m crinoidal limestones or black shales with phosphate nodules (Garcia-Alcalde *et al.* 2002b).	Originated in subtidal to supratidal, shallow to very shallow water environments (Garcia-Alcalde *et al.* 2002b).

Vegamian Fm. and Baleas Fm.	**Thickness:** 5-10 m in the eastern Baleas Fm. and 10-60 m in the western Vegamian Fm. **Age of the Vegamian Fm. and Baleas Fm.:** Abundant conodonts within the limestones of the Baleas Fm. indicate a late Famennian - early Tournaisian age. The Vegamian Fm. a mid Tournaisian - early Visean age has been documented (Sánchez de Posada *et al.* 1990; Colmenero *et al.* 2002)**.**	Either 5-10 m of sandy crinoidal limestone and/or pure grainstone and packstone limestones of the eastern Baleas Fm., or 10-60 m of black, poorly fossiliferous shales with phosphate nodules and radiolarites in the western Vegamian Fm. The Baleas and Vegamian Fms and maybe the uppermost Ermita Fm. overlap the Devonian/Carboniferous boundary (Colmenero *et al.* 2002).	The Baleas Fm. limestones represent submarine shoals, a shallow-water well oxygenated shelf sea with benthic communities. Separated by the slightly deeper channels (Ermita Fm.) sandstones and (Vegamian Fm.) shales on the shelf edge (Colmenero *et al.* 2002).
Alba/Genicera Fm. (also called the Carboniferous griotte limestones)	**Thickness:** 20-30 m **Age of the Alba/Genicera Fm.:** Visean. Pelagic fauna are dominant including cephalodos and subordinate benthic faunal debris (Colmenero *et al.* 2002).	Laterally uniform unit that gradationally overlies the Baleas and Vegamian Fms. The unit comprises red nodular limestones with red shale partings and beds including a radiolarite horizon (Colmenero *et al.* 2002).	The Fm. is considered to be a condensed unit and was deposited on a well oxygenated pelagic platform with gentle slopes within several hundred metres of water (Sánchez de la Torre *et al.* 1983; Colmenero *et al.* 2002).
Barcaliente and Olleros Fms.	**Thickness:** 300-350 m **Age of the Barcaliente and Olleros Fm.:** Serpukhovian, contains few fossils (Colmenero *et al.* 2002).	300-350 m of laminated, dark grey limestones and mudstones within the Barcaliente Fm. which thins towards the east (Colmenero *et al.* 2002).	Restricted, highly stressed shallow marine platform environment (González Lastra 1978; Eichmüller and Seibert 1984; Colmenero *et al.* 2002).
Valdeteja Fm.	**Thickness:** up to 1000 m **Age of the Valdeteja Fm.:** Bashkirian (Colmenero *et al.* 2002).	Thick limestone deposits (~1000m thick in parts) (Colmenero *et al.* 2002).	This Fm. was deposited on raised shallow water platforms above sub-marine highs produced by the incipient emplacement of new thrust units (Fernández 1993; Colmenero *et al.* 2002).
San Emiliano Fm.	**Thickness:** 1500 m **Age of the San Emiliano Fm.:** upper Bashkirian (Colmenero *et al.* 2002).	Terrigenous sediments that filled the foredeep towards the southern and western flanks of the Valdeteja Fm. Consists of shales, turbiditic sandstones, calcareous breccias, coal seams and limestone bands (Colmenero *et al.* 2002).	Shallowing upwards succession deposited in a coastal, shallow marine setting near to progradating deltas (Bowman 1982; Fernández 1993; Colmenero *et al.* 2002).

Table 2.1: Synoptic overview of the lithostratigraphic units of the uppermost Precambrian to Late Carboniferous, as used and discussed within the present study, their chronostratigraphic postion, thickness, lithology and palaeoenvironmental interpretation. Corresponding references are given within the table.

2.1.2 Precambrian and Lower Palaeozoic: an overview

2.1.2.1 Precambrian

Precambrian strata are represented by the sediments of the Narcea Gp. of Comte (1937), which are an equivalent to the Narcea Schists of Lotze (1956, 1961 in: Valladares *et al.,* 2002). An Upper Proterozoic age was demonstrated by Vidal *et al.* (1994) in: Valladares *et al.* (2002); Garciá-López and Bastida (2002) on the basis of acritarch findings. The Narcea Gp. forms the core of the so called Narcia Antiform (see **Figure 2.1**), which bounds the **CZ** and the **WALZ** to the west (Valladares *et al.,* 2002).

The Narcea Gp. (1000-2000 m) consists of three informal units: [1] a lower unit of interbedded porphyritic volcanic rocks, sandstones and shales, [2] a middle unit made up of turbiditic shales and greywackes and finally [3] an upper unit consisting of shales and interbedded sandstones (Pérez-Estaún, 1973; Carballo, 1984; Valladares *et al.,* 2002). Marcos (1973 in: Valladares *et al.,* 2002) distinguished two differing facies areas within in the northern sector of the Narcea Gp. (a western area and an eastern area). The eastern area comprised predominantly low metamorphic fine to medium grained siliciclastic sediments, that have been interpreted as the deposits of an outer deep-sea fan. The western facies area on the other hand displays a higher metamorphic gradient and is comprised of predominantly volcanic and volcaniclastic rocks of rhyolitic, dacitic and andesitic composition (Valladares *et al.,* 2002).

2.1.2.2 Cambrian

A prominant angular unconformity separates the Precambrian Narcea Gp. from the lowermost Cambrian Herreria Gp. (Comte, 1959). This unconformity is widely regarded to be the expression of tectonic movements due to the Cadomian Orogeny. As described above, the dip of this angular unconformity decreases systematically from the east to the west across the CZ (Valladares *et al.,* 2002).

The **Herreria Fm.** (Comte, 1937, 1959; Lotze, 1961 in: Linan *et al.,* 2002) forms the base of the Palaeozoic succession. It consists of conglomerate, quartzite, feldspathic sandstone, rare dolomitic levels and interbedded mudstones (Garciá-López and Bastida, 2002). Its thickness increases from ~600 m in the south near the area of Barrios de Luna, to ~1500 m in the Narcea Valley towards the north (Rupke, 1965 in: Meer Mohr, 1969; Garciá-López and Bastida, 2002). Three members were

proposed by Aramburu *et al.* (1992) and Linan *et al.* (2002): The [1] lower member consists of sandstones, siltstones, shales and dolomites, with some conglomeratic intervals, especially at the base. Acritarchs suggest a Lower Cambrian (Cordubian) age (Garciá-López and Bastida, 2002). The [2] middle member contains coarse-grained sandstones, with conglomerates and rare shale horizons based on its ichnofossil content and lithostratigraphic context, a Lower Cambrian age was assigned by Crimes *et al.* (1977 in: Aramburu-Zabala Higuera and García Ramos, 1993) and Garciá-López and Bastida (2002). The [3] upper member, originally termed Barrios beds (Lotze, 1961 in: Álvaro *et al.,* 2003), is formed by interbedded sandstones, shales and dolomites, which have yielded mid Early Cambrian (Upper Ovetian) trilobites and acritarchs (Garciá-López and Bastida, 2002; Vidal *et al.,* 1999 in: Linan *et al.,* 2002). The Herreria Fm. was deposited in a transitional fluviatile-marine environment (Bosch, 1969), most likely a braided delta, where an alternation of littoral and shallow sublittoral environments developed into persistent sublittoral conditions (Álvaro *et al.,* 2003). The sediments were supplied from the east (Garciá-López and Bastida, 2002).

The Herreria Fm. is conformably overlain by the **Lancara Fm.** (Comte, 1937, 1959; Lotze, 1961 in: Martínez García, 1981; Álvaro *et al.,* 2003). The Lancara Fm. as described by Meer Mohr (1969); Aramburu-Zabala Higuera and García Ramos (1993); Linan *et al.* (2002), is a sucession of ~150 – 225 m of Cambrian (Acadian) dolomites, limestones and nodular red shales. The formation consists of two informal members: a [1] lower member, that consists of a persistent dolomite level, followed by a horizon of grey limestones and oolitic limestones including minor archeocyathan-build ups and trilobites, which are probably of Bilbilian age (Sdzuy, 1995 in: Linan *et al.,* 2002). Aramburu *et al.* (1992) and Álvaro *et al.* (2003) interpreted the environment of deposition as supralittoral–littoral in the western parts of the CZ and shallow sublittoral in its eastern parts. The [2] upper member (‘Griotte Mb.’) is formed by widespread limestone deposits overlain by nodular red limestones. Brachiopods, echinoderms, molluscs and porifera are abundant, suggesting a sublittoral environment of deposition. Deposition is assumed to have taken place on tectonically induced palaeohighs (Álvaro *et al.,* 2003). A diachronous boundary has been inferred for the ‘Griotte Mb.’ based on its trilobite record (Martínez García, 1981; Linan *et al.,* 2002). The lower dolomitic member of the Lancara Fm. represents in many cases the decollement horizon for most of the tectonic nappes of the CZ (Díaz Rodríguez, 1989).

The **Oville Fm.** (Comte, 1937; Meer Mohr, 1969; Martínez García, 1981) is a siliciclastic unit consisting of 80–800 m of mainly glauconitic sandstones and green shales. It exhibits many facies changes with the intercalation of some quartzitic beds towards the top. Three members, all with diachronous boundaries have been defined (Aramburu, 1989 in: Aramburu-Zabala Higuera and García Ramos, 1993; Garciá-López and Bastida, 2002; Linan *et al.,* 2002). The [1] Genestosa Mb. consists of green shales with abundant trilobites, brachiopods, gastropods, palynomorphs and echinoderms. The stratigraphic position for the base of the Genestosa Mb. ranges regionally from the upper Leonian to the upper Caesaraugustan (Garciá-López and Bastida, 2002), highlighting the diachronous nature of this stratigraphic boundary. The [2] Adrados Mb. consists of sandstones (frequently with glauconite) and shales/siltstones. The sandstones become more prominent towards the top of the Mb. Fombella (1978) reported an undiagnostic mid Cambrian to Tremadocian aged acritarch assemblage for the Adrados Mb. (Linan *et al.*, 2002). Aramburu (1989) suggested a more narrow stratigraphic range concluding that the Mb. comprises just parts of the mid Cambrian in age (Garciá-López and Bastida, 2002). Finally, the [3] La Barca Mb. contains sandstones, sometimes glauconitic, and grey-green shales. Ichnofossils like *Cruziana* and *Skolithos* are very abundant, together with isolated lingulid shell beds. According to Garciá-López and Bastida (2002) the prescence of *Cruziana barbata* and certain acritarch assemblages seem to indicate a mid Cambrian age for the entire La Barca Mb.

The **Barrios Fm.** (Comte, 1937; Martínez García, 1981) comprises ~80–1020 m of white quartz arenites. These quartz arenites form a widespread deposit that has been documented throughout western and central Europe. Within the literature concerning the geology of Iberia this distinctive quartz arenite has also been termed as the so called ‘Amorican Quartzite’. The Barrios Fm. contains sparce intercalated shale and conglomerate horizons and has been dated with the help of acritarch and ichnofossil assemblages to be of latest mid Cambrian to Early Ordovician (Tremadoc) in age (Garciá-López and Bastida, 2002; Aramburu *et al.,* 1992 in: Linan *et al.,* 2002). The lower parts of this quartzarenitic Fm. are interpreted to be the facies equivalent to the upper part of the Oville Fm. due to lateral facies change. Rocks of phreatomagmatic origin and volcanic pipes have been demonstrated to be intercalated and to cross-cut the quartzarenitic beds of the Barrios Fm. (Heinz *et al*., 1985). The increased magmatic activity documented by the aforementioned volcaniclastic beds is commonly regarded to be associated with the initial extensional tectonic regime, that finally leads to the opening of the Rheic Ocean (Aramburu-Zabala Higuera and García Ramos, 1993). A subdivision into three members has been proposed for the Barrios Fm.

(Aramburu-Zabala Higuera and García Ramos, 1993; Garciá-López and Bastida, 2002). The [1] La Matosa Mb. consists of a coarsening upward megasequence, ranging from thin-grained sandstones at the base, to pebbly coarse-grained sandstones at the top. It contains lingulid shell beds and trace fossil assemblages (*Cruziana* and *Skolithos*) (Martínez García, 1981; Aramburu-Zabala Higuera and García Ramos, 1993) and has been assigned a mid to Late Cambrian maybe even Tremadocian age (Garciá-López and Bastida, 2002). Albani *et al.* (2006) was able to isolate a well preserved Late Cambrian acritarch assemblage from the La Matosa Mb., hence corroborating earlier age assignments.

The [2] Ligueria Mb. is almost exclusively confined to the Nappes Province and consists of siliceous pebble-supported conglomerates and interbedded sandstones and shales. It is considered to be of Tremadocian age (Garciá-López and Bastida, 2002). Finally, the [3] Tanes Mb. expresses similar lithologies to the La Matosa Mb., yet following a fining upwards megasequence. In the upper parts of this member, there are common units of interbedded shales and sandstones, that have been reported to contain lingulid brachiopods of Arenigian age (Garciá-López and Bastida, 2002). This biostratigraphic age consignment was recently coorborated by a U-Pb radiometric age determination performed on zircon crystals from a bentonite layer of the Tanes Mb. U-Pb analysis of single zircon grains yielded concordant and overlapping error ellipsis with a pooled concordia age of 477.47 +/- 0.93 Ma (Gutiérrez-Alonso *et al*., 2007).

According to Linan *et al.* (2002), the Barrios Fm. was deposited within a tidal to supratidal environment. A nowadays unexposed area towards the east is assumed to be the source for the sediments of the Barrios Fm. This assumption is based on the observation of a systematic and consistent decrease in grain-size from the east to the west, which in turn is used as an explanation for the observable lateral facies change between the Oville Fm. and the Barrios Fm. (Garciá-López and Bastida, 2002).

2.1.2.3 Ordovician

As a consequence of the lateral facies change between the Oville Fm. and the Barrios Fm. (described above), the Cambro-Ordovician boundary (see **Figure 2.3**) is interpreted to be either within the uppermost parts of the Oville Fm. or above a hiatus within the Barrios Fm. (Gutierrez-Marco *et al.,* 2002).

Whereas the Barrios Fm. and Oville Fm. are developed in a relatively uniform way, all the overlying Middle Ordovician to lowermost Silurian strata exhibit significant facies changes and drastic regional changes of their overall thickness (Garciá-López and Bastida, 2002).

In most areas of the CZ younger Ordovician rocks do not exist, therefore the Barrios Fm. is directly overlain by Silurian to Lower Carboniferous rocks (Gutierrez-Marco *et al.,* 2002). However, two thin bands of post-Arenigian rocks are recorded. Firstly, a band close to the Narcea antiform (in the western part of the 'fold and nappes region') which includes the **Luarca** and **Castro** formations and secondly a band that can be found in the Laviana-Sueve thrust sheet of the 'nappe region', east of the Central Coal Basin (see **Figure 2.2**) known as the **Sueve Fm.** (Garciá-López and Bastida 2002). Between the eastern and the western band only the thin, condensed succession of the so called 'Getino Beds' occurs.

Thicker developed stratigraphic equivalents to the Getino Beds can be found and will be briefly described and discussed in the following text.

Within the western 'fold and nappes region' of the West Asturian Leonese Zone (WALZ) the Barrios Fm. is directly overlain by the mid Ordovician Luarca Fm. with a distinct and sharp contact. Having a maximum thickness of ~350 m, the Luarca Fm. was first described by Barrois (1882) and has been subsequently divided into two members (Aramburu-Zabala Higuera and García Ramos, 1993): The [1] Penas Mb. shows typically grey sandstones and interbedded black shales at its base, followed locally by a mafic sill overlain by lenticular ooidal ironstones. The black shale layers contain sulphides that are interpreted to indicate an euxinic depositional environment (Rodrigues Sastre and Gonzalez Menendez, 2011). Lingulid brachiopods and graptolites indicate an age ranging from Arenig to Llanvirn (Garciá-López and Bastida, 2002; Gutierrez-Marco *et al.,* 2002). The [2] Vidrias Mb. is composed of dominant, siderite and carbonate nodule containing black shales, thin dolomitic intercalations, and shell beds composed mainly of brachiopods (Garciá-López and Bastida, 2002; Gutierrez-Marco *et al.,* 2002). At Portilla de Luna (3 km south east of

Barrios de Luna, see **Figure 2.2** for location), a 14 m thick layer of fossil-rich, grey limestones indicating a Hirnantian (Ashgill) age, have been described as directly overlaying the Luarca Fm. (Garciá-López and Bastida, 2002). Recently, Gutierrez-Marco *et al.* (2002) interpreted these successions as the deposits of a terrigenous marine shelf. Evaluating the low diversity benthic cold water fauna, that has been found within these sequences, Rodrigues Sastre and Gonzalez Menendez (2011) concluded, that these deposits were indicative of a high palaeolatitude setting.

The Luarca Fm. in turn is overlain by the younger Castro Fm. (Truyols *et al.,* 1996 in; Gutierrez-Marco *et al.,* 2002). It varies between ~200-450 m in thickness. The Castro Fm. has been assigned three members: a Lower, a Middle and the so called Viodo Mb. The Lower Mb. consists of volcaniclastic rocks, sandstones, shales and a minor amount of conglomeratic intercalations. It contains a diverse fauna, that was used to determine a late Dobrotivian (see **Figure 2.3B**) age (Truyols *et al.,* 1996). The Middle Mb. comprises intrusive basalts, volcanic breccias, volcanogenic shales, sandstones, and a subordinate amount of quartzitic layers that have not yielded any fossils yet. Nonetheless, a late Ordovician age has been assumed for this succession (Gutierrez-Marco *et al.,* 2002). Finally, the Viodo Mb. is composed of two calcareous units that are separated by an alternation of sandstones and volcanogenic shales. Its fossil assemblages indicate a earliest Silurian (Rhuddanian to lower Aeronian) age (Aramburu-Zabala Higuera and García Ramos, 1993). The Castro Fm. in its entirety is interpreted to have been deposited in a shallow marine environment, above the storm wave base (Sarmiento *et al.,* 1994; Villas and Cocks, 1996 in: Gutierrez-Marco *et al.,* 2002; Gutiérrez-Marco and Rábano, 1998; Garciá-López and Bastida, 2002).

Within the eastern Laviana-Sueve thrust sheet (east of the Central Coal Basin), the second band of post-Arenigian rocks occurs. The Sueve Fm. is considered to be the stratigraphic equivalent to the Luarca Fm. in the west (Garciá-López and Bastida, 2002). It directly overlies the Barrios Fm., again with a sharp contact. The Sueve Fm. consists of three members: [1] the Cerracin Mb., [2] the Bayo Mb. and at the top the [3] Cofino Mb. The Cerracin Mb. shows near its base typically a lenticular ooidal ironstone level, that is overlain by highly fossiliferous black shales. Graptolites from within these black shale horizons indicate an Upper Oretanian (compare **Figure 2.3B**) age (Garciá-López and Bastida, 2002; Gutierrez-Marco *et al.,* 2002). The Bayo Mb. consists of interbedded sandstones and dark-grey shales. A distinct faunal assemblage that can be found at the middle of this member marks the Oretanian-Dobrotivian boundary (Gutierrez-Marco *et al.,* 2002). Lastly, lenticular ooidial ironstones are to be found at the base of the Cofino Mb.. These ironstones are

followed by prominent, fossil rich black shales layers that indicate a Dobrotivian age (Garciá-López and Bastida, 2002; Gutierrez-Marco *et al.,* 2002).

The dark shales of the Sueve and Luarca formations suggest, a slightly deeper environmental setting for deposition, and most probably more distal shelf areas (according to Gutierrez-Marco *et al.,* (2002) this interpretation is also supported by the wide spread prescence of faunal immigrants like brachiopods, graptolites and ostracods). The facies development and faunal changes across Iberia within the Lower and Middle Ordovician suggest an overall SE to NNW deepening trend (Gutierrez-Marco *et al.,* 2002). The Luarca and Sueve Formations were deposited in a storm dominated shallow epeiric sea (Aramburu, 1989; Aramburu-Zabala Higuera and García Ramos, 1993; Gutiérrez-Marco *et al.,* 1996a; Garciá-López and Bastida, 2002). A few horizons within the succession may represent shallower sublittoral environments above the storm wave base, especially the lenticular ooidal ironstone beds.

- ***The Cambro-Ordovician succession: palaeoenvironmental and geotectonic discussion***

The Rheic Ocean (compare **Figures 2.4** and **2.5**) started opening from the late mid or early Late Cambrian onwards as a result of the Avalonian microplate separating from the northern margin of Gondwana (Dias and Ribeiro, 1995; Gutiérrez-Alonso *et al.,* 2003). According to Gutiérrez-Alonso *et al.* (2003) and Nance *et al.,* (2010), this ocean broadened during the Ordovician at the expense of the Iapetus Ocean in the north and attained its greatest width of ~4000 km by the Silurian with an approximate average spreading rate between 8-10 cm/yr. The tectonic processes leading to the opening of the Rheic Ocean resulted in a change of the overall geotectonic regime affecting the entire northern rim of Gondwana. Whereas the lower to lower mid Cambrian successions were deposited within an compressional, active continental margin setting, caused by the southward directed subduction of Iapetus, the mid Cambrian to Ordovician aged strata were laid down in an extensional, rift related environment. This extensional, rift related setting led to crustal thinning and further fragmentation of the northern Gondwanan margin accompanied by extensive bi-modal, rift related magmatism, not just only affecting Iberia but also for example large parts of present day France and Sardinia (Weil *et al.,* 2001; Crowley *et al.,* 2002; Gutiérrez-Alonso *et al.,* 2008; Linnemann *et al.,* 2008; von Raumer and Stampfli, 2008; Keller *et al.,* 2008; Ballèvre *et al.,* 2009;

Díez Fernández and Martínez Catalán, 2009; Martínez Catalán *et al.,* 2009b; Romer and Hahne, 2010; Barba *et al.,* 2011).

During the upper Ordovician Gondwana experienced a large scale temperature drop leading to end Ordovician Hirnantian glaciation (e.g. Le Heron *et al.,* 2008). The formation of the vast ice sheets led to a dramatic sea-level drop affecting the northern regions of Gondwana. The maximum extent of the Hirnantian ice sheets is still a matter of ongoing, controversial discussions. Glacial deposits (diamictites) within the CZ have been described by Bernárdez Rodríguez *et al.* (2006) and Gutierrez-Marco *et al.* (2010). These authors infer, that the palaeovalleys, which have been interpreted as subglacial tunnel valleys by Le Heron *et al.* (2004), and their infill may in fact be related to the Hirnantian glaciation. This seems to be corroborated by the finding of typical Hirnantian fauna within these deposits (Gutierrez-Marco *et al.,* 2010). The diamictites are considered to be either related to an ice sheet lobe or to be part of a peri-Gondwanan satellite ice cap (Gutierrez-Marco *et al.,* 2010). The glacial incisions that truncate Cambro-Ordovician strata (e.g. the Barrios Fm.) are 200−250 m deep and 1−3 km wide (Gutierrez-Marco *et al.,* 2010). The Hirnantian glacial deposits were deposited in a brief, ~500,000 year time-window (Gutierrez-Marco *et al.,* 2002; Le Heron *et al.,* 2005) and are capped in some cases by the so called Luna quartzite, a unit that pinches out laterally (compare **Figure 2.3**). Above the Luna quartzite or directly above the diamictites, the Silurian Formigoso Fm. normally starts with the aforementioned, glauconitic sandstones of the Getino Beds. It is important to note, that the glaciomarine diamictites mentioned above do not exist for most regions of the CZ.

The drastic variations in thickness recorded for the Barrios Fm. are most likely the combined outcome of larger scale tectonic processes and palaeoclimatological changes, that affected Iberia during the time of deposition and immediately afterwards. The rift related extensional tectonic led via the initiation of horst and graben structures to the formation of a significant palaeotopographical relief. Horst areas were subjected to erosion and partly stratigraphic condensation, grabens provided at the same time increased volumes of accommodation space. The Hirnantian glaciation caused a dramatic drop in sea-level and hence the erosional formation of palaeovalleys (Brenchley *et al.,* 2003 in: Keller *et al.,* 2008), therefore diminishing the local thickness of the Barrios Fm. A prominent pre-diamictite hiatus is observed within the Barrios Fm. throughout the entire CZ. This hiatus is regarded to have been produced by the increased rate of erosion caused by the sea-level drop prior to the deposition of the Hirnantian diamictites (Gutiérrez-Marco and Rábano, 1998;

Gutierrez-Marco *et al.,* 2002). The palaeotopographical relief that resulted from the extensional tectonics and the following glaciogenic processes contributed significantly towards the development of the Silurian black shales of the Formigoso Fm.

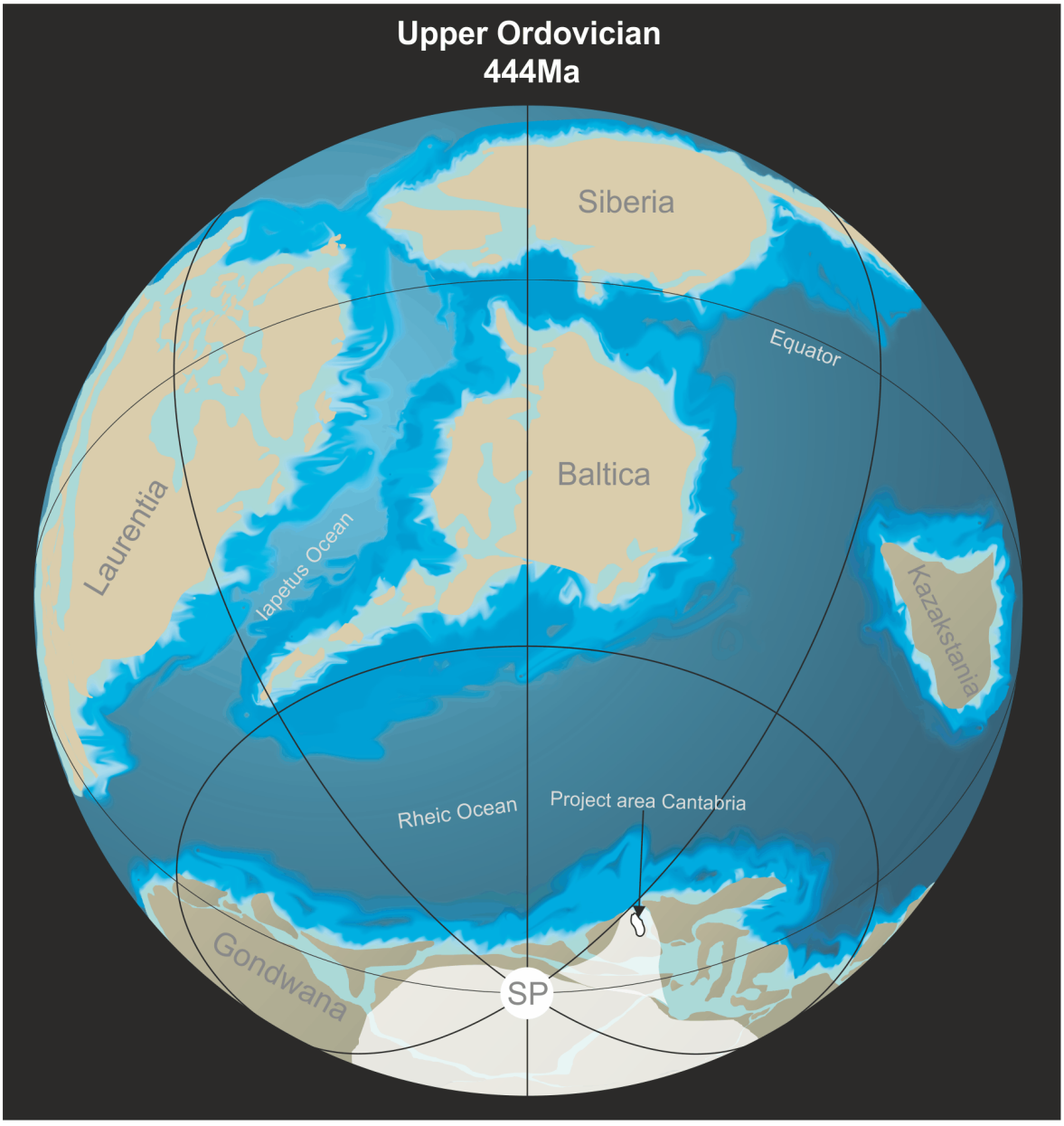

Figure 2.4: Palaeogeographical reconstruction for the time of the Upper Ordovician (440Ma), illustrating the continent-continent configuration and the extent of the Late Ordovician 'Hirnantian' ice mass, plate reconstructions. Note the Hirnantian Ice mass has extended as far as Iberia. The position of the project area 'Cantabria' is marked, SP = South Pole. Note that during the Late Ordovician the South Pole is positioned over northern Africa. Modified after Scotese *et al.* (1999); Monod *et al.* (2003); Le Heron *et al.* (2004); Le Heron *et al.,* (2005); Bernárdez Rodríguez *et al.* (2006); Gutiérrez-Marco *et al.* (2010).

2.1.2.4 Silurian

The Silurian in most regions of the southern CZ (Correcillas unit, see **Figure 2.2**) is represented by black shales belonging to the Lower Silurian Formigoso Fm. In most cases the Formigoso Fm. overlies directly the Getino Beds (see above). The other Middle to Upper Ordovician formations (Luarca Fm., Castro Fm. and Sueve Fm.), which were previously mentioned and discussed, are not developed within the southern CZ. In areas where the Getino Beds have not been deposited, a significant hiatus spanning from the Arenigian (top Barrios Fm.) to the Areonian/Telychian boundary (base of the Formigoso Fm.) exists. The Formigoso Fm. is conformably overlain by the San Pedro Fm. As the Silurian of the CZ forms the most fundamental part of the present study, it will be reviewed and discussed in greater detail within a separate chapter.

2.1.2.5 Devonian

The base of the Devionian is marked by the ferrigenous beds of the uppermost parts of the San Pedro Fm. (which will be discussed later on in more detail). These beds are overlain conformably by the sediments of the La Vid Gp. (Comte, 1936; Gutiérrez-Marco and Rábano, 1998; Suárez de Centi *et al.,* 1989; Garcia-Alcalde *et al.,* 2002a), which is sub-divded into four members: the [1] Felmin Mb. consists of 150-200 m dolostones, dolomitized, bioclastic, stromatolitic limestones and thick sandstone intercalations that are considered to be Lochkovian-earliest Emsian in age. The [2] La Pedrosa Mb. compises ~130-140 m fossiliferous grey argillaceous limestones with intercalations of dark shales. Parts of the highly fossiliferous beds have been interpreted to be storm deposits and an Emsian age has been determined. The [3] Valporquero Mb., considered to be late Emsian in age, consists of olive green shales with limestone lenses and finally the [4] Coladilla Mb. contains ~200 m of red fossiliferous limestones and marlstones interbedded with shales. Biostroms and patch reef complexes are frequent (Garcia-Alcalde *et al.,* 2002a). Overall the carbonate sedimentological patterns that can be observed within the deposits of the La Vid Gp. points towards a sedimentation within a warm and tropical environmental setting. The La Vid Gp. is conformably overlain by the Santa Lucia Fm. The Santa Lucia Fm. comprises ~250-260 m thick argillaceous limestones which are sandwiched between heavily bioturbated shales at the base and at the top, a Late Emsian-Eifelian age was assigned to this Fm. (Hofmann and Keller, 2006). The following Huergas Fm. (early Eifelian-Givetian in age) is highly variable with regards to its thickness (50-500 m). It marks a change to siliciclastic sedimentation series that are characterised by

ferruginous red sandstones and euxinic nodular black shales (Brouwer, 1967). A return to a calcareous, reefal succession is marked by the overlying Portilla Fm. which consists of 100-200 m of thick fossiliferous limestones of Givetian-earlier Frasnian age (Mohanti, 1972; Keller, 1997).

The increased siliciclastic input characterising the Late Devonian sucessions is regarded to be the result of enhanced tectonic uplift. The Frasnian-age Nocedo Fm. (Comte, 1936) overlies conformably the Portilla Fm. that was discussed above it is constituted of ~300 m of thick calcareous sandstones with interbedded limestone and shale horizons. The Fueyo Fm. (Comte, 1936) that is of upper Frasnian age, comprises ~130 m nodular black shales with pelagic faunas. The following Famennian aged Ermita Fm. (Comte, 1936) is up to 60 m in thickness and heralds cross-bedded sandstones, siltstones with thin shale and sandy limestone lenses (Raven, 1983; Garcia-Alcalde *et al.,* 2002a).

2.1.2.6 Carboniferous

The Baleas Fm. ~5-10 m thick conformably overlies the Devonian sediments in the west of the CZ. It is comprised of skeletal grainstones to wackstones and is considered to be late Famennian-Tournaisian in age (Higgins, 1971). The Vegamian Fm. is the stratigraphic equivalent towards the eastern parts of the CZ and comprises there a 10-60 m thick sucession of black shales and mudstones. Both formations were deposited in a shallow marine setting (the Vegamian Fm., slightly deeper, most likely on a shelf edge) following the early Carbonifeous transgression over the Devonian continental margin. The Alba Fm. or Genicera Fm. (Higgins, 1971; Maas, 1974 in: Martínez García, 1981) was deposited during the time of maximum sea-level high stand (Visean) and comprises ~20-30 m condensed red nodular limestones, that are considered to have been deposited within a well oxygenated pelagic platform setting (Colmenero *et al.* 2002). This Carboniferous sequence records the transformation of the passive continental margin into an active continental margin setting, associated with the onset of early Variscan deformation (Dias and Ribeiro, 1995; Colmenero *et al.,* 2002; Keller *et al.,* 2008).

During the Serpukhovian (Namurian A), the sedimentary basin hosted a thick slightly marine devoloped carbonate platform succession. This sucession comprises the Barcaliente and Olleros formations (Maas, 1974 in: Martínez García, 1981; Bahamonde *et al.,* 1997). A Variscan foredeep was located towards the west documented by ~300-350 m of thinly bedded grey limestones and

mudstones of the Barcaliente Fm. in the west and predominantly turbidite deposition of the Olleros Fm. towards the south (Colmenero *et al.,* 2002).

The Valdeteja Fm. (Maas, 1974 in: Martínez García, 1981) comprise up to 1000 m thick carbonates, these carbonates are the stratigraphic equivalent to parts of the Pinos and La Majua Mb's of the San Emiliano Fm. (Bowman, 1982). The drastic change in sedimentation patterns observable over relatively short distances is regarded to be the product of extensive facies differentiation in front of the developing Variscan Orogen (Colmenero *et al.,* 2002). The San Emiliano Fm. is subdivided into three members: the siliclclastic sediments of the [1] Pinos Mb. are overlain by the [2] La Majua Mb. that consists of predominantly shale and sandstone sucession with minor intercalations of coal seams and shallow marine limestone bands. The faunal content of the limestone bands together with plant fossils from the coal seams demonstrate a late Baskirian to early Moscovian age (Bowman, 1982). The overall transgressive trend is documented by the deltaic sediments of the [3] Candemuela Mb. Siliciclastic sedimentation continued into the late Westphalian (Langsettian) when the basin was finally filled by terrigenous sediments, terminating the carbonate platform deposition within the CZ (Colmenero *et al.,* 2002).

2.1.3 The Silurian of the Cantabrian Zone: a review

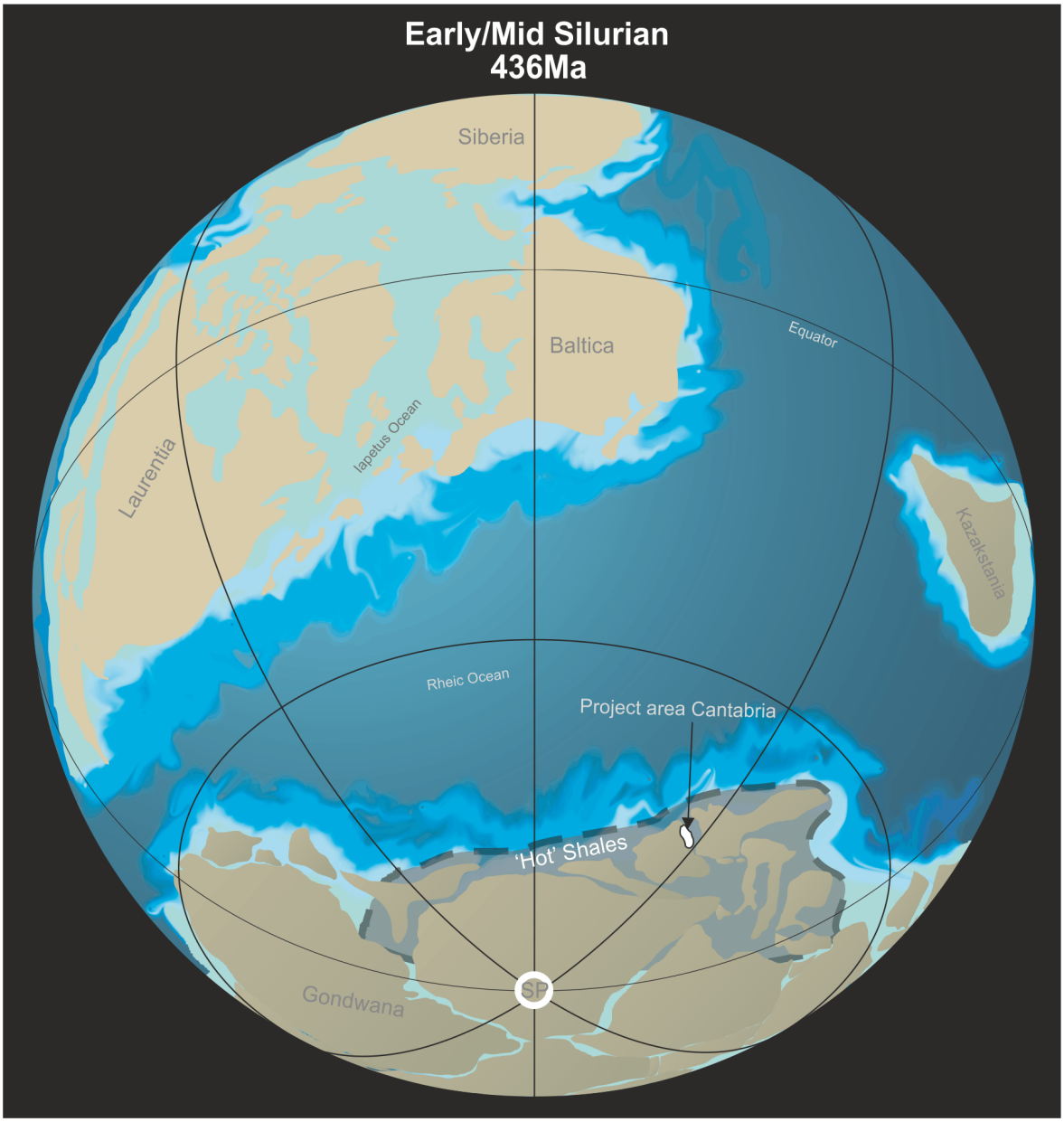

Figure 2.5: Showing inferred 'hot' shale deposition across the northern rim of Gondwana during the lower/middle Silurian. The project area 'Cantabria', northern Spain is highlighted, plate reconstructions modified after Scotese *et al.* (1999) and Lüning *et al.* (2000). SP donating the South Pole.

The Silurian rocks of the Iberian region are mainly terrigenous sediments dominated by pelagic faunas as in many other regions of northern Gondwana e.g. the 'hot' shales of northern Africa (Lüning *et al.,* 2000). They occur in all regions except for the South Portuguese Zone that most likely belonged to Avalonia (Gutiérrez-Marco and Rábano, 1998; Robardet and Gutierrez-Marco, 2002). The most characteristic Silurian rocks in the Cantabrian Zone belong to the graptolitic black shales of the Formigoso Fm.

After the Late Ordovician glaciation (described in the previous section) the early Silurian sea-level fluctuated greatly, most likely related to the waxing and waning of ice-sheets in NW Gondwana (Sachanski *et al.,* 2010), which in turn is considered to be related to orbital forcing (Sutcliffe *et al.,* 2000 in; Le Heron *et al.,* 2005; Le Heron *et al.,* 2008; Le Heron *et al.,* 2009; Armstrong *et al.,* 2009). Zhang *et al.* (2006, with previous references herein), state that the Latest Ordovician-Early Silurian sea level was not only affected by the melting of the Hirnantian ice sheet, but also by three short lived Early Silurian glacial eposides (early Aeronian, latest Aeronian to early Telychian, and latest Telychian to earliest Wenlock). The relative sea-level low stand of the Hirnantian was followed by a major eustatic Silurian transgression (Rubino, 2003). The onset of this relative sea-level rise (see **Figure 2.7**) is dated to be within the late *crispus*–early *griestoniensis* Biozone and it reached its maximum in the Telychian *Spiralis* graptolite Biozone (Sachanski *et al.,* 2010). As a consequence large parts of the continental shelf areas of Gondwana were invaded by marine waters (Paris and Robardet, 1990; Tait *et al.,* 1997). Anoxic conditions prevailed over North Gondwana most probably as a result of the stratification of the water column caused by fresh water capping and subsequent shut down of the oceanic circulation as a result of the melting Hirnantian ice masses (Paris and Robardet, 1990). These environemtal conditions led to the deposition of predominantly fine grained siliciclastic sediments (black shale sequence) during the Lower Silurian within the CZ.

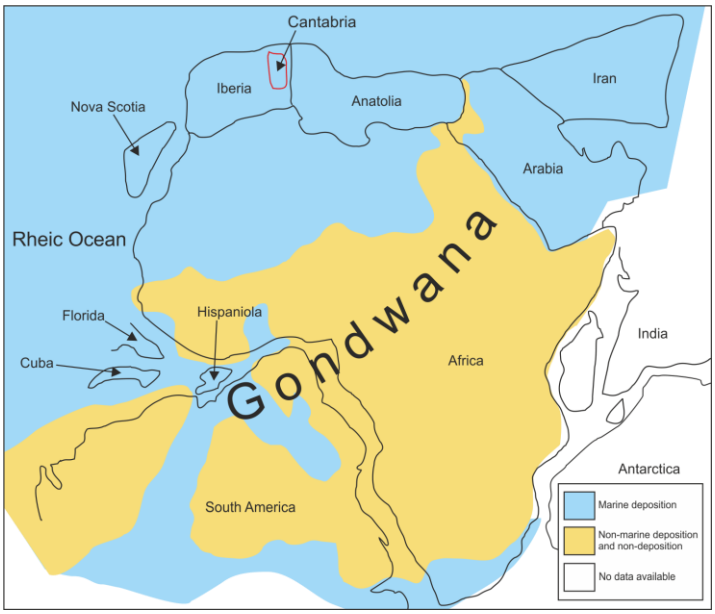

Figure 2.6: Illustrating the land sea relationship, large parts of the Gondwanan shelf are flooded by the sea enabling the deposition of marine developed sediments. The position of the project area 'Cantabria' is highlighted. Modified after Lüning *et al.* (2000).

The base of the black shale sequence is diachronous across the Iberian Peninsula. Black shale deposition began during the Rhuddanian, as seen within the OMZ, Catalonian Coastal Ranges, restricted areas of the WALZ and in the northernmost CIZ. They can also be found across large parts of northern Africa (Lüning *et al.,* 2000). Yet in most regions of the Iberian Peninsula (for example, Penalba and Mondonedo domains of the WALZ, in the Iberian Cordillera and in most areas of the CIZ) the black shale deposition was delayed until the Aeronian and, more commonly, Telychian times, as seen within the CZ (Robardet and Gutierrez-Marco, 2002).

Rapid deepening affected the whole Cantabrian area, the sedimentation of the lowermost Silurian Formigoso Fm. commenced above a transgressive surface (see **Figure 2.6**). Overall the Formigoso Fm. exhibits a shallowing and coarsening upward succession towards the overlying San Pedro Fm. Most likely the Formgoso Fm. has been deposited during repeated minor transgressive-regressive cycles (this study).

The thickness changes in the Silurian Formigoso Fm. are drastic ranging from <50 m in the southern areas of the Cantabrian Zone to >400 m in the Northern Cantabria regions. The lateral variation in thickness of the Silurian Formigoso Fm. is controlled by a combination of the extensional tectonics related to the opening and widening of the Rheic Ocean and the Hirnantian glacial processes as previously mentioned. Various models for the deposition of the Silurian black shales of the Cantabrian region and the northern Gondwanan region as a whole are discussed in the following chapter.

Within the CZ, Silurian rocks are present both in the 'folds and nappes region' and the Pisuerga-Carrion unit (see **Figure 2.2**) of the Palentian region in the SE (Gutiérrez-Marco and Rábano, 1998; Robardet and Gutierrez-Marco, 2002). The thickest and most complete Silurian succession is seen within the 'Fold and Nappe Province'. The approximatly 400 m thick succession is composed in its lower part by the shales and sandstones of the Formigoso Fm. and in its upper part by the coaser clastic siliciclastic of the lower San Pedro Fm. (Garciá-López and Bastida, 2002). The best preserved and most complete Silurian sequences can be found in the southern CZ, within the Correcillas Unit (compare **Figure 2.2(B)**; area highlighted).

The questionably earliest Silurian rocks occur at the Cabo Penas area within the 'folds and nappes region'. The upper parts of the El Castro Fm. (Viodo Mb., as previously mentioned) have yielded a

fossil assemblage that probably indicate a pre-Telychian age (Robardet and Gutierrez-Marco, 2002).

Early Silurian conodonts (?Rhuddanian) were discovered on the southern slope of the Cantabrian Mountains, at Getino. The conodonts occur in a band of dolomitic limestone at the top of a siliclastic sucession that has been previously described as the so called 'Transitional Beds' (Bosch, 1969; García-Ramos *et al.,* 1989). Within the more recent literature these 'Transtitional Beds' have also been described under the name of the 'Getino Beds' and have some times even been assigned formation status dispite their relatively thin development (García-Ramos *et al.,* 1989; Aramburu-Zabala Higuera and García Ramos, 1993; Sarmiento *et al.,* 1994). In most areas of the southern Correcillas unit, these 'Getino Beds' overlie the Cambro-Ordovician Barrios Fm. and precede the lower Silurian Formigoso Fm. The Ordovician Luarca, Sueve and El Castro Formations are not developed. The Getino Beds have been described as heterolithic, tidal deposits, consisting of a few meters of alternating sandstones, siltstones, mudstones and carbonates (predominantly dolomites and siderites). All beds are highly bioturbated and show frequent enrichments with glauconite and Fe-oxides. Their thickness and lithologies are extremely variable (Garciá-López and Bastida 2002). It has been mentioned, that the transiton from underlying Barrios Fm. is normally gradual (Sarmiento *et al.,* 1994). However, it was observed during the fieldwork leading to the present study that the contact is always sharp and discrete.

The Getino Beds occur as a condensed succession, the age constraints remain uncertain due to the lack of fossils (other than in the top of the succession). Based on their lithostratigraphic relationship and positioning between the Barrios and overlying Formigoso Fm. a most likely age ranging from the Dapingian up to the lower Aeronian may be inferred.

Previously these beds have been included within the lower part of the overlying Formigoso Fm. (Kegel, 1929; Comte, 1959; Evers, 1967 in: Sarmiento *et al.,* 1994). Biostratrigraphic evidence supporting this stratigraphic assumption was provided by the finding of fossils assemblages from near the top of the succession at two localities (Pontido and Getino). These fossil assemblages included graptolites (*Pristiograptus* sp., *Metaclimacograptus* aff. *hughesi*), trilobites (*Leonaspis* sp., *Calymene* sp.), bivalves, crinoids and conodonts (*Panderodus unicostatus, Walliserodus sancticlairi*) and is indicative of a late Rhuddanian to early Aeronian age (Garciá-López and Bastida, 2002). Furthermore Sarmiento *et al.* (1994), compared a small number of conodonts from the upper parts of the Getino Beds to the fauna that was previously published from the Viodo Mb.

of the Castro Fm., concluding that the top of the Getino beds could be tentatively assigned to either the *A. petila* Zone or the *A. fluegeli* Zone, confirming the late Rhuddanian to early Aeronian age (see **Figure 2.7** 'biostratigraphy'). Based on the degree and development of the bioturbation, the fossil content and the presence of glauconite it is assumed that the Getino Beds were at least partly deposited within a shallow marine environment (Garciá-López and Bastida, 2002).

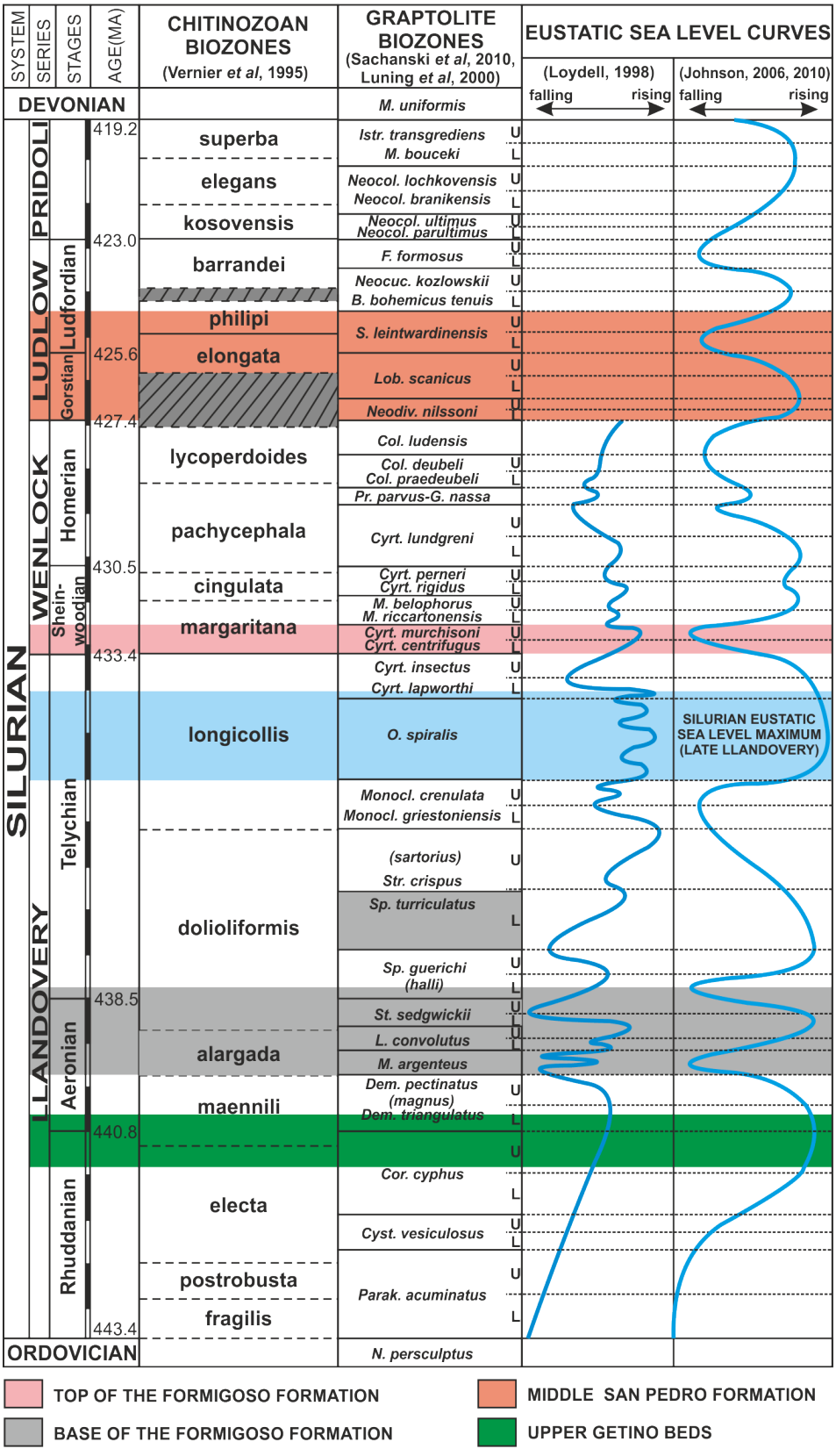

Figure 2.7: Biostratigraphy of the Silurian formations of Cantabria. Highlighted by colour are the stratigraphic sections for which reliable biostraqtigraphic dating are available; Biostratigraphy compiled after Sachanski *et al.* (2010); Verniers *et al.* (1995); Lüning *et al.* (2000); Gutierrez-Marco and Štorch (1998). The sea-level curves are compiled after Loydell (1998); Johnson (2006); Johnson (2010).

The Formigoso Fm. (Kegel, 1929; Comte, 1959) consists of 100-300 m of black/grey siltstones and shales with an increasing number of sandstone intercalations towards the top of the formation. The

sandstones typically show a large amount of bioturbation, ripple marks and hummocky cross-stratifications (Suárez de Centi *et al.,* 1989; Robardet and Gutierrez-Marco, 2002). The Formigoso Fm. can be found overlying the Castro Fm. in the Cabo Penas area (northern coast), yet in most regions of the Fold and Nappe Province (particularly the southern 'Correcillas Unit' (compare **Figure 2.2**) it is seen overlying the basal Silurian rocks (Getino Beds) or the Floian aged Barrios Fm. with a paraconformity or disconformity (Comte, 1959 in: Schneider *et al.,* 2004; Rupke, 1965; Garciá-López and Bastida, 2002). Kegel (1929) distinguished two members: the [1] Pizarras del Bernesga Mb. consists of graptolite rich black shales from which graptolites *M. convolutus* and *M. turriculatus* indicate an age of late mid Aeronian to early Telychian (Comte, 1959; Truyols *et al.,* 1974; Truyols and Julivert, 1983 in: Sarmiento *et al.,* 1994; Paris *et al.,* 1995; Gutiérrez-Marco and Rábano, 1998; Garciá-López and Bastida, 2002). The age constraints for the lower Bernesga Mb. were confirmed by organic walled microfossils, mainly chitinozoans (Cramer and Diez, 1978).

The [2] Capas de Villasimpliz Mb. is characterised by the intercalation of silt and sandstones the sandstones become more prominent towards the top of the Mb. as previously mentioned. Fossils are less abundant within this upper member, yet it has yielded graptolites (*Monoclimacis* cf. *vomerina, Monograptus priodon*), brachiopods and palynomorphs suggesting a Late Llandovery to Early Wenlock age (Upper Telychian boundary or Lower Sheinwoodian *centrifuges-murchisoni* Biozone (Schweineberg, 1987; Aramburu *et al.,* 1992 in: Gutiérrez-Marco and Rábano, 1998; Garciá-López and Bastida, 2002).

The Bernesga Mb. was deposited in open marine to off-shore conditions within a shallow epeiric sea with little circulation and a lack of oxygen (Evers, 1967; Suarez de Centi, 1988 in: Garciá-López and Bastida, 2002; García-Ramos *et al.,* 1989). The shallowing upward trend throughout the Formigoso Fm. is documented by the increased amount of coarser siliciclastic intercalations within the overlying Villasimpliz Mb. Many of these intercalations have been previously interpreted to be tempestites, hence indicating deposition above the storm wave base (Suárez de Centi *et al.,* 1989; Barba and Fernández, 1991 in: Veselovsky, 2004; Robardet and Gutierrez-marco, 2002). The low abundance of graptolites within the Villasimpliz Mb. and the following San Pedro Fm. is probably due to environmental conditions (change in salinity) and not post depositional destruction, as organic walled microfossils (chitinozoans) have been found within these rocks (Robardet and Gutierrez-Marco, 2002).

The Furada-San Pedro Fm. is present in all the Silurian sections of the Fold and Nappes Province. The formation was originally described from two main areas, the so called 'Ferruginous Sandstones of Furada' (Barrois, 1882) from the northern flank of the Cantabrian Mountains and the San Pedro Fm. (Comte, 1937) from the south (Richardson *et al.,* 2001). The contact with the Formigoso Fm. has been described as sharp and erosive in the areas closer to the Central Coal Basin and to be transitional in the area around the Narcea Antiform. Its thickness ranges from 5–250 m (Garciá-López and Bastida, 2002) and consists of grey to reddish ferruginous sandstones with shaley intercalations, thin oolitic ironstone beds and in the upper parts some sandy limestone lenses. The thickness increases from the Central Coal Basin to the Narcea Antiform (Bosch, 1969; in: Garciá-López and Bastida, 2002). The San Pedro Fm. has been sub-divided into three informal members:

The [1] Lower Mb., consists of red ferruginous, coarse-grained sandstones, sometimes oolitic, that show trough cross-stratification. At some localities conglomeratic beds with phosphatic, sideritic and silty clasts as well as intraclasts can be observed. Some of these clasts have been described to be of volcanic origin (Bosch, 1969; Suarez de Centi, 1988 in: Richardson *et al.,* 2001). Locally late Wenlockian palynomorphs have been described from the lowermost part of the lowermost member of the The San Pedro Fm. (Richardson *et al.,* 2001).

The [2] Middle Member is characterised by medium to fine grained sandstones with current and wave ripples with grey to green intensively bioturbated mudstones and siltstones horizons (Garciá-López and Bastida 2002). Ludlow and Pridoli brachiopods (*Orbiculoidea striata*, '*Spirifer' Vulcani,* Comte, 1959; Poll, 1970 in: Garciá-López and Bastida, 2002; García-Ramos *et al.,* 1989) have been described from its middle part (Gutiérrez-Marco and Rábano, 1998).

The [3] Upper Member, contains fine-grained quartzitic sandstones either white or light grey with cross-stratification, interbedded with dark to black shales. Around 50 m from the top of the formation, graptolites from the *nilssoni* and *scanicus* zones and probably the *leintwardinensis* zone (*Saetograptus fritschi fritschi, S. chimaera saandweyi*) have been described, indicating a Gorstian and lowermost Ludfordian age. The upper member has also yielded early Devonian (Lochkovian) conodonts, trilobites (*Acastella tiro, Acastella heberti*), brachiopods (*Platyorthis verneuili, Mesodouvillina triculta*, *Howellella mercuri, Platyorthis* ex gr. *monnieri*), molluscs, bryozoans, echinoderms, conulariids, acritarchs and chitinozoans (Truyols *et al.,* 1974; Truyols *et al.,* 1990; Aramburu *et al.,* 1992 in: Robardet and Gutierrez-marco, 2002; Garciá-López and Bastida, 2002).

The Silurian–Devonian boundary is therefore positioned within the upper member of the San Pedro Fm., and indeed, most studies suggest that the boundary lies between ~13-15 m below the top (Suárez de Centi *et al.,* 1989; Richardson *et al.,* 2001; Robardet and Gutierrez-Marco, 2002).

The deposition of the San Pedro Fm. took place in a shallow marine environment (littoral to very shallow sublittoral), dominanted by the supply of coarser clastic detritus (Garciá-López and Bastida, 2002). A transgressive-regressive cycle is suggested, with the middle member representing the deepest conditions (Richardson *et al.,* 2001). Grain size is seen to decrease from 'an emerged land area' located in the core of the Asturian Arc in the east towards the west. Most of the iron in the formation is derived from subarial weathering of basic volcanic rocks (Garciá-López and Bastida, 2002). The transition to the overlying formation (Raneces or La Vid Group) is gradual and characterised by an increase in dolomitic cement within the sandstones. González (1983) determined, that the nature of this boundary is diachronous, younging towards the Narcea Antiform in the west (Garciá-López and Bastida, 2002).

- ***Palaeogeographic remarks on the Cantabrian Silurian***

The positioning of the Iberian Peninsula during the Silurian cannot be defined precisely with palaeomagnetic data (at Almaden, southern CIZ, basaltic lavas interbedded within Llandovery shales were remagnetised during the Late Devonian/Early Carboniferous (Perroud *et al.,* 1991; Parés and Van Der Voo, 1992 in: Robardet and Gutierrez-Marco, 2002). The San Pedro Fm. has been affected by pre-folding magnetisation during the Early Carboniferous (Van der Voo, 2005; Perroud and Bonhommet, 2007 in: Robardet and Gutierrez-Marco, 2002). Therefore the positioning the Iberian Penisula is based on the high or cold temperature latitudes of the latest Ordovician Hirnantian glacial deposits (~ 50^{o}S, Robardet and Gutierrez-marco, 2002; Paris and Robardet, 1990) and the warm temperate to subtropical latitudes of the Lower Devonian (limestones with local reefs) (~ 35^{o}S, Robardet and Gutierrez-marco, 2002). Gutiérrez-Marco and Rábano (1998) suggest that during the Early Silurian the positioning was 40-50^{o}S and 35-40^{o}S during the Late Silurian.

Chapter 3
Black shale genesis

Contents

3.1 Black shales: an introduction

3.1.1 Definitions and general remarks

Definition:
1) 'Black shale is a dark-coloured fine grained sedimentary rock, containing organic matter and silt- and clay-size mineral grains that accumulated together' (Swanson, 1961 in: Tourtelot, 1979)

2) 'Dark coloured, fine grained mudrocks having the sedimentological, palaeoecological and geochemical characteristics associated with deposition under oxygen-deficient or oxygen-free bottom waters' (Tyson, 1987 in: Wignall 1994).

Synonyms; organic-rich shale, bituminous shale and alum shale (Swanson, 1961; Wignall, 1994; Lavergren, 2005).

Black shales are dark-coloured mudrocks that comprise clay/silt and sand sized mineral grains, carbonate, chert and phosphate with varying ratios of organic matter. The black colour comes from two constituents: [1] the contained organic matter and [2] the finely disseminated pyrite (Schieber, 2003). They are fine grained strata usually deposited under oxygen-poor bottom waters which typically accumulate in deep-water, basinal locations (Wignall and Newton, 2001; Ketris and Yudovich, 2009). The oxygen poor (or anoxic) bottom waters are maintained either by a stratified water column that isolates the photic zone from the anoxic nutrient rich bottom waters (**Preservation Model**), or high productivity rates, where the flux of organic matter (OM) and in turn the demand for dissolved O_2 exceeds the supply (**Productivity Model**). These oxygen-poor conditions lead to the preservation of organic material (mostly planktonic algae) within the black shales. Most black shales are generated in marine environments and may have present day areal extents of thousands of square kilometres (Arthur and Sageman, 1994). The back shales or 'oil shales' may contain 'shale oil' which can be extracted by pyrolysis (Ketris and Yudovich, 2009). When black shales are subjected to pyrolysis the levels of organic content present and the type of organic material determine the type of hydrocarbons produced if any (Tourtelot, 1979; Tyson, 1995). The global 'oil shale' reserves exceed petroleum reserves (Ketris and Yudovich, 2009). Mineralogically, typical muds are characterised by approximately 40-60% clay minerals, 30% quartz and 10% each of feldspars and carbonate-iron oxide cements (Boggs, 2009 In: Sethi and Schieber, 1998; Cox and Lowe, 1995).

The majority of shales that meet the classification above tend to have a Total Organic Carbon (TOC) percentage of 1 or more; a few shales can reach in excess of 20% TOC as seen in the Lower Silurian transgressive 'hot' shales of Northern Africa (Lüning *et al.,* 2000; Lüning *et al.,*

2003a; Lüning *et al.,* 2003b; Lüning and Kolonic, 2006). Black shales are major source rocks for oil reserves (Wignall, 1994; Werne *et al.,* 2002; Piper and Calvert, 2009), the black shales of the lower Palaeozoic equate to 80-90% of the Palaeozoic sourced hydrocarbons in North Africa (Lüning *et al.,* 2000; Lüning *et al.,* 2005).

Many black shale units are enriched in metals severalfold above expected amounts in ordinary shale (Oschmann, 2000; Piper and Calvert, 2009). Some black shale units have served as host rocks for syngenetic metal deposits (Swanson, 1961; Tourtelot, 1979). Vine and Tourtelot (1970) determined that some black shales may contain horizons enriched in metals by factors greater than 50 such as Ag, Mo, Zn, Ni, Cu, Cr, V and less commonly Co, Se, and U. These elements together form part of the redox sensitive (adsorbed to organic matter and Fe-Mn hydroxides) and or sulfide forming trace metals (mainly FeS), they can be utilised to reconstruct environmental conditions during black shale deposition. For example, U within black shales can be used to signify the redox state during the time of deposition, it can also be used as a proxy for the levels of organic carbon present, as it is adsorbed to organic content under reducing conditions (Fertl and Chilingar, 1988; Lüning and Kolonic, 2003; Lüning and Kolonic, 2006).

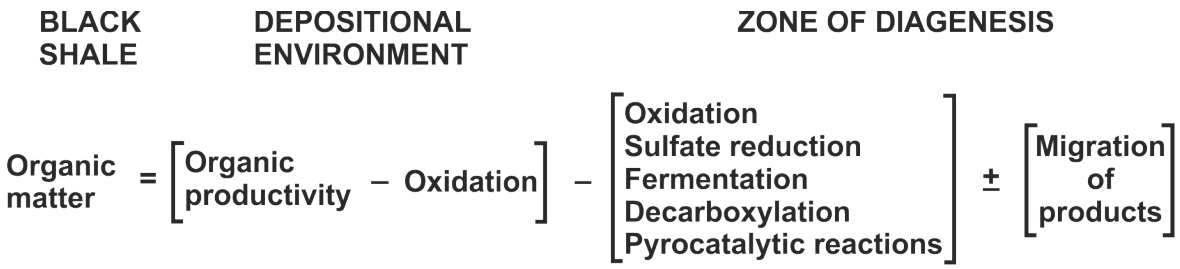

Figure 3.1 Chemical processes and relationships between the original depositional environment, diagenetic alterations and resulting black shales. Note the large amount of processes that finally lead to destruction or diminishing of the organic matter preserved within the geological record, highlighting the importance of the high original organic productivity for black shale genesis (slightly modified after Tourtelot, 1979).

Black shales occur throughout the Earth's geological history (see **Figure 3.2**). They are formed at times when specific geological settings and palaeoenvironmetal controls are suitable for the deposition of organic-rich sediments. The basic concept for generating organic-rich sediments is, that they form when and where organic material accumulates at a faster rate than it can be destroyed (Tourtelot, 1979).

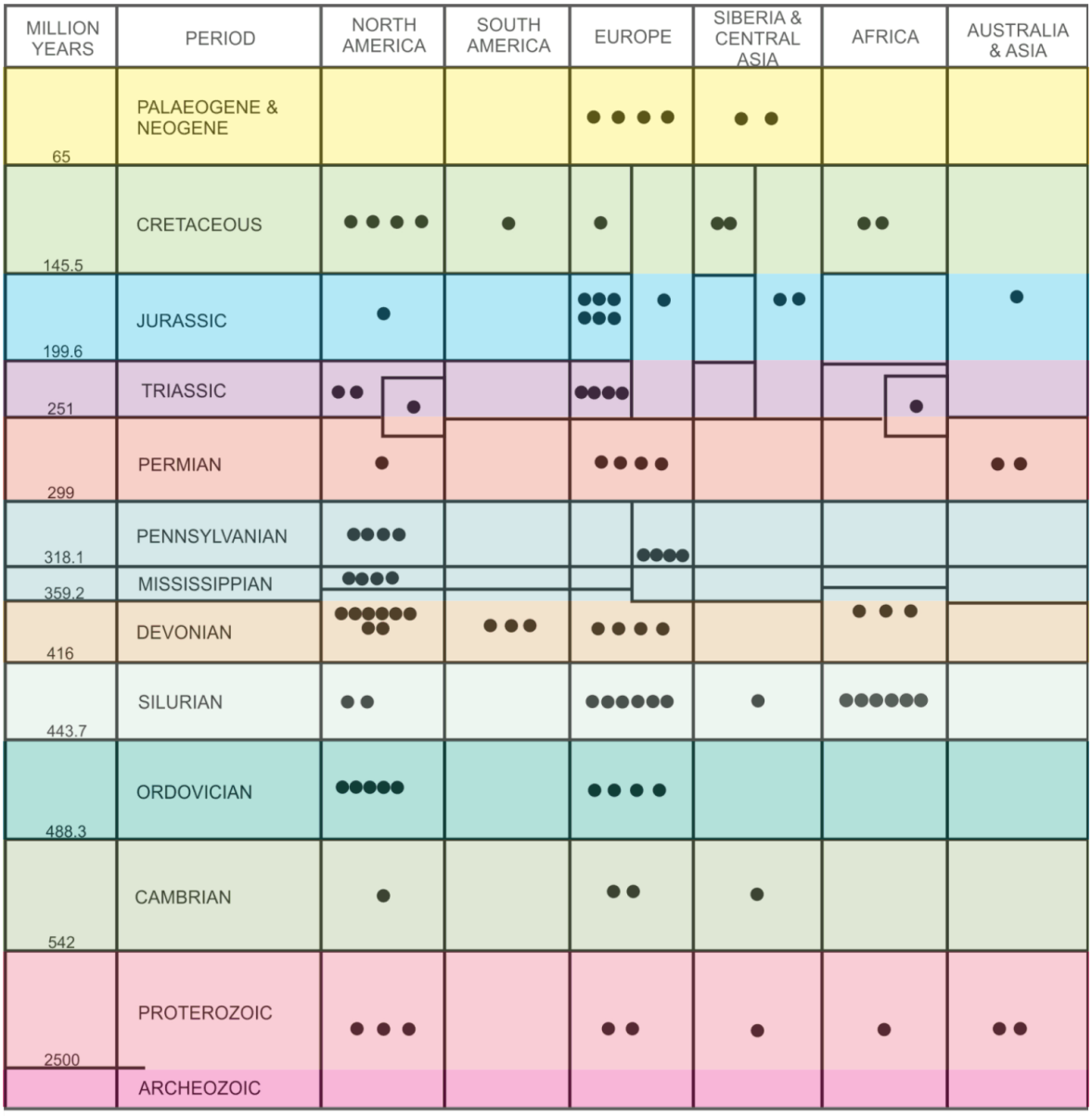

Figure 3.2: Distribution of prominent black shales through time and space. The filled black circles represent occurrences. The occurrences differ greatly in thickness, areal extent and other characteristics. Background colour code after the International Chronostratigraphic Chart (Gradstein *et al*., 2012). Modified after Tourtelot (1979) and Lüning *et al.* (2000).

3.1.2 Depositional mechanisms

A wide variety of different models have been proposed in order to explain the necessary processes and mechanisms which lead to the generation of black shale deposits. Amongst these, two models attracted the most attention within the previously published literature. The **productivity model** (Pedersen and Calvert, 1990) and the **preservation model** (Demaison and Moore, 1980), both of which have led to and stimulated debate over the formation of organic rich sediments. The **productivity model** suggests that the enrichment of organic matter in the sediment is a consequence of high settling rates of OM related to high primary productivity in the surface waters (the nutrients being supplied by upwelling or terrestrial influxes). The **preservation model** argues

that it is the conditions within the water column that lead to the formation of organic rich sediments (depletion of dissolved O_2 in the water column (dysoxia/anoxia), stratification (presence of a pycnocline, as in the modern Black Sea) and low sedimentation rates (Arthur and Sageman, 1994; Tyson, 1995; Nijenhuis *et al.,* 1999; Murphy *et al.,* 2000; Harris *et al.,* 2004; Meyers, 2006; Killops and Killops, 2009; Wei *et al.,* 2012). Tyson (1987) in: Wignall (1994) pointed out that the two models are incompatible because high productivity and enhanced preservation conditions do not coincide. High productivity rates suggest sustained nutrients and hence vigorous circulation (upwelling) of the water column, whereas the preservation model is typically generated by stratification of the water column, preventing nutrient circulation and leading to generally low productivity (Wignall, 1994). However, recent studies (Calvert and Fontugne, 2001; Werne *et al.,* 2002; Rimmer, 2004; Rinna *et al.,* 2002 in; Wei *et al.,* 2012) suggest that the processes of anoxia in the water column and high productivity may not be completely independent of one another, instead favouring a combination of both processes. Despite the major differences in the two models, they are notoriously difficult to infer within ancient organic rich sediments, due to poor palaeoproductivity proxies and the inability to constrain sedimentation rates (Wignall, 1994; Werne *et al.,* 2002).

The marine depositional environments can be classed as either 'marine shelfal deposits' or 'enclosed silled basin systems' the later being deep, enclosed, strongly stratified basins, characterised by a redox boundary high in the water column, such as for example the modern day Black Sea (Wignall and Hallam, 1991; Arthur and Sageman, 1994; Wignall, 1994; Killops and Killops, 2009).

The widespread deposition of organic rich shelfal deposits occurs during the mid Cambrian, early mid Ordovician, early Silurian, the Devonian, early and late Jurassic and the mid and late Cretaceous. These periods correspond to polar ice cap minima and resulting global eustatic marine transgressions (Killops and Killops, 2009). Many of the World's best source rocks are associated to this 'transgressive' black shale category (Wignall, 1994). Marine transgressions introduce large amount of nutrients into the shallow marine areas, resulting in high levels of primary productivity. Water circulation may be restricted (due to post-glacial stratification of the water column) leading to the intense anoxia with the degradation of the OM and the formation of organic rich sediments (Killops and Killops, 2009). Tourtelot (1979) suggested there are essentially two groups of transgressive sediments: the first group is characterised by alternating marine and non-marine

deposition, and the second dominated by exclusively marine deposition. The deposition of transgressive black shales (see **Figure 3.3)** can either occur during the initial stages of the relative sea-level rise under starved basin conditions ('puddle model' of Wignall and Hallam, 1991), forming commonly on erosive or hiatal surfaces or during the peak of transgression (maximum flooding black shales) at the time of maximum shoreline retreat ('expanding puddle model' of Wignall and Hallam, 1991) the later is a variation of the silled basin model (Black Sea model) proposed by Stanley and Blanpied (1980) in: Wignall (1994); Armstrong *et al.* (2005).

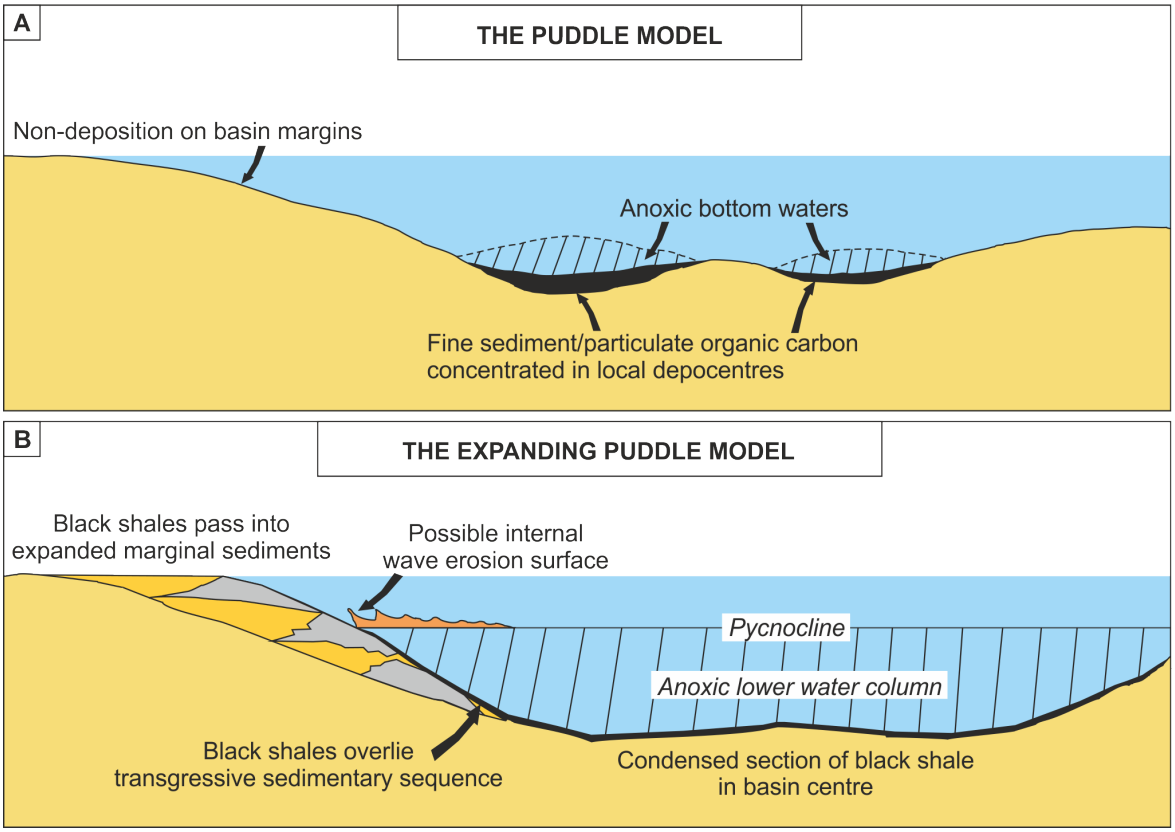

Figure 3.3: Schematic illustration of the processes leading to black shale formation according to the **[A]** 'The Puddle Model' (for basal transgressive black shales) and **[B]** 'The Expanding Puddle Model' (for maximum flooding black shales). Redrawn and modified after (Wignall, 1994).

The depositional environments of marine black shales can also be described by using the following three models of Tourtelot (1979), as illustrated by the **Figures 3.4 – 3.6**.

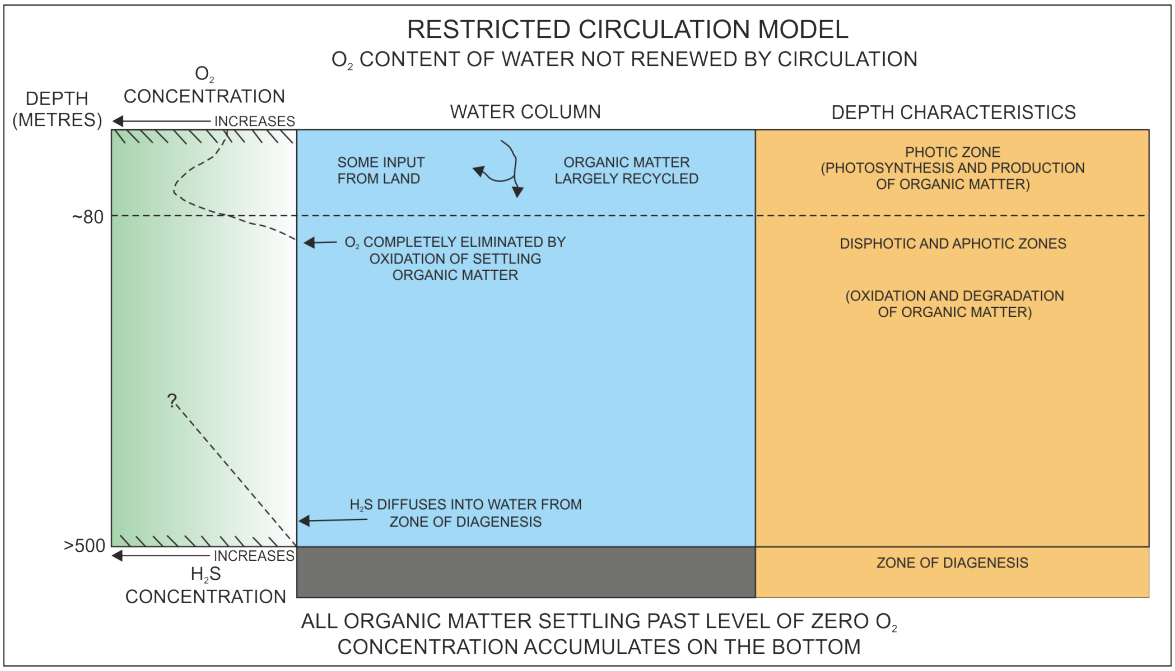

Figure 3.4: Restricted circulation model for accumulation of organically rich black shales. Modified after Tourtelot (1979); Didyk *et al.* (1978).

Restricted circulation model (see **Figure 3.4**): This model is used to explain the processes that are apparent within the modern day Black Sea - enclosed stratified basin. The oxygen contents of the water column are not renewed by circulation, meaning the renewal of oxygen is not fast enough, or equal to the oxygen consumed by the oxidation of organic matter. With this model organic rich sediments can accumulate even if the rates of bioproductivity are relatively small (Tourtelot, 1979).

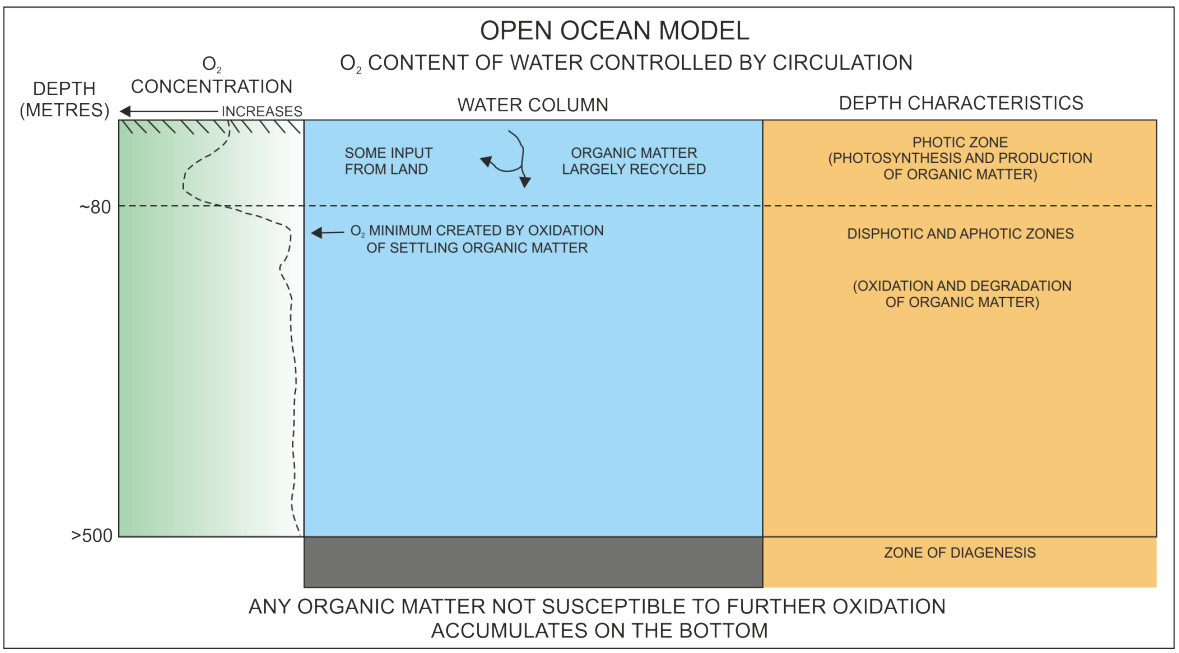

Figure 3.5: Open ocean model for accumulation of organically rich black shales. Modified after Tourtelot (1979); Didyk *et al.* (1978).

Open ocean model (see **Figure 3.5)**: this can be easily applied to modern day deep marine environments. The oxygen content of the water column is controlled by circulation (thermohaline circulation), yet it is heavily influenced by the rates of oxidation of organic matter escaping the photic zone. The oxygen minimum is created by the oxidation of the organic material. Organic rich sediments can accumulate even when the sedimentary environment is completely oxic (Tourtelot, 1979).

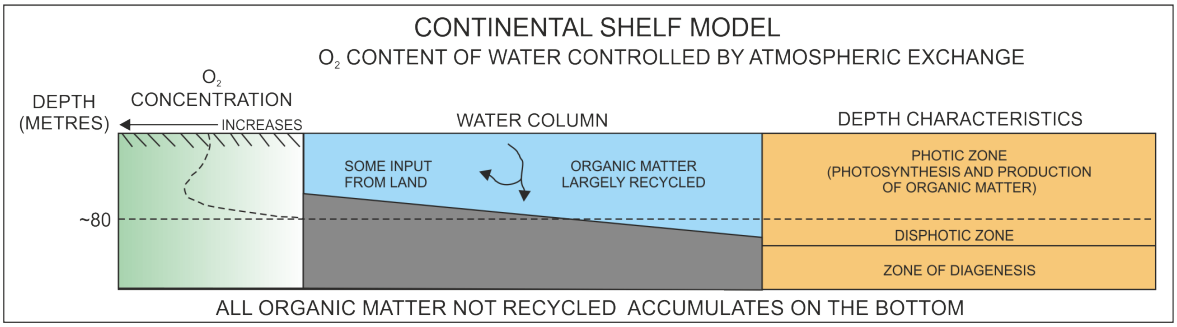

Figure 3.6: Continental shelf model for accumulation of organically rich black shales. Modified after Tourtelot (1979); Didyk *et al.* (1978).

Continental shelf model (see **Figure 3.6**): This model contains the same input factors as the others yet there is a water column with significantly reduced thickness between the photic zone and the sediment surface. Thus the organic material is recycled in the photic zone to a lesser extent due to a more rapid settling to the sediment surface. In this environment the sediments become anoxic in a very short distance below the surface because of bacterial processes and the breakdown of the organic content (Tourtelot, 1979).

3.1.3 *Organic carbon and Bioproductivity (Palaeoproductivity)*

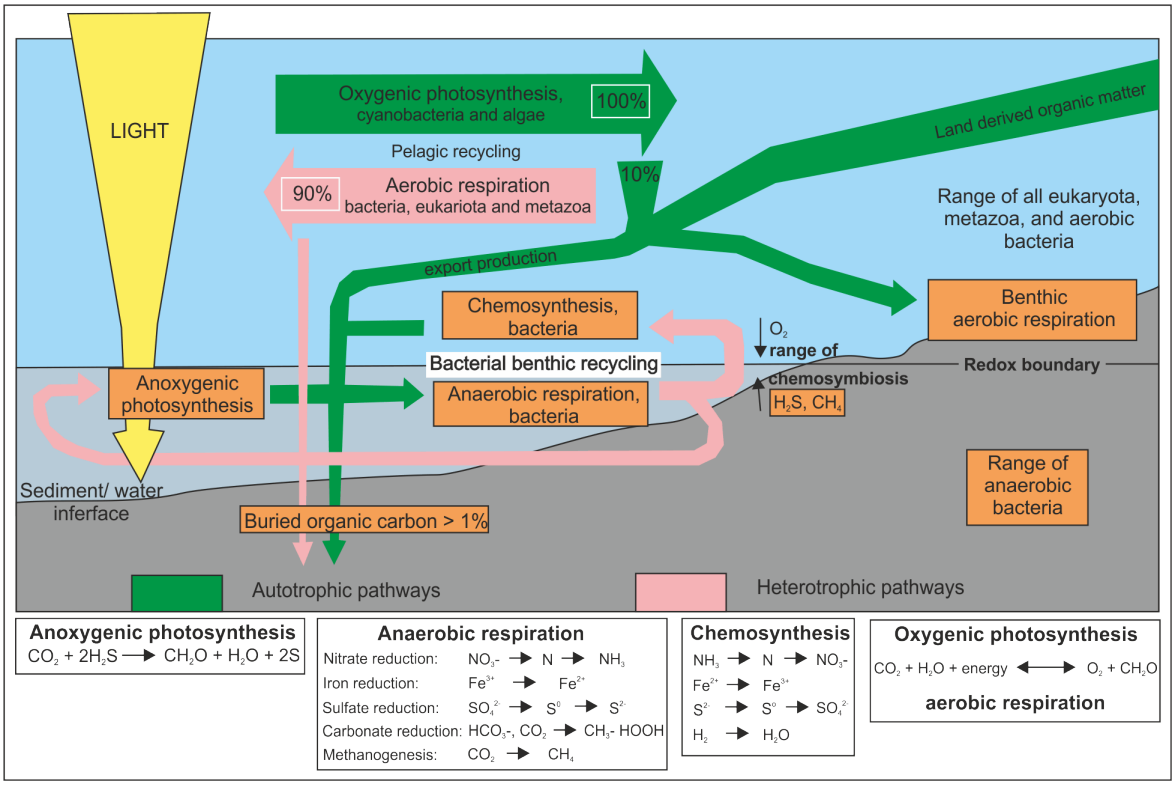

Figure 3.7: The organic carbon cycles and the main related redox reactions. Modified after Oschmann (2000).

It is commonly accepted that the organic matter preserved within black shales is a result of the organic carbon cycle depicted in **Figure 3.7** (Hedges and Keil, 1995; Oschmann, 2000; Walther, 2009). The fixation of carbon occurs during oxygenic photosynthesis (Methanal, CH_2O). Müller and Suess (1979) in: Meyers (2006) concluded that less than 1% of the organic matter produced in the photic zone reaches the sea floor. The organic matter that accumulates at the sea floor is dominated by the single celled photosynthetic phytoplankton within the photic zone (Meyers 2006). A combination of these primary producers and both land and marine derived organic matter is more apparent in marine sediments close to river mouths (Meyers 1997). The burial of organic carbon occurs when it accumulates faster than it can be destroyed by processes such as aerobic degradation in the upper most parts of the oxic water column and bacterial oxidation in the sediment (see early diagenesis covered in **sections 3.1.4. + 3.1.5**). Stow *et al.* (2001); Arthur (1979); Sageman *et al.* (2003); Bohacs *et al.* (2005) and Meyers *et al.* (2005) highlight the three fundamental processes controlling the burial of organic carbon. These being dilution (caused by variations in sedimentation rates, terrigenous clastic and skeletal flux), production (rates of marine and terrigenous organic matter flux) and decomposition (preservation). The productivity and/or

preservation models (see **section 3.1.2**) will also explain the levels of organic carbon burial in the sediments.

Bioproductivity is variable, controlled and sustained by the levels of nutrients available in the photic zone. The level of nutrients in turn are controlled by (limited to depths of), seasonality (light and temperature), oceanic circulation, salinity and variation in atmospheric CO_2 (Bonn *et al.,* 1998; Hillaire-Marcel and De Vernal, 2007). The vast majority of productivity is limited to depths of 100 m (Meyers 2006). Variations of atmospheric CO_2 are believed to result from changes in the productivity rates and the burial of carbon (Pfeifer *et al.* 2001), hence the productivity extent can be used to infer palaeoclimatic conditions. Nutrient recycling, mainly the replenishment of nitrate, phosphate and silicate of the surface waters, is controlled by the vertical movement of the water masses, upwelling, vertical mixing and nutrient delivery from the land (Tyson, 1995; Meyers, 2006; Bernárdez *et al.,* 2008; Piper and Calvert, 2009; Chester, 2009). The salinity levels also have an impact on the rates of productivity. Fully marine organisms cannot cope with the changes in salinity levels (Killops and Killops, 2009) and more importantly, brackish surface waters can lead to salinity driven water column stratification (Tyson, 1995; Meyers, 2006), preventing the replenishment of nutrients via upwelling (Challands *et al.,* 2009). The excess productivity leads to a greater demand for oxygen and ultimately results in a depletion of dissolved oxygen with depth (Prakash Babu *et al.* 2002). One might suggest that high surface water productivity leads to high fluxes of OM to the sea-floor sediment. However, this assumption proves to be invalid in many cases, as the OM accumulation is heavily dependent on the levels of dissolved O_2 within the water column and the depth related decrease with the OM flux. In other words a high palaeoproductivity (and carbon content) in the photic zone is not always recorded within the sediments (Wignall, 1994; Bonn *et al.,* 1998; Paytan and Gornitz, 2008). Brumsack (1981) in: Tyson (1995) demonstrated that a high productivity is not essential to produce marine sediments with TOC values up to 10%; it can be achieved by decreasing sediment dilution and enhancing the preservation by increased levels of anoxia. The concentrations of OM matter within sediments, represents only a fraction of the biological productivity in the surface waters. Under normal marine settings approximately 10% of the original productivity leaves the euphotic zone, in upwelling areas this may increase to up to 30%, however, the amount of OM that actually reaches the sediment may only represent a few percent (Tyson, 1995; Reitz *et al.,* 2004; Tribovillard *et al.,* 2006). Phosphorus (P) and nitrogen (N) concentrations have been used as productivity indicators (Schmitz *et al.,* 1997; Hetzel *et al.,* 2011), yet these elements are recycled intensely (biocycling) within the water column, and P in particular

is known to be poorly correlated with surface water productivity (Wignall, 1994). P contents can also be affected by post burial redox conditions (Delaney, 1998 in: Paytan and Gornitz, 2008). Biogenic silica (Si) concentrations produced by siliceous plankton and biogenic opal have also been used as an indicator for bioproductivity (Bonn *et al.,* 1998; Schmitz *et al.,* 1997). Over 90% of the organic silica is preserved in the sediments (Wignall 1994). However factors such as Si dissolution within the water column, at the sediment/water interface and within the sediment make it difficult to calculate original bioproduction rates for the surface waters (Bonn *et al.,* 1998; Hillaire-Marcel and De Vernal, 2007). By far the most commonly used palaeoproductivity indicator is barium (Ba) or biogenic Ba (Ba_{bio}). As a result of reducing conditions, and the sulphate release from decaying OM within the oxygen minimum zone Ba is removed from solution as syngenetic barite ($BaSO_4$). It can also be incorporated into the siliceous phytodetritus (Wignall, 1994; Schmitz *et al.,* 1997; Bonn *et al.,* 1998; Pfeifer *et al.,* 2001; Reitz *et al.,* 2004; Kiipli *et al.,* 2004; Chun and Delaney, 2006; Scopelliti *et al.,* 2006; Turgeon and Brumsack, 2006; Calvert and Pedersen, 2007; Paytan and Gornitz, 2008) resulting in a positive correlation between the Ba_{bio} and OM fluxes (Dymond *et al.* 1992 in: Paytan and Gornitz, 2008; Prakash Babu *et al.,* 2002). The use of Ba as a palaeoproductivity proxy is however not unproblematic. The relationship between Ba and the environment as described above was demonstrated to work effectively in deep water environments (>1000m), however only minor correlations between Ba and productivity exists in shallow water settings (Wignall, 1994; Hetzel *et al.* 2011). A further problem for the interpretation of Ba concentrations within the geological record arises from the highly mobile nature of Ba during diagenesis, specifically within the sulphate reduction zone (Wignall, 1994; McManus *et al.,* 1998; Prakash Babu *et al.,* 2002; Hetzel *et al.,* 2006; Turgeon and Brumsack, 2006; Calvert and Pedersen, 2007). Ba associated to terrigenous silicates, like for example K-feldspars and micas, where it can substitute K (Calvert and Pedersen, 2007), and Fe-Mn oxides and hydroxides (Anderson and Winckler, 2005), as well as post-depositional hydrothermal activity, can mask the original biogenic Ba signal (Paytan and Gornitz, 2008; Wei *et al.,* 2012).

3.1.4 Anoxia and its relation to OM preservation

Oxygen deficiency (or anoxia) occurs when the oxygen demand for the oxidation of OM exceeds the rate of oxygen supply, which is determined by climatic, hydrographic or oceanographic factors (Dean *et al.,* 1984; Tyson, 1995).

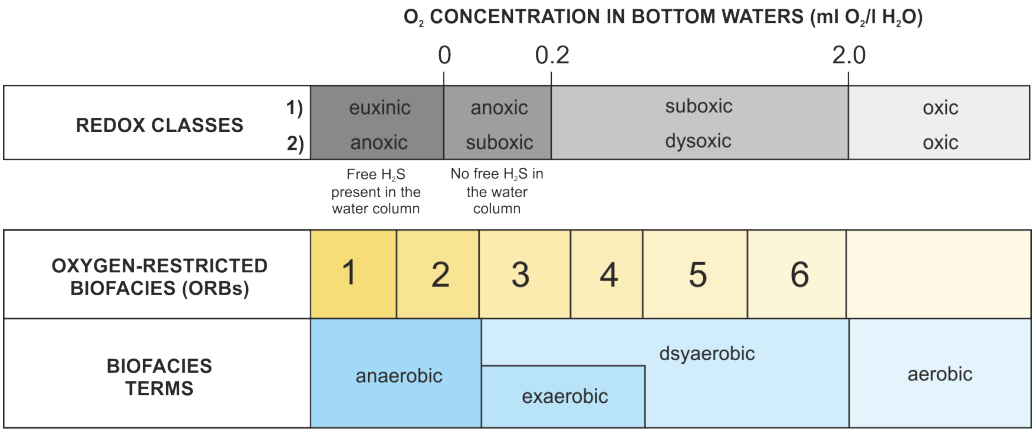

Figure 3.8: Redox classes, biofacies and biofacies terminology. Terminology from Tyson and Pearson (1991). Within the redox classes section [1] is the terminology from Tribovillard *et al.* (2006) and [2] is after Wignall (1994). Modified after Wignall (1994) and Tribovillard *et al.* (2006).

The redox classification of sedimentary environments is based on the concentration of dissolved O_2 (see **Figure 3.8**) and comprises: [1] oxic (>~2.0 ml O_2 1^{-1} H_2O), [2] dysoxic or suboxic (~2.0–0.2 ml O_2 1^{-1} H_2O), and [3] the anoxic facies. The last one can be further on sub-divided into the nonsulfidic (<~0.2 ml O_2 1^{-1} H_2O, no free H_2S) and sulfidic or euxinic (0 ml O_2 1^{-1} H_2O, with free H_2S) subfacies (Wignall, 1994; Tyson, 1995; Algeo and Maynard, 2004; Algeo *et al.,* 2004). There has been considerable confusion about the various terms (Jorissen *et al.,* 2007), however the above definitions will be used within the present study.

Anoxic conditions are classed as either nonsulfidic or sulfidic, the sulfidic conditions - also termed euxinic meaning 'Black Sea-like', from the Greek *Pontos Euxinus* (King, 2004 in: Piper and Calvert, 2009) - prevail when free hydrogen sulphide (H_2S) percolates from the underlying sediments into the water column (Wignall, 1994). The H_2S is a by-product of sulphate-reducing bacteria in the sediments (the euxinic conditions may even extend as far as the photic zone, such as in the modern day Black Sea). Suboxic conditions are characterised by low O_2 concentrations, where the H_2S concentrations are restricted to the pore waters below the sediment-water interface (Tribovillard *et al.,* 2006).

Under oxic conditions, where surface waters contain between 4.5 – 8.0 ml O_2 l^{-1} H_2O (Wright and Colling, 1995 in: Algeo and Maynard, 2004), degradation of OM by aerobic bacteria and other organisms occurs, decreasing the dissolved levels of O_2 within the water column. The oxygen consumption rates vary with the nature of the OM present (Tyson, 1995). Under depleted O_2 conditions (amount of OM exceeds the O_2 present) the OM is further degraded by anaerobic microbes which can utilise secondary oxidant sources such as iron and manganese oxides/sulphates and dissolved species of Cr, Re, U and V, which are reduced to less soluble states and accumulate on the sea-floor (Piper and Calvert, 2009). Anoxic conditions prevail when

all the oxidants have been depleted and H_2S is produced by the sulphate reducing bacteria. Evidence for the reduced species of Cr, Re, U and V including FeS, CdS and ZnS in the sediments demonstrate the presence of the sulphate reducing bacteria (Calvert and Pedersen, 2007; Piper and Calvert, 2009). At increased depth, below the sediment/water interface, methanogenic bacteria begin to break down the OM, mostly via oxidative-reductive disproportionation of carbon (Tribovillard *et al.,* 2006). The boundaries between the differing oxygenation regimes (see **Figure 3.9** and **Figure 3.10**) are largely controlled by microbial-driven oxidation reactions (Riding and Awramik, 2000; Piper and Calvert, 2009).

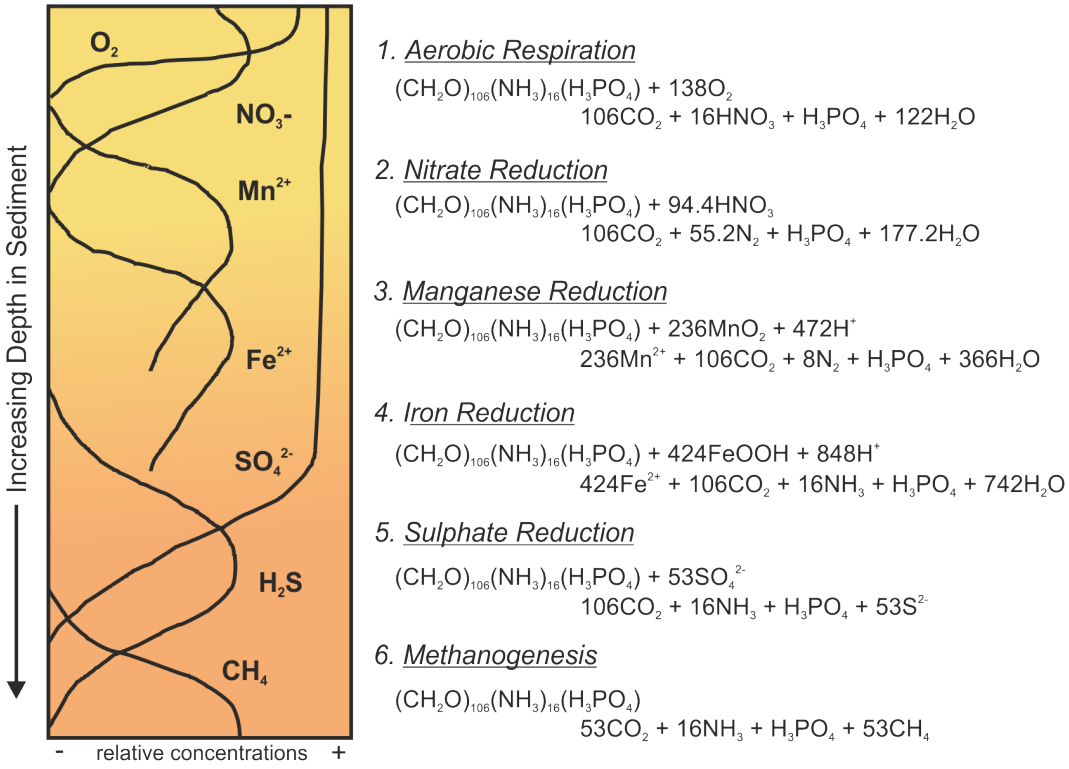

Figure 3.9 Relationship between increasing depth and the chemical reactions facilitating the break-down of organic matter. Modified after Calvert and Pedersen (2007).

Anoxia can also occur within a stratified water column which is controlled by vertical temperature and salinity gradients and exacerbated by the presence of OM and bacterial respiration, effectively restricting the circulation of O_2 (Piper and Calvert, 2009). Under these circumstances a well oxygenated surface layer is separated from the underlying anoxic waters by the establishment of the pycnocline (Wignall and Hallam, 1991; Wignall and Maynard, 1993; Wignall 1994), enhancing the development of the anoxic/euxinic conditions towards the sediment/water interface. Tyson (1995) suggested that there is generally less potential for oxygen depletion in the deep sea environments than there is within the shallower shelfal environments. This might be related to the establishment of the oceanic thermohaline circulation, which is providing O_2 to the deep ocean, at

least under present day conditions. The extent of the anoxic conditions and O_2 replenishment of the pore-waters below the sediment-water interface is considered to be controlled by a wide variety of factors, such as the intensity of bioturbation (O_2 replenishment), the mineralogical composition (clays or sands), the texture (varying grain sizes) of the sediments, turbiditic flow deposits (introducing oxygen rich sediments into the system) and strength of bottom currents (Dean *et al.* 1984; Wignall, 1994; Tribovillard *et al.,* 2006).

Pyrite in black shales has often been used to infer deposition under anoxic bottom water conditions. However pyrite formation can also occur under fully oxygenated water columns. Fine grained shallow marine sediments can contain substantial amounts of pyrite as a result of high settling fluxes of OM due to high productivity rates and shallow depths where the settling flux of the OM decreases systematically with the water depth (Piper and Calvert, 2009). Various elemental proxies and concentrations can be used to infer the palaeoredox states, this will be described and discussed in **Chapter 3.1.15**.

3.1.5 Diagenesis and degradation of organic matter

The early diagenetic processes affecting marine sediments are dependent on a series of typical chemical redox reactions that are bound to the major zones of diagenesis. These zones, with increasing depth are the aerobic oxidation zone (oxic zone), the nitrate reduction, the manganese zone, the iron reduction zone, the sulphate reduction zone and finally the zone of methanogenesis (see **Figure 3.9**). The hierarchy of these zones reflects the decreasing availability of oxygen, as in OM-rich sediments O_2 is the primary oxidant, and the free energy yields of the specific reactions (Froelich *et al.,* 1979 in; Martens *et al.,* 1992; Bloch *et al.,* 1999).

Under anoxic bottom waters the same hierarchy of reactions and consequently the same types of diagenetic zones are developed with a major difference that the oxic zone is absent and a lack of burrowing. The organic matter that is subject to the early diagenetic overprint is considered to have an overall Redfield composition: $(CH_2O)_{106}(NH_3)_{16}(H_3PO_4)$, (Chester 2009).

Aerobic degradation (oxic zone). Most marine environments are oxic, as a result ~90% or more of the OM that reaches the sea-floor (via particle flux) is oxidised close to the sediment/water interface, only <10% of the OM flux is oxidised by secondary oxidants (Chester 2009). Under oxic conditions and the presence of aerobic organisms (see **Figure 3.9**), decomposition (re-

mineralisation and degradation) of the OM occurs rapidly, and most of the OM is destroyed at this stage. The CO_2 released from the oxidation of the OM can lead to carbonate dissolution, and ammonia (NH_3) can be oxidised (**nitrification**) to nitrate (Chester, 2009). At the sediment/water interface (under oxic bottom waters) the rate of oxidation can be accelerated by the bioturbation and mixing of the sediments. Levels of oxygen in the sediment are affected by sedimentary particle size, the reduced pore space within silts and clays leads to a rapid reduction of water circulation with depth, limiting the levels of dissolved O_2 replenishment via diffusion (Killops and Killops, 2009). Open marine pelagic sediments are often oxygenated to depths of 0.5 m, whereas the oxygenation of shelfal fine-grained deposits, in the absence of bioturbation, is limited to the upper (1-2 mm). Even with intense bioturbation the diffusion of O_2 will only extend as far as 20-30 mm (Tyson, 1995; Killops and Killops, 2009).

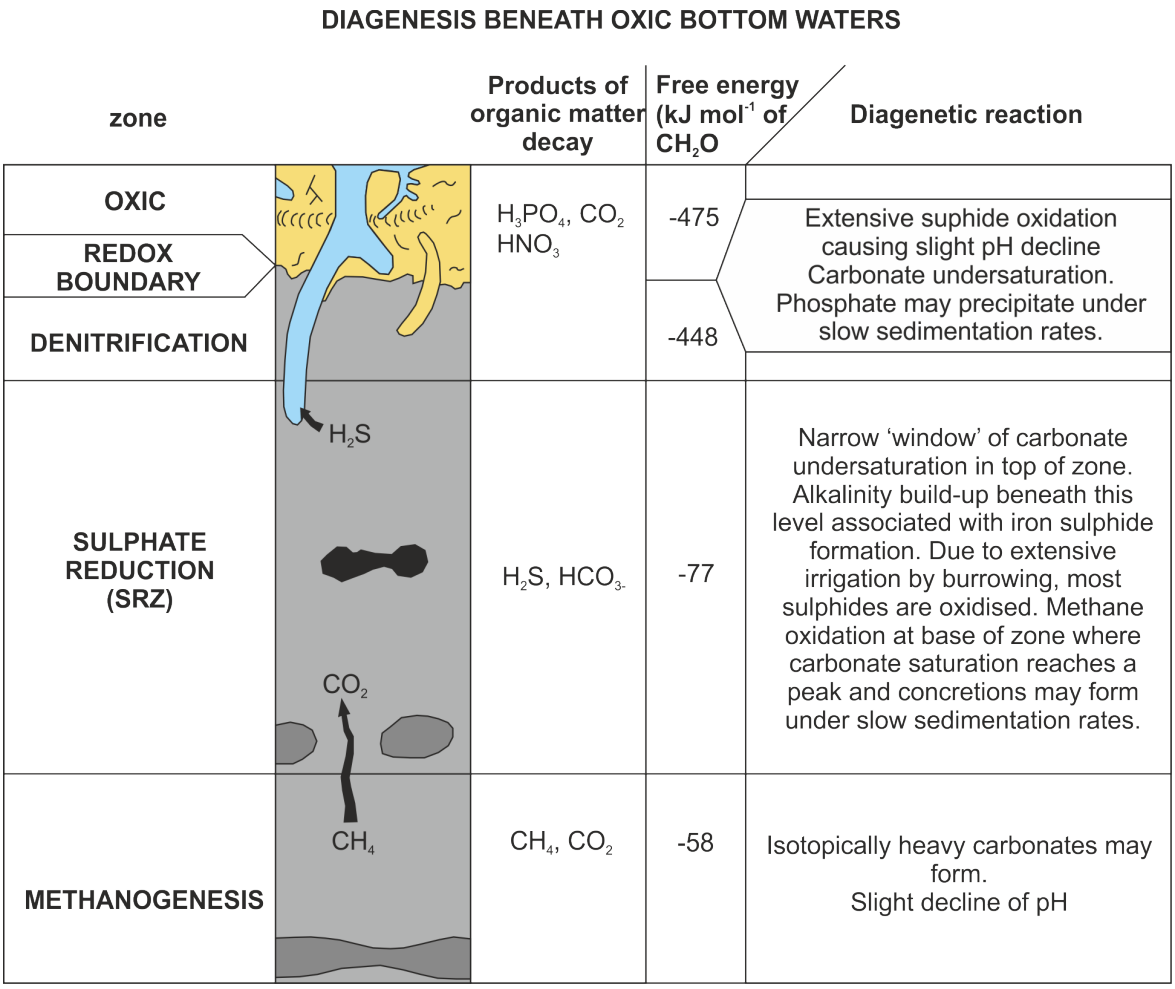

Figure 3.10; Characteristics of diagenetic zones beneath oxic bottom waters defined by organic matter oxidation pathways. Modified after Wignall, 1994.

When the levels of dissolved O_2 fall below the levels of demand (according to Tyson (1995) aerobic degradation is apparent until suboxic conditions of <0.2ml l^{-1}), anoxic conditions occur within the sediments and possibly the overlying water column. This leads to the degradation of OM via anaerobic processes. The anaerobes (most of which are facultative, so can also use oxygen, if in sufficient supply) can utilise other inorganic oxidising agents in the absence of O_2. These are in order of decreasing energy return manganese (IV) to (II), nitrate, iron (III) to (II), sulphate and bicarbonate (Hedges and Keil, 1995; Killops and Killops, 2009; Chester, 2009). Nitrate reduction (**Denitrification zone**), occurs under depleted O_2 conditions, when the dissolved O_2 levels reach ~5% of the respective concentration in oxic waters. The oxygen from nitrate (or nitric acid, HNO_3) is used to degrade the OM further (Tyson, 1995; Chester, 2009). The vertical extent of the **Denitrification zone** is usually very limited in marine sediments, as a result of low nitrate concentrations (Killops and Killops, 2009). Only approximately 3% of the OM in shelf sediments is thought to be oxidised by denitrifying bacteria (Tyson, 1995). Examples for the use of other secondary oxidants, like manganese oxides or iron oxides is depicted and explained in **Figure 3.9**.

Sulphate reduction occurs when the dissolved O_2 and nitrate levels are depleted (Tyson, 1995). Most of the OM degradation occurs within the **sulphate reduction zone (SRZ)**. The depth of the SRZ is dependent on the relative concentration of OM present (Killops and Killops, 2009). The vertical magnitude of the SRZ zone is two to three times thicker than the oxic zone, as sulphate concentrations (20-30mM) in sea-water exceed those of O_2, which is typically less than or equal to 0.25-0.30mM (Tyson, 1995). The degradation of OM leads to the build up of hydrogen sulphide (H_2S) a by-product and consequent activity of the sulfate reducing bacteria (Riding and Awramik, 2000). High concentrations of H_2S can ultimately inhibit the sulfate reducing chemical reactions carried out by anaerobic bacteria (Wignall, 1994; Tyson, 1995). Pyrite (FeS_2) formation is dependent on the levels of free reactive iron. Under euxinic conditions and reactive iron depletion, H_2S can accumulate (sulphurization) and act as a week acid, leading to poor preservation of OM (Wignall, 1994). The production of methane is predominantly facilitated within the **Methanogenesis Zone.** The chemical processes leading to the formation of methane are initiated when all available sulphates are depleted (Tourtelot, 1979). Anaerobes (methanogens) synthesize biogenic methane (CH_4) from the smallest fermentation products (mostly alcohols with $>C_1$). CO_2 and H_2 are necessary, where CO_2 is used as an electron donor during the reaction with H_2. Some methanogens can synthesize methane using simple C_1 compounds like methanol and formates, or methylated amines - C_1-units (Killops and Killops, 2009).

There are essentially two factors controlling the successions within the diagenetic zone. Firstly the magnitude of the OM flux to the sea-floor, which is controlled by the extent of the bioproductivity, secondly the rates at which the sediment accumulates. Both of these factors tend to decrease from the continental margins areas to the deep sea environments. Variations of these two factors, ultimately determines the amount of OM preserved within the sediments, and the extent to which it consumes the various oxidants (Chester, 2009).

During the late diagenesis, mineral reactions occur in response to burial and consequent increase in pressure and temperature. The common reactions are the dissolution-precipitation of silicates and carbonates, whereas, calcite is depleted with increasing depth. Quartz and feldspars undergo dissolution and mixed-layer clay/illite is authigenetically precipitated. The OM undergoes drastic diagenetic maturation with increasing depth (Boggs, 1995; Bloch *et al.,* 1999). Within the clay mineralogy the most significant diagenetic changes occur with the transformation of smectite (montmorillonite) layers into illite layers (termed the I/S transformation, the substitution of Al^{3+} and K^{+} for Si^{4+} in the clay mineral structure). The I/S transformation occurs at around 4 km in depth and 120-140^{o}C (Walther, 2009). At around 2.5 km depth chlorite appears. The autogenesis is believed to be controlled by the amounts of Mg^{2+} and Fe^{2+} in solution. Chloride formation below 3.4 km in depth is considered to be related to the reaction of kaolinite with quartz, below 4 km to be the by-product of the aforementioned I/S transformation. Under temperatures exceeding 300^{o}C and depths of >5.5 km illite is recrystallized, forming sericite and finally a muscovite structure (Walther, 2009).

3.1.6 Clay Geochemistry and Mineralogy

Clays or phyllosilicate minerals in general are sheet silicates, in which layers of silica tetrahedral are bound to layers of hydroxides. They are one of the major components of mudrocks or shales and form because of the weathering and breakdown (hydrolytic decomposition) of primary aluminosilicate feldspars. The most common types of clays (<2 µm) are kaolinite, illite, chlorite, vermiculite, montmorillonite (or smectite), and mixed-layer (illite/smectite, I/S) clays (Fagel, 2007; Chester, 2009). The original mineralogy of mudstones is controlled by the varying relative proportions of these clays, affecting the overall geochemistry of clay-rich sediments (Sethi and Schieber, 1998). The genesis of clay minerals is predominantly controlled by prevailing climatological conditions and the original rock type. The original clay mineralogy of sediments can

change due to lithification and post-diagenetic processes. During burial the clay fraction can undergo illitization (addition of K^+ ions to kaolinite forming illite) and authigenesis of kaolinite. Authigenesis is however, only a minor process as it accounts for only less than 10% of the total of clay minerals (Fagel, 2007; Sethi and Schieber, 1998). By their ability to exchange ions (ions in the clay interlayers can be exchanged for ions in the surrounding solution), and because of the adsorption and desorption of ions, particularly oxides and hydroxides on their surfaces, clay minerals play an important role in controlling the chemical composition of aqueous fluids (White 2013). Selective accumulation of clay minerals may occur in certain environments, such as kaolinite, which is seen to accumulate more readily in shallow marine settings (Sethi and Schieber, 1998).

The presence of kaolinite in marine sediments is commonly interpreted to be indicative for humid/warm, tropical climates and well drained topographies in the source area, conditions that lead to an extensive and complete weathering of feldspars. As kaolinite is also regarded to be a typical outcome of desert weathering, it is termed a so called 'low-latitude' clay mineral (Pettijohn *et al.,* 1987; Weaver, 1989 in: Sethi and Schieber, 1998; Chamley, 1989 in: Diester-Haass *et al.,* 1998; Chester, 2009). The presence of illite can indicate humid temperate climates (Einsele, 2000), whereas Chamley (1989) and Weaver (1989) in Diester-Haass *et al.* (1998) suggest chlorite and illite to be derived from areas subject to rapid uplift, enhanced mechanical erosion and cold/desert area conditions. Illites are the most common of the clay minerals in deep sea sediments and are present mostly at mid-latitudes, where the clay mineral assemblages are less diluted by chlorite and kaolinite. Chlorite is termed a high-latitude clay mineral and is mainly confined to Polar Regions - related to ice rafting - and is considered to be a primary mineral and not a weathering product (Chester, 2009). Mixed-layer clays are considered to form under conditions of mild chemical weathering (Chamley, 1989 in: Diester-Haass *et al.,* 1998). Montmorillonite (smectite) clay types indicate temperate to subtropical climates (Einsele, 2000), with smectite forming within warm, poorly drained continental areas (Chamley, 1989 in: Diester-Haass *et al.,* 1998).

Marine muds formed in colder climates tend to contain a higher concentration of feldspars and fewer phyllosilicates, which is interpreted to be the result of lower chemical weathering intensities. The different clay minerals present within mud-rocks are commonly used as a proxy for weathering conditions and hence as a palaeoclimatological indicator (Calvert and Pedersen, 2007).

- **Ideal compositions of clay minerals**

Kaolinite. $Si_4Al_4O_{10}(OH)_8$ - 46.54% SiO_2, 39.5% Al_2O_3 and 13.96% H_2O (Weaver, 1989). Kaolinite is a so called 1:1 clay or two layered clay, that is characterised by having a single tetrahedral layer and a single octahedral (hydroxide) layer (Fagel, 2007; Chester, 2009). The tetrahedral layer consists of Si^{4+} and Al^{3+} tetrahedrons that are interconnected by O^{2-}. The octahedral (or hydroxide) layer consists of Al^{3+}, Mg^{2+} or Fe^{2+} bonded to 6 O^{2-} or OH^- in an octahedron structure (Walther, 2009). Fe_2O_3, TiO_2, MgO and CaO are ubiquitous within kaolinite samples and K_2O + Na_2O are common (Weaver, 1989). Impurities such as quartz, anatase, rutile, pyrite, limonite, feldspar, montmorillonite and various other oxides and oxyhydroxides (Fe, Ti and Mn including Si and Al hydroxides) can occur within kaolinite dominated mudstones and as coatings (Weaver, 1989).

The 2:1 clays (or 3 layered clays) are formed by a single hydroxide (octahedral) layer bounded by two tetrahedral layers (Fagel, 2007; Chester, 2009) and they are commonly sub-divided into the following groups, the pyrophyllite group, the most simple clays being pyrophyllite ($Al_2Si_4O_{10}(OH)_2$ and talc ($Mg_3Si_4O_{10}(OH)_2$), the smectite group, the biotite group and the vermiculite group.

Illite. Illite is the name applied to clay sized micas (biotite and muscovite), illite may form by the breakdown of primary minerals, including feldspars, micas, kaolinite, smectite, detrital aluminosilicates and glauconite (Djarnia and Fekirine, 1998). Illite belongs to the 2:1 clays, a single hydroxide layer bounded by two tetrahedral layers (Fagel, 2007). Micas (illite) are related to pyrophyllite and talc, by the substitution of Al^{3+} for Si^{4+} within the tetrahedral site, and the presence of K^+ cations in the interlayer as a result of the charge deficit of the Al/Si substitution (Fagel, 2007; White, 2013).

Vermiculite. The Vermiculite group (2:1 or 3 layered clay) has structures similar to those of pyrophyllite and talc (see above). Due to cation deficiency clays of the vermiculite group exhibit a higher net charge on the 2:1 layer, which in turn causes the layers (hydroxide layer and tetrahedral layers) being held together by greater electrostatic forces. Therefore the interlayer spaces are less expandable and the cations less exchangeable (White, 2013).

Montmorillonites. $X_{1/3}(Mg_{1/3}Al_{5/3})Si_4O_{10}$ $(OH)_2$ $.nH_2O$. Belonging to the smectite group (2:1 or 3 layered clay). They generally incorporate water molecules within the interlayers, and the water volumes are largely controlled by cations present and by humidity levels. The interlayer cations of smectites are variable (X = exchangeable, Na and/or Ca), dependent on the chemical properties of the surrounding solution (Fagel, 2007; White, 2013).

Mixed-layer clays (I/S). Because of the structural similarities to 2:1 clays I/S clays form crystals consisting of more than one type of clay (by regular or irregular stacking of the clay minerals). For example, illite-smectite layers (Fagel, 2007; White, 2013).

Chlorite. $(Mg,Fe,Al)_6$ $(SiAl)_4O_{10}(OH)_8$. Chlorite is characterised by having two tetrahedral layers and two hydroxide layers, hence a typical 2:2 clay structure (White, 2013). It is also characterised by having 3 sheets; two tetrahedral layers and an octahedral one and its interlayer space is taken up by a hydroxide layer, forming a so called 2:1:1 layer type (Fagel, 2007).

3.1.7 Elemental Geochemistry

In the following the contribution of major and trace elements towards black shale genesis and their importance and use as palaeoenvironmental indicators is described and discussed, in particular the major elements magnesium (as MgO), aluminium (as Al_2O_3), silicon (as SiO_2), potassium (as K_2O), calcium (as CaO), titanium (as TiO_2), manganese (as MnO) and iron (as Fe_2O_3), as well as the trace elements phosphorous (P), sulphur (S), scandium (Sc), vanadium (V), chromium (Cr), cobalt (Co), nickel (Ni), copper (Cu), zinc (Zn), arsenic (As), rubidium (Rb), strontium (Sr), zirconium (Zr), molybdenum (Mo), silver (Ag), cadmium (Cd), tin (Sn), antimony (Sb), barium (Ba), mercury (Hg), lead (Pb), bismuth (Bi), thorium (Th) and uranium (U).

Shales are composed of clay minerals and hence are also known as alumosilicates, and normally act as ‘element dustbins’ or sinks. The elemental geochemistry (specifically at the trace element level) can be vast and varied, depending on the composition of the detrital material derived from the hinterland and the overall sea-water chemistry. Within marine settings, black shales tend to form because of restricted circulation and/or elevated bioproductivity. A product of these factors are anoxic or reducing conditions within the sediment and also, under certain circumstances, the water column. These changes in redox conditions can drastically effect the absolute concentrations of certain redox sensitive trace elements. In the past, these redox sensitive elements have proven to be a powerful tool in the reconstruction of environmental conditions that prevailed during the sedimentation and diagenesis of black shales. In the following the geochemical behaviour is briefly described and discussed. The major elements will be discussed in ascending order of their relative atomic mass.

3.1.7.1 Major elements

- **Magnesium** (as MgO). MgO is commonly associated with detrital, light silicates. It also forms an important component of the dissolved ions in the seawater. It is prominently represented within dolomites due to cation exchanges (de Barry Barnett and Wilson, 1960; Burgan *et al.,* 2008; März *et al.,* 2009). Burgan *et al.* (2008) demonstrated that elevated values of MgO and depletions of CaO are related to weathering effects on the original source material.
- **Aluminium** (as Al_2O_3). The bulk of Al_2O_3 in shales belongs to the clay mineral fraction (detrital silicates – terrigenous), a result of the weathering and breakdown of alumosilicates, most prominently feldspars (de Barry Barnett and Wilson, 1960; Cox *et al.,* 1995; Djarnia and Fekirine, 1998; Wei *et al.,* 2003; Galindo *et al.,* 2007; März *et al.,* 2009). High concentrations of SiO_2, Al_2O_3, K_2O, Fe_2O_3 combined with low CaO and MgO contents are commonly interpreted to reflect the dominance of silicate minerals (e.g. illite, kaolinite, chlorite, smectite) and only a subordinate contribution of carbonates, like calcite and dolomites (Burgan *et al.,* 2008). High Al_2O_3 contents can indicate a relatively high intensity of weathering and increased maturity of the sediment. Al enrichments can be associated to scavenging of Fe-oxyhydroxides, biogenic opal (acting as a vessel transferring most of the aluminium to the sea-floor) and clay minerals from the water column (Wei *et al.,* 2003). It can also be related to the organic particle flux via adsorption of dissolved Al from the sea-water, and it has consequently been used as a proxy-element for palaeo-bioproductivity (Murray and Leinen, 1996; Calvert and Pedersen, 2007). Al/Ti ratios are used to track opal accumulations and siliceous bioproductivity. Aeolian dust transported via storm events into the sedimentary basin can have a major impact on absolute Al_2O_3 concentrations (Wei *et al.,* 2003; Calvert and Pedersen, 2007). Long-term, multiple recycling leads to sediments enriched in quartz (sand and silt size fractions) and illite (within the clay minerals). This recycling process increases the compositional maturity of the sediments. As a consequence, the coarser grained sediments will start to exhibit trends towards pure quartz arenites and the finer grained, mudrocks will become more potassic and aluminous (Cox and Lowe, 1995).
- **Silicon** (as SiO_2). In sedimentary rocks, silicon is generally associated with components such as clastic quartz, siliceous fossils and alumosilicate minerals (de Barry Barnett and

Wilson, 1960; Kuroda *et al.,* 2005). Enrichments of silica can be related to an increased influx of terrigenous material and biogenic processes, such as the biomineralisation of skeletons and shells (Calvert and Pedersen, 2007).

- **Potassium** (as K_2O). K_2O is considered to represent the detrital fraction in shales (Wei *et al.,* 2003), originating from the weathering and breakdown of feldspars. It is typical for light silicates (März *et al.,* 2009) such as feldspars, micas and slightly hydrated clays (Serra, 1984). The relative proportions of Al, Si, K and Ti in shales are mainly controlled by weathering, transport and depositional processes (Burgan *et al.,* 2008). If the contents of K_2O are high then it can signify the abundance of illite, formed by the addition of K^+ (which is a major soluble cation within the sea-water) to kaolinite (Wei *et al.* 2003). This process is also known as 'illitization' of kaolinite (Pearce *et al.,* 1991; Fedo *et al.,* 1997). High K_2O levels can also indicate, that the sediments have not undergone extensive leaching during the erosional processes (Burgan *et al.,* 2008). A positive correlation of K_2O to Al_2O_3 indicates that these elements are of detrital origin (Abdou and Shehata, 2007; Burgan *et al.,* 2008). K_2O/Al_2O_3 ratios are used to elucidate the original composition of mudrocks (Cox *et al.,* 1995). Elevated K values are interpreted to be typical for granitc source areas. Another enrichment process for K is the long-term recycling of sediments as described under the Al_2O_3 section.
- **Calcium** (as CaO). Can occur as carbonates, phosphates, and within aluminosilicate minerals in sedimentary rocks (Kuroda *et al.,* 2005). Within black shales calcium co-exists in various mobile forms (Galindo *et al.,* 2007), predominantly as calcite and/or dolomite. However it can also be present within silicate minerals such as anorthite. For black shales, typically low CaO values document the carbonate deficiency of the environment. This depletion in Ca can be the result of the palaeogeographical positioning of the respective sedimentary basin or it can be the result of Sr substituting Ca (Burgan *et al.,* 2008). Lipinski *et al.* (2003) suggested that carbonate contents are lower in TOC-rich sediments due to dilution effects.
- **Titanium** (as TiO_2). TiO_2 is considered to represent the detrital (terrigenous) fraction in shales (Murray and Leinen, 1996; Wei *et al.,* 2003). It is commonly associated with the heavy mineral rutile, that can also contain considerable amounts of the elements Cr, V, Mn and Sn (de Barry Barnett and Wilson, 1960). The source of excess titanium in pelagic marine sediments is interpreted to be predominately aeolian dust (Sageman *et al.,* 2003).

Positive correlations of Mg and Ti with Al indicate their association with the alumosilicate fraction (Burgan *et al.,* 2008). Ti/Al and Ti vs. Al plots are used to discriminate between various source areas, in particular to distinguish between areas of predominantly granitic or basic composition (Abdou and Shehata, 2007). Ti is considered to be a better proxy for the terrestrial influx compared to Al, as the total Al concentrations can be partly of authigenic or biogenic origin (Wei *et al.,* 2003).

- **Manganese** (as MnO). Under oxic conditions Mn tends to form highly insoluble Mn(IV)-oxyhydroxides, which can act as a substantial trace element sink, preventing the recycling of trace elements into the overlying water column (Calvert and Pedersen, 2007). In anoxic sediments at the sediment/water interface, Mn is reduced and transformed from insoluble Mn(IV)-oxide to highly soluble Mn(II)-sulphide. Mn(II) is not found in black shales, as it is not readily adsorbed to organic matter (Calvert and Pedersen, 1993; Algeo and Maynard, 2004). As Mn(II) is highly soluble it easily migrates within the sediment column upwards or downwards. The downwards migration commonly leads to $MnCO_3$ precipitation within concretions under oxic bottom waters conditions, the upwards diffusion finally results in the dissolution of Mn(II) into the water column and hence its removal from the sediment. This usually occurs in anoxic basins (Tribovillard *et al.,* 2006). Mn is usually associated with other redox sensitive elements and is consequently used as a proxy for redox conditions (Elbaz-Poulicheet *et al.,* 1997; Wei *et al.,* 2003; Elbaz-Poulichet *et al.,* 2005; Chun and Delaney, 2006; Schröder and Grotzinger, 2007). However, Tribovillard *et al.* (2006) cautioned the use of Mn as a redox proxy, due to its highly mobile nature in chemically reducing sediments.
- **Iron** (as Fe_2O_3). Iron is generally associated with alumosilicates, iron oxides and sulfides such as pyrite in sedimentary rocks (Kuroda *et al.,* 2005). The main source of iron can be located to be within the detrital influx. Under oxygen depleted (anoxic - euxinic) conditions Fe oxide and oxyhydroxides are commonly reduced, either biologically or non-biologically (März *et al.,* 2009). If free hydrogen sulphide (H_2S) is present then Fe-oxides (reactive iron) are transformed into Fe-sulphides, most commonly pyrite (FeS_2) in the form of framboidal pyrite (Werne *et al.,* 2002). If there is no free Fe available for H_2S to react with, then the accumulated H_2S at the sediment-water interface usually reacts with the organic material present: a process known as 'sulfurization' (Wignall, 1994; März *et al.,* 2009). High Fe concentrations can also be related to the formation of Fe-hydroxides and/or the presence

of detrital biotite (Burgan *et al.,* 2008). Ciglenečki *et al.* (2006) noted, that FeS_2 can adsorb trace elements to its reactive surface and therefore act as an important sink for Mo, Mn, Co, Cu, Ni and Cr. The presence of H_2S and the thereby induced reactions result in the removal of Ag, Cd, Cu, Ni and Zn out of solution, forming generally insoluble sulphides (Calvert and Pedersen, 2007). The absence of a strong correlation with Al_2O_3 can be interpreted to indicate an authigenic origin of Fe-oxides and may hence be used as a proxy for the prevailing redox conditions during Fe-oxide formation (Abdou and Shehata, 2007). Fe concentrations (and speciation) as well as Fe/Al ratios are widely used as a proxy for pyrite formation and redox conditions using the 'Degree of Pyritization' (DOP), which will be reviewed later in this chapter (Lyons *et al.,* 2003; Wei *et al.,* 2012). In the presence of sufficient amounts of detrital iron and times of enhanced organic matter burial, the amount of diagenetic pyrite formed will show a highly significant, positive correlation to TOC due to H_2S formation at the sediment-water interface (Schultz, 2004). If the iron does not show any correlation with S, then the iron may reside within the residual fraction, which is commonly composed of iron containing silicate minerals (Galindo *et al.,* 2007). A negative correlation between iron and silicon is commonly regarded to indicate changes within the environment or the provenance area of the original source material (Burgan *et al.,* 2008).

3.1.7.2 Trace elements

In the following only the geochemistry and the chemical behaviour of trace elements analysed for this study will be briefly discussed, again they have been sorted into ascending relative atomical mass.

- **Phosphorous (P)**. P is mainly present as HPO_4^{2-} in modern day oceans, where it is strongly coupled to the cycles of Fe and OM (März *et al.,* 2009). Under oxic conditions Fe oxides and oxyhyroxides can adsorb substantial amounts of P along with OM both acting as carriers of P to the sea-floor (Tribovillard *et al.,* 2006; Calvert and Pedersen, 2007). The formation of Fe oxides can also lead to the co-precipitation of phosphates. Within reducing environments P is separated from Fe oxides and OM, subsequently released as PO_4^{3-} back into the water column and there re-utilised as a readily available nutrient for phytoplankton. It becomes hence re-introduced to the biological cycle resulting in low burial rates of P together with OM. High bioproductivity combined with a high accumulation rate

of OM may therefore develop without any significant P burial. Because of the rather intricate processes described above, the use of P as a productivity proxy is not straight forward (Tribovillard *et al.,* 2006; März *et al.,* 2009). In detrital form P exists predominantly as the calcium phosphate mineral apatite (de Barry Barnett and Wilson, 1960).

- **Sulphur (S)**. Sulphur is present in anoxic, OM rich sediments as a result of bacterial sulphate reduction. The bacterial sulphate reduction requires sulphate dissolved in pore-waters as an electron donor for the oxidation of OM in the absence of oxygen (Dean *et al.,* 1984). Sulphate reduction occurs once all other oxidants (such as O_2 > Mn-oxides > NO_3 > Fe-oxides) have been used and are hence depleted (Dean *et al.,* 1984). Excess S is locked within metal sulphides in the overlying water column, if there are free reactive trace metals available (März, 2009; Lipinski *et al*., 2003; Dean *et al.*, 1984).
- **Scandium (Sc)**. Little is known about the chemical behaviour of Sc in organic rich shales. Sc concentrations in sea-water are very low. It is associated mostly with detrital terrestrial material in marine sediments. It is a highly compatible chemical element in the continental crust, which means that it is not highly concentrated in any non-biological mineral (Wei *et al.,* 2003). However, Sc can be slightly enriched within biogenic apatite and ferromanganese oxide minerals in pelagic sediments (Wei *et al.,* 2003). Sc behaves like REE's in sedimentary rocks and is enriched in weathering residues (Wei *et al.,* 2003).
- **Vanadium (V)**. Vanadium is a redox sensitive element with strong euxinic affinity like U, Mo and Zn (Algeo *et al.,* 2004). Its geochemical behaviour is similar to that of Ni (Wignall, 1994). V is present in a wide variety of minerals, but by far the most important being patronite (VS_4) (Hillebrand, 1907) and vanadinite (Pb_5)(VO_4)$_3$Cl (Trotter and Barnes, 1958). Under oxic conditions V is normally present as an oxy-anion (HVO_4^{2-}, $H_2VO_4^-$) or as V(V). It can be incorporated into Mn + Fe – oxides and hydroxides, possibly also into kaolinite, which all act as vessels to the sea-floor. When dissolved, vanadium tends to occur as a V(IV) - vanadyl ion, that is easily adsorbed to clay particles once reduced to V(III) during burial (Wignall, 1994; Elbaz-Poulicheet *et al.,* 1997; Jones and Manning, 1994 in: Schröder and Grotzinger, 2007). The removal from the water column and the subsequent transfer to the sediment are facilitated by principally two processes: [1] Under anoxic conditions V(V) is reduced to V(IV) because of the simultaneous oxidation of organic compounds, like humic and fulvic acids. This chemical reduction process leads to the formation of soluble ($VO(OH)_3^-$) - hydroxyl species, which remain dissolved within the water column, as well as

insoluble ($VO(OH)_2$ - hydroxides that precipitate out of solution and are adsorbed onto clay minerals at the sediment-water interface. The direct participation of organic substances (humic and/or fulvic acids) during this chemical reactions generally results in a strong positive correlation between V and TOC (Brumsack, 1986; Calvert and Pedersen, 1993; Arthur and Sageman, 1994; Algeo and Maynard, 2004; Abanda and Hannigan, 2006; Tribovillard *et al.,* 2006; Abdou and Shehata, 2007; Schröder and Grotzinger, 2007; März *et al.,* 2009; Pi *et al.,* 2013). [2] Under sulphidic conditions (characterised by the presence of H_2S) V(IV) is further reduced to V(III) and forms insoluble ($V(OH)_3$) - hydroxides and (V_2O_3) – oxides which directly precipitate out of solution and are subsequently transferred to the sediment. As these reactions are carried out without any involvement of organic materials, V shows typically no correlation with TOC values (Calvert and Pedersen, 1993; Arthur and Sageman, 1994; Tribovillard *et al.,* 2006; März *et al.,* 2009; Pi *et al.,* 2013). A third process is offered by the incorporation of V into FeS during sulphide formation. However, evidence in support of this process is currently scarce and controversial, leaving this model as a matter of still ongoing debate (Algeo and Maynard, 2004; Tribovillard *et al.,* 2006). During the lithification and following diagenesis, V(III) readily substitutes Al at the octahedral sites of authigenic clay minerals, a reaction known also to take place extensively in the course of the recrystalisation of clay minerals (Tribovillard *et al.,* 2006).

- **Chromium (Cr)**. Cr belongs to the group of redox sensitive elements (Lipinski *et al.,* 2003). Cr can be fixed in high amounts in sediments under reducing conditions either by OM via biocycling (according to Brumsack (1986) Cr is regarded to be an important nutrient for phytoplankton) or by the adsorption to Fe- and Mn- oxyhydroxides (Calvert and Pedersen, 1993). In oxic environments Cr is present as Cr(VI) within the anion ($CrO^{2}_{4}^{-}$). Under anoxic conditions is Cr(VI) typically reduced to Cr (III) to form aquahydroxyl or hydroxyl cations ($Cr(OH)_2^{+}$. Cr(III) containing molecular complexes are being precipitated as insoluble $Cr(OH)_3$ or Cr_2O_3 under high pH levels and incorporated into humic or fulvic acids under low ph conditions. Cr(III) is not known to form an insoluble sulphide and is hence not incorporated into pyrite due to its structural and electronic incompatibilities (Tribovillard *et al.,* 2006), unlike other trace elements such as Mo, Pb, Cu, Ni and Zn (Algeo and Maynard, 2004). Consequently, when OM/oxyhydroxides are remineralised by sulphate-reducing bacteria, Cr may be lost to the overlying water column (Tribovillard *et al.,* 2006). Cr is frequently used together with V (V/Cr ratio) to evaluate and quantify redox conditions

(Wignall, 1994; Abdou and Shehata, 2007) within the diagenetic nitrate reduction zone (see also **Chapter 3.1.5** Diagenesis and degradation of organic matter). V/Cr values above 2 are interpreted to indicate anoxic conditions, whereas values below 2 are thought to be indicative for oxic conditions (Schröder and Grotzinger, 2007; Nagarajan *et al.,* 2007). Aside the phases that undergo changes and alterations whilst being metabolised through the biocycle, Cr is mainly hosted within the detrital fraction of sediments by minerals such as chromite, clay minerals where Cr substitutes Al and a wide range of ferromagnesian minerals where Cr substitutes Mg (Calvert and Pedersen, 1993; Wignall, 1994; Algeo and Maynard, 2004; Tribovillard *et al.,* 2006; Nagarajan *et al.,* 2007).

- **Cobalt (Co)**. Co belongs to the redox-sensitive/sulphide forming trace elements (Lipinski *et al.,* 2003). Within sediments Co is strongly tied to the detrital fraction, limiting its use as a reliable redox proxy (Brumsack, 1986; Algeo and Maynard, 2004; Tribovillard *et al.,* 2006). In oxic environments Co is typically present as a dissolved cation (Co^{2+}), although it can also be associated with humic and fulvic acids (Algeo and Maynard, 2004; Tribovillard *et al.,* 2006; Charriau *et al.,* 2011). Co can be accumulated in high amounts within sediments under reducing conditions, either by being bound to OM or by forming autonomous sulphides (CoS) or co-precipitated together with Fe-sulphides (Lipinski *et al.,* 2003; Algeo and Maynard, 2004). Co uptake is kinetically slow, its concentrations in authigenic sulphides are therefore low (Algeo and Maynard, 2004). In unaltered sediments formed under euxinic conditions Co shows positive correlations with other redox sensitive elements such as U, V and Zn.
- **Nickel (Ni)**. Is considered a redox sensitive and sulphide forming element (Lipinski *et al.,* 2003). It is present in both the organic and detrital fractions of sediments, in the form of Fe oxides, hydrous Fe and Mn oxides and clay minerals (Algeo and Maynard, 2004; Charriau *et al.,* 2011). In oxic to suboxic waters Ni appears either as a soluble cation (Ni^{2+}, $NiCl^{+}$) or adsorbed to humic and fulvic acids (Algeo and Maynard, 2004; Tribovillard *et al.,* 2006; März *et al.,* 2009). As an important nutrient Ni is a strong biolimiting element and involved within the biological cycle during primary production (Calvert and Pedersen, 1993; Wignall, 1994; Tribovillard *et al.,* 2006; März *et al.,* 2009; Piper and Calvert, 2009). The resulting OM serves as a carrier for Ni to the sea-floor. Under dysoxic conditions Ni tends to form molecular complexes with OM. Under anoxic conditions the presence of H_2S leads to the precipitation of NiS. However, it may also be incorporated into FeS (Wignall, 1994; Algeo

and Maynard, 2004; Tribovillard *et al.,* 2006). Secondary coupling of Ni to OM can form during the process of OM sulfurisation, although in the course of the same process Ni can also be released (März *et al.,* 2009). The overall geochemical behaviour of Ni is very similar to that of V.

- **Copper (Cu)**. Is considered to be a redox sensitive element (Lipinski *et al.,* 2003). It is either fixed in sediments under reducing conditions by being bound to OM (acting as a nutrient within biocycling (Calvert and Pedersen, 1993; Algeo and Maynard, 2004), or is precipitated as autonomous sulphides or co-precipitated together with Fe-sulphides (Lipinski *et al.,* 2003). The transfer of Cu from the water column to the sediment via the soluble $CuCl^{+}$ ions is either facilitated by forming organic metal ligands in humic acids (Tribovillard *et al.,* 2006; Algeo and Maynard, 2004) or by the adsorption to Fe-Mn-oxyhydroxides. Cu may be lost to the overlying water column when the OM and/or oxyhydroxides are being remineralised by sulphate-reducing bacteria (Algeo and Maynard, 2004; Tribovillard *et al.,* 2006). Under anoxic conditions Cu(II) is reduced to Cu(I) and is subsequently precipitated as CuS or Cu_2S as an independent sulphide phase or it is incorporated into FeS (Algeo and Maynard, 2004; Tribovillard *et al.,* 2006). In unaltered sediments Cu shows therefore show strong associations to OM and other redox sensitive elements (e.g. Ni, Zn and U). In (hemi-) pelagic sediments with low accumulation rates Cu may be fixed during the authigenic formation of nontronite or smectite minerals (Tribovillard *et al.,* 2006). Cu/Zn ratios are being used as redox indicators, with high values indicating reducing conditions and low values specifying oxidising conditions (Nagarajan *et al.,* 2007).
- **Zinc (Zn)**. Zn is a redox sensitive, sulphide forming element (Lipinski *et al.,* 2003) of strong euxinic affinity comparable to Mo, U and V (Algeo *et al.,* 2004). It is present under oxic to suboxic conditions in form of a soluble Zn^{2+} and $ZnCl^{+}$ - cations or, as an important bio-limiting nutrient for phytoplanktonic organisms, directly incorporated into OM (Brumsack, 1986; Calvert and Pedersen, 1993; Algeo and Maynard, 2004; Tribovillard *et al.,* 2006). The OM resulting from the planktonic biomass serves as the main carrier from the water column to the sediment (Brumsack, 1986). It can also be adsorbed to precipitating Fe-Mn oxides and hydroxides, that will act as additional vessels for the transfer to the sea-floor (Tribovillard *et al.,* 2006). Zn in the absence of OM and Fe-Mn oxides and hydroxides adsorbs to the reactive surface of clay minerals and is hence used as a proxy to estimate the clay fraction within siliciclastic sediment (Svendsen and Hartley, 2001). For this

purpose it is regarded to be far more reliable than the obvious Al_2O_3, as Al_2O_3 is also present within other minerals than clays, such as for example feldspars (Svendsen and Hartley, 2001). Under reducing conditions and in the presence of H_2S, zinc sulphides (e.g. galena, ZnS – sphalerite ((Zn/Fe)S)) are more readily formed than FeS, yet Zn can also be incorporated into the FeS crystal lattice (Algeo and Maynard, 2004; Tribovillard *et al.,* 2006). The correlation or the non-correlation of the elemental ratios Zn/Al to TOC/Al and S/Al is used to determine, whether the sedimentary Zn is localised within the sulfurised OM or directly in pyrite (März *et al.,* 2009). The decay of OM by sulphate reducing bacteria can liberate Zn from the organic-metal complexes, which is then commonly taken up by authigenic FeS (Algeo and Maynard, 2004), thus leading to an systematic Zn - enrichment of the sulphide phase and a consequent depletion of Zn within the OM. High amounts of Zn within coarser clastic sediments are sometimes related to syn- or post-depositional hydrothermal activity (Lipinski *et al.,* 2003; Charriau *et al.,* 2011).

- **Arsenic (As)**. As can be adsorbed to Fe/Mn hydroxides. Under reducing conditions the dissolution of these hydroxides result in the release of As. The inorganic species of As (As(III) and As(V)) are largely controlled by the redox state of the environment, with the reduction of As(V) leading to the formation of As(III). During the formation of pyrite As(III) is readily adsorbed to its reactive surfaces leading to so called ‘arsenical pyrite’ (de Barry Barnett and Wilson, 1960). The oxidation of arsenopyrite is also known to be a prominent mechanism responsible for the accumulation of As (Xie *et al.,* 2009). The organic species, monomethylarsonate (MMAs) and dimethylarsonate (DMAs) are frequently found within natural waters, and contribute significantly to As speciation. It has been shown that malcroalgae and phytoplankton have the capability to reduce or methylate As(V) within the water column. The subsequent degradation of phytoplankton and associated organic matter through bacterial activity is known to generate a wide variety of organoarsenical species (Elbaz-Poulicheet *et al.,* 1997). Brumsack (1986) suggested, that the biocycling of As may not be significant, as modern day sea-water exhibits little concentration changes with increasing depth, unlike for example Cd and Zn (discussed below). As a redox sensitive element As is used to evaluate the environmental redox conditions.
- **Rubidium (Rb)**. Rb is considered a detrital element, that is normally enriched in shales and siltstones. In shales it is associated with the fine grained detrital fraction and resides within clays and micas, hence commonly showing positive correlations with Al_2O_3 and K_2O

(Dypvik and Harris, 2001; Kampunzu *et al.,* 2005; Xu *et al.,* 2010). For the geochemical characterisation of siliciclastic sediments Rb is often used as a grainsize indicator. K/Rb ratios have been demonstrated to be indicative for different salinity levels (Burgan *et al.,* 2008), with K/Rb ratios between 250-300 for non-marine to brackish and 150-200 for marine shales (Campbell and Williams, 1965 in: Abdou and Shehata, 2007).

- **Strontium (Sr)**. The chemical behaviour and systematics of Sr in sedimentary rocks is complicated (Veizer and Demovič, 1974). Sr is a major component of sea-water, being present in modern day oceans in concentrations of ~8 mg/l (Turekian, 1964). According to Turekian (1964) the oceanic Sr concentrations are mostly controlled by the weathering of limestones (adding Sr to the oceanic Sr pool) and diagenetic processes (responsible for the removal of Sr). Sr is considered to be a non-essential biological element, however, because of its intermitting ion radius it can substitute for Ca^{2+} and Ba^{2+} in living organisms (Turekian, 1964; De Vos *et al*. 2006). Sedimentary processes can strongly influence the distribution of Sr. The Sr content can be controlled by its adsorption to various clay minerals. However, Turekian (1964) suggested that clay minerals are not an efficient device for the removal of Sr in deep sea environments, as clay minerals exhibit only extremely low exchange adsorption rates as defined by the respective mass-action equilibrium equations (Wahlberg *et al*., 1965). The major sink for Sr is deemed to be deep-sea carbonate deposits via the extensive substitution of Sr^{2+} for Ca^{2+} ions in carbonate minerals (such as aragonite), and to a lesser extent by the exchange of K^{+} ions in rock forming minerals such as K-feldspar and plagioclase (De Vos *et al*., 2006). Feldspars are considered to be the principal carrier of Sr in sedimentary rocks. Ba^{2+} ions within baryte ($BaSO_4$) and witherite ($BaCO_3$) can also, under certain circumstances, be substantially substituted by Sr (De Vos *et al*., 2006). Low temperature palaeoenvironmental conditions (as normally in higher latitudes) of deposition can significantly influence the distribution of sedimentary Sr concentrations (Dypvik and Harris, 2001; Kiipli *et al.,* 2004). Sr shows a similar geochemical behaviour as Ca and Ba, which implies that it can substitute both of these elements easily (Krauskopf and Burg, 1995; De Vos *et al*., 2006). The generally low concentrations of Sr in black shales are considered to be related to the low concentrations of Ca within this type of sediment and the absence of certain Sr containing rock forming minerals such as gypsum ($CaSO_4.2H_2O$), celestite ($SrSO_4$), strontianite ($SrCO_3$), hornblende and plagioclase. The very rare occurrence of celestite and strontianite within

fine-grained siliciclastic deposits is most commonly interpreted to indicate post-depositional hydrothermal activity or evaporitic conditions within extreme shallow water environments (Turekian, 1964; De Vos *et al*., 2006). Burgan *et al.* (2008) suggested that low concentrations of Sr in sediments are related to deposition under chemically reducing environmental conditions. In aqueous environments with pH values below 4.5, Sr is apparent as the highly mobile Sr^{2+} ion. Under neutral (pH 5 – 7.5) environmental conditions $SrSO_4$ forms, and finally, under alkaline (>pH 8) conditions $SrCO_3$ is dominant (De Vos *et al*., 2006). Within the published literature Rb/Sr ratios have been used to infer the intensity of the chemical weathering that affected the hinterland from which the sediments derived (Taylor *et al*., 1983; Xu *et al.,* 2010; Romer and Hahne, 2010). Higher values are interpreted to indicate intense weathering, lower values are thought to point towards more moderate weathering conditions. Chemical weathering can ultimately lead to leaching of the Ca-Sr system, leaving a residue enriched in K-Rb and depleted in Ca-Sr (Xu *et al.,* 2010; Romer and Hahne, 2010). Higher Sr concentrations can occur within granitic rocks, where Sr and Ba correlate with Ca, particularly within feldspar minerals (Burgan *et al.,* 2008). The fractionation of these two elements can occur during the selective weathering of these feldspars. Weathering of plagioclase results in the depletion of Sr relative to Ba as plagioclase is easier to weather than K-Feldspar, furthermore, Sr is more mobile relative to Ba (Nyakairu and Koeberl, 2001; De Vos *et al*., 2006). Sr/Ca ratios have been utilised as a salinity proxy with low values indicating fresh water conditions and opposing high values relating to the development of marine saline conditions (Turekian, 1955; Dodd and Crisp, 1982; Limburg, 1995; Chang *et al*., 2004).

- **Zirconium (Zr)**. Zirconium resides in the heavy mineral fraction (Zr is the cation in zircon) and is commonly associated with the coarser grained fraction of otherwise fine grained sediments (Svendsen and Hartley, 2001). Typically, higher Zr values are found in sandstones than in shales. Zr is commonly used as a terrigenous (detrital) proxy element along with Ti (Zr/Ti ratios). Higher Zr/Ti – ratios are considered to indicate an input of siliciclastic sediments sourced from shallower and more energetic environments (de Barry Barnett and Wilson, 1960; Lipinski *et al.,* 2003; März *et al.,* 2009).
- **Molybdenum (Mo)**. Mo is considered a redox sensitive element with a strong euxinic affinity. It has been demonstrated to be a useful and important palaeoredox indicator (Calvert and Pedersen, 1993; Lipinski *et al.,* 2003; Algeo *et al.,* 2004; Wilde *et al.,* 2004). In

sea-water under oxic to suboxic conditions Mo is present as Mo(VI), mostly in the form of the soluble oxy-anion molybdate - MoO_4^{2-} (Calvert and Pedersen, 1993; Tribovillard *et al.,* 2006; März *et al.,* 2009). With concentrations up to 10 ppb, Mo is one of the most abundant trace metals in modern oceans (Brumsack, 1986; Wignall, 1994; Werne *et al.,* 2002; Algeo and Maynard, 2004; Schröder and Grotzinger, 2007; Piper and Calvert, 2009) and it is also one of the most enriched trace metals in organic rich black shales (Brumsack, 1986; Wignall, 1994). The concentrations of Mo can be correlated to the amount of OM within an environment (Vine and Tourtelot, 1970), as it is incorporated into OM via the adsorption to humic acids (Brumsack, 1986; Tribovillard *et al.,* 2006). High concentrations of Mo have been regarded to be a powerful proxy for high palaeo-bioproductivity. Mo in its oxic form is considered to play an important role during the biological processes of N fixation and is rapidly scavenged by Mn oxides or oxyhydroxides (Calvert and Pedersen, 1993; Lipinski *et al.,* 2003; März *et al.,* 2009). In the presence of H_2S, which is an essential component to Mo fixation (Lyons *et al.,* 2003; Meyers *et al.,* 2005), the Mo oxy-anion is converted to particle-reactive (MoS_4^{2-}) - thiomolybdates (März *et al.,* 2009; Pi *et al.,* 2013). These are readily extracted by and added into sinking OM (predominantly humic substances) and also incorporated into FeS (Brumsack, 1986; Algeo and Maynard, 2004; Elbaz-Poulichet *et al.,* 2005; Tribovillard *et al.,* 2006; Schröder and Grotzinger, 2007; Calvert and Pedersen, 2007; März *et al.,* 2009). Element ratios such as Mo/Al, S/Al and the ratio of TOC/Al are used to determine whether Mo is incorporated within the non-biogenic particles of the sediment, sulphurised OM or FeS (e.g. Hild and Brumsack, 1998; Warning and Brumsack, 2000; März *et al*., 2008).

- **Silver (Ag)**. Is regarded to belong to the group of redox sensitive elements. It can be fixed in high amounts within sediments under reducing conditions as it is readily adsorbed to organic matter and sometimes even acting as a nutrient (Calvert and Pedersen, 2007). However, little is known about the exact chemical behaviour of Ag under reducing conditions (Lipinski *et al.* 2003).
- **Cadmium (Cd)**. Cd is an important nutrient for phytoplankton within the marine water column (Cullen *et al*., 1999; Lane *et al.,* 2005; Xu and Morel, 2013). It is present under oxic to suboxic conditions as a soluble cation ($CdCl^+$ or Cd(II)) within the water column as is there incorporated into OM which serves as its main carrier to the sea-floor (Calvert and Pedersen, 1993; Tribovillard *et al.,* 2006). Cd forms cadmium sulphide (CdS) in the

presence of H_2S – far more readily than FeS, and forms separate sulphide phases rather than being incorporated together with FeS (Tribovillard *et al.,* 2006; März *et al.,* 2009). As Cd may be bound to OM via the biological cycle, the Cd/Al ratio is used as a palaeo-bioproductivity indicator within the geological record (Lipinski *et al.,* 2003). Cd is enriched in both mildly and strongly reducing sediments (Tribovillard *et al.,* 2006). FeS_2 may incorporate/adsorb Cd which makes it necessary to determine to what extent the sedimentary Cd is related to OM or pyrite by analysing the correlations between Cd/Al, TOC/Al or S/Al (März *et al.,* 2009; Charriau *et al.,* 2011).

- **Tin (Sn)**. Sn is considered to be detrital in nature. Within the water column the surface concentrations are high due to fluvial/aeolian input, but Sn is depleted rapidly with increasing depth throughout the water column because of its highly reactive nature (Brumsack, 1986).
- **Antimony (Sb)**. Sb has a similar geochemical behaviour to As (Elbaz-Poulicheet *et al.,* 1997) and under oxic conditions occurs as two stable forms (Sb(III) and Sb(V)). Sb is considered a redox sensitive element (Lipinski *et al.,* 2003) that is fixed to the sediment under reducing conditions either by OM or as autonomous sulphides that are co-precipitated together with FeS. A reduction step is required at the redox boundary in order to immobilise Sb in reducing environments (Lipinski *et al.,* 2003).
- **Barium (Ba)**. Ba within marine systems is most commonly associated with detrital plagioclase crystals and micas. Concentrations of Al, K or Ti are used to correct for this detrital fraction (Tribovillard *et al.,* 2006). A further prominent Ba containing mineral phase is baryte ($BaSO_4$). The enrichment of Ba in pelagic sediments relative to crustal values is normally associated to baryte (Calvert and Pedersen, 2007). Ba concentrations are widely applied as an indicator for palaeoproductivity levels (Arnaboldi and Meyers, 2006), using the concentrations of biogenic Ba or Ba_{excess}, (see **Chapter 4.10.5** Bioproductivity for a detailed discussion). Under reducing conditions the baryte is commonly adsorbed to decaying organic detritus (Kiipli *et al.,* 2004; Tribovillard *et al.,* 2006; Chun and Delaney, 2006). Ba is also present in environments without significant organic detritus yet in far lower proportions (Brumsack, 1986; Bonn *et al.,* 1998). It should be noted, that the Ba proxy should be used with caution as baryte dissolution is known to occur within sulphate-depleted pore waters, similar to the chemical behaviour of Mn (Brumsack, 1986; Lipinski *et al.,* 2003). In other words, Ba may accumulate in sediments with high OM fluxes, but may

migrate with the onset of the early diagenesis (Tribovillard *et al.,* 2006). Hydrothermal fluids are commonly associated with Ba, Sr, Pb, Zn and Mn indicating that these fluids could affect/overprint the biogenic barium signal (Tribovillard *et al.,* 2006).

- **Mercury (Hg)**. Its main occurrence is in cinnabar (HgS). Cinnabar is known to form post depositional and is related to hydrothermal activity.
- **Lead (Pb)**. A redox sensitive/sulphide forming element. In oxic marine environments Pb is present as both, the Pb^{+}-cation and in form of the soluble ($PbCO_3$) Pb-carbonate (Algeo and Maynard, 2004). Under anoxic conditions Pb is rapidly removed from the water column, the depletion of Pb with increasing depth as it is more readily scavenged than it is released (Brumsack, 1986). As insoluble PbS it is commonly precipitated independent from FeS (Algeo and Maynard, 2004). Because of the rapid depletion (as described above) Pb exhibits only weak positive correlations with TOC, but it tends to correlate well with Mo and V, as Pb and Mo can together be incorporated in pyrite and V is co-precipitated as an oxyhydroxide (Algeo and Maynard, 2004; Charriau *et al.,* 2011).
- **Bismuth (Bi)**. Little is known about the chemical behaviour of Bi. It is considered to be a redox sensitive and sulphide forming element. It is easily bound to organic matter and precipitated as autonomous sulphides or co-precipitated together with Fe-sulphides, along with other redox sensitive elements such as commonly Co, Cu, Cr, Ni and to a lesser extent together with Ag, Cd, Mo, Re, Sb, Ti, U and V (Lipinski *et al.,* 2003). Slightly elevated Bi values are regarded to indicate its fixation in sulphides under anoxic conditions. However, these slight enrichments may also simply be related to its overall low abundance and relatively short residence time in sea-water.
- **Thorium (Th)**. Th concentrations mostly correspond to the detrital infux (silicate and Th-baring clay minerals) originating from acidic igneous rock types (Serra, 1984). Th is mainly found in clays of detrital origin, where it is adsorbed to the platelets, and to a lessor extent humic acids are known to act as a minor sink for Th. A considerable amount of Th was demonstrated to reside within in FeS fraction (Galindo *et al.,* 2007). The ratios of Th and U concentrations have been widely used as a redox indicator (Jones and Manning, 1994 in: Dypvik and Harris, 2001; Nagarajan *et al.,* 2007), with U/Th values below 1.25 suggesting oxic environments and values greater than 1.25 indicating suboxic to anoxic conditions (Arthur and Sageman, 1994; Svendsen and Hartley, 2001; Nagarajan *et al.,* 2007).

- **Uranium (U)**. U preserved in sedimentary basins derives from two fundamentally different sources. The [1] detrital U (U_{detr}) stems from detrital, U bearing minerals (e.g. zircon) that have been extracted from rocks exposed to weathering and erosion in the hinterland, whereas the [2] authigenic U (U_{auth}) ultimately results from redox driven precipitation of U out of solution from the water column. The major source of U in sea-water is the weathering of igneous (acidic), metamorphic and sedimentary rocks (Serra, 1984). The U is dissolved within ground waters and transported to the sea (Swanson, 1961). U is a highly redox sensitive element and strongly related to anoxic bottom waters (Lipinski *et al.,* 2003). Therefore, U can appear in relative high concentrations (Lüning *et al.,* 2000) of up to approximately 200 ppm (Fisher and Wignall, 2001) within organic rich black shales, compared to just 2.5 ppm within the average Upper Crust (Wedepohl, 1991) or 3.1 ppm within the international PAAS-(Post-Archaean Australian Shale) standard (Taylor and McLennan, 1985). However, under oxic water conditions U occurs predominantly as a soluble uranyl (U^{6+}) (tri)carbonate complex $UO_2(CO_3)_3^{4-}$, only near the redox boundary it appears in the form of the also highly soluble uranyl (UO_2^{+}) ion (Calvert and Pedersen, 1993; Wignall, 1994; Fisher and Wignall, 2001; Algeo and Maynard, 2004; Tribovillard *et al.,* 2006; Nagarajan *et al.,* 2007). Under anoxic conditions U is reduced to an insoluble state and will precipitate in form of authigenic minerals out of solution: in anoxic environments with active sulphate reduction the uranyl (U^{6+}) - complexes are reduced to insoluble (U^{4+} or U^{5+}) - fluoride complexes that are strongly adsorbed to organic matter and particle surfaces (Fisher and Wignall, 2001; Lev and Filer, 2004; Elbaz-Poulichet *et al.,* 2005; Schröder and Grotzinger, 2007; Nagarajan *et al.,* 2007). In particular the fixation of uranyl - ions to the organo-metal ligands of humic acids forms one of the major OM-driven sinks for authigenic U (Wignall, 1994; Elbaz-Poulicheet *et al.,* 1997; Lüning *et al.,* 2000). It can also precipitate unrelated to biological matter as crystalline uraninite (UO_2), mainly in the presence of H_2S (Algeo and Maynard, 2004; Pi *et al.,* 2013). It has been suggested that the U associated with settling OM and adsorption, only equates to a minor component of the total U budget in sediments. The concentration of U in diagenetic phases (such as apatite and monazite) is the main U sink in OM rich sediments (Lev and Filer, 2004). Permanent pore-water anoxia is required for a constant U fixation, as diagenetically induced re-oxygenation of the sediment will remobilise U^{4+} as it is converted back to soluble U^{6+}, resulting in its escape back into the overlying water column (Wignall, 1994;

Tribovillard *et al.,* 2006). Three important factors control the concentrations of authigenic U within sediments: [1] the intensity of the anoxia, [2] the abundance of fixing components (OM) and [3] the sedimentation rates (Wignall, 1994). The relationship between U and TOC in sediments is regarded to be strongly influenced by the [1] U content of the water column, the [2] carbonate content, the [3] sedimentation rate and finally, the [4] productivity vs. preservation of OC in sediments (Lüning *et al.,* 2003b). The U-TOC proxy is considered to be useful for even strongly weathered black shale successions, where the original OM has been largely destroyed by oxidation and dissolution (Lüning *et al.,* 2003b).

When interpreting the total U concentrations of sedimentary rocks, it is important to determine and separate the authigenic and detrital fractions of U in order to identify, reconstruct and quantify the extent of potential anoxia that may have prevailed during the time of deposition. Wignall and Myers (1988, in: Nagarajan *et al.,* 2007) introduced a formula, in which the total U is formed as the sum of the concentrations of the detrital and the authigenic U. They noted, that the amount of Th present within detrital U-bearing minerals is always on average three times higher than the concentration of U within these minerals. This allowed them to express the detrital amount of U as the equivalent of Th/3 and to arrive at the following equation: $\mathbf{U_{auth} = U_{tot} - (Th/3)}$. Authigenic U values below 5 are normally considered to represent oxic environments, whereas values above 5 are thought to be indicative for suboxic to anoxic conditions (Nagarajan *et al.,* 2007).

3.1.8 Elemental associations and environmental control

The main constituents of marine sediments are detrital minerals (mainly clays and quartz), authigenic FeS (and other sulphide phases), authigenic phosphate and finally OM (Chester, 1990; Wignall, 1994). The intensity of chemical weathering of the original source rocks greatly effects the major element composition of mudrocks (Cox *et al.,* 1995), such as the weathering and breakdown of feldspars ultimately controls the major elemental abundances of, for example K and the trace elements Sr and Ba (see Sr element description **Chapter 3.1.7**). The concentrations of specific elements within any siliciclastic sediment are predominantly controlled by the presence or absence of the following mineral classes (**Table 3.1**). The silicates correspond mostly to the detrital fraction of the sediments, whereas the formation of Fe- / Mn- hydroxides/oxides and sulphides is depending on and associated with the redox conditions of the water column. The hydroxides/oxides formed in

the oxic top waters act as carriers for various trace elements towards the sea-floor (see **Chapter 3.1.7**). The hydroxides/oxides are subsequently reduced in the presence of H_2S and the trace elements released are adsorbed/incorporated into OM or authigenic sulphides (mainly FeS). The chemical composition of the waters (and trace element enrichment in the sediment) at the sediment/water interface is reliant on [1] the sedimentation of metal-rich particulate material (detrital component), [2] trace metal adsorption onto clays, OM and Fe- / Mn- hydroxides/oxides, and [3] the reduction of the OM, Fe- / Mn- hydroxides/oxides and consequent capture of the released trace elements within solid phase authigenic sulphides.

Mineral classes	Mineral phases	Elements and oxides
Silicates (detrital component)	quartz, feldspars, mica, clay minerals	**SiO_2, Al_2O_3, TiO_2**, Fe_2O_3, MgO, CaO, **Na_2O, K_2O, Rb,** Sr, **Zr**, Ba and transition metals (adsorbed)
Carbonates	calcite, dolomite, siderite, etc	**CaO, MgO,** Fe_2O_3, MnO, Sr, Ba C, O
Phosphates	apatite	**P_2O, CaO,** Ce
Metal-oxides/Hydroxides/ Sulphides (authigenic component)	goethite, hematite, pyrite etc.	**Fe, Mn, transition metals (adsorbed)**, Zr, Ba
Organic Matter		**C, transition metals (absorbed)**, Ba

Table 3.1 Main components of siliciclastic sediments divided into mineral classes, associated mineral phases and their chemical composition. The most significant elements are highlighted in bold. Modified after Scheffler (2004) and Boggs (1995).

The enrichment of certain chemical elements within sediments is controlled by the following six factors: [1] heterolithic sedimentary successions and associated partial element mobilisation during diagenesis, [2] prevailing redox conditions within the water column and the sediment, [3] potential hydrothermal alteration, [4] aeolian influx, [5] fluvial runoff and [6] elemental composition of the seawater (Nijenhuis *et al.* 1999).

Piper and Calvert (2009) suggest that the concentrations of elements within marine sediments is controlled by two fundamental parameters: [1] terrestrial-derived clastics and subsequent transport

to the oceans via rivers and the atmosphere, and [2] syn- and postdepostional hydrothermal activity affecting the elemental concentrations for e.g. Ba, Sr Pb, Zn, Mn and Fe within deep ocean settings (Tribovillard *et al.,* 2006)

Trace elements in marine settings are either classified as lithogenous (detrital) or seawater sourced (authigenic). Algeo and Maynard (2004) developed and applied the following formulas in order to determine, whether a trace element is related to one of these two classes or to the organic fraction of the sediment.

$$\mathbf{X_{detr} = X/Al_{back} * Al} \quad \mathbf{(1)}$$

Where X_{detr} is the detrital concentration of trace element X (ppm); X/Al_{back} is the average Al-normalised ''background'' concentration of trace element X ($x\ 10^{-4}$); and Al is the Al concentration of the sample (wt.%).

$$\mathbf{X_{org} = [b_{at} + m_{at} \times TOC] \times Al - X_{detr}} \quad \mathbf{(2)}$$

X_{org} and X_{detr} are the 'organic' and 'detrital' concentrations of element X (ppm); b_{at} and m_{at} relate to the y-intercept, and slope of the 'anoxic trend' of element X respectively, with the 'anoxic trend' referring to sediments forming under nonsulphidic anoxic conditions, the y-intercept, and slope are taken from the correlation coefficients of the analysed redox sensitive elemental pairs (see Table 2 of Algeo and Maynard, 2004); TOC and Al are the TOC and Al concentrations of the sample in (wt.%).

$$\mathbf{X_{sulf} = X_{tot} - (X_{org} + X_{detr}).} \quad \mathbf{(3)}$$

X_{sulf} and X_{tot} are the ''sulfidic'' and total concentrations of element X (ppm), and X_{org} and X_{detr} are the previously calculated values.

Detrital Elements. Detrital elements are the major, and in some circumstances, trace elements, whose concentrations within a sediment are controlled by the amount of siliciclastic sediment influxes from the hinterland (mainly Si, Al, K, Ti and Zr). The sedimentary detrital fraction consists principally of silicate minerals such as quartz, feldspars, mica and clay minerals (see **Table 3.1**). For the important clay minerals illite and smectite, a strong positive correlation between Al_2O_3 and

K_2O is assumed to indicate their detrital origin (Burgan *et al.,* 2008). According to Tribovillard *et al.* (2006), the detrital fraction of any given element can be calculated using the formula:

$$\mathbf{X_{detr} = (X/Al)_{average\ shale} \times Al_{sample}} \quad \mathbf{(4)}$$

Where X_{detr} is the calculated detrital amount of the element in question, $(X/Al)_{average\ shale}$ corresponds to the X/Al ratio of the average shale within the analysed section in regards to the element in question, and Al_{sample} relates to the absolute Al concentrations of the sample in question.

The authigenic elemental fraction is calculated using:

$$\mathbf{X_{auth} = X_{tot} - X_{detr}} \quad \mathbf{(5)}$$

Where X_{auth} is the calculated authigenic amount of the element in question, X_{tot} is the total concentration of the element in question and X_{detr} is the previously calculated (**equation 4**) detrital component of the given element.

The determination of the detrital fraction of the sediments (or normalising to Al or Ti) is necessary to assess and quantify the enrichment of redox sensitive elements relative to given international standards.

Redox sensitive and sulphide-forming elements. Redox sensitive elements are major and trace elements whose sedimentary concentrations vary dependent on the extent of detrital siliciclastic influx, levels of OM and productivity rates, oxygen levels within the water column, and ultimately the sediment-type and the sedimentation rates (Arthur and Sageman, 1994; Killops and Killops, 2009). During anoxic conditions the trace elements Ag, As, Bi, Cd, Co, Cr, Cu, Fe, Mn, Mo, Ni, P, Pb, Sb, U, V and Zn are fixed either by incorporation into Mn/Fe-oxides and hydroxides, or by adsorption onto OM and clay minerals within the oxic, uppermost parts of an otherwise anoxic water column (Algeo and Maynard, 2004; Lipinski *et al*., 2003, März *et al*., 2009; Charriau *et al*., 2011) and transferred to the sediment-water interface, where they become incorporated into authigenic sulphides (Tribovillard *et al*., 2006, März *et al*., 2009). For euxinic and H_2S-enriched environmental conditions, the redox sensitive trace elements can be divided into two major groups depending on their chemical behaviour towards H_2S: [1] Trace elements of 'strong euxinic affinity' are Mo, U, V, Zn (Pettijohn, 1957 in: Berry and Wilde, 1978; Dean *et al.,* 1984; Algeo and Maynard, 2004), which usually showing strong correlations with OM and are taken up as solid solution in FeS or other sulphide phases. [2] Trace elements of 'weak euxinic affinity' (Cu, Ni, Cr, Co) which are not

strongly influenced by the presence of H_2S (Algeo and Maynard, 2004), yet reside within the OM or detrital fractions of the sediment (see **Figure 3.11**). The redox sensitive trace element concentrations and ratios can be used to reconstruct environmental conditions for the time of deposition.

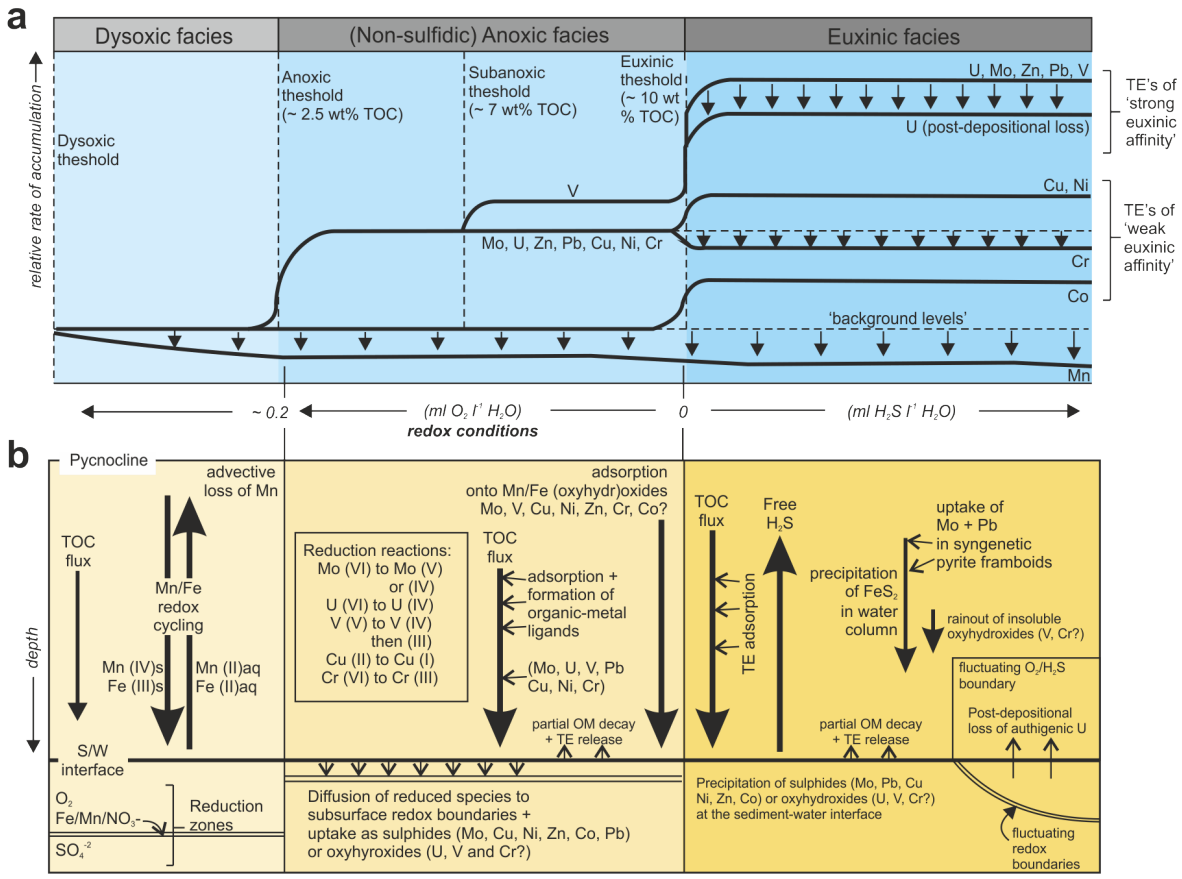

Figure 3.11. (a) Redox dependent enrichments of trace elements (TE) and enrichment-thresholds. The 'anoxic threshold' is defined to be at 2.5 wt% TOC and permits only minor enrichments of trace elements (with the exception of Co, that can act as a chemical catalyst); the 'sub-anoxic' threshold is set at 7wt% TOC, where moderate enrichment takes place, and the 'euxinic threshold' at 10wt% TOC at which drastic and rapid enrichment of trace elements occurs. Downward pointing arrows indicate the rapid depletion of [1] Mn within low-oxygen environments followed by [2] Cr in euxinic facies and [3] U in euxinic facies through post-depositional re-mobilisation. Benthic O_2-levels increase from the right to the left, whereas H_2S levels increase from the left to the right. **(b)** Process model showing the various chemical reaction-types and reaction-chains leading to systematic enrichment of shales by trace elements. Oxygen-content decreases from left to right. Boundaries between 'dysoxic' / 'anoxic' facies and 'anoxic' / 'euxinic' facies are set at thresholds of 0.2 and 0 ml O_2 l^{-1} H_2O respectively (modified from Algeo and Maynard, 2004).

3.1.9 Mobile, immobile and re-mobilised elements

Most of the redox sensitive elements described previously are highly mobile, dependent on the oxygen concentration within the water column and the sediment as well as on specific post-diagenetic conditions. When using trace element concentrations and ratios to reconstruct palaeoenvironmental conditions (i.e. productivity or redox state), it is important to use multiple elements as proxies, as single elemental data can be unreliable and misleading (Rollinson and Rollinson, 1993). In the absence of post-depositional re-oxygenation metal sulphides are stable

and not affected by diagenetic processes (Tribovillard *et al.,* 2006; Calvert and Pedersen, 2007), hence effectively trapping the incorporated redox sensitive elements within the sediments (see **Chapter 3.1.7**). However, relatively abrupt environmental changes caused by e.g. bioturbation or larger scaled turbiditic flows, but also climatically induced glacial-interglacial transitions can perturb the water column and re-suspend sediments resulting in the replenishment of oxidizing agents (Rollinson and Rollinson, 1993). For example, only small amounts of O_2 are needed in order to affect the U contents of the upper most parts of the sediments. The U is remobilised via its oxidation back to the soluble U^{6+} - state and escapes into the overlying water column (Wignall, 1994). Other elements such as V, Cd and Mo may also be affected by these reoxygenation- and remobilisation processes (Tribovillard *et al.,* 2006; Calvert and Pedersen, 2007), which have the potential to effectively mask if not completely obliterate the original palaeoenvironmental signal archived within the geochemical signatures.

Elements that are considered relatively immobile in aqueous solutions are Ti, Zr, Y, Nb and P (Rollinson and Rollinson, 1993). They are also relatively stable in the presence of hydrothermal fluids, during sea-floor weathering and remain immobile even up to medium metamorphic grades, making them ideal for palaeoenvironmental reconstructions but also plate-tectonic provenance discriminations (Floyd and Winchester, 1978; Bhatia, 1983; Floyd *et al.,* 1989; Rollinson and Rollinson, 1993).

3.1.10 Normalisation of major and trace elements and enrichment factor (EF) calculation

As mentioned previously, the major and trace element concentrations of marine sediments are a combination of detrital and authigenic components. Marine sediments often contain varying amounts of mineral phases of biogenic origin, like $CaCO_3$ and opal. These additional mineral phases dilute and alter the trace element abundances of the sediment (Tribovillard *et al.,* 2006). In fine grained marine sediments Al is commonly used as a normalising factor (Calvert and Pedersen, 2007) to eliminate the effects of this dilution and to smoothen the variability linked to the clay fraction, hence avoiding the influence of organic carbon, biogenic carbonate and silica contents on the original elemental composition. Normalisation to Al is only applicable, if the Al resides within the detrital clay fraction of the sediments and is demonstrated to have remained immobile during the diagenesis (Calvert and Pedersen, 1993; Dellwig *et al.,* 2000; Algeo and Maynard, 2004; Arnaboldi and Meyers, 2006; Herut and Sandler, 2006; Scopelliti *et al.,* 2006). The Al normalised values of

the trace elements are usually given as x 10^{-4}. The elemental X/Al - normalised values of the samples are used within enrichment factor (EF) plots, the elemental EF's are calculated as described in the following (Rule, 1986; Dellwig *et al.,* 2000; Tribovillard *et al.,* 2006; Scopelliti *et al.,* 2006; Turgeon and Brumsack, 2006):

$$\mathbf{EF_{element\ X} = X/Al_{sample} / X/Al_{average\ shale}} \quad \mathbf{(6)}$$

The $X/Al_{average\ shale}$ component will vary depending on the selected standard for comparison. The EF plots compare the elemental concentrations of the analysed sample in terms of enrichments (values greater than 1) and depletions (values less than 1) relative to a known standard. For the present study, the international standards for the 'upper continental crust' (Taylor and McLennon, 1985) and various shales: the 'Average Shale' (Turekian and Wedepohl, 1961; Wedepohl, 1971, 1991), 'Average black shale' (Vine and Tourtelot, 1970), Post-Archean Australian Shale 'PAAS' (Taylor and McLennon, 1985) and the North American Shale Composite 'NASC' (Gromet *et al.*, 1984) have been used.

Al normalisation must be used with caution as highlighted by Van der Weijden (2002), as the concentrations of Al can also be affected biologically to a certain extent (see **Chapter 3.1.7**). It is necessary to determine and quantify this potential error source by carefully analysing the correlation coefficients (r^2) of Al to relatively immobile elements of the detrital fraction such as Sc, Th or Zr (Tribovillard *et al.,* 2006; Pi *et al.,* 2013). Ti is also used as a normalising element, as it is associated with the heavy minerals of the detrital fraction (Kato *et al.,* 2002). This normalisation is again not without potential problems, as the post-depositional formation of authigenic rutile can compromise the significance of the total Ti readings and hence hamper the interpretation of the resulting Ti-normalised values (Calvert and Pedersen, 2007).

3.1.11 Gamma ray signals and API units

Gamma-ray spectrometry (Rider and Kennedy, 2011, with previous references therein) is used to measure the concentrations of the three most abundant natural radioactive elements in sediments: ^{40}K, ^{232}Th and ^{238}U (Adams and Weaver, 1958). A total gamma-ray (GR) log combines the three elemental signals into one curve, whereas a spectral gamma-ray (SGR) log displays the three components individually. A computed gamma-ray (CGR) log is generated by excluding the U

values. The K and Th concentrations reside within the detrital clay fractions of sediments (see **Chapter 3.1.7**). The U contents can be of detrital and authigenic origin as previously described (see **Chap 3.1.7**). Under oxic environmental conditions the U can either occur primarily, within the siliciclastic detrital fraction of for example zircon crystals, and secondarily, be incorporated within the detrital clay fraction via adsorption onto the reactive surface of the clay minerals. Within oxygen deficient environments, U will be incorporated into the sediment via the reduction-induced precipitation of authigenic U containing phases (Parkinson, 1996). Using the varying concentrations of K, Th and U differing lithologies can be determined and palaeoenvironmental conditions be inferred (Serra, 1984). For this purpose, K is normally assumed to determine the un-weathered detrital influx, Th is taken to indicate the degree of weathering and U is used as a powerful redox indicator (Rider and Kennedy, 2011).

In order to enable correlations and comparisons between various gamma-ray based datasets, it is often necessary to standardise these. This standardisation is carried out by converting the geochemical data for K, Th and U into the conventional American Petroleum Institute (API) units. The API units relate to an artificially radioactive concrete slab constructed at the University of Houston with known concentrations of K, Th and U (Serra, 1984; Doveton and Merriam, 2004). The artificial radioactive concrete is considered to have twice the radioactivity of a typical shale. In order to convert the measured geochemical values to API units the following calculation has to be applied, where the Th and U values are in ppm and the K values in wt% prior to the conversion (Doveton and Merriam, 2004):

API = 8U + 4Th + 16K **(7)**

The conversion factors used in **Equation 7** are the most commonly used.

3.1.12 Degree of pyritization

The degree of pyritization, DOP (Raiswell and Berner, 1985 in: Wignall, 1994; Wortmann *et al.,* 1999; Fisher and Wignall, 2001) is calculated by using the following calculation:

DOP = pyritic iron / pyritic iron + acid soluble Fe **(8)**

The DOP has been demonstrated to be a reliable redox indicator for marine sediments (Schultz, 2004). DOP values ranging from 0 – 0.45 indicate aerobic, oxygenated conditions (leading to little

or no pyrite formation), 0.45 - 0.75 a dysaerobic or dysoxic to anoxic environment, and finally, values ranging from 0.75 – 1 are taken to specify bituminous euxinic settings (Raiswell *et al.,* 1988 in: Arthur and Sageman, 1994; Murphy *et al.,* 2000; Werne *et al.,* 2002; Schultz, 2004). The sedimentation rates are known to have an effect on the DOP, with slower sedimentation rates leading to higher DOP values, especially, if clay-bound iron is included within the reactive iron component (Wignall, 1994; Murphy *et al.,* 2000).

3.1.13 Sediment recycling: Index of compositional variation (ICV)

The ICV is a parameter that can be used to determine the maturity of sediments and extent of sediment recycling (Cox *et al.,* 1995). The ICV allows the discrimination between sediments consisting of first-cycle material and sediments that have been formed by re-working of this first-cycle material, which typically leads to increased maturity. Within tectonically inactive settings such as cratons, siliciclastic sediments will normally express significantly higher calculated ICV values, indicating and reflecting the higher order recycling processes and consequent reworking of older sediments, and hence increased sediment maturity. In contrast, within tectonically active settings, the calculated ICV values will be typically low due to the relatively minor reworking and recycling of first-cycle sediments, and therefore exhibit a lower degree of compositional maturity (Cox *et al.,* 1995). The ICV is calculated by a formula, in which relatively mobile major elements are normalised to the relatively immobile aluminium:

$$\mathbf{ICV = [Fe_2O_3 + K_2O + Na_2O + CaO + MgO + MnO + TiO_2] / Al_2O_3} \qquad \mathbf{(9)}$$

The non-clay minerals have typically a higher ratio of the major cations to Al_2O_3 than the clay minerals (Cullers and Podkovyrov, 2000), thus giving a higher ICV index (see **Figure 3.12**). Immature shales may express ICV values greater than one, due to a high influx of non-clay minerals such as plagioclase, K-feldspar, amphiboles and pyroxenes, which are generally found within tectonically active settings and/or within first-cycle deposits (Cox *et al.,* 1995; Cullers and Podkovyrov, 2000; Campos Alvarez and Roser, 2007). Mature shales have higher contents of clay minerals, such as kaolinite, illite, and muscovite. As a consequence they will normally display ICV values below one. These types of shales may form on cratons and other tectonically quiescent environments, like e.g. within ‘passive margin settings’, where sediment recycling is active. However, some first cycle deposits have been documented to display high ICV values, as they were subjected to intense weathering (Cox *et al.,* 1995; Cullers and Podkovyrov, 2000). The

combination of ICV values with the ratio of certain alkali-elements to aluminium, e.g. the ratio of K_2O/Al_2O_3, is used to determine the alkali-feldspar to plagioclase and clay mineral ratio (Cox *et al.,* 1995), which in turn is utilised to estimate the original mineralogy and the maturity of ancient mudrocks (see **Figure 3.12**). A K_2O/Al_2O_3 ratio of ≥0.5 indicates significant feldspar quantities relative to the clay content and is typical for immature sediments. Values ≤0.4 suggest minimal concentrations of feldspar within the original shale and point towards highly mature sediments (Cox *et al.,* 1995; Cullers and Podkovyrov, 2000). The ICV and K_2O/Al_2O_3 values are commonly described alongside the weathering indices (Chemical index of alteration [CIA] and Chemical index of weathering [CIW], see below) to infer the intensity of the weathering, the degree of recycling and the maturity of sediments (Cullers and Podkovyrov, 2000; Barbera *et al.,* 2006; Okunlola *et al.,* 2009).

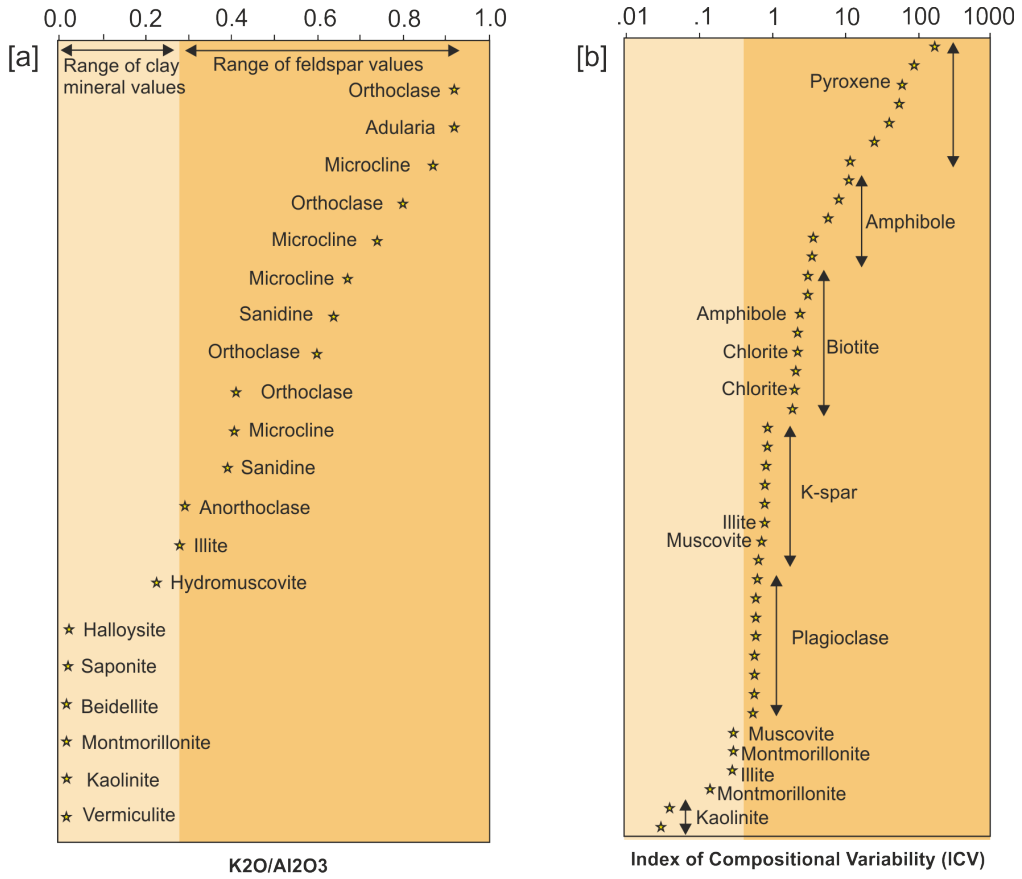

Figure 3.12: [a] K_2O/Al_2O_3 ratios for various K-Feldspars and clay minerals. The stars represent the specific values for the minerals indicated. **[b]** Index of Compositional Variation (ICV), the stars locate typical values for the specific minerals. The arrows indicate the range of values for a particular mineral group. The background colours highlight un-weathered minerals (darker colouration) and weathering products (lighter coloration). Data from Deer and Howie (1966), modified after Cox *et al.* (1995).

3.1.14 Weathering indices: CIA, PIA and CIW

The following weathering indices are used to determine the degree of alteration of a given sediment by assessing the clay fraction of the unit in question. The **chemical index of alteration** 'CIA' (Nesbitt and Young, 1982; Taylor and McLennan, 1985 in: Hetzel *et al.,* 2006; Rollinson and Rollinson, 1993; Fedo *et al.,* 1995; Price and Velbel, 2003; Campos Alvarez and Roser, 2007) can be calculated by applying the following formula:

$$\mathbf{CIA = (Al_2O_3 / (Al_2O_3 + CaO^* + Na_2O + K_2O)) \times 100} \qquad \mathbf{(10)}$$

Where CaO* is the CaO incorporated into the silicate fraction.

The CIA is a well-established parameter for determining the degree of weathering and is the most accepted of the available weathering indices (Bahlburg and Dobrzinski, 2011). The CIA index can also be displayed on a ternary plot (($CaO^* + Na_2O$) – Al_2O_3 – K_2O or 'A-CN-K' diagram) after (Nath *et al.,* 2000; Mongelli *et al.,* 2006; Nesbitt and Young, 1982 in: Rahman and Suzuki, 2007; Rahman and Suzuki, 2007; Lee, 2009; Descourvieres *et al.,* 2011) which can display significant K enrichment trends. During the degradation of feldspars, Na^+, K^+ and Ca^{2+} are mobilised and clay minerals with a higher fraction of Al are formed, for e.g. illite and kaolinite (Mongelli *et al.,* 2006; Bahlburg and Dobrzinski, 2011). The CIA is estimated from the proportion of Al_2O_3 which derives from secondary clay products relative to the weathering-prone oxides, provided predominantly from feldspar decomposition (Hetzel *et al.,* 2006). CIA values of about 50 indicate fresh bedrock subject to minimal amounts of chemical weathering, and hence feldspar crystals undergo low if no chemical alteration. These conditions are commonly interpreted to indicate cold-arid glacial environmental conditions (Wang *et al.,* 2006). CIA values of 75-100 indicate complete conversion of feldspars to aluminous clay minerals, under these conditions an intense chemical weathering can be inferred, predominantly occurring under warm-damp interglacial conditions (Wang *et al.,* 2006; Scheffler *et al.,* 2006). An increase in CIA values relative to Rb/K ratios are commonly interpreted to represent rising temperatures and warm-humid conditions (see Fedo *et al.,* 1995; Abdou and Shehata, 2007). The CIA values of the most common sediment forming minerals vary significantly. Kaolinite has a CIA value of 100 and represents the highest degree of weathering. The CIA values for illite range between 75 and c. 90, muscovite is usually evident at 75 (70-75 for the average shales, Rahman and Suzuki, 2007) and finally the feldspars occur at values of 50. Igneous and metamorphic rocks typically exhibit the following CIA systematics. Fresh basalts

commonly display CIA values ranging between 30 and 45, fresh granites and granodiorites between 45 to 55 (Nesbitt, 1982; Fedo *et al.,* 1995; Bahlburg and Dobrzinski, 2011).

The **chemical index of weathering** (Harnois, 1988 in: Moosavirad *et al.,* 2011):

$$\mathbf{CIW = (Al_2O_3 / (Al_2O_3 + Na_2O + CaO^*)) \times 100} \quad \mathbf{(11)}$$

Where CaO* is the CaO incorporated into the silicate fraction.

The CIW is identical to the previously described CIA yet it eliminates K_2O concentrations from the equation (Price and Velbel, 2003). The CIW index increases with the degree of depletion of the soil or sediment in Na and Ca, relative to Al, which in turn suggests intense or prolonged source area weathering (Barbera *et al.,* 2006). The value of this index increases as the degree of weathering increases, and the difference between CIW index values of the silicate parent rock and soil or sediment reflects the amount of weathering experienced by the weathered material (Harnois, 1988). The CIW can also be displayed in the A-C-N (Al_2O_3 – CaO – Na_2O) diagram, where trends between the three components are more apparent (Mongelli *et al.,* 2006).

Source weathering can also be calculated by using the **plagioclase index of alteration** (PIA) after Fedo *et al.* (1995) in: Moosavirad *et al.* (2011):

$$\mathbf{PIA = ((Al_2O_3 - K_2O) / ((Al_2O_3 - K_2O) + CaO + Na_2O)) \times 100} \quad \mathbf{(12)}$$

The PIA was developed as an alternative method to the CIW (described previously) as plagioclase is abundant in siliceous sediments and dissolves relatively rapidly (Price and Velbel, 2003). The PIA index quantifies the degree of plagioclase destruction. High PIA values (towards 100) indicate that the plagioclase content has been almost entirely destroyed during weathering and transport of the source sediments (Fedo *et al.,* 1995; Campos Alvarez and Roser, 2007). PIA values of around 50 represent unaltered crystalline bedrock and values approaching 100 indicate significant production of secondary aluminous clay minerals (Fedo *et al.,* 1995). High CIA and PIA values (i.e., 75–100) indicate intensive weathering in the source area whereas low values (i.e., 60 or less) indicate low weathering in the source area. The high variations in CIA and PIA values may, however, be due to the low concentrations (sometimes below or near detection limits) of the alkalis and alkaline earth elements rather than variable degrees of source area weathering (Osae *et al.,* 2006).

3.1.15 Elemental proxies

The following **Table 3.2** displays various elemental proxies that can be used in order to reconstruct the palaeoenvironmental conditions during the time of deposition, including: provenance (composition of the original source material), chemical weathering extents, redox conditions, grain size, salinity, humidity, TOC proxy and bioproductivity:

Factor	Elemental Proxy	Interpretation	References
Provenance	Cr/Ni	Ratio indicating mafic to ultra-mafic input	(Abdou and Shehata, 2007)
	Cr vs. Ni	A positive correlation indicates of mafic to ultra-mafic input	(Abdou and Shehata, 2007)
	Zr/Ti	Discriminates between granitic and mafic source rocks	(Scheffler *et al.,* 2006)
	TiO_2 vs. Ni	Discriminates between granitic and mafic source rocks	(Floyd *et al.,* 1989 in: Nagarajan *et al.,* 2007)
	Ti/Al and Zr/Ti	Discriminates between granitic and mafic source rocks	(Lipinski *et al.,* 2003; Scheffler *et al.,* 2006; Abdou and Shehata, 2007)
	Al_2O_3/TiO_2	Discriminates between granitic and mafic source rocks	(Taylor and McLennan, 1985 in: Barbera *et al.,* 2006)
	K_2O/Na_2O	high ratios indicate (illite) - felsic source, low ratios intermediate + basic	(Abdou and Shehata, 2007)
Source weathering	Rb/Sr	high values (0.8) intensive weathering, low values (0-0.2) weak weathering	(Burgan *et al.,* 2008; McLennan, 1993 in: Abdou and Shehata, 2007; Xu *et al.,* 2010)
	CIA	Weathering index (see **Chapter 3.1.14** 'CIA')	(Nesbitt and Young, 1982)
	A-CN-K	Weathering index (see **Chapter 3.1.14** 'CIA')	(Nesbitt and Young, 1982 in: Rahman and Suzuki, 2007)
	PIA	Weathering index (see **Chapter 3.1.14** 'PIA')	(Fedo *et al.,* 1995)
	CIW	Weathering index (see **Chapter 3.1.14** 'CIW')	(Harnois, 1988)
	ICV	Weathering index (see **Chapter 3.1.13** 'ICV')	(Cox *et al.,* 1995)
	K_2O/Al_2O_3	Weathering index (see **Chapter 3.1.13** 'ICV')	(Cox *et al.,* 1995)
	Th/U	Values >3 generally indicate weathering effects (oxidation of U)	(McLennan and Taylor, 1991 in: Campos Alvarez and Roser, 2007; Nath *et al.,* 2000)
	K/Rb	Lower ratios indicate intense weathering (weathering depletes K relative to Rb)	(Nath *et al.,* 2000)
Clay typing	Th vs. K	Identification of clay groups	(Schlumberger, 2009)
Redox conditions	Ni/V	Lower ratio values indicating more reducing conditions.	(Jones and Manning, 1994 in: Harris *et al.,* 2004)
	V/Cr	< 2 'oxic', 2 - 4.25 'dysoxic', > 4.25 'suboxic to anoxic'	(Jones and Manning, 1994; Dill, 1986 in: Wignall, 1994; Abdou and Shehata, 2007; Scheffler *et al.,* 2006)
	DOP	<0.5 'oxic', 0.5 - 0.75 'dysoxic', >0.75 'anoxic to euxinic' (see **Chapter 3.1.12**)	(Raiswell and Berner, 1985 in: Wignall, 1994; Rimmer, 2004)
	V(V+Ni)	< 0.46 'oxic', 0.46-0.6 'dysoxic', 0.54-0.82 'suboxic to anoxic', >0.84 'Euxinic'	(Hatch and Leventhal, 1992; Arthur and Sageman, 1994; Scopelliti *et al.,* 2006; Rimmer, 2004)
	V/Sc	< 9.1 indicative of oxic conditions	Kimura and Watanabe (2001)
	Ni/Co	< 5 'oxic', 5 -7 'dysoxic', > 7 'suboxic to anoxic'	(Dypvik 1984; Dill, 1986 in: Wignall, 1994; Jones and Manning, 1994; Rimmer, 2004; Abanda and Hannigan, 2006)
	U/Th	< 0.75 'oxic', 0.75 -1.25 'dysoxic', > 1.25 'suboxic to anoxic'	(Jones and Manning, 1994; Marynowski *et al.,* 2012; Nagarajan *et al.,* 2007)
	Th/U	< 2 implies anoxic conditions	(Fertl, 1979; Arthur and Sageman, 1994; Dypvik and Harris, 2001; Harris *et al.,* 2004)
	Rb/Sr	High ratios (3.8-6.1) can result under Anoxic conditions	(Burgan *et al.,* 2008)

	Mn/Al	Low values indicate reducing conditions	(Brumsack, 1986)
	Cu/Zn	High Cu/Zn ratios indicate reducing conditions, low suggest oxic conditions	(Hallberg and Халлберг, 1976 in: Nagarajan *et al.,* 2007)
	Ni/Co	< 5 'oxic, 5 - 7 'dysoxic', >7 'suboxic to anoxic' conditions.	(Dypvik, 1984 in: Rimmer, 2004; Ross and Bustin, 2009)
Grain size	SiO_2/Al_2O_3	Lower ratios indicate finer grain sizes.	(Dean and Arthur, 1998 in: Werne *et al.,* 2002; Hetzel *et al.,* 2011)
	K_2O/Al_2O_3	Lower ratios indicate finer grain sizes.	(Challands *et al.,* 2009)
	Zr/Rb	Lower ratios indicate finer grain sizes.	(Dypvik and Harris, 2001)
(detrital proxies)	Ti/Al or Al/Ti	Compositional variation in detrital flux	(Scopelliti *et al.,* 2006; Sageman *et al.,* 2003; Challands *et al.,* 2009; Zabel *et al.,* 1999; Hetzel *et al.,* 2011)
	Zr/Ti	Compositional variation in detrital flux	(Scheffler *et al.,* 2006)
	Zr/Al	Compositional variation in detrital flux	(Hetzel *et al.,* 2011)
Salinity	Rb/K	< 0.004 indicate fresh water, 0.004-0.006 brackish, > 0.006 fully marine	(Campbell and Williams, 1965 in: Scheffler *et al.,* 2006; Burgan *et al.,* 2008)
	K/Rb	250-300 for non-marine and brackish water shales and 150-200 for marine shales	(Campbell and Williams, 1965 in: Abdou and Shehata, 2007)
Humidity	SiO_2 vs. (Al_2O_3 + K_2O + Na_2O)	Discriminates between 'humid', 'semi-humid' and 'arid' environmental conditions.	(Suttner and Dutta, 1986 in: Moosavirad *et al.,* 2011)
	Al_2O_3/TiO_2	< 20 'humid', 20 - 30 'semi-humid', >30 'semi-arid	(Akul'shina, 1976 in: Kiipli *et al.,* 2012)
TOC Proxy	Using U ppm concentrations	Using the relationship between TOC and U (see **Chapter 4.10.2** '	(Fertl and Chilingar, 1988)
Bioproductivity	Using biogenic Ba concentrations	See **Chapter 4.10.5**	
	Si/Al ratio	See **Chapter 4.10.5**	(Scopelliti *et al.,* 2006)
	Authigenic U	See **Chapter 3.1.7.2**	(Wignall, 1994)
	Sr/Al	Indicating fluxes in productivity	(Reolid and Martínez-Ruiz, 2012)

Table 3.2 Elemental proxies that are used to reconstruct palaeoenvironmental conditions at the time of deposition. The elemental proxies cover: provenance (sediment source), source weathering, clay typing, redox conditions, grain-size (detrital proxies), salinity, humidity, TOC and bioproductivity (compiled after references mentioned in table).

3.2 Silurian Gondwana: pre-requisite for Llandovery black shales

3.2.1 Llandovery black shales: previous models and interpretations

During the Late Ordovician Gondwana drifted over the palaeo South Pole (Mac Niocaill *et al*., 1997; Scotese *et al*., 1999; Cocks and Torsvik, 2002; Torsvik and Van der Voo, 2002; Fortey and Cocks, 2003). This together with a drop of global temperatures (Harland, 1972; Stanley, 1988; Leton *et al*., 2012) promoted the growth of ice sheets (see **Figure 2.4**) that extended as far as 65^{o}S palaeolatitude (Scotese *et al.,* 1999). The glaciation was almost entirely restricted to the Hirnantian, which was of <0.5 My in duration (Sutcliffe *et al.,* 2000; Cocks, 2007; Le Heron *et al.,* 2009), and led to a global eustatic sea-level fall of 50–100 m, triggering the second largest global mass extinction amongst life forms, during which 85% of all species were eliminated (Sheehan, 2001; Craig *et al.,* 2002). The Silurian black shales were deposited along the northern rim of Gondwana during the Early Silurian transgression as a result of the melting of the Hirnantian ice masses (e.g.

Fekirine and Abdallah, 1998; Lüning *et al.,* 2000). These black shales form a 6000 km belt extending from Mauritania to Saudi Arabia and are composed of partly strongly organically enriched deposits, with TOC values locally exceeding >20% (Lüning *et al.,* 2000; Le Heron *et al.,* 2013). There are two horizons within the Silurian black shales of the nowadays Northern African region that are termed 'hot shales' (see 'U' within **Chapter 3.1.7.2** and **Figure 3.13**), with API values exceeding 200API, due to a strong enrichment of U (Lüning *et al.,* 2000; Lüning *et al.,* 2003a; Lüning *et al.,* 2005; Loydell *et al.,* 2009). These 'hot' shales are of highest economical importance as they form the source rock for 80-90% of the Palaeozoic sourced hydrocarbons in North Africa (Lüning *et al.,* 2000; Lüning *et al.,* 2005).

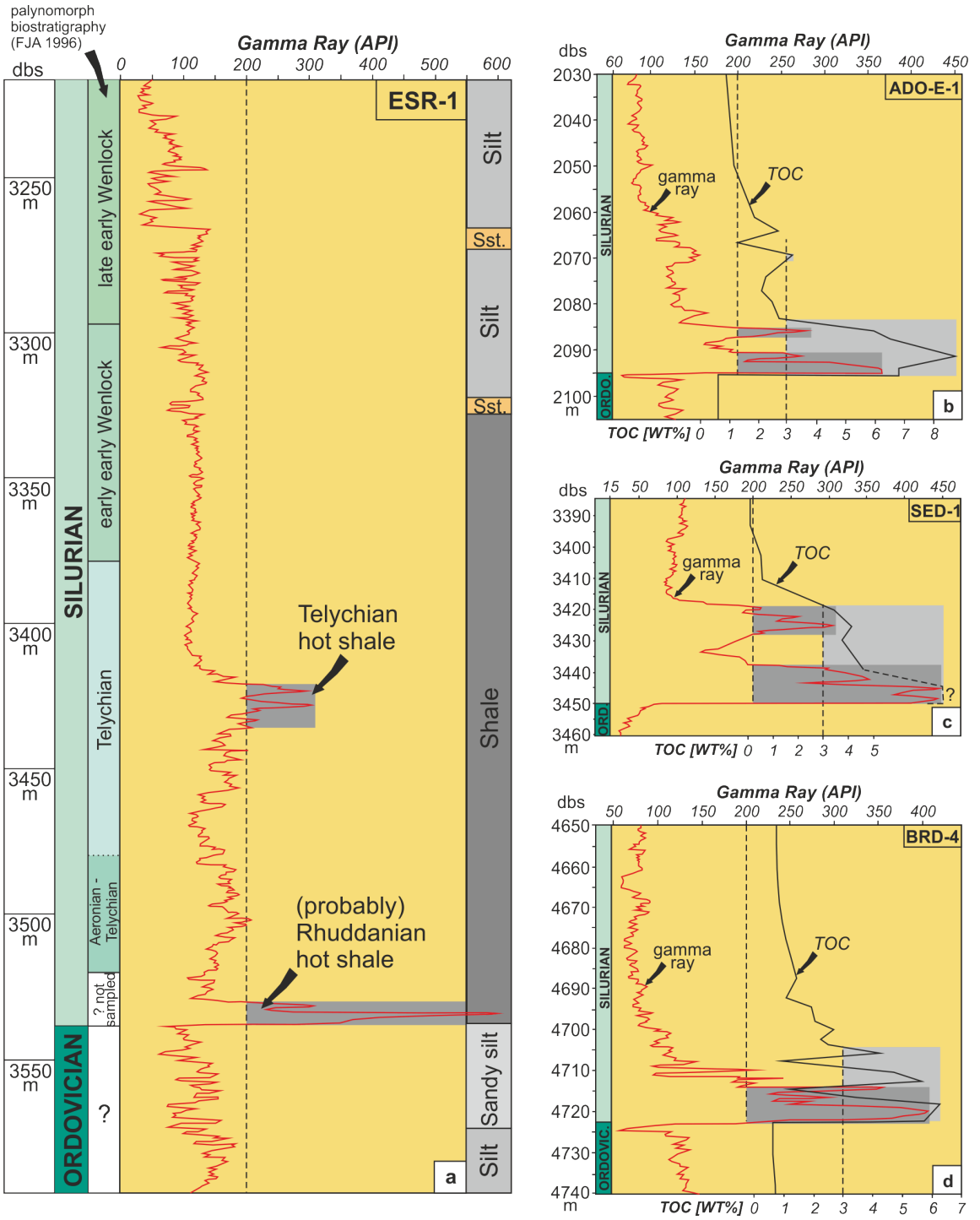

Figure 3.13: Gamma-ray and TOC signatures of Llandovery black shale successions from Algeria and Libya. **A)** Gamma-ray signature of a black shale sequence, Ghadames Basin, Libya. Showing the two 'hot' shale horizons. Biostratigraphy after Futyan, Jawzi and Associates (FGA 1996 in: Lüning *et al.,* 2000). **B, C** and **D)** Gamma-ray signals and TOC contents of coeval black shales from the Algerian part of the Ghadames basin and the Illizi basin of Algeria, showing the relationship between TOC and the gamma-ray signal (total API). The peaks in the gamma-ray signal correspond to the peaks in TOC. API: American Petroleum Institute units, dbs: depth below surface, Sst.: sandstone and TOC: Total Organic Carbon. Modified after Lüning *et al.* (2000).

The regional distribution varies between the lower Rhuddanian 'hot' shale horizon and the upper Telychian 'hot' shale horizon. The Rhuddanian deposits are confined to palaeo-lows during the initial transgression as a result of the relief and the tunnel valleys generated by the Hirnantian glaciation (Le Heron *et al.,* 2004; Le Heron *et al.,* 2007; Le Heron and Craig, 2008; Le Heron *et al.,*

2009). The relief created by the glaciogenic processes was superimposed on and locally exaggerated the pre-existing shelf topography that was caused by the Pan-African and Infracambrian tectonics (Lüning *et al.,* 2000; Le Heron *et al.,* 2004; Lüning *et al.,* 2005). These black shales are considered to be a large scale synchronous anoxic event that is apparent across northern Gondwana (Lüning *et al.,* 2000; Lüning *et al.,* 2005). Sea-level rise continued during the post-Rhuddanian leading to the deposition of 'lean' shales with depreciated TOC content and API values of ~120 (Lüning *et al.,* 2000; Fello *et al.,* 2006). These organically 'lean' shales are difficult to date and correlate by means of biostratigraphy, as they contain only few fossils of biostratigraphical value (Butcher, 2009). The following Upper Telychian 'hot' shale deposits were formed by a second synchronous large scale anoxic event (Lüning *et al.,* 2000; Lüning *et al.,* 2005). A second wave of 'lean' shale deposits overlies the Telychian 'hot' shales, both lean shale deposits and the Telychian 'hot' shales are laterally extensive (see **Figure 3.14**). It is important to note, that only the basal Rhuddanian 'hot' shales are restricted to the palaeo-depressions (Lüning *et al.,* 2000; Lüning *et al.,* 2005). Le Heron *et al.* (2013) suggested that the patchy nature of the 'hot' shales may be related to lingering ices sheets that locally moderated the extent of anoxia.

The nowadays surface extent of the Rhuddanian 'hot' shales is difficult to trace as they tend to lose their diagnostic features such as the elevated OM content and the corresponding dark, black colour in the course of elevated weathering. However, the U distribution appears to remain largely unaltered by the weathering processes (Lüning and Kolonic, 2006; Fello *et al.,* 2006), implying that it can potentially be used as a proxy for the original OM content and hence indicate the presence of 'hot' shales (Fertl and Chilingar, 1988; Lüning and Kolonic, 2006; Fello *et al.,* 2006).

Using tectonic and biogeographical data it has been advocated, that Iberia was, at least until the Early Silurian, part of the northern Gondwanan margin (Scotese *et al*., 1999; Robardet, 2003; Cocks and Torsvik, 2006; Bassett, 2009; Servais and Sinbutin, 2009). This assumption is further corroborated by the presence of Hirnantian glacial deposits and tunnel valleys in Iberia, comparable to those found across northern Africa (Gutiérrez-Marco *et al.,* 2010). In the following the depositional models for the Silurian 'hot' shales of northern Africa and the Middle East proposed by Lüning *et al.* (2000) and Armstrong *et al*. (2005) will be described and discussed in detail, as they provide valuable insights into the processes that may have also operated in Iberia and in particular within the Cantabrian basin.

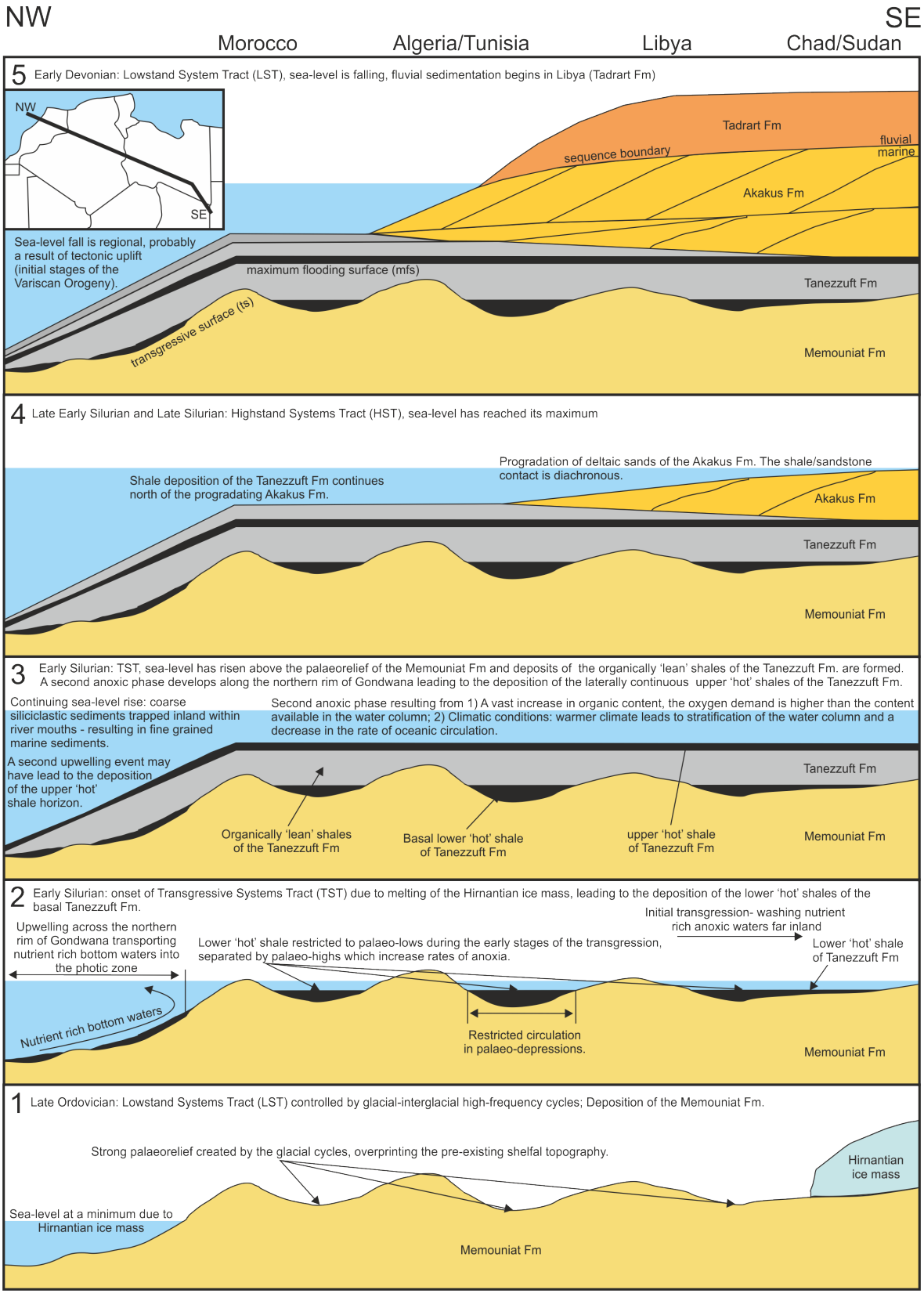

Figure 3.14: Depositional model for the lower and upper 'hot' shales across northern Africa (Northern Gondwana from the (**1**) Late Ordovician to the (**5**) Early Devonian). Cross sections 1-5 spanning from Morocco (North West) to the Chad/Sudan (South East) as indicated by inset in sketch number 5. Modified after Lüning *et al.* (2000).

3.2.2 Parameters controlling anoxia and the deposition of Llandovery black shales

In the following, the processes and parameters that may have led to the development of the Silurian 'hot' shales across Northern Gondwana are summarised and discussed. Many of the proposed models and theories addressing the problem of black shale formation invoke only one or just a very limited number of controlling factors. However, it has to be stressed that it may not have been necessarily just one or a few parameters that initiated and sustained the formation of black shales, but a combination and maybe even complex interaction of varied processes.

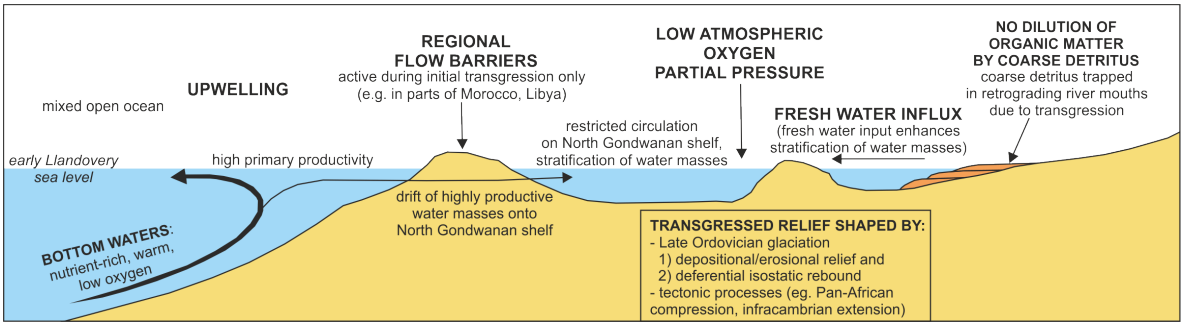

Figure 3.15: Palaeo-oceanographical, sedimentological and palaeobiological processes that may have operated during the Early Silurian leading to the development of the Llandovery 'hot' shales. Modified after Lüning *et al.* (2000).

3.2.2.1 Upwelling along the northern rim of Gondwana

Upwelling transfers relatively nutrient rich waters from moderate to deep marine depths up to the photic zone (Moore *et al.,* 1993; Tyson, 1995). Demaison (1993, in Tyson, 1995) estimated that only 8% of the World's petroleum reserves are derived from 'upwelling areas', in contrast to 78% being generated within dysoxic-anoxic 'silled basins' (see **Chapter 3.1.2**, Black Sea model). Upwelling creates a favourable environment for the biological cycle, leading to an increase in the plankton bioproductivity. However, it can also enhance the levels of anoxia by bringing low oxygenated bottom waters onto the shallow marine shelf areas. Pedersen and Calvert (1990) suggest that the upwelling induced palaeoproductivity contributes more towards the formation of organically enriched sediments than the primary water-column anoxia (see **Chapter 3.1.2**, productivity model), and that the key to black shale production is the large-scale influx of organic carbon and not necessarily the redox status (see **Chapter 3.1.2**, preservation model) of the water column within the depositional basin (Lüning *et al.,* 2000). Moore *et al.* (1993) modelled the extents of the upwelling and the palaeoproductivity for the early Silurian using modern day oceanographic circulation analogues and bioproductivity rates. The model showed that during the Silurian the

largest upwelling zone was within the Southern hemisphere, between 70°S and 35°S, along the extensive Northern Gondwanan margin. The model assumed that the westerly winds, resulting from the palaeogeographical positioning of Gondwana, promoted intense upwelling. The high amount of available organic matter in the water-column and the sediment triggered the development of dysoxic to anoxic conditions, as large proportions of the dissolved oxygen were removed by the oxygenation and subsequent break-down of OM. The computer simulations also suggested that the prevailing winds and related upwelling were not only active during the Llandovery, but also persisted throughout the Wenlock, thus predicting a prolonged and continuous period of time for black shale formation. However, only two discrete black shale successions have been documented from the Rhuddanian and the Telychian respectively (Lüning *et al.,* 2000; Armstrong *et al.,* 2005). The confinement of these two black shale deposits to distinct stratigraphic levels emphasises that additional processes, not considered within the computer-based modelling, must have been responsible for the interruption and finally termination of the black shale generation (Lüning *et al.,* 2000). The nature of these processes is currently a matter of ongoing debate, but the most widely discussed involve short-termed seasonal changes, geographical variations in nutrient sources, the effects of high-frequency sea-level fluctuations, sedimentological condensation versus dilution due to under or over supply of terrestrial material and the punctuated, glacial–interglacial related development of a stratified water column (Walliser, 1996, with previous references therein; Štorch, 1998; Lüning *et al.,* 2000; Lüning *et al.,* 2003a; Nielsen, 2004; Page *et al*., 2007; Armstrong *et al.,* 2009; LaPorte *et al*., 2009; Le Heron *et al.,* 2009; Małkowski and Racki, 2009).

Wilde *et al.* (1991) and Berry *et al.* (1998, both in Lüning *et al,* 2003a), proposed a monsoonal setting for northern Gondwana, with seasonal intense upwelling and the associated development of a pronounced oxygen minimum zone. Page *et al.* (2007) and Le Heron *et al.* (2009), on the other hand, argue that upwelling is unlikely to be the mechanism leading to black shale formation, as the necessary nutrient-laden sediments stem, according to their model, from glacial melt waters derived from the hinterland, which reinforce the development of a shallow pycnocline and hence the development of a salinity driven water column stratification.

3.2.2.2 Transgressions and shelf geometries

The deposition of the Silurian black shales across northern Gondwana correlates to relative sea-levels highs (see **Chapter 2.1.3** Silurian Cantabria), that reached their maximum during the

Telychian *Oktavites spiralis* graptolite biozone (Arthur and Sageman, 1994; Loydell, 1998; Johnson, 2006; Johnson, 2010 in: Sachanski *et al.,* 2010). The maximum extent of this transgression and the resulting land-sea relationship is illustrated in **Figure 3.16**. It highlights, that not only the majority of the Gondwanan shelf areas were submerged beneath the sea, but also a vast amount of the Gondwanan mainland, pushing the palaeo-coastline as far southwards as present day Niger and Chad.

It is the initial stage of this eustatic sea-level rise that is regarded to be of importance for the deposition of the Rhuddanian black shale (Lüning *et al.* 2000). Most of the processes that were initiated during the early phase of this transgression and the geological features that were left behind by it, can be explained straightforwardly by applying the basal transgressive 'puddle model' of Wignall and Hallam (1991).

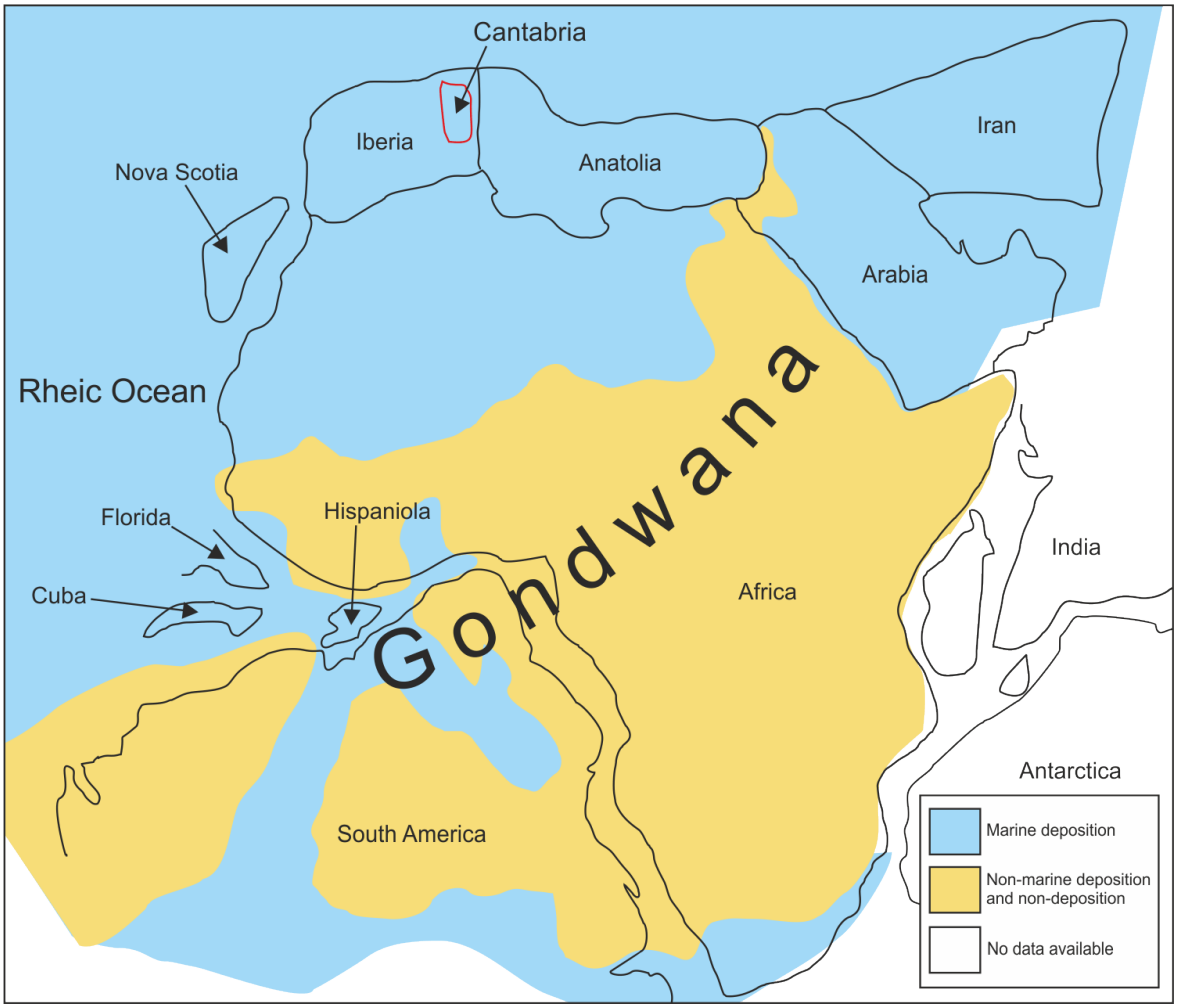

Figure 3.16: Continental configuration of "western" Gondwana, land/sea distribution and the approximate position of the Cantabrian Basin during the early Silurian. Large parts of the peri-Gondwanan shelf and of the Gondwanan main-land are flooded by the sea as a result of the global eustatic sea-level rise caused by the melt-down of the Hirnantian ice masses. Modified after Clifford (1986) and Lüning *et al.* (2000).

The initial stages of the lower Silurian transgression immersed substantial parts of the Northern Gondwanan continental platform. The onset of this transgression is considered to be of significant importance for the development of the Silurian black shales. There are a number of smaller factors that could have further controlled the development of the black shales, these parameters are directly related to the initial flooding of the continental margins. The controlling factors are briefly discussed in the following: [1] **Sub basins**. Palaeo-lows or topographical 'depressions' are flooded during the initial stages of the marine transgression, these shelfal depressions are separated from open-ocean circulation by localised flow barriers or 'palaeo-highs'. Shelfal oxygen defiency, created by the upwelling of oxygen depleted bottom waters and high productivity rates is therefore enhanced. These depressions lead to the localised 'focusing' or concentration of OM (Lüning *et al.,* 2000; Lüning *et al.,* 2005; Fello *et al.,* 2006; Le Heron *et al.,* 2009). The flooding of these palaeo-depressions and the environmental conditions that operate within, can be interpreted by applying the 'puddle model' of Wignall and Hallam (1991). Based on the observation, that organically lean Hirnantian black shales have been found in Jordan, pre-dating the basal Rhuddanian 'hot' shales deposits of Lüning *et al*. (2000), Armstrong *et al.* (2005) concluded that the depositional model for the Rhuddanian 'hot' shales would be closer related to the maximum transgression 'expanding puddle model' of Wignall (1994). However, Lüning *et al.* (2006) stress that the age constraints for the lean shale are poorly confined, and hence, support their original idea of an initial transgressive 'puddle' model interpretation for the Rhuddanian black shales. Furthermore, Lüning *et al.* (2006) pointed out that the basal 'hot' shales are clearly Rhuddanian in age and that there is no evidence for Hirnantian 'lean' shales. [2] **Entrapment of coarse siliciclastics**. The transgression during the latest Ordovician/earliest Silurian was extremely rapid (Fekirine and Abdallah, 1998). The sea had transgressed more than 1000 km inland (**Figure 3.16**) within a few hundred thousand years (Lüning *et al.,* 2000). The rapid immersion left the shelfal areas to be starved of coarser grained siliciclastic sediments. The coarser sediments were trapped inland, within river mouths towards the south and around palaeohighs, leading to relatively undiluted OM content in the more distal shelf areas (Lüning *et al.,* 2000). [3] **Incomplete re-colonization after seasonal anoxia**. Tyson and Pearson (1991) and Tyson (1995) proposed seasonal anoxia. During the summer a thermocline/pycnocline developed, predominantly restricting the water column circulation, thus leading to the stratification of the water column. This water column stratification led to the establishment of a well oxygenated, warm, lower density, mixed surface layer. This surface layer created a film, capping the cooler, denser, oxygen depleted waters below. This scenario, ultimately

leads to the ideal conditions for black shale formation and effectively terminating the aerobic benthic ecosystem (Wignall, 1994; Tyson, 1995). The stratification of the water column effectively starves the surface waters of nutrients, nutrients that the bottom waters have in plentiful supply. The extent of oxygen depletion within a water column, subjected to stratification depends on the following factors: [1] the organic loading, [2] the intensity of the pycnocline, [3] the initial oxygen contents of the bottom waters, [4] the duration of water column stratification, and finally [5] the volumes of sub-pycnocline bottom water (Tyson and Pearson, 1991 in: Wignall, 1994).

During the winter the thermocline and/or pycnocline may not be developed, leading to the re-establishment of full water-column circulation. The circulation may be aided by vigorous wind driven turbulence powered by winter storms, allowing nutrients from the deep bottom waters to reach the photic zone (Wignall, 1994). However, on wide continental shelf areas, the distances can be too vast for complete biological re-colonization during the winter months. This could explain the rarity or absence of aerobic benthic faunas in most black shales sequences (Wignall, 1994; Tyson, 1995; Lüning *et al.,* 2000).

3.2.2.3 Postglacial fresh water stratification

The melting of the Hirnantian ice masses led to a significant release of fresh water into the earliest Silurian sea. Fresh water has a lower density than that of saline water, as a result, it will form a fresh water cap. This fresh water cap restricted the vertical exchange of shelfal water masses (Combaz, 1967; Combaz, 1986 in: Lüning *et al.,* 2000). Brackish surface waters are known to cause salinity driven water column stratification (Tyson, 1995; Page *et al.,* 2007 in: Le Heron *et al.,* 2009), effectively preventing the replenishment of nutrients from upwelling processes and exacerbating the levels of anoxia. The majority of the ice masses had disappeared during the early Llandovery, resulting in the weakening and finally disappearance of the capping effect. However, this model strictly implies the existence of low salinity surface waters, which contradicts with the high abundance of graptolites found in the Rhuddanian 'hot' shales (Lüning *et al.,* 2000). Le Heron *et al.* (2013) interpreted the patchy nature of the Silurian 'hot' shales to be related to lingering Hirnantian ices sheets, that in turn, locally moderated the extent of anoxia.

3.2.2.4 Episodic climatic changes

The black 'hot' shales of the northern Gondwanan region were deposited during the Rhuddanian and Telychian respectively. The deposition of the basal Rhuddanian 'hot' shales coincide with the 'Spirodden Secundo Episode', spanning from the latest, post-Hirnantian Ordovician to the Mid-Areonian (Aldridge *et al.,* 1993 in Lüning *et al.,* 2000). Jeppsson (1990 in Lüning *et al.* 2000) describes 'Secundo Episodes' as being characteristic of warm climates in high latitudes, dry conditions in low latitudes and warm, saline anoxic oceanic bottom waters. In contrast the 'Primo Episodes' relate to cooler, more humid climates and cold, oxic oceanic bottom waters. The differing episodes are controlled by climatic differences linked to the concentrations of atmospheric CO_2. The cold oceanic bottom waters of a 'Primo Episode' have a higher storage capacity for CO_2 than the saline bottom waters of a 'Secundo Episode' (Aldridge *et al.,* 1993 in: Lüning *et al.,* 2000). As the northern rim of Gondwana was subject to upwelling conditions, warm, anoxic, nutrient rich bottom waters of the Secundo Episode could have been transported onto the shelf margins. These waters may have exacerbated the shelfal oxygen deficiency produced by the high influx of oxygen-consuming organic matter (Lüning *et al.,* 2000). However, in many cases graptolite diversities do not correspond to the Primo–Secundo model, as a consequence, the model should be used with caution (Lüning *et al.,* 2000).

Chapter 4
Methodology

Contents

4.1 Localities and sampling

Prior to field work, the geological maps (Spanish Geological Survey, Instituto Tecnológico GeoMinero de España) of the Cantabrian region (**Figure 4.1**) were studied. Aerial photographs (kindly provided by the Facultad de Geología, Universidad de Oviedo, Spain) were analysed and interpreted. All areas where the Silurian formations occurred were noted, in particular the black shales of the Formigoso Fm. and its relation to road cuttings. Road cuttings were selected for further analysis as they provided the best exposure and preservation of the organically enriched sediments. All localities visited during the reconnaissance trips are marked on **Figure 4.1**. An overall decrease in preservation and increase in alteration of the Silurian Formigoso Fm. was seen towards the north of the Cantabrian Zone, especially within the northern coastal sections. It was therefore decided to concentrate on the far better preserved sections of the Southern Cantabrian Zone.

Five representative localities were selected for logging and sampling, all of which are confined to the southern margin of the Cantabrian Zone, within the Correcillas unit (see **Chapter 2** 'Geological Setting' and **Figure 2.2**). The localities were selected based on the preservation of the material and completeness of the Silurian succession. The locations were: [1] Aralla, [2] Caldas de Luna, [3] La Majua, [4] Sena de Luna and [5] Villanueva. The GPS coordinates for these localities can be found in **Table 4.1** and a detailed map is provided within **Chapter 2** 'Geological Setting' and **Figure 2.2**.

All localities were logged and systematically sampled. The resulting sedimentary logs are provided within **Chapter 5** 'Geochemical Results', information for the samples and sample numbers are listed in **Table 4.2** 'Samples numbers, localities and lithology'. The sampling interval was consistently 25 cm for all localities. For each of the locations the uppermost bed of the Barrios Fm. was probed and used as a control sample. The overlying Getino Beds, which are not always developed, varied in thickness drastically from ~ 30 cm at the Aralla section up to ~ 10 m at the La Majua section, and were sampled bed by bed. The Aralla section was by far the best locality in terms of completeness and preservation, and was the only locality that permitted the sampling of the upper Formigoso Fm. (Villasimpliz Mb.). Approximately 25 g were sampled per sampling point to allow for repeated preparation and analysis. A total of 599 samples were collected, processed, pelleted and geochemically analysed under laboratory conditions. In addition to the laboratory samples, a further *in situ* high-resolution geochemical log was generated covering the basal parts of the Formigoso Fm. at the Aralla locality (see **Chapter 2.1**, **Figure 2.2**). For this a portable Niton

XL3t XRF analyser was used (see **Chapter 4.3** 'Niton XL3t portable XRF analyser'). *In situ* analysis was carried out equidistantly every 10mm for the first 3.39 m, consequently resulting in 339 geochemical readings.

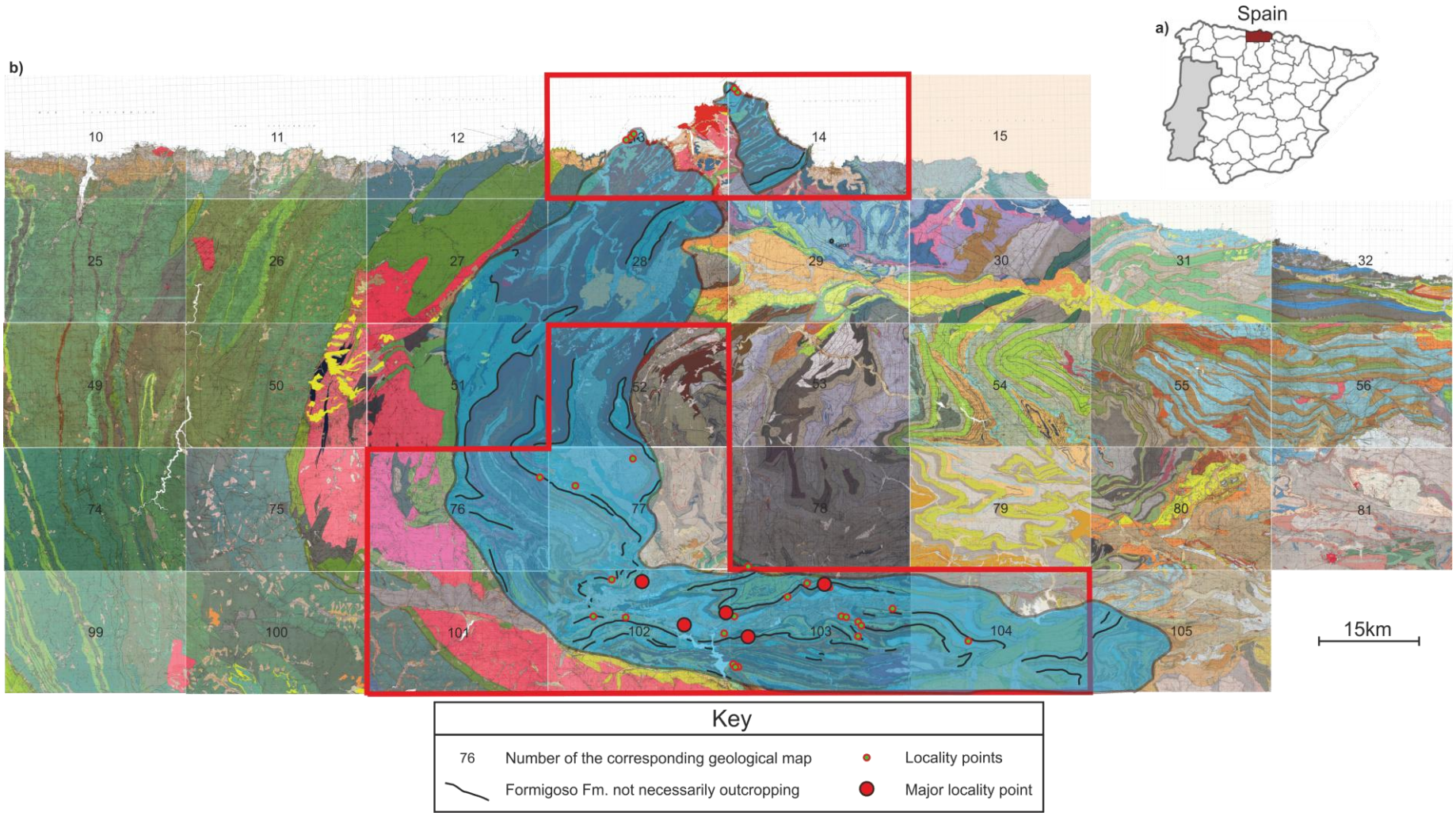

Figure 4.1 (a) Overview map of Spain, highlighted in red the studied area. (b) A collation of maps of the Spanish Geological Survey, numbered according to the Spanish geological map index (IGME, Instituto Geológico y Minero de España, 2002). The red outline indicates the investigated areas. The area shaded in blue represents the Somiedo-Corrcillas Unit of the Cantabrian Zone (see **Chapter 2** 'Geological Setting'). Black lines indicate the Silurian Formigoso Fm. Sections investigated are marked by red circles, localities selected for detailed analysis are high-lighted by the larger red points.

Locality No.	Latitude	Logitude	Elevation (m)
1	N43 34.794	W6 02.190	3
2	N43 34.496	W6 02.482	12
3	N43 34.302	W6 02.944	3
4	N43 34.258	W6 03.093	9
5	N42 54.134	W5 53.122	1129
6	N42 50.912	W5 51.575	1144
7	N42 50.976	W5 51.997	1063
8	N42 51.127	W5 52.047	1117
9	N42 55.724	W6 04.878	1359
10	N42 55.651	W6 04.911	1372
11	N42 55.831	W5 51.984	1324
12	N42 54.549	W5 49.501	1370
13	N42 54.451	W5 49.525	1383
14	N42 59.596	W6 02.310	1340
15	N42 54.549	W5 49.494	1379
16	N42 56.691	W5 33.207	1113
17	N42 56.608	W5 33.149	1066
18	N42 53.859	W5 37.279	1162
19	N42 59.405	W6 06.517	1109
20	N42 55.780	W6 08.717	1359
21	N42 53.382	W5 24.125	1122
22	N42 55.822	W5 39.264	1193
23	N42 55.710	W5 38.617	1307
24	N43 38.346	W5 49.634	0
25	N43 38.345	W5 49.704	25
26	N43 38.360	W5 49.762	4
27	N43 38.541	W5 49.871	3
28	N43 38.581	W5 50.004	8
29	N43 38.342	W5 49.669	9
30	N43 09.358	W6 15.063	713

Locality No.	Latitude	Logitude	Elevation (m)
31	N43 08.574	W6 10.870	1100
32	N43 11.159	W6 04.057	1037
011	N42 55.650	W6 04.912	1375
021	N42 56.463	W5 51.363	1425
041	N42 57.683	W5 45.667	1187
051	N43 00.683	W5 50.267	1187
061	N42 59.017	W5 43.267	1187
071	N42 58.679	W5 40.855	1400
081	N42 58.765	W5 40.912	1225
091	N42 58.875	W5 41.106	1270
0101	N42 58.884	W5 41.227	1278
0111	N42 58.678	W5 40.960	1214
0121	N42 56.672	W5 51.382	1432
0131	N42 56.685	W5 51.346	1380
0141	N42 56.686	W5 51.416	1438
0151	N42 59.600	W6 02.291	1344
0161	N42 59.598	W6 02.310	1343
0171	N42 54.933	W5 57.899	1187
0181	N42 55.260	W5 37.190	1545
0191	N42 54.954	W5 36.939	1652

Analysed Localities

Grid: Lat/Lon hddd^{o} mm.mmm'

Datum: WGS 84

Table 4.1 GPS coordinates for the sections investigated. Sections analysed are highlighted in red: #12 (Aralla section), #0101 (Villanueva section), #0121 (Caldas de Luna section), #0161 (La Majua section) and #0171 (Sena de Luna section); See also **Figure 4.1**.

Samples numbers, localities and lithology:

Aralla	Aralla 1	Barrios Fm. (upper) - at contact with Getino Bed
	Aralla 2 + 3	Getino Bed (beds 1+ 2)
	Aralla 4-184	Lower Formigoso Fm. (Bernesga Mb.) 37m+
		after Aralla.184 - 27.3m gap in section
	Aralla 185-241	Upper Formigoso Fm. (Villasimpliz Mb.)
Aralla HR	HR 1-31	Getino bed at a 1cm resolution
	HR 32-252	Formigoso Fm. (Bernesga Mb.) at a 1cm resolution
		after HR 252 – 39cm gap in section
	HR 253-339	Formigoso Fm. (Bernesga Mb.) at a 1cm resolution
Caldas de Luna	Caldas 1 - 98	All samples taken from the basal Formigoso Fm. (Bernesga Mb.)

La Majua	La Majua 1	Upper Barrios Fm.
	La Majua 2-31	Getino Beds (bed by bed sampled)
	La Majua 32-46	Formigoso Fm. (Bernesga Mb.) after 46 – 3m gap
	La Majua 47-70	Formigoso Fm. (Bernesga Mb.) – from quarried section
Sena de Luna	Sena 1	Barrios Fm. (upper) - at contact with Getino Bed
	Sena 2-10	Getino Beds (bed by bed sampled)
	Sena 11-47	Lower Formigoso Fm. (Bernesga Mb.)
		after Sena 47 – 2m gap in section
	Sena 8-79	Lower Formigoso Fm. (Bernesga Mb.)
Villanueva	Villa 1 - 111	All samples taken from the basal Formigoso Fm. (Bernesga Mb.)

Table 4.2: Analysed localities, section labels, sample numbers and corresponding lithostratigraphic units. All sedimentary logs are documented within **Chapter 5** 'Geochemical Results'.

4.2 Sample preparation

For the geochemical XRF analysis samples were prepared following two different protocols, in order to assess and quantify any potential effects of the preparation method on the geochemical results. The first method (see **Chapter 4.2.2**) resulted in the generation of conventional XRF-pressed powder discs. The second consisted of simply using plastic capsules enclosing the powdered sediment samples and being sealed by an ultra-thin film of low molecular weight. Both methods require the samples to be milled to a fine powder. Cross-contamination of samples was avoided by carefully cleaning the equipment after the preparation of each sample. In the following, the different working steps and the equipment used will be summarised:

4.2.1 Milling process

- The samples were left in a laboratory oven at 40^{o}C for 48 hrs prior to the milling, to ensure the samples were moisture free.
- Samples were then reduced to smaller pieces (roughly 2 cm^{3}) using a hydraulically operated rock splitter.
- Once the sample was successfully reduced to smaller pieces, it was passed through a jaw crusher. The jaw crusher reduced the samples to fine gravel size.
- Finally, an agate ring mill was used to produce the very fine uniform analytical powders.

4.2.2 Preparation of pressed powder discs (after Watson, 1996)

- Polyvinylpyrrolidone-methylcellulose was used as a binding solution.

- The binding solution was produced by combining two different solutions (Solution A and Solution B).
- Solution A: Add 35 g of polyvinylpyrrolidone (PVP) added to 175 ml of alcohol.
- Solution B: 200 ml of distilled water were heated to a temperature of 90^{o}C in a 1 litre beaker and 20 g of methylcellulose were gradually introduced. The solution was allowed to cool to a temperature of approximately 40^{o}C
- Solution A was added to solution B, stirring continuously until a viscous, slightly yellow solution was formed. If to viscous the solution can be thinned by introducing ethanol before use.
- 8 g of sample powder was weighed out and transferred to a small sample bags.
- 1 ml of the PVP binding solution was added to the powder.
- The binder and the powder are then intensively mixed.
- The pellets were then pressed with the help of a mechanical die (with a pressure of 10 ton applied for 20 seconds).
- The pressing process led to the formation of the analytical discs. All discs were labelled systematically with the corresponding sample number.
- The discs were finally placed in a laboratory oven at a temperature of 40^{o}C for 48 hrs in order to lose their moisture content.

4.2.3 Powder capsule

8 g of the powered rock samples were placed in analytical plastic mini-capsules. The plastic capsule consists of an open top and a plastic base. The capsules were sealed using an ultra-thin (12.5 µm) plastic film of low molecular weight (low density polyethylene, LDPE).

4.3 Niton XL3t portable XRF analyser

The Niton XL3t XRF analyser used (see **Figure 4.2**), more commonly known simply as XRF analyser, allows for a fast, non-destructive and cost effective way to determine elemental compositions of rocks and soil samples, metals, slurries and liquid samples, dust collected on wipe

samples, airborne heavy elements collected on filters and also painted surfaces including wood, concrete, plaster, drywall and many other building materials.

The purpose of this section is to describe the advantages and limitations of a handheld XRF Niton XL3t (operating with an energy dispersive analyser) opposed to conventional laboratory based wavelength dispersive XRF. The detector resolution is an important factor as it determines the range of elements that can be analysed. Higher resolutions are generally achieved by applying lower electron voltage (eV). According to Brouwer (2003) wave-length dispersive XRF generally provides higher resolutions between 5eV and 20eV, while energy-dispersive XRF commonly operates between 150eV to 220eV range. The Niton XL3t XRF analyser used to generate the data for the present study has a resolution of 185eV. Wave-length dispersive XRF analysers have despite their higher resolution, the disadvantage that they can only detect one element at a time, whereas energy-dispersive XRF analysers are designed to detect groups of elements simultaneously. Both technologies are comparable in their capability to eliminate background radiation effects, which otherwise would affect the detection limits and the reproducibility. Energy-dispersive XRF analysers do not utilise a diffraction crystal like wave-length dispersive XRF, therefore energy dispersive systems allow for a greater X-ray source efficiency and lower operating costs. A wave-length dispersive XRF achieves similar counts only by exciting the sample up to 1000 times, leading usually to higher operational costs (Brouwer, 2003).

Each element when exposed to an X-ray of sufficient energy re-emits a unique characteristic x-ray that can be utilised as a ‘fingerprint’ to determine that particular element. XRF analysers determine the sample chemistry by measuring the spectrum of these characteristic re-emitted X-rays. The primary X-ray beam emitted is either from an X-ray tube (as in the Niton XL3t) or from a small sealed capsule of radioactive material.

A fluorescent X-ray is generated when an X-ray of sufficient energy hits an atom within the sample. As the X-ray strikes the atom it dislodges an electron from one of the atoms inner orbital shells. This electron is replaced by an electron from one of the atoms higher energy orbital shells, in order for to regain atomic stability (see **Figure 4.3**). As the electron drops from a higher energy state to a lower energy state it releases a fluorescent X-ray. This fluorescent X-ray is equal to the specific and unique difference in energy between the electrons two quantum states (Brouwer, 2003).

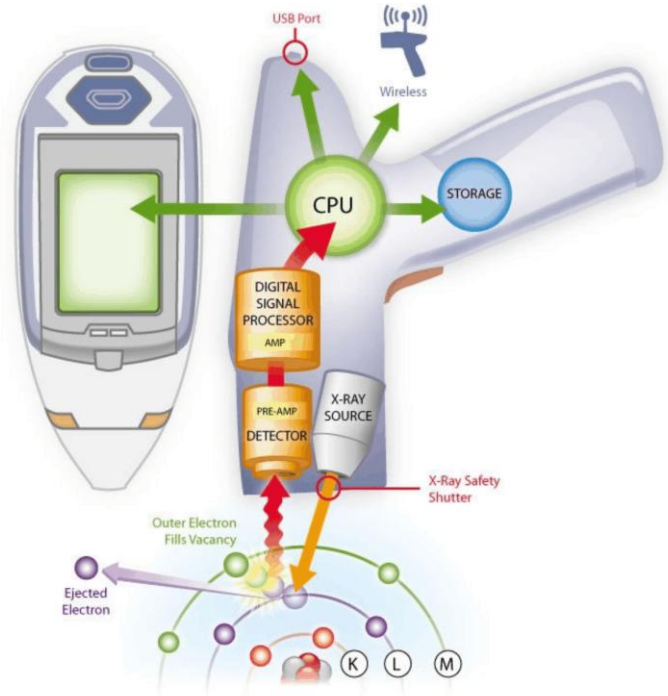

Figure 4.2: Configuration of the Niton XL3t, showing the principle analytical steps and operational flow of data processing during analysis. An internal X-Ray source is used to generate a primary X-ray beam that is emitted directly by the XRF analyser. Upon interaction with matter composed of materials with an atomic weight heavier than $_{11}$Na, element diagnostic secondary fluorescent X-rays are emitted by the sample. The X-rays are perceived by the detector, amplified by the signal processor and finally identified by a central processing unit (CPU). Figure reproduced with kind permission of Thermo Fisher Scientific (2012).

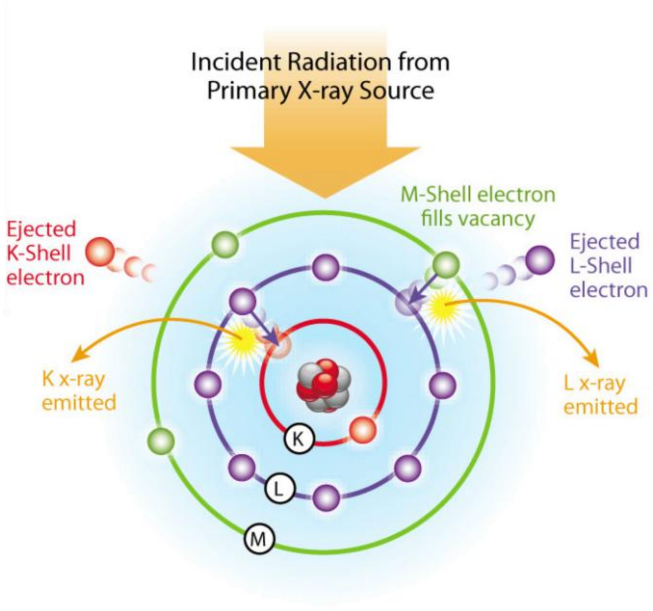

Figure 4.3 Atom structure. Showing how the atom reacts once an X-Ray of sufficient energy has collided. An electron from the inner orbital shell has been ejected, this is replaced with an electron from a higher energy state to stabilise the atom. When an electron moves from a higher to lower energy state a fluorescent X-Ray is emitted. Figure reproduced with kind permission of Thermo Fisher Scientific (2012).

For a given element to be detected by the Niton XL3t XRF analyser, the measured concentration within the sample must be at least three times the standard deviation of the measurement (error). The detection limits will vary between samples with differing compositions.

There are approximately 30 or more elements that can be identified from any unknown sample using XRF analysers. The Niton XL3t XRF analyser is able to detect and analyse elements ranging from the light magnesium ($_{12}$Mg) to the heavier ($_{92}$U) uranium (see **Table 4.3**). X-ray energies measured range from 1.25 kilo-electron volts (keV) up to 85 keV. The elastic (Raleigh) and inelastic (Compton) scattered X-rays emitted by the samples during analysis are also detected and quantified. These scattered X-rays are used to give an approximation for the samples density and the percentage of light elements within.

Analysis Mode	Elements available (Mg only when detector is purged with He)
Soil Mode:	Ca, Fe, K, Mn, Ti, Ba, Cr, Cu, Ni, Pb, Rb, S, Sc, Sn, Sr, Th, U, V, Zn and Zr
Mining Cu/Zn Mode:	Mg, Al, Si, P, S, Cl, As, K, Ca, Ti, V, Cr, Mn, Fe, Co, Ni, Cu, Zn, W, Pb, Bi, Zr, Nb, Mo, Sn, Ba, Sb, Cd, Pd, Sr, Rb, Se, Ag and Au
Mining Ta/Hf Mode:	Mg, Al, Si, P, S, Cl, As, K, Ca, Ti, V, Cr, Mn, Fe, Co, Ni, Hf, Re, W, Pb, Bi, Zr, Ta, Nb, Mo, Sn, Ba, Sb, Cd, Pd, Sr, Rb, Se, Ag and Au

Table 4.3 Elements suites detectable within the differing analytical modes of the Niton XL3t XRF analyser.

4.4 Analytical modes of the Niton XL3t XRF analyser

As mentioned previously (see **Chapter 4.3**) there are different analytical modes available that can be selected within a Niton XL3t XRF analyser. These modes allow for separate suites of elements to be detected (see **Table 4.3**). The main difference between these modes is that the 'mining' modes will allow the analysis of the lightest elements (most importantly the analysis of Mg – only possible when the detector is purged with helium) whereas the 'soil' mode focuses on heavier elements such as Th and U.

4.5 Effect of helium detector purging

Helium purging of the detector is required for the optimal detection of light elements, specifically Mg, Al, Si, and P. The purpose of the helium purging of the detector is to eliminate any heavier elements present within the nose cone, that may mask the detection of the lighter elements, such as Magnesium. Mg can only be detected whilst the nose cone is purged with helium. The 2 sigma errors for Al, Si and P are greatly reduced by the use of helium. For helium purging of the nose cone the helium ferrule must be attached to the rear of the Niton XL3t XRF analyser. The regulator that is included with the XRF analyser governs the helium flow rate to 70 cc/min. Once the helium

has been turned on, allow a minimum of 5 minutes for the helium purging of the nose cone needs to be allowed for before commencing analysis.

4.6 Creating calibration files

In order to calibrate raw data from the Niton XL3t XRF analyser international and inter-laboratory standards (see **Table 4.4)** were utilised. The readings of these standards were then cross-plotted against the known standard elemental values (see for example **Figure 4.5** - Iron calibration). The cross-plotting for all elements used against the respective published standard readings provided the relationship that was used to establish the equations for the various calibration curves. The equations of these curves and intercepts (varying from element to element) were applied to raw data in order to shift the readings accordingly towards the calibration.

STANDARD	Description	Origin	Year	Institution	Reference
AC-E	GRANITE	Ailsa Craig island in the Firth of Clyde, SW Scotland	1987	GIT-IWG	(Potts and Holbrook, 1987)
AGV-1	ANDESITE	East wall of Guano Valley, Lake Caunty,Oregon, USA	1967	USGS	(Flanagan, 1976)
AL-I	ALBITE	Pinzele, Trente, Italy	1984	GIT-IWG	(Govindaraju, 1984)
AN-G	ANORTHOSITE	Stratified basic complex of Fiskenaesset, Western Greenland	1980	GIT-IWG	(Govindaraju, 1980)
ATT-1 (IL)	ATTALPULGITE				
BCR-1	BASALT	Columbia River Group basalt, Bridal Veil Flow Quarry, Washington USA	1967	USGS	(Flanagan, 1976)
BCS-267	SILICA BRICK	Bureau of analysed samples LTD., *, Newham Hall, Newby, Middlesbrough TS8 9EA, England*		BAS	
BCS-269	FIREBRICK	Bureau of analysed samples LTD., *, Newham Hall, Newby, Middlesbrough TS8 9EA, England*		BAS	
BCS-313	SILICA BRICK	Supplied by pilkington Brothers plc, St. Helens.	1989	BAS	
BCS-314	SILICA BRICK	Bureau of analysed samples LTD., *, Newham Hall, Newby, Middlesbrough TS8 9EA, England*		BAS	
BCS-315	FIREBRICK	Bureau of analysed samples LTD., *, Newham Hall, Newby, Middlesbrough TS8 9EA, England*		BAS	
BCS-368	DOLOMITE	Bureau of analysed samples LTD., *, Newham Hall, Newby, Middlesbrough TS8 9EA, England*	1989	BAS	
BCS-375	SODA FELDSPAR	Island off south-west coast of Sweden	1989	BAS	
BCS-376	POTASH FELDSPAR	Lillesand,Glamsland, South Norway	1989	BAS	
BE-N	BASALT	Old volcano near Essey-la-Côte, near Nancy, Meurthe et Moselle, France	1980	GIT-IWG	(Govindaraju, 1980)
BHVO-1	BASALT	Kilauea caldera, Kilauea volcano, Hawaii	1976	USGS	(Flanagan, 1976)
BIR-1	BASALT	12 km east of Reykjavik (Iceland)	1984	USGS	(Flanagan and Geological Survey (US), 1984)
BL-3571 (IL)	AMPHIBOLITE			Bristol	

BMS (IL)	BLACK MARINE SHALE			Southampton	
BOB-1 (IL)	BASALT			Birmingham	
BR	BASALT	Essey-la Côte, near Nancy, Meurthe et Moselle, France	1964	CRPG	(Roubault *et al.,* 1970)
BX-N	BAUXITE	Mine de Marou, Brignoles (Var), France	1967	ANRT	(La Roche, 1971)
CGM (IL)	MUDSTONE				
DNC-1	DIABASE	Braggstown, North Carolina	1984	USGS	(Flanagan and Geological Survey (US), 1984)
DR-N	DIORITE	Neuntelstein, Massif du Champ du Feu (Vosges), France	1967	ANRT	(La Roche, 1968)
DT-N	KYANITE	Nanga,Eboko (Cameroun)	1967	ANRT	(La Roche, 1971)
DTS-1	DUNITE	Twin Sisters area, Hamilton (Washington)	1967	USGS	(Flanagan, 1976)
FK-N	POTASH FELDSPAR	Madras (now Tamil Nadu), India	1967	ANRT	(De la Roche and Govindaraju, 1976)
G-1 (IL)	GRANITE	Smith Granite Company, Westerly, Rhode Island, USA	1951	USGS	(Flanagan, 1976)
G-2	GRANITE	Westerly Granite, from Sullivan quarry, Bradford, Rhode Island, USA	1967	USGS	(Flanagan, 1976)
GA	GRANITE	Andlau, Bas-Rhin (France)	1964	CRPG	(Roubault *et al.,* 1970)
GD-1 (IL)	GRANODIORITE			Aberdeen	
GH	GRANITE	Massif du Tauorirt Tan Afella, Hoggar (Algèrie)	1964	CRPG	(Roubault *et al.,* 1970)
GS-N	GRANITE	Senones Vosges mountains, France	1967	ANRT	(De la Roche and Govindaraju, 1976)
GSP-1	GRANODIORITE	Silver Plume Quarry, Colorado, USA	1967	USGS	(Flanagan, 1976)
I-1 (IL)	APLITIC GRANITE			QMC	
I-3 (IL)	DOLERITE			QMC	
IF-G	IRON FORMATION	Iron-ore deposit, Isua supracrustal belt, West Greenland	1984	GIT-IWG	(Govindaraju, 1984)
JB-1	ALKALI BASALT	Kitamatsuura basalt, Myokanji Toge, Sasebo, Nagasaki	1968	GSJ	(Govindaraju, 1994)
JG-1	GRANODIORITE	Sori granodiorite, Azuma-mura, Gunma Prefecture, Japan	1967	GSJ	(Govindaraju, 1994)
M-2 (IL)	PELITE			QMC	
M-3 (IL)	CALC SILICATE			QMC	
MAG-1	MARINE SHALE	Wilkinson Basin of the Gulf of Maine	1976	USGS	(Flanagan, 1976)
MA-N	GRANITE	Beauvoir (Clermont-Ferrand, Massif Central), France	1980	GIT-IWG	(Govindaraju, 1980)
MCM (IL)	CALCAREOUS MUDSTONE			Southampton	
MICA-FE	BIOTITE MICA	Massif de Saint-Sylvestre (Massif Central) France	1967	CRPG	(Roubault *et al.,* 1970)
MICA-MG	PHOLOPITE	Bekily, Southern Madacasgar	1967	CRPG	(Roubault *et al.,* 1970)
MRG-1	GABBRO	Mount Royal, Montreal	1975	CCRMP	(Abbey, 1981)
NBS-1B (IL)	ARGILLACEOUS SHALE			NBS	
NBS-99 (IL)	FELDSPAR			NBS	
NIM-D (SARM 6)	DUNITE	Ultrabasic pipe, Bushveld Igneous Complex, South Africa	1978	SABS	(Steele *et al.,* 1978)
NIM-G (SARM 1)	GRANITE	Acid portion of Bushveld Igneous Complex, South Africa	1978	SABS	(SARM Program., 2006)
NIM-L (SARM 3)	LUJAVORITE	Council for Mineral Technology (MINTEK) Randburg 2125		SABS	(SARM Program., 2006)
NIM-N (SARM 4)	NORITE	Council for Mineral Technology (MINTEK) Randburg 2125		SABS	(SARM Program., 2006)

NIM-P (SARM 5)	PYROXENITE	Critical zone of the Bushveld Igneous Complex, South Africa	1978	SABS	(Steele *et al.,* 1978)
NIM-S (SARM 2)	SYENITE	Council for Mineral Technology (MINTEK) Randburg 2125		SABS	(SARM Program., 2006)
PCC-1	PERIDOTITE	East Austin Creek, Sunoma County, California, USA	1967	USGS	(Flanagan, 1976)
PH-8 (IL)	RHYOLITE			Bristol	
PK-170 (IL)	PHYLLITE			Bristol	
PK-180 (IL)	MARBLE			Bristol	
PM (IL)	MARL			Southampton	
QLO-1	QUARTZ LATITE	South-eastern Oregon	1976	USGS	(Flanagan, 1976)
RGM-1	RHYOLITE	Glass Mountain, Siskiyou County, California, USA	1976	USGS	(Flanagan, 1976)
RJH-440 (IL)	PELITE			Bristol	
SCO-1	SHALE	Natrona County,Wyoming, USA	1976	USGS	(Flanagan, 1976)
SDC-1	MICA SCHIST	Rock Creek Park,Washington,D.C	1976	USGS	(Flanagan, 1976)
SGR-1	SHALE	Green River Formation	1976	USGS	(Flanagan, 1976)
STM-1	NEPHELINE SYENITE	Table Mountain, Oregon, USA	1976	USGS	(Flanagan, 1976)
SY-1 (IL)	SYENITE			CCRMP	
SY-2	SYENITE	Bancroft area, Eastern Ontario, Canada	1975	CCRMP	(Abbey, 1981)
SY-3	SYENITE	Bancroft area, Eastern Ontario, Canada	1975	CCRMP	(Abbey, 1981)
T-1 (IL)	TONALITE			Tanzania	
TL-214 (IL)	GLAUCOPHANE SCHIST				
UB-N	SERPENTINE	Col de Bagenelles (Vosges), France	1967	ANRT	(La Roche, 1968)
W-1	DIABASE	Bull Run Quarry, near Centerville, Fairfox county, Virginia, USA	1951	USGS	(Flanagan, 1976)
W-2	DIABASE	About 5 km of Centerville,Virginia	1984	USGS	(Flanagan and Geological Survey (US), 1984)

Table 4.4 The international and inter-laboratory standards utilised for calibration of the Niton XL3t XRF analyser. **(IL)** refers to inter-laboratory standards. Data taken from Jochum (2011) 'GeoReM Database (2012)' accessed online - 28/02/2012 - http://georem.mpch-mainz.gwdg.de/

Below (see **Figure 4.5**) is an example of the calibration generated for iron and the formula used, the 2 sigma errors for the Niton XL3t XRF analyser have been included.

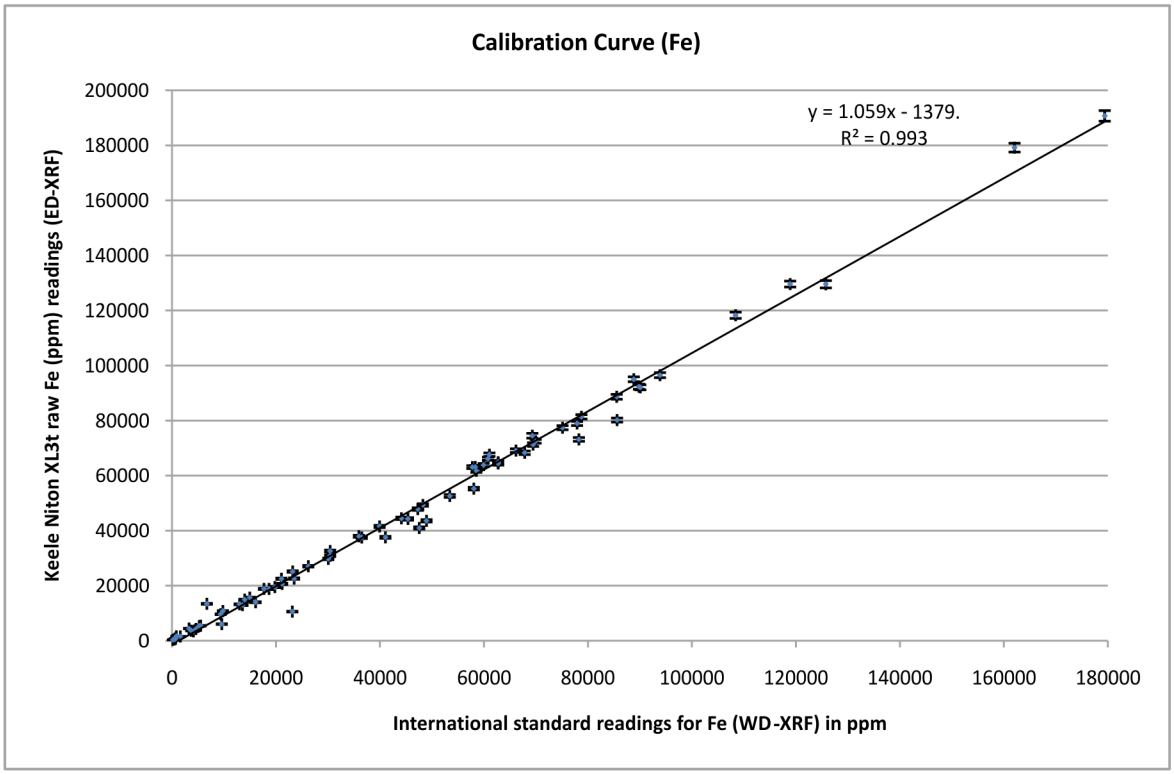

Figure 4.5 The calibration of iron. Keele Niton XL3t XRF analyser values (in ppm) plotted against the known international standard data (in ppm). The Intercept and slope of the calibration curve is applied to raw Fe data to shift it accordingly towards the calibration.

The following formula is applied in order to calibrate raw iron data, the intercept and slope values were taken from **Figure 4.5**. This is an example of the calibration method, the formula can be applied to any element:

Corrected Fe value = (raw Fe value – intercept of Fe calibration)/slope of Fe calibration **[13]**

The intercept in this case being: -1379, and the slope being: 1.059

The calibration curves for all other elements can be found in **Appendix A** 'Calibration curves'.

4.7 Effects of sample preparation techniques, helium purging, analytical time and machine error on the geochemical results

The analytical Mining Cu/Zn mode (see **Table 4.3**) of the Niton XL3t XRF analyser was consistently used for the entirety of the data collection. This mode was selected as it allows for light element detection not available in soil mode (see **Table 4.3)**. The analytical time was set to the maximum of 360 seconds, other than when the analytical time-span was varied to test effects on 2 sigma error.

This was so the effects of sample preparation, helium purging and machine error could be evaluated for the lighter elements. A description of the standards used is given in table **Table 4.4**.

4.7.1 Comparison of the differing preparation methods

The purpose of this experiment was to determine whether the differing sample preparation methods mentioned previously (see **Chapter 4.2.2**) had a significant impact on the analysed geochemical data. The samples chosen for this experiment were Villa 1, Villa 2 and Villa 3 (see **Table 4.2**). These samples were representative of the black shales belonging to the Formigoso Fm. collected at the Villanueva locality. The samples of the Formigoso Fm. were selected to determine the direct relationship between the various sample preparation methods and the potential effects they may have on the analysed geochemical data.

The data from samples prepared in accordance with the methods described earlier (see **Chapter 4.2.2**) were compared to readings obtained from unprepared (raw) sample. The following **Table 4.5** illustrates the significantly varying geochemical data, especially for the lighter elements, in relation to the different sample preparation methods used (see also **Figure 4.6** and **Figure 4.7**).

SAMPLE	Ti [ppm]	Ti 2σ	Ti 2σ(%)	K [ppm]	K 2σ	K 2σ(%)	Al [ppm]	Al 2σ	Al 2σ(%)	Si [ppm]	Si 2σ	Si 2σ(%)
Villa 1 Raw	5195.73	60.08	1.16	18884.04	252.65	1.34	58884.63	1241.88	2.11	171250.30	1063.30	0.62
Villa 1 Disc	5228.53	53.59	1.02	26966.78	272.17	1.01	103293.70	1919.61	1.86	200118.00	1206.65	0.60
Villa 1 Capsule	5290.84	55.13	1.04	26807.66	276.43	1.03	48452.21	1184.96	2.45	129073.00	950.11	0.74
SAMPLE	**Ti [ppm]**	**Ti 2σ**	**Ti 2σ(%)**	**K [ppm]**	**K 2σ**	**K 2σ(%)**	**Al [ppm]**	**Al 2σ**	**Al 2σ(%)**	**Si [ppm]**	**Si 2σ**	**Si 2σ(%)**
Villa 2 Raw	2034.73	41.71	2.05	9605.63	207.13	2.16	38578.75	843.07	2.19	74370.45	571.58	0.77
Villa 2 Disc	5318.84	56.34	1.06	26475.54	280.13	1.06	107168.80	1979.51	1.85	203359.70	1217.73	0.60
Villa 2 Capsule	5195.30	55.42	1.07	25176.05	271.45	1.08	42797.07	1082.78	2.53	118676.60	891.20	0.75
SAMPLE	**Ti [ppm]**	**Ti 2σ**	**Ti 2σ(%)**	**K [ppm]**	**K 2σ**	**K 2σ(%)**	**Al [ppm]**	**Al 2σ**	**Al 2σ(%)**	**Si [ppm]**	**Si 2σ**	**Si 2σ(%)**
Villa 3 Raw	4779.07	50.42	1.06	24170.35	254.79	1.05	84149.19	1503.88	1.79	172873.70	1070.26	0.62
Villa 3 Disc	5299.17	56.70	1.07	26347.83	282.08	1.07	107738.30	1991.62	1.85	204846.50	1216.99	0.59
Villa 3 Capsule	5159.93	54.95	1.06	24681.89	267.28	1.08	41146.83	1063.34	2.58	115272.00	878.35	0.76

Table 4.5 Geochemical data representative of the three samples Villa 1, Villa 2 and Villa 3. Two different sample preparation methods (pressed discs and plastic capsules, see **Chapter 4.2**) have been applied. The resulting analytical data are compared to data obtained from unprepared, raw samples. Measurements were taken using the analytical Cu/Zn mining mode for a duration of 360s per sample.

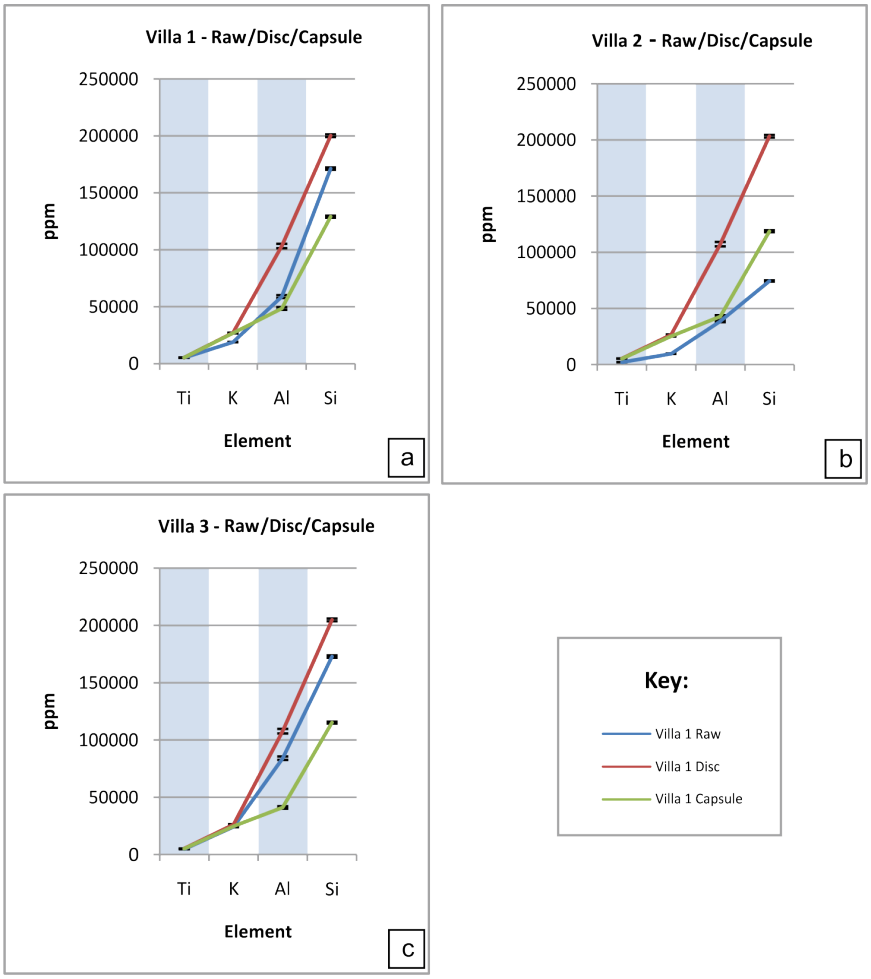

Figure 4.6: Absolute geochemical values (from **Table 4.5**) for the various samples measured (Villa 1, Villa 2 and Villa 3). The figure shows that different sample preparation methods (as described above), has a significant effect on the absolute elemental concentrations detected. The light elements Al and Si show the most significant variation in absolute values. In each case are the highest absolute concentration values generated from press-disc prepared samples.

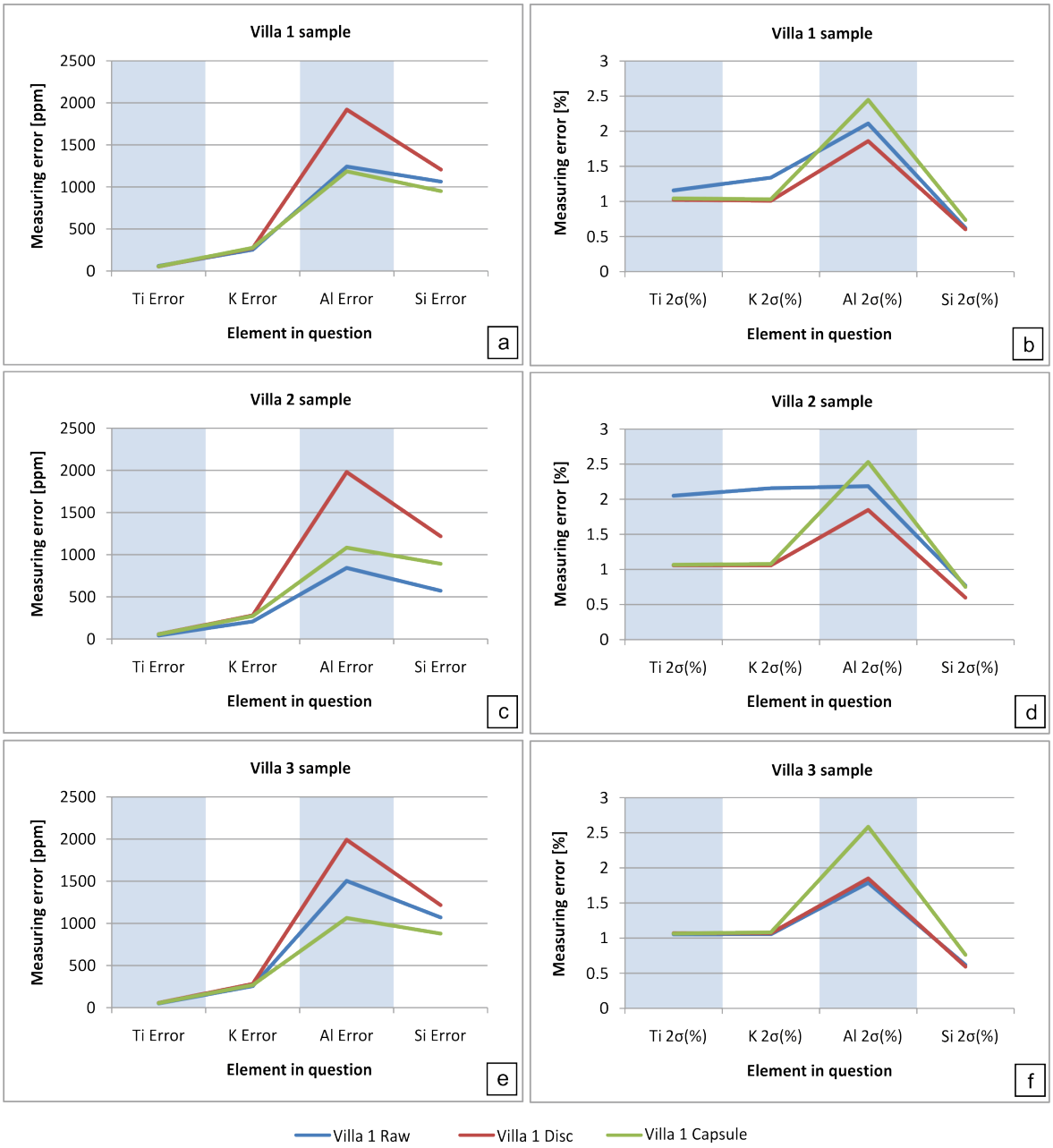

Figure 4.7 (a, c and **e**): Illustrate the measuring-2-sigma errors in ppm for the samples Villa 1, Villa 2 and Villa 3. The absolute measuring error in ppm is consequently the highest for the press-disc prepared samples, as this preparation method produces systematically the highest concentration readings (see **Figure 4.6**). (**b, d, f**) measuring-2-sigma errors expressed as percentage. The press-disc prepared samples show the lowest error-percent values.

4.7.2 Helium purged and non-purged analysis: the effects on lighter elements

The purpose of this testing was to determine how helium-purging of the detector effects the analysis of lighter elements. To assess and quantify this effect, data were generated using helium-purging and compared to data obtained from non-purged analysis (see **Table 4.6**). As described above (see **Chapter 4.5** 'Effect of helium detector purging'), purging of the XRF detector with helium greatly increases the detectors sensitivity for lighter elements, mainly Mg, Al and P.

SAMPLE	Mg [ppm]	Mg Error	Al [ppm]	Al Error	Si [ppm]	Si Error	K [ppm]	K Error
SCO-1 (Helium)	10530.26	752.75	71452.23	715.17	289222.2	1355.3	19894.64	227.57
SCO-1 (non-Helium)	0	9266.18	54347.32	1272.1	258858	1401.8	17029.51	206.31
BMS (Helium)	9166.17	1033.96	92575.13	967.12	212177.5	985.66	20788.38	267.65
BMS (non-Helium)	0	14022.16	71439.06	1884.86	188453.6	1081.64	17830.86	246.15
MAG-1 (Helium)	0	4683.89	5910.96	503.93	23776.77	263.98	8322.17	152.46
MAG-1 (non-Helium)	31751.03	15226.16	7213.53	1504.16	22044.23	405.31	6915.17	132.66

Table 4.6: Variation of the lighter elements between helium-purged and non-purged readings using the international standards SCO-1, BMS and MAG-1(see **Table 4.4** 'international and inter-laboratory standards'). The lighter elements Mg, Al, Si and K were selected for analysis. The comparison between the helium-purged and non-purged data shows the systematically lower measuring errors and therefore higher quality of the data produced with helium-purging. Measuring errors **in percent** are for sample **SCO-1**: Mg (non-helium):N/A, Mg (helium): 7.14, Al (non-helium): 2.34, Al (helium): 1.00, Si (non-helium): 0.54, Si (helium): 0.46, K (non-helium): 1.21 and K (helium): 1.14. Sample **BMS**: Mg (non-helium): N/A, Mg (helium): 11.2, Al (non-helium): 2.63, Al (helium): 1.04, Si (non-helium): 0.57, Si (helium): 0.46, K (non-helium): 1.38 and K (helium): 1.28. Sample **MAG-1**: Mg (non-helium): 47.95, Mg (helium): N/A, Al (non-helium): 20.85, Al (helium): 8.52, Si (non-helium): 1.83, Si (helium): 1.11, K (non-helium): 1.91 and K (helium): 1.83. The analytical Cu/Zn mining mode of the Niton XRF was used for a maximum analysis time of 360s for each sample.

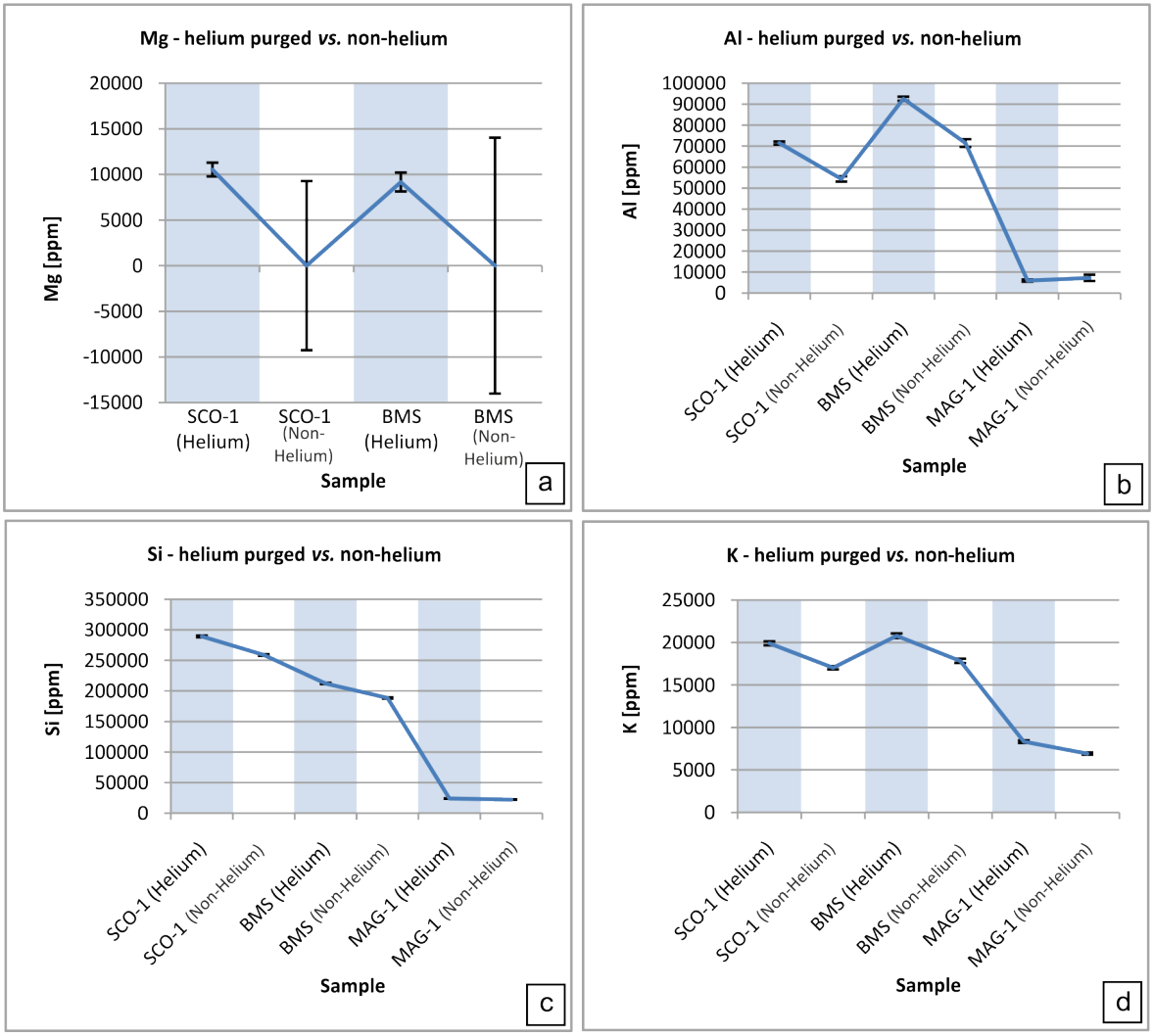

Figure 4.8: Cross-plots of element *vs.* helium purged and non-helium purged sample using the data documented in **Table 4.6**. Error bars (2 sigma) are given for each measurement. The effect of the helium-purging is evident in the significantly reduced statistical errors (2 sigma).

4.7.3 Analytical time vs. 2-sigma error

Using the original factory configuration, the Niton XL3t XRF analyser utilises four different analytical filters for the detection of different groups of elements: **[1]** the 'main-range filter' is used for the analysis of the transition group elements with an atomic number (Z) between 21 and 80, **[2]** the 'low-range filter' for elements Z = 19-24, **[3]** the 'high-range filter' for elements Z = 47-56, and **[4]** the 'light-range filter' for light element analysis (elements with Z < 17). The combination of these filters and the time allowed for analysis has a great influence on the absolute concentration measured and the respective 2-sigma errors. In order to evaluate this effect, a test series was designed. For the purpose of this experiment the 'main-range filter', 'low-range filter' and 'light-range filter' were used. Measuring time was 30 seconds for the 'main-range filter' and 'low-range filter' and 60 seconds for the 'light-range filter'. One analytical cycle using all relevant filters lasted for 120 seconds.

The international standards MAG-1, SCO-1 and BMS were used for this test. Each standard was analysed for 60, 120, 240 and a maximum reading time of 360 seconds. Note that for each of the samples there are no values for Al at 60 seconds, as Al is only detected using the Niton XL3t 'light-range filter'. The 'light-range filter' is set up only to initiate after the first 60 seconds (see above). The time allocation for the differing filters can be adjusted as required.

SAMPLE/Time (s)	Al [ppm]	Al 2σ-Error	K [ppm]	K 2σ-Error
MAG-1/ 60	-	-	7138.16	237.28
MAG-1/ 120	8408.6	2516.13	6847.52	230.73
MAG-1/ 240	6534.67	1734.71	6967.26	164.78
MAG-1/ 360	7213.53	1504.16	6915.17	132.66
SAMPLE/Time (s)	**Al [ppm]**	**Al 2σ-Error**	**K [ppm]**	**K 2σ-Error**
SCO-1/ 60	-	-	16647.64	332.18
SCO-1/ 120	52998.71	2087	16755.75	336.68
SCO-1/ 240	53329.35	1536.5	17044.39	252.05
SCO-1/ 360	54347.32	1272.1	17029.51	206.31
SAMPLE/Time (s)	**Al [ppm]**	**Al 2σ-Error**	**K [ppm]**	**K 2σ-Error**
BMS/ 60	-	-	17413.98	402.18
BMS/ 120	68336.16	3077.68	18089.35	411.11
BMS/ 240	72142.13	2309.41	17846.89	302.35
BMS/ 360	71439.06	1884.86	17830.86	246.15

Table 4.7: Analytical results for varying analytical durations (60,120,240 and 360 seconds) for the standards MAG-1, SCO-1 and BMS.

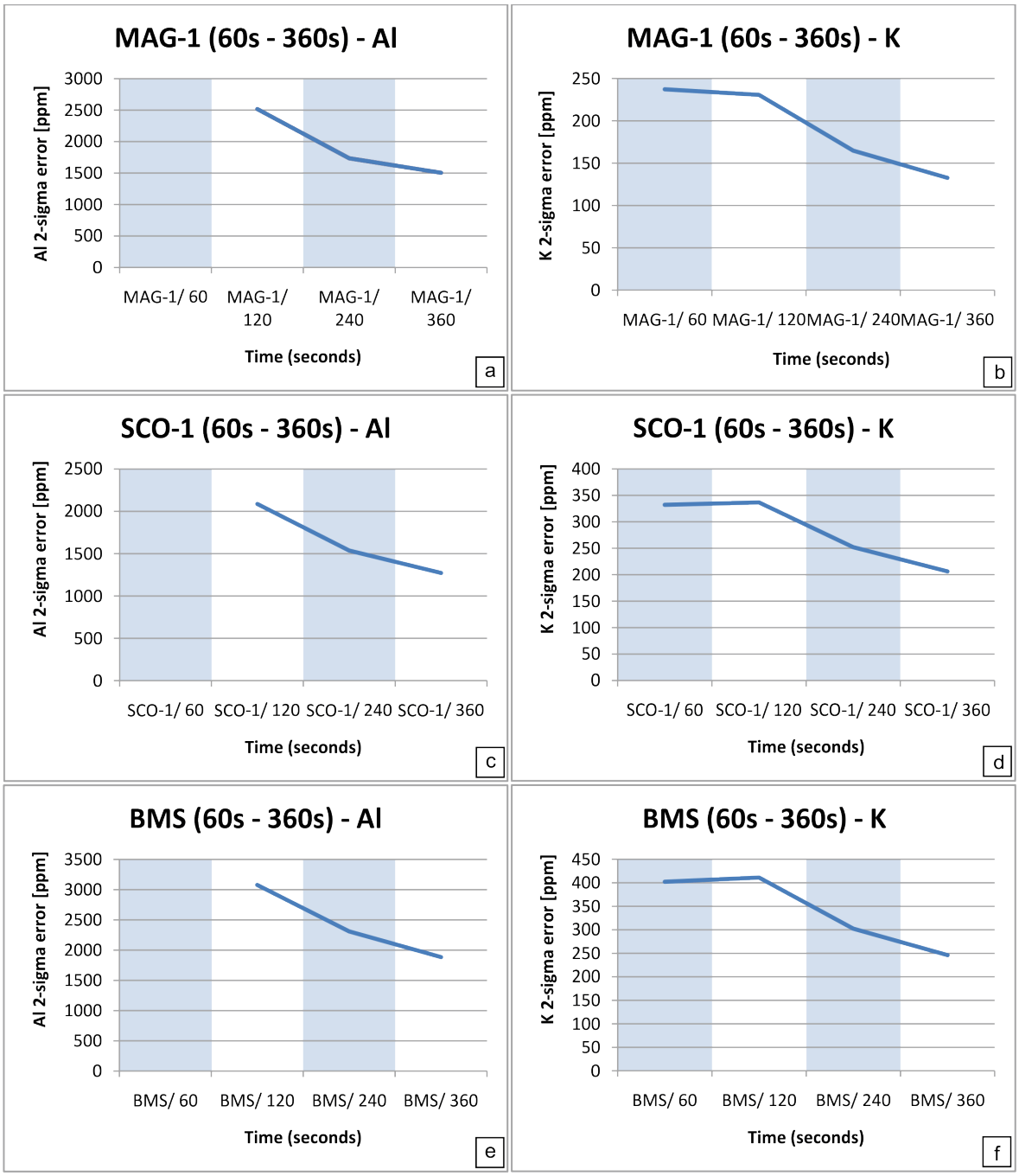

Figure 4.9: Analytical time and its effect on the 2-sigma error. The international standards MAG-1, SCO-1 and BMS were analysed. The analytical Cu/Zn mining mode was used to obtain readings for analytical durations of 60, 120, 240 and a maximum of 360s. Note that in each case Al is not detected within 60s, only after (for explanation see text). The 2-sigma error is seen to reduce significantly between 120s and 240s of analytical time.

4.7.4 Precision of the measurements

In order to test the reproducibility of the data generated with the help of the Niton XL3t analyser the inter-laboratory BMS (black marine shale) standard was selected and analysed at the same point 30 times applying the analytical Cu/Zn Mining mode for 240s.

SAMPLE	No.	Al	Al 2σ	Al 2σ (%)	Zr	Zr 2σ	Zr 2σ (%)	Rb	Rb 2σ	Rb 2σ (%)	Mn	Mn 2σ	Mn 2σ (%)
BMS	1	94996.4	3031.82	3.19	67.14	2.71	4.04	52.7	1.71	3.24	781.92	60.66	7.76
BMS	2	95052.6	3019.82	3.18	67.14	2.7	4.02	52.02	1.7	3.27	754.96	59.86	7.93
BMS	3	96714.27	3054.14	3.16	69.56	2.78	4.00	53.89	1.76	3.27	756.23	60.93	8.06
BMS	4	96214.2	3035.28	3.15	70.44	2.77	3.93	53.73	1.74	3.24	787.26	61.21	7.78
BMS	5	95544.52	3077.98	3.22	66.72	2.7	4.05	52.6	1.71	3.25	748.26	59.66	7.97
BMS	6	95284.27	2989.62	3.14	68.02	2.72	4.00	52.79	1.71	3.24	801.8	61	7.61
BMS	7	95801.87	3099.77	3.24	68.62	2.73	3.98	52.99	1.72	3.25	750.57	60.35	8.04
BMS	8	94125.47	3015.56	3.20	68.01	2.71	3.98	52.76	1.7	3.22	724.04	59.2	8.18
BMS	9	96022.66	3088.64	3.22	69.31	2.76	3.98	53.4	1.74	3.26	697.82	59.1	8.47
BMS	10	95876.04	3033.21	3.16	69.91	2.76	3.95	51.49	1.7	3.30	762.68	60.26	7.90
BMS	11	96196.98	3100.82	3.22	67.29	2.71	4.03	53.13	1.72	3.24	773.72	60.43	7.81
BMS	12	95571.05	3005.02	3.14	68.52	2.74	4.00	52.18	1.71	3.28	728.84	59.99	8.23
BMS	13	95110	3041.08	3.20	67.69	2.68	3.96	51.42	1.67	3.25	779.62	59.84	7.68
BMS	14	97900.21	3102.78	3.17	68.42	2.73	3.99	51.71	1.7	3.29	713.04	59.14	8.29
BMS	15	96219.93	3030.4	3.15	69.25	2.74	3.96	53.18	1.72	3.23	794.55	60.69	7.64
BMS	16	98817.63	3124.19	3.16	69.6	2.77	3.98	53.1	1.73	3.26	822.89	61.73	7.50
BMS	17	93586.19	2979.92	3.18	69.24	2.72	3.93	52.39	1.7	3.24	759.71	59.94	7.89
BMS	18	97033.55	3113.52	3.21	71.87	2.76	3.84	52.03	1.7	3.27	741.1	59.37	8.01
BMS	19	95911.48	3075.17	3.21	70.78	2.75	3.89	51.72	1.69	3.27	756.03	59.92	7.93
BMS	20	95346.94	3041.43	3.19	67.73	2.7	3.99	51.89	1.69	3.26	709.48	58.66	8.27
BMS	21	95279.17	3002.29	3.15	67.38	2.71	4.02	52.44	1.7	3.24	746.5	59.6	7.98
BMS	22	96751.66	3035.06	3.14	69.8	2.72	3.90	51.45	1.68	3.27	735.99	59.17	8.04
BMS	23	96040.87	3082.31	3.21	68.56	2.74	4.00	52.92	1.72	3.25	758.98	60.42	7.96
BMS	24	95813.5	3046.39	3.18	68.31	2.73	4.00	52.3	1.71	3.27	734.51	59.88	8.15
BMS	25	97682	3121.55	3.20	68.64	2.71	3.95	51.66	1.68	3.25	773.74	60.15	7.77
BMS	26	99018.96	3154.6	3.19	67.51	2.72	4.03	53.15	1.72	3.24	743.97	59.89	8.05
BMS	27	99008.55	3114.68	3.15	69.09	2.73	3.95	53.48	1.72	3.22	736.84	59.61	8.09
BMS	28	95263.96	3030.06	3.18	68.18	2.71	3.97	53.65	1.72	3.21	741.12	60.19	8.12
BMS	29	98048.44	3109.03	3.17	67.58	2.71	4.01	53.29	1.72	3.23	760.06	59.66	7.85
BMS	30	99352.22	3109.74	3.13	66.99	2.71	4.05	51.98	1.7	3.27	784.38	60.65	7.73

Table 4.8: Measuring the BMS standard at the same point 30 times testing the reproducibility of data generated by the Niton XL3t. The analytical Cu/Zn mining mode was used, analytical time was 240s. The elemental concentrations remain constant within the analytical error.

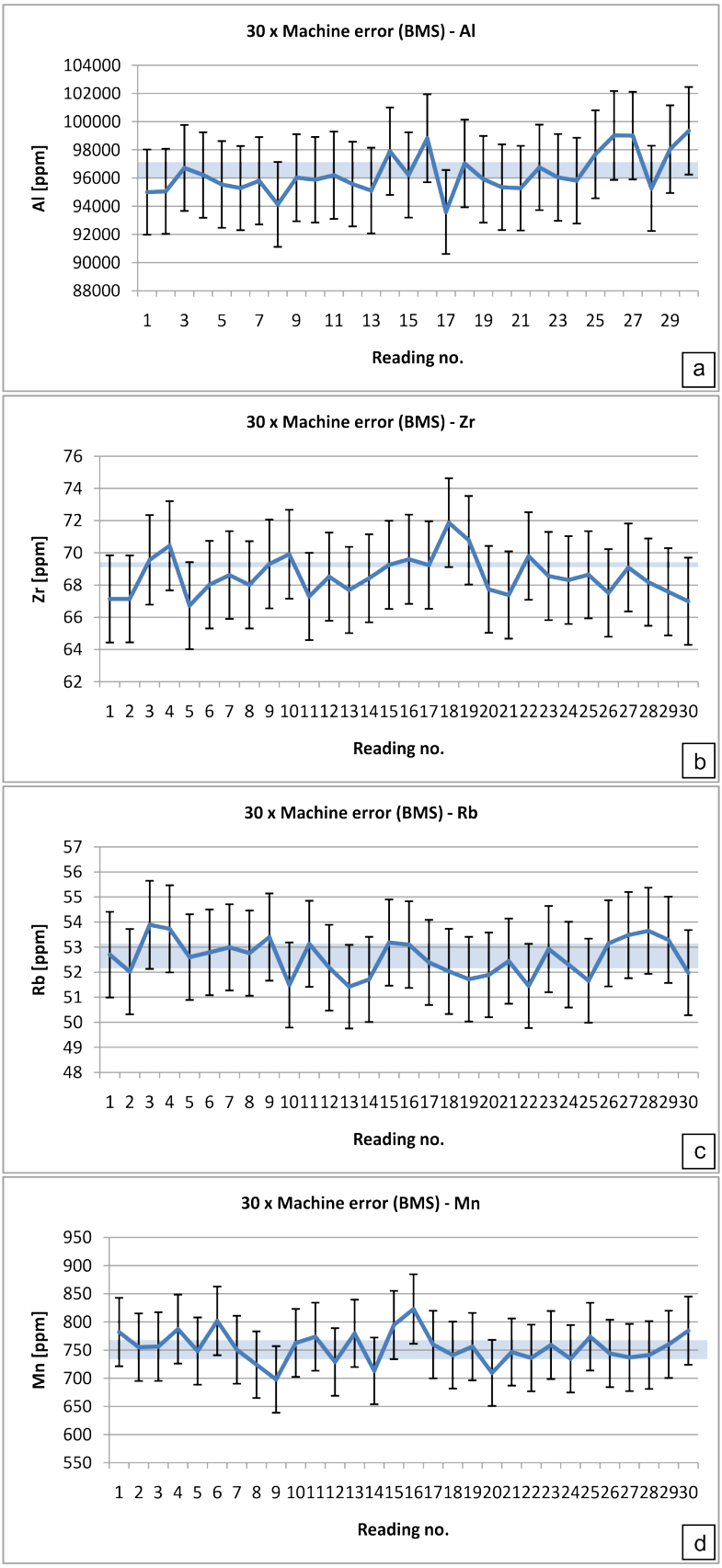

Figure 4.10: Reproducibility of Niton XL3t XRF analyser results using the data documented in **Table 4.8**. The Cu/Zn mining mode was selected, 240s was the set analytical time for each reading. The data remain consistent. The elements selected (Al, Zr, Rb and Mn) best represent the slightly irregular pattern observed within the data. This irregular pattern is interpreted to be caused by the Niton XL3t internal cooling system (controlling the detectors analytical temperature). Note that all readings are nonetheless within the range of the analytical 2-sigma error. In order to compensate for this irregular signal the values of 3 consecutive readings were averaged.

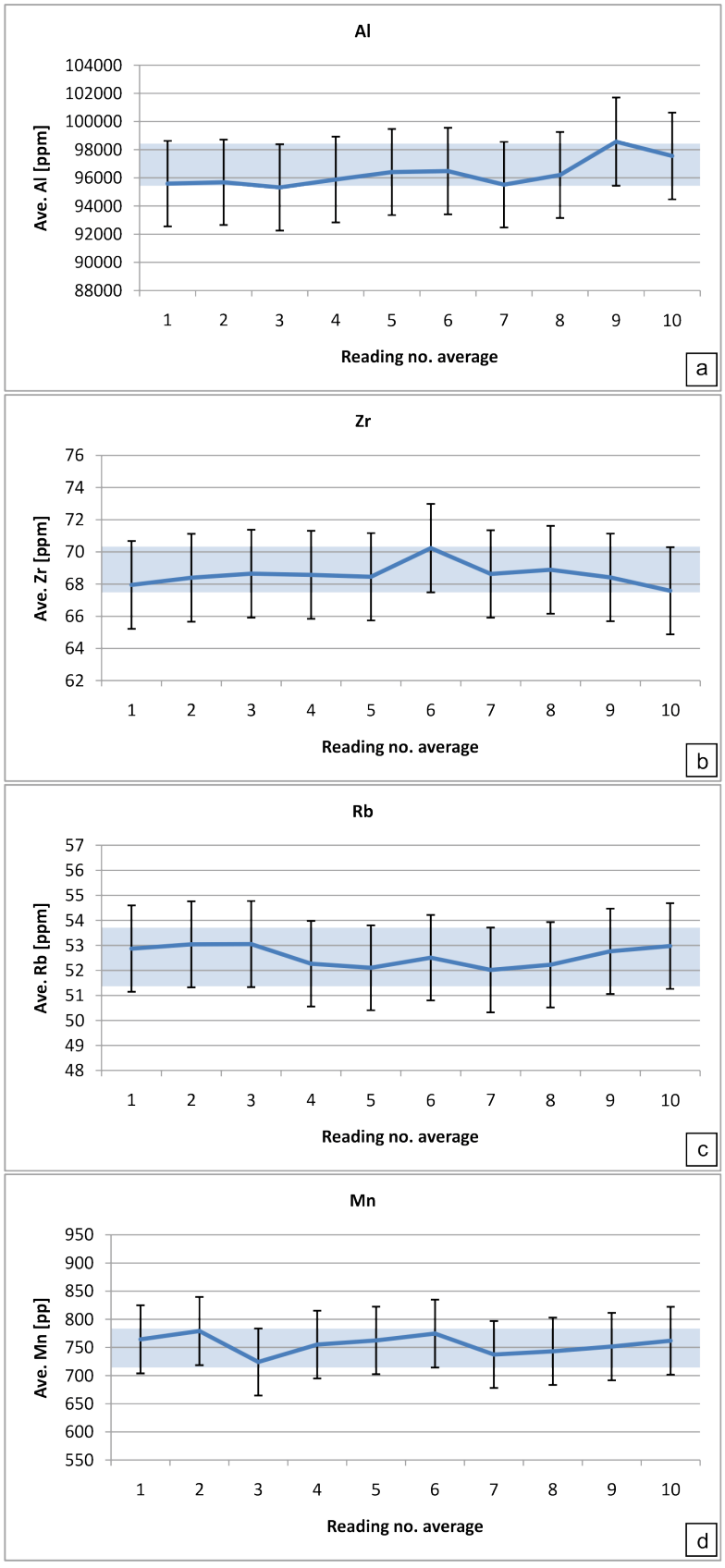

Figure 4.11 The effects of averaging the values of 3 consecutive readings (**Table 4.8**). Note how the irregular signal for each of the elements is flattened out.

4.8 Evaluation and discussion of the differing analytical procedures

4.8.1 Sample preparation technique

The purpose of this experiment (see **Chapter 4.7.1**), was to determine the effects of different sample preparation methods on the geochemical results.

The black shale samples Villa 1, Villa 2 and Villa 3 were split three ways to provide sufficient material for the three differing sample preparation methods (powder capsule, pressed powder disc and finally the comparison to unprepared raw sample, see **Chapter 4.4**). The geochemical results of this experiment are given in **Table 4.5** and illustrated in **Figures 4.6** and **4.7**. The differing sample preparation methods are seen to have a significant effect on the absolute values and 2-sigma errors determined by the Niton XL3t XRF analyser. The different methods largely effect the detection of the lighter elements Al and Si (see **Figure 4.6** and **4.7**). Analysis of the pressed powder-disc results in the highest readings for absolute elemental Al concentrations in comparison to the samples prepared by using the powder capsule method (see **Figure 4.6**). As a result, the corresponding absolute 2-sigma errors (given in ppm) increase systematically with the increase in absolute elemental concentrations detected. The 2-sigma error percentages of the light element Al decrease dramatically when utilising the pressed powder disc in comparison to the powder capsule. Readings of the powder capsule samples were associated with the highest 2-sigma errors (see **Figure 4.7 - b,d** and **f**).

The absolute values and related elemental 2-sigma errors alter significantly and systematically with the sample preparation method used (see above). The reason for this systematic offset of the geochemical data and the significant changes in the related 2-sigma errors is interpreted to be largely controlled by the following parameters: within the [1] raw, un-prepared sample, the elemental distribution is in many cases not homogenous. This effect is also strongly related to the grain-size of the sediment. Furthermore, raw, natural samples extracted from any geological section and directly analysed will often exhibit an irregular, uneven surface, thus increasing the amount of deflected primary X-rays and subsequently decreasing the total count-rate per element. The readings of the [2] powder capsules show much lower absolute values for the light element Al and systematically higher 2-sigma errors. This shift is partly related to a masking and absorption effect caused by the thin plastic film used to seal the capsules. Additionally, the loading of the capsules turned out to be systematically less dense than the packing of the pressed discs. The

pore-space provided by the less dense packing enabled moisture to adsorb to the fine powder particles of the sample, hence increasing the overall volatile content and consequently also increasing the analytical error. In contrast to the aforementioned preparation methods the [3] powder disc provides a completely homogenous element distribution. The amount of pore space and associated adsorption of volatiles is essentially negligible, as a near perfect loading is achieved due to the high pressures applied during the pressing process. Furthermore, the preparation of discs leads to very flat and even surfaces, significantly reducing the amount of deflected primary X-rays during analyses.

In summary, the power capsules are here deemed to be the most ineffective way to analyse lighter elements. The powder discs are the preferred sample preparation method as they lead to the most reduced 2-sigma errors and hence to data of the highest quality achievable with XRF analysis. The analysis of the raw samples is not completely ruled out, as valuable insights can be gained from the elemental ratios resulting from *in situ* analysis. However, the absolute concentrations may vary significantly due to the reasons described above, and caution must be taken when interpreting this data.

4.8.2 Helium purging of the detector

Two international standards (SCO-1 and MAG-1) along with an inter-laboratory standard (BMS) were chosen to test the effects of helium purging. The purging with helium is assumed to clear the detector of heavier chemical elements, with whom the primary X-ray beam may already start to interact before being emitted onto the sample, hence leading to unwanted, artificial signals that will reduce the overall quality of the data. The resulting data are documented in **Table 4.6** and displayed in **Figure 4.8**. The lighter elements selected and analysed were Mg, Al, Si and K. All elements show significantly reduced 2-sigma errors when the helium purging is introduced.

4.8.3 Analytical time and its effect on 2-sigma errors

The standards SCO-1, MAG-1 and BMS were selected for this test. The results are given in **Table 4.7** and illustrated in **Figure 4.9**. The purpose of this test was to determine the most practical time span. The elements selected to show the relationship between the variation of analytical time and

2-sigma errors are Al and K. From analysing the data (see **Figure 4.9**) it is evident that increasing the length of analytical time significantly reduces the related 2-sigma errors. The Al concentrations are not available for the first 60s of analysis, as the special configuration of the 'light-range filter', which is measuring the lighter elements such as Al, requires a 60s duration for initial signal acquisition. The 2-sigma errors for the Al and K concentrations are significantly reduced between the 120s and 240s analytical time-spans (see **Figure 4.9**), whereas, the difference in the 2-sigma errors between the 240s and maximum analytical time-span of 360s is noticeably less prominent. When the analytical time is increased, the total number of counts of the particular element in question will also increase, thus leading to a systematically lower statistical 2-sigma error and higher quality readings.

4.8.4 How reliable is the Niton XL3t for geochemical data

The inter-laboratory standard BMS was used in this experiment to determine how reproducible the Niton XL3t data are. The results are given in **Table 4.8** and displayed in **Figures 4.10** and **4.11**. The elements selected for analysis and comparison were Al, Zr, Rb and Mn. The BMS standard was consecutively spot measured 30 times (240s per analysis) to test the machines ability to reproduce data under replicable and constant analytical conditions. In each case the absolute elemental values are within the 2-sigma error ranges, as indicated and highlighted by the blue horizontal bars in **Figure 4.10**. The absolute elemental concentrations for Al, Zr, Rb and Mn exhibit irregular patterns. These irregular patterns are thought to be related to the cooling and ventilation system of the analyser's detector. The averaging of 3 data points proved to be sufficient to compensate for this artificially introduced variation in the data (see **Figure 4.11**). Based on this test, the reliability of the data generated is regarded to be high.

4.9 Summary: Material and methods

The pressed powder discs were demonstrated to be the best sample preparation method for use with the Niton XL3t XRF analyser, as the discs allowed for the unhindered detection of light elements and lowest 2-sigma errors. Helium purging of the detector is a necessity when analysing light elements in the analytical Cu/Zn mining mode, as it greatly reduces the 2-sigma errors and

allows for the detection of Mg. For reliable results, the analytical time should be no less than 240 seconds in the Cu/Zn mining mode. The samples are to be measured at the same point three times and averaged in order to eliminate the artificial signal generated by the machine's cooling system. The calibration files for all major and trace elements are based on the standards described in **Table 4.4**. The raw Niton XL3t data plotted against published standard values, resulted in correlation coefficients (R^2) of 0.9 and higher (Fe calibration for example 0.993, see **Figure 4.6**), suggesting the data produced by the energy dispersive Niton XL3t XRF analyser are comparable to wave-length dispersive XRF systems.

The advantages of the energy-dispersive Niton XL3t XRF analyser is that its portable and detects groups of elements instantaneously in contrast to the single element analysis of wave-length dispersive XRF systems. This leads to a very high time, energy and importantly, cost efficiency. The absolute detector resolution of the Niton XL3t XRF analyser is far from the standards of available wave-length dispersive XRF systems, however it has been demonstrated to generate under controlled laboratory conditions meaningful and reproducible data. The limitations are the inability to detect elements lighter than Mg and various rare earth elements. The accuracy in the field is limited by compositional heterogeneities, the amount of volatiles and inconsistent measuring geometries.

To generate the geochemical major and trace element data set for the present study, all samples (see **Table 4.2**) were processed and pressed powder discs formed. Each sample was analysed three times and the readings subsequently averaged to eliminate any artificial signals caused by the machine's cooling system. Measuring time for one analysis was 240 seconds for the analytical Cu/Zn Mining mode and 120 seconds for the analytical Soil mode. The application of both analytical modes was required, as the mining mode enabled the analysis of the lighter elements and the soil mode the heavier elements. The elemental data were then selected from either one of the two analytical routines, based on the highest R^2 values of the calibration data, and compiled into a final dataset. For the generation of the high resolution field-data (see **Chapter 4.1**), particular emphasise was laid on the concentrations of redox sensitive elements like V and U, therefore the soil mode with a measuring time of 120s was selected for this *in situ* analysis to generate the best results.

4.10 Calculating specific parameters & proxies

This section details the formulas applied to the geochemical dataset in order to calculate specific parameters and proxies. Detailed explanations and descriptions for each calculation are provided in **Chapter 3** 'Black Shale Genesis'.

4.10.1 Calculating elemental enrichment factors

In order to estimate the enrichment or depletion of a given element relative to a known standard, enrichment factors (EF) are used. The EF calculation typically uses Al to normalise the elemental concentrations as described in **Chapter 2.2.12**. The following EF formula **[14]** was applied (Rule, 1986; Dellwig *et al.,* 2000; Scopelliti *et al*., 2006; Tribovillard *et al*., 2006; Turgeon and Brumsack, 2006):

$$\mathbf{EF_{element\ X} = X/Al_{(unknown\ sample)} / X/Al_{(known\ standard)}} \qquad \mathbf{[14]}$$

If the value calculated is greater than 1 then the particular element in question is enriched relative to the standard it is compared to. If the value is less than 1 then it is depleted. The EF calculated are illustrated by EF plots, which were generated with the help of the software GCDkit 3.0 (Janoušek *et al.,* 2006; Janoušek *et al.,* 2011). For the normalisation process the following standards (see **Table 8.3.3.1**, 'Results appendix B: part 1') were used: [1] **Average Shale** (Turekian and Wedepohl, 1961), [2] **Average Shale** (Wedepohl, 1971; Wedepohl, 1991), [3] **Average black shale** (Vine and Tourtelot, 1970), [4] **SCO-1** (Abbey and Geological Survey of Canada, 1983; Gladney and Roelandts, 1988; Govindaraju, 1989, 1994), [5] **Post-Archean Australian Shale (PAAS)** (Taylor and McLennan, 1985), [6] **Post-Archean Upper Continental Crust (PA-UCC)** (Taylor and McLennan, 1985, 1995), [7] **Upper Crust** (Wedepohl, 1991 Largly derived from Shaw *et al.* (1967); Shaw *et al.* (1976 in: Rudnick and Gao, 2003) and finally, [8] **North American Shale Composite (NASC)** (Gromet *et al.,* 1984).

4.10.2 Total Organic Carbon (TOC) proxy

The TOC values were calculated using total uranium ppm values as a proxy for organic matter (Fertl and Chilingar, 1988; Fello *et al.* 2006; Lüning and Kolonic, 2006). The relationship between U

and organic matter is described in **Chapter 3** 'Black Shale Genesis'. Using the relationship between TOC and U as described by Fertl and Chilingar (1988), the formula **[15]** was developed:

$$\mathbf{TOC = 3.9637 \times \ln(U\ ppm) - 5.6873.} \qquad \mathbf{[15]}$$

Where TOC is the amount of total organic carbon in wt%, ln is the natural logarithm applied to the total U ppm values.

4.10.3 Degree of Pyritization (DOP)

The DOP is described in **Chapter 3** 'Black Shale Genesis', has been used as a reliable redox indicator. In order to calculate the DOP, the concentrations of pyritic iron and acid soluble iron (or reactive iron) are needed. These variables have been approximated using the following formulas: **[16]** Mosher (2006 in: Hetzel *et al.,* 2006); Hetzel *et al.* (2011), **[17]** Kuroda *et al.* (2005), **[18]** Kuroda *et al.* (2005).

$$\mathbf{Reactive\ Iron\ (Fe_x) = Fe_2O_3 - (0.25 \times Al_2O_3)} \qquad \mathbf{[16]}$$

$$\mathbf{Fe_{alum} = 0.54 \times Al_2O_3} \qquad \mathbf{[17]}$$

$$\mathbf{Fe_{pyrite}\ (FeS_2) = Fe_2O_3 - Fe_{alum}} \qquad \mathbf{[18]}$$

The DOP is then calculated by combining the calculated, $\mathbf{Fe_{pyrite}}$ and $\mathbf{Fe_x}$ values using formula **[19]**, (Wignall, 1994):

$$\mathbf{DOP = Fe_{pyrite} / (Fe_{pyrite} + Fe_x)} \qquad \mathbf{[19]}$$

4.10.4 Sodium proxy

The Niton XL3t XRF analyser is unable to detect elements lighter than Magnesium (see **Chapter 4.5**). Therefore the following formula was implemented in order to approximate the Na_2O values, using the observed relationship between Na_2O and K_2O in a selection of black shale standards and the weak positive correlation of Na_2O to K_2O with $R^2 \geq 0.4$ described from floodplain sediments (Salminen and De Vos, 2005). The black shale standards selected were the **[1]** North American Shale Composite (NASC) of Gromet *et al.* (1984), the **[2]** three average shale composites of (i) Pettijohn (1975), (ii) Turekian and Wedepohl (1961) and (iii) Heinrich *et al.* (1980) in: Wedephol (1971 & 1991), the **[3]** average black shale composite of Vine and Tourtelot (1970), the **[4]** SCO-1

shale standard of Abbey and Geological Survey of Canada (1983) and finally, the **[5]** Post-Archean Australian Shale (PAAS) of Taylor and McLennan (1985). The K_2O and Na_2O values for each of the aforementioned black shale standards were cross-plotted in order to determine the correlation (R^2 = 0.437). The equation of this curve was applied to total K_2O values within this project in order to give a rough approximation as to the Na_2O values. The following equation **[20]** was applied:

$$\mathbf{Na_2O = [0.277 \times (K_2O_{total\ wt\%})] + 0.281} \qquad \mathbf{[20]}$$

4.10.5 Palaeobioproductivity calculations using barium

The quantification of palaeobioproductivity using geochemical proxy data is under certain circumstances an intricate issue. Various calculation steps are needed in order to approximate the palaeobioproductivity. The following methods were applied (Pfeifer *et al.,* 2001):

4.10.5.1 Calculation of biogenic barium and its accumulation rates

A normative analysis was applied to correct for lithogenic Ba, as lithogenic Ba is not related to the bioproductivity within surface waters (Pfeifer *et al.,* 2001). Barium in marine sediments occurs as biogenic barite or associated with alumosilicates (as terrigenous/lithogenic Ba) which is the main source of detrital Ba. The ratio of the detrital Ba/Al is the crucial factor (Bernárdez *et al.,* 2008) for the calculation of biogenic Ba (Ba_{bio}) from the total Ba (Ba_{total}). The terrigenous Ba (Ba_{terr}) is estimated by the ratio of total Ba to the conservative elements Al or Ti ($Ba/Al_{aluminosilicate}$ or $Ba/Ti_{aluminosilicate}$). The Ba_{bio} is then calculated by subtracting the Ba_{terr} from the Ba_{tot} concentration. Ti can also be used as a proxy for the terrigenous fraction as part of the Al concentrations may be of biogenic origin (Murray *et al.*, 1993 in: Bonn *et al.,* 1998). The following formulas **[21]** from Pfeifer *et al.* (2001) and **[22]** from Bonn *et al.* (1998) were applied to calculate Ba_{bio}. Ti and Al concentrations were used to normalise the Ba concentrations.

$$\mathbf{Ba_{bio}\ (Ba_{excess}) = Ba_{tot} - (Al\ X\ Ba/Al_{aluminosilicate})} \qquad \mathbf{[21]}$$

$$\mathbf{Ba_{bio}\ (Ba_{excess}) = Ba_{tot} - (Ti\ X\ Ba/Ti_{aluminosilicate})} \qquad \mathbf{[22]}$$

Under certain circumstances the applied formula **[21]** and **[22]** generated non-realistic negative values. Therefore, the approximation for Ba(bio) developed by Prakash Babu *et al.* (2002) was also tested and subsequently used for the present study. The proxy of Prakash Babu *et al.* (2002) is

based on the assumption that the lowest Ba/Al ratios are always equivalent to the local Ba background.

In order to calculate the accumulation rates of biogenic Ba (AR Ba_{bio}) the equations of Pfeifer *et al.,* (2001) were applied:

$$\mathbf{AR\ Ba_{bio} = Ba_{bio}\ X\ MAR/100} \qquad \mathbf{[23]}$$

Where MAR is the mass accumulation rate in g cm^{-2} kyr^{-1}

$$\mathbf{MAR = SR\ X\ DBD} \qquad \mathbf{[24]}$$

Where SR is the sedimentation rate in cm kyr^{-1} and the DBD is the dry bulk density in g cm^{-3}

The sedimentation rate (SR) was calculated by using the available biostratigraphic age constraints for the base and the top of the lower part of the Formigoso Fm. (Bernesga Mb.) and the number of samples taken. The Bernesga Mb. spans the time from the Mid-Late Aeronian to the Mid-Telychian (see **Chapter 2.1.3** 'The Silurian of the Cantabrian Zone: a review'). Using the numerical ages of Gradstein *et al.* (2012), a duration of ~4 Myr can be assigned to the Bernesga Mb. A total of 181 shale samples were taken from the Bernesga Mb. at the Aralla section at intervals of 25 cm. Applying the certainly simplistic assumption, that the Bernesga Mb. does not include horizons affected by stratigraphic condensation and/or dilution an average time-span of 22099.44 yrs is represented by 25 cm of sediment, and therefore, 1cm of sediment represents ~883.97 yrs. From this an approximate average sedimentation rate of ~**1.12 cm kyr^{-1}** was calculated (~11.2 m per million years). This estimate corresponds very well to previously published sedimentation rates for other black shales (Stein, 1990; Erbacher *et al.,* 2004; Erbacher *et al.,* 2005; Turgeon and Brumsack, 2006).

The Dry Bulk Density (DBD) was estimated by applying the average shale DBD ranges of 1.8 – 2.8 g cm^{-3} (Rieke and Chilingarian, 1974). Both the lower range value and upper range value for DBD along with the SR was used to calculate the minimum and maximum Mass Accumulation Rate (MAR):

$$\mathbf{Minimum\ MAR} = 1.11603 \times 1.8 = \mathbf{2.008854\ g\ cm^{-2}\ kyr^{-1}} \qquad \mathbf{[25]}$$

$$\mathbf{Maximum\ MAR} = 1.11603 \times 2.8 = \mathbf{3.124884\ g\ cm^{-2}\ kyr^{-1}} \qquad \mathbf{[26]}$$

4.10.5.2 Calculation of new production (P_{new})

In order to calculate the new production (P_{new}) the flux of Ba (F_{ba}) to the seafloor has to be calculated first using equation **[27]** (Pfeifer *et al.,* 2001). Dymond *et al.* (1992) related the amount of Ba_{bio} preserved to the MAR (in mg cm^{-2} kyr^{-1}) of the sediment (equation **[28]**). To estimate F_{ba} on the basis of Ba accumulation rates the amount of preserved biogenic Ba ($\%Ba_{pres}$) is calculated (equation **[28]**). Dissolved Ba at the sediment/water interface (F_{ba}) is calculated by dividing the AR Ba_{bio} by $\%Ba_{pres}$ (equation **[27]** incorporates equation **[28]**):

$$F_{ba} = AR\ Ba_{bio} / 0.209 \log(MAR) - 0.213 \quad [27]$$

$$\%Ba_{pres} = 20.9 \log(MAR) - 21.3 \quad [28]$$

Consequently, the new production rate (P_{new}) is expressed by equation **[29]** in gC m^{-2} yr^{-1} (Francois *et al*., 1995 in: Pfeifer *et al.,* 2001):

$$P_{new} = 1.95(F_{ba})^{1.41} \quad [29]$$

4.10.5.3 Calculation of primary production (PP)

The primary production (or PP in gC m^{-2} yr^{-1}) is calculated using formula **[30]** of Eppley and Peterson (1979 in: Pfeifer *et al.,* 2001) based on the P_{new} values calculated by using equation **[29]**:

$$PP = 20(P_{new})^{0.5} \quad [30]$$

4.10.6 Cyclicity (Fourier analysis)

The following functions were applied to the redox sensitive element geochemistry of the Silurian black shales from the Formigoso Fm., Cantabria. The functions and plots were created using the analytical PAST software (Hammer *et al.,* 2001; Hammer and Harper, 2006). To calculate and describe the data **[1]** matrix plot functions, **[2]** spectral analysis and finally, **[3]** short-time Fourier analysis was used.

- *Matrix function*

The matrix function is a two-dimensional plot of the data matrix. The data is displayed using a gray-scale with white for the lowest value and black for the highest, or a colour scale. The matrix plots are used to get an overview over a large data matrix (Hammer *et al.,* 2001).

- *Spectral Analysis*

Spectral analysis of the geochemical data was carried out in order to identify and describe any potential periodicities or other spectral characteristics. For this, the datasets were taken as the sum of superimposed parts, therefore decomposed into 'sum of sines' (Hammer and Harper, 2006) and subsequently analysed by using

$$F(t) = \cos\left(2\frac{\quad}{\quad}\right) \qquad [31]$$

Where F(t) is the time series of a total duration of T, a_i are the amplitudes and ω_i are the phases (Hammer and Harper, 2006).

The frequency axis is in units of *1/(x unit)*. If for example, your *x* values are given in millions of years, a frequency of 0.1 corresponds to a period of 10 million years. The power axis is in units proportional to the square of the amplitudes of the sinusoids present in the data.

The highest peak in the spectrum is presented with its frequency and power value, together with a probability that the peak could occur from random data. The 0.01 and 0.05 significance levels ('white noise lines') are shown as red dashed lines (Hammer *et al.,* 2001).

- *Short-time Fourier*

The Short-time Fourier function is a spectral analysis which utilises discrete Fourier transform (FFT) functions, however, it divides the signal into a sequence of overlapping windows, which are analysed individually (Hammer and Harper, 2006). This allows the development of the spectrum in time, in contrast to the global analysis provided by other spectral analysis modules. The sample position is shown on the *x* axis, frequency (in periods per sample) on the *y* axis, and power on a logarithmic scale as colour or grey scale (Hammer *et al.,* 2001). The discrete Short-time Fourier analysis was carried by using the equations and algorithms of Hammer and Harper (2006):

$$c_i = \frac{\quad}{\quad} \cos(2 \quad (j - 1)/N) \qquad [32]$$

$$d_i = \frac{}{} \sin(2 \quad (j - 1)/N) \qquad [33]$$

$$a_i = \frac{}{} \qquad [34]$$

$$\omega_i = \tan^{-1} \frac{}{} \qquad [35]$$

Where a_i and ω_i are the expressions of the spectral coefficients. F is the time series, j are the increments and N is the total number of samples.

4.11 Scanning Electron Microscopy (SEM)

Scanning Electron Microscopic imaging and elemental analysis was carried out with a Hitachi TM3000 Scanning Electron Microscope with EDX analytical attachment.

4.12 Selected elements and calibration files used

There are several differing analytical modes available for use with the Niton XL3t XRF analyser, as described above (**Chapter 4.4**). This meant that individual elements had to be selected from one of the various analytical modes. The elements were selected based on their correlation coefficients when plotted against the international and inter-laboratory standards. The following table (**Table 4.9**) displays all major and trace elements and from which analytical mode they were selected.

Element	Type	Mode
MgO	%	Mining Cu/Zn
Mg	ppm	Mining Cu/Zn (Cal)
Al_2O_3	%	Mining Cu/Zn
Al	ppm	Mining Cu/Zn (Cal)
SiO_2	%	Mining Cu/Zn
Si	ppm	Mining Cu/Zn (Cal)
K_2O	%	Mining Cu/Zn
K	ppm	Mining Cu/Zn (Cal)
CaO	%	Mining Cu/Zn
Ca	ppm	Mining Cu/Zn (Cal)
TiO_2	%	Mining Cu/Zn
Ti	ppm	Mining Cu/Zn (Cal)
MnO	%	Soil
Mn	ppm	Soil
Fe_2O_3	%	Soil
Fe	ppm	Soil (Cal)
Co	ppm	Soil
P	ppm	Mining Cu/Zn
S	ppm	Mining Cu/Zn (Cal)
Cl	ppm	Mining Cu/Zn
Sc	ppm	Soil
V	ppm	Soil
Cr	ppm	Soil
Ni	ppm	Soil (Cal)

Element	Type	Mode
Cu	ppm	Soil
Zn	ppm	Mining Cu/Zn (Cal)
As	ppm	Mining Cu/Zn
Se	ppm	Soil
Rb	ppm	Mining Cu/Zn (Cal)
Sr	ppm	Soil (Cal)
Zr	ppm	Mining Cu/Zn (Cal)
Nb	ppm	Mining Cu/Zn (Cal)
Mo	ppm	Mining Cu/Zn
Pd	ppm	Soil
Ag	ppm	Mining Cu/Zn
Cd	ppm	Soil
Sn	ppm	Mining Cu/Zn
Sb	ppm	Soil
Te	ppm	Soil
Cs	ppm	Soil
Ba	ppm	Soil (Cal)
W	ppm	Soil
Au	ppm	Soil
Hg	ppm	Soil
Pb	ppm	Mining Cu/Zn (Cal)
Bi	ppm	Mining Cu/Zn
Th	ppm	Soil
U	ppm	Soil

Table 4.9 Analytical modes for which the various elements listed were selected. The table also indicates the various elements that were calibrated (Cal).

The calibration method is described in **Chapter 4.6**. Elemental calibrations are documented in **Table 4.9**. The majority of the major element values were calibrated other than the Mn values, whereas for the trace elements only a select few were calibrated. This was because the majority of the trace element absolute concentrations were very low, or near to the detection limits (D.L). The elemental absolute concentrations of the international and inter-laboratory standards were significantly higher. As a result, when the calibration process was applied it had a significant effect on the results. For the low elemental abundances of certain trace elements the calibration process resulted in even negative ppm values.

4.13 Elemental errors

The previous section indicates which elements were selected from the differing analytical modes of the Niton XL3t analyser. The following table (**Table 4.10**) displays the average 2-sigma error ranges for these selected elements. The elemental error ranges were calculated from the entirety of the geochemical dataset, consisting of 3594 analysis points.

Element	Mode	Average Form. Value	Ave. Lab Error %	Ave. Lab Error value	Ave. Field Error %	Ave. Field Error value
Major		**Wt%**	**(+/-) %**	**(+/-) wt%**	**(+/-) %**	**(+/-) wt%**
MgO	Mining	1.11	**31.42**	**0.35**	**N/A**	**N/A**
Al_2O_3	Mining	29.94	**1.1**	**0.33**	**N/A**	**N/A**
SiO_2	Mining	51.54	**0.6**	**0.31**	**N/A**	**N/A**
K_2O	Mining	3.81	**1.51**	**0.06**	**1.77**	**0.07**
CaO	Mining	0.24	**30.83**	**0.07**	**35.48**	**0.09**
TiO_2	Mining	1.14	**1.31**	**0.01**	**2.11**	**0.02**
MnO	Soil	0.06	**35.02**	**0.02**	**46.81**	**0.03**
Fe_2O_3	Soil	6.71	**0.6**	**0.04**	**0.79**	**0.05**

Trace		ppm	(+/-) %	(+/-) ppm	(+/-) %	(+/-) ppm
Co	Soil	125.74	**55.94**	**70.34**	**26.05**	**32.75**
P	Mining	320.82	**14.78**	**47.43**	**N/A**	**N/A**
S	Mining	927.73	**12.78**	**118.54**	**47.6**	**441.6**
Cl	Mining	615.85	**4.35**	**26.8**	**N/A**	**N/A**
Sc	Soil	22.36	**56.22**	**12.57**	**49.77**	**11.13**
V	Soil	214.28	**14.15**	**30.32**	**18.78**	**40.24**
Cr	Soil	121.02	**11.76**	**14.24**	**20.64**	**24.98**
Ni	Soil	84.17	**28.26**	**23.78**	**35.81**	**30.14**
Cu	Soil	36.45	**29.23**	**10.65**	**34**	**12.39**
Zn	Mining	62.44	**25.4**	**15.86**	**48.69**	**30.4**
As	Mining	25.59	**14.56**	**3.73**	**9.46**	**2.42**
Se	Soil	2.74	**57.1**	**1.57**	**53.94**	**1.48**
Rb	Mining	155.18	**3.09**	**4.79**	**4.82**	**7.48**
Sr	Soil	190.26	**2.63**	**5**	**2.43**	**4.62**
Zr	Mining	134.45	**2.5**	**3.36**	**3.25**	**4.37**
Nb	Mining	19.5	**8.25**	**1.61**	**N/A**	**N/A**
Mo	Mining	4.77	**39.3**	**1.88**	**40.99**	**1.96**
Pd	Soil	15.11	**61.38**	**9.28**	**54.4**	**8.22**
Ag	Mining	59.03	**33.18**	**19.58**	**12.83**	**7.57**
Cd	Soil	13.31	**57.62**	**7.67**	**41.18**	**5.48**
Sn	Mining	26.85	**45.7**	**12.27**	**27.53**	**7.39**
Sb	Soil	27.74	**48.59**	**13.48**	**24.09**	**6.68**
Te	Soil	51.59	**44.96**	**23.2**	**21.78**	**11.24**
Cs	Soil	29.26	**29.41**	**8.6**	**11.57**	**3.39**
Ba	Soil	461.37	**8.56**	**39.47**	**6.38**	**29.44**
W	Soil	29.05	**57.19**	**16.62**	**60.13**	**17.47**
Au	Soil	8.88	**62.71**	**5.57**	**58.03**	**5.15**
Hg	Soil	6.64	**54.47**	**3.61**	**56.76**	**3.77**
Pb	Mining	42.65	**26.96**	**11.5**	**28.37**	**12.1**
Bi	Mining	61.81	**24.26**	**14.99**	**N/A**	**N/A**
Th	Soil	13.91	**24.12**	**3.36**	**28.18**	**3.92**
U	Soil	10.91	**44.95**	**4.91**	**55.42**	**6.05**

Table 4.10 The average 2-sigma errors were calculated from the entirety of the geochemical database consisting of 3594 readings per element. The 2-sigma errors that are relatively high are associated to the lower absolute elemental concentrations predominantly within the trace elements. For example, a U value of 9.35ppm has a 2-sigma error of 44.95% (or +/- 4.2 ppm). This table allows for a direct comparison between the lab based 2-sigma errors and the field based 2-sigma errors. The 'Average Formigoso Fm.' values (Average Form. Value) were calculated from 496 shale samples, excluding zero values (values below D.L.). The colours represent the differing analysis modes. Pink represents the analytical Mining Cu/Zn mode and the blue signifies the analytical Soil mode of the Niton XL3t XRF analyser. The field readings only contain analytical Soil mode readings, as helium was not taken into the field for the purging of the detector. N/A denotes elements that were not analysed in the specific analytical mode, in this case the Soil mode of the Niton XL3t.

Chapter 5
Geochemical results

Contents

This chapter documents and describes all geochemical data obtained from the analysed sections: **[1]** Aralla section, **[2]** the high-resolution Aralla section, **[3]** Caldas de Luna section, **[4]** La Majua section, **[5]** Sena de Luna section and finally, **[6]** the Villanueva section. The systematic labelling and sample identification for the locations listed above can be found in **Table 4.2** of **Chapter 4** 'Methodology'. The sedimentary logs for the localities are provided within the corresponding sections. The specific sampling horizons for each locality are indicated on the sedimentary logs. The photo-plates associated with each of the sedimentary logs are provided in **Sedimentary Log appendix C**.

In the following, the sedimentological background and the geochemical data for the sections listed above are systematically described. The description of the absolute concentrations of the major elements, ordered by their increasing atomic number (Z), starting with the Getino Beds (which are not present at all locations), followed by the Bernesga Mb. and finally the Villasimpliz Mb., which is only available for the Aralla section. The absolute concentrations of the trace elements are then described in the same systematic order and fashion as the previously mentioned major elements. The absolute values are documented for each section in **Results appendix B (part 2)**.

5.1 Aralla Section

The analysed part of the Aralla section comprises the following formations and members: **[1]** the uppermost part of the Barrios Fm., **[2]** the Getino Beds and the Formigoso Fm., which is subdivided into the **[3]** Bernesga Mb. and **[4]** the Villasimpliz Mb. (see **'Sedimentary log of the Aralla section**').

The Aralla log begins with the uppermost bed of the Barrios Fm., consisting of coarse-grained quartzarenite. The contact with the overlying Getino Beds is sharp. The Getino Beds are represented by 31 cm of interbedded fine grained sand- and siltstones. A distinct iron staining can be observed at the top of the succession. The boundary to the overlying Bernesga Mb. of the Formigoso Fm. is again discrete. The Bernesga Mb. consists of 37 m of clay/silt grade organically enriched black shales that are followed by 7 m of very fine-grained sandstone/shale alternations. At the base are the black shales rich in monograptid graptolites. The relative abundance of the graptolites diminishes towards the top of the Bernesga Mb. as the number of very fine-grained sandstone intercalations increases. Due to non-exposure a gap of 27.3 m obscures the boundary to the overlying Villasimpliz Mb. The Villasimpliz Mb. consists of 74 m of interbedded sand- and

siltstones. The thickness of these sandstone beds increases in a cyclic fashion. The vast majority of the thicker sandstone beds are heavily bioturbated at the base and symmetrical ripple marks are usually developed at the top. Channel deposits with planar cross-bedded sandstones occur towards the top of the succession. The contact of the Villasimpliz Mb. to the overlying San Pedro Fm. is gradational.

Locality No.	GPS Coor.	Log total length	Total Samples
12	N42° 54.549' W5° 49.501'	148m	241

Sedimentary log of the Aralla section, Cantabrian Mountains, Northern Spain

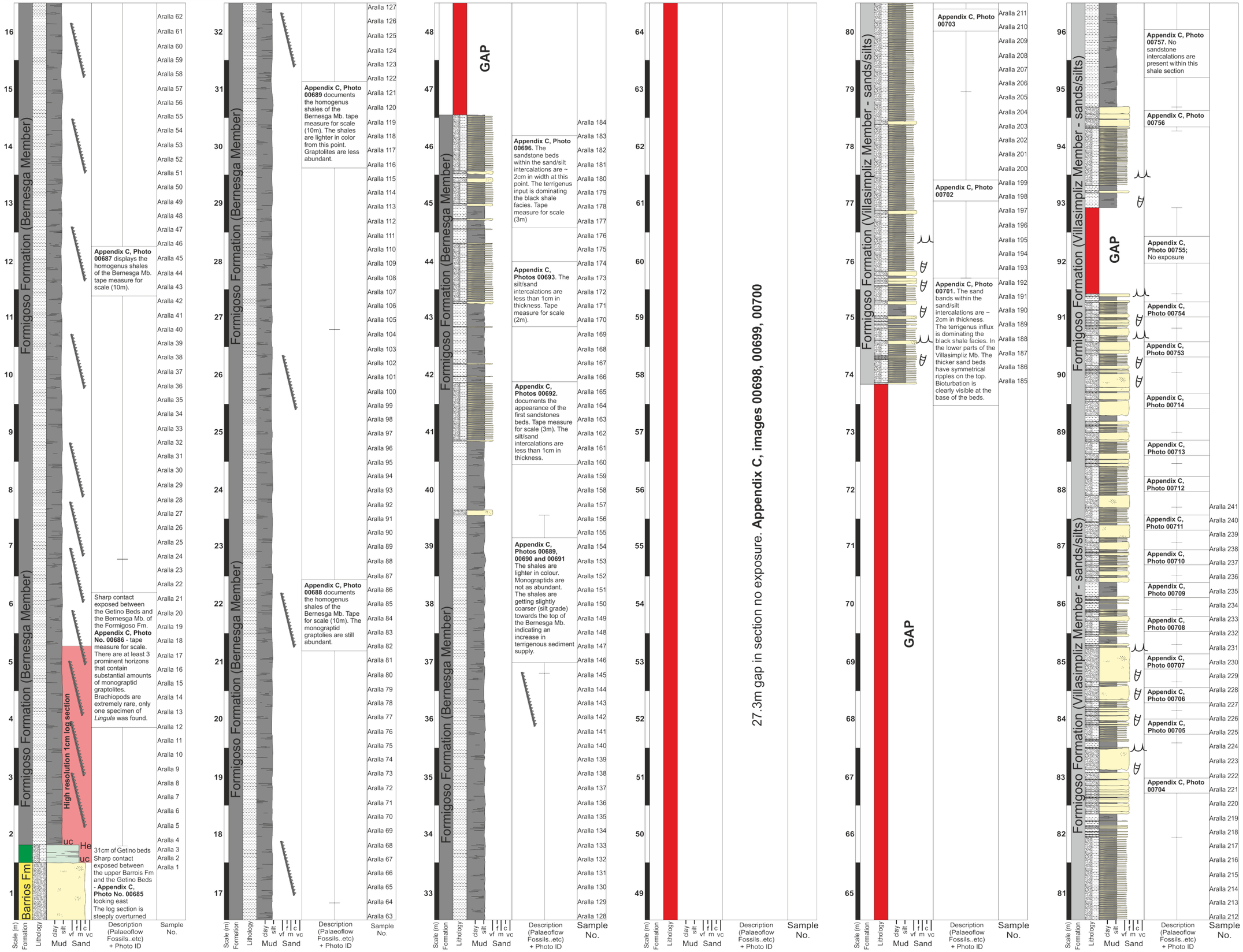

Locality No.	GPS Coor.	Log total length	Total Samples
12	N42° 54.549' W5° 49.501'	148m	241

Sedimentary log of the Aralla section, Cantabrian Mountains, Northern Spain continued...

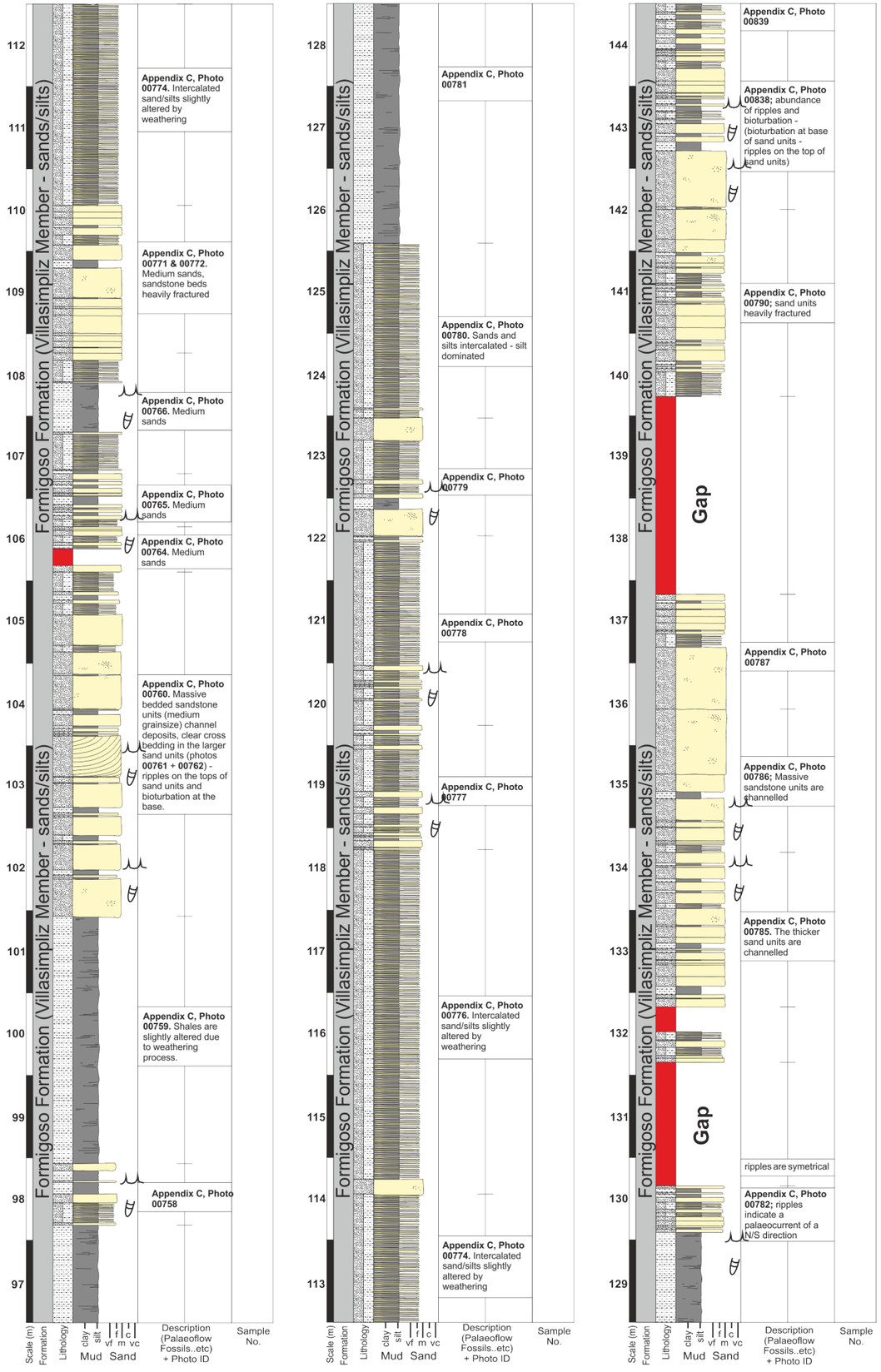

Figures (field images) associated with the Aralla section

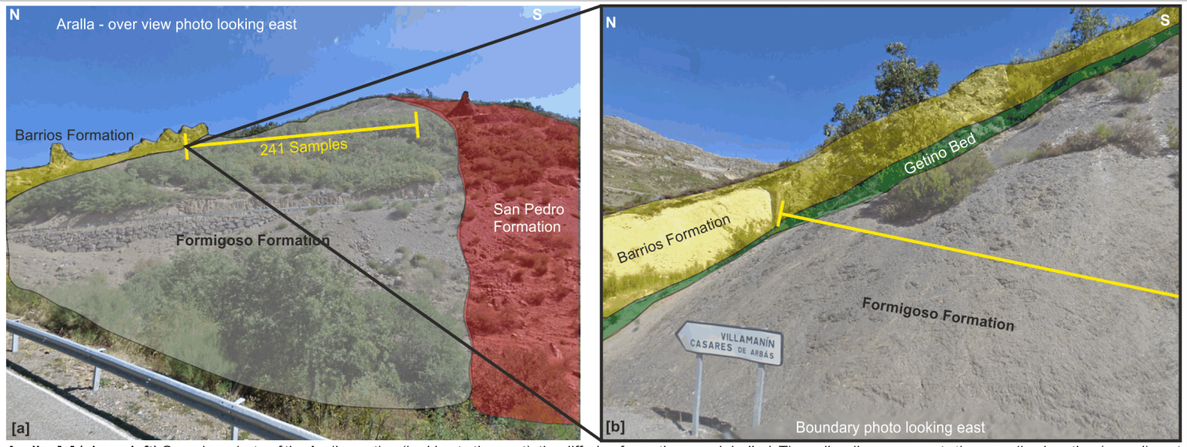

Aralla: [a] (above left) Overview photo of the Aralla section (looking to the east), the differing formations are labelled. The yellow line represents the sampling location (sampling at 25cm intervals (yellow line represents ~ 150m). **[b] (above right - expanded photo of the contact - Log starting point)** Displays the nature of the contact between the underlying Barrios Fm, Getino Beds and the Formigoso Fm.

Photo 00685 (left); Displaying the contact between the underlying Barrios Fm and the Getino Fm, The black shales Bernesga Mb. can be seen towards the right hand side of the photo. (Hammer and tape for scale).

Photo 00686 (right); The contact with the underlying Getino/Barrios Fm can be seen in the top left corner of the photo - The tape is for scale (5m) documenting the homogenus shales of the Bernesga Mb.

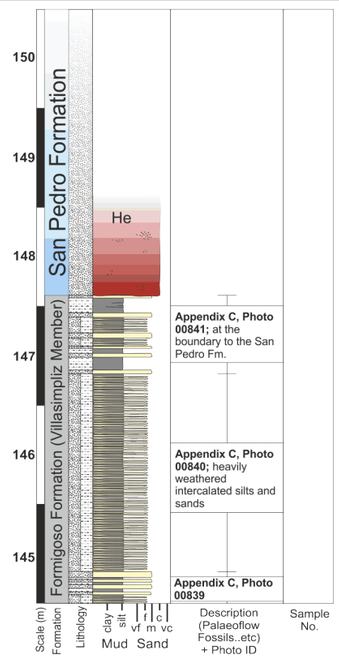

Sedimentary log key

Lithology Symbols

- Shales (organically enriched mudstones)
- Siltstones
- Sandstone bodies
- Intercalated sands and silts - less than 1cm in width

Sedimentary symbols

uc	Unconformity		Wave Ripples
Py	Pyrite		Nodular Weathering
He	Hematised		Planar Tabular Cross Bedding
	Bioturbation		Monograptid Graptolites

Left scale; representing 1m of the log section.

Left symbol; representing the sand/silt intercalations where the intercalations are less than 1 cm in width.

Aralla 1
Caldas 1
La Majua 1
Sena 1
Villa 1

Text (left); Represents the sample numbers for the individual log sections.

5.1.1 Major element variations

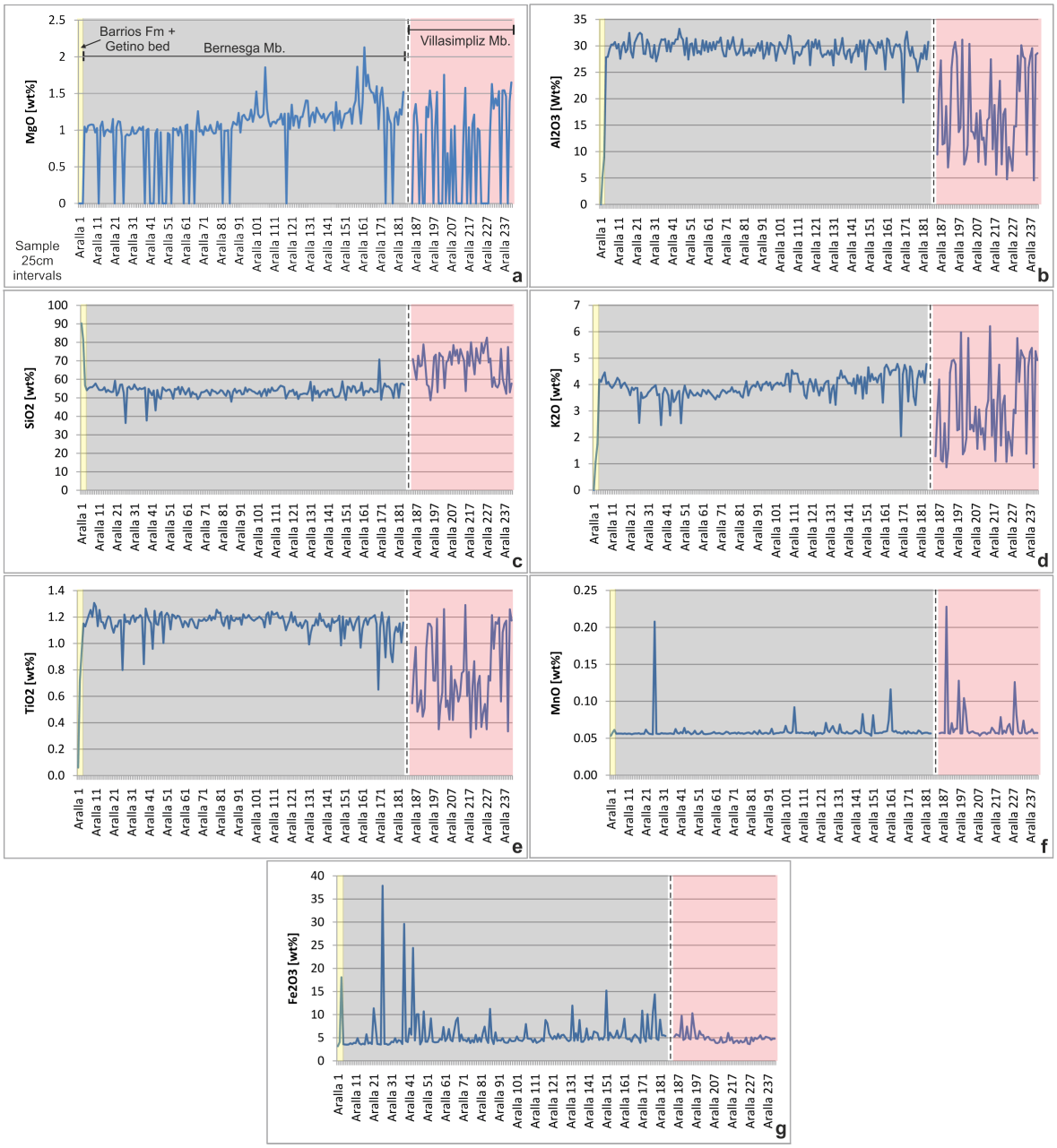

Figure 5.1 Major element variations for the Aralla section. Each sample number represents a 25 cm interval. The coloured areas indicate the different litho-stratigraphic units, starting with the Barrios Fm., followed by the Getino Beds (yellow), the Bernesga Mb. (Grey) and finally the Villasimpliz Mb. (red). The dashed line represents a gap of 27.3 m. A single sample (Aralla 1) from the Barrios Fm. was analysed as a control sample, the Getino Beds are represented by Aralla 2 and Aralla 3. Only the major elements of the Bernesga Mb. and Villasimpliz Mb. are illustrated and will be described within the text. The absolute elemental values for the Barrios Fm. and Getino Beds are documented in **Results appendix B** (part 2). Due to limitations of the Niton XL3t XRF analyser is the determination of lighter geochemical elements restricted. Hence, absolute Na values are not available for this dataset. The Na values are approximated (see **Chapter 4.10.4** 'Sodium proxy') for the use within discrimination diagrams reviewed later (**Chapter 6.2** 'Geochemical classification'), but are not discussed here. Ca values are mostly below detection limits (D.L.), therefore are not included in this section, however the data can be found in the **Results appendix B** (part 2).

Major elements for the Bernesga Mb. (Aralla 4 - 184)

The Bernesga Mb. at Aralla is represented by 181 geochemical samples (see **Table 5.3**). MgO concentrations are relatively low at the base and increase towards the top of the Bernesga Mb. The MgO concentrations vary from below detection limit (D.L.) to 2.12 wt%, with an average 1.15 wt%

and a standard deviation (S.D) of 0.4. Al_2O_3 values are relative consistent throughout the Bernesga Mb., ranging from 19.28 to 33.2 wt%, with an average concentration of 29.45 wt% and a S.D. of 1.66. SiO_2 concentrations vary between 36.4 and 70.81 wt% and increase systematically towards the top of the Bernesga Mb. Sample 'Aralla 170' (70.81 wt%) documents the onset of the increased input of terrigenous material. The SiO_2 values show an average of 53.59 wt% with a S.D. of 3.14. The K_2O values exhibit a depletion affecting the most basal units of the section and then increase consistently towards the upper most parts of the Bernesga Mb. with values ranging from 2.04 to 4.77 wt%, an average of 3.92 wt% and a S.D. of 0.42. TiO_2 values are relatively consistent, with a slight enrichment at the base of the section and systematic depletion towards the top. The values range from 0.65 to 1.3 wt%, averaging at 1.15 wt% and show a S.D. of 0.08. The MnO concentrations are consistent throughout, varying between 0.05 to 0.2 wt%, averaging 0.05 with a S.D. of 0.01. Some samples, e.g. Aralla 27 and 161 (see Aralla table in **Results appendix B, part 2**) are highly enriched in MnO. This is most likely related to localised mineralisation. Fe_2O_3 values show a general increase from the base to the top of the Mb., varying from 3.47 to 37.86 wt%, and average of 5.74 wt% and a S.D of 3.89. Three samples, Aralla 26, 38 and 43 (see Aralla table in **Results appendix B, part 2**) show substantial enrichments, again most likely related to localised mineralisation.

Major elements for the Villasimpliz Mb. (Aralla 185 - 241)

The Villasimpliz Mb. at the Aralla section is represented by 57 geochemical samples (see **Table 5.3**). MgO concentrations are highly erratic within the sands and silts, varying between below D.L. and 1.75 wt%, with an average 0.71 wt% and S.D. of 0.66. Al_2O_3 concentrations are significantly lower than that of the Bernesga Mb., ranging from 4.57 to 31.15 wt%, averaging 17.4 wt% with a S.D. of 8.37. SiO_2 values show a marked increase varying from 48.73 to 82.57 wt%, averaging at 67.42 wt% with a S.D. of 8.86. The K_2O values show a wide range, from 0.85 to 6.2 wt%, averaging 3.11 wt% and a S.D. of 1.58. TiO_2 concentrations vary between 0.28 and 1.29 wt%, averaging at 0.76 wt% with a S.D. of 0.29. The MnO values vary between 0.05 and 0.22, averaging 0.06 wt% with a S.D. of 0.02. Fe_2O_3 concentrations are more consistent than in the lower Mb, ranging from 3.62 to 10.3 wt%, averaging at 5 wt% with a S.D. of 1.23.

5.1.2 Trace element variations

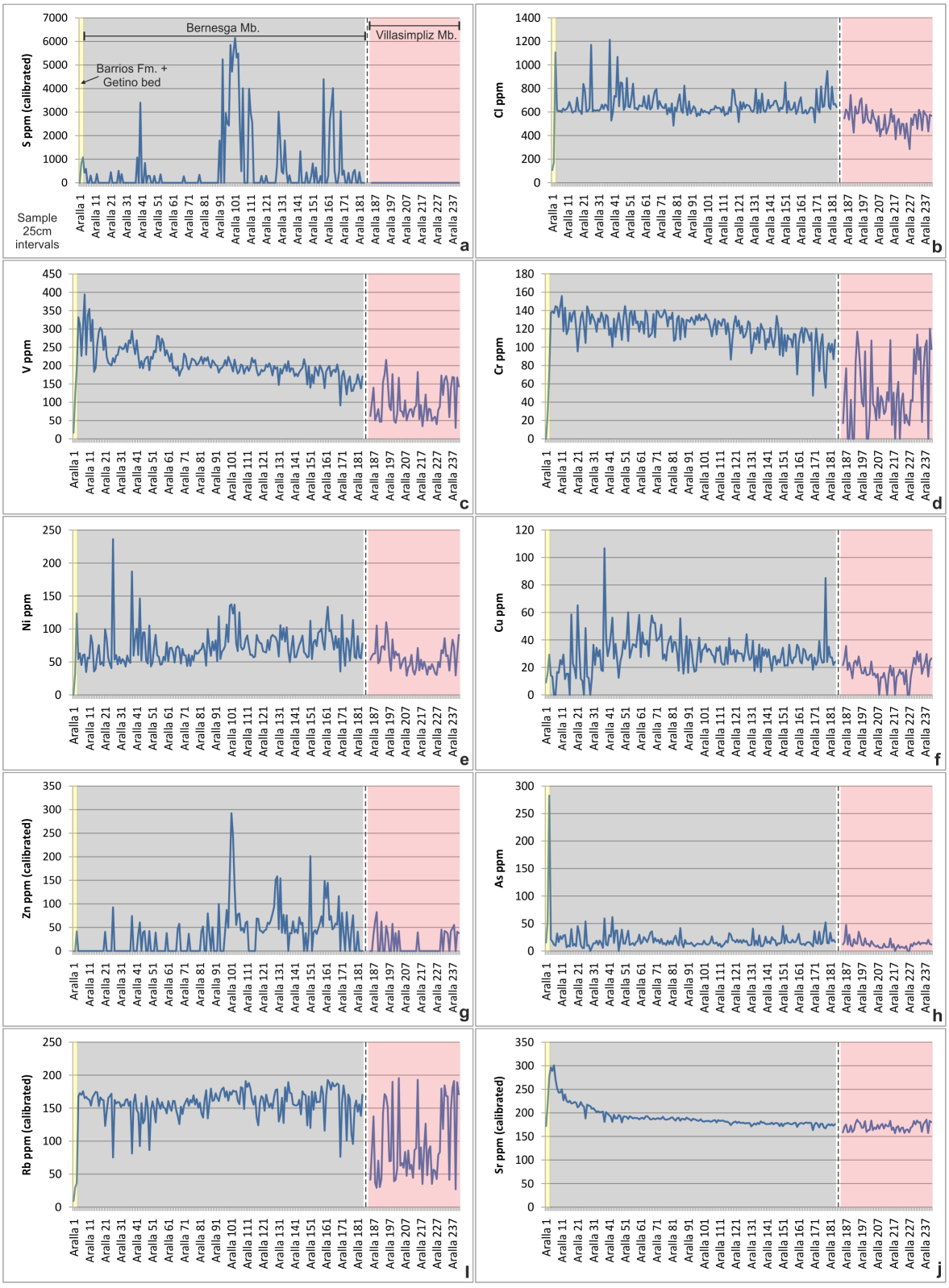

Figure 5.2 Trace element variations for the Aralla log section, plotted against stratigraphy. Every sample number represents a 25 cm interval. The coloured areas indicate the different litho-stratigraphic units, starting with the Barrios Fm., followed by the Getino Beds (yellow), the Bernesga Mb. (Grey) and finally the Villasimpliz Mb. (red). The dashed line represents a gap of 27.3 m. A single sample (Aralla 1) from the Barrios Fm. was analysed as a control sample, the Getino Beds are represented by Aralla 2 and Aralla 3. Only the trace elements of the Bernesga Mb. and Villasimpliz Mb. are illustrated and will be described within the text. The absolute elemental values for the Barrios Fm. and Getino Beds are documented in **Results appendix B** (part 2). P and Bi concentrations are below D.L. and not further discussed. The elements Sc, Co, Se, Mo, Pd, Ag, Cd, Sn, Sb, Te, W, Au and Pb are near to the D.L. and hence neither illustrated nor discussed, however the data can be found in the **Results appendix B** (part 2).

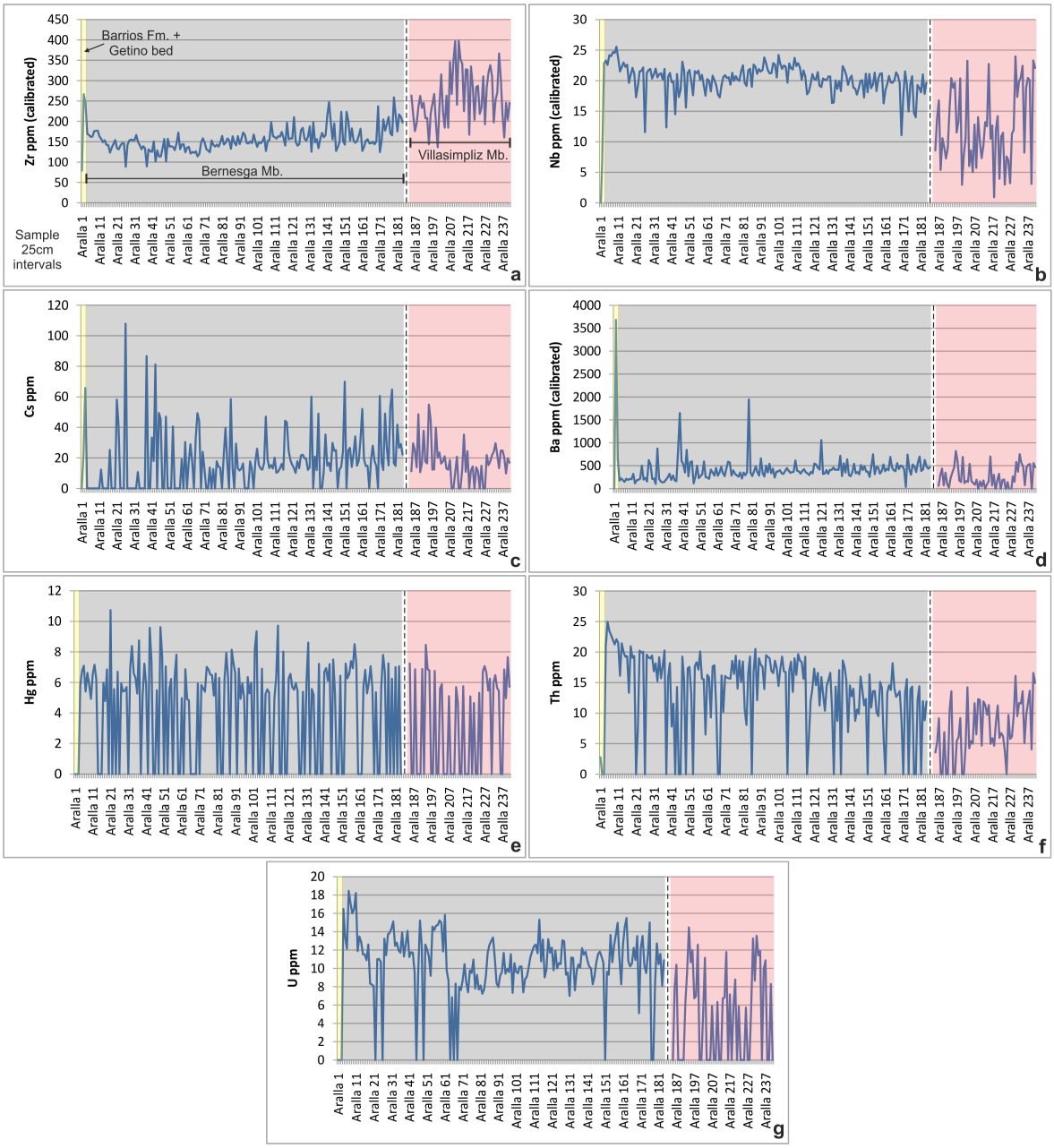

Figure 5.3 Trace element variations for the Aralla log section, plotted against stratigraphy. Every sample number represents a 25 cm interval. The coloured areas indicate the different litho-stratigraphic units, starting with the Barrios Fm., followed by the Getino Beds (yellow), the Bernesga Mb. (Grey) and finally the Villasimpliz Mb. (red). The dashed line represents a gap of 27.3 m. A single sample (Aralla 1) from the Barrios Fm. was analysed as a control sample, the Getino Beds are represented by Aralla 2 and Aralla 3. Only the trace elements of the Bernesga Mb. and Villasimpliz Mb. are illustrated and will be described within the text. The absolute elemental values for the Barrios Fm. and Getino Beds are documented in **Results appendix B** (part 2). A number of element concentrations were near to the detection limits (see **Figure 5.2** caption) and consequently not discussed within this chapter.

Trace elements for the Bernesga Mb. (Aralla 4 - 184)

The Bernesga Mb. at the Aralla section is represented by 181 geochemical samples (see **Table 5.3**). The S concentrations are mostly below D.L. yet a few intervals towards the top of the Mb. show significant enrichments. The S values vary between below D.L. to 6148 ppm, with an average of 1743.9 ppm and a S.D. of 1340.4. Cl concentrations are relatively consistent with a few enrichments at the base and towards top of the Mb. The values vary between 484 and 1213 ppm,

with an average of 659.7 ppm and a S.D. of 96.6. The V values are again enriched at the base of the Mb. A rhythmic pattern can be observed in the basal parts of the section (3 distinct peaks). The values decrease gradually towards the top of the Mb. The V values vary throughout from 91 to 394 ppm with an average of 208.6 ppm and a S.D. of 42.8. Cr values are enriched at the base of the Mb. decreasing towards the top, with a rhythmic pattern seen near the base. The Cr values range from 47 to 155 ppm, averaging at 120.2 ppm with a S.D. of 16.6. The Ni values increase from the base of the Mb. towards the top, the values range from 34 to 236 ppm, averaging at 73.4 with a S.D. of 26.5. The Cu values are near D.L. at the base of the Mb. The values increase rapidly and begin to decrease gradually towards the top of the Mb. The Cu values range from below D.L. to 106 ppm, averaging at 30 ppm with a S.D. of 13.4. Zn values are mostly below D.L. at the base of the Mb., the values increase from the middle of the Mb. in what appears to be a rhythmic pattern. The values range from below D.L. to 292 ppm, averaging at 69.6 ppm with a S.D. of 47.7. The As values are relatively consistent throughout the Mb. ranging from below D.L. to 61 ppm, averaging at 18.4 ppm with a S.D. of 10.3. Rb values are consistent throughout the Mb. increasing slightly towards the top, the values range from 75 to 192 ppm, averaging at 157.7 ppm with a S.D. of 21.1. The Sr values are enriched at the base of the Mb., but decrease throughout in a logarithmic fashion, with values ranging from 163 to 300 ppm, averaging at 190.6 ppm with a S.D. of 21.9. Zr concentrations are low at the base and then gradually increase throughout, the values range from 88 to 258 ppm, averaging at 154.7 ppm with a S.D. of 26.9. Nb values are consistent throughout the Mb., with values ranging from 11 to 25 ppm, averaging at 20.3 ppm with a S.D. of 2.2. Cs concentrations increase throughout the Mb., the values are below D.L. at the base followed by a series of enriched horizons before settling into a steady increase. Cs values range from below D.L. to 107 ppm, averaging at 26.1 ppm with a S.D. of 19. Ba values increase steadily from the base to the top of the Mb. with a few enriched horizons near the base, the values range from 38 to 1942 ppm, averaging at 398.7 with a S.D. of 215.8. The Hg concentrations are just above D.L. yet remain consistent from the base to the top, the values range from below D.L. to 10 ppm, averaging at 6.4 ppm with a S.D. of 3.2. Th values are enriched at the base of the Mb. decreasing towards the top. A rhythmic pattern of the Th concentrations is again seen, with values ranging from below D.L. to 24 ppm, averaging at 15.6 ppm with a S.D. of 6.2. The U concentrations are enriched at the base of the Mb. A rhythmic pattern is seen at the base much like that of the V concentrations described previously (three distinct peaks), the values range from below D.L. to 18 ppm, averaging at 11.2 ppm with a S.D. of 3.4.

Trace elements for the Villasimpliz Mb. (Aralla 185 - 241)

The Villasimpliz Mb. at the Aralla section is represented by 57 geochemical samples (see **Table 5.3**). The S concentrations are below D.L. for this Mb. and consequently not further discussed. Cl values are depleted in relation to the lower Mb., with values ranging from 285 to 744 ppm, averaging 529.5 ppm with a S.D. of 89.6. The V values are depleted relative to the lower Mb., values range from 29 to 215 ppm, averaging at 98 ppm with a S.D. of 48.8. Cr values are erratic when compared with the lower Mb. The values range from below D.L. to 120 ppm, averaging at 49 ppm with a S.D. of 36.9. The Ni values are depleted relative to the lower Mb., the values range from 29 to 110 ppm, averaging at 55.9 ppm with a S.D. of 18.8. The Cu values are depleted relative to the lower Mb. the values range from below D.L. to 35 ppm, averaging at 17.5 ppm with a S.D. of 7.9. Zn values are near D.L., the values range from below D.L. to 82 ppm, averaging at 15.8 ppm with a S.D. of 23.6. The As values are slightly depleted relative to the lower Mb. The concentrations range from below D.L. to 47 ppm, averaging at 12.5 ppm with a S.D. of 8. Rb values are depleted and highly erratic relative to the lower Mb., the values range from 26 to 195 ppm, averaging at 95.7 ppm with a S.D. of 55.1. Sr values are slightly erratic yet average near to the values of the lower Mb. The values range from 156 to 185 ppm, averaging at 170.5 ppm with a S.D. of 8.5. The Zr values are drastically enriched relative to the lower Mb. with the values ranging from 136 to 398 ppm, averaging at 257.4 ppm with a S.D. of 63.3. Nb values are depleted and highly erratic relative to the lower Mb. with values ranging from 1 to 23 ppm, averaging at 12.5 ppm with a S.D. of 6.2. The Cs values are near D.L. however, remain relatively consistent, ranging from below D.L. to 54 ppm, averaging at 17.4 ppm with a S.D. of 12.1. Ba values are lower relative to the lower Mb. and are slightly more erratic, with values ranging from below D.L. to 816 ppm, averaging at 255.4 ppm with a S.D. of 229.7. The Hg concentrations remain consistent to the lower Mb. again close to the D.L., the values range from below D.L. to 8 ppm, averaging at 3.1 ppm with a S.D. of 3.1. The Th values are lower and more erratic than that of the lower Mb, ranging from below D.L. to 16 ppm, averaging at 7.4 ppm with a S.D. of 4.6. U concentrations are lower and more erratic in comparison to the lower Mb, with values ranging from below D.L. to 14 ppm, averaging at 4.8 ppm with a S.D. of 4.9.

5.2 Aralla high resolution (HR) Section

The following section documents all geochemical results for the Aralla HR section. The Aralla HR section consists of 339 *in-situ* field readings. The interval for the analysis within the Getino Beds and Bernesga Mb. was set at 1 cm. The analysis numbers for the Aralla HR section are documented in **Table 4.2** of **Chapter 4** 'Methodology'. The *in-situ* log section is indicated at the base of 'Sedimentary log of the Aralla section'. The absolute elemental concentrations can be found in the **Results appendix B** (part 2).

5.2.1 Major element variations

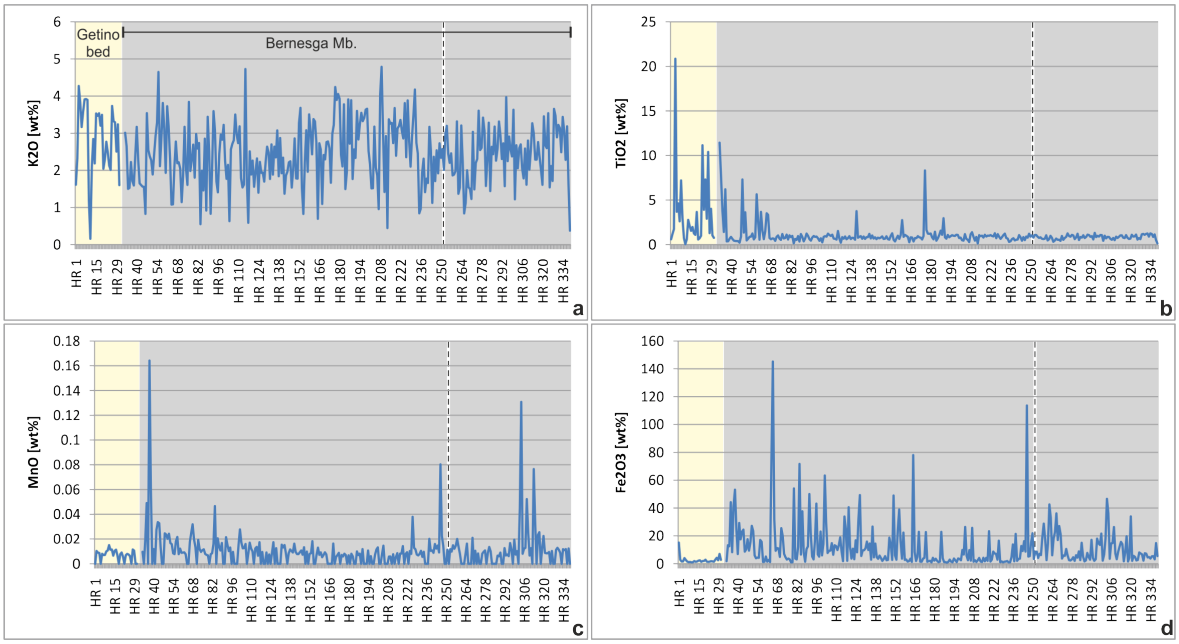

Figure 5.4 Major element variations for the Aralla HR section. Each sample number represents a 1 cm interval. The coloured areas indicate the different litho-stratigraphic units, starting with the Getino Beds (yellow) followed by the Bernesga Mb. of the Formigoso Fm. (Grey). The dashed line represents a gap of 39 cm. The Getino Beds are represented by analysis numbers HR 1 to HR 31, and the Bernesga Mb. HR 32 to HR 339. See **Results appendix B** (part 2) for absolute elemental values. The purpose of the Aralla HR log section was to determine whether there were any higher order rhythmic pulses superimposed on the previously described V and U curves of the Aralla section. Due to limitations of the Niton XL3t XRF analyser, analysis of the lightest geochemical elements is hindered in the field. Various factors affect the geochemical analysis of the light elements, these being, **[1]** the uneven analysis surface, **[2]** the changes in moisture content and finally, **[3]** the inability to purge the detector with helium in the field, as described in the previous **Chapter 4** 'Methodology'. The Ca values are mostly below D.L., therefore not discussed further, however the geochemical data for Ca can be found in the **Results appendix B** (part 2).

Major elements for the Getino Bed (HR 1 - 31)

The Getino Beds for the Aralla HR section are represented by 31 analysis points (see **Table 5.3**). The K_2O concentrations deplete towards the top of the beds, the values are fairly erratic, ranging from 0.15 to 4.27 wt%, with an average of 2.82 wt% and S.D. of 0.94. TiO_2 values show depletion from the base towards the top, ranging from 0.04 to 20.85 wt%, averaging at 3.42 wt% with a S.D.

of 4.25. The MnO concentrations are consistent throughout, varying between below D.L. and 0.01 wt%, averaging 0.006 wt% with a S.D. of 0.004. Fe_2O_3 values are depleted in relation to the overlying Bernesga Mb. varying from 0.97 to 15.14 wt%, and averaging 2.58 wt% with a S.D of 2.62.

Major elements for the Bernesga Mb. (HR 32 - 339)

The Bernesga Mb. for the Aralla HR section is represented by 308 analysis points (see **Table 5.3**). The K_2O values range dramatically from 0.37 to 4.78 wt%, averaging 2.44 wt% and a S.D. of 0.82, the K_2O values express a rhythmic pattern. TiO_2 concentrations vary between 0.13 and 11.43 wt% showing an enrichment at the very base (boundary with underlying Getino Beds), averaging at 1.02 wt% with a S.D. of 1.1. The MnO values vary between below D.L. and 0.16 wt%, again showing enrichment at the very onset, averaging 0.01 wt% with a S.D. of 0.01. Fe_2O_3 concentrations are erratic, decreasing towards the top, ranging from 0.75 to 149.2 wt%, averaging at 12.03 wt% with a S.D. of 16.1.

5.2.2 Trace element variations

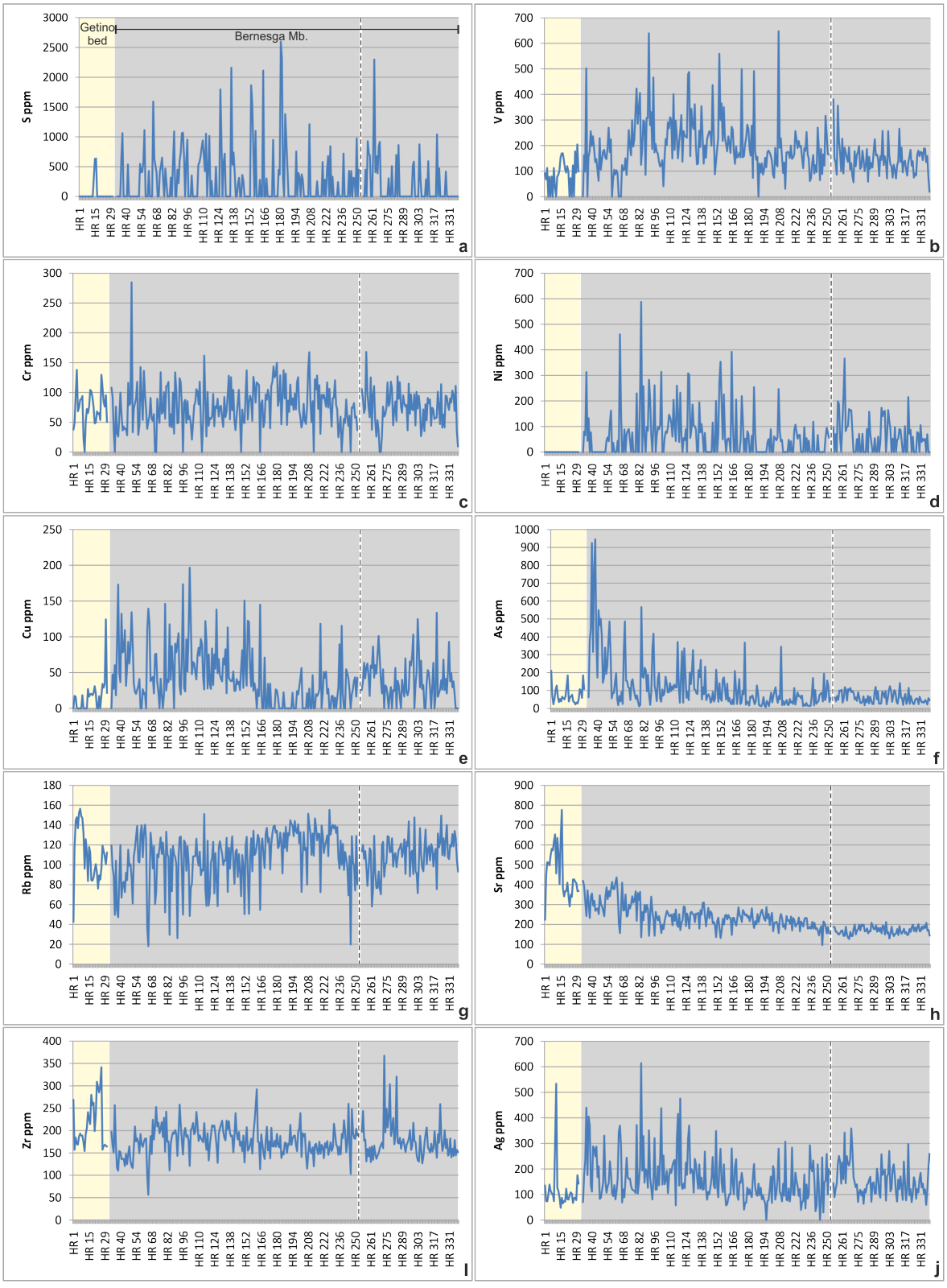

Figure 5.5 Trace element variations for the Aralla HR section. Each sample number represents a 1 cm interval. The coloured areas indicate the different litho-stratigraphic units, starting with the Getino Beds (yellow) followed by the Bernesga Mb. of the Formigoso Fm. (Grey). The dashed line represents a gap of 39 cm. See the **Results appendix B** (part 2), for absolute elemental values of the Getino Beds and Bernesga Mb. The following elements are close to the D.L. and have been excluded from any further description and discussion: Sc, Co, Zn, Se, Mo, Pd, W, Au, Hg and Pb. Their values have been documented in the **Results appendix B** (part 2).

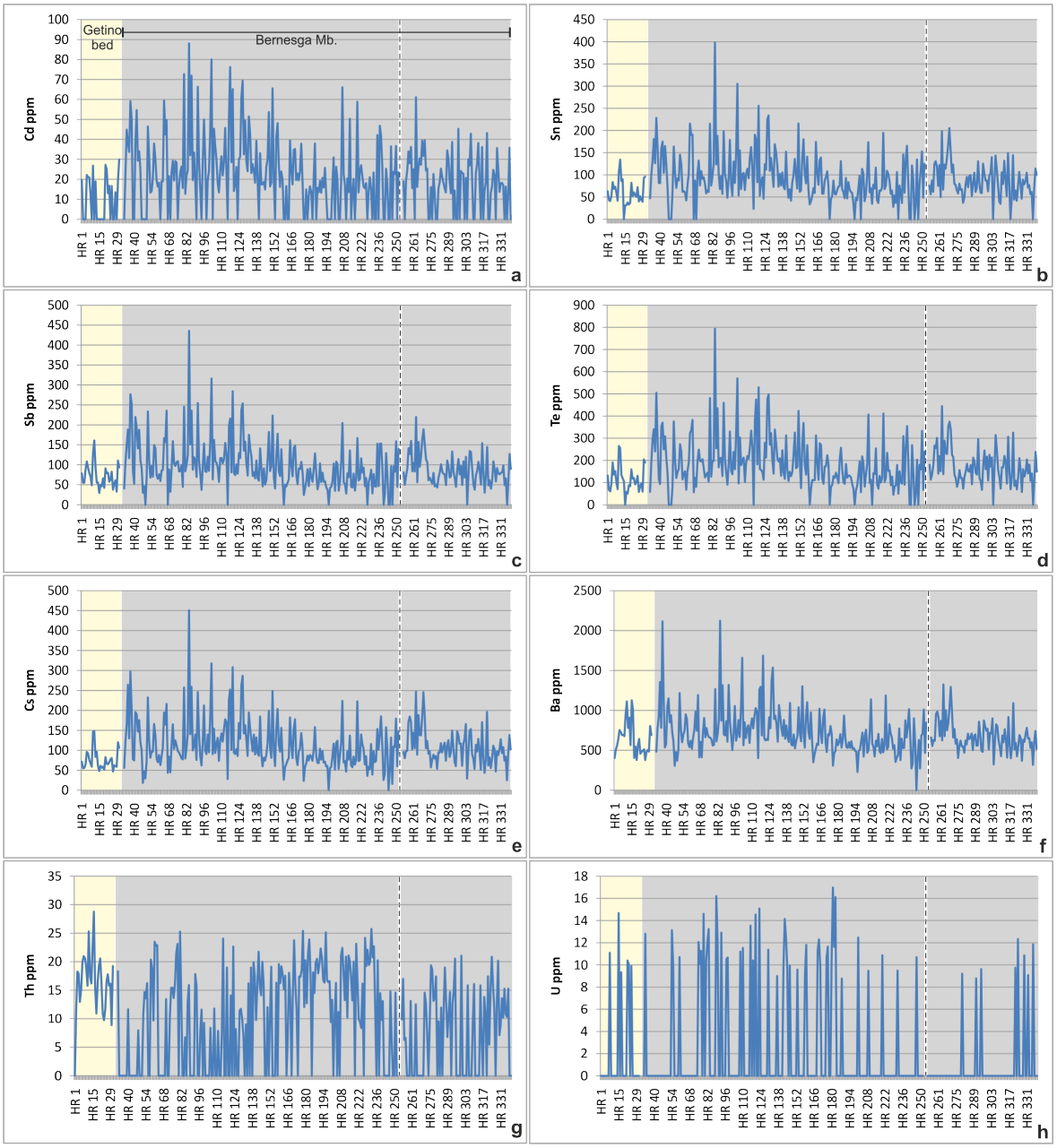

Figure 5.6 Trace element variation curves for the Aralla HR section. Each sample number represents a 1 cm interval. The coloured areas indicate the different litho-stratigraphic units, starting with the Getino Beds (yellow) followed by the Bernesga Mb. of the Formigoso Fm. (Grey). The dashed line represents a gap of 39 cm. The absolute elemental values for the Getino Beds and Bernesga Mb. are documented in **Results appendix B** (part 2). A number of element concentrations were near to the detection limits (see **Figure 5.5** caption) and consequently are not discussed within this chapter.

Trace elements for the Getino Bed (HR 1 - 31)

The Getino Bed for the Aralla HR section is represented by 31 analysis points (see **Table 5.3**). The S concentrations are mostly below D.L. for the Getino Beds. However, there were three values above the D.L., 318, 628 and 637 ppm. The V values are enriched towards the top of the beds, the values increase gradually throughout with a rhythmic pattern. The values vary from below D.L. to 204 ppm with an average of 85.9 ppm and S.D. of 58.7. The Cr values are erratic throughout, ranging from below D.L. to 137 ppm, averaging at 73.7 ppm with a S.D. of 29. The Ni values are below D.L. within the Getino Bed. The Cu values are near D.L. at the base of the bed the values

increase rapidly towards the boundary of the overlying Bernesga Mb. the values range from below D.L. to 124 ppm, averaging at 16.2 ppm with a S.D. of 23.3. As values are relatively depleted in relation to the overlying Bernesga Mb. shales, the concentrations vary from 22 to 210 ppm, averaging at 75.3 ppm with a S.D. of 48.4. Rb values are enriched towards the base and decrease rapidly before increasing again close to the top of the unit, the values range from 42 to 156 ppm, averaging at 110.3 ppm with a S.D. of 26.7. The Sr values are enriched relative to the overlying Bernesga Mb. The same logarithmic decrease is seen within the values, ranging from 223 to 776 ppm, averaging at 459.1 ppm with a S.D. of 124.9. Zr values increase towards the top of the beds and are enriched relative to the overlying Bernesga Mb. The values range from 154 to 341 ppm, averaging at 216 ppm with a S.D. of 53.6. Ag values are depleted relative to the overlying Bernesga Mb., with one horizon showing enrichment. The values range from 47 to 533 ppm, averaging at 117.7 ppm with a S.D. of 89.1. Cd values are consistent, and near to the D.L., the values range from below D.L. to 29 ppm, averaging at 9.7 ppm with a S.D. of 10.9. The Sn concentrations are depleted relative to the overlying Bernesga Mb. The values range from below D.L. to 134 ppm, averaging at 59.6 ppm with a S.D. of 27.4. Sb concentrations are depleted in relation to the overlying Bernesga Mb. The values range from 29 to 160 ppm, averaging at 72.4 with a S.D. of 29. The Te concentrations are depleted relative to the Bernesga Mb., with values ranging from below D.L. to 264 ppm, averaging at 115.3 ppm with a S.D. of 59.1. Cs values are depleted relative to the overlying Bernesga Mb. The values range from 46 to 148 ppm, averaging at 75.6 ppm with a S.D. of 25.7. The Ba concentrations show an enrichment towards the centre of the Getino Beds and are slightly lower in concentration relative to the overlying Bernesga Mb. The values range from 378 to 1125 ppm, averaging at 642.1 ppm with a S.D. of 207. Th values increase towards the centre of the Getino Beds, the rhythmic pattern is again evident, with values ranging from below D.L. to 28 ppm, averaging at 16.3 ppm with a S.D. of 5.3. The U concentrations are consistent, near D.L., the values range from below D.L. to 14 ppm, averaging at 2.1 ppm with a S.D. of 4.4.

Trace elements for the Bernesga Mb. (HR 32 - 339)

The lower Bernesga Mb. for the Aralla HR section is represented by 308 analysis points (see **Table 5.3**). The S concentrations are mostly below or near D.L., the values vary between below D.L. to 2593 ppm, with an average of 266 ppm and S.D. of 447.6. The V values display a rhythmic pattern towards the base. The V concentrations vary throughout from below D.L. to 646 ppm with an average of 183.4 ppm and S.D. of 98.5. Cr values are relatively consistent, with a rhythmic pattern

seen throughout, the values range from below D.L. to 284 ppm, averaging at 75.4 ppm with a S.D. of 35. The Ni values increase from the base of the Mb., with values near to D.L., ranging from below D.L. to 587 ppm, averaging at 65 with a S.D. of 86.6. The Cu values display a rhythmic pattern with values varying from below D.L. to 196 ppm, averaging at 42 ppm with a S.D. of 37.6. As values display a logarithmic decrease from the base of the Bernesga Mb., similar to the Sr values. The concentrations vary from 5 to 944 ppm, averaging at 108.4 ppm with a S.D. of 126.5. Rb values are consistent throughout the Mb. increasing slightly towards the top, the values range from 18 to 155 ppm, averaging at 108 ppm with a S.D. of 24.8. The Sr values are enriched at the base of the Mb. the values then decrease throughout in a logarithmic fashion, with values ranging from 96 to 436 ppm, averaging at 223.3 ppm with a S.D. of 62.6. Zr values are enriched at the top of the Mb. increasing throughout. The values range from 56 to 367 ppm, averaging at 176.6 ppm with a S.D. of 34.9. Ag values are enriched towards the base and gradually decrease throughout. The values range from below D.L. to 613 ppm, averaging at 161 ppm with a S.D. of 84.5. Cd values are higher towards the base of the Mb. the values range from below D.L. to 88 ppm, averaging at 21.6 ppm with a S.D. of 17.4. The Sn concentrations show depletion from the base, the values range from below D.L. to 398 ppm, averaging at 92.3 ppm with a S.D. of 52. Sb values display a depletion at the base and towards the top of the Mb., with a few enriched horizons towards the base. The values range from 0 to 435 ppm, averaging at 95.6 with a S.D. of 57. The Te concentrations display a depletion at the base and then systematically increase towards the top of the Mb., with a few enriched horizons towards the base. The values range from below D.L. to 793 ppm, averaging at 182.7 ppm with a S.D. of 109.1. Cs values are enriched at the base of the Mb. decreasing towards the top. A rhythmic pattern is again seen, with values ranging from below D.L. to 450 ppm, averaging at 112.7 ppm with a S.D. of 57.7. The Ba concentrations are enriched at the base of the Mb. With values ranging from below D.L. to 2123 ppm, averaging at 712.5 ppm with a S.D. of 263.4. Th values are depleted at the base of the Mb. increasing towards the top. A rhythmic pattern is again seen, with values ranging from below D.L. to 25 ppm, averaging at 9.1 ppm with a S.D. of 8.3. The U concentrations are enriched towards the base of the Mb. The values range from below D.L. to 16 ppm, averaging at 2 ppm with a S.D. of 4.4.

5.3 Caldas de Luna section

The analysed part of the Caldas de Luna section consists of the Bernesga Mb. of the Formigoso Fm. (see **'Sedimentary log of the Caldas de Luna section**').

The Caldas de Luna section consists of the Bernesga Mb. of the Formigoso Fm. The boundary with the underlying Barrios Fm. is sharp. The Getino Beds are completely missing at this particular locality. The first 30 m of the Bernesga Mb. were logged in detail, after this point the Formigoso Fm. is covered in thick vegetation. Subsequently the boundary to the overlying Villasimpliz Mb. is not evident. The Bernesga Mb. consists of clay/silt grade organically enriched black shales. These black shales are rich in monograptid graptolites at their basal parts, as with the previously described Aralla section **Chapter 5.2**.

Locality No.	GPS Coor.	Log total length	Total Samples
121	N42° 56.672' W5° 51.382'	54m	98

Sedimentary log of the Caldas de la Luna section, Cantabrian Mountains, Northern Spain

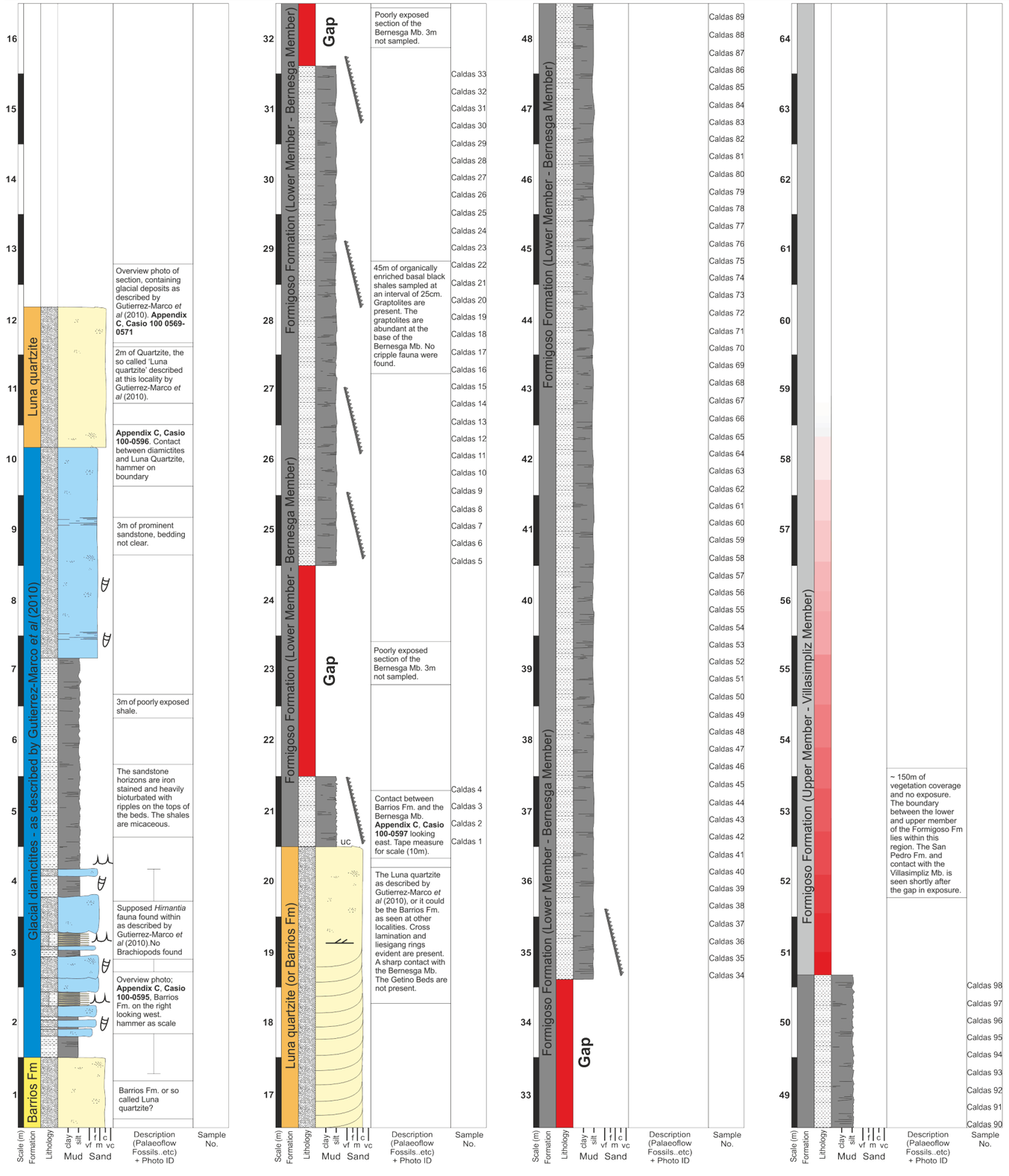

Figures (field images) associated with the Caldas de la Luna section

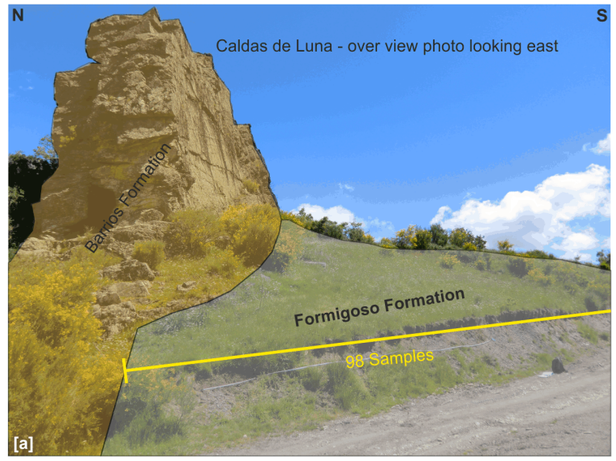

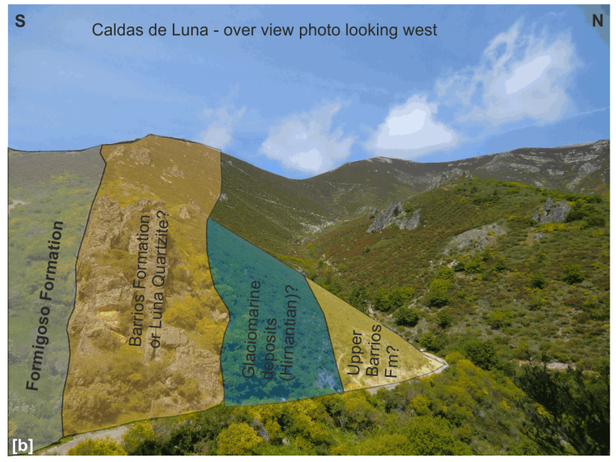

Caldas de Luna: [a] Overview photo (**Appendix C, 100-0597**) of the Caldas de Luna section (orientated towards the east), the differing formations are labelled. The yellow line represents the sampling location (Formigoso Fm. sampled at 25cm intervals). **[b]** Overview photo (**Appendix C, 100-0569**) of the locality orientated towards the west (opposite side of the valley). **Suggested glaciomarine location as in Gutierrez-Marco *et al.* (2010).**

Sedimentary log key

Lithology Symbols

- Shales (organically enriched mudstones)
- Siltstones
- Sandstone bodies
- Intercalated sands and silts - less than 1cm in width

Sedimentary symbols

uc	Unconformity	Wave Ripples
Py	Pyrite	Nodular Weathering
He	Hematised	Planar Tabular Cross Bedding
	Bioturbation	Monograptid Graptolites

Left scale; representing 1m of the log section.

Left symbol; representing the sand/silt intercalations where the intercalations are less than 1 cm in width.

Araila 1
Caldas 1
La Majua 1
Sena 1
Villa 1

Text (left); Represents the sample numbers for the individual log sections.

5.3.1 Major element variations

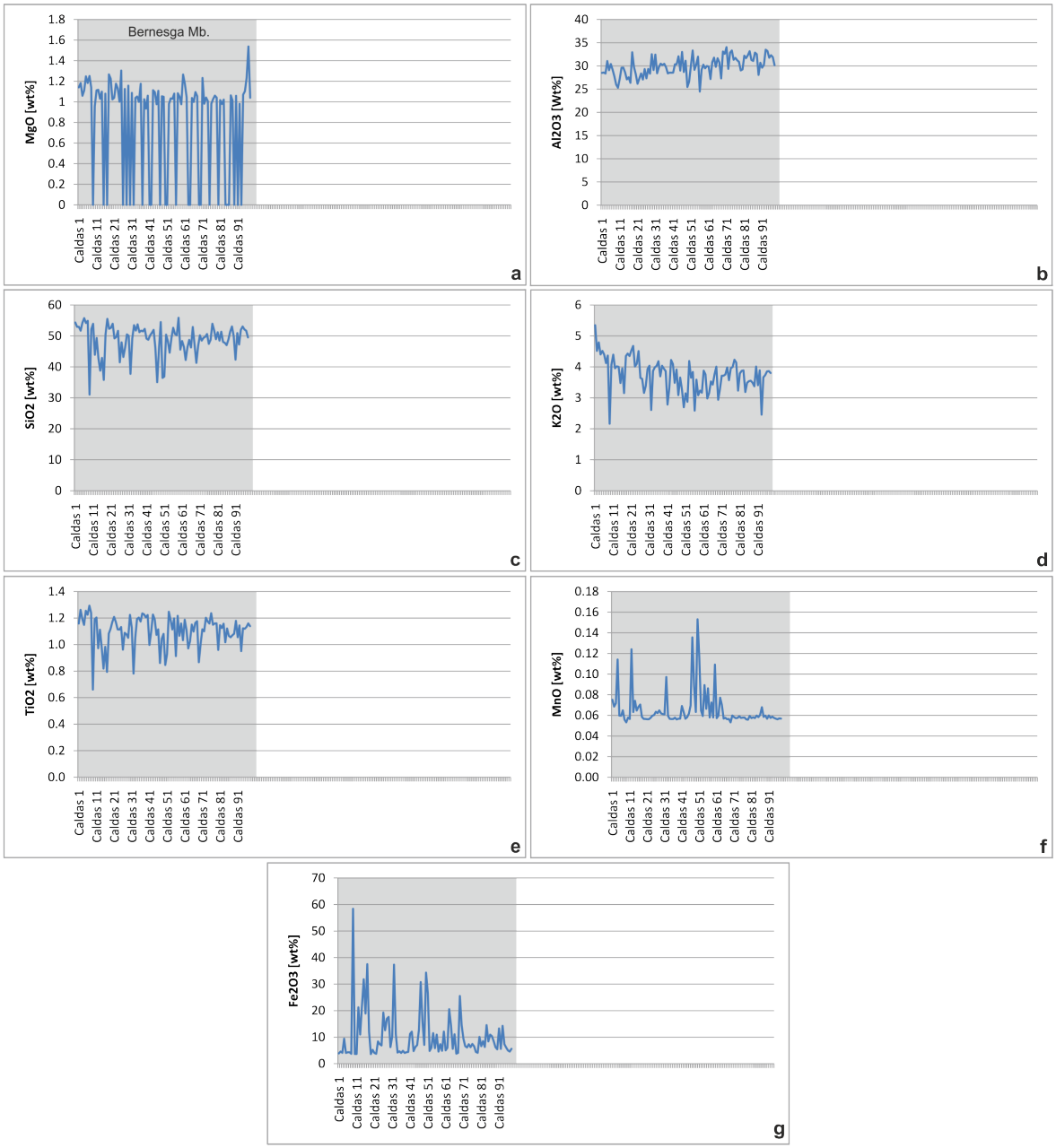

Figure 5.7 Major element variations for the Caldas de Luna section. Each sample number represents a 25 cm interval. All samples are representative of the Bernesga Mb. See **Results appendix B** (part 2) for absolute elemental values for the Formigoso Fm. As previously mentioned in **Chapter 5.2** 'Aralla section', the Na values were approximated and hence are not displayed here. The Na proxy data can however be found in the **Results appendix B** (part 2). Ca and Mg values are mostly below or near to D.L., the Ca concentrations can be found in the **Results appendix B** (part 2).

Major elements for the Bernesga Mb. (Caldas 1 - 98)

The Bernesga Mb. at the Caldas de Luna section is represented by 98 geochemical samples (see **Table 5.3**). The MgO concentrations are consistent throughout Bernesga Mb, nearing the D.L. The MgO values show a decline towards the upper parts of the Mb. The MgO concentrations vary from below D.L. to 1.53 wt%, with an average 1.09 wt% and standard deviation (S.D) of 0.49. Al_2O_3 values are pretty consistent throughout, showing a slight increase towards the top of the Mb.

Ranging from 24.4 to 34 wt%, an average of 29.93 wt% and S.D. of 2.1. SiO_2 concentrations range from 31 to 55.8 wt% decreasing towards the top of the Bernesga Mb., averaging at 48.81 wt% with a S.D. of 4.9. The K_2O values decrease throughout the Bernesga Mb. the values range from 2.16 to 5.34 wt%, an average of 3.73 wt% and S.D. of 0.53. TiO_2 values are relatively consistent, with a slight enrichment towards the base of the section. The values range from 0.66 to 1.29 wt%, averaging at 1.1 wt% with a S.D. of 0.11. The MnO concentrations are consistent throughout. However, a few enriched horizons are seen towards the middle of the section. The MnO values vary between 0.05 to 0.15 wt%, averaging 0.06 wt% with a S.D. of 0.01. Fe_2O_3 values show a general decrease from the base to the top of the Mb. varying from 3.6 to 58.3 wt%, with an average of 10.42 wt% and a S.D of 9, there are a number of enrichments (decreasing from the base), most likely related to localised mineralisation.

5.3.2 Trace element variations

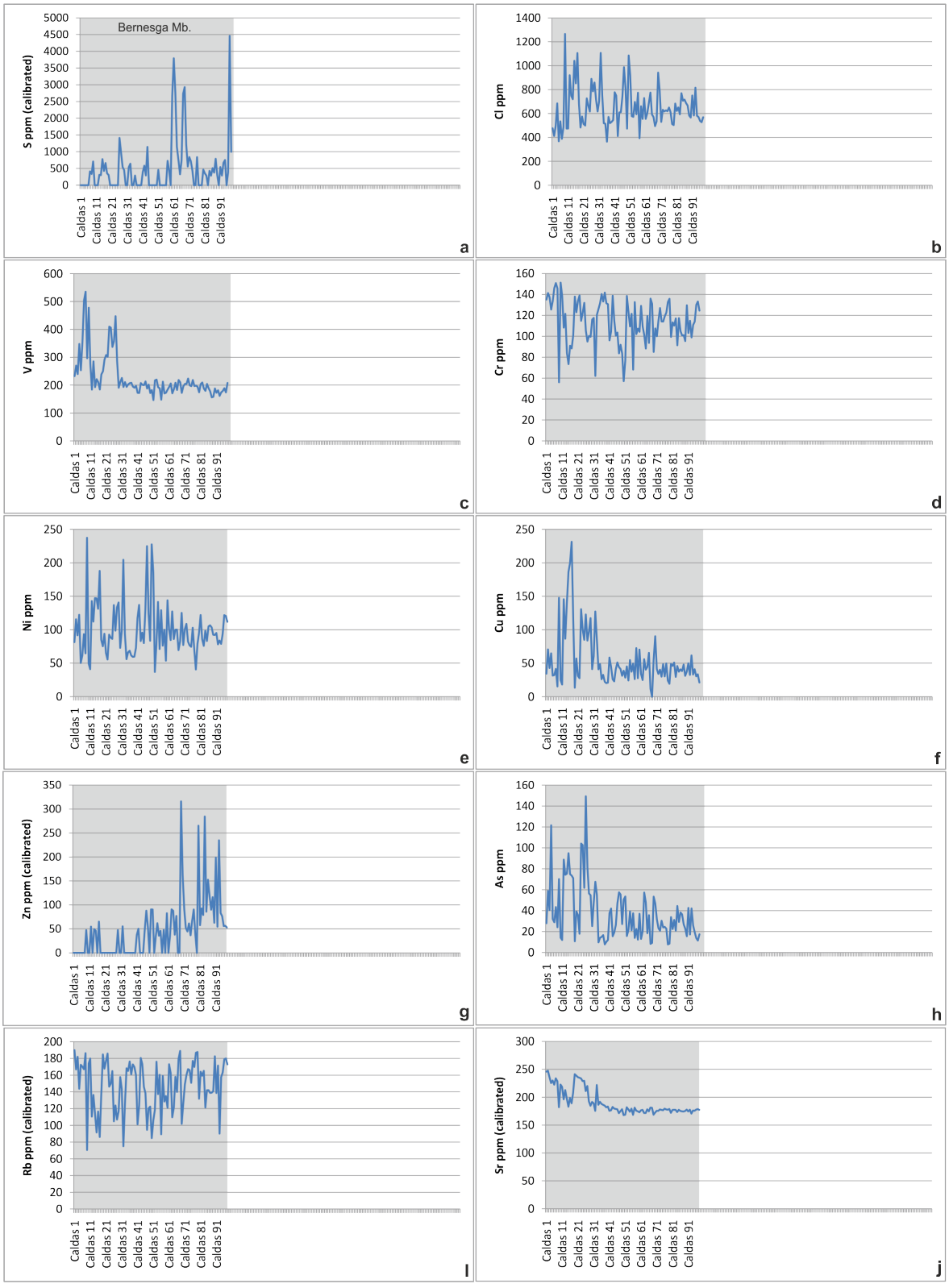

Figure 5.8 Trace element variations for the Caldas de Luna section. Each sample number represents a 25 cm interval. All samples are representative of the Bernesga Mb. See **Results appendix B** (part 2) for absolute elemental values for the Formigoso Fm. P and Bi concentrations are below D.L. and subsequently not further discussed. The following elements are close to the D.L., and not further discussed: Sc, Co, Se, Mo, Pd, Ag, Cd, Sn, Sb, Te, W, Au and Pb. These elements have not been included in the following descriptive section, however the data can be found in **Results appendix B** (part 2).

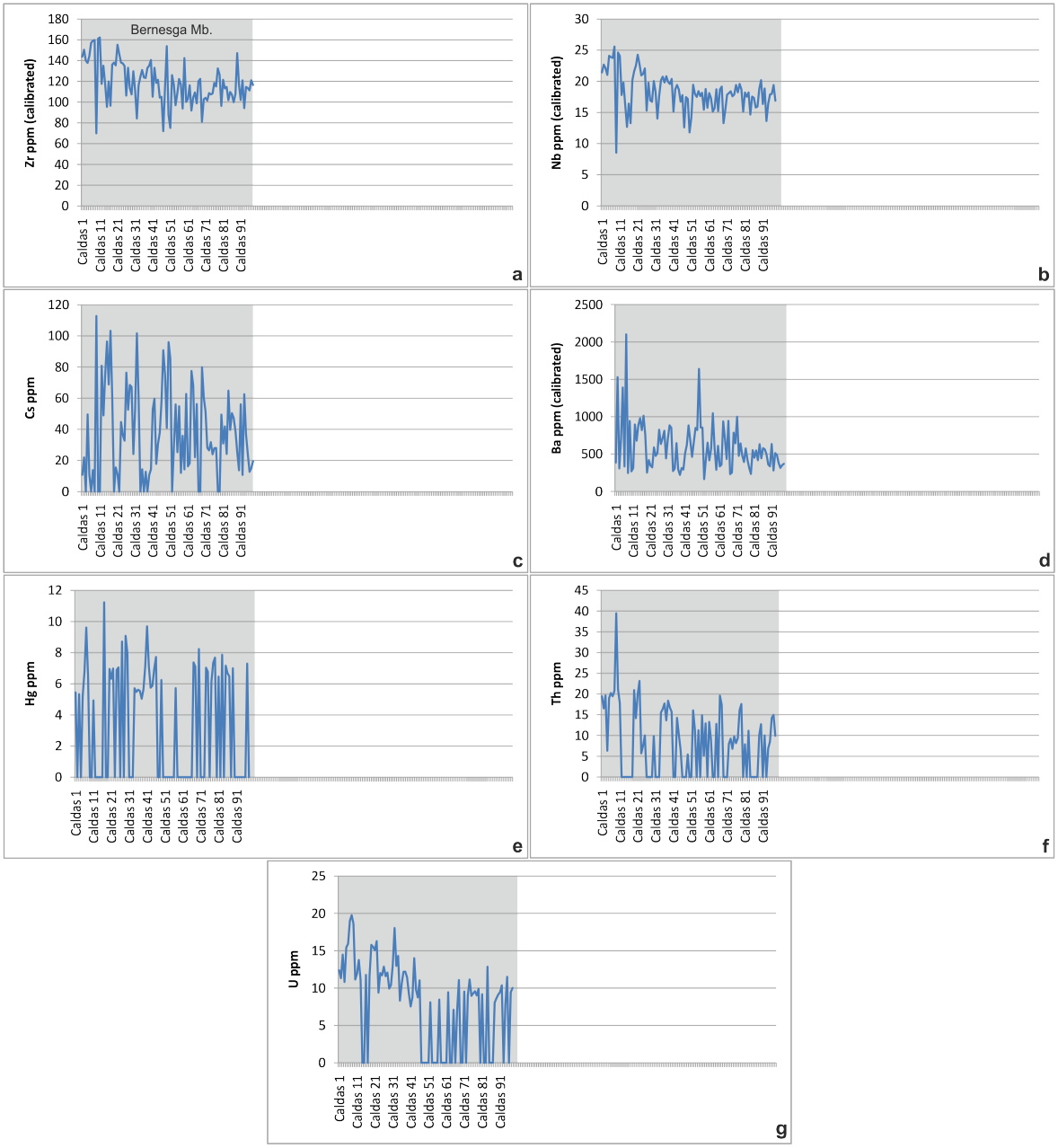

Figure 5.9 Trace element variation curves for the Caldas de Luna section. Each sample number represents a 25 cm interval. All samples are representative of the Bernesga Mb. A number of element concentrations were near to the detection limits (see **Figure 5.8** caption) and consequently are not discussed within this chapter.

Trace elements for the Bernesga Mb. (Caldas 1 - 98)

The Bernesga Mb. at the Caldas de Luna section is represented by 98 geochemical samples (see **Table 5.3**). The S concentrations are mostly near to D.L. yet a few intervals towards the top of the Mb. show enrichments. The values vary between below D.L. to 4460 ppm, with an average of 869.8 ppm and S.D. of 799.8. Cl concentrations are relatively consistent with a few enrichments at the base and towards the top of the Mb. The values vary between 364.5 and 1265 ppm, with an average of 652.4 ppm and S.D. of 170.8. The V values are enriched at the base of the Mb. the values decrease gradually towards the top of the Mb. A rhythmic pattern is seen towards the base

in the form of two distinct peaks. The V values vary throughout from 146.4 to 535 ppm with an average of 225.9 ppm and S.D. of 75.7. Cr values are enriched at the base of the Mb. decreasing towards the top, with a rhythmic pattern seen at the base. The values range from 56 to 151.2 ppm, averaging at 113.6 ppm with a S.D. of 20.9. The Ni values increase from the base of the Mb. towards the top, the values range from 36.8 to 237.3 ppm, averaging at 99.9 ppm with a S.D. of 38.8. The Cu values are relatively consistent throughout the Mb. with an enrichment at the base. The values increase rapidly and then begin to decrease gradually towards the top of the Mb. The values range from below D.L. to 231.4 ppm, averaging at 55.3 ppm with a S.D. of 41.2. Zn values are below D.L. at the base of the Mb. the values increase from the middle of the Mb. showing an enrichment towards the top. The values range from below D.L. to 316 ppm, averaging at 85.9 ppm with a S.D. of 63.6. The As values show a decrease from the base of the Mb., ranging from 7.7 to 149.3 ppm, averaging at 37.6 ppm with a S.D. of 26.7. Rb values are consistent throughout the Mb. decreasing slightly towards the top. The values range from 70.6 to 189.8 ppm, averaging at 146.6 ppm with a S.D. of 30. The Sr values are enriched at the base of the Mb. the values then decrease throughout in a logarithmic fashion, with values ranging from 167.7 to 247.4 ppm, averaging at 189.9 ppm with a S.D. of 22.1. Zr values are enriched at the base of the Mb. decreasing throughout. The values range from 69.9 to 162.2 ppm, averaging at 118.5 ppm with a S.D. of 20.1. Nb values decrease from the onset of the Mb. the values range from 8.5 to 25.5 ppm, averaging at 18.2 ppm with a S.D. of 3. The Cs concentrations decrease throughout the Mb. there are a number of horizons with values below the D.L. at the base, followed by a series of enriched horizons before settling into a steady decrease. The values range from below D.L. to 112.7 ppm, averaging at 44.1 ppm with a S.D. of 28.8. Ba values decrease steadily from the base to the top of the Mb. with a few enriched horizons at the base. The values range from 166 to 2100.9 ppm, averaging at 594.2 ppm with a S.D. of 319.4. The Hg concentrations are just above D.L. yet remain consistent from base to top. The values range from below D.L. to 11.2 ppm, averaging at 6.8 ppm with a S.D. of 3.5. Th values are enriched at the base of the Mb. decreasing towards the top. The Th values range from below D.L. to 39.4 ppm, averaging at 13.8 ppm with a S.D. of 8.2. The U concentrations are enriched at the base of the Mb. a rhythmic pattern is seen at the base much like that of the V concentrations described previously. The values range from below D.L. to 19.7 ppm, averaging at 11.4 ppm with a S.D. of 5.8.

5.4 La Majua Section

The analysed part of the La Majua section comprises of the following formations and members: **[1]** the uppermost part of the Barrios Fm. **[2]** the Getino Beds, and finally **[3]** the Bernesga Mb. (see '**Sedimentary log of the La Majua section**').

The La Majua log section begins with the uppermost bed of the Barrios Fm., consisting of a coarse-grained quartzarenite. The contact with the overlying Getino Beds is sharp. The Getino Beds are represented by 9.5 m of interbedded fine grained sand- and siltstones. The sandstones show grading, varying from coarse-grained sands to very-fine-grained sands. The Getino Beds are heavily bioturbated throughout. Symmetrical ripple marks are present on the tops of many of the sandstone beds. A number of the siltstone intercalations contain high amounts of crystalline pyrite. There are also infrequent hematised sandstone horizons throughout. The contact with the overlying Bernesga Mb. shales is very sharp and angular. 6 m of the basal shales of the Bernesga Mb. were logged and sampled at this location. The shales are organically enriched and contain vast numbers of monograptid graptolites, some of which are >25 cm in length. This suggests that the environment at the time of deposition was extremely calm. The boundary with the overlying Villasimpliz Mb. is not evident at this location.

Locality No.	GPS Coor.	Log total length	Total Samples
161	N42° 59.598' W6° 02.310'	24m	70

Sedimentary log of the La Majua section, Cantabrian Mountains, Northern Spain

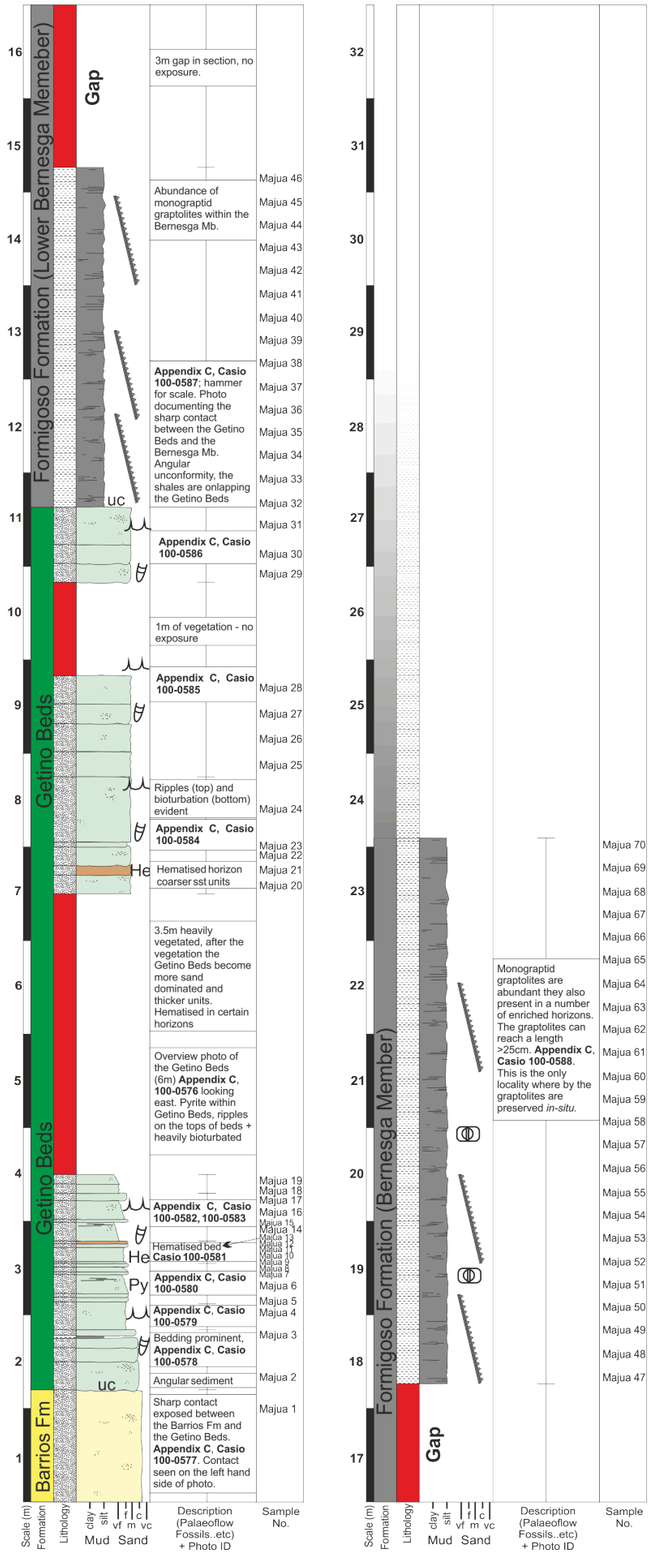

Figures (field images) associated with the La Majua section

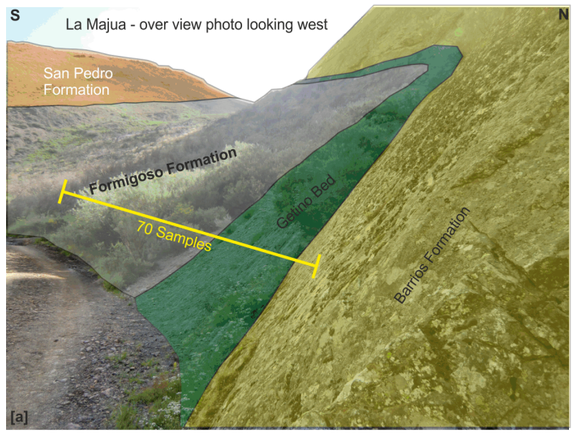

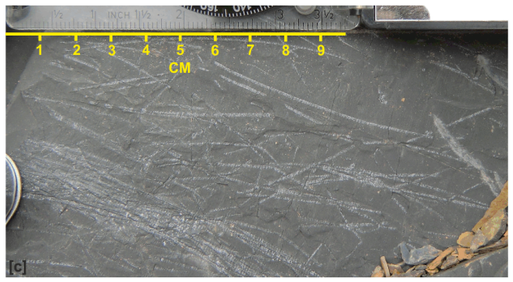

La Majua: [a] Overview photo (**Appendix C**, **100-0573**) of the La Majua section (looking towards the west), the differing formations are labelled. The yellow line represents the log section. All of the Getino Beds were sampled, the Bernesga Mb. at 25cm intervals. **[b]** Showing the monograptid graptolites *in-situ*, the Hammer is for scale (30cm). For graptolites to be preserved at this length, it suggests that the environmental conditions were extremely calm. The graptolites shown in **[c]** are aligned, suggesting a gentle continuous current.

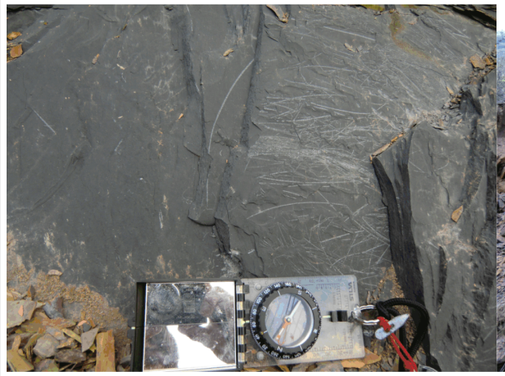

Appendix C, Photo 100-0588; Graptolites found *in-situ* within fresh quarried section. The quarried section represents the upper part of the La Majua log section. The graptolites are up to 30cm in length, and appear to be aligned. The size and orientation can be used to infer very calm environment of deposition with a slight current.

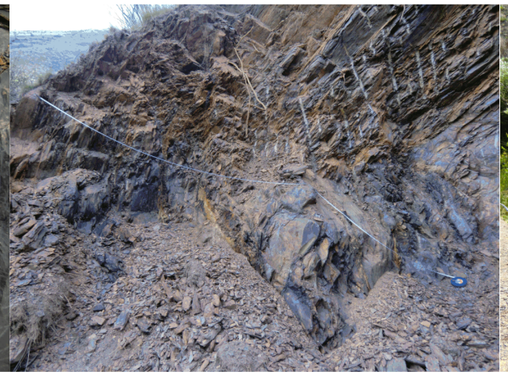

Appendix C, Photo 100-0589. Quarried section of the Bernesga Mb.). Nodular weathering patterns can be seen towards the centre of the image. It is within this quarried section that the large monograptid graptolites can be found (Figure to the left (**100-0588**) and above **[b]**).

Appendix C, Photo 100-0576. Contact between the upper Barrios Fm. (seen towards the right of the image) and the Getino Beds. Hammer for scale (30cm).

Sedimentary log key

Lithology Symbols

- Shales (organically enriched mudstones)
- Siltstones
- Sandstone bodies
- Intercalated sands and silts - less than 1cm in width

Sedimentary symbols

uc	Unconformity		Wave Ripples
Py	Pyrite		Nodular Weathering
He	Hematised		Planar Tabular Cross Bedding
	Bioturbation		Monograptid Graptolites

Left scale; representing 1m of the log section.

Left symbol; representing the sand/silt intercalations where the intercalations are less than 1 cm in width.

Araila 1
Caldas 1
La Majua 1
Sena 1
Villa 1

Text (left); Represents the sample numbers for the individual log sections.

5.4.1 Major element variations

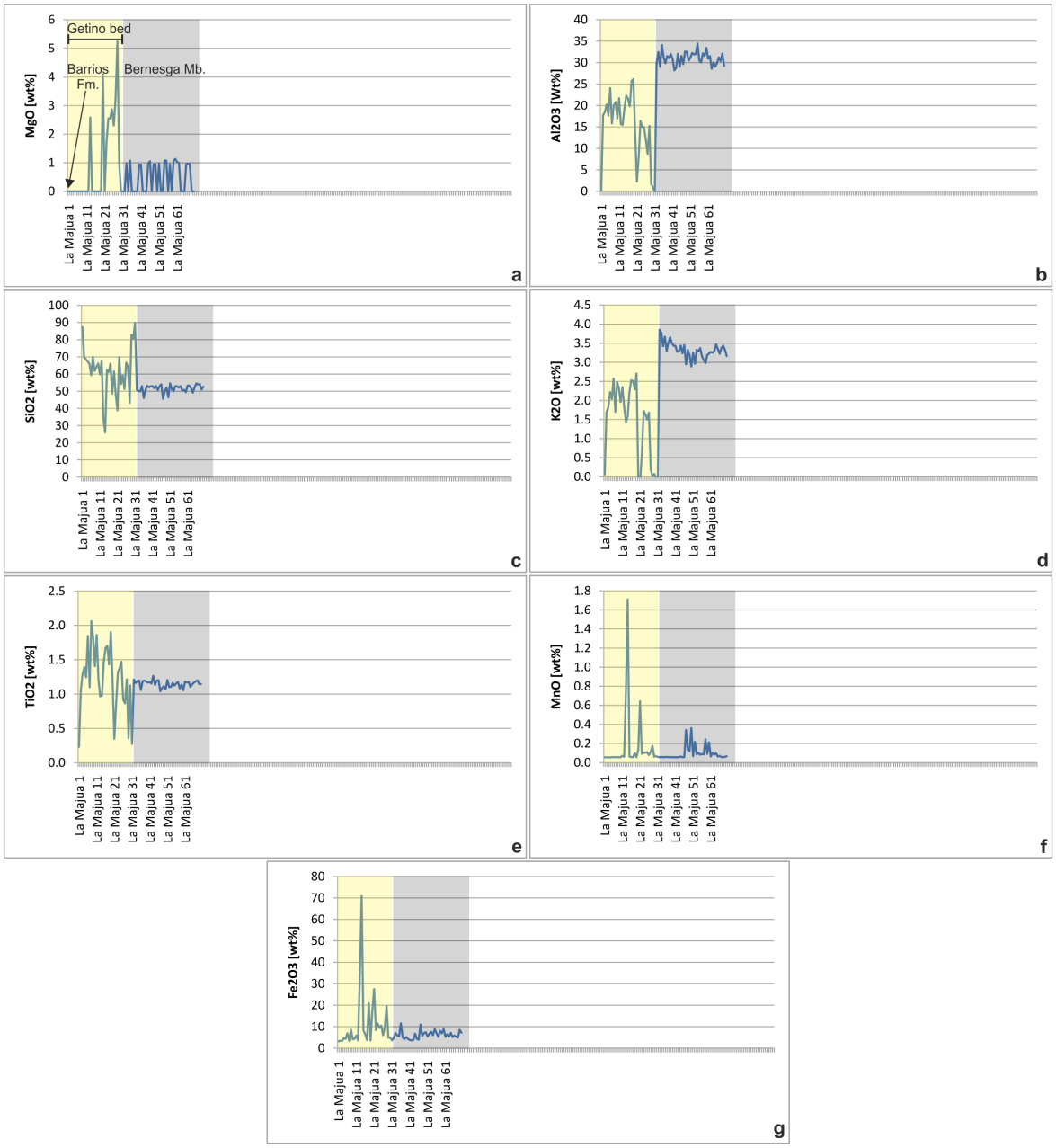

Figure 5.10 Major element variations for the La Majua section. Each sample number represents a 25 cm interval within the Bernesga Mb. However, the Getino Beds were sampled bed by bed. The coloured areas indicate the different litho-stratigraphic units, starting with the Barrios Fm. and Getino Beds (yellow) followed by the Bernesga Mb. (Grey). A single sample (La Majua 1) from the underlying Barrios Fm. was analysed as a control sample. The Getino Beds are represented by La Majua 2 to La Majua 31, and the Bernesga Mb. is represented by samples La Majua 32 to La Majua 70. See **Results appendix B** (part 2) for absolute elemental values for the Barrios Fm., Getino Beds and Formigoso Fm. As previously mentioned in **Chapter 5.2** 'Aralla section', the Na values were approximated and hence are not displayed here. The Na proxy data can however be found in the **Results appendix B** (part 2). Ca values are mostly below detection limits (D.L.), therefore are not included in this section, however the data can be found in **Results appendix B** (part 2).

Major elements for the Getino Beds (La Majua 2 - 31)

The Getino Beds at the La Majua section are represented by 30 geochemical samples (see **Table 5.3**). The MgO concentrations are below D.L. at the base and increase significantly towards the top of the Getino Bed. The MgO concentrations vary from below D.L. to 5.2 wt%, with an average 0.9 wt% and standard deviation (S.D) of 1.5. Al_2O_3 values are pretty consistent throughout, showing a

depletion towards the top of the Getino Beds ranging from below D.L. to 26.1 wt%, an average of 15.6 wt% and S.D. of 7.1. SiO_2 concentrations range from 26 to 89.9 wt% decreasing towards the top of the Getino Beds with an enriched horizon at the very top. The values average at 61 wt% with a S.D. of 13.6. The K_2O values show a depletion at the base of the Getino Beds. The values range from below D.L. to 2.7 wt%, an average of 1.5 wt% and S.D. of 0.9. TiO_2 values are relatively consistent, with a slight depletion towards the top. The values range from 0.2 to 2 wt%, averaging at 1.2 wt% with a S.D. of 0.4. The MnO concentrations are consistent throughout, with a slight increase towards the top. The concentrations vary between 0.05 and 1.7 wt%, averaging 0.17 wt% with a S.D. of 0.33. There are number of samples that are highly enriched, and are most likely related to localised mineralisation. Fe_2O_3 values show a systematic increase from the base to the top of the Fm., varying from 3.3 to 70.8 wt%, and average of 11.1 wt% and a S.D of 13.6. A number of horizons show substantial enrichments, again most likely related to localised mineralisation.

Major elements for the Bernesga Mb. (La Majua 32 - 70)

The Bernesga Mb. at the La Majua section is represented by 39 geochemical samples (see **Table 5.3**). The MgO concentrations are relatively consistent just above the D.L. The values vary between below D.L. to 1.1 wt%, with an average 1.0 wt% and S.D. of 0.5. Al_2O_3 concentrations are significantly higher than that of the underlying Getino Beds, ranging from 28.2 to 34.4 wt%, averaging 31 wt% with a S.D. of 1.4. SiO_2 values show a marked depletion relative to the underlying Getino Beds, varying from 45.5 to 54.6 wt%, averaging at 51.6 wt% with a S.D. of 2.1. The K_2O values range from 2.8 to 3.8 wt%, showing a systematic decrease towards the top. The values average at 3.3 wt% and have a S.D. of 0.2. TiO_2 are depleted relative to the underlying Getino Beds, the concentrations vary between 1 and 1.2 wt%, averaging at 1.1 wt% with a S.D. of 0.04. The MnO values vary between 0.05 and 0.36 wt%, averaging 0.09 wt% with a S.D. of 0.07, again with a number of enriched horizons, most likely related to localised mineralisation. Fe_2O_3 concentrations are consistent, increasing slightly towards the top of the Mb. The concentrations range from 3.5 to 11.5 wt%, averaging at 6.2 wt% with a S.D. of 1.8.

5.4.2 Trace element variations

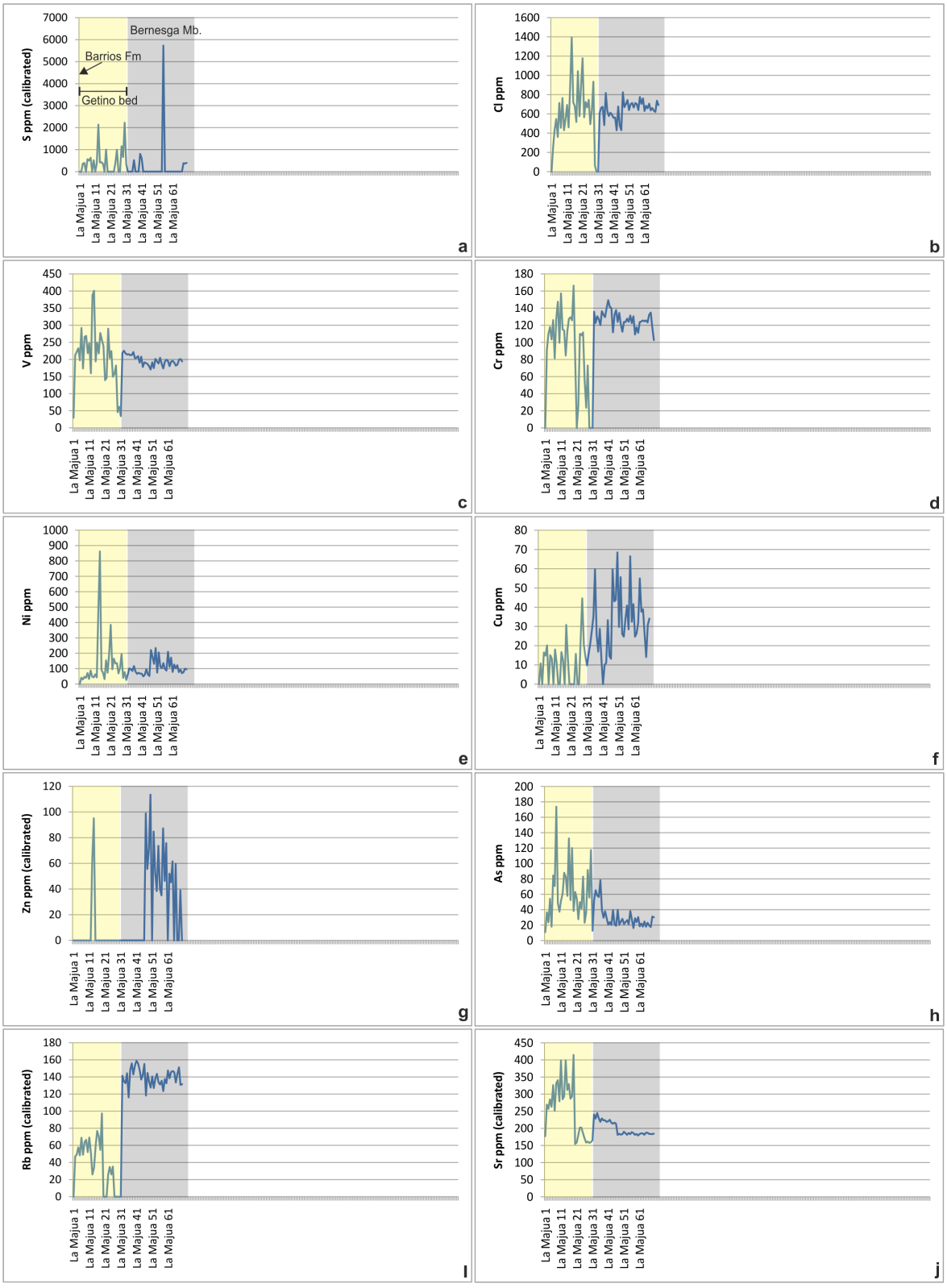

Figure 5.11 Trace element variations for the La Majua section. Each sample number represents a 25 cm interval within the Bernesga Mb. However, the Getino Beds were sampled bed by bed. The coloured areas indicate the different litho-stratigraphic units, starting with the Barrios Fm. and Getino Beds (yellow) followed by the Bernesga Mb. (Grey). As with the previous major element description, a single sample (La Majua 1) from the underlying Barrios Fm. was analysed as a control sample, the Getino Beds are represented by La Majua 2 to La Majua 31, and the Bernesga Mb. is represented by samples La Majua 32 to La Majua 70. See **Results appendix B** (part 2) for absolute elemental values of the Barrios Fm., Getino Beds and Formigoso Fm. P and Bi concentrations are below D.L. and not further discussed. The following elements are close to the D.L. and not further discussed: Sc, Co, Se, Mo, Pd, Ag, Cd, Sn, Sb, Te, W, Au and Pb. The data for these elements can be found in **Results appendix B** (part 2).

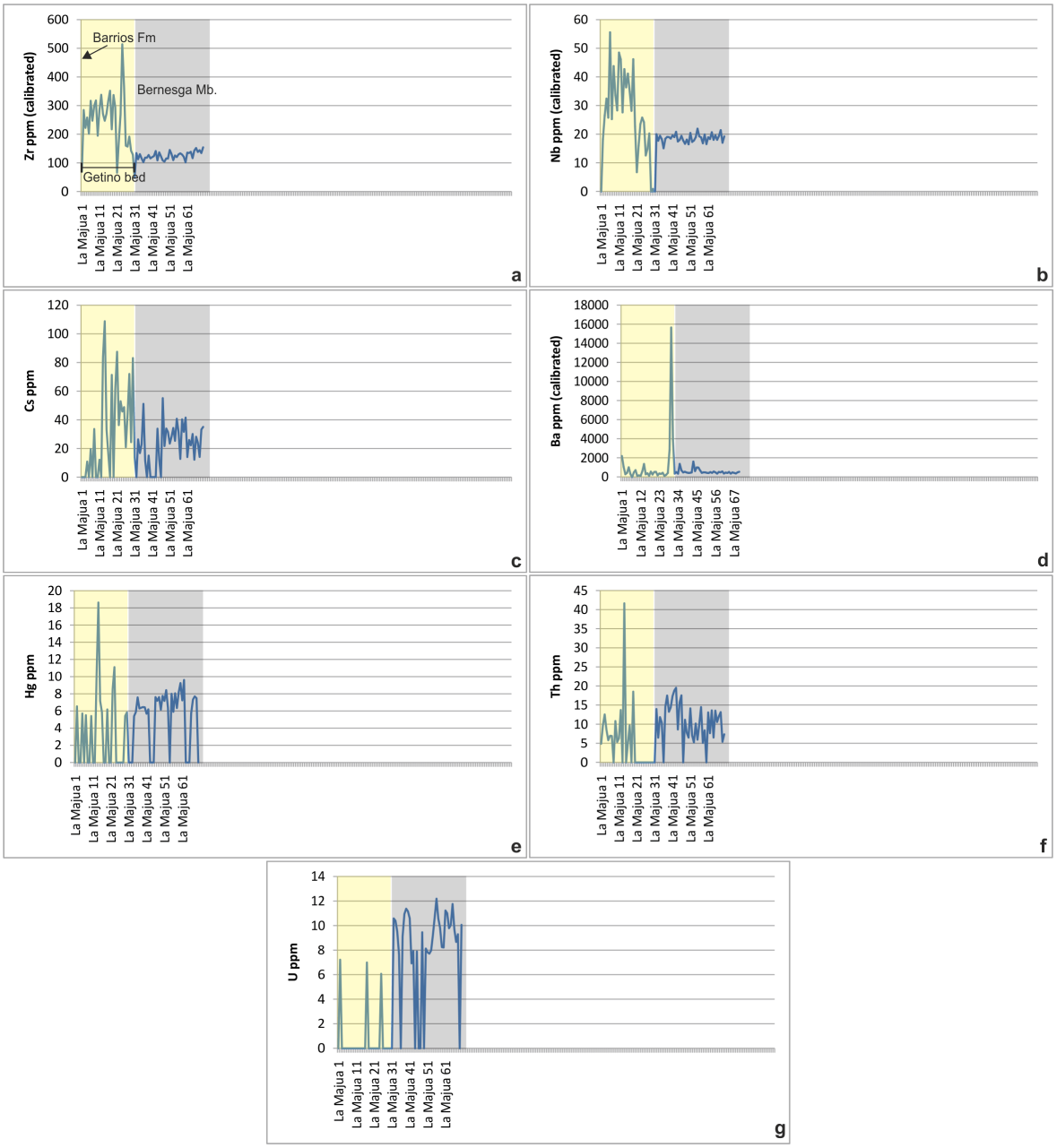

Figure 5.12 All trace element variations for the La Majua section. Each sample number represents a 25 cm interval within the Bernesga Mb. However, the Getino Beds were sampled bed by bed. The coloured areas indicate the different litho-stratigraphic units, starting with the Barrios Fm. and Getino Beds (yellow) followed by the Bernesga Mb. (Grey). A number of element concentrations were near to the detection limits (see **Figure 5.11** caption) and consequently are not discussed within this chapter.

Trace elements for the Getino Beds (La Majua 2 - 31)

The Getino Beds at the La Majua section are represented by 30 geochemical samples (see **Table 5.3**). The S concentrations are elevated relative to the overlying Bernesga Mb. A few horizons are substantially enriched. The values vary between below D.L. to 2222 ppm, with an average of 448.1 ppm and S.D. of 576.7. Cl concentrations increase from the base to the top, with values varying between below D.L. and 1393.4 ppm, with an average of 612.3 ppm and S.D. of 313.3. The V values show a maximum towards the middle of the Getino Beds, which then diminish towards the top. The V values vary from 34.3 to 400.7 ppm with an average of 211.6 ppm and S.D. of 82.9. Cr

values are enriched at the base of the Getino Beds decreasing towards the top. The values range from below D.L. to 166.3 ppm, averaging at 90.9 ppm with a S.D. of 48.2. The Ni values increase from the base of the Mb. towards the top, with a few enriched horizons related to localised mineralisation. The Ni values range from 26.5 to 861.5 ppm, averaging at 131.4 with a S.D. of 171.4. The Cu values are near D.L. with values ranging from below D.L. to 44.5 ppm, averaging at 10.6 ppm with a S.D. of 10.9. The majority of the Zn values are below D.L. Only one sample displayed a value of 95.1 ppm. The As values rise significantly from the base towards the middle of the Getino Beds, these values then diminish gradually. The As concentrations fall between 12.7 and 173.7 ppm, they average at 62.9 ppm with a S.D. of 36.6. Rb values show a slight increase from the base of the Getino Beds and deplete towards the top (below D.L.). The values range from below D.L. to 97.2 ppm, averaging at 38.7 ppm with a S.D. of 28.3. The Sr values increase towards the middle of the Getino Beds which then fall dramatically towards the top. The Sr concentrations vary from 154 to 414.7 ppm, averaging at 255.7 ppm with a S.D. of 80.4. Zr values increase towards the top of the beds before decreasing drastically at the very top. The Zr values range from 47.4 to 514.1 ppm, averaging at 249.4 ppm with a S.D. of 95.6. Nb values increase towards the middle of the beds, the values fall rapidly towards the very top. The Nb values range from below D.L. to 55.5 ppm, averaging at 26.7 ppm with a S.D. of 14.9. The Cs concentrations increase throughout the beds. The values are below D.L. at the base followed by a series of enriched horizons, the values range from below D.L. to 108.8 ppm, averaging at 32.6 ppm with a S.D. of 32.3. Ba values decrease steadily from the base to the top of the Mb. with an enriched horizon at the very top. The values range from below D.L. to 15648.4 ppm, averaging at 1117 ppm with a S.D. of 2865.1. The Hg concentrations are near D.L. and remain consistent from the base to the top. One sample shows a significant enrichment towards the middle of the beds. The values range from below D.L. to 18.6 ppm, averaging at 3.3 ppm with a S.D. of 4.6. Th values are above the D.L. at the base of the Getino Beds. However, the concentrations fall below the D.L. towards the top. The Th values range from below D.L. to 41.6 ppm, averaging at 5.3 ppm with a S.D. of 8.6. The U concentrations are mostly below D.L., there are three horizons with values of 7.2, 6.9 and 6 ppm.

Trace elements for the Bernesga Mb. (La Majua 32 - 70)

The Bernesga Mb. at the La Majua section is represented by 39 geochemical samples (see **Table 5.3**). The S concentrations are mostly below D.L. for this Mb. with one enriched horizon of 5726.1 ppm. Cl values show a steady increase from the base of the Mb., with values ranging from 430.2 to 824.3 ppm, averaging 651.4 ppm with a S.D. of 90.7. The V values decrease from the base of the

Mb. The values range from 170.4 to 225.2 ppm, averaging at 196.8 ppm with a S.D. of 14. Cr values are enriched relative to the underlying Getino Beds. The values decrease gradually from the base, ranging from 102.7 to 149.2 ppm, averaging at 126.5 ppm with a S.D. of 9.6. The Ni values show a steady increase throughout the section, including the underlying Getino Beds. The values range from 50.2 to 234 ppm, averaging at 106.5 ppm with a S.D. of 47.5. The Cu values are enriched relative to the underlying Getino Beds, and are erratic. The Cu values range from below D.L. to 68.4 ppm, averaging at 32.6 ppm with a S.D. of 16.1. Zn values are below D.L. at the base, the values increase drastically and then decrease towards the top. The Zn values range from below D.L. to 113.5 ppm, averaging at 62.8 ppm with a S.D. of 35.1. The As values are slightly depleted relative to the underlying Getino Beds, and show a gradual decline throughout. The concentrations range from 16.7 to 78.2 ppm, averaging at 30.3 ppm with a S.D. of 14.4. The Rb values show a substantial enrichment relative to the underlying Getino Beds and remain consistent, with values ranging from 116 to 158.8 ppm, averaging at 139.7 ppm with a S.D. of 10.1. Sr values are elevated at the base and deplete through the section. The Sr values range from 179.2 to 244.7 ppm, averaging at 199.5 with a S.D. of 20.6. The Zr values are significantly depleted relative to the Getino Beds, showing a slight increase from the base. The values range from 101.8 to 154.2 ppm, averaging at 125.9 ppm with a S.D. of 13.5. Nb values are depleted relative to the underlying Getino Beds yet remain consistent with values ranging from 15 to 21.9 ppm, averaging at 18.6 ppm with a S.D. of 1.4. The Cs values are near D.L. at the base and remain relatively consistent thereafter. The values range from below D.L. to 55.1 ppm, averaging at 27.5 ppm with a S.D. of 14.6. Ba values are slightly elevated relative to the underlying Getino Beds, with values ranging from 341.9 to 1602.2 ppm, averaging at 545.7 ppm with a S.D. of 262.7. The Hg concentrations remain consistent to the lower Getino Beds, again close to the D.L. The values range from below D.L. to 9.6 ppm, averaging at 7.08 ppm with a S.D. of 3.2. The Th values show a marked increase relative to the underlying Getino Beds, and decrease slightly from the base. The concentrations range from below D.L. to 19.5 ppm, averaging at 11.3 ppm with a S.D. of 5. U concentrations are enriched relative to the underlying Getino Beds, with values ranging from below D.L. to 12.1 ppm, averaging at 9.5 ppm with a S.D. of 3.7.

5.5 Sena de Luna Section

The analysed part of the Sena de Luna section comprises of the following formations and members: **[1]** the uppermost part of the Barrios Fm. **[2]** the Getino Beds, and finally **[3]** Bernesga Mb. (see **'Sedimentary log of the Sena de Luna section**').

The Sena de Luna log begins with the uppermost bed of the Barrios Fm., consisting of a coarse-grained quartzarenite. The contact with the overlying Getino Beds is not clear as there is dense vegetation present. The Getino Beds are represented by 10 m of interbedded fine grained sand- and siltstones. The sandstones show grading, varying from coarse-grained sands to fine-grained sands. The Getino beds are heavily bioturbated throughout. Symmetrical ripples are present on many of the sandstone beds. The contact with the overlying Bernesga Mb. shales is very sharp. 27 m of the basal shales belonging to the Bernesga Mb. were logged this location. The very base of the Bernesga Mb. is poorly exposed at this location due to heavy coverage by vegetation. Consequently there is a gap of 5.3 m at the very base of the log section. The shales are organically enriched and contain vast numbers of monograptid graptolites. The boundary with the overlying Villasimpliz Mb. is not evident at this location.

Locality No.	GPS Coor.	Log total length	Total Samples
171	N42° 54.933' W5° 57.899'	36m	79

Sedimentary log of the Sena de Luna section, Cantabrian Mountains, Northern Spain

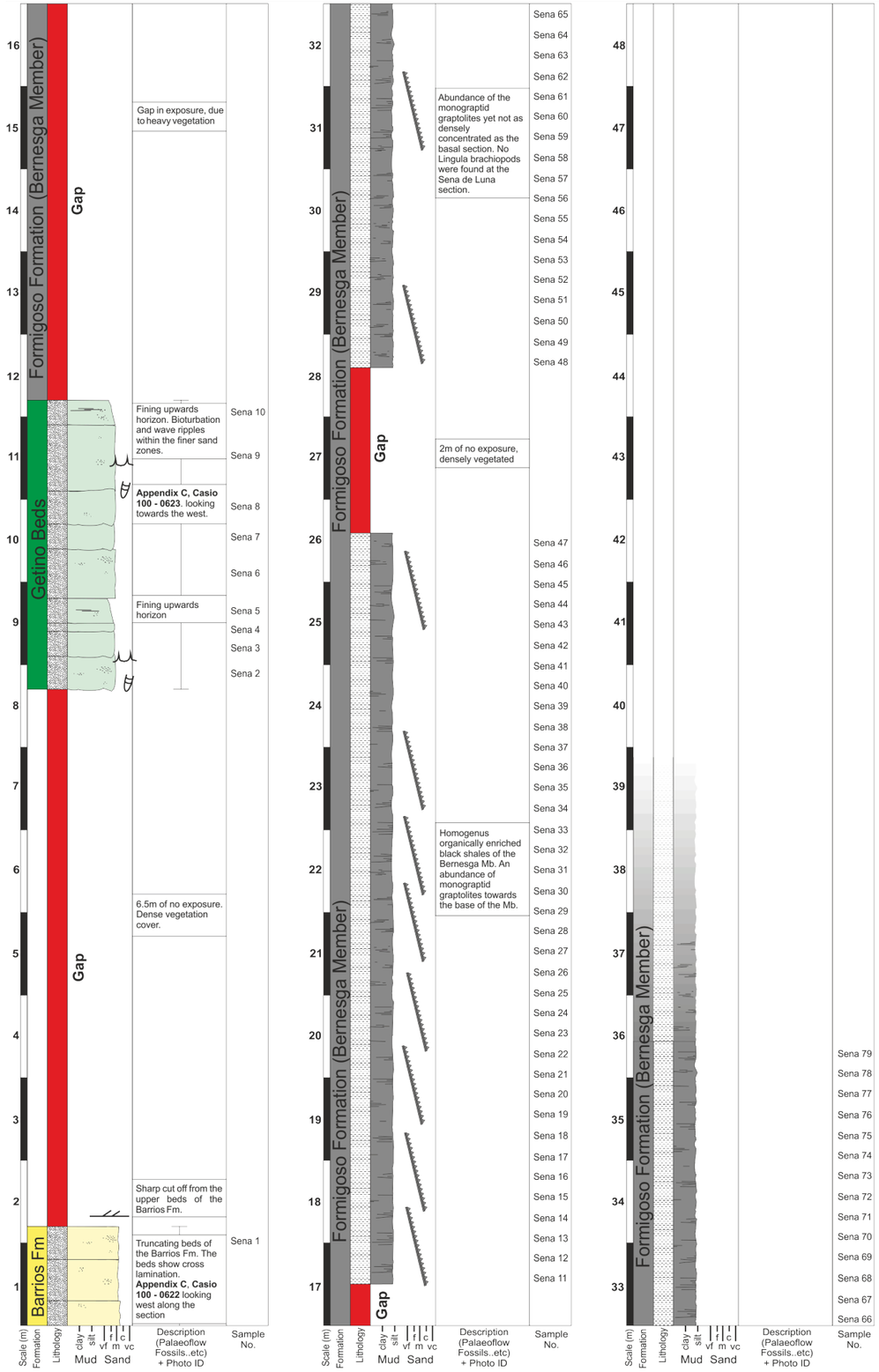

Figures (field images) associated with the Sena de Luna section

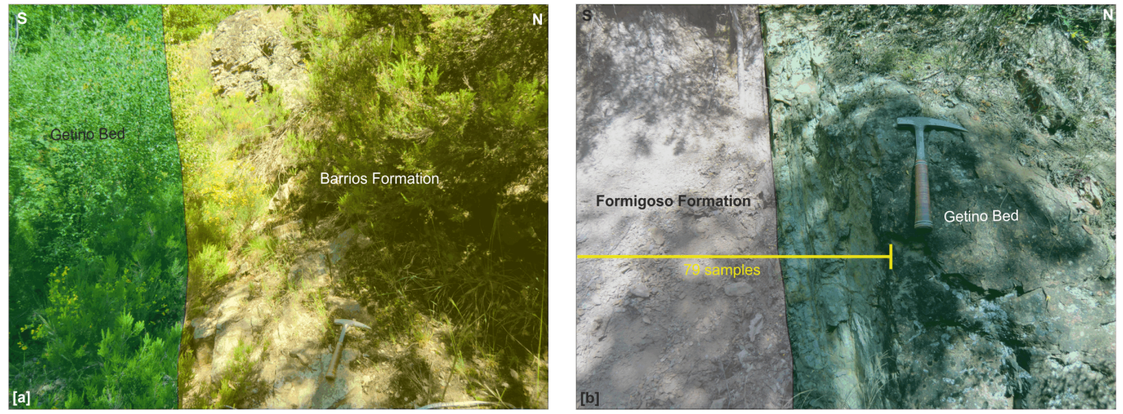

Sena de Luna: [a] The boundary between the Barrios Fm. and the Getino Bed. However, there is a substantial gap in the section due to heavy vegetation as seen towards the left of the image ~6m before the Getino Beds outcrop. **[b]** Contact between the Getino Beds and the overlying Bernesga Mb. (hammer for scale in both instances 30cm in length). The yellow line in **[b]** represents the beginning of the sampling region (79 samples taken at 25cm intervals throughout the Bernesga Mb.. The basal Bernesga Member of the Formigoso Fm does not outcrop for ~5m after the end of the Getino Beds (very poor exposure). Every bed of the Getino Beds were sampled at this locality.

Sedimentary log key

Lithology Symbols

- Shales (organically enriched mudstones)
- Sandstone bodies
- Siltstones
- Intercalated sands and silts - less than 1cm in width

Sedimentary symbols

uc	Unconformity		Wave Ripples
Py	Pyrite		Nodular Weathering
He	Hematised		Planar Tabular Cross Bedding
	Bioturbation		Monograptid Graptolites

Left scale; representing 1m of the log section.

Left symbol; representing the sand/silt intercalations where the intercalations are less than 1 cm in width.

Araila 1
Caldas 1
La Majua 1
Sena 1
Villa 1

Text (left); Represents the sample numbers for the individual log sections.

5.5.1 Major element variations

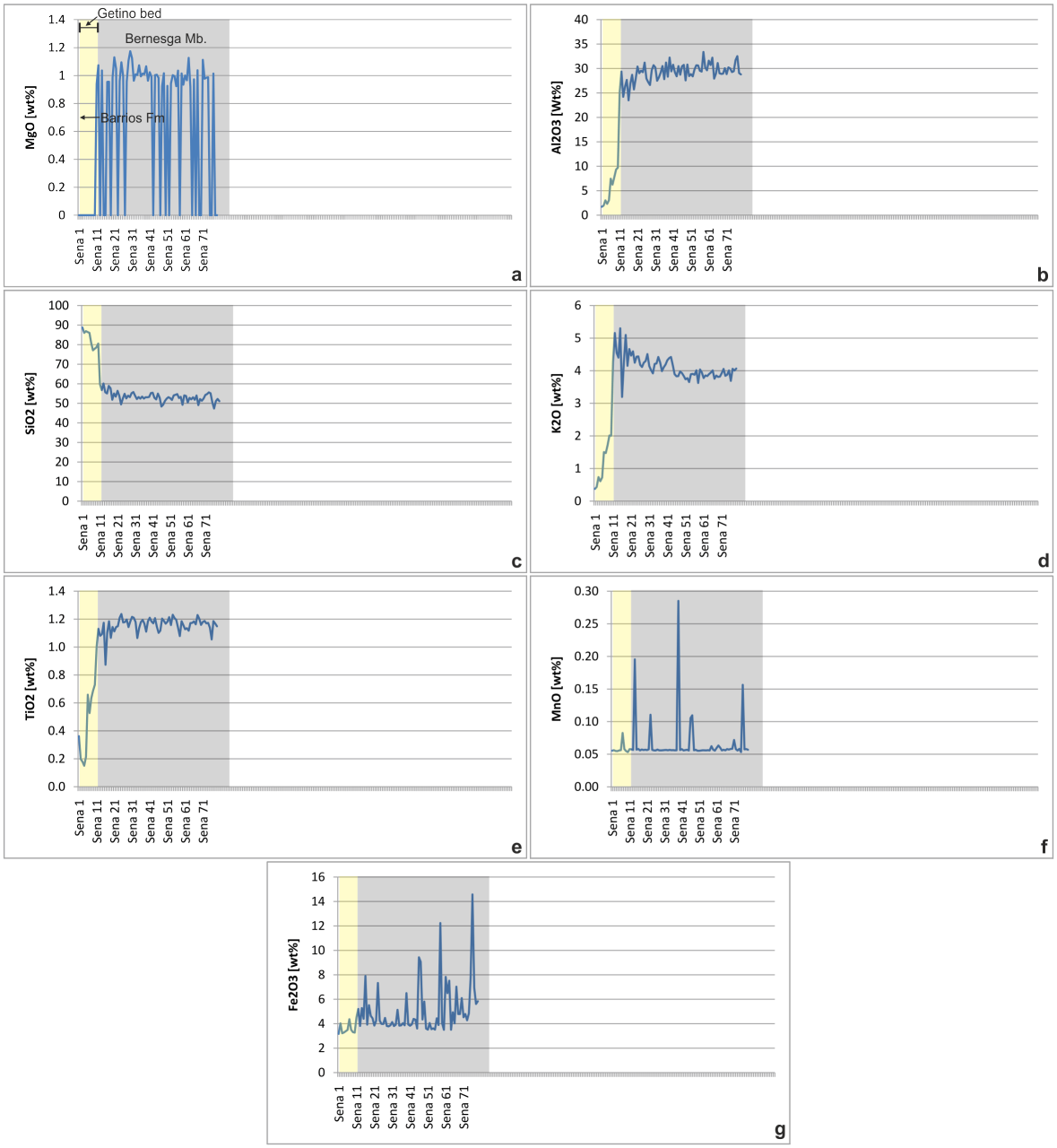

Figure 5.13 Major element variations for the Sena de Luna section. Each sample number represents a 25 cm interval within the Bernesga Mb. However, the Getino Beds were sampled bed by bed. The coloured areas indicate the different litho-stratigraphic units, starting with the Barrios Fm. and Getino Beds (yellow) followed by the Bernesga Mb. (Grey). A single sample (Sena 1) from the underlying Barrios Fm. was analysed as a control sample. The Getino Beds are represented by Sena 2 to Sena 10 and the Bernesga Mb. is represented by samples Sena 11 to Sena 79. See **Results appendix B** (part 2) for absolute elemental values for the Barrios Fm., Getino Beds and Formigoso Fm. As previously mentioned in **Chapter 5.2** 'Aralla section', the Na values were approximated and hence are not discussed here. The Na proxy data can however be found in the **Results appendix B** (part 2). Ca values are mostly below D.L., therefore are not included in this section, however the geochemical data can be found in the **Results appendix B** (part 2).

Major elements for the Getino Beds (Sena 2 - 10)

The Getino Beds at the Sena de Luna section are represented by 9 geochemical samples (see **Table 5.3**). The MgO concentrations fall below the D.L. for the Getino Beds and are not further discussed. Al_2O_3 values increase significantly from the base to the top of the beds, ranging from 1.9 to 9.7 wt%, an average of 5.6 wt% and S.D. of 3. SiO_2 concentrations range from 77.1 to 86.9

wt% decreasing towards the top of the Getino Beds, averaging at 82.2 wt% with a S.D. of 4. The K_2O values increase systematically from the base to the top of the Getino Beds. The values range from 0.4 to 2 wt%, an average of 1.2 wt% and S.D. of 0.6. TiO_2 values increase significantly towards the top of the Getino Beds, the values range from 0.1 to 0.7 wt%, averaging at 0.4 wt% with a S.D. of 0.2. The MnO concentrations are consistent throughout, varying between 0.05 and 0.08 wt%, averaging 0.05 with a S.D. of 0.009. The sample 'Sena de Luna 27' shows a slight enrichment most likely related to localised mineralisation (see **Results appendix B,** part 2). Fe_2O_3 values show a systematic increase from the base to the top of the Getino Beds, varying from 3.2 to 4.3 wt%, with an average of 3.5 wt% and S.D of 0.3.

Major elements for the Bernesga Mb. (Sena 11 - 79)

The Bernesga Mb. at the Sena de Luna section is represented by 69 geochemical samples (see **Table 5.3**). The MgO concentrations are relatively consistent just above the D.L., varying between below D.L. to 1.1 wt%, with an average 1.01 wt% and S.D. of 0.4. Al_2O_3 concentrations are significantly higher relative to the underlying Getino Beds., ranging from 23.4 to 33.3 wt%, averaging 29.2 wt% with a S.D. of 1.8. SiO_2 values show a marked decrease relative to the Getino Beds, varying from 47.3 to 60.1 wt%, averaging at 53.3 wt% with a S.D. of 2.3. The K_2O values range from 3.1 to 5.3 wt% decreasing towards the top, averaging 4.1 wt% and a S.D. of 0.3. TiO_2 concentrations are enriched relative to the underlying Getino Beds. The concentrations vary between 0.8 and 1.2 wt%, averaging at 1.1 wt% with a S.D. of 0.05. The MnO values vary between 0.05 and 0.28, averaging 0.06 wt% with a S.D. of 0.03 again with a number of enriched horizons, most likely related to localised mineralisation. Fe_2O_3 concentrations are consistent at the base increasing towards the top. The values range from 3.5 to 14.5 wt%, averaging at 5 wt% with a S.D. of 2. A few enriched horizons towards the top could suggest localised mineralisation.

5.5.2 Trace element variations

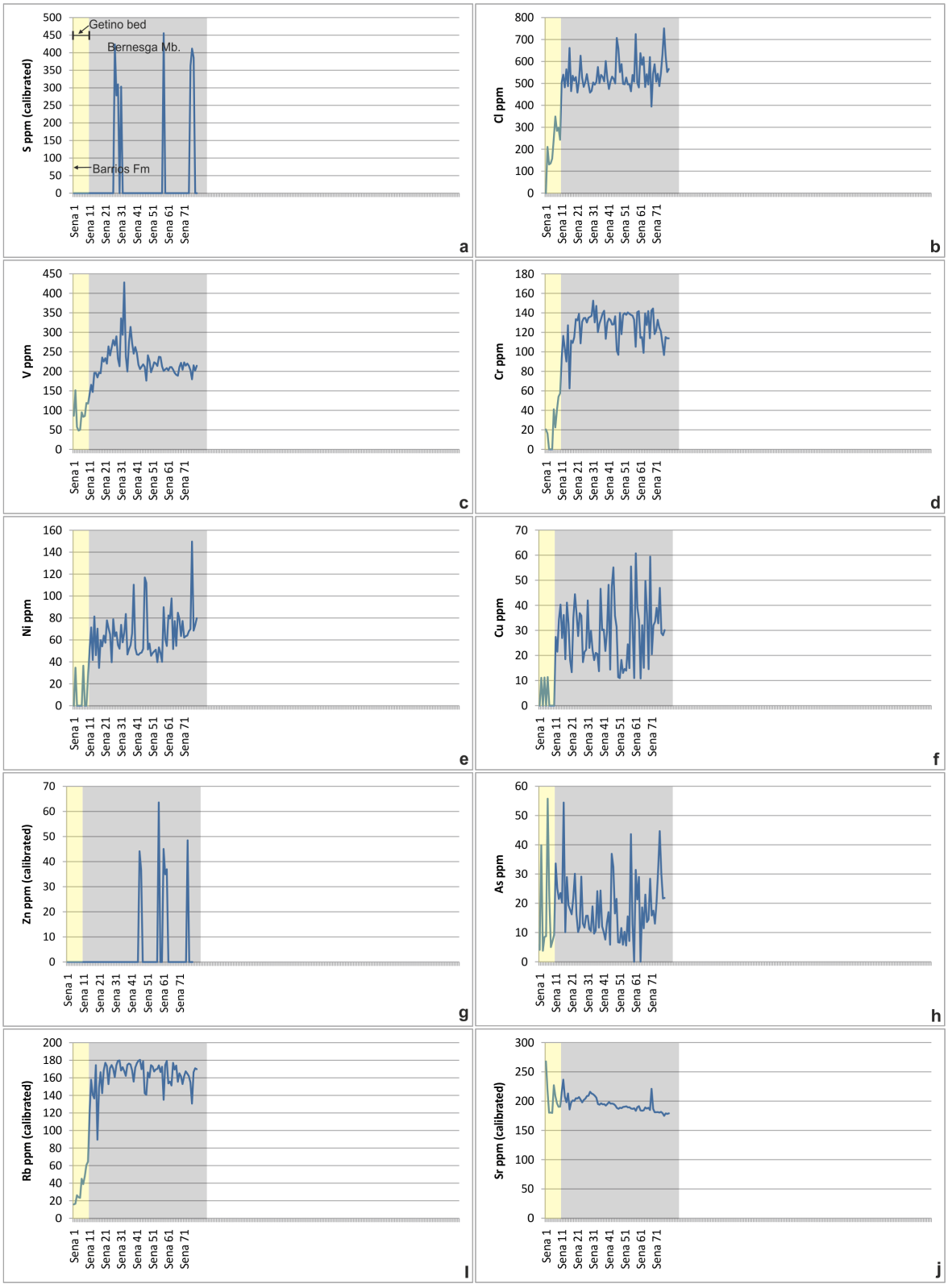

Figure 5.14 Trace element variations for the Sena de Luna section. Each sample number represents a 25 cm interval within the Bernesga Mb. However, the Getino Beds were sampled bed by bed. The coloured areas indicate the different litho-stratigraphic units, starting with the Barrios Fm. and Getino Beds (yellow) followed by the Bernesga Mb. (Grey). As with the previous major element description, a single sample (Sena 1) from the underlying Barrios Fm. was analysed as a control sample, the Getino Beds are represented by Sena 2 to Sena 10, and the Bernesga Mb. is represented by samples Sena 11 to Sena 79. See **Results appendix B** (part 2) for absolute elemental values for the Barrios Fm., Getino Beds and Formigoso Fm. P and Bi concentrations are below D.L. and not further discussed. The following elements are near to the D.L. and not included: Sc, Co, Se, Mo, Pd, Ag, Cd, Sn, Sb, Te, W, Au and Pb. However, the data for these elements can be found in **Results appendix B** (part 2).

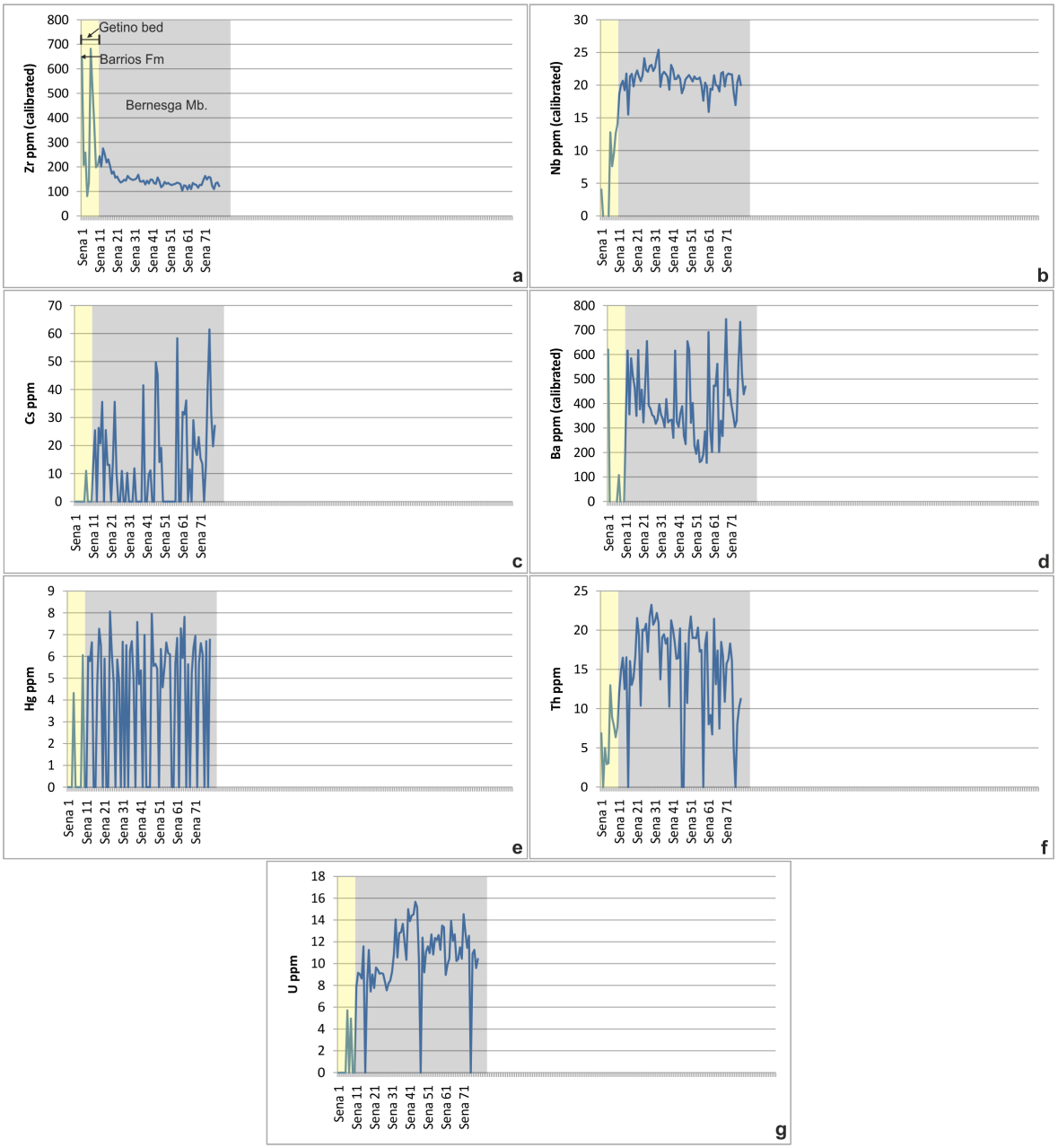

Figure 5.15 Trace element variation curves for the Sena de Luna section. Each sample number represents a 25 cm interval within the Bernesga Mb. However, the Getino Beds were sampled bed by bed. The coloured areas indicate the different litho-stratigraphic units, starting with the Barrios Fm. and Getino Beds (yellow) followed by the Bernesga Mb. (Grey). A number of element concentrations were near to the detection limits (see **Figure 5.14** caption) and consequently are not discussed within this chapter.

Trace elements for the Getino Beds (Sena 2 - 10)

The Getino Beds at the Sena de Luna section are represented by 9 geochemical samples (see **Table 5.3**). The S concentrations are below D.L. and subsequently are not further discussed. Cl concentrations increase from the base to the top, with values varying between 130.2 and 348.9 ppm, with an average of 228.4 ppm and S.D. of 76.4. The V values reach a maximum at the base of the Getino Beds, which then decrease rapidly before increasing again towards the top. The V values vary from 48 to 151.2 ppm with an average of 89.6 ppm and S.D. of 35. Cr values increase towards the top of the Getino Beds, the values range from below D.L. to 57.3 ppm, averaging at

25.6 ppm with a S.D. of 23.2. The Ni values are mostly below D.L. with three horizons showing values of 34.6, 36.4 and 28 ppm. The Cu values are mostly below D.L. with three values of 11.1, 11.2 and 11.3 ppm. The Zn values fall below the D.L. and not further discussed. The As values rise dramatically from the base and are erratic, ranging from 3.7 to 55.7 ppm, averaging at 17.7 ppm with a S.D. of 18.2. Rb values show an increase from the base of the beds, the values range from 16.6 to 64.4 ppm, averaging at 38.5 ppm with a S.D. of 17.1. The Sr values are elevated at the base, decreasing throughout. The Sr values range from 179.9 to 227.1 ppm, averaging at 196.7 ppm with a S.D. of 17.2. Zr values increase towards the top of the bed before decreasing significantly at the top. The values range from 80.8 to 681.8 ppm, averaging at 296.9 ppm with a S.D. of 195.8. Nb values increase towards the top of the beds. The values range from below D.L. to 14 ppm, averaging at 6 ppm with a S.D. of 6.5. The Cs concentrations are mostly below the D.L. with one value of 10.9 ppm. Ba values are mostly below the D.L. with two values of 8 and 107.5 ppm. The Hg values are mostly below the D.L. with two values of 4.3 and 6 ppm. Th values increase from the base, with values ranging from below D.L. to 12.9 ppm, averaging at 6 ppm with a S.D. of 3.8. The U concentrations are mostly below D.L., with two horizons displaying values of 5.7 and 4.9 ppm.

Trace elements for the Bernesga Mb. (Sena 11 - 79)

The Bernesga Mb. at the Sena de Luna section is represented by 69 geochemical samples (see **Table 5.3**). The S concentrations are mostly below D.L. for this Mb. There are however a number of enriched horizons of 423.4, 278.2, 309.8, 303.2, 455.3, 362, 411.5 and 385.9 ppm. Cl values show a steady increase from the base of the Mb. with values ranging from 394.3 to 750.6 ppm, averaging 537.9 ppm with a S.D. of 66.1. The V values increase from the base of the Mb. and then decrease after peaking. The values range from 141.2 to 427.8 ppm, averaging at 224.4 ppm with a S.D. of 42.5. Cr values are enriched in relation to the underlying Getino Beds, they decrease gradually from the base. The values range from 62.5 to 152.5 ppm, averaging at 125 ppm with a S.D. of 16.4. The Ni values show a steady increase throughout the section, including the underlying Getino Beds. The Ni values range from 34.4 to 149.6 ppm, averaging at 64.7 ppm with a S.D. of 20.1. The Cu values are enriched relative to the Getino Beds and are erratic. The values range from 10.8 to 60.7 ppm, averaging at 29.4 ppm with a S.D. of 12.6. Zn values are below D.L. at the very base, there are a few enriched horizons towards the top of the Mb. with values of 44.1, 36.7, 63.5, 45, 34.9, 36.9 and 48.4 ppm. The As values are slightly depleted relative to the underlying Getino Beds, and show a gradual decline from the base before increasing again towards the top.

The As concentrations range from below D.L. to 54.4 ppm, they average at 19.0 ppm with a S.D. of 10.3. The Rb values show a significant enrichment relative to the underlying Getino Beds and remain consistent. The values range from 89.4 to 180.4 ppm, averaging at 163.2 ppm with a S.D. of 15.9. Sr values are elevated at the base and deplete through the section, the values range from 174.9 to 236.7 ppm, averaging at 194.6 ppm with a S.D. of 11.8. The Zr values are significantly depleted relative to the underlying Getino Beds, showing a decrease from the base. The values range from 102.5 to 275.3 ppm, averaging at 147.6 ppm with a S.D. of 33.3. Nb values are enriched relative to the underlying Getino Beds yet remain consistent. The values range from 15.5 to 25.3 ppm, averaging at 20.8 ppm with a S.D. of 1.7. The Cs values are near D.L. at the base and remain relatively consistent thereafter. The values range from below D.L. to 61.4 ppm, averaging at 24.6 ppm with a S.D. of 16. Ba values are enriched relative to the underlying Getino Beds, with values ranging from 157.7 to 744.2 ppm, averaging at 393.8 ppm with a S.D. of 142.6. The Hg concentrations are enriched relative to the underlying Getino Beds. However, the concentrations are near to D.L. The values range from below D.L. to 8 ppm, averaging at 6.1 ppm with a S.D. of 3. The Th values show a significant increase relative to the underlying Getino Beds, and decrease slightly from the base. The values range from below D.L. to 23.2 ppm, averaging at 16.4 ppm with a S.D. of 6. U concentrations are enriched relative to the underlying Getino Beds, with values ranging from below D.L. to 15.6 ppm, averaging at 11.09 ppm with a S.D. of 3.

5.6 Villanueva Section

The analysed part of the Caldas de Luna section consists of the Bernesga Mb. of the Formigoso Fm. (see **'Sedimentary log of the Villanueva section**').

The Villanueva section consists of the Bernesga Mb. The Barrios Fm. is exposed at this locality, however, it was inaccessible. The contact with the overlying Getino Beds was not evident. There is a small outcrop of the Getino Beds, yet it is poorly exposed. The boundary to the overlying Bernesga Mb. shales is not exposed. The analysed section of the Villanueva section consists of 28 m of the Bernesga Mb. shales. The Bernesga Mb. consists of clay/silt grade organically enriched black shales. These black shales are rich in monograptid graptolites at their basal parts, as with the previously described Aralla section **Chapter 5.2**. The upper part of the Bernesga Mb. is not exposed and is covered by dense vegetation. Consequently, the contact with the overlying Villasimpliz Mb. is not visible.

Locality No.	GPS Coor.	Log total length	Total Samples
101	N42° 58.884' W5° 41.227'	84m	111

Sedimentary log of the Villanueva section, Cantabrian Mountains, Northern Spain

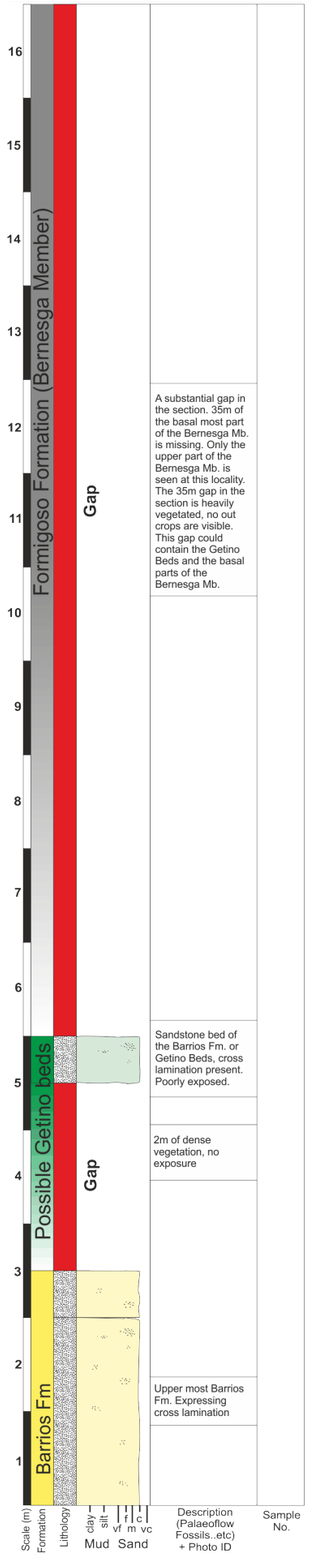

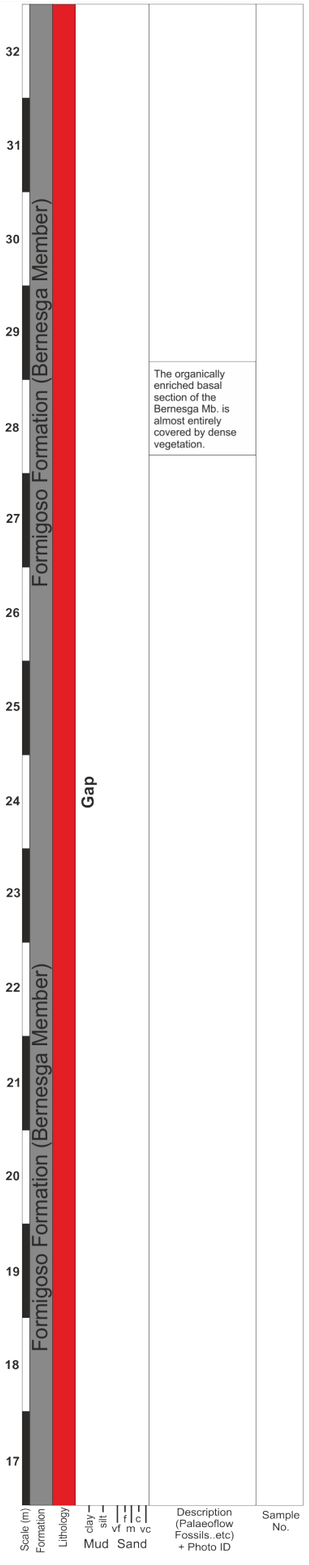

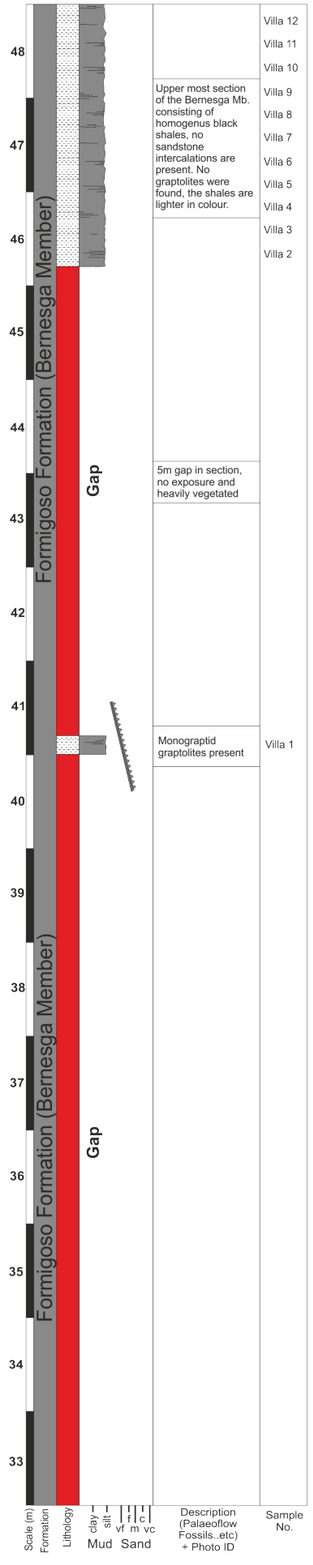

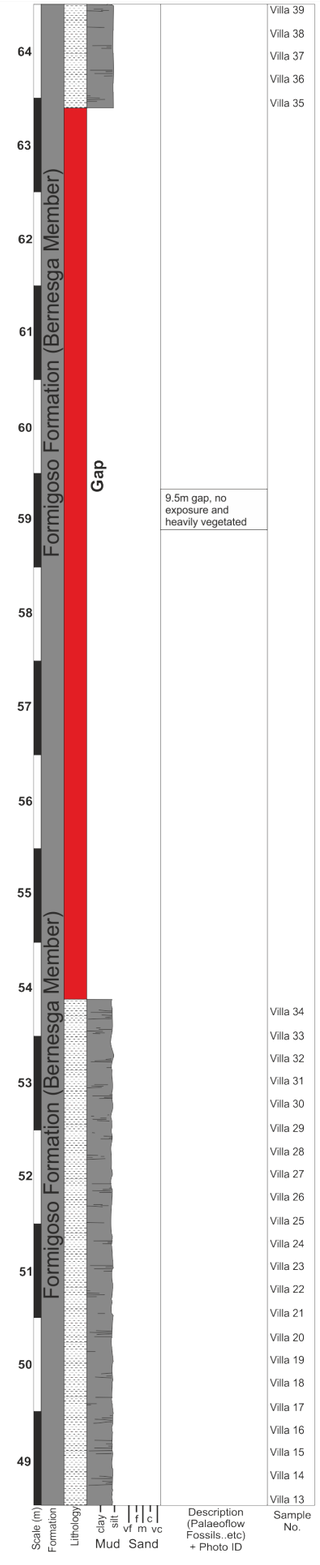

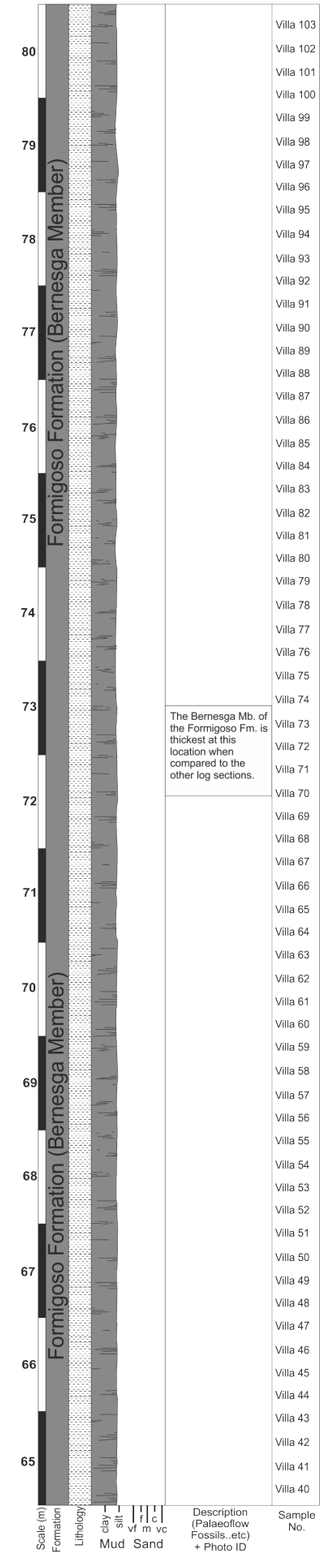

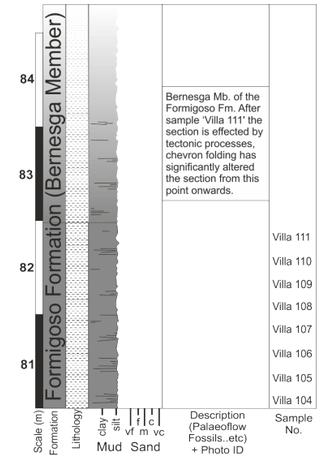

Sedimentary log key

Lithology Symbols

- Shales (Organically enriched mudstones)
- Siltstones
- Sandstone bodies
- Intercalated sands and silts - less than 1cm in width

Sedimentary symbols

uc	Unconformity
Py	Pyrite
He	Hematised
	Bioturbation
	Wave Ripples
	Nodular Weathering
	Planar Tabular Cross Bedding
	Monograptid Graptolites

Left scale; representing 1m of the log section.

Left symbol; representing the sand/silt intercalations where the intercalations are less than 1 cm in width.

Araldia 1
Caldas 1
La Majua 1
Sena 1
Villa 1

Text (left); Represents the sample numbers for the individual log sections.

5.6.1 Major element variations

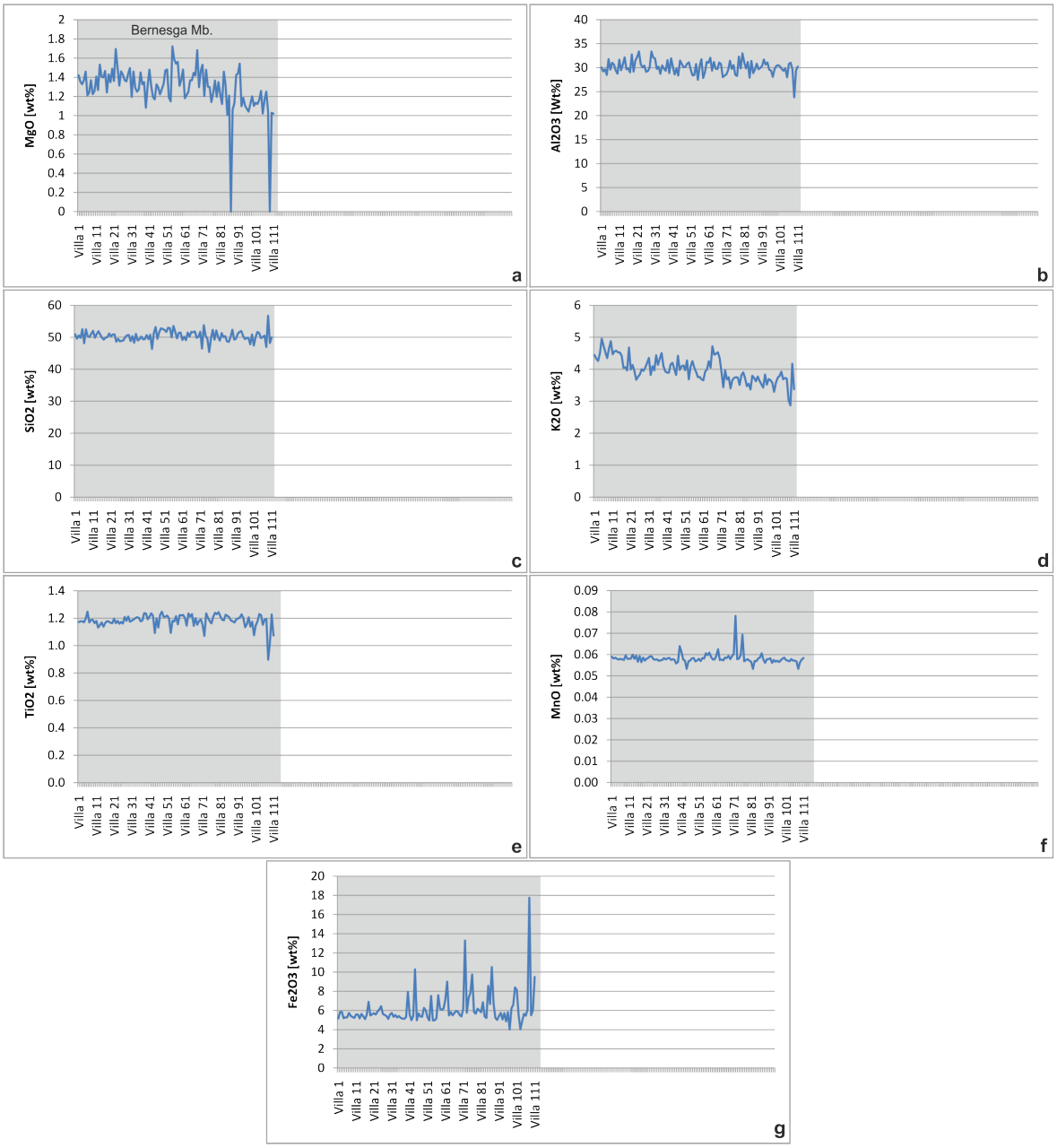

Figure 5.16 Major element variations for the Villanueva log section. Each sample number represents a 25 cm sampling interval. See **Results appendix B** (part 2) for absolute elemental values for the Formigoso Fm. As previously mentioned in **Chapter 5.2** 'Aralla section', the Na values were approximated and hence are not displayed here. The Na proxy data can however be found in the **Results appendix B** (part 2). Ca values are mostly below D.L., therefore are not included in this section, however the data can be found in the **Results appendix B** (part 2).

Major elements for the Bernesga Mb. (Villa 1 - 111)

The Bernesga Mb. at the Villanueva section is represented by 111 geochemical samples (see **Table 5.3**). The MgO concentrations decline towards the top of the Mb. The MgO values vary between below D.L. and 1.72 wt%, an average concentration of 1.3 wt% and a S.D. of 0.23. Al_2O_3 concentrations are consistent throughout the Mb., ranging from 23.8 to 33.3 wt%, averaging 30.1 wt% with a S.D. of 1.39. SiO_2 values are consistent varying from 45.3 to 56.7 wt%, averaging at

50.3 wt% with a S.D. of 1.62. The K_2O values show a gradual decline from the base, ranging from 2.8 to 4.9 wt%, averaging 3.9 wt% and a S.D. of 0.39. TiO_2 concentrations are consistent, showing a slight decline towards the top of the Mb. the values vary between 0.89 and 1.24 wt%, averaging at 1.1 wt% with a S.D. of 0.04. The MnO values show a slight decline from the base, with concentrations varying between 0.05 and 0.07 wt%, averaging 0.05 wt% with a S.D. of 0.002, a number of samples towards the middle of the Mb. are enriched, most likely related to localised mineralisation. Fe_2O_3 concentrations increase towards the top of the Mb. and become more erratic throughout. Again a number of enriched horizons occur within the Fe_2O_3 concentrations and may be related to localised mineralisation, the values range from 4.01 to 17.7 wt%, averaging at 6.1 wt% with a S.D. of 1.7.

5.6.2 Trace element variations

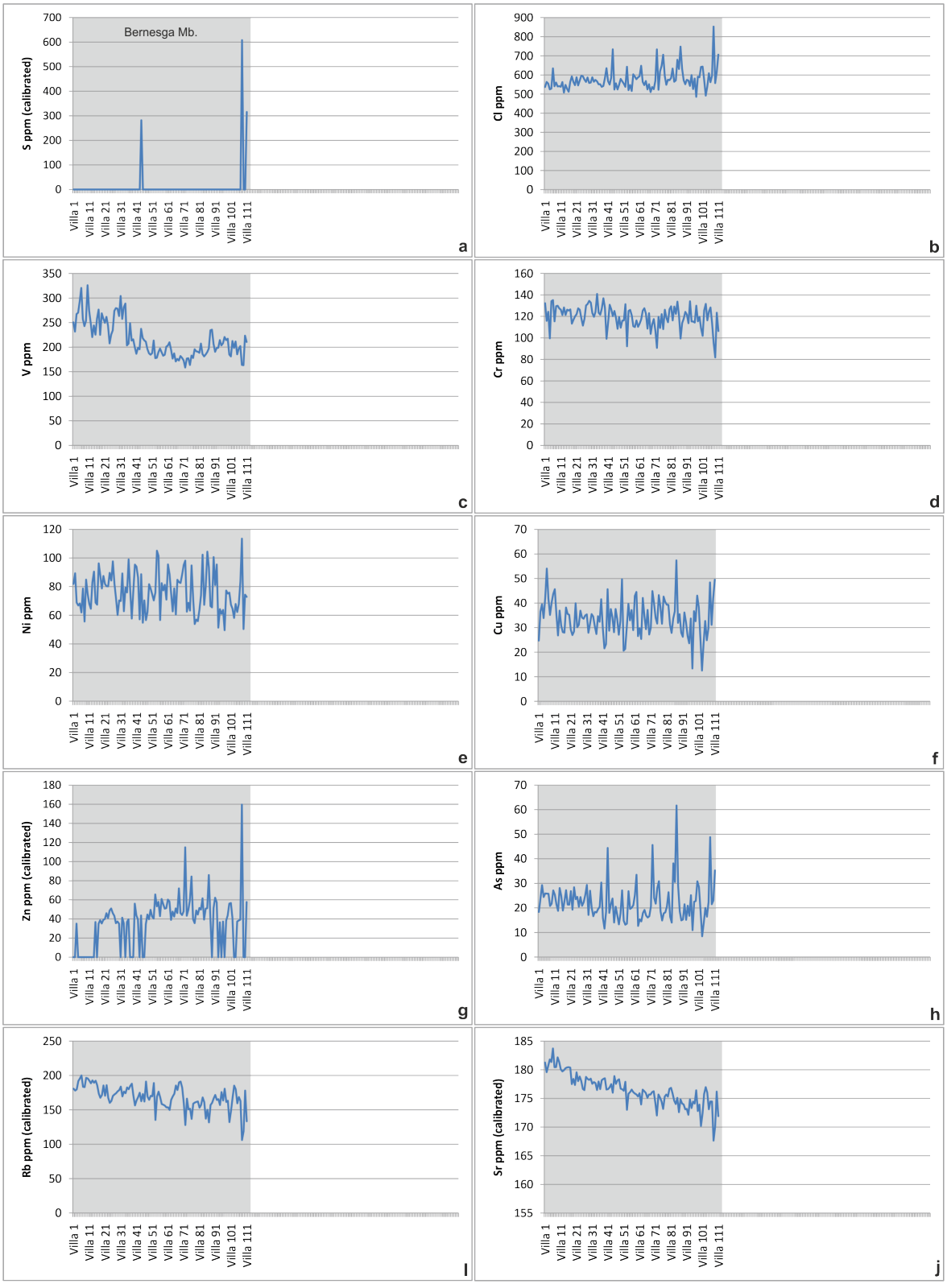

Figure 5.17 Trace element variations for the Villanueva log section. Each sample number represents a 25 cm sampling interval. See **Results appendix B** (part 2) for absolute elemental values of the Formigoso Fm. P and Bi concentrations are below D.L. and not further discussed. The following elements are near the D.L. and are not further discussed: Sc, Co, Se, Mo, Pd, Ag, Cd, Sn, Sb, Te, W, Au and Pb. However, the data for these elements is documented in **Results appendix B** (part 2).

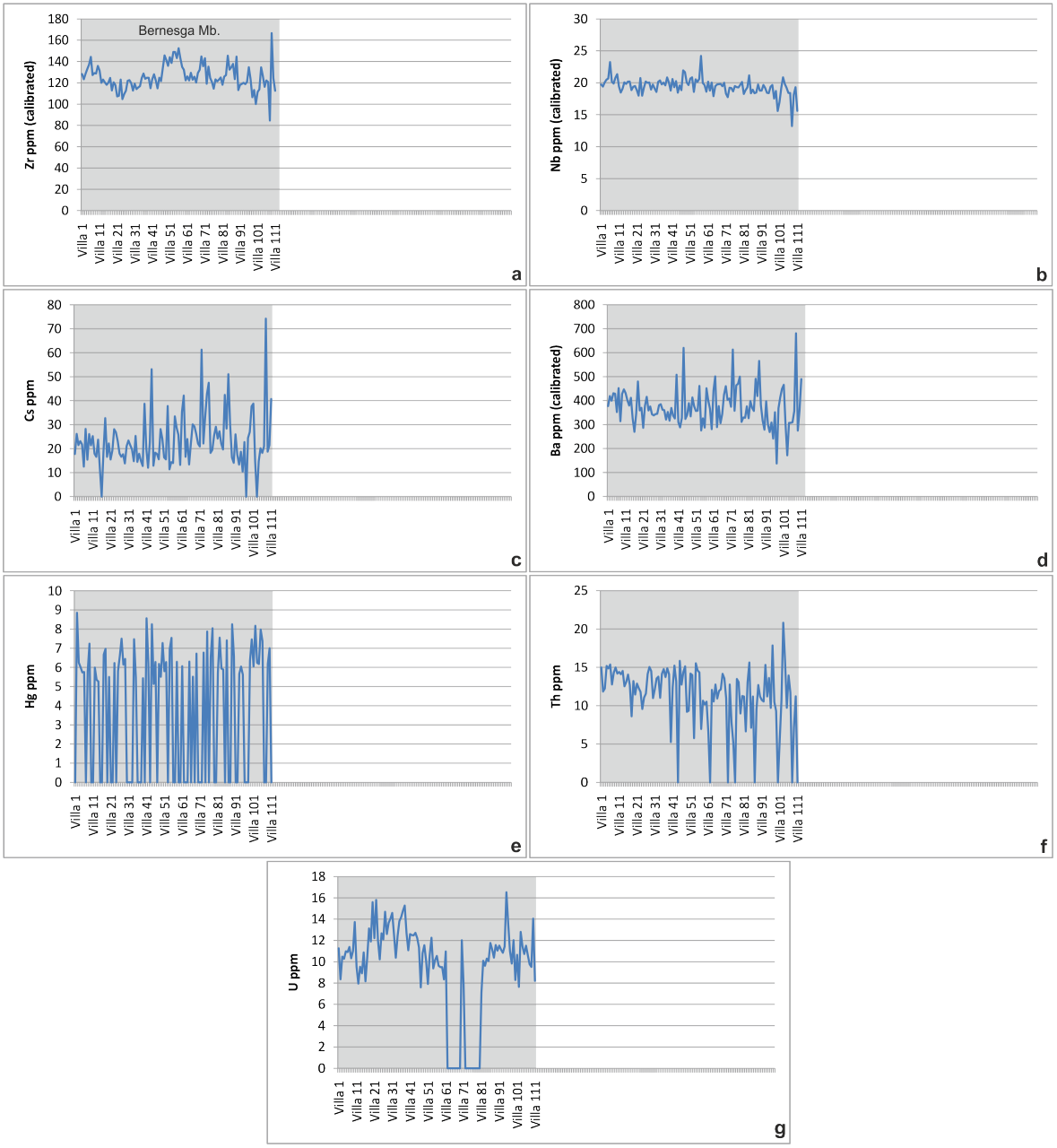

Figure 5.18 Trace element variations for the Villanueva log section. Each sample number represents a 25 cm sampling interval. A number of element concentrations were near to the detection limits (see **Figure 5.17** caption) and consequently are not discussed within this chapter.

Trace elements for the Bernesga Mb. (Villa 1 - 111)

The Bernesga Mb. at the Villasimpliz section is represented by 111 geochemical samples (see **Table 5.3**). The S concentrations are mostly below D.L. for this Mb. However, there are three samples with values of 281.8, 608.1 and 315.5 ppm. Cl values increase from the very base with values ranging from 485.6 to 853.1 ppm, averaging 577.6 ppm with a S.D. of 55.2. The V values show a gradual decline from the base before increasing slightly towards the top of the analysed section. The V values range from 158.4 to 325.9 ppm, averaging at 215.5 ppm with a S.D. of 36.7. The Cr values are relatively consistent, yet show a slight decline towards the top of the Mb. The

values range from 81.8 to 140.8 ppm, averaging at 119.5 ppm with a S.D. of 10.3. The Ni values are erratic ranging from 49.5 to 113.5 ppm, averaging at 76.1 ppm with a S.D. of 13.9. The Cu values are consistent showing a slight depletion towards the top of the Mb. The values range from 12.5 to 57.3 ppm, averaging at 33.9 ppm with a S.D. of 7.5. Zn values are near D.L. at the base, the values then increase throughout, ranging from below D.L. to 159.6 ppm, averaging at 49.2 ppm with a S.D. of 26.7. The As values show an overall decline from the base of the Mb. with a few enriched horizons towards the top, most likely related to localised mineralisation. The As concentrations range from 8.46 to 61.6 ppm and average at 22.3 ppm, the S.D. is 7.7. The Rb values are showing a decline throughout, the values range from 106.1 to 200 ppm, averaging at 168.5 ppm with a S.D. of 17.1. Sr values show a gradual decline throughout the Mb., the values range from 167.6 to 183.7 ppm, averaging at 176.4 ppm with a S.D. of 2.7. The Zr values are relatively consistent, showing a slight rhythmic pattern throughout. The Zr values range from 84.5 to 166.6 ppm, averaging at 125.4 ppm with a S.D. of 11.8. Nb values are consistent showing a slight decline towards the top of the Mb. The values range from 13.2 to 24.1 ppm, averaging at 19.4 ppm with a S.D. of 1.3. The Cs values are near D.L. and become erratic towards the top of the Mb., ranging from below D.L. to 74.22 ppm, averaging at 23.8 ppm with a S.D. of 11.2. Ba values are erratic, with values ranging from 137.5 to 680.7 ppm, averaging at 374.2 ppm with a S.D. of 81.1. The Hg concentrations remain consistent, yet are close to the D.L. The values range from below D.L. to 8.8 ppm, averaging at 6.5 ppm with a S.D. of 3.3. The Th values show a decline towards the top of the Mb., with values ranging from below D.L. to 20.8 ppm, averaging at 12.2 ppm with a S.D. of 4.1. U concentrations show a rhythmic pattern with a depletion towards the middle of the Mb. The values range from below D.L. to 16.5 ppm, averaging at 11.2 ppm with a S.D. of 4.4.

Chapter 6
Interpretation of Geochemical results

Contents

The interpretations of the geochemical data documented in the previous **Chapter 5** 'Geochemical results' involved a number of proxies and elemental ratios that will be briefly described below. Firstly, the geochemical data for all of the log locations were averaged and plotted in enrichment factor diagrams, in order to determine which elements are depleted or enriched relative to a selection of international standards. The geochemical data are then classified according to the schemes of Herron (1988), Roser and Korsch (1988), Floyd *et al*. (1989), and Pearce *et al*. (2010). The redox proxies of Fertl (1979), Hatch and Leventhal (1992), Jones and Manning (1994), Wignall (1994) and Kimura and Watanabe (2001) are applied systematically and described accordingly for each of the log localities. The palaeosalinity proxy of Cambell and Williams (1965) is used in order to reconstruct salinity levels during the time of deposition for the individual log locations. The proxies of Akul'shina (1976) and Kiipli *et al.* (2012) are used to reconstruct the palaeohumidity conditions. The geochemical data for all of the log locations are systematically plotted in the clay discriminations diagrams of Cullers and Podkovyrov (2000), Eickmann *et al.* (2009) and Schlumberger (2009). The index of compositional variation (ICV) of Cox *et al*. (1995) is used in order to reconstruct the extent of weathering and ultimately the level of sediment recycling. The weathering proxies of Nesbitt and Young (1982), Harnois (1988) and Fedo *et al*. (1995) are calculated and used to reconstruct the extent of chemical weathering. The salinity, redox and grain-size proxies mentioned above are systematically presented in 3D plots in order to determine and evaluate the relationships between the changing environmental conditions. The hydrothermal indicator of Boström (1973) is used to establish whether the sediments had been subject to any significant hydrothermal alteration. The quantification of any potential hydrothermal overprint is crucial to the development of the then following palaeobioproductivity reconstructions. The palaeobioproductivity proxies of Pfeifer *et al*. 2001, Bonn *et al*. 1998 and Prakash Babu *et al*. (2002) are applied to the Ba concentrations. API units are calculated for the K_2O, Th and U concentrations following the steps detailed in **Chapter 3.1.11**, in order to produce synthetic gamma-ray logs for the localities investigated. Finally, a spectral analysis is applied to the cyclic redox sensitive elements U and V for all of the investigated locations to determine the nature of the cyclic signals observed.

6.1 Enrichment factor plots

In order to determine and quantify relative elemental enrichments and depletions within the black shales of the Bernesga Mb, but also to identify and highlight differences between the investigated sites, all available data for the Bernesga Mb. have been averaged for the individual localities. The averaged data were also combined to create a representative composite for the entire black shale containing lower Formigoso Fm. Only elemental values clearly above the D.L. were introduced to the data matrix. The averaged Bernesga Mb. data are documented in Appendix B (Part 1). The values were compared to the following international standards: [1] **Average Shale** (Turekian and Wedepohl, 1961), [2] **Average Shale** (compiled from: Wedepohl, 1971, 1991; Heinrich *et al.,* 1980), [3] **Average black shale** (Vine and Tourtelot, 1970), [4] **SCO-1** (compiled from: Abbey and Geological Survey of Canada, 1983; Gladney and Roelandts, 1988; Govindaraju, 1989, 1994), [5] **Post-Archean Australian Shale** (PAAS, Taylor and McLennan, 1985), [6] **Post-Archean Upper Continental Crust** (PA-UCC, Taylor and McLennan, 1985, 1995), [7] **Upper Crust** (Hans Wedepohl, 1995 largely derived from Shaw *et al.,* 1967, 1976), [8] **North American Shale Composite** (NASC, Gromet *et al.,* 1984).

6.1.1 Enrichment factor plots (individual localities)

Figure 6.1 Enrichment factor diagrams for all localities. The shale values of the Bernesga Mb. were averaged for each locality, values below the detection limit were excluded from the averaging process. Aralla (**|**, black upright dash): samples Aralla 4 - 184, Caldas de Luna (**Δ**, red triangle): samples Caldas 1 - 98, La Majua (**+**, green upright cross): samples La Majua 32 - 70, Sena de Luna (**x**, dark blue diagonal cross): samples Sena 11 – 79 and Villanueva (◊, light bluediamond): samples Villa 1 - 111. Normalised to the international standards Average black shale **(a)**, Average shale **(b + c)**, SCO-1 **(d)**, NASC (e) and PAAS **(f)**. The high enrichments of Ag, Te and Hg is interpreted to be related to localised, post-depositional fluid flow activity.

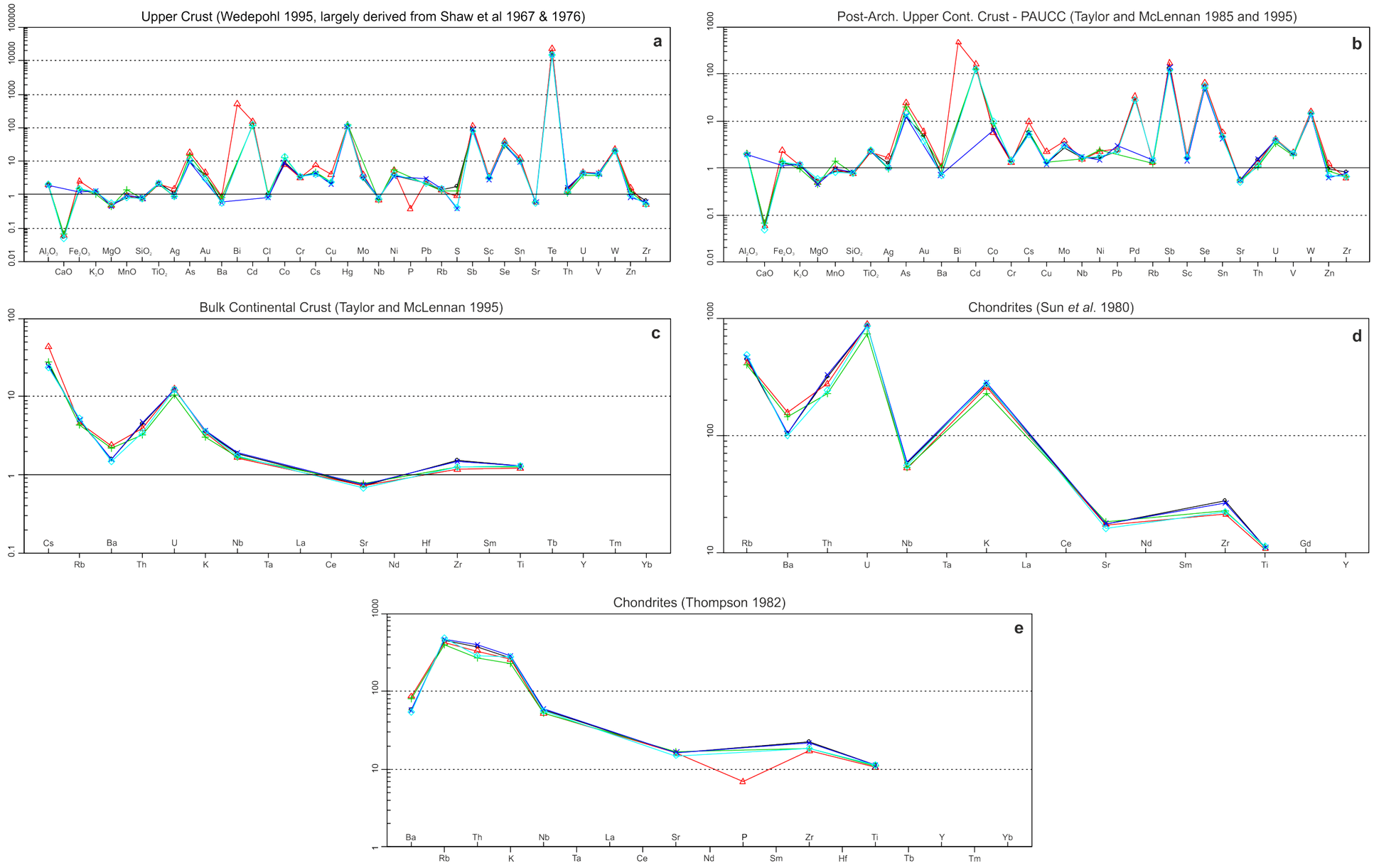

Figure 6.2 Enrichment factor diagrams for all localities, just the shale values of the Bernesga Mb. were averaged for each locality, values below the detection limit were excluded from the averaging process. (**|**, black upright dash): samples Aralla 4 - 184, Caldas de Luna (**Δ**, red triangle): samples Caldas 1 - 98, La Majua (**+**, green upright cross): samples La Majua 32 - 70, Sena de Luna (**x**, dark blue diagonal cross): samples Sena 11 – 79 and Villanueva (◊, light blue diamond): samples Villa 1 - 111. Normalised to the international standards, Upper crust **(a)**, PA-UCC **(b)**, Bulk continental crust **(c)** and Chondrites **(d + e)**.

6.1.2 Enrichment factor plots (composite)

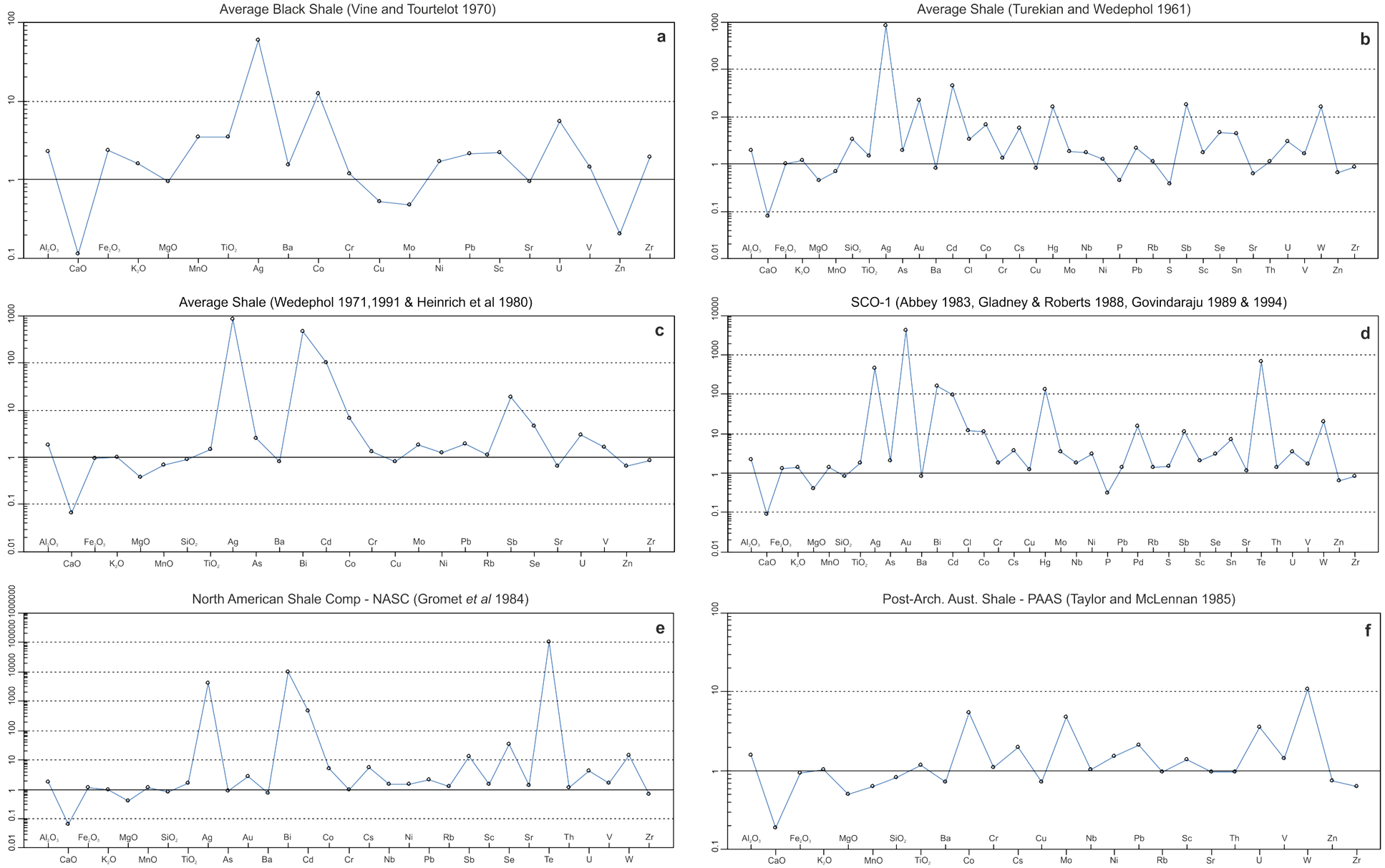

Figure 6.3 Enrichment factor diagrams for the Bernesga Mb. composite. The composite was calculated using the data from a total of 496 samples. Values below D.L. were excluded. Normalised to the international standards, Average black shale **(a)**, Average shale **(b + c)**, SCO-1 **(d)**, NASC **(e)** and PAAS **(f)**. The high enrichments of Ag, Te and Hg is interpreted to be related to localised, post-depositional fluid flow activity.

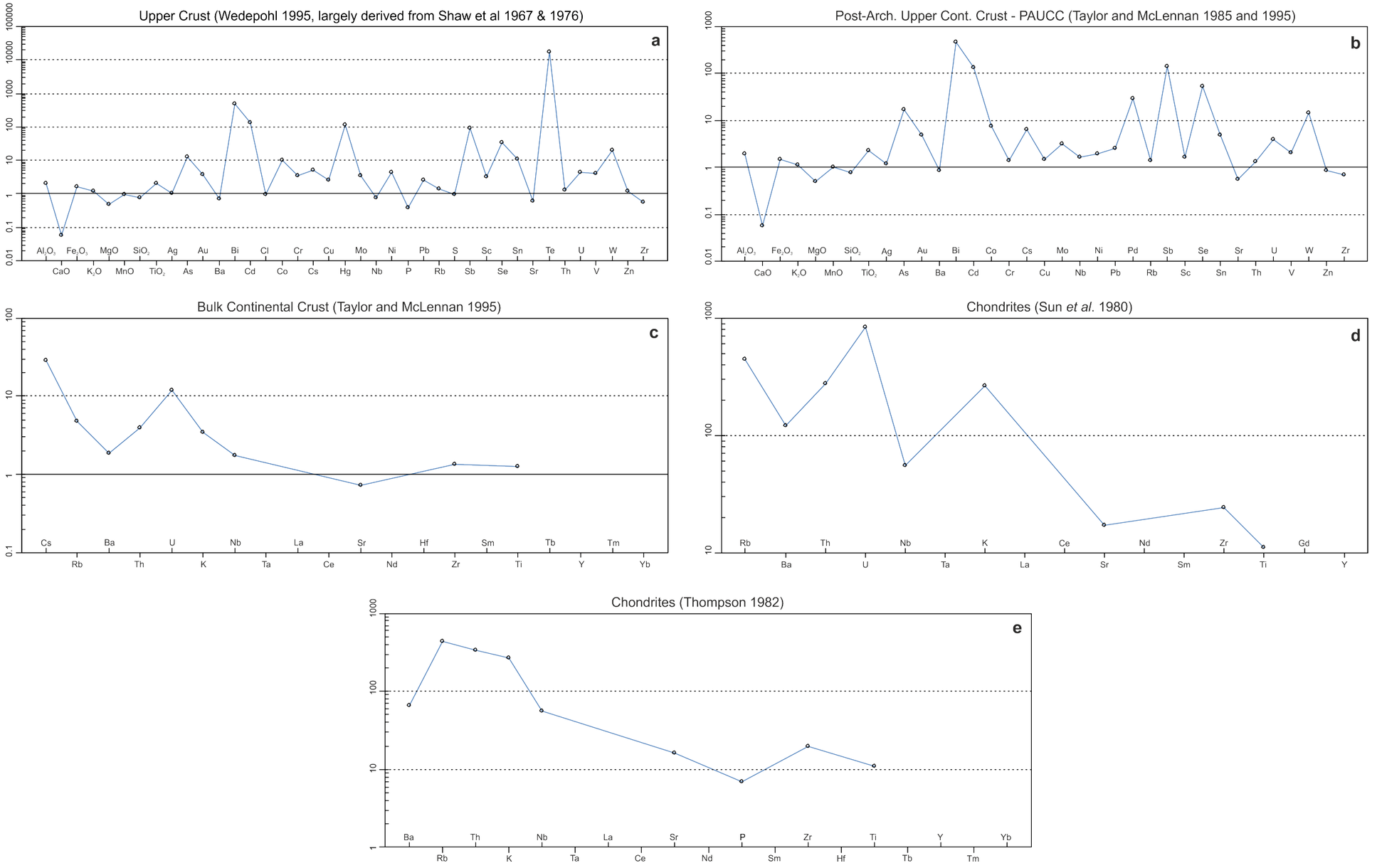

Figure 6.4 Enrichment factor diagrams for the average Formigoso Fm. Shale (Bernesga Mb.) all locality data averaged (496 samples) excluding values below detection limits. Normalised to the international standards, Upper crust **(a)**, PA-UCC **(b)**, Bulk continental crust **(c)** and Chondrites **(d + e)**.

When normalised to the international standard '**Average black shale**' of Vine and Tourtelot (1970), the Bernesga Mb. shales show similar elemental concentrations with regards to MgO, Cr, and Sr. A slight enrichment (~1 x) in the concentrations of Al_2O_3, Fe_2O_3, K_2O, Ba, Ni, Pb, Sc, V and Zr is observed. MnO and TiO_2 concentrations are more strongly enriched (up to ~2.5 x). The elements that are significantly enriched are Ag, Co and U (~60, 12 and 6 x respectively). On the other hand, Cu and Mo concentrations show a slight depletion (~0.5 x) and CaO and Zn are significantly depleted (~0.95 and 0.9 x respectively). The normalisation to the '**Average shale**' of Turekian and Wedepohl (1961) reveals that the elemental concentrations of Fe_2O_3, K_2O, Ba, Cr, Cu, Ni, Rb, Th and Zr are comparable. The elements Al_2O_3, SiO_2, As, Cl, Cu, Hg, Pb, Se, Sn, U and V are moderately enriched (~2 x), whereas the elemental concentrations of Ag, Au, Cd, Hg, Sb and W are significantly enriched (~ 900, 11, 50, 11, 11 and 11 x respectively). MgO, MnO, Sr and Zn are very slightly (~0.5 x) and CaO and S concentrations significantly depleted (~0.09 and 0.5 respectively). The Bernesga Mb. when normalised to the '**Average shale**' of Wedepohl (1971, 1991) and Heinrich *et al*. (1980), shows comparable Fe_2O_3, K_2O, SiO_2, Ba, Cr, Cu, Ni, Rb and Zr concentrations. The elemental enrichments of Al_2O_3, TiO_2, As, Mo, Pb and V are insignificant (~2 x). Whereas, the concentrations of Ag, Bi, Cd, Co, Sb, Se and U show significant enrichments (~900, 600, 100, 8, 11, 5 and 3 x respectively). CaO, MgO, Sr and Zn are relatively depleted (0.08, 0.5, 0.7 and 0.7 respectively). The normalisation of the Bernesga Mb. to the '**SCO-1**' standard of Abbey (1983), Gladney and Roberts (1988) and Govindaraju (1989, 1994) determines that Fe_2O_3, K_2O, MnO, Ba, Cu, Pb, Rb, Sr, Th and Zr concentrations are comparable. The concentrations of Al_2O_3, TiO_2, As, Cr, Cs, Mo, Nb, Ni, S, Sc, Se, U and V show mild enrichments (~2 x). Ag, Au, Bi, Cd, Cl, Co, Hg, Pd, Sb, Sn, Te, U and W show significant enrichments (~600, 5000, 200, 100, 10, 10, 150, 11, 10, 9, 700, 5 and 11 respectively). The elements CaO, MgO, P and Zn are depleted (~0.1, 0.4, 0.4 and 0.8 respectively). The Bernesga Mb. elemental concentrations of Al_2O_3, Fe_2O_3, K_2O, MnO, SiO_2, As, Ba, Cr, Sr, Th and Zr are comparable to that of the '**NASC**' international standard of Gromet *et al*. (1984). The elements that show slight enrichments are TiO_2, Au, Co, Cs, Nb, Ni, Pb, Rb, Sc, U, V and W (~1-2 x). The concentrations of Ag, Bi, Cd, Sb, Se and Te are significantly enriched (~5000, 10000, 6000, 10, 13 and 100000 x respectively), whereas, CaO and MgO are depleted (~0.08 and 0.4 x respectively). When normalised to the '**PAAS**' international standard of Taylor and McLennon (1985) the elemental concentrations of K_2O, TiO_2, Cr, Nb, Rb, Sr and Th are comparable. Al_2O_3, Cs, Ni, Sc and V concentrations are mildly enriched (~1.5 x). The elements strongly enriched are Co, Mo, Pb, U and W (~5, 4, 2 and 3 x respectively). CaO, MgO, MnO, SiO_2, Ba, Cu, Zn and Zr are depleted (~0.2, 0.4, 0.6, 0.8, 0.7, 0.7, 0.8 and 0.7 respectively).

The Bernesga Mb. has elemental concentrations of K_2O, MnO, SiO_2, Ag, Ba, Cl, Nb, Th and Zn comparable to that of the international standard '**Upper Crust**' of Wedepohl (1995). The elements that are mildly enriched are Al_2O_3, Fe_2O_3, TiO_2, Cr, Cs, Cu, Mo, Ni, Pb, Rb, S, Sc, U and V (~3 x). As, Bi, Cd, Hg, Sb, Se, Sn, Te and W concentrations are significantly enriched (~11, 600, 150, 100, 100, 5, 10, 20000 and 11 x respectively). Whereas the CaO, MgO, Ba, Cl, Nb, P, Sr and Zr concentrations are relatively depleted (~0.07, 0.7, 0.8, 0.9, 0.8, 0.4, 0.7 and 0.6 x respectively). When normalised to the international standard '**PA-UCC**' of Taylor and McLennon (1985, 1995) the elements that are comparable are K_2O, MnO, SiO_2 and Ba. Elemental concentrations that are slightly enriched are Al_2O_3, Fe_2O_3, TiO_2, Ag, Cr, Cu, Nb, Ni, Pb, Rb, Sc, Th and V (~2 x). As, Au, Bi, Cd, Co, Cs, Pd, Sb, Se, U and W show significant enrichments (~11, 7, 500, 150, 8, 8, 30, 150, 60, 5 and 11 x respectively). The elements Sr, Zr and TiO_2, are comparable when normalised to the '**Bulk continental crust**' of Taylor and McLennon (1995). Ba, K_2O and Nb concentrations are mildly enriched (~2 x). The concentrations of Cs, Rb, Th and U are significantly enriched (~30, 4, 4 and 10 x respectively). When normalised to the international standard '**Chondrites**' of Sun *et al*. (1980) the elemental concentrations of Rb, Ba, Th, U and K_2O are significantly enriched (~450, 150, 300, 900 and 250 respectively), whereas the elements Nb, Sr, Zr and TiO_2 are mildly enriched (~60, 20, 20, 10.5 x respectively). Finally the normalisation to the '**Chrondrites**' of Thompson (1982) determines that the elemental concentrations of Ba, Rb, Th, K_2O and Nb are significantly enriched (~80, 450, 400, 300 and 50 x respectively). The elements Sr, P, Zr and TiO_2 are enriched to a lower extent (~20, 8, 20 and 10 x respectively).

The enrichment of Al_2O_3 within the Formigoso Fm. relative to the average shale composites is most likely the result of maturity effects. This interpretation is further corroborated by the consistently high weathering indices, which will be reviewed later (**Chapter 6.4.5**). The Fe_2O_3 enrichments could be related to localised mineralisation, as are the Ag and Pb concentrations. The TiO_2 and Zr enrichments could indicate an increased detrital fraction, which is slightly elevated in contrast to the average shale composites. The U enrichment could be related to the organically rich basal shales of the Bernesga Mb. These shales were most likely subject to high redox conditions (euxinic) and consequent accumulation of organic matter. The U enrichment is related directly to the quantity of organic matter as it is adsorbed to its surface under reducing conditions (reviewed in **Chapter 6.4**).

Other elemental enrichments in relation to the upper continental crust composites are Bi, Cd, Hg, Sb, Te and W. These are most likely related to the geochemical signature of the detrital source and/or the sea-water chemistry during the time of deposition.

6.2 Geochemical classification

All major and trace elemental concentrations obtained from the analysed sections were used to classify the sediments geochemically. The **[1]** Ni *vs.* TiO_2 plot of Floyd *et al.* (1989), **[2]** provenance discrimination diagram of Roser and Korsch (1988), **[3]** SiO_2-Al_2O_3-CaO ternary plot of Ross and Bustin (2009), **[4]** Zr-$15Al_2O_3$-$300TiO_2$ diagram of Mongelli *et al*. 2006 and finally, **[5]** the TOC-Fe(wt%)-TS10(wt%) resulted all in very similar signatures and patterns. For this reason, only the data of the Aralla locality will be discussed and showcased here. The classification and discrimination of the remaining localities are documented in **Results appendix B** (part 1).

The entirety of the dataset (all major and trace elements for all locations) is cross-plotted utilising the log(Fe_2O_3/K_2O) *vs.* log(SiO_2/Al_2O_3) of Herron (1988), see **Figure 6.5**. This discrimination diagram was originally developed to separate aluminium-rich fine-grained sediments from coarser-grained immature sediments using the diagnostic differences within the ratios of the oxides for Fe and K and Si and Al respectively. These plots show that the bulk of the Bernesga Mb. shales fall into the 'shale' window, a couple of samples from the various localities can be seen to push up towards the 'Fe-shale' category, fitting with the Fe_2O_3 enrichments seen in the elemental distribution plots documented in **Chapter 5** 'Geochemical results'. The majority of the sand- and siltstones of Villasimpliz Mb. from the Aralla section (**Figure 6.5**, **a**) fall into the 'Wacke' window, with a number of samples pushing towards the 'Fe-sand'.

The bivariate plot TiO_2 *vs.* Ni of Floyd *et al.* (1989), see **Figure 6.6**. This diagram was engineered for use with immature greywackes. It allows for the discrimination between sediments comprised of either a bulk acidic or basic composition when cross-plotting the concentrations of TiO_2 and Ni. This diagram has worked effectively for discriminating between the mature shales of the Bernesga Mb. and the sand- and siltstones of the Villasimpliz Mb. A clear grain-size effect is observed. In terms of the provenance discrimination fields, the data do not discriminate within the predictable areas. For example, the shales of the Bernesga Mb. are not plotting near or at the trend line for mudstones, as they were expected to do. The sand- and siltstones of the Villasimpliz Mb. do however fall within the proximity of the 'acidic' composition field, which is not too farfetched, as the sediments have certainly been sourced from the predominantly acidic basement of the hinterland.

The provenance discrimination diagram of Roser and Korsch (1988), see **Figure 6.7.** This diagram is used to distinguish between different sedimentary provenance sources, such as the 'quartzose sedimentary', 'mafic igneous', intermediate igneous' and finally 'felsic igneous' provenances. Two

different discriminant functions are used: [1] **Discriminant function 1 (F1) =** $(-1.773 \times TiO_2\%) + (0.607 \times Al_2O_3\%) + (0.76 \times Fe_2O_3^T\%) + (-1.5 \times MgO\%) + (0.616 \times CaO\%) + (0.509 \times Na_2O\%) + (-1.22 \times K_2O\%) + (-9.09)$. [2] **Discriminant function 2 (F2)** = $(0.445 \times TiO_2\%) + (0.07 \times Al_2O_3\%) + (-0.25 \times Fe_2O_3^T\%) + (-1.142 \times MgO\%) + (0.432 \times Na_2O\%) + (1.426 \times K_2O\%) + (-6.861)$. During the Silurian the Formigoso Fm. is interpreted to have been deposited in a passive margin setting (see **Chapter 2** 'Geological Setting'). The hinterland and hence the source for the sediments is regarded to have been primarily a granitic basement. However, this is not shown in and can't be deduced from the discrimination diagrams (see also **Figure 6.8**). Although, the discriminant functions applied do show a clear systematic variation between the shales of the Bernesga Mb. and the sand- and siltstones of the Villasimpliz Mb. The maturity and grain-size effects are again clearly seen. These hinterland- and tectonic discrimination diagrams have previously been widely used in order to elucidate the lithological composition of provenance areas and the very nature of their larger scale geodynamic setting (see e.g. Johnsson and Basu, 1993; Arribas *et al*., 2007 with previous references therein). However, a detailed critical evaluation of these diagrams and related discrimination functions by Armstrong-Altrin and Verma (2005) highlighted, that they are not always reliable and consequently have to be applied with caution.

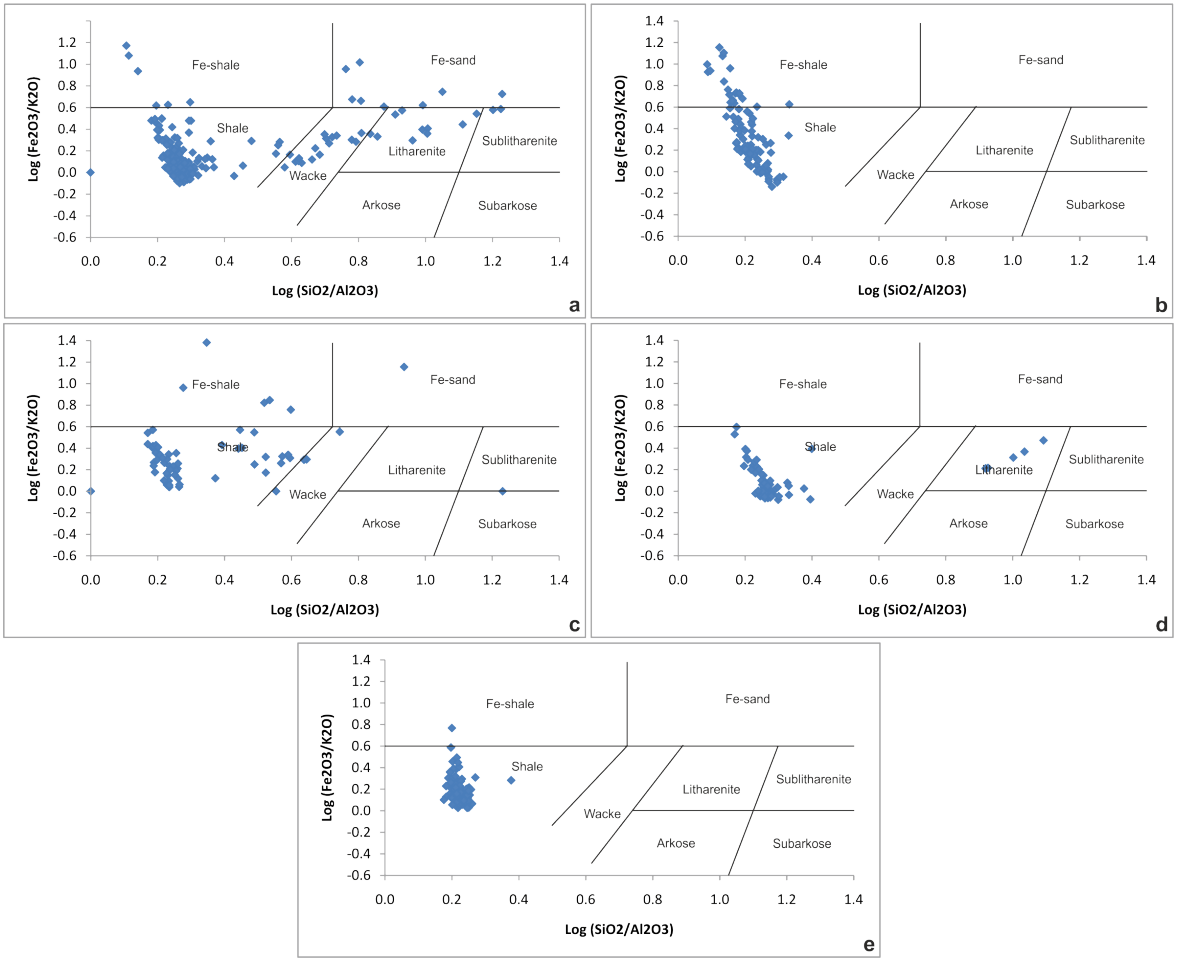

Figure 6.5 Chemical classification and discrimination of the sediments analysed using the $\log(SiO_2/Al_2O_3)$ vs. $\log(Fe_2O_3^t/K_2O)$-system of Herron (1988). **a)** Aralla, the shales of the Bernesga Mb. are grouped within the 'Shale' category a select few samples are plotting within the 'Fe-shale, the sand- and siltstones of the Villasimpliz Mb. trend towards the 'Fe-sand' **b)** Caldas de Luna, the Bernesga Mb. shales are confined to the 'Shale' category, displaying a trend into the 'Fe-shale' category **c)** La Majua, the sand- and siltstones of the Getino beds cluster towards the 'Wacke', whereas the Bernesga Mb. is confined to the 'Shale' category **d)** Sena de Luna, a select few sands of the Getino Beds plot in the 'Litharenite' realm, the Bernesga Mb. is within the 'Shale' category and finally, **e)** Villanueva section plotting almost entirely within the 'Shale' category with one sample in the 'Fe-shale' zone.

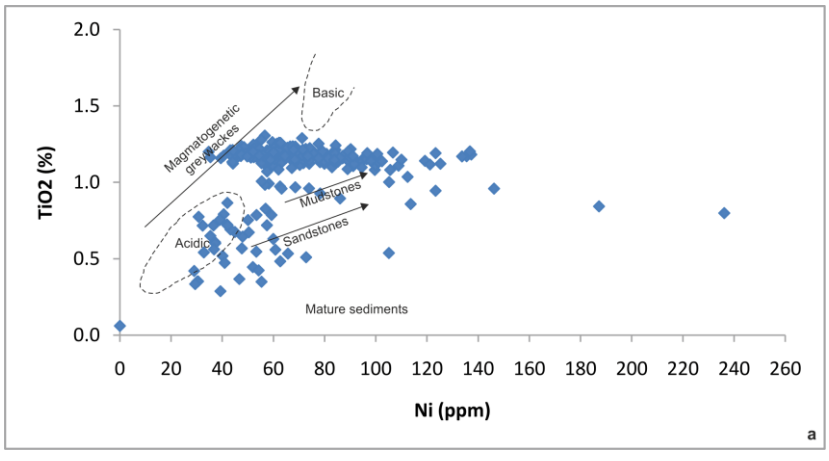

Figure 6.6 TiO_2 *vs*. Ni after Floyd *et al.*, (1989). Illustrated are data of the Aralla section (241 samples). The shales of the Bernesga Mb. display relatively uniform TiO_2 concentrations, with concentrations of Ni varying from ~35 ppm to 140 ppm. The sand- and siltstones of the Villasimpliz Mb. cluster towards the 'Acidic' zone.

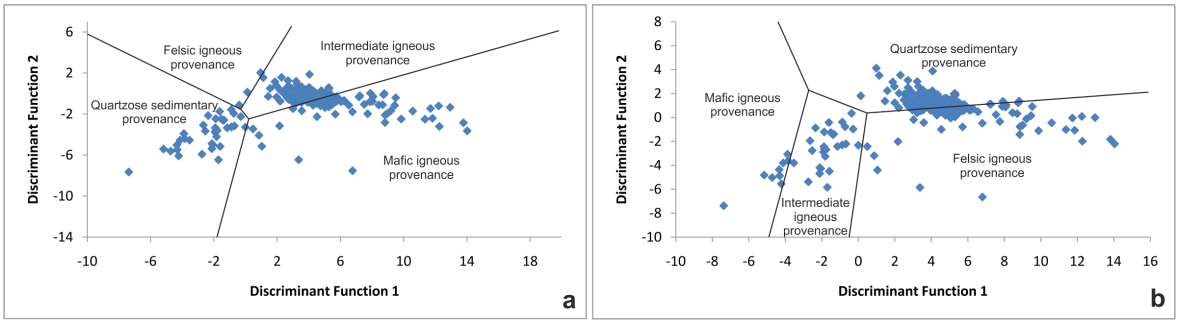

Figure 6.7 Displaying all geochemical data from the Aralla section (241 samples). **(a)** and **(b)**: Provenance discrimination diagrams for shales, after Roser and Korsch (1988). **a) Discriminant function 1** = (−1.773×TiO_2%) + (0.607×Al_2O_3%) + (0.76×$Fe_2O_3^T$%) + (−1.5×MgO%) + (0.616×CaO%) + (0.509×Na_2O%) + (−1.22×K_2O%) + (−9.09). **Discriminant function 2** = (0.445×TiO_2%)+(0.07×Al_2O_3%) +(−0.25×$Fe_2O_3^T$%) + (−1.142×MgO%) + (0.432×Na_2O%) +(1.426×K_2O%) + (−6.861). **b) Discriminant function 1** = –1.773 TiO_2 + 0.607 Al_2O_3 + 0.76 Fe_2O_3(total) –1.5 MgO + 0.616 CaO + 0.509 Na_2O – 1.224 K_2O – 9.09, **Discriminant function 2** = 0.445 TiO_2 + 0.07 Al_2O_3 – 0.25 Fe_2O_3(total) –1.142 MgO + 0.438 CaO + 1.475 Na_2O + 1.426 K_2O – 6.861. **(a)** displays a clear compositional differentiation between the shales of the Bernesga Mb. and the sand- and siltstones of the Villasimpliz Mb. The sands are seen to trend towards the 'Quartzose sedimentary provenance' field, whereas the shales of the Bernesga Mb. span from the 'Intermediate igneous provenance' to the 'Mafic igneous provenance'. **(b)** Discriminating to a higher extent the shales of the Bernesga Mb. from the sand- and siltstones of the Villasimpliz Mb. The Villasimpliz Mb. clusters within the 'Mafic igneous provenance' and 'Intermediate igneous provenance', whereas, the shales of the Bernesga Mb. trend from the 'Quartzose sedimentary provenance' to the 'felsic igneous provenance'.

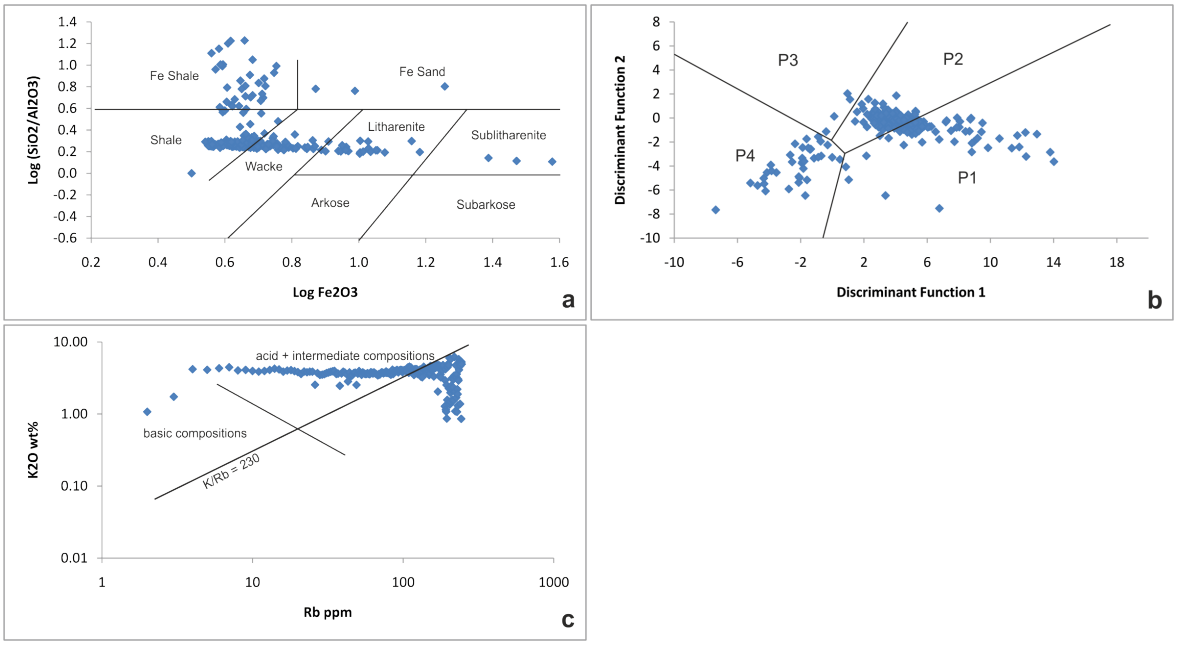

Figure 6.8 Aralla section (241 samples). **a**) Chemical classification, after Herron (1988). **b**) Plot of discriminant functions F1 and F2. Provenance fields are after Roser and Korsch (1988). **P1** = mafic and lesser intermediate igneous provenance, **P2** = intermediate igneous provenance, **P3** = felsic igneous provenance and finally **P4** = recycled-mature polycyclic quartzose detritus. **c**) Distribution of K and Rb relative to a K/Rb ratio of 230 (=main trend of Shaw, 1968). **(a)** a clear discrimination is seen between the Bernesga Mb. and the Villasimpliz Mb. The shales and silts of the Bernesga Mb. trend from the 'Shale' category to the 'Litharenite', whereas the sand- and siltstones of the Villasimpliz Mb. are clustering towards the 'Fe shale'. **(b)** the provenance discrimination diagram of Roser and Korsch (1988) clearly discriminates between the Bernesga Mb. and the Villasimpliz Mb. The shales span from 'P3' to 'P1', whereas the sand- and siltstones plot between 'P4' and 'P1'.

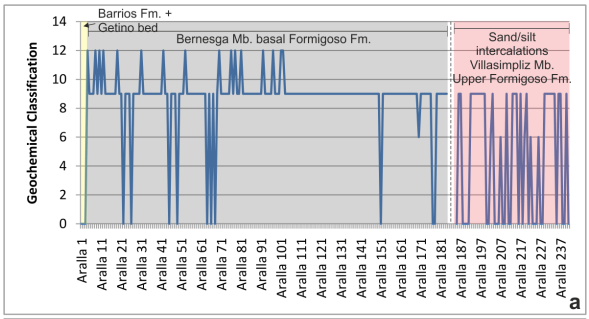

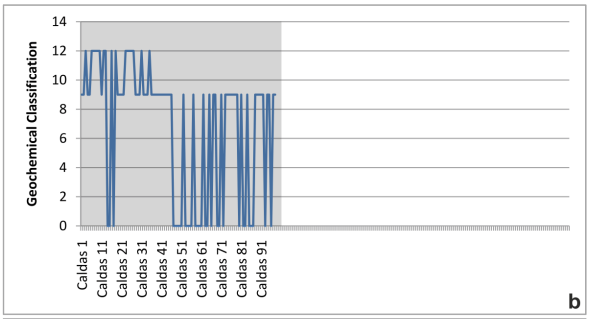

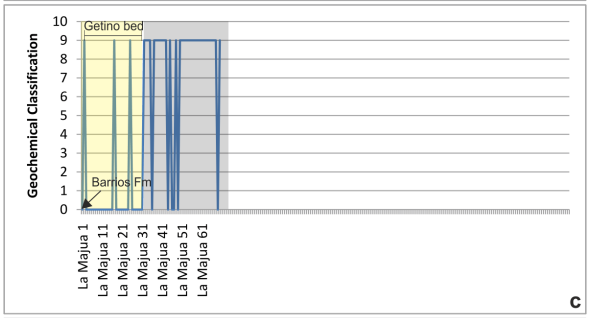

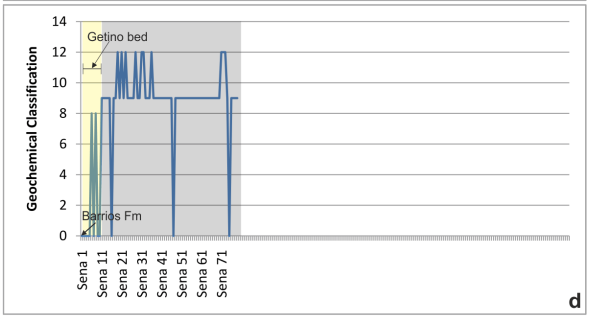

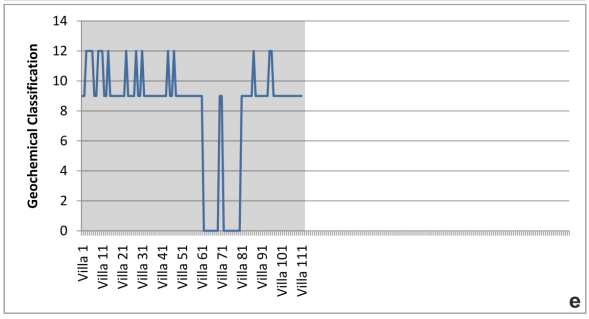

Criteria used for geochemical classification

Parameter	Criteria	Score	Average values for each locality
U	> 6ppm < 6ppm	4 1	**a)** 9.1 **b)** 7.9 **c)** 4.8 **d)** 9.4 **e)** 9.5
Th/U	> 3.0 < 3.0	1 4	**a)** 1.2 **b)** 0.9 **c)** 1.1 **d)** 1.4 **e)** 1.0
P2O/Al2O3	> 0.02 < 0.02	4 1	**a)** n/a **b)** n/a **c)** n/a **d)** n/a **e)** n/a P2O values are below detection limit
Mo/Al2O3	> 0.08 < 0.08	4 1	**a)** 0.009 **b)** 0.04 **c)** 0 **d)** 0.02 **e)** 0.02
Zr/U	> 65	2	**a)** 17.5 **b)** 11.4 **c)** 16.6 **d)** 16.4 **e)** 11.5

f

Figure 6.9 Geochemical classification based on Pearce *et al.*, (2010). Criteria used are listed in **Table f** (above). **a**) Aralla, **b**) Caldas, **c**) La Majua, **d**) Sena de Luna, **e**) Villanueva. The geochemical classification values (0 to 14) indicate: >0 yet ≤4 = floodplain mudstone, >4 and ≤ 7 = brackish water or lacustrine, >7 and ≤ 10 = marginal marine mudstone, >10 to 16 = marine mudstone. If a sample has a very high Zr/U value (above 65), it is presumed to contain abundant heavy minerals and is awarded a final score of 2. If a sample is derived from coal, it is awarded a default score of 0, after Pearce *et al*. (2010). The P_2O and Mo values were near/below detection limits. The P_2O/Al_2O_3 ratio was excluded from the classification scheme calculation.

Pearce *et al*. (2010) developed a geochemical classification scheme to discriminate between floodplain-, brackish to lacustrine-, marginal marine-, and fully marine developed mudstones. The parameters that are used to classify the sediments are quantified by a scoring system: **[1]** U ppm values ≥6 are awarded a score of 4, concentrations <6 are given a value of 1, **[2]** a Th/U ratio of ≥3 is awarded a score of 1, values <3 are given a value of 4, **[3]** a P_2O/Al_2O_3 ratio ≥0.02 is given a score of 4, <0.02 are given a value of 1, **[4]** the ratios of Mo/Al_2O_3 are awarded a score of 4 if ≥0.08 and a value of 1 if <0.08, finally **[5]** a Zr/U ratio >65 is awarded score of 2, a Zr/U ratio <65 gains 0. The sum of these parameters for each sample results in a geochemical classification value. These diagnostic values are then used to identify the environmental setting in which the sediments were deposited in. Geochemical classification values of >0 yet ≤ 4 are interpreted to be indicative of floodplain sediments, values of >4 and ≤ 7 suggest a brackish to lacustrine environment of deposition, values of >7 and ≤ 10 infer marginal marine settings and finally, values of >10 to 16 indicate fully marine developed sediments.

When applying the scheme of Pearce *et al*. (2010), the depositional environment of most of the lower part of the Bernesga Mb. at Aralla (**Figure 6.9 a**) can be classified as fully marine developed. The succession is however punctuated by three distinct phases, which exhibit values indicative for a strong floodplain influence. Towards the middle of the Bernesga Mb. a drop in the classification values can be observed, these shales can be interpreted to be of marginal marine origin. Most of the sand- and siltstones of the overlying Villasimpliz Mb. carry low values diagnostic for marginal marine settings. Furthermore, there are a number of horizons intercalated, that suggest a brackish to lacustrine environment of deposition. Overall, the Formigoso Fm. at the Aralla section can be interpreted to display a decline in salinity levels from the fully marine developed conditions at the base over the marginal marine mud, silt and sandstones of the upper Bernesga Mb. to the brackish – lacustrine environment inferred for parts of the Villasimpliz Mb.

The lower part of the Bernesga Mb. at Caldas de Luna (**Figure 6.9 b**) developed under fluctuating fully and marginal marine environmental conditions. The middle of the Bernesga Mb. was deposited under erratic environmental changes between marginal marine to floodplain sedimentation. When interpreting this scenario, the Caldas de Luna section displays a decline in salinity levels from the very onset of black shale deposition.

The Getino Beds of the La Majua section (**Figure 6.9 c**) were deposited under interacting marginal marine and floodplain environments. The shales of the Bernesga Mb. show values typical for marginal marine sedimentation with a few horizons at its base influenced by the introduction of floodplain conditions. It is important to note that the lowermost 'fully marine' section of the Bernesga Mb. is here absent. It is suggested that the region around La Majua was situated on a palaeo-high, resulting in the deposition of the basal shales under non-marine conditions.

The Sena de Luna section (**Figure 6.9 d**) is characterised by the presence of the floodplain Getino Beds. The environmental conditions change rapidly to marginal marine conditions. The base of the Bernesga Mb. is characterised by a high-order oscillation between marginal marine to fully marine developed conditions. The basal section of the Bernesga Mb. is overlain by shales formed under consistent marginal marine conditions. Towards the top a rapid transition to fully marine and floodplain environmental conditions is developed.

The Bernesga Mb. at Villanueva (**Figure 6.9 e**) is dominated by an interaction of fully marine and marginal marine conditions. There is a brief interval towards the middle of the section where

floodplain conditions are apparent. The section culminates with the predominantly marginal marine conditions punctuated by infrequent fully marine conditions.

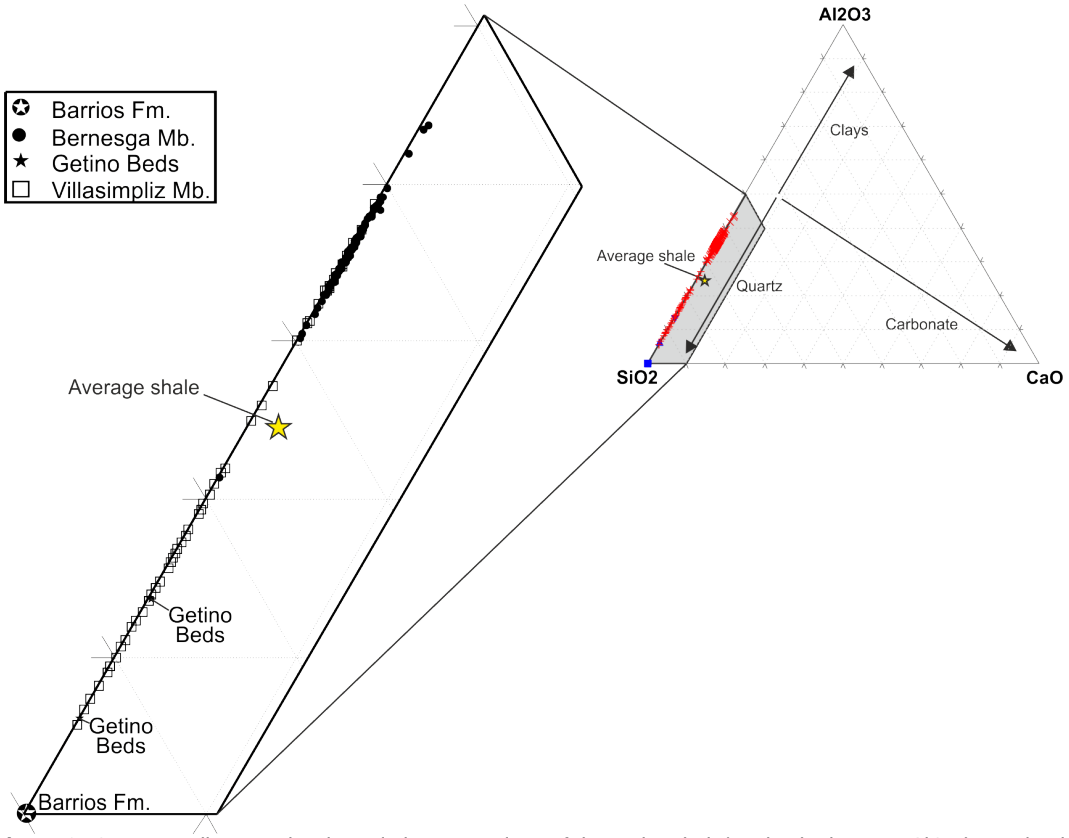

Figure 6.10 Ternary diagram showing relative proportions of the major shale/mudrock elements SiO_2 (quartz), Al_2O_3 (clays) and CaO (carbonates). Data from the Aralla section (241 samples). The 'Average shale' international standard after Wedepohl (1971) shown as star. The shales of the Bernesga Mb. (black circle) show an enrichment in Al_2O_3 relative to the 'Average shale'. The sand- and siltstones of the Villasimpliz Mb. (square) exhibit a compositional maturity trend towards higher SiO_2 concentrations. The control sample of the highly mature Barrios Fm. (black circle with inset star) as an example for an end member of such a maturity trend is plotting directly into the SiO_2 corner.

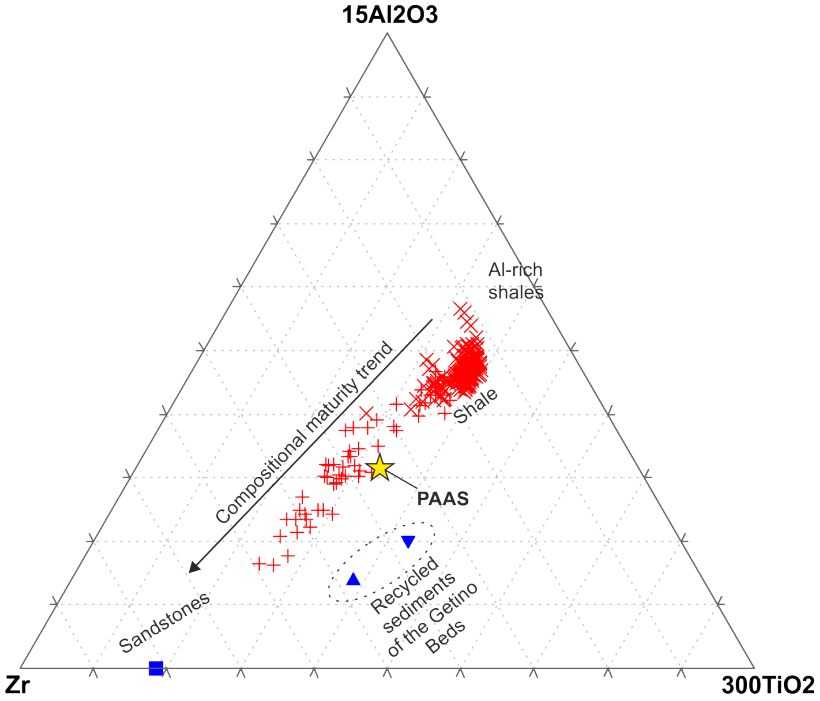

Figure 6.11 Ternary $15Al_2O_3$-$300TiO_2$-Zr plot of Mongelli *et al*. (2006), the international standard 'PAAS' of Taylor and McLennon (1985) has been plotted for comparison. The plot illustrates all geochemical data from the Aralla section (241 samples). The Barrios Fm. is represented by a blue square, the Getino Beds by blue triangles, the Bernesga Mb. by the diagonal red cross (x) and finally the Villasimpliz Mb. an upright cross (+). A compositional maturity trend is present within the sand- and siltstones of the Villasimpliz Mb. towards increased Zr concentrations. See text for details.

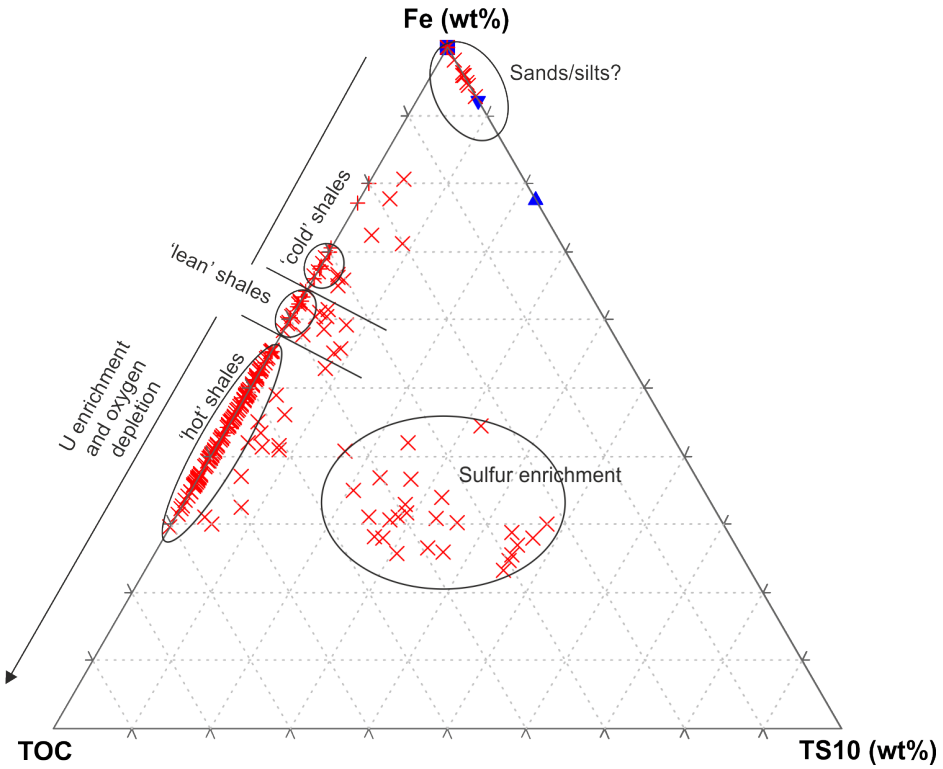

Figure 6.12 TOC–TS–Fe ternary diagram of Dean and Arthur (1989) and Arthur and Sageman (1994). **TOC**= total organic carbon, **TS**= total sulphur. Illustrating all geochemical data for the Aralla section (241 samples). Discrimination fields are indicated, based on U concentrations: **[1]** the 'hot' shales, **[2]** the 'lean' shales and, **[3]** the 'cold' shales. The Barrios Fm. is represented by a blue square, the Getino Beds by blue triangles, the Bernesga Mb. by the diagonal red cross (x) and finally the Villasimpliz Mb. an upright cross (+).

The SiO_2-Al_2O_3-CaO ternary plot (**Figure 6.10**) of Ross and Bustin (2009) utilises SiO_2 concentrations to determine the relative proportions of Quartz, Al_2O_3 to approximate the clays concentrations and CaO values to represent the carbonate fraction. The shales of the Bernesga Mb. display an enrichment in Al_2O_3 relative to the 'Average shale' of Wedepohl (1971), as determined by the previously described elemental EF plots (**Chapter 6.1** 'Enrichment factor plots'). The sand- and siltstones of the Villasimpliz Mb. show a compositional maturity trend towards SiO_2 as expected. In general it is assumed, that weathering and sedimentary recycling processes will lead to the demise of less resistant alumosilicates, and hence to a relative enrichment of the resistant heavy minerals and quartz. As a consequence, higher mature sediments will start plotting towards the SiO_2. It is notable, that all of the sediments belonging to the Formigoso Fm. are, compared to the international standards, strongly depleted with regards to CaO, indicating that no dilution of the siliciclastic sediments with a carbonate-phase took place.

The $15Al_2O_3$-$300TiO_2$-Zr plot (**Figure 6.11**) after Mongelli *et al*. (2006) uses the three elemental components Al_2O_3, TiO_2 and Zr to discriminate different lithologies. The Al_2O_3 concentrations represent the clay content, whereas the TiO_2 and Zr concentrations are residing in the heavy mineral phases. The TiO_2 and Zr components are used to discriminate between either, **[1]** a acidic

provenance with the enrichment of Zr, indicating the presence of zircon crystals originally formed within melts of granitic composition, and **[2]** a basic composition of the provenance, typified by the elevated concentrations of TiO_2 indicating the presence of Ti-oxides, for example rutile. The increased Zr values are interpreted to be indicative for higher mature sandstones. The shales of the Bernesga Mb. plot within the 'shale' category and are consequently trending towards the Al-rich shales. The shales display an overall enrichment of Al_2O_3 in comparison to the international standard 'PAAS' of Taylor and McLennon (1985). The sand- and siltstones of the Villasimpliz Mb. are trending towards Zr, indicating a higher compositional maturity. The Getino Beds, represented by the blue triangles, have comparable concentrations of Al_2O_3 and Zr relative to the sand- and siltstones of the Villasimpliz Mb. However, they show a significant relative enrichment of TiO_2. The Getino Beds are the product of recycled sediments, with the predominant sediment source being the Barrios Fm., combined with an influx of clay-content from the hinterland as a result of elevated chemical weathering rates. Most likely, the Getino beds represent transgression-related lag sediments with a relatively high content of heavy minerals such as zircon and rutile, with the latter causing the high TiO_2 concentrations.

The TOC–TS10–Fe ternary plot after Dean and Arthur (1989) and Arthur and Sageman (1994) seen in **Figure 6.12**. The differing concentrations of the parameters TOC, total sulphur (TS) and Fe are used to discriminate sediments formed under different redox conditions. The majority of the shales of the Bernesga Mb. trend towards high TOC values, whereas the Barrios Fm., Getino Beds and Villasimpliz Mb. show no enrichment. As the TOC values of this research were approximated based on U ppm concentrations, there is a clear differentiation or grouping of the shales, **[1]** the U enriched basal shales or 'hot shales', **[2]** the U lean shales and finally **[3]** the shales or siltstones that are depleted in U relative to the very basal shales. A number of shale samples show elevated TS values, which do not coincide with Fe_2O_3 peaks on the variation plots (see **Chapter 5** 'Geochemical results), indicating that these S enrichments are not solely related to the formation of pyrite but also to other sulphide phases, such as sphalerite (ZnS).

6.3 Sr systematic within the Bernesga Mb

The geochemically analysed black shales show significant strontium enrichments (up to 300 ppm) at the base of the Bernesga Mb. This strontium enrichment diminishes to approximately 175 ppm in a logarithmic fashion throughout the Bernesga Mb. (see **Chapter 5.1.2** 'Sr element variation', **Figure 5.2j**). An explanation for the strontium enrichments at the very onset of black shale deposition could be the presence of celestine crystals ($SrSO_4$), that were found in high concentrations on the black shale bedding planes (see **Figure 6.13** and **Figure 6.14**).

Within marine environments, Sr originates from two potential sources, **[1]** hydrothermal via leaching of oceanic crust and, **[2]** riverine, from terrestrially derived sediments (MacKenzie, 2005). In order to determine the Sr source it is necessary to determine the isotopic signature of Sr. However, the analysis of Strontium-isotopes was not available for this study. Sr is commonly enriched in immature sediments as it is associated due to the K-Sr exchange processes to the relatively high feldspar contents. In addition to this, it is commonly enriched within carbonates. The Sr abundance in carbonates is related to the presence of aragonite, as the Ca^{2+} ions are substituted by Sr^{2+} ions (De Vos *et al*., 2006). Sr is also mildly enriched within oceanic bottom waters (Villiers, 1999). During the initial transgression of the early Silurian, upwelling processes may have brought the Sr rich bottom waters upon the shelfal margin. This upwelling process may have contributed to the overall Sr enrichment observed in the sediments. The Sr enrichment observed at the base of the Bernesga Mb. complies with the Sr values of the international shale standards, **[1]** the 'Average shale' of Turekian and Wedepohl (1961) and **[2]** the 'Average shale' of Wedepohl (1971, 1991). This indicates that the majority of the overlying shales of the Bernesga Mb. are significantly Sr-depleted. If the Sr concentrations observed within the lower Bernesga shales are directly related to the concentrations of Sr within the original sediment source, then the Sr depletions within the upper Bernesga Mb. shales could indicate a depletion of Sr within the source material. The average Sr concentration of the Bernesga Mb. (~190 ppm) is remarkably similar to the average Sr-content (~192 ppm) of glacial till derived palaeo-soils and loess (De Vos *et al*., 2006). Large areas of the peri-glacial Gondwanan hinterland were exposed to increased physical and minor chemical weathering because of the melt-down of the Hirnantian ice-masses. The melting of the glacial masses led to the deposition of 'out-wash' glacial tills and the formation of significant quantities of loess. These sediments and their associated Sr content were subsequently transported into the predominantly anoxic black shale regime via river systems and possible aeolian influx.

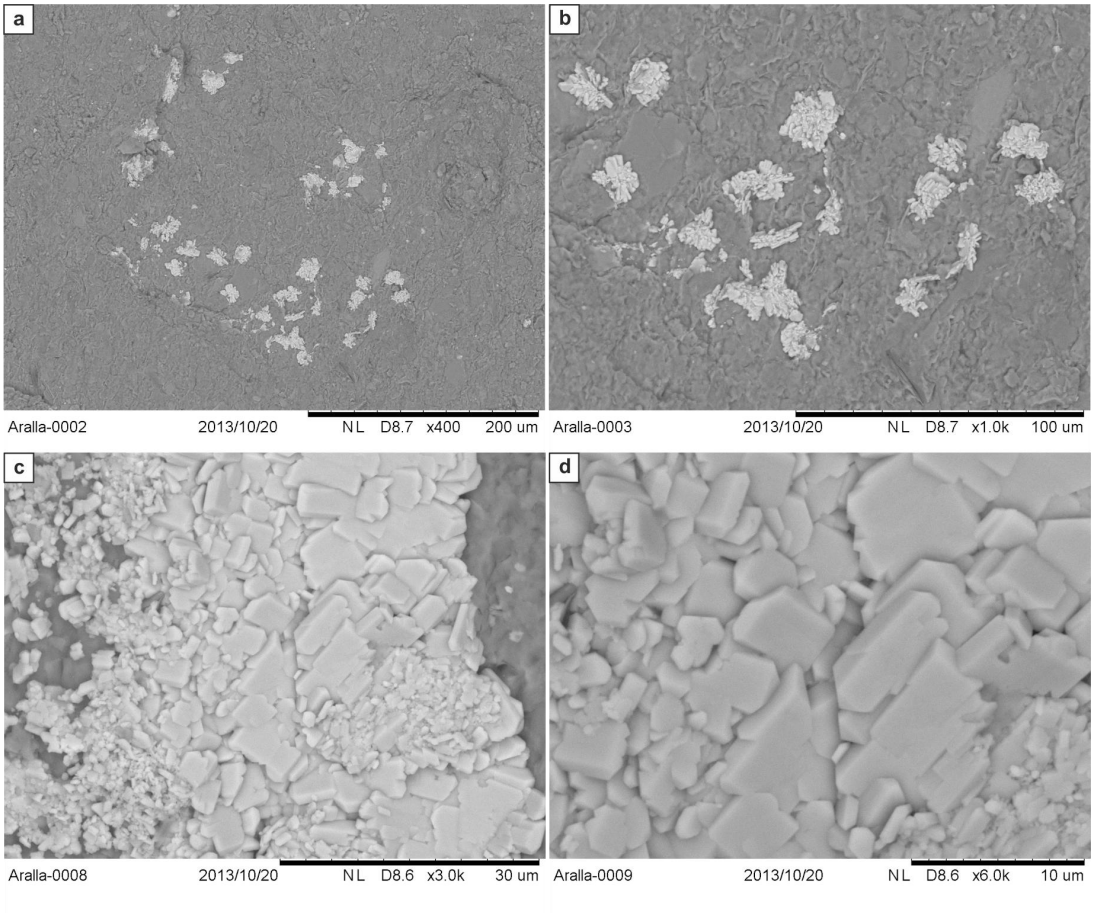

Figure 6.13 Scanning electron microscope (SEM) micrographs showing the celestine crystals within the shales of the lowermost Bernesga Mb. of the Aralla section. **(a)** The distribution of the celestine is not uniform, external factors are mitigating the formation of celestine. **(b)** The crystal aggregates show a wide range of different morphologies ranging from spherical, angular to completely irregular. They show a size-range between 15µm and 130 µm. **(c and d)** Increased magnification of a crystal in **b)**, the size of the platey individual celestine crystals vary from ~1µm to 8µm.

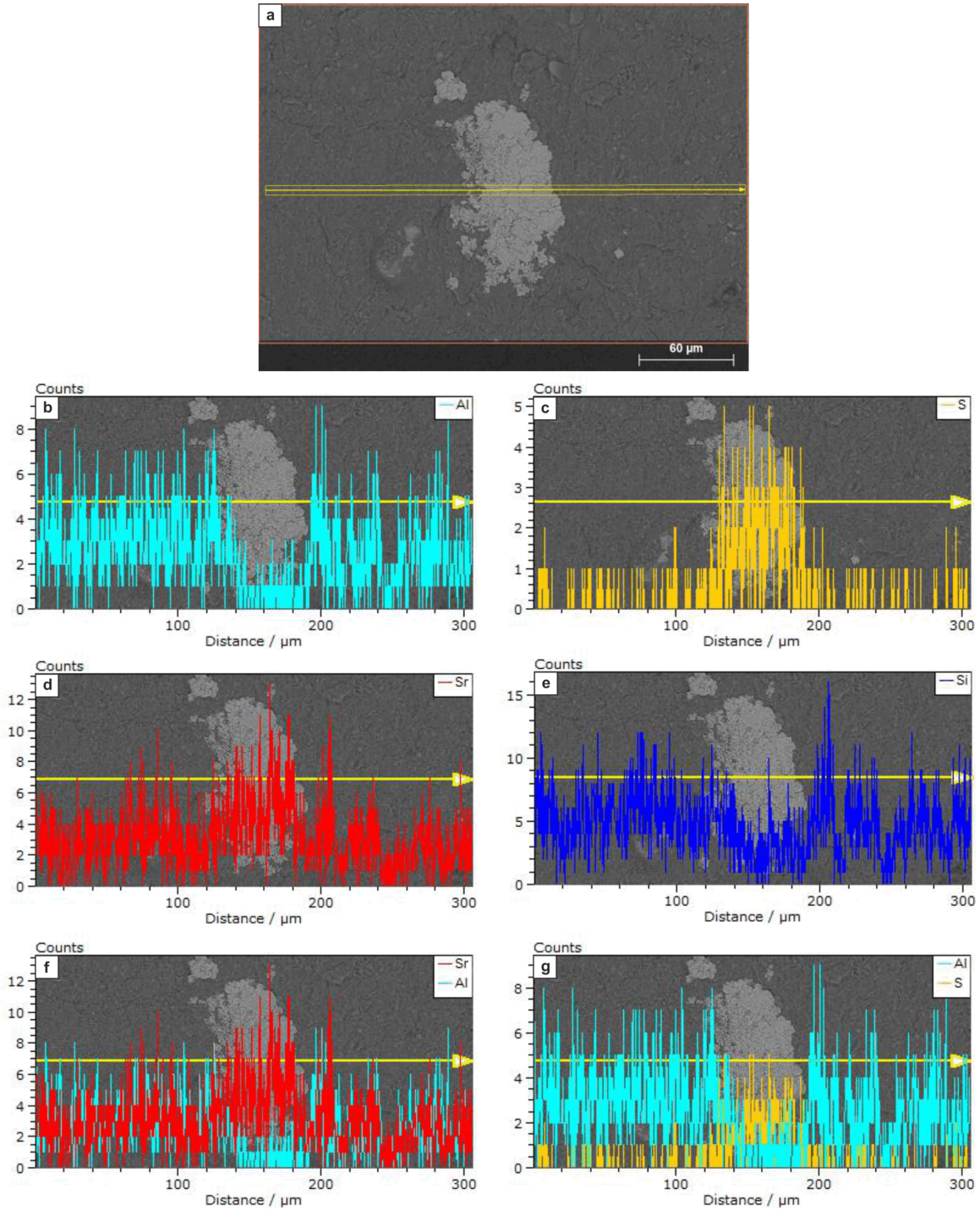

Figure 6.14 Elemental line-scan measurements (SEM ED-XRF) across a celestine crystal and the background clay-matrix. (**a**) BSE image of the analysed sample, showing the orientation of the line-scan. **(b)** Analysed aluminium concentrations across the sample, the values are higher in the clay-rich background matrix relative to the celestine complex. **(c)** Sulfur enrichment observable within the celestine crystal relative to the background matrix. **(d)** Sr enrichment is apparent in the crystal analysed relative to the background matrix, although the matrix also shows a significant Sr enrichment either side of the crystal. **(e)** Analysed Si concentrations, displaying an overall depletion in the crystal relative to the background matrix. However, there is a Si rich horizon within the middle of the celestine complex, most likely the result of impurities within. **(f)** Relationship between Sr and Al concentrations, the Al concentrations fall in contrast to the enrichment in Sr. **(g)** Illustrating lower Al concentrations with higher S values within the crystal complex.

6.4 Environmental reconstructions

For the environmental reconstruction a number of variables were approximated: **[1]** the palaeo-redox states, **[2]** palaeosalinity variations, **[3]** palaeohumidity fluctuations, **[4]** clay-typing, **[5]** the chemical weathering conditions, **[6]** the palaeobioproductivity reconstruction, and finally **[7]** the effects of potential hydrothermal overprinting on the concentrations of certain elements. The combination of these parameters was used to establish the palaeoenvironmental conditions during the deposition of the **[1]** Getino beds, **[2]** Bernesga Mb. shales and **[3]** the sand- and siltstones of the Villasimpliz Mb.

6.4.1 Anoxia reconstructions

A number of geochemical proxies involving different chemical elements and elemental ratios were used to estimate the palaeo-redox conditions for the sediments of the Formigoso Fm., but also to critically test the value and robustness of the applied proxies compared to each other.

The **Ni/V** and **V/Cr** redox proxies of Jones and Manning (1994) rely on the sensitivity of V to changing redox conditions. Under oxic conditions V is relatively insoluble and accumulates in sediments, leading to low Ni/V and high V/Cr ratios. In contrast, under reducing conditions it is soluble and is incorporated into the water column (Harris *et al*., 2004). A V/Cr ratio ≤ 2 is interpreted to represent oxic environmental conditions, > 2 for ≤ 4.25 dysoxic and >4.25 sub-oxic to anoxic conditions. Kimura and Watanabe (2001) suggested that the degree of enrichment of V is best represented by the **V/Sc** ratio, as both the reduced forms of V and Sc are equally insoluble. Generally, the V abundance in shales varies significantly relative to Sc, and not to other insoluble elements such as Ti and Al. A V/Sc ratio ≤9.1 is used to infer an oxic environment of deposition, and values above oxygen depleted. The **V/(V+Ni)** proxy of Hatch and Leventhal (1992) considers that both the V and Ni occur in highly stable organically derived tetrapyrrole structures (such as porphyrin), which are preserved under anaerobic conditions. Oxidised OM tends to exhibit a lower tetrapyrrole content and hence low Ni and V concentrations. The V may also be adsorbed onto the clay minerals, a process that is thought to occur post-depositional (Rimmer, 2004). V/(V+Ni) ratios ≤ 0.46 are interpreted to represent oxic conditions, >0.46 to ≤0.60 dysoxic, >0.54 to ≤0.82 suboxic to anoxic and >0.84 indicates a euxinic environment of deposition. Jones and Manning (1994) also engineered the **U/Th** redox proxy, the uranyl ion U^{+6} is highly soluble under oxic environmental conditions, but is reduced and precipitates under reducing conditions. The Th resides in the detrital

fraction that is not affected by the redox state. A U/Th ratio ≤ 0.75 indicates oxic conditions, >0.75 to ≤1.25 dysoxic and >1.25 can be used to interpret a suboxic to anoxic environment of deposition. The **Th/U** proxy of Fertl (1979) uses the same principles highlighted above for the U/Th ratio. Values ≤ 2 relate to anoxic environmental conditions. The degree of pyritisation (**DOP**) is considered to be one of the most effective ways for reconstructing the extent of anoxia and is described in detail in **Chapters 3.1.12** and **4.10.3** 'Degree of Pyritisation'. The above proxies are systematically described and interpreted for Aralla, Caldas de Luna, La Majua, Sena de Luna and Villanueva.

6.4.1.1 Aralla section

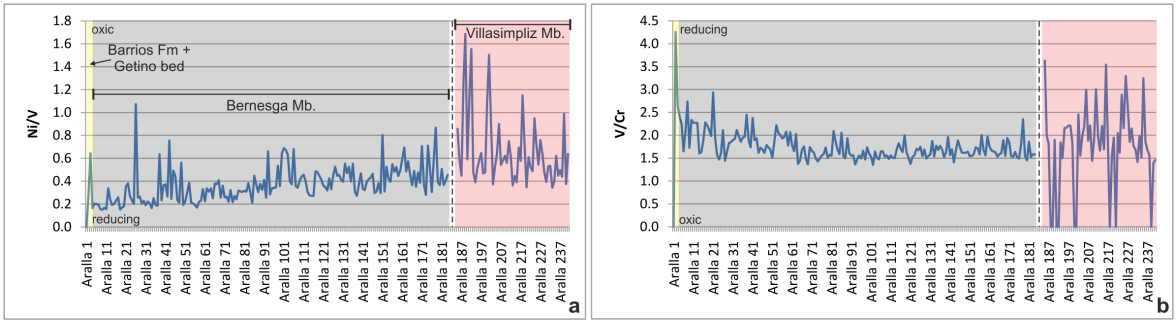

Figure 6.15 (a) the Ni/V ratio of Jones and Manning (1994), the lowest values are observed at the base of the Bernesga Mb. indicating a oxygen depleted environment of deposition, the values increase gradually throughout the Mb. The sand- and siltstones of the Villasimpliz Mb. show erratic and relatively higher values than the Bernesga Mb. indicating the increased presence of free oxygen, and **(b)** the V/Cr ratio of Jones and Manning (1994), the values are elevated at the base of the Bernesga Mb. indicating reducing conditions. These values decrease throughout the section and then become relatively stable. The sand- and siltstones of the Villasimpliz Mb. have increased values, suggesting deposition under a reducing environment (this does not concur with the field observations) a few horizons display low values indicating sedimentation under oxic conditions.

The values of the Ni/V and V/Cr redox ratios of Jones and Manning (1994) are used to interpret that the basal shales of the Bernesga Mb. are highly reduced (**Figure 6.15**). The shales are then deposited under progressively oxygenated conditions towards the top of the Bernesga Mb. The sands and silts of the Villasimpliz Mb. are interpreted as oxic sediments when applying the Ni/V ratio. However, when applying the V/Cr proxy, the Villasimpliz Mb. is displaying a higher state of anoxia than the basal shales of the Bernesga Mb. This interpretation conflicts with the field observations of heavy bioturbation for the Villasimpliz Mb. The redox proxies V/Cr, V/Sc, V/(V+Ni), of Jones and Manning (1994), Kimura and Watanabe (2001), Hatch and Leventhal (1992) respectively (**Figure 6.16**), determine, that elevated redox conditions prevailed during the deposition of the basal shales of the Bernesga Mb. In contrast, the U/Th ratio of Jones and Manning (1994) resulted in values interpreted to suggest a predominantly oxic environment of deposition, hence demonstrating that this redox proxy has to be interpreted with caution. The Th/U

ratio of Fertl (1979) suggested that the increased reducing conditions did indeed take place during the deposition of the basal shales. However, the ratio suggests that oxic conditions prevailed during the sedimentation of the mid-Bernesga Mb. The upper Bernesga Mb. and the overlying Villasimpliz Mb. have ratios that suggest a more reducing environment of deposition than the basal shales of the Bernesga Mb. When applying the proxies to the elemental concentrations of the Bernesga Mb., it is evident, that the ratios V/Sc, U/Th and Th/U do not work as effectively as the V/(V+Ni) ratio. However, when the V/(V+Ni) ratio is applied to the elemental concentrations of the Getino Beds, the values suggest an 'euxinic' environment of deposition. This interpretation significantly contradicts the field observations, as the Getino Beds are heavily bioturbated indicating an oxic environment during the time of deposition.

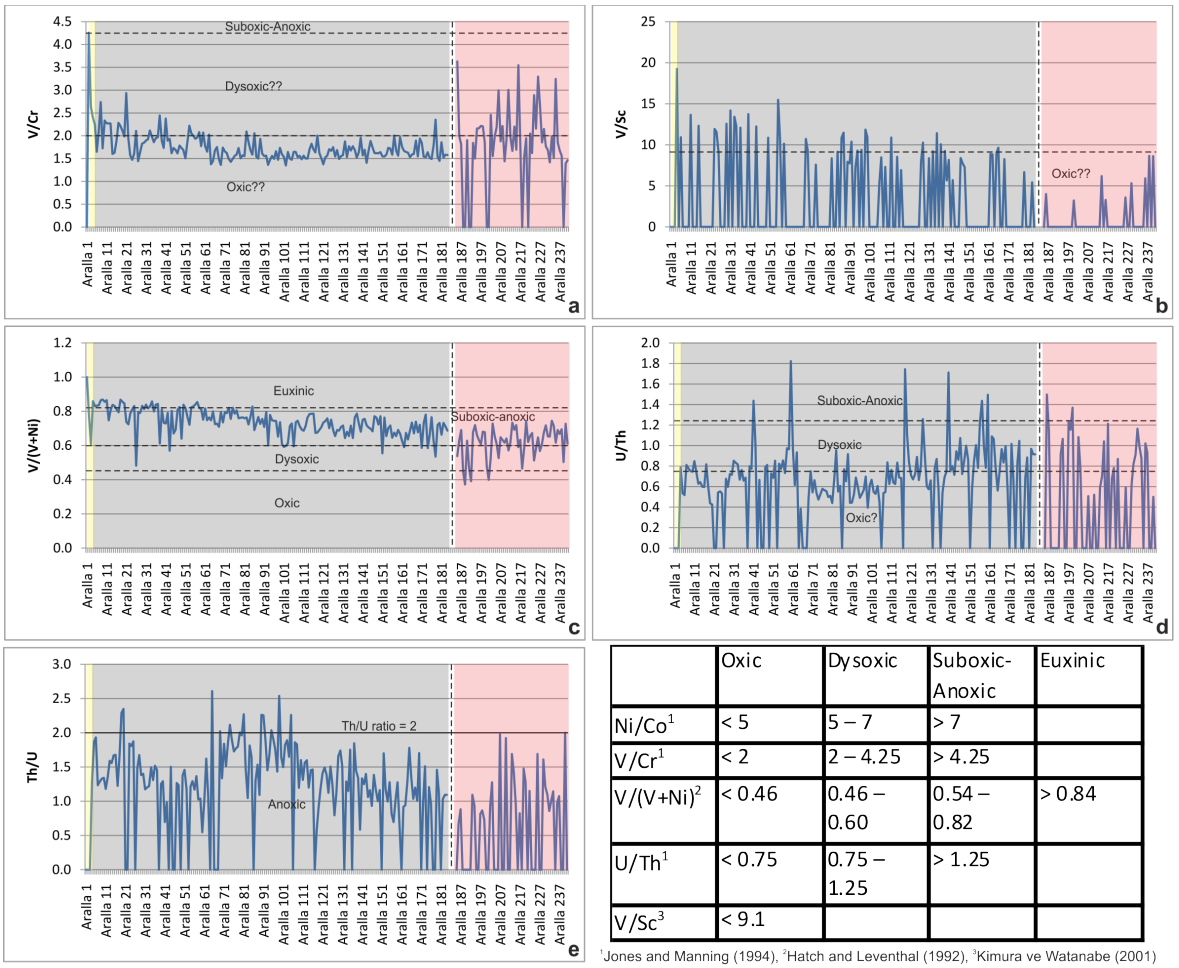

	Oxic	Dysoxic	Suboxic-Anoxic	Euxinic
Ni/Co[1]	< 5	5 – 7	> 7	
V/Cr[1]	< 2	2 – 4.25	> 4.25	
V/(V+Ni)[2]	< 0.46	0.46 – 0.60	0.54 – 0.82	> 0.84
U/Th[1]	< 0.75	0.75 – 1.25	> 1.25	
V/Sc[3]	< 9.1			

[1]Jones and Manning (1994), [2]Hatch and Leventhal (1992), [3]Kimura ve Watanabe (2001)

Figure 6.16 Various proxies used to reconstruct palaeoenvironmental redox conditions. **(a)** V/Cr ratios, illustrating the elevated reducing conditions at the base of the Bernesga Mb. the sediments are progressively oxygenated towards the top of the Mb. However, the Villasimpliz Mb. shows increased reducing conditions relative to the Bernesga Mb. shales. **(b)** V/Sc ratios suggesting elevated reducing environments at the base of the Bernesga Mb. the sediments are deposited under progressively oxygenated conditions towards the top of the Mb. including the overlying Villasimpliz Mb. **(c)** V/(V+NI) redox proxy, illustrating the progressive oxygenation of the environment from the 'euxinic' base to the 'dysoxic-suboxic' top. **(d)** U/Th values contradicting all other ratios, indicating that the vast majority of the Formigoso Fm. is deposited under an oxic environment of deposition. **(e)** Th/U redox proxy, interpreted to show reducing conditions at the base of the Bernesga Mb., and oxic environment towards it middle, and progressively more reducing conditions towards the top, including the Villasimpliz Mb. The table indicates the various proxy values indicative of different environmental conditions.

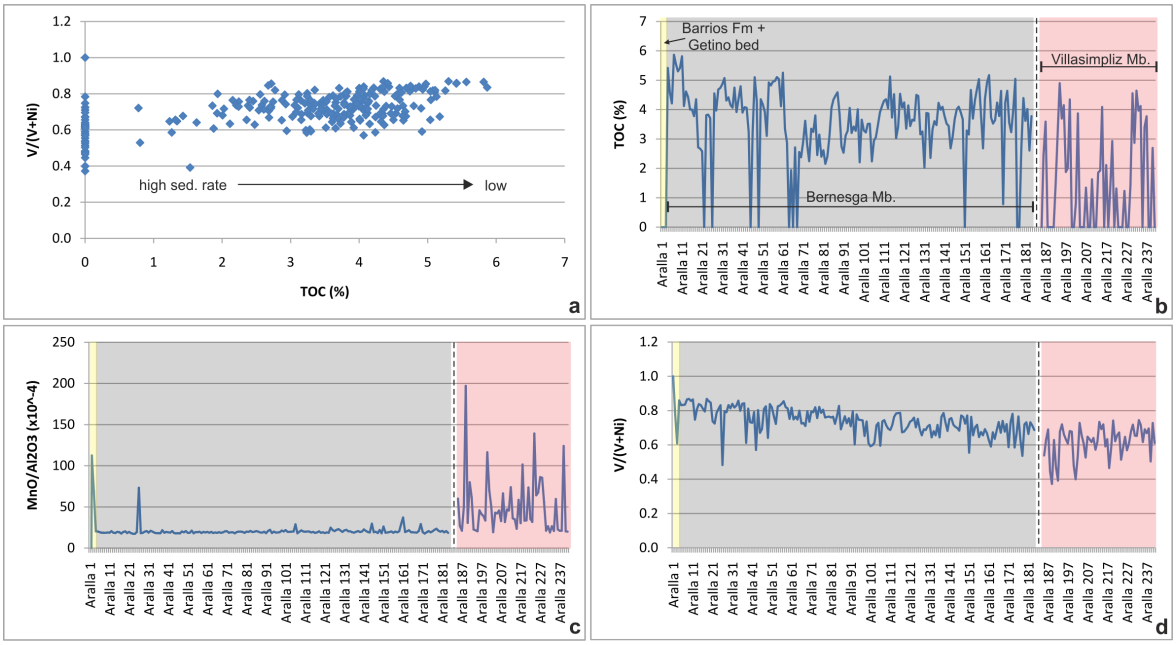

Figure 6.17 a) V/(V+Ni) *vs.* TOC. The basic assumption of this proxy is the reciprocal relationship between the TOC values and the sedimentation rate (Arthur and Sagemann,1994). The V/(V+Ni) values have to be above 0.5 in order for the organic carbon to be preserved and not to be oxidised (Rimmer, 2004). The TOC values are seen to increase with the increasing reducing conditions, interpreted by higher V/(V+Ni) ratios. **b)** TOC values *vs.* stratigraphy. **c & d)** MnO/Al_2O_3 ratio and V/(V+Ni) *vs.* stratigraphy respectively.

When the TOC concentrations and V/(V+Ni) ratios decrease (see **Figure 6.17**) are the Mn/Al ratios seen to increase (samples 185 onwards) suggesting oxygenation of the sediments. The sand- and siltstone intercalations of the Villasimpliz Mb. are interpreted to be oxygen rich sediments within the otherwise anoxic black shale regime.

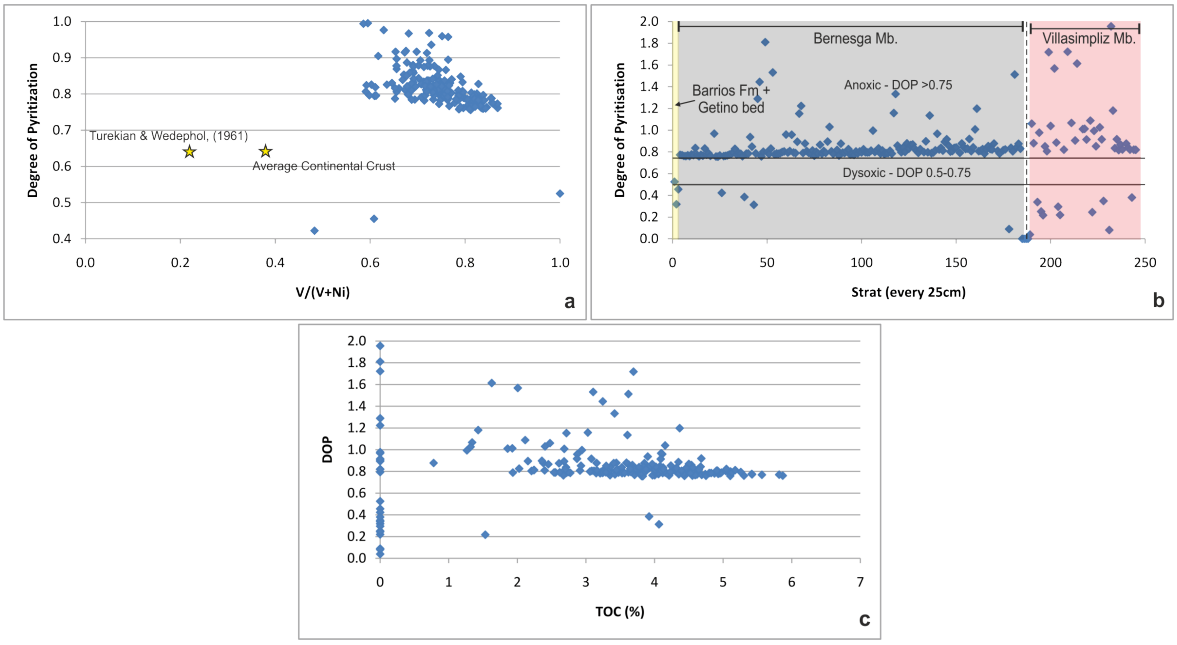

Figure 6.18 a) V/(V+Ni) *vs.* degree of pyritization (DOP), with the average shale of Turekian and Wedepohl (1961) and average continental crust for comparison. The Formigoso Fm. shows significantly elevated DOP values and V/(V+Ni) ratios relative to the international standards. **b)** DOP *vs.* stratigraphy, the lines indicating the varying redox states are after Wignall (1994). The majority of the Bernesga Mb. has DOP values indicative of anoxic conditions >0.75. The Villasimpliz Mb. displays anoxic conditions >0.75, most of these values are related to the siltstone intercalations, whereas the sandstone beds indicate oxic conditions <0.5. **c)** Non-coupling between DOP and TOC (%), illustrating the uniform DOP and increasing TOC.

The Degree of Pyritization (DOP) is widely considered to be one of the most effective ways to determine the extent of anoxia. The majority of the Bernesga Mb. is set within the anoxic regime with DOP values >0.75. The shales of the Bernesga Mb. have higher DOP and V/(V+Ni) values in relation to the 'Average shale' of Turekian and Wedepohl (1961) and the upper continental crust (see **Figure 6.18 a**). Varying the levels of TOC does not necessarily affect the redox state (see **Figure 6.18 c**). It is generally accepted that increased levels of TOC lead to elevated reducing environmental conditions. However, in this instance, all the free reactive Fe may have been utilised in pyrite formation and euxinic conditions may have prevailed. H_2S in these conditions may have been present at the sediment water interface leading the sulphurisation of the organic material. Framboidal pyrite is evident within the basal Bernesga Mb. (**Figure 6.20**). The pyrite formation leads to the relative enrichment of Fe and S as shown in the elemental maps of **Figure 6.20**.

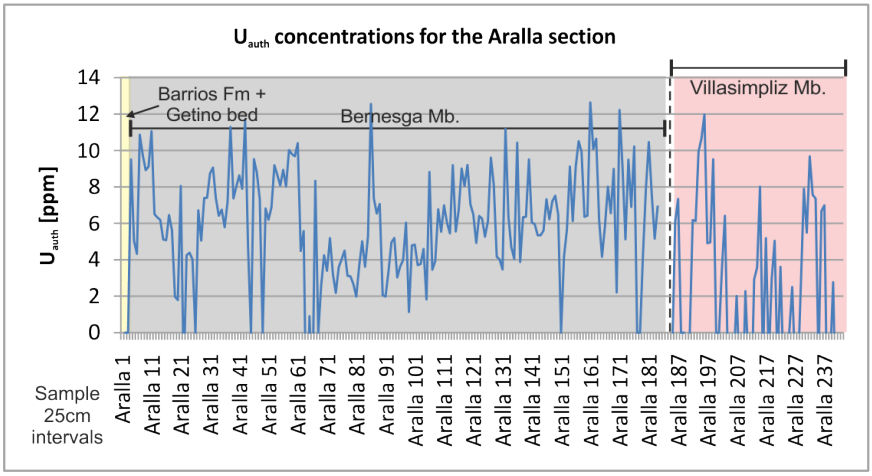

Figure 6.19 Authigenic U (U_{auth}) concentrations for the Aralla section. The U_{auth} shows the same similar cyclic signal as the absolute U concentrations (see **Chapter 3.1.7.2** 'U description').

The authigenic U (U_{auth}) concentrations were calculated following the method of Wignall and Myers (1988), as described previously (**Chapter 3.1.7.2** 'U description'). The U_{auth} (see **Figure 6.19**) equates to a significant proportion of the absolute U concentrations illustrated in **Chapter 5** 'Geochemical results'. The average U_{auth} concentrations for the Bernesga Mb. equate to ~6 ppm, whereas the absolute U concentrations average at ~11 ppm. Therefore the U_{auth} concentrations make up ~54% of the total U values analysed. These high overall concentrations of the U_{auth} are associated to the reducing conditions of the environment at the time of deposition. The high concentrations of U_{auth} within the Bernesga Mb. of the Aralla section correspond well to the 'euxinic' conditions of the previously calculated V/(V+Ni) ratio (see **Figure 6.16** and **6.17**). The cyclic signal observed in the U_{auth} concentrations is also present within the absolute U values (see **Chapter**

5.1.2 'U element variation', **Figure 5.2**). This indicates that the cyclic U signal is the response to prevailing environmental conditions at the time of the black shale deposition.

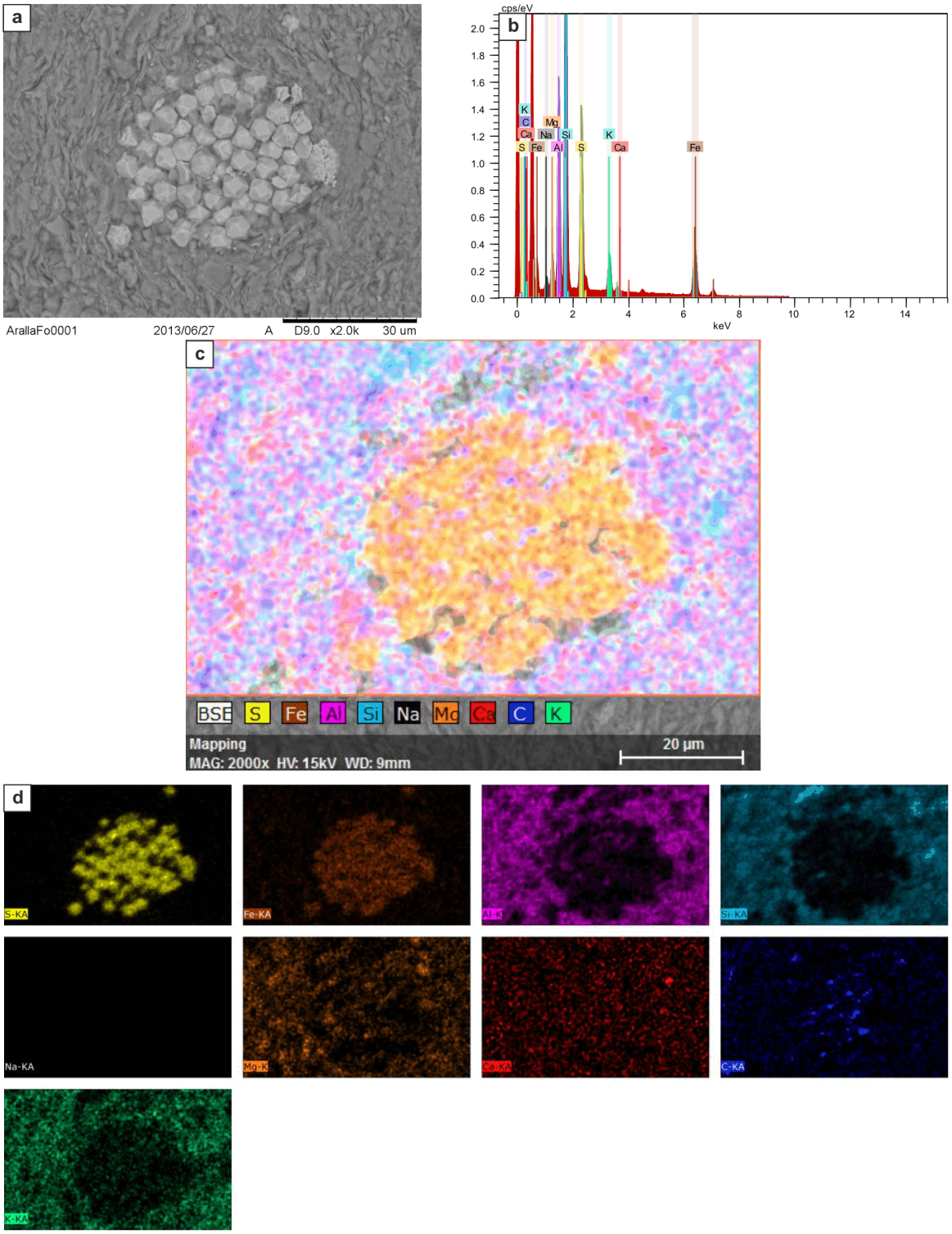

Figure 6.20 (a) SEM micrograph of framboidal pyrite found within the basal shales of the Bernesga Mb. at Aralla. **(b)** Elemental spectrum of the analysed section. **(c)** Combined elemental map (SEM ED-XRF), high-lighting the areas of the various elemental enrichments. **(d)** Individual element maps (SEM ED-XRF), note in particular the enrichments in S and Fe within the pyrite formation, and the relative depletions in Al and Si within. The Al and Si concentrations are related to the background clay mineralogy.

6.4.1.2 Caldas de Luna section

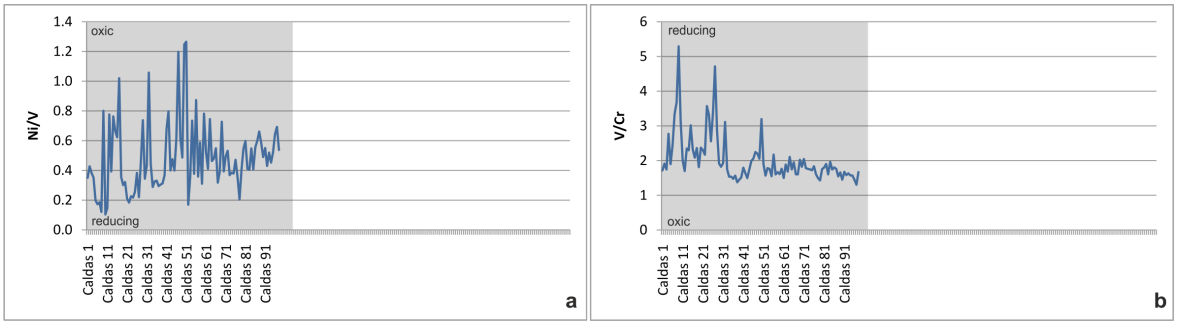

Figure 6.21 (a) Ni/V ratio of Jones and Manning (1994). The lowest values are observed at the base of the Bernesga Mb. indicating a oxygen depleted environment of deposition, the values increase erratically throughout the Mb. **(b)** the V/Cr ratio of Jones and Manning (1994). The values are elevated at the base of the Bernesga Mb., with a few peaks indicating highly reducing conditions. These values deplete throughout the section and then become relatively stable.

The Ni/V and V/Cr redox proxies of Jones and Manning (1994) were used to interpret the basal shales of the Bernesga Mb. to be deposited within a reduced environment, with a number of intercalated horizons pointing towards elevated reducing conditions. The sediments become gradually more oxygenated towards the top of the Bernesga Mb (**Figure 6.21**). The various redox proxies V/Cr, V/Sc, V/(V+Ni), U/Th and Th/U of Jones and Manning (1994), Kimura and Watanabe (2001), Hatch and Leventhal (1992), Jones and Manning (1994) and Fertl (1979) respectively (see **Figure 6.22**), showed that there were elevated redox conditions, even 'euxinic', during the onset of black shale deposition. However, the V/Cr and V/Sc ratios suggest, that the majority of the Bernesga Mb. formed under oxygen rich environmental conditions. The U/Th ratios also seem to indicate, that there were a number of black shale horizons forming under oxic conditions. The Th/U proxy of Fertl (1979) and the V/(V+Ni) redox proxy of Hatch and Leventhal (1992) were deemed the most effective proxies in this instance for reconstructing the palaeoenvironmental conditions during the time of black shale deposition.

The majority of the shales of the Bernesga Mb. are set within the Anoxic regime with DOP values >0.75 (see **Figure 6.24b**). However, a number of horizons display lower DOP values, which is regarded to indicate oxic conditions. The shales of the Bernesga Mb. have a higher DOP index and V(V+Ni) ratio in relation to the average shale of Turekian and Wedepohl (1961) and the upper continental crust (see **Figure 6.24a**). The TOC levels vary significantly whereas the DOP values remain relatively consistent (see **Figure 6.24c**).

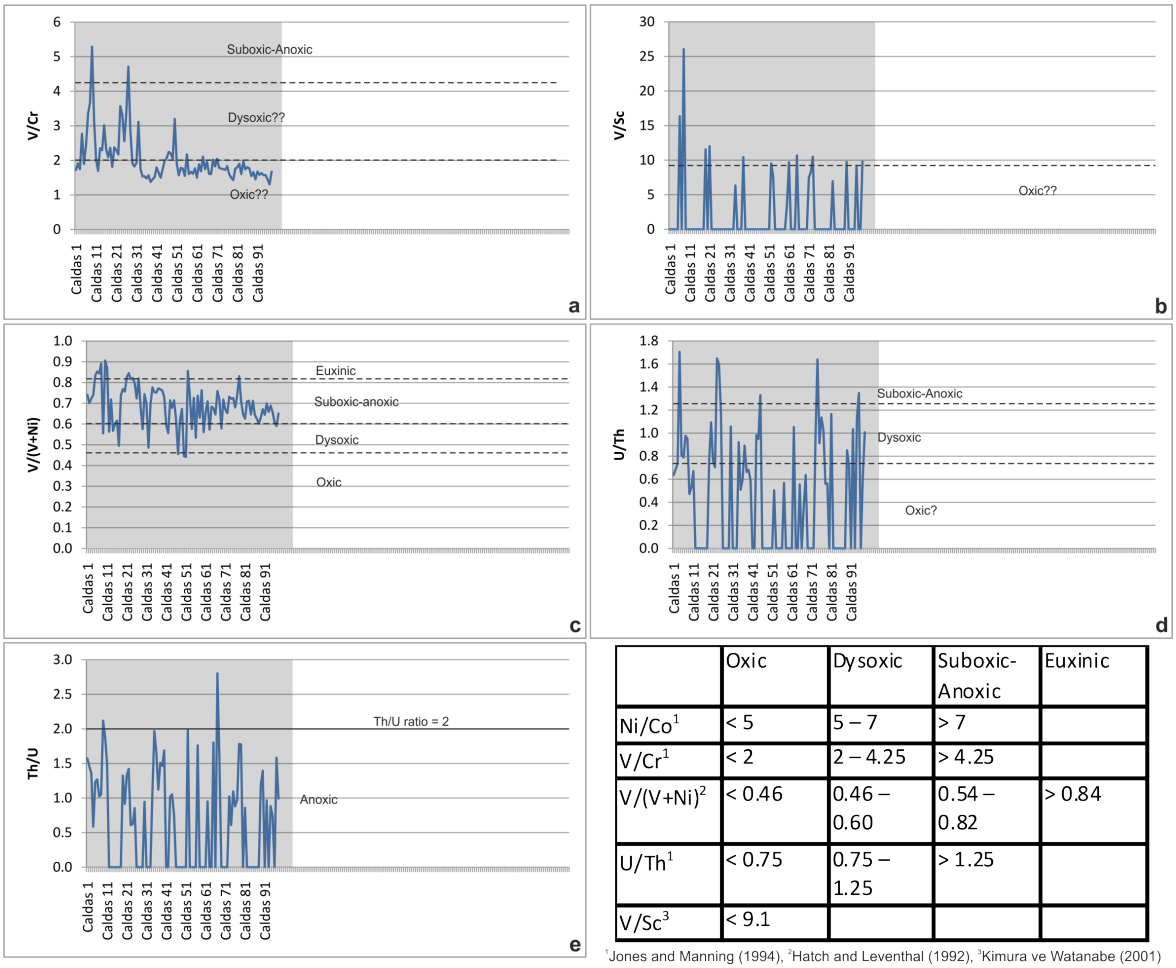

	Oxic	Dysoxic	Suboxic-Anoxic	Euxinic
Ni/Co[1]	< 5	5 – 7	> 7	
V/Cr[1]	< 2	2 – 4.25	> 4.25	
V/(V+Ni)[2]	< 0.46	0.46 – 0.60	0.54 – 0.82	> 0.84
U/Th[1]	< 0.75	0.75 – 1.25	> 1.25	
V/Sc[3]	< 9.1			

[1]Jones and Manning (1994), [2]Hatch and Leventhal (1992), [3]Kimura ve Watanabe (2001)

Figure 6.22 Various proxies used to reconstruct palaeoenvironmental redox conditions. **(a)** V/Cr ratios, illustrating the elevated reducing conditions at the base of the Bernesga Mb. the sediments are progressively oxygenated towards the top of the Mb. **(b)** V/Sc ratios suggesting elevated reducing conditions at the base of the Bernesga Mb. the sediments are deposited under progressively oxygenated conditions towards the top of the Mb. **(c)** V/(V+NI) redox proxy, illustrating the progressive oxygenation of the environment from the 'euxinic' base to the 'suboxic' top. **(d)** U/Th values contradicting all other ratios, indicating that significant parts of the Formigoso Fm. are deposited under oxic environmental conditions. **(e)** Th/U redox proxy, interpreted to show erratic reducing conditions throughout the Bernesga Mb. The table indicates the various proxy values indicative of different environmental conditions.

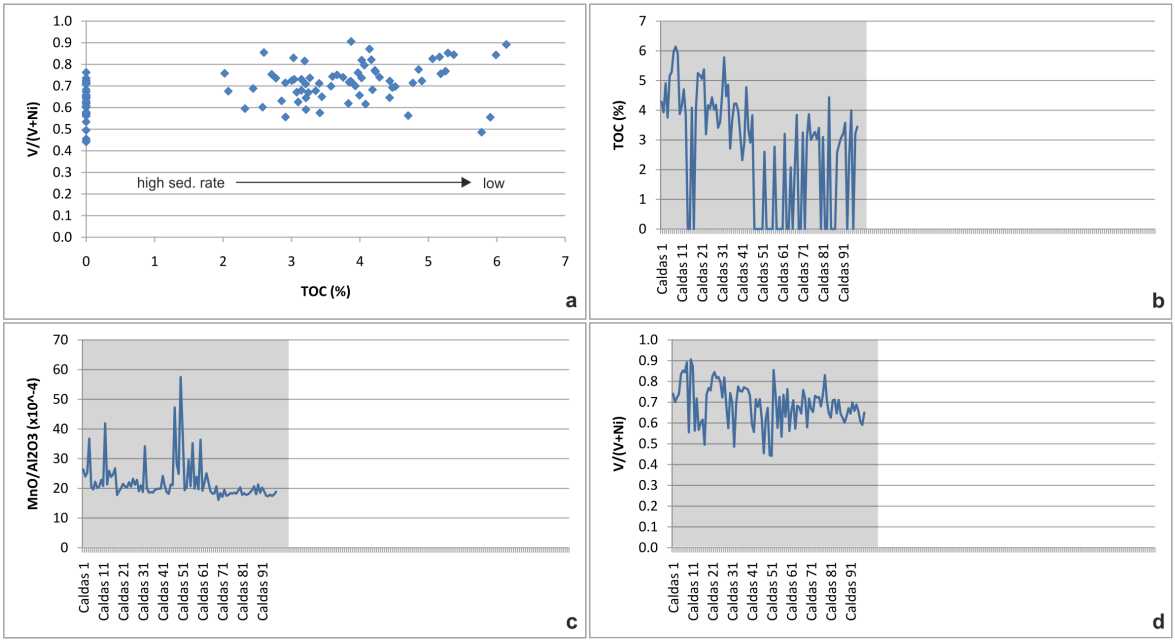

Figure 6.23 a) V/(V+Ni) *vs.* TOC (Arthur and Sagemann,1994). The V/(V+Ni) values have to be above 0.5 in order for the organic carbon to be preserved and not to become oxidised (Rimmer, 2004). The TOC values are seen to increase with the increasing reducing conditions, interpreted by higher V/(V+Ni) ratios. **b)** TOC values *vs.* stratigraphy. **c & d)** MnO/Al_2O_3 ratio and V/(V+Ni) *vs.* stratigraphy respectively.

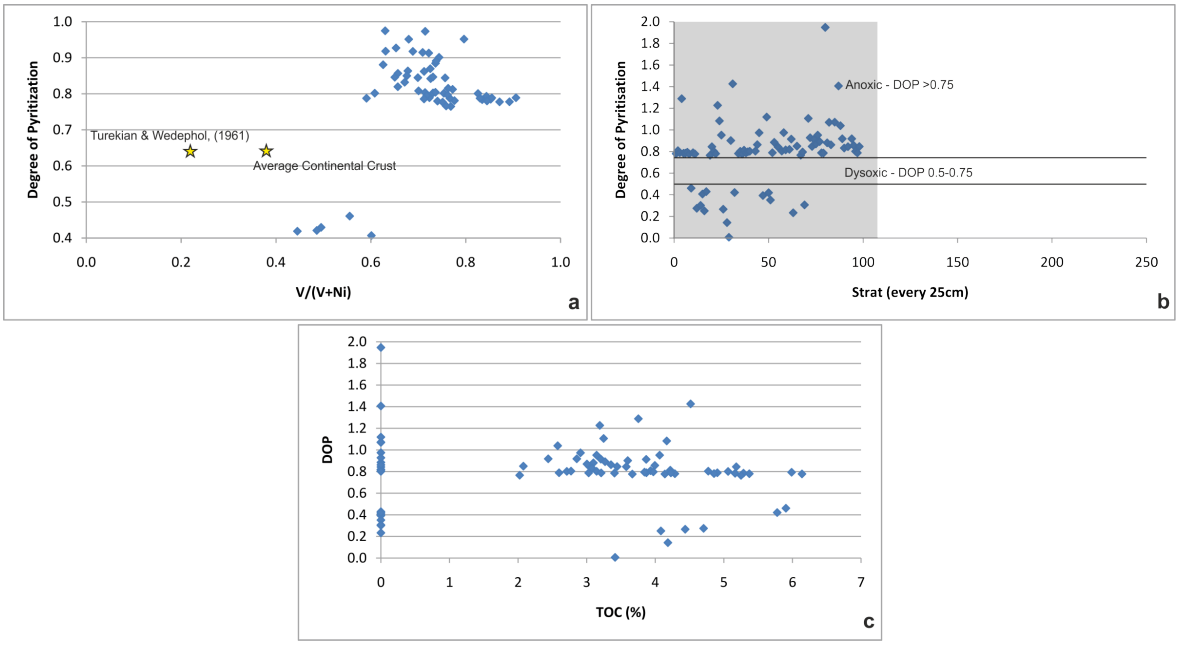

Figure 6.24 a) V/(V+Ni) *vs.* degree of pyritization (DOP), with the average shale of Turekian and Wedepohl (1961) and average continental crust for comparison. The Formigoso Fm. shows significantly elevated DOP values and V/(V+Ni) ratios relative to the international standards. **b)** DOP *vs.* stratigraphy, the lines indicating the varying redox states are after Wignall (1994). The majority of the Bernesga Mb. has DOP values indicative of anoxic conditions >0.75. A number of horizons are present within the oxic zone. **c)** Illustrates an idealized plot of a uniform DOP with increasing TOC.

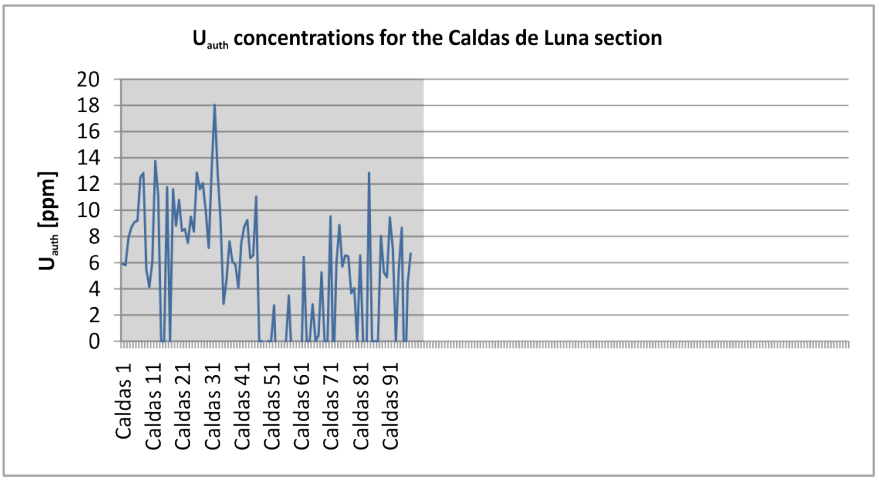

Figure 6.25 Authigenic U concentrations for the Caldas de Luna section. Note that the values are significantly elevated at the base relative to the overlying middle to upper Bernesga Mb. shales.

U_{auth} values are significantly enriched in the basal shales of the Bernesga Mb. The U_{auth} concentrations of the Caldas de Luna section (see **Figure 6.26**) are regarded to relate to the highly 'euxinic' conditions as indicated by the previously interpreted V/(V+Ni) of the Caldas de Luna section (see **Figure 6.22** and **6.23**). The average U_{auth} concentrations for the Bernesga Mb. equate to ~5 ppm, whereas the absolute U concentrations average at ~11 ppm. Therefore the U_{auth} concentrations make up ~45% of the total U values analysed. These high overall concentrations of the U_{auth} are associated to the reducing conditions of the environment at the time of deposition.

6.4.1.3 La Majua section

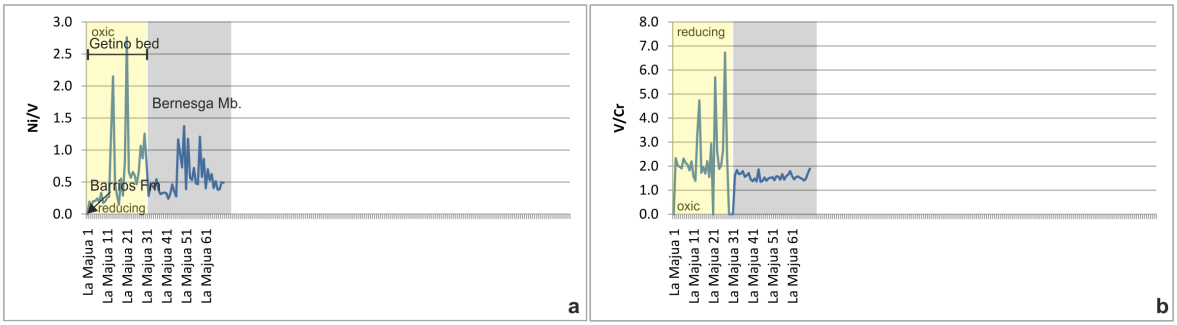

Figure 6.26 (a) the Ni/V ratio of Jones and Manning (1994), the lowest values are observed within the Getino Beds, with a number of elevated horizons towards the top suggesting an increased oxygenation of the environment. The base of the Bernesga Mb. displays low values indicating an oxygen depleted environment of deposition, the values increase gradually throughout the Mb. **(b)** the V/Cr ratio of Jones and Manning (1994), the values are higher in the Getino Beds especially towards the top relative to the overlying Bernesga Mb. indicating extreme reducing conditions. This interpretation does not concur with the field observations of the Getino Beds (see text). The Bernesga Mb. has relatively consistent values throughout.

The values of the Ni/V and V/Cr redox ratios of Jones and Manning (1994) are used to interpret that the sediments of the Getino Beds were deposited under elevated reducing conditions compared to the overlying Bernesga Mb. (see **Figure 6.26**). This interpretation is clearly contradicted by the field observations, as the Getino Beds are heavily bioturbated, indicating an oxic environment during the time of deposition. However, the Ni/V ratios of the Getino Beds do display a number of peaks interpreted to represent an oxygen-rich environment of deposition. The basal shales of the Bernesga Mb. are highly reduced at the base (see **Figure 6.26a**). When applying the V/Cr proxy, the Getino Beds are displaying a higher state of anoxia then the basal shales of the Bernesga Mb. This interpretation again conflicts with the field observations of heavy bioturbation. The V/Sc ratio of Jones and Manning (1994) indicates that the Getino beds were deposited under an oxic to dysoxic environment. It also suggests that the Bernesga Mb. is entirely oxic (see **Figure 6.27b**). When the V/(V+Ni) redox proxy of Hatch and Leventhal (1992) is interpreted, it too suggests that the Getino Beds were formed under elevated reducing conditions relative to the Bernesga Mb. The U/Th ratio in this instance rightfully infers, that the Getino Beds are deposited under oxic environmental conditions and the Bernesga Mb. under dysoxic to anoxic conditions. The Th/U redox proxy insinuates that all sediments at the La Majua section were affected by prevailing anoxic conditions. The V/(V+Ni) and U/Th redox proxies are here the most effective tools for reconstructing the palaeoenvironmental redox conditions.

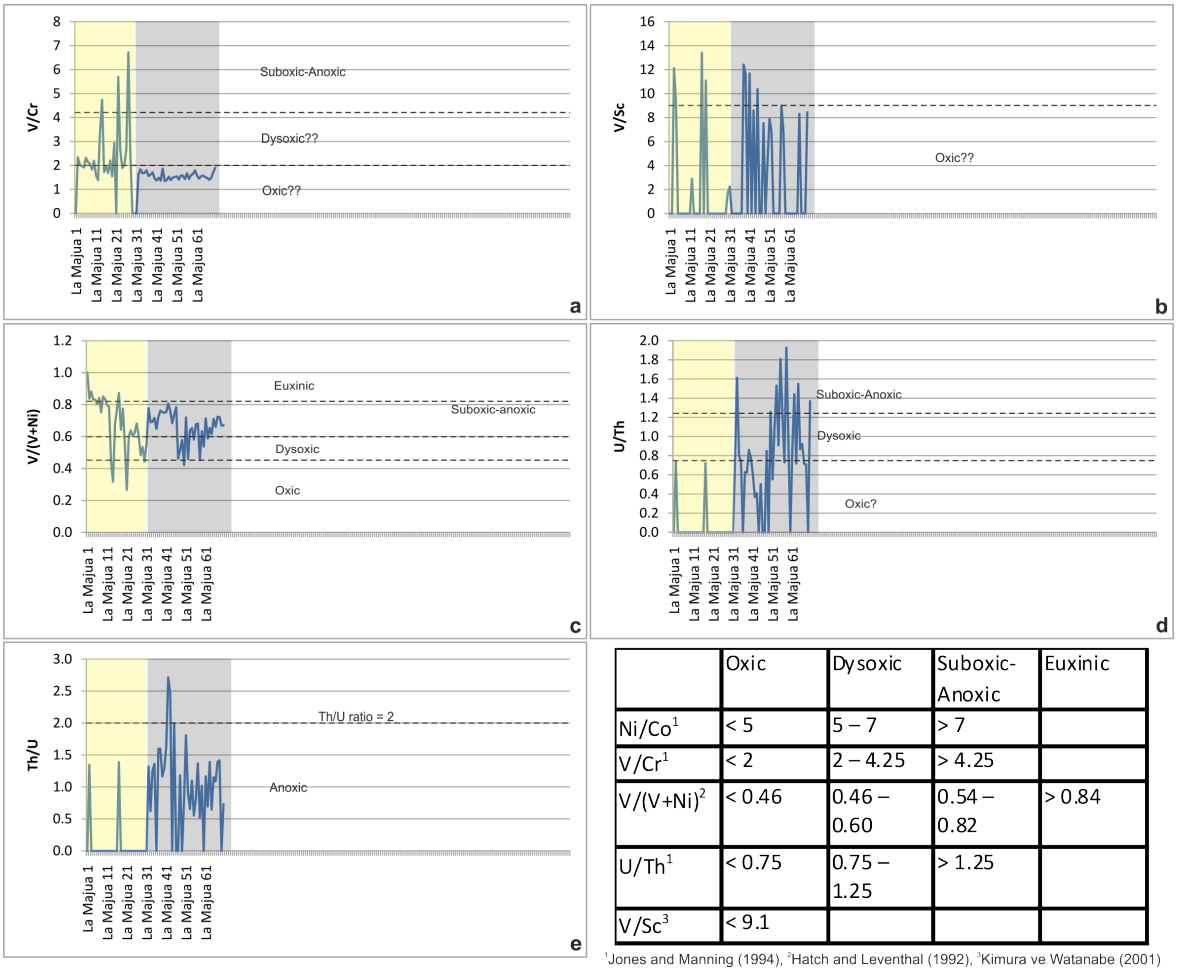

	Oxic	Dysoxic	Suboxic-Anoxic	Euxinic
Ni/Co[1]	< 5	5 – 7	> 7	
V/Cr[1]	< 2	2 – 4.25	> 4.25	
V/(V+Ni)[2]	< 0.46	0.46 – 0.60	0.54 – 0.82	> 0.84
U/Th[1]	< 0.75	0.75 – 1.25	> 1.25	
V/Sc[3]	< 9.1			

[1]Jones and Manning (1994), [2]Hatch and Leventhal (1992), [3]Kimura ve Watanabe (2001)

Figure 6.27 Various proxies used to reconstruct palaeoenvironmental redox conditions. **(a)** V/Cr ratios, illustrating the elevated reducing conditions for the Getino Beds relative to the overlying Bernesga Mb. The sediments of the Bernesga Mb. are here plotted within the oxic zone. **(b)** V/Sc ratios suggesting elevated reducing environments for the Getino Beds and oxic environmental conditions for the overlying Bernesga Mb. **(c)** V/(V+NI) redox proxy, again the sediments of the Getino Beds are displaying higher reducing conditions than the overlying Bernesga Mb. The Bernesga Mb. shows the progressive oxygenation of the environment from the near 'euxinic' base to the 'suboxic' top. **(d)** U/Th values contradicting all other ratios, correctly indicating that the Getino Beds are forming under oxygenated conditions and the vast majority of the Bernesga Mb. is deposited under dysoxic-anoxic environment of deposition. **(e)** Th/U redox proxy, interpreted to show reducing environmental conditions for the Getino Beds, and anoxic conditions of the Bernesga Mb. The table indicates the various proxy values indicative of different environmental conditions.

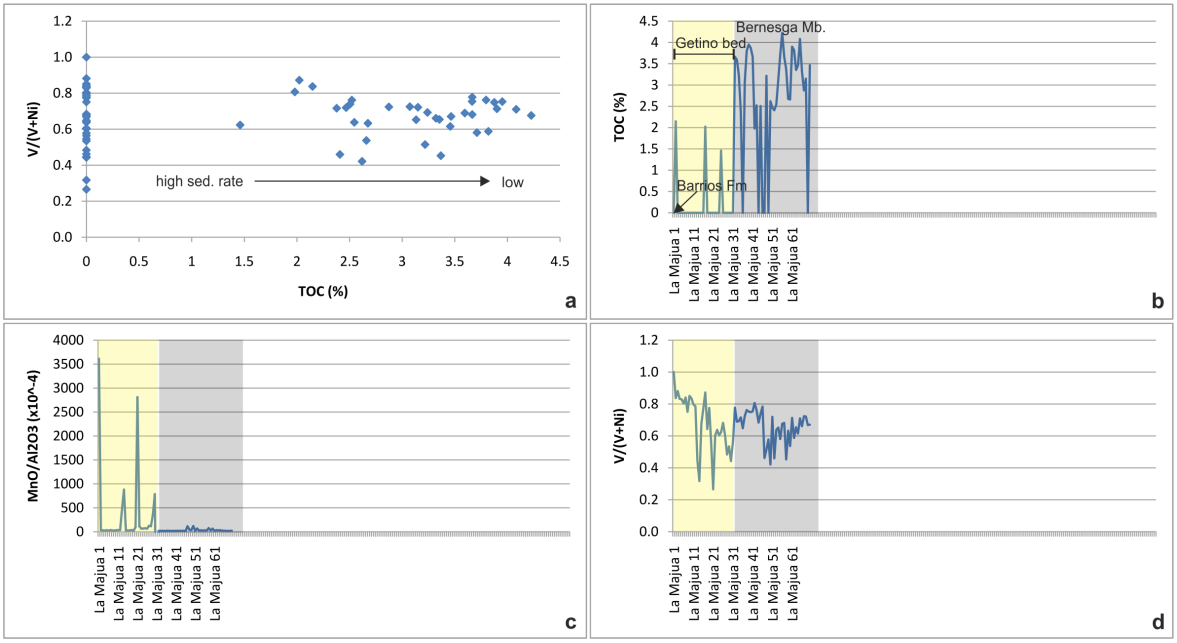

Figure 6.28 a) V/(V+Ni) *vs.* TOC (Arthur and Sagemann,1994) The V/(V+Ni) values have to be above 0.5 in order for the organic carbon to be preserved and not oxidised (Rimmer, 2004). The TOC values are seen to increase with the increasing reducing conditions, interpreted by higher V/(V+Ni) ratios. **b)** TOC values *vs.* stratigraphy. **c & d)** MnO/Al_2O_3 ratio and V/(V+Ni) *vs.* stratigraphy respectively.

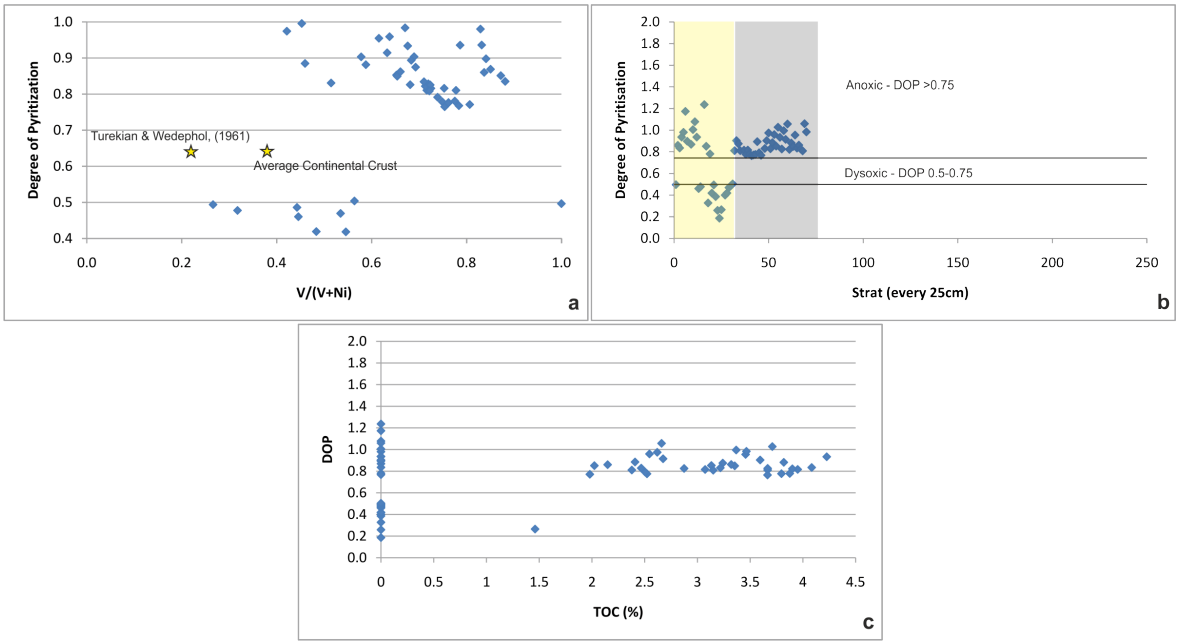

Figure 6.29 a) V/(V+Ni) *vs.* degree of pyritization (DOP), with the average shale of Turekian and Wedepohl (1961) and average continental crust for comparison. The Formigoso Fm. shows significantly elevated DOP values and V/(V+Ni) ratios relative to the international standards. In contrast, the Getino Beds show substantial depletions of the DOP values relative to the international standards. **b)** DOP *vs.* stratigraphy, the lines indicating the varying redox states are after Wignall (1994). The base of the Getino Beds display DOP value >0.75, indicating anoxic conditions, the top of the beds show values <0.5 suggesting oxygenation of the sediments. The majority of the Bernesga Mb. has DOP values indicative of anoxic conditions >0.75. **c)** Illustrates an idealized plot of a uniform DOP with increasing TOC.

The majority of the basal Getino Beds have DOP values >0.75 indicating that these sediments were forming under reducing conditions, hence contradicting the heavily bioturbated field observations. However, the top of the Getino Beds display DOP values <0.5 suggesting oxygenation of the sediments. The entirety of the Bernesga Mb. is set within the anoxic regime with

DOP values >0.75 (see **Figure 6.29b**). The shales of the Bernesga Mb. have higher DOP and V/(V+Ni) values relative to the average shale of Turekian and Wedepohl (1961) and the upper continental crust (see **Figure 6.29a**). Varying levels of organic content do not necessarily affect the redox state (see **Figure 6.29c**), however, typically higher levels of TOC lead to an increased redox state as mentioned previously (**Chapter 6.4.1.1**).

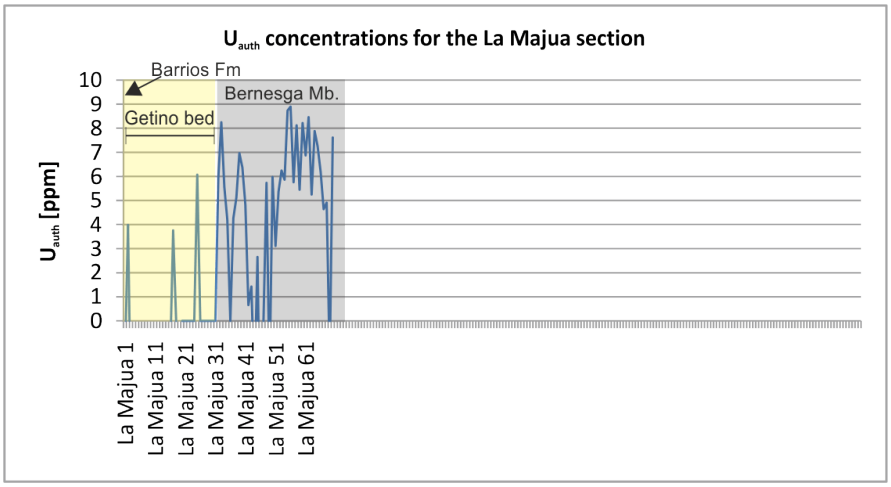

Figure 6.30 Authigenic U concentrations for the La Majua section. Note that the U_{auth} concentrations are significantly depleted in the oxygen rich sediments of the Getino Beds relative to the Bernesga Mb. shales.

It is important to note that the U_{auth} concentrations within the Getino Beds are extremely low (see **Figure 6.30**). This interpretation is enforced by the strong bioturbation of the sediments, suggesting increased amounts of oxygen in the sediments. The U_{auth} concentrations are enriched in the basal shales of the Bernesga Mb. relating to the high ('euxinic') redox conditions as indicated by the previously interpreted V/(V+Ni) ratios (see **Figure 6.27** and **6.28**). The average U_{auth} concentrations for the Bernesga Mb. equate to ~4.6 ppm, whereas the absolute U concentrations average at ~9 ppm. Therefore the U_{auth} constitutes up to ~51% of the total U observed.

6.4.1.4 Sena de Luna section

The values of the Ni/V and V/Cr redox ratios of Jones and Manning (1994) are used to interpret reducing conditions for the Getino Beds compared to the seemingly more oxygenated Bernesga shales (see **Figure 6.31**). However, the V/Cr ratios of the Getino Beds do display a horizon interpreted to represent an oxygen rich environment of deposition. The basal shales of the Bernesga Mb. are highly reduced at the base followed by a progressive oxygenation of the environment towards the top (see **Figure 6.31**). The V/Sc ratios indicate that the Getino beds were

deposited under an oxic environment. It also suggests that the Bernesga Mb. is predominantly deposited under anoxic conditions (see **Figure 6.32b**). When the V/(V+Ni) redox proxy of Hatch and Leventhal (1992) is interpreted, it too suggested that the Getino Beds were forming under elevated reducing conditions relative to the overlying Bernesga Mb. The Bernesga Mb. is deposited under borderline 'euxinic' to 'anoxic' conditions. The U/Th ratio in this instance rightfully infers that the Getino Beds are deposited under oxic environmental conditions and the Bernesga Mb. under elevated reducing conditions. The Th/U redox proxy may lead to the assumption, that the majority of the sediments analysed at the Sena de Luna section were affected by prevailing anoxic conditions. However, the proxy suggests that the basal Bernesga Mb. shales were deposited under oxic conditions. The V/(V+Ni) and U/Th redox proxies are here the most effective for reconstructing the palaeoenvironmental redox conditions. The proxies that determine the Getino Beds were deposited under reducing conditions contradict the field observations, as the Getino Beds are significantly bioturbated indicating an oxic environment during the time of deposition.

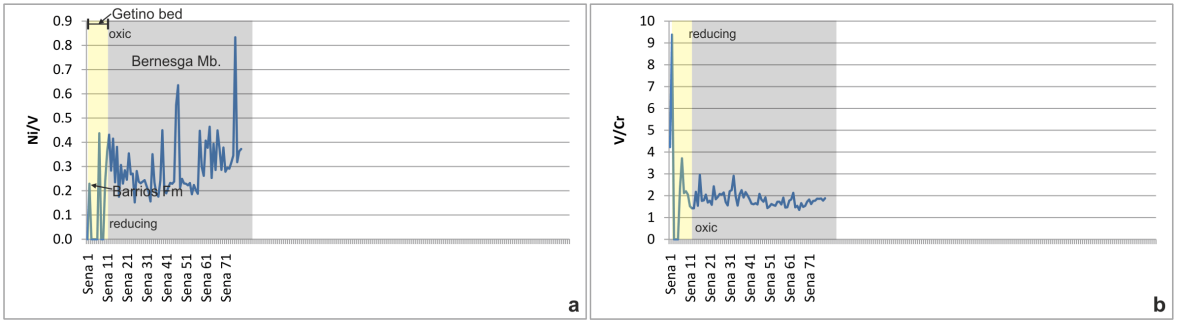

Figure 6.31 (a) the Ni/V ratio of Jones and Manning (1994), the lowest values are observed within the Getino Beds, with a number of elevated horizons towards the top suggesting an increased oxygenation of the environment. The base of the Bernesga Mb. displays low values indicating an oxygen depleted environment of deposition, the values increase erratically throughout the Mb. **(b)** the V/Cr ratio of Jones and Manning (1994), the values are higher in the Getino Beds especially at the base relative to the overlying Bernesga Mb. indicating extreme reducing conditions. This interpretation does not concur with the field observations of the Getino Beds. The Bernesga Mb. has relatively consistent values throughout.

The majority of the base of the Getino Beds have DOP values <0.5 indicating an oxic environment of deposition, concurring with the heavy bioturbation observed in the field. The entirety of the Bernesga Mb. is set within the anoxic regime with DOP values >0.75 (see **Figure 6.34b**). The shales of the Bernesga Mb. have higher DOP and V/(V+Ni) values relative to the average shale of Turekian and Wedepohl (1961) and the upper continental crust (see **Figure 6.34a**).

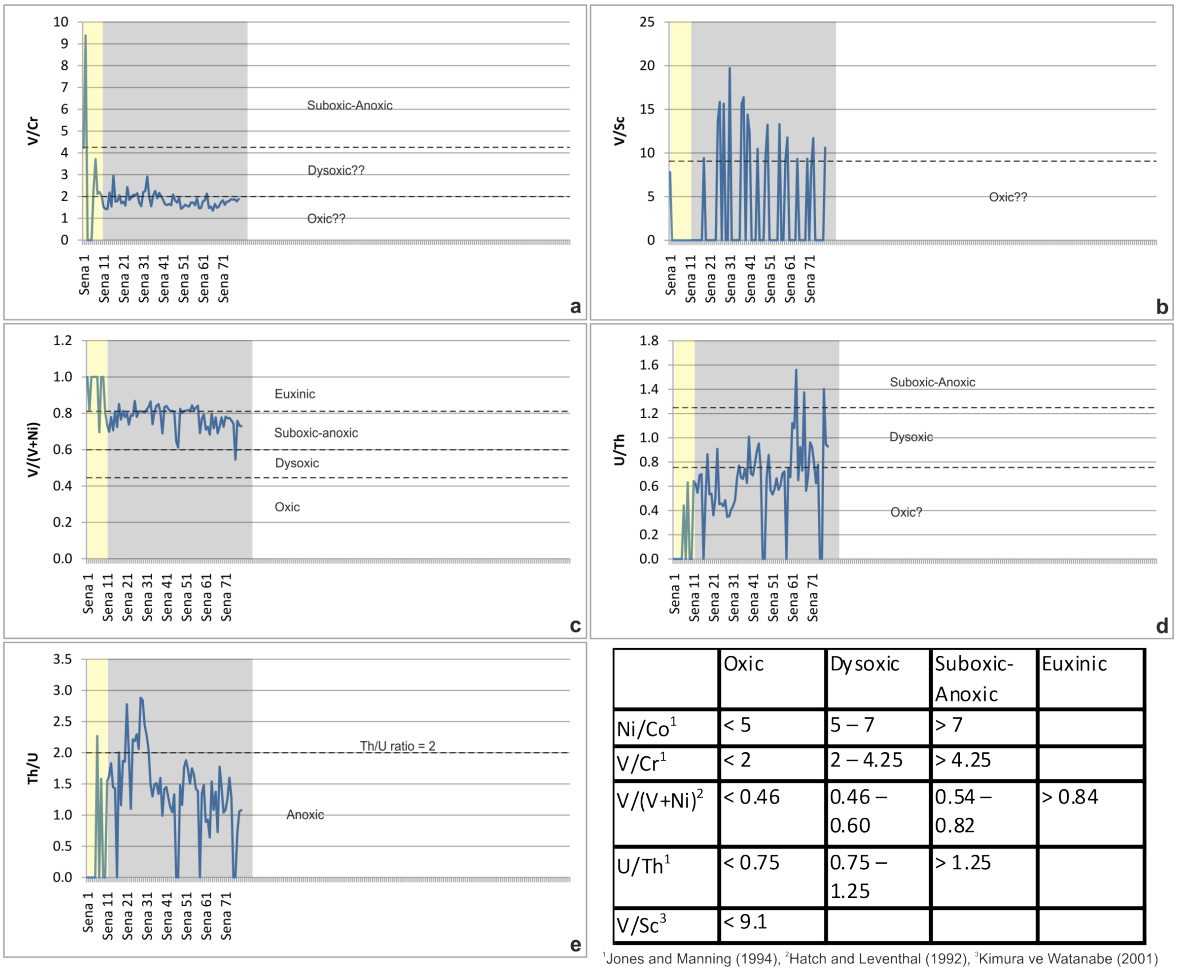

	Oxic	Dysoxic	Suboxic-Anoxic	Euxinic
Ni/Co[1]	< 5	5 – 7	> 7	
V/Cr[1]	< 2	2 – 4.25	> 4.25	
V/(V+Ni)[2]	< 0.46	0.46 – 0.60	0.54 – 0.82	> 0.84
U/Th[1]	< 0.75	0.75 – 1.25	> 1.25	
V/Sc[3]	< 9.1			

[1]Jones and Manning (1994), [2]Hatch and Leventhal (1992), [3]Kimura ve Watanabe (2001)

Figure 6.32 Various proxies used to reconstruct palaeoenvironmental redox conditions. **(a)** V/Cr ratios, illustrating the elevated reducing conditions for the Getino Beds relative to the overlying Bernesga Mb. The sediments of the Bernesga Mb. are here plotting predominantly within the oxic zone. **(b)** V/Sc ratios suggesting an oxic environment of deposition for the Getino Beds and anoxic environmental conditions for the overlying Bernesga Mb. **(c)** V/(V+NI) redox proxy, again the sediments of the Getino Beds are displaying higher reducing conditions than the overlying Bernesga Mb. The Bernesga Mb. shows the progressive oxygenation of the environment from the near 'euxinic' base to the 'suboxic' top. **(d)** U/Th values indicate that the Getino Beds are forming under oxygenated conditions and the vast majority of the Bernesga Mb. is deposited under an oxic to dysoxic-anoxic environment of deposition. **(e)** Th/U redox proxy, interpreted to show reducing environmental conditions for the Getino Beds and anoxic conditions of the Bernesga Mb. However, the values for the base of the Bernesga Mb. suggest oxic conditions. The table indicates the various proxy values indicative of different environmental conditions.

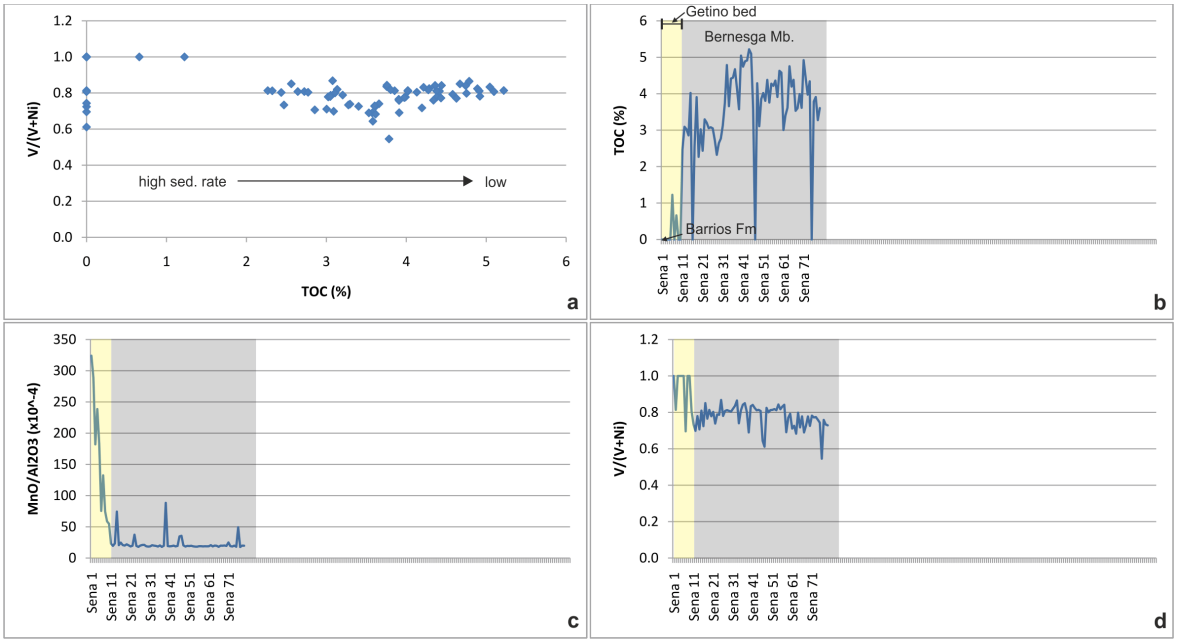

Figure 6.33 a) V/(V+Ni) *vs.* TOC, the higher the TOC values the lower the sedimentation rate (Arthur and Sagemann,1994), the V/(V+Ni) values have to be above 0.5 in order for the organic carbon to be preserved and not oxidised (Rimmer, 2004). The TOC values are seen to increase with the increasing reducing conditions, interpreted by higher V/(V+Ni) ratios. **b)** TOC values *vs.* stratigraphy. **c & d)** MnO/Al_2O_3 ratio and V/(V+Ni) *vs.* stratigraphy respectively.

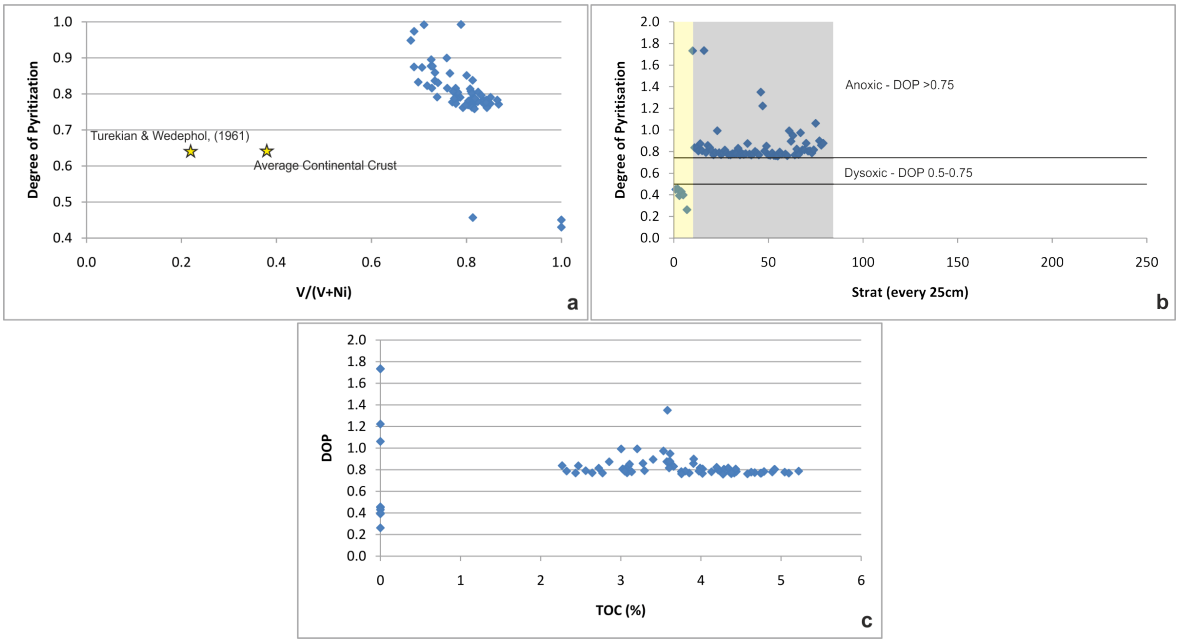

Figure 6.34 a) V/(V+Ni) *vs.* degree of pyritization (DOP), with the average shale of Turekian and Wedepohl (1961) and average continental crust for comparison. The Formigoso Fm. shows significantly elevated DOP values and V/(V+Ni) ratios relative to the international standards. **b)** DOP *vs.* stratigraphy, the lines indicating the varying redox states are after Wignall (1994). The Getino Beds display DOP values <0.5, indicating oxic conditions. The majority of the Bernesga Mb. has DOP values indicative of anoxic conditions >0.75. **c)** Illustrates an idealized plot of a uniform DOP with increasing TOC.

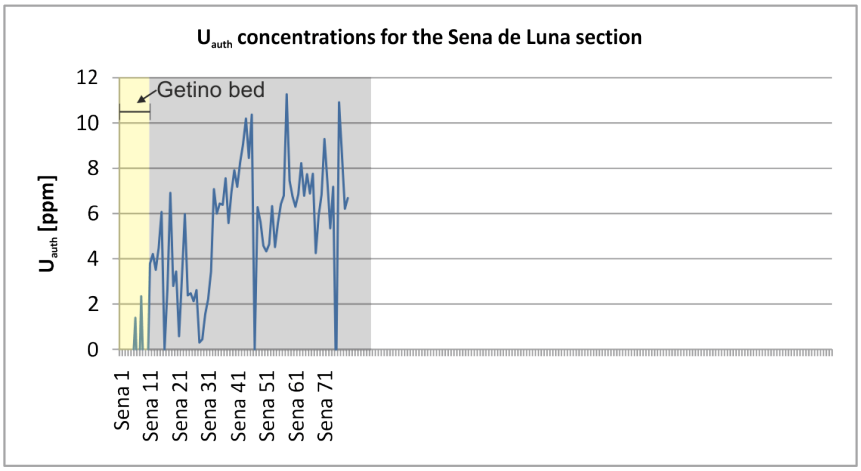

Figure 6.35 Authigenic U concentrations for the Sena de Luna section. Note that the U_{auth} concentrations are significantly depleted in the oxygen rich sediments of the Getino Beds relative to the Bernesga Mb. shales.

The U_{auth} concentrations for the Getino beds are considerably lower than the overlying Bernesga Mb. shales (see **Figure 6.35**). The Getino Beds are heavily bioturbated as determined by field observations, indicating the high oxygen content of the sediments. The shales at the base of the Bernesga Mb. show relatively low concentrations of U_{auth} in contrast to the elevated values of the middle to upper Bernesga Mb. The high amount of U_{auth} present within the upper part of the Bernesga Mb. relates to the high redox conditions 'anoxic' to 'euxinic' as indicated by the previously interpreted V/(V+Ni) ratios (see **Figure 6.32** and **6.33**). The average U_{auth} concentrations for the Bernesga Mb. equate to ~5.5 ppm. In contrast, the absolute U concentrations average at

~11 ppm. Therefore, the U_{auth} component forms ~50% of the total U values analysed for the Sena de Luna section.

6.4.1.5 Villanueva section

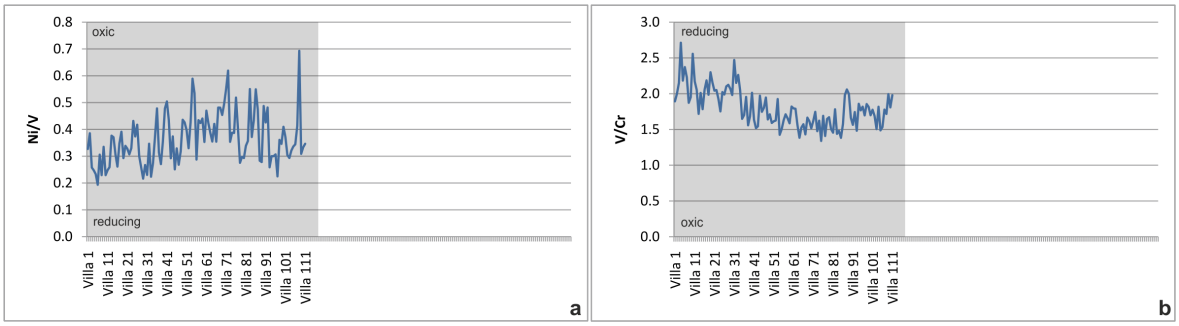

Figure 6.36 (a) the Ni/V ratio of Jones and Manning (1994), the lowest values are observed at the base of the Bernesga Mb. indicating a oxygen depleted environment of deposition, the values increase erratically throughout the Mb. **(b)** the V/Cr ratio of Jones and Manning (1994), the values are elevated at the base of the Bernesga Mb., with a few peaks indicating highly reducing conditions. These values deplete throughout the section and then become relatively stable before increasing again towards the top.

The Ni/V and V/Cr redox proxies of Jones and Manning (1994) were used to interpret that the basal shales of the Bernesga Mb. were deposited under reducing environmental conditions. The sediments become gradually more oxygenated towards the top of the Bernesga Mb (**Figure 6.36**). The various redox proxies V/Cr, V/Sc, V/(V+Ni), U/Th and Th/U of Jones and Manning (1994), Kimura and Watanabe (2001), Hatch and Leventhal (1992), Jones and Manning (1994) and Fertl (1979) respectively (see **Figure 6.37**), showed that there were heightened redox conditions, even 'euxinic', during the onset of black shale deposition. However, the V/Sc and U/Th ratios suggested that the parts of the Bernesga Mb. formed under oxygen rich environmental conditions. The Th/U ratios indicated that the entirety of the black shales formed under anoxic conditions. The Th/U proxy of Fertl (1979) and the V/(V+Ni) redox proxy of Hatch and Leventhal (1992) were deemed the most effective proxies in this instance for reconstructing the palaeoenvironmental conditions during the time of black shale deposition.

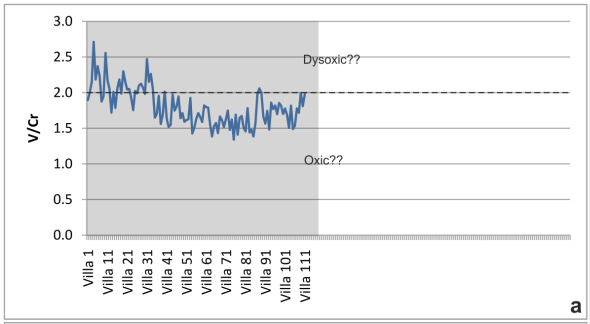

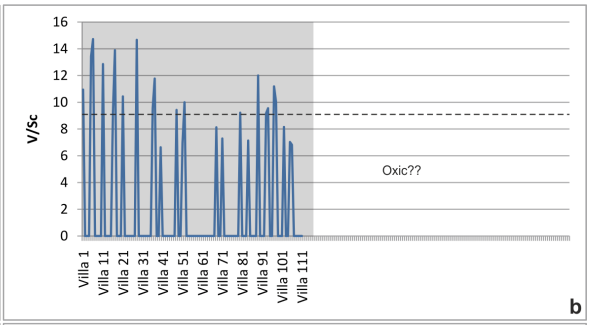

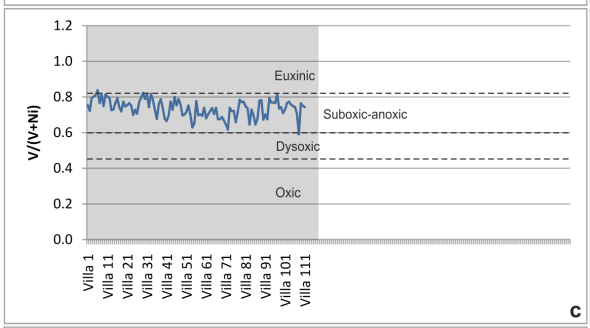

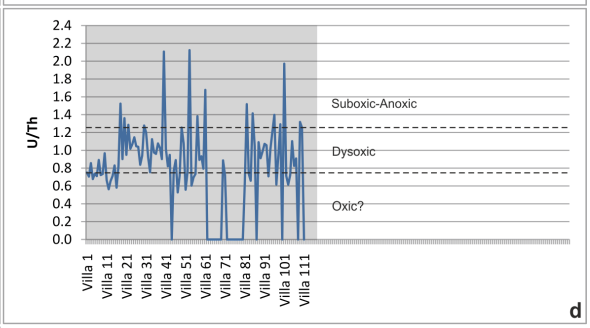

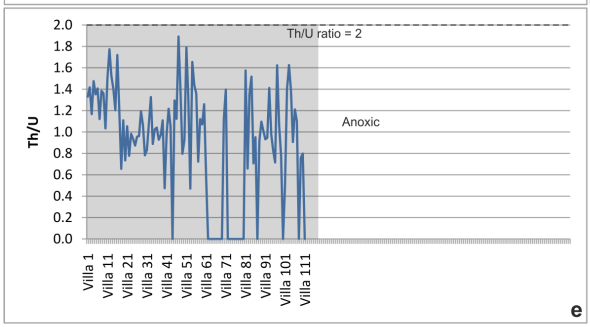

	Oxic	Dysoxic	Suboxic-Anoxic	Euxinic
Ni/Co[1]	< 5	5 – 7	> 7	
V/Cr[1]	< 2	2 – 4.25	> 4.25	
V/(V+Ni)[2]	< 0.46	0.46 – 0.60	0.54 – 0.82	> 0.84
U/Th[1]	< 0.75	0.75 – 1.25	> 1.25	
V/Sc[3]	< 9.1			

[1]Jones and Manning (1994), [2]Hatch and Leventhal (1992), [3]Kimura ve Watanabe (2001)

Figure 6.37 Various proxies used to reconstruct palaeoenvironmental redox conditions. **(a)** V/Cr ratios, illustrating the elevated reducing conditions at the base of the Bernesga Mb. the sediments are progressively oxygenated and then become slightly reduced towards the top of the Mb. **(b)** V/Sc ratios suggesting elevated reducing conditions at the base of the Bernesga Mb. the sediments are deposited under progressively oxygenated conditions towards the top of the Mb. **(c)** V/(V+NI) redox proxy, illustrating the progressive oxygenation of the environment from the 'euxinic' base to the 'suboxic' top. **(d)** U/Th values contradicting all other ratios, indicating that significant parts of the Formigoso Fm. are deposited under oxic environmental conditions. **(e)** Th/U redox proxy, interpreted to show erratic reducing conditions throughout the Bernesga Mb. The table indicates the various proxy values indicative of different environmental conditions.

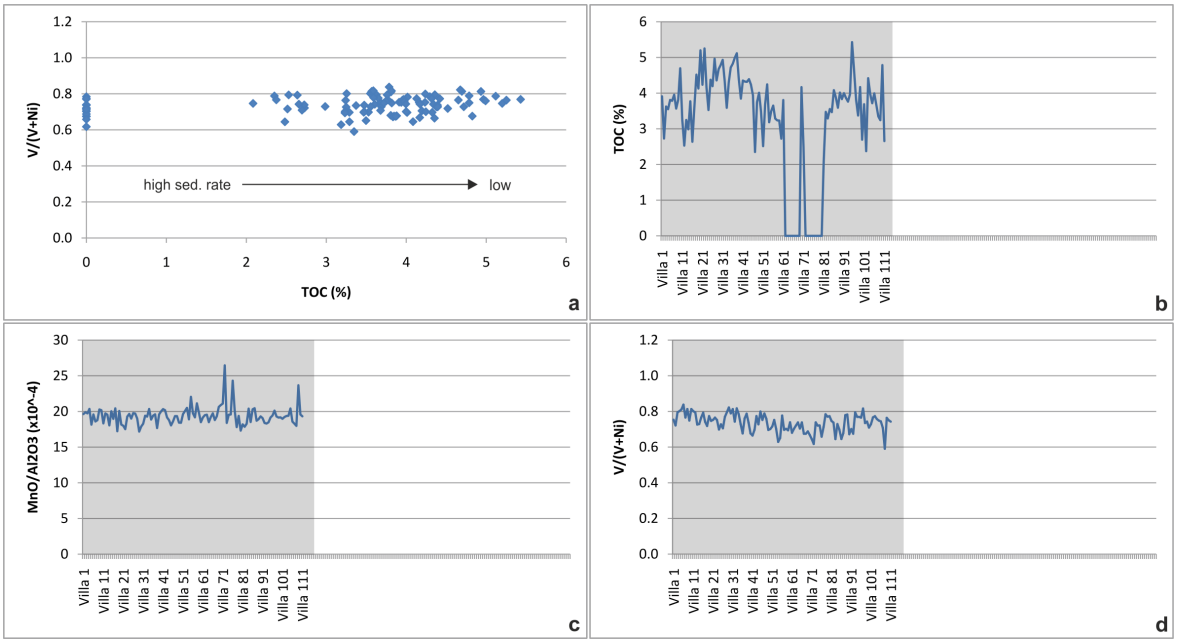

Figure 6.38 a) V/(V+Ni) *vs.* TOC, the higher the TOC values the lower the sedimentation rate (Arthur and Sagemann,1994), the V/(V+Ni) values have to be above 0.5 in order for the organic carbon to be preserved and not oxidised (Rimmer, 2004). The TOC values are seen to increase with the increasing reducing conditions, interpreted by higher V/(V+Ni) ratios. **b)** TOC values *vs.* stratigraphy. **c & d)** MnO/Al_2O_3 ratio and V/(V+Ni) *vs.* stratigraphy respectively.

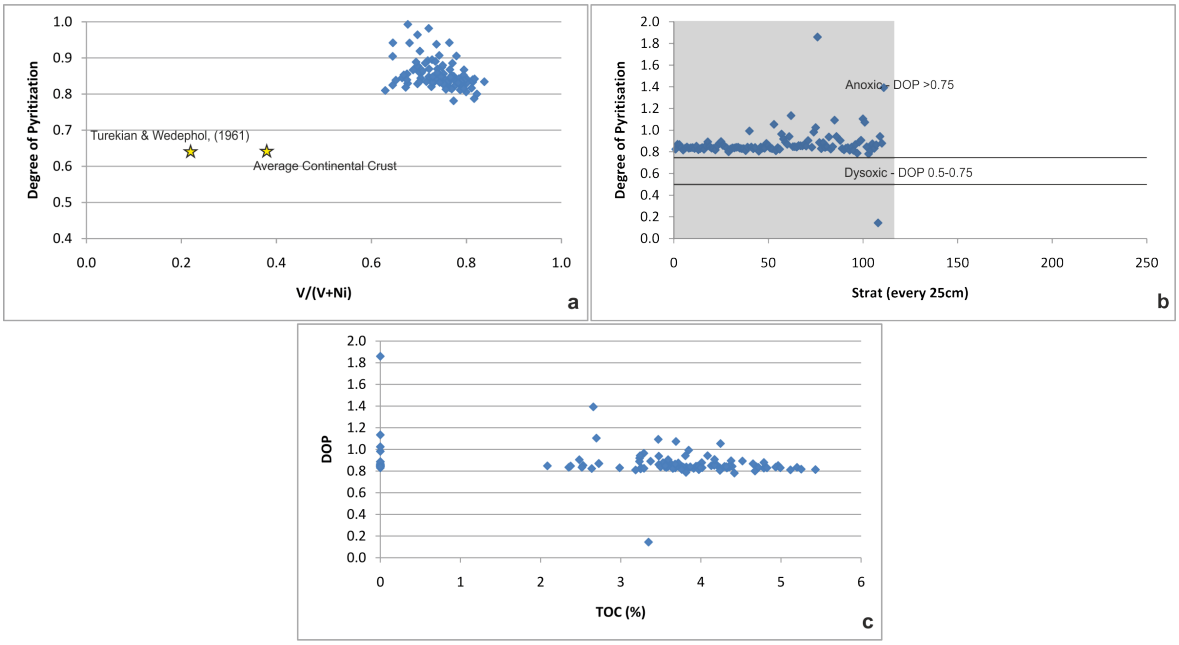

Figure 6.39 a) V/(V+Ni) *vs.* degree of pyritization (DOP), with the average shale of Turekian and Wedepohl (1961) and average continental crust for comparison. The Formigoso Fm. shows significantly elevated DOP values and V/(V+Ni) ratios relative to the international standards. **b)** DOP *vs.* stratigraphy, the lines indicating the varying redox states are after Wignall (1994). The majority of the Bernesga Mb. has DOP values indicative of anoxic conditions >0.75 other than one sample towards the top indicating oxic conditions. **c)** Illustrates an idealized plot of a uniform DOP with increasing TOC.

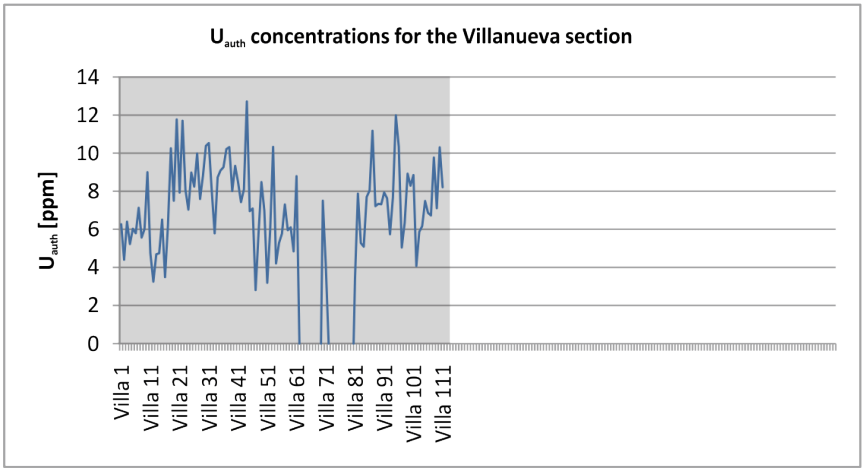

Figure 6.40 Authigenic U concentrations for the Villanueva section.

The majority of the shales of the Bernesga Mb. are within the Anoxic regime with DOP values >0.75 (see **Figure 6.39b**). The shales of the Bernesga Mb. have a higher DOP index and V(V+Ni) ratio in relation to the average shale of Turekian and Wedepohl (1961) and the upper continental crust (see **Figure 6.39a** displays that. The TOC levels vary significantly whereas the DOP values remain relatively consistent (see **Figure 6.39c**).

The U_{auth} concentrations of the Villanueva section are erratic. The basal shales contain a low amount of U_{auth}, comparable to the concentrations of the Sena de Luna section. The middle to upper part of the Bernesga Mb. contain higher U_{auth} concentrations. The elevated U_{auth} concentrations relate to the high redox conditions 'euxinic' as indicated by the previously interpreted V/(V+Ni) ratio (see **Figure 6.37** and **6.38**). The U_{auth} concentrations for the Bernesga Mb. average at ~5.7 ppm, whereas the absolute U concentrations average at ~11 ppm. Therefore, the U_{auth} fraction equates to ~52% of the absolute U concentrations analysed for the Villanueva section.

6.4.2 Palaeosalinity reconstruction

The palaeosalinity reconstructions were calculated following the method of Campbell and Williams (1965). The ratio of the elements Rb and K are used to interpret varying levels of salinity. The use of this elemental ratio is based on the assumption that marine shales contain higher Rb concentrations due to the increased concentrations of Rb in sea-water (0.12 ppm) relative to fresh water environments (0.0013ppm). The K concentrations are used to represent the clay fraction. The ratio values are interpreted as the following: **[1]** Rb/K ratio of ≤0.004 indicates fresh-water

conditions, **[2]** >0.004 to ≤0.006 suggests fresh-water to brackish conditions and, **[3]** >0.006 relates to fully marine developed environments.

Figure 6.41 Palaeosalinity reconstructions for the various localities using the Rb/K ratio, the dashed line values after Campbell and Williams (1965). Rb/K values above 0.004 indicate fresh water to brackish environments of deposition, whereas values above 0.006 are indicative of fully marine saline conditions. **(a)** Rb/K ratios from the Aralla section (241 samples). The Getino Beds are here interpreted to be fresh-water deposits, the Bernesga Mb. deposited under brackish conditions and the Villasimpliz Mb. under predominantly fresh-water conditions, **(b)** Rb/K ratios from the Caldas de Luna section (98 samples), the Bernesga Mb. is formed under brackish water conditions, with an gradational increase in salinity towards the top of the Mb. **(c)** Rb/K ratios from the La Majua section (70 samples), the Getino Beds were deposited under fresh-water conditions, the Bernesga Mb. under brackish conditions **(d)** Rb/K ratios from the Sena de Luna section (79 samples) here the Getino Beds show a salinity trend from brackish at the base to fresh-water at its top and **(e)** the Rb/K ratios from the Villanueva section (111 samples), the Bernesga Mb. is deposited under brackish water conditions, with a significant increase in salinity towards the top.

The sediments of the Getino Beds in most cases have been interpreted as fresh-water deposits. The black shales of the lower Bernesga Mb. were deposited under brackish-water conditions. The Caldas de Luna and Villanueva sections show elevated salinity levels towards the top of the Bernesga Mb., yet they never reach fully marine conditions. This interpretation contradicts the previously discussed classification scheme of Pearce *et al.* (2010), where it was concluded that the most basal shales of the Bernesga Mb. can be classified as 'fully marine sediments' (see **Chapter 6.2**). The Rb/K proxy suggests that the shales of the Formigoso Fm. were never subject to fully marine conditions. Under this assumption were the shales most likely confined to the 'restricted shelfal margins', which relates well to the basal transgressive puddle model of Wignall (1994). The

fact that certain redox element cycles or horizons are missing (i.e. V and U cycles laterally) at the base of a number of sections (for e.g. the La Majua section) could point towards certain palaeo-topographical effects, that would lead to a diachronous onset of deposition of the basal black shales belonging to the Bernesga Mb. in different areas. The overlying Villasimpliz Mb. is typified by an increased influx of terrestrially derived material, interpreted to be the response to an overall relative sea-level fall. The salinity levels reduce with the extensive fresh-water input from the Gondwanan hinterland.

6.4.3 Palaeohumidity reconstructions

The humidity proxy of SiO_2 *vs.* (Al_2O_3+K_2O+Na_2O) of Suttner and Dutta (1986) uses the relationship between the relative weathering resistant SiO_2 *vs.* the weathering prone oxides Al_2O_3, K_2O, Na_2O related to the degradation of feldspars under elevated chemical weathering conditions to approximate the relative sediment maturity. The Al_2O_3/TiO_2 proxy of Akul'shina (1976) is applied under the assumption that Al and Ti are relatively immobile in near-neutral (pH) environment conditions. It is considered that under pH levels of <4 and >10 aluminium is mobilised, whereas Ti is mobile under pH conditions of <2. Ti is known to replace Al in the clay lattice dependant on the prevailing intensity of chemical weathering. An Al_2O_3/TiO_2 ratio of ≤20 is used to interpret humid environmental conditions, >20 to ≤ 30 semi-humid and, >30 semi-arid.

6.4.3.1 Aralla section

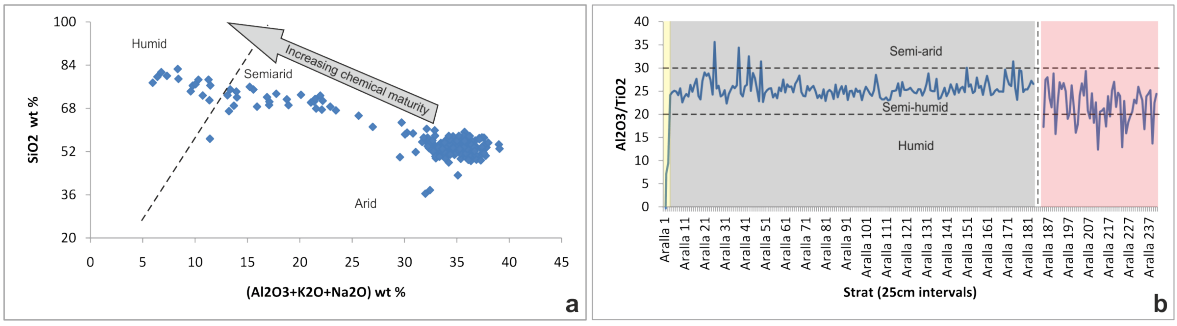

Figure 6.42 a) Bivariate SiO_2 *vs.* (Al_2O_3 +K_2O+Na_2O) palaeoclimate discrimination diagram, fields after Suttner and Dutta (1986). The shales of the Bernesga Mb. cluster towards the 'Arid' field, the Villasimpliz Mb. trends towards 'Humid' conditions **b**) The Al/Ti proxy of Akul'shina (1976) inferring palaeoclimatic conditions **[1]** ratios <20 represent humid environments, **[2]** 20–30 indicate semi-humid, and **[3]** >30 are related to semi-arid climatic settings. The Getino Beds are deposited under 'Humid' conditions, the Bernesga Mb. within a predominantly semi-humid enviroment and the Villasimpliz Mb. displays an erratic decline towards a 'Humid' palaeoenvironment.

Following the humidity reconstruction of Suttner and Dutta (1986), the Bernesga Mb. is seen to cluster towards the 'Arid' climatic conditions, whereas the Villasimpliz Mb. trends towards the

'Humid' environment (see **Figure 6.42 a**). This scenario is compatible with the larger scale geotectonic settings. The interpretation that the Bernesga Mb. was deposited under 'Arid' conditions during the lowermost Silurian, coincides with the southern palaeolatitude reconstruction of Scotese *et al*. (1999) see (**Figure 2.4** 'Geological Setting Chapter'). According to this palaeogeographical reconstruction the Iberian Peninsula is positioned to the north of the South Pole during the Early/Mid Silurian. A cool dry 'Arid' climate corresponds well with a polar to sub-polar setting. The sands of the upper Villasimpliz Mb. are trending towards 'semi-arid' to 'humid' environments. During the Mid Silurian the Iberian Peninsula drifted northwards (along with the northernmost rim of Gondwana) towards the palaeoequator, thus leading to an overall increase in temperature and humid climatic conditions. The palaeohumidity proxy of Akul'shina (1976) indicates that the Getino beds were deposited under a 'Humid' environment, the Bernesga Mb. under predominantly 'Semi-humid' and the Villasimpliz Mb. with increasingly 'Humid' climatic conditions (see **Figure 6.42 b**). This scenario is again compatible with the larger scale geotectonic plate configuration. With the increased humidity levels of the Getino Beds, it is interpreted that they were deposited during an interglacial period.

6.4.3.2 Caldas de Luna section

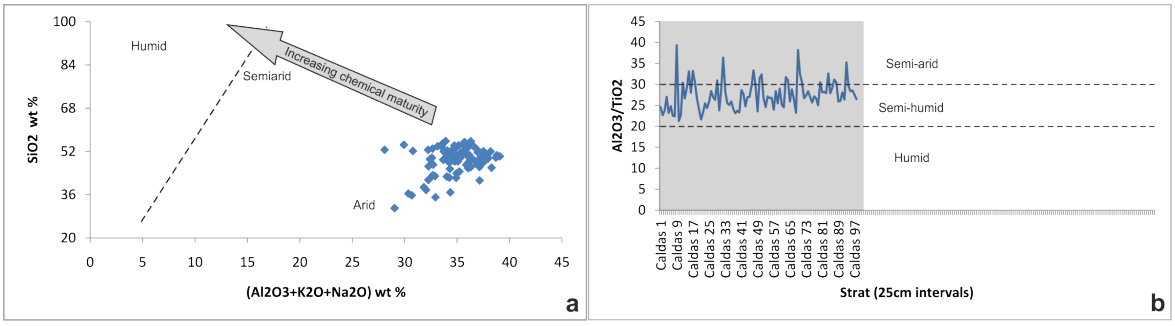

Figure 6.43 a) Bivariate SiO_2 *vs.* (Al_2O_3 +K_2O+Na_2O) palaeoclimate discrimination diagram, fields after Suttner and Dutta (1986). The shales of the Bernesga Mb. cluster towards the 'Arid' field. **b**) The Al/Ti proxy of Akul'shina (1976) inferring palaeoclimatic conditions **[1]** ratios <20 represent humid environments, **[2]** 20–30 indicate semi-humid, and **[3]** >30 are related to semi-arid climatic settings. The Bernesga Mb. is forming under predominantly semi-humid to semi-arid enviroments.

The humidity proxy of Suttner and Dutta (1986) determines that the Bernesga Mb. is deposited under 'Arid' climatic conditions (see **Figure 6.43 a**). The inferred 'arid' climatic conditions are again compatible with the polar setting described in **Chapter 6.4.3.1**. When applying the humidity proxy of Akul'shina (1976) it is interpreted that the Bernesga Mb. shales are deposited under fluctuating semi-humid to semi-arid climatic conditions (see **Figure 6.43 b**).

6.4.3.3 La Majua section

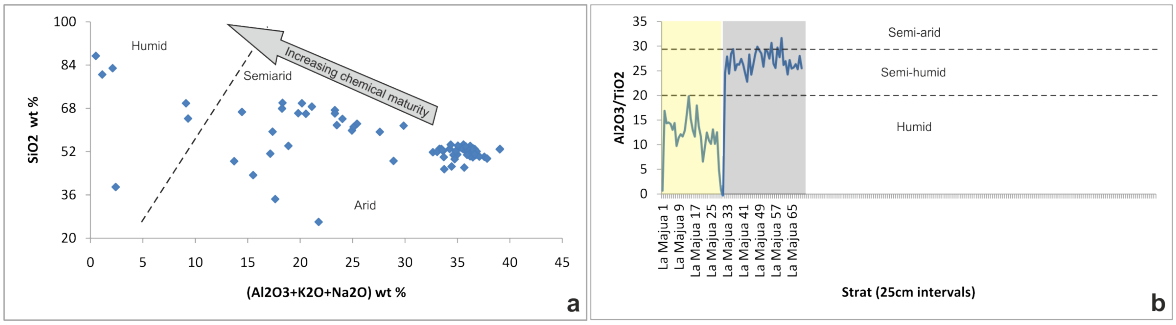

Figure 6.44 a) Bivariate SiO_2 *vs.* (Al_2O_3 +K_2O+Na_2O) palaeoclimate discrimination diagram, fields after Suttner and Dutta (1986). The shales of the Bernesga Mb. cluster towards the 'Arid' field, the Getino Beds trend towards 'Humid' conditions **b**) The Al/Ti proxy of Akul'shina (1976) inferring palaeoclimatic conditions **[1]** ratios <20 represent humid environments, **[2]** 20–30 indicate semi-humid, and **[3]** >30 are related to semi-arid climatic settings. The Getino Beds are affected by 'Humid' conditions, the Bernesga Mb. by a predominantly semi-humid environment.

The palaeohumidity proxy of Suttner and Dutta (1986), suggests that the Getino Beds are trending towards increasing humidity levels, the shales of the Bernesga Mb. cluster around the 'arid' field (see **Figure 6.44 a**). The increased humidity levels during the deposition of the Getino Beds is interpreted to be the response to fluctuating glacial – interglacial periods (Sachanski *et al.* 2010) with the Getino beds forming under the latter. The 'arid' conditions of the Bernesga Mb. are compatible with the polar setting as described above. The Al_2O_3/TiO_2 proxy of Akul'shina (1976), is used to interpret that the Getino beds are being deposited under 'Humid' climatic conditions and the Bernesga Mb. under predominantly 'Semi-humid' conditions (see **Figure 6.44 b**).

6.4.3.4 Sena de Luna section

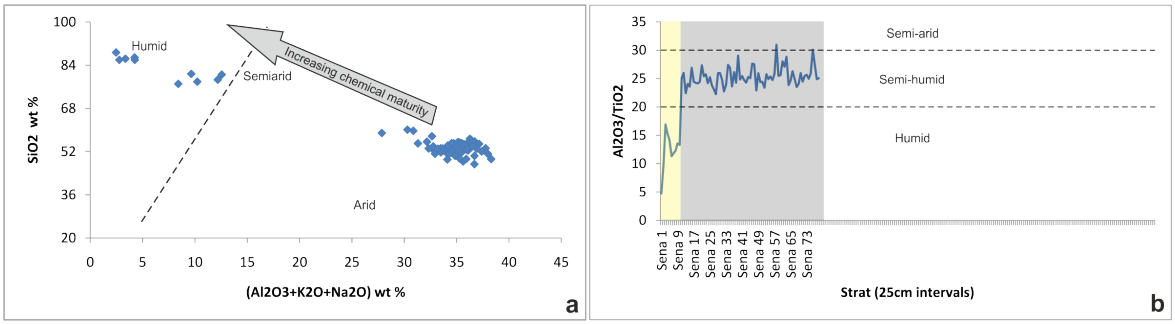

Figure 6.45 a) Bivariate SiO_2 *vs.* (Al_2O_3 +K_2O+Na_2O) palaeoclimate discrimination diagram, fields after Suttner and Dutta (1986). The shales of the Bernesga Mb. cluster towards the 'Arid' field, the Getino Beds trend towards 'Humid' conditions **b**) The Al/Ti proxy of Akul'shina (1976) inferring palaeoclimatic conditions **[1]** ratios <20 represent humid environments, **[2]** 20–30 indicate semi-humid, and **[3]** >30 are related to semi-arid climatic settings. The Getino Beds are affected by 'Humid' conditions and the overlying Bernesga Mb. by a semi-humid environment.

The palaeohumidity proxy of Suttner and Dutta (1986), suggests that the Getino Beds were deposited under increasing humidity levels, the shales of the Bernesga Mb. cluster around the 'arid' field (see **Figure 6.45 a**). The increased humidity levels during the deposition of the Getino Beds is

interpreted to be the response to fluctuating glacial – interglacial periods (Sachanski *et al.* 2010), with the Getino beds forming under the latter. The 'arid' conditions of the Bernesga Mb. are compatible with the geotectonic setting of the lower Silurian described above. The Al_2O_3/TiO_2 proxy of Akul'shina (1976), is used to interpret that the Getino beds are being deposited under 'Humid' climatic conditions and the Bernesga Mb. under predominantly 'Semi-humid' conditions (see **Figure 6.45 b**).

6.4.3.5 Villanueva section

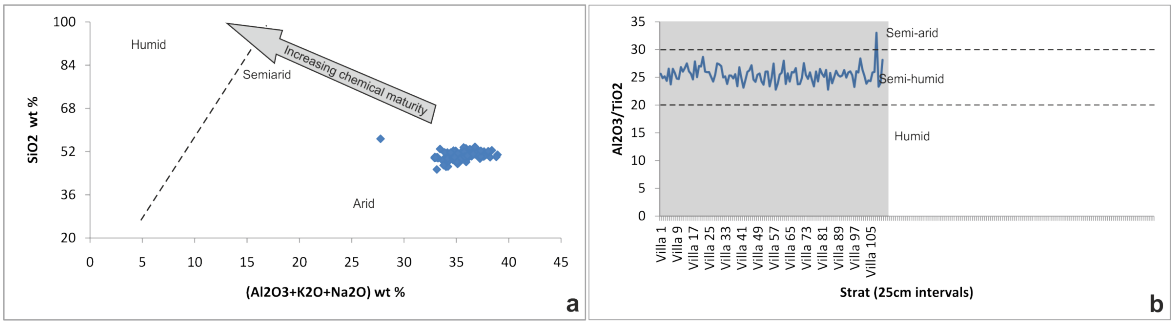

Figure 6.46 a) Bivariate SiO_2 *vs.* (Al_2O_3 +K_2O+Na_2O) palaeoclimate discrimination diagram, fields after Suttner and Dutta (1986). The shales of the Bernesga Mb. cluster towards the 'Arid' field. **b**) The Al/Ti proxy of Akul'shina (1976) inferring palaeoclimatic conditions **[1]** ratios <20 represent humid environments, **[2]** 20–30 indicate semi-humid, and **[3]** >30 are related to semi-arid climatic settings. The Bernesga Mb. is affected by predominantly semi-humid environmental conditions.

The humidity proxy of Suttner and Dutta (1986) determines that the Bernesga Mb. is deposited under 'Arid' climatic conditions (see **Figure 6.46 a**). The inferred 'arid' climatic conditions are again compatible with the polar setting described in **Chapter 6.4.3.1**. When applying the humidity proxy of Akul'shina (1976) it is interpreted that the Bernesga Mb. shales are deposited under predominantly semi-humid environmental conditions (see **Figure 6.46 b**).

6.4.4 Clay typing

The following section utilises a number of cross-plots and ternary diagrams in order to discriminate the common rock forming minerals present, **[1]** the Th vs. K cross plot of Schlumberger (2009), **[2]** the SiO_2 vs. Al_2O_3 and Fe_2O_3 vs. Al_2O_3 plots of Cullers and Podkovyrov (2000) and **[3]** SiO_2-Fe_2O_3-Al_2O_3 ternary plot of Konhauser (1998).

The Schlumberger (2009) plot discriminates the clay mineralogy using the varying concentrations of the Th and K_2O present (see **Figure 6.47**). Only the shales of the Bernesga Mb. were plotted in this diagram. Lateral variations in the clay mineralogy can be seen across the southern Cantabrian

region. The majority of the locations show a maturity trend towards the 100% kaolinite, montmorillonite and illite 'clay line' with the bulk of the shale data residing within the illite/mixed layer clay zones. The Villanueva and la Majua localities (see **Figure 6.47 c** and **e**) show a mass grouping of the shale data in the Illite zone, only one sample in each case sits within the '100% kaolinite, montmorillonite and illite 'clay line''. It is interpreted that the shales at these locations are less mature, the local source sediments may have undergone a lower degree of chemical weathering.

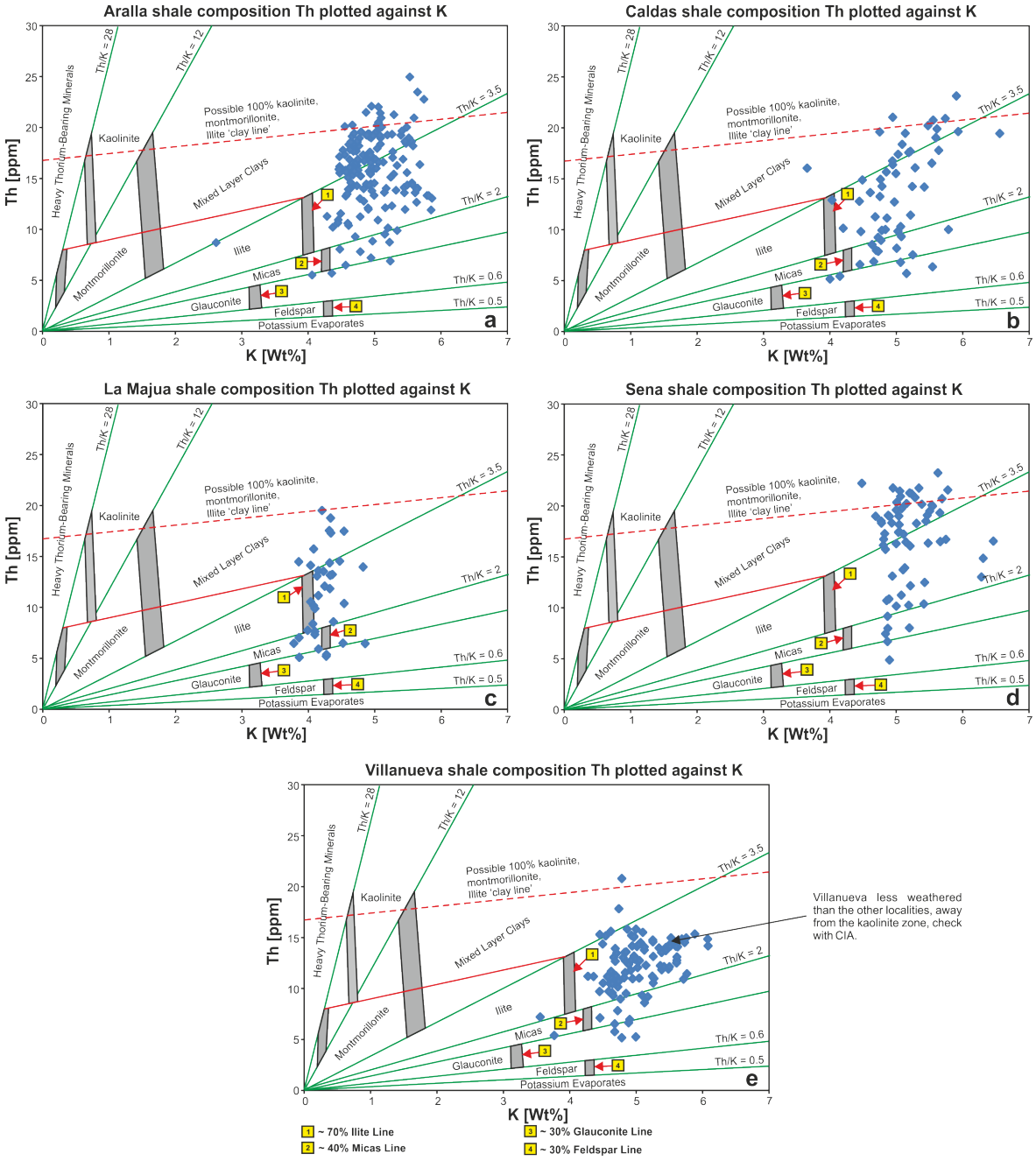

Figure 6.47 Cross-plot of K_2O (Wt%) vs. Th (ppm) after Schlumberger (2009), discriminating common rock forming minerals according to their thorium and potassium concentrations. Only the shale data was used from each of the five localities. **a**) Aralla section, the samples show a compositional maturity trend towards the 100% kaolinite, montmorillonite and illite 'clay line' with the bulk of the shale data residing within the illite/mixed layer clay zones, **b**) Caldas de Luna section, samples showing a maturity trend towards the 100% kaolinite, montmorillonite and illite 'clay line', the bulk of the data resides in the illite/mixed layer clay zones, **c**) La Majua section, the bulk of the data residing across the Mica – mixed-clay layer zones **d**) Sena de Luna section and, a compositional maturity trend is evident towards the 100% kaolinite, montmorillonite and illite 'clay line' with the bulk of the samples residing in the illite/mixed layer clay zones and, **e**) Villanueva section, the bulk of the samples belong to the illite zone with only one sample present within the 100% kaolinite, montmorillonite and illite 'clay line' zone.

As previously stated the majority of the localities show shale data residing across the two zones 'Illite' and 'mixed layer clays' (**Figure 6.47**). The presence of these clays can be used to infer the degree of weathering of the source rocks or maturity of the shales respectively. It has also been used to infer palaeolatitudes and climatic conditions for the time of deposition. The presence of Illite can indicate humid temperate climates (Einsele, 2000). However, Chamley (1989) and Weaver (1989 in: Diester-Haass *et al.,* 1998) suggest chlorite and illite are being derived from areas subject to uplift (leading to increased active mechanical erosion) and cold-desert area conditions. Illites are the most common of the clay minerals in deep sea sediments and are present mostly at mid-latitudes. The presence of the 'mixed-layer clays' suggests a weak development of chemical weathering (Chamley, 1989 in Diester-Haass *et al.,* 1998). Montmorillonite (smectite) clay types indicate temperate to subtropical climates (Einsele, 2000). The smectite commonly develops under warm, poorly drained continental areas (Chamley, 1989 in: Diester-Haass *et al.,* 1998).

Illite is the predominant clay mineral in marine shales as it is more stable than montmorillonite and kaolinite, the latter dominating freshwater sediments (Weaver, 1989). Montmorillonite forms under the lowest precipitation rates, illite and vermiculite at intermediate rates and kaolinite/halloysite at the highest leaching intensities (Calvert and Pedersen, 2007).

6.4.4.1 Aralla section

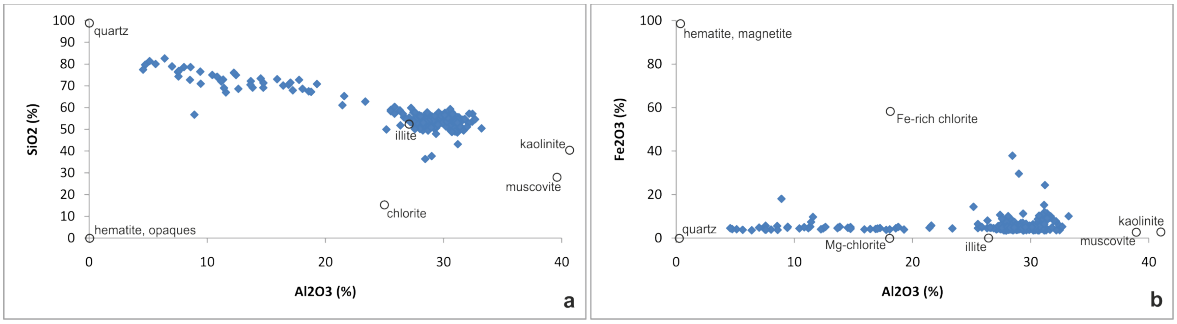

Figure 6.48 a) SiO_2 vs. Al_2O_3 of Cullers and Podkovyrov (2000), concentrations are plotted relative to the ideal composition of the observed minerals. Much of the variation in composition may be accounted for by different concentrations of the end-members quartz and muscovite. The Bernesga Mb. shales are clustering around 'illite', with the bulk of the samples trending towards 'kaolinite'. The Villasimpliz Mb. sand- and siltstones trend towards the compositionally mature 'quartz'. **b**) Fe_2O_3 total vs. Al_2O_3 of Cullers and Podkovyrov (2000), concentrations plotted relative to the composition of the observed minerals, again much of the variation in composition may be accounted for by the relative abundance of quartz and/or muscovite. The Bernesga Mb. shales again cluster around the 'illite' trending towards a 'kaolinite' enrichment. The Villasimpliz Mb. is trending towards 'quartz'.

The sediments of the Aralla section display a wide variation of minerals present (see **Figure 6.48**). The Barrios Fm. plots towards a pure 'quartz' composition, the organically enriched shales of the Bernesga Mb. pool around the 'illite' zone, but show a trend towards 'kaolinite'. The sand- and

siltstones of the overlying Villasimpliz Mb. also exhibit a compositional maturity trend towards the 'quartz' end-member (**Figure 6.48 a** and **b**).

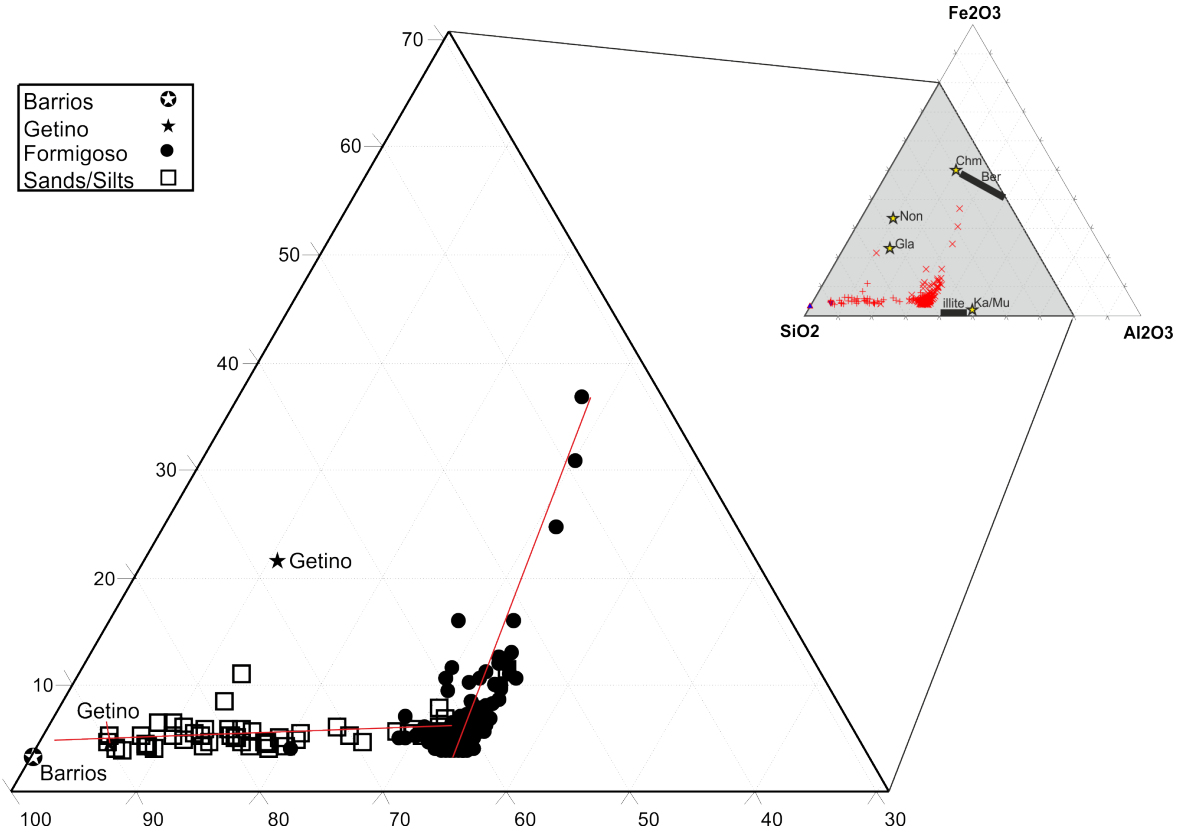

Figure 6.49 Distribution of the elements Fe, Al and Si within the Aralla section (241 samples), compared to several ideal clay minerals, including chamosite (Chm) and berthierine (Ber), kaolin and muscovite (Ka/Mu), nontronite (Non), illite and glauconite (Gla) after Konhauser (1998), Konhauser and Urrutia (1999) and Eickmann *et al.* (2009). Black rectangles indicate the existence of solid solutions between end-members. The Barrios Fm. plots at the SiO_2 corner, the shales of the Bernesga Mb. pool towards illite with a number of samples trending towards an enrichment with chamosite. The sand- and siltstones of the Villasimpliz Mb. display a compositional maturity trend towards SiO_2.

When plotting the samples of the Aralla section in the SiO_2-Fe_2O_3-Al_2O_3 discrimination diagram (see **Figure 6.49**), the Barrios Fm. plots at the SiO_2 corner. The Getino Beds, represented as black stars, show a wide compositional distribution ranging from SiO_2 enrichment to an enrichment of Fe_2O_3, which may indicate the presence of the mineral Glauconite. The black shales of the Bernesga Mb. (black circles) cluster around the illite zone, with a number of samples trending towards chamosite. The presence of chamosite is interpreted to be the product of localised Fe_2O_3 mineralisation. When referring to the 'elemental variations' in **Chapter 5.1.1** 'Fe_2O_3 element variation', the Fe_2O_3 peaks are apparent towards the base of the Bernesga Mb. The sand- and siltstones of the overlying Villasimpliz Mb. display a compositional maturity trend towards the SiO_2 component. Other ternary diagrams (MgO-CaO-Al_2O_3, Garnier *et al*. (2008); K_2O-Al_2O_3-SiO_2, Konhauser (1998) and Konhauser and Urrutia (1999); Al_2O_3–(CaO+Na_2O+K_2O)–(Fe_2O_3+MgO), Moosavirad *et al.* (2011) were utilised for the clay discrimination, these diagrams all showed that

the shales of the Bernesga Mb. pool around the illite zone. These diagram are not included here, but are documented in the **Results Appendix B** (Part 1) under 'ternary diagrams'.

6.4.4.2 Caldas de Luna section

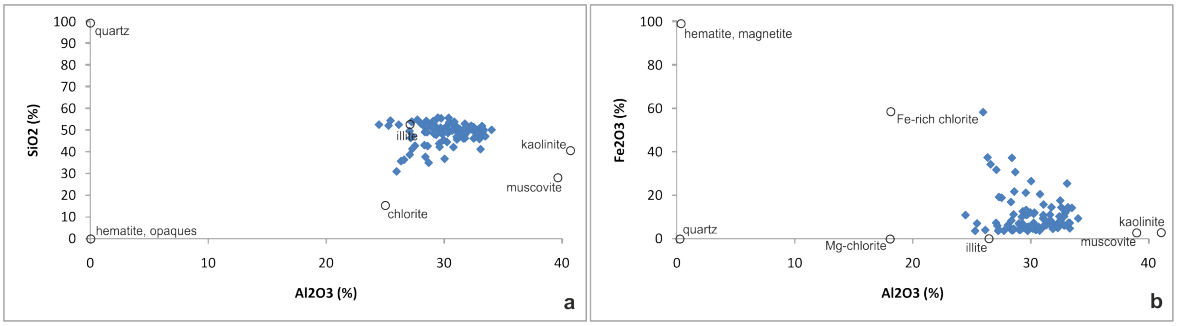

Figure 6.50 All data from the Caldas de Luna section (98 samples). **a**) SiO_2 vs. Al_2O_3 of Cullers and Podkovyrov (2000), concentrations are plotted relative to the idealized composition of the observed minerals. Much of the variation in composition may be accounted for by variation in quartz and clay minerals-muscovite. The Bernesga Mb. shales are clustering around 'illite', with the bulk of the samples trending towards 'kaolinite'. **b**) Fe_2O_3 total vs. Al_2O_3 of Cullers and Podkovyrov (2000), concentrations plotted relative to the composition of the observed minerals, again much of the variation in composition may be accounted for by variation in quartz and clay minerals-muscovite. The Bernesga Mb. shales again cluster around the 'illite' trending towards an enrichment of 'kaolinite', a number of samples display significant Fe_2O_3 enrichments. The enrichments of Fe_2O_3 is interpreted to represent the presence of Fe-rich chlorite.

The sediments of the Caldas de Luna section comprise the black shales of the Bernesga Mb. The shales mostly cluster around the 'illite' zone (see **Figure 6.50**). A number of the shales trend towards Fe-chlorite (**Figure 6.50 a** and **b**), this is interpreted to be the result of localised Fe_2O_3 mineralisation, the Fe_2O_3 rich horizons can be seen towards the base of the Bernesga Mb. in the results section (see **Chapter 5.3.1** 'Fe_2O_3 element variation').

When plotting the shales of the Caldas de Luna section in the SiO_2-Fe_2O_3-Al_2O_3 discrimination diagram (see **Figure 6.51**), they cluster around the illite zone, with a number of samples trending towards chamosite. The presence of chamosite is interpreted to be the product of localised Fe_2O_3 mineralisation. When referring to the 'elemental variations' in **Chapter 5.3.1** 'Fe_2O_3 element variation', the Fe_2O_3 enrichments are evident towards the base of the Bernesga Mb.

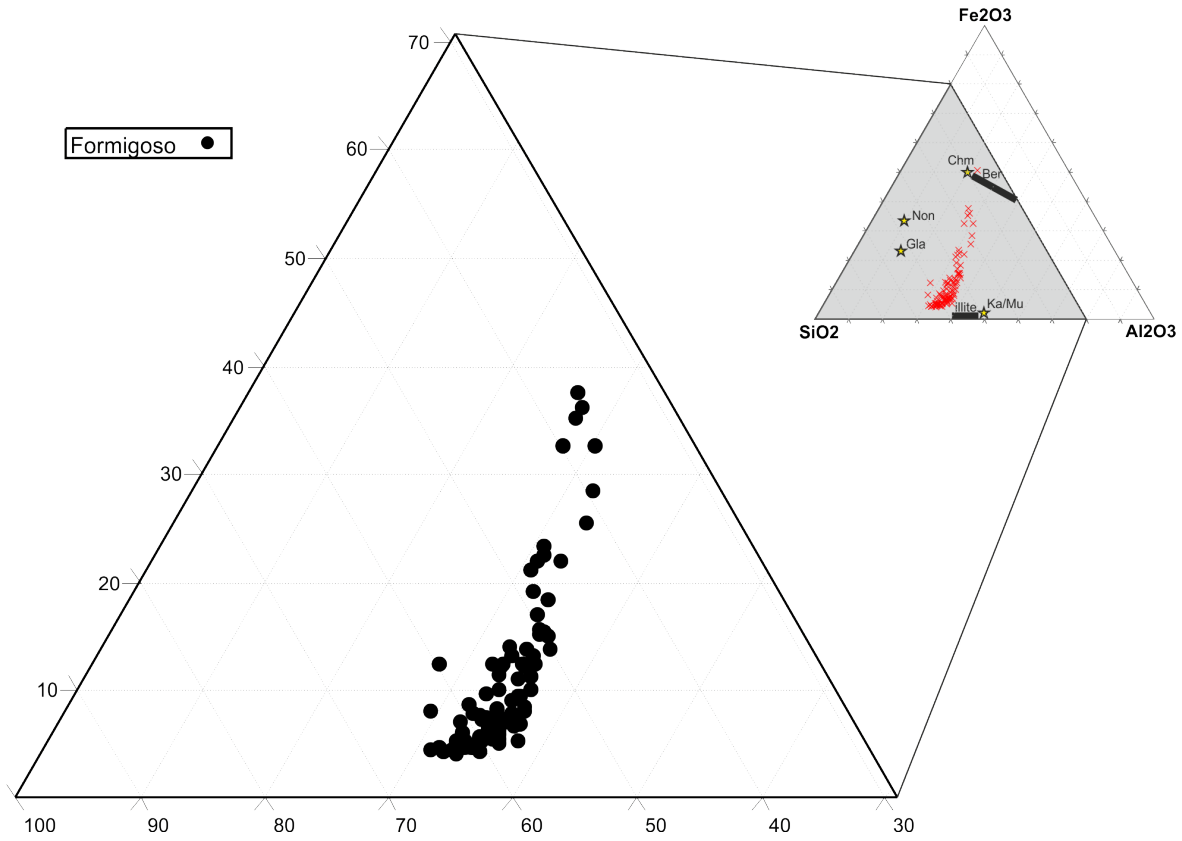

Figure 6.51 Distribution of the elements Fe, Al and Si within the Caldas de Luna section (98 samples), compared with several ideal clay minerals, including chamosite (Chm), berthierine (Ber) thin/long rectangle to represent variable compositions, kaolin and muscovite (Ka/Mu), nontronite (Non), illite thick/long rectangle and glauconite (Gla) after Konhauser (1998), Konhauser and Urrutia (1999) and Eickmann *et al.* (2009). The shales of the Bernesga Mb. pool towards illite with a number of samples trending towards an enrichment of chamosite.

6.4.4.3 La Majua section

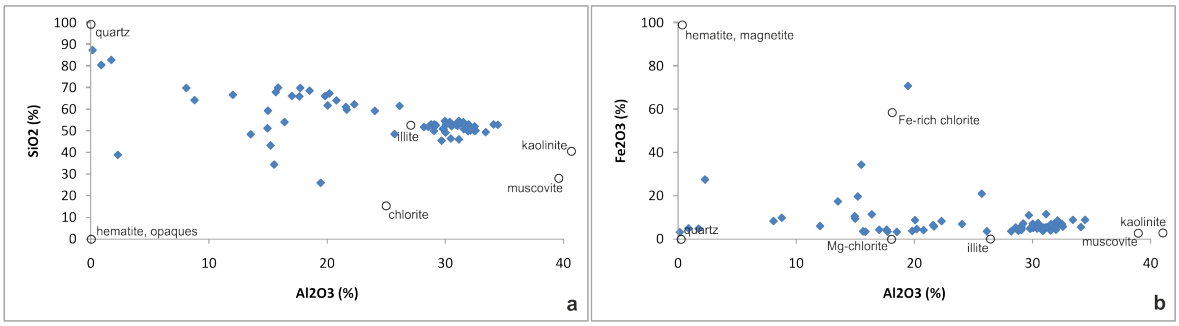

Figure 6.52 All data from the La Majua section (70 samples). **a**) SiO_2 vs. Al_2O_3 of Cullers and Podkovyrov (2000), concentrations are plotted relative to the idealized composition of the observed minerals. Much of the variation in composition may be accounted for by variation in quartz and clay minerals-muscovite. The Getino Beds trend towards the compositionally mature 'quartz', the Bernesga Mb. shales are clustering around 'illite', with the bulk of the samples trending towards 'kaolinite'. **b**) Fe_2O_3 total vs. Al_2O_3 of Cullers and Podkovyrov (2000), concentrations plotted relative to the composition of the observed minerals, again much of the variation in composition may be accounted for by variation in quartz and clay minerals-muscovite. The Getino Beds are trending towards 'quartz' and the Bernesga Mb. shales cluster around the 'illite' trending towards a 'kaolinite' enrichment.

The sediments of the La Majua section display a wide variation of minerals present (see **Figure 6.52**). The Barrios Fm. plots towards a pure 'quartz' composition, The sand- and siltstones of the Getino Beds show predominantly a compositional maturity trend towards 'quartz' yet there is a significant range with a number of samples showing significant Fe_2O_3 enrichments, interpreted to

indicate the presence of Fe-rich chlorite. The overlying organically enriched shales of the Bernesga Mb. pool around the 'illite' zone, yet trend towards an enrichment of 'kaolinite'. (**Figure 6.52 a** and **b**).

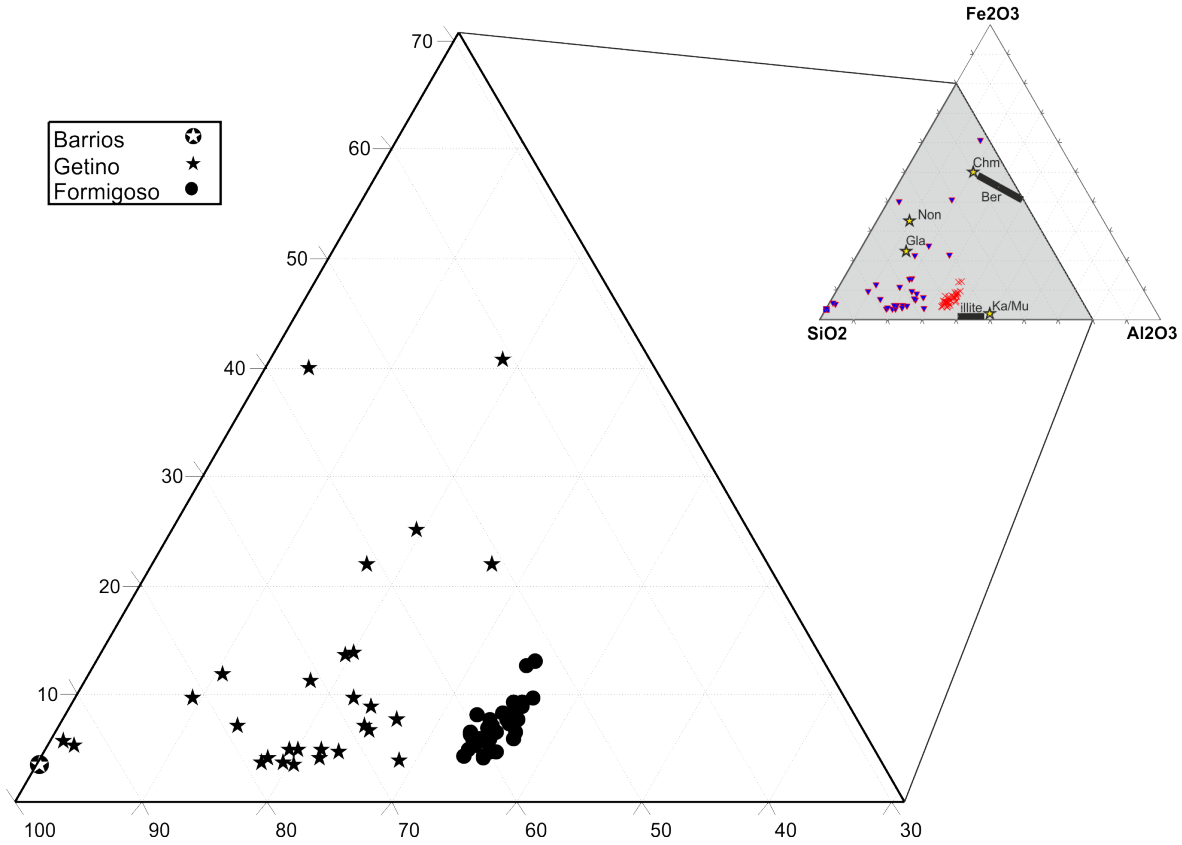

Figure 6.53 Distribution of the elements Fe, Al and Si within the La Majua section (70 samples), compared with several ideal clay minerals, including chamosite (Chm), berthierine (Ber) thin/long rectangle to represent variable compositions, kaolin and muscovite (Ka/Mu), nontronite (Non), illite thick/long rectangle and glauconite (Gla) after Konhauser (1998), Konhauser and Urrutia (1999) and Eickmann *et al.* (2009). The Barrios Fm. plots at the SiO_2 corner, the sand- and siltstones of the Getino Beds display a compositional maturity trend towards SiO_2. However, the compositional range is significant, with samples plotting towards glauconite and chamosite. The overlying shales of the Bernesga Mb. pool towards illite.

When plotting the sediments of the La Majua section in the SiO_2-Fe_2O_3-Al_2O_3 discrimination diagram (see **Figure 6.53**), the Barrios Fm. plots at the SiO_2 corner. The Getino Beds, represented as black stars, show a wide compositional range ranging from SiO_2 enrichment to an enrichment of Fe_2O_3, here indicating the presence of the minerals glauconite and chamosite. The Fe_2O_3 enrichments are interpreted to be the product of localised Fe_2O_3 mineralisation. When referring to the 'elemental variations' in **Chapter 5.4.1** 'Fe_2O_3 element variation', the Fe_2O_3 peaks are apparent at the mid-section of the Getino Beds. The overlying black shales of the Bernesga Mb. (black circles) cluster around the illite zone.

6.4.4.4 Sena de Luna section

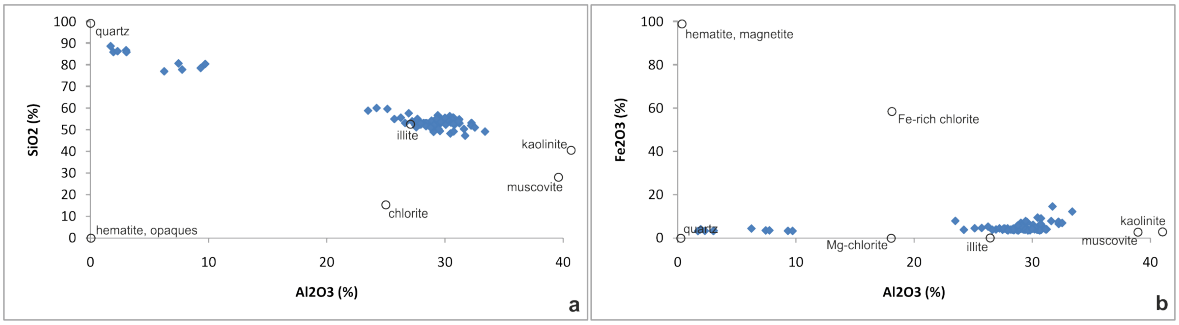

Figure 6.54 All data from the Sena de Luna section (79 samples). **a**) SiO_2 vs. Al_2O_3 of Cullers and Podkovyrov (2000), concentrations are plotted relative to the idealized composition of the observed minerals. Much of the variation in composition may be accounted for by variation in quartz and clay minerals-muscovite. The Getino Beds trend towards the compositionally mature 'quartz', the Bernesga Mb. shales are clustering around 'illite', with the bulk of the samples trending towards 'kaolinite'. **b**) Fe_2O_3 total vs. Al_2O_3 of Cullers and Podkovyrov (2000), concentrations plotted relative to the composition of the observed minerals, again much of the variation in composition may be accounted for by variation in quartz and clay minerals-muscovite. The Getino Beds are trending towards 'quartz' and the Bernesga Mb. shales cluster around the 'illite' trending towards a 'kaolinite' enrichment.

The Sena de Luna section comprises wide variations of minerals (see **Figure 6.54**). The Barrios Fm. plots towards a pure 'quartz' composition, the sand- and siltstones of the Getino Beds show a compositional maturity trend towards 'quartz'. The overlying organically enriched shales of the Bernesga Mb. pool around the 'illite' zone, yet trend towards an enrichment of 'kaolinite'. (**Figure 6.52 a** and **b**).

The sediments of the La Majua section when plotted within the SiO_2-Fe_2O_3-Al_2O_3 discrimination diagram (see **Figure 6.55**), the Barrios Fm. plots at the SiO_2 corner. The Getino Beds, represented as black stars, show a compositional maturity trend towards SiO_2. The overlying black shales of the Bernesga Mb. (black circles) cluster around the illite zone, with a number of samples showing slight enrichments in Fe_2O_3. The Fe_2O_3 enrichments are interpreted to be the product of localised Fe_2O_3 mineralisation. When referring to the 'elemental variations' in **Chapter 5.5.1** 'Fe_2O_3 element variation', the Fe_2O_3 peaks are apparent towards the top of the Bernesga Mb.

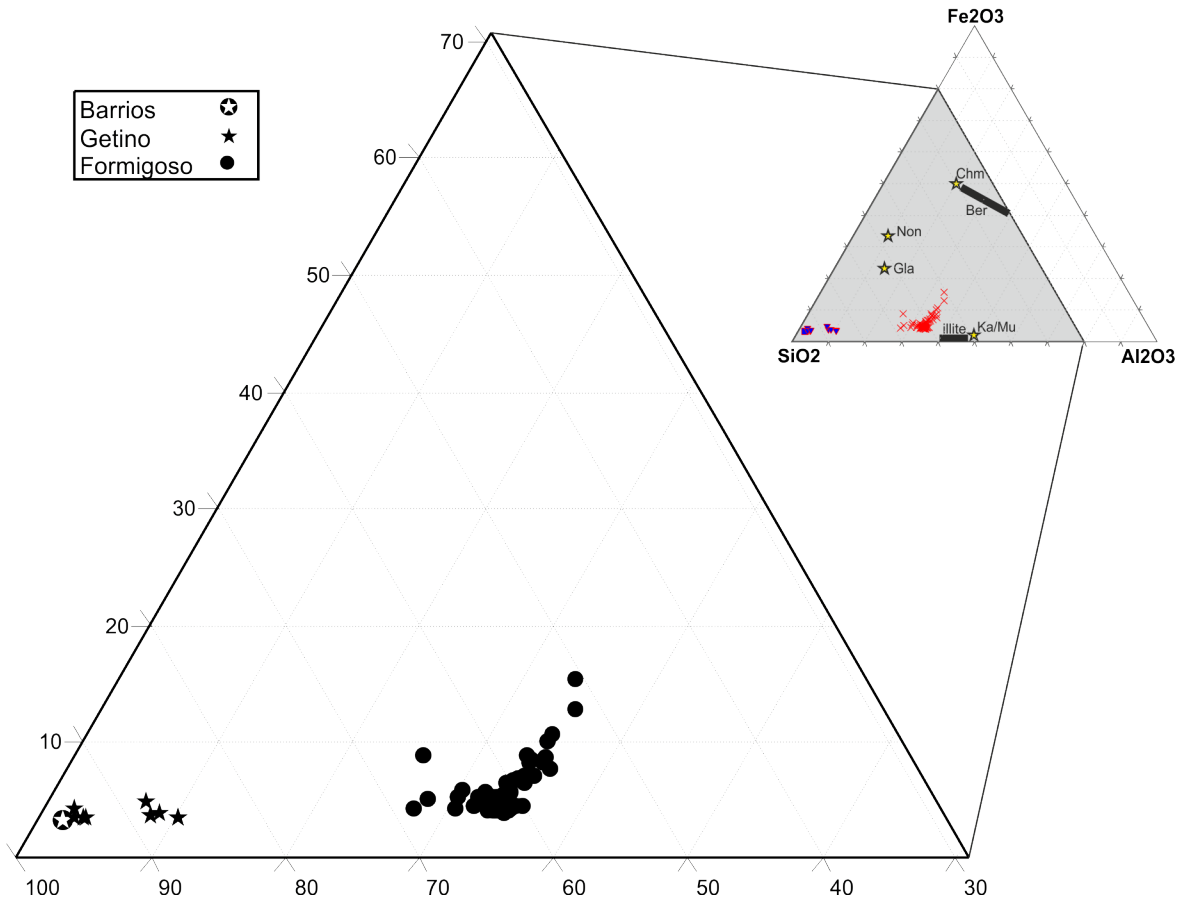

Figure 6.55 Distribution of the elements Fe, Al and Si within the Sena de Luna section (79 samples), compared with several ideal clay minerals, including chamosite (Chm), berthierine (Ber) thin/long rectangle to represent variable compositions, kaolin and muscovite (Ka/Mu), nontronite (Non), illite thick/long rectangle and glauconite (Gla) after Konhauser (1998), Konhauser and Urrutia (1999) and Eickmann *et al.* (2009). The Barrios Fm. plots at the SiO_2 corner, the sand- and siltstones of the Getino Beds display a compositional maturity trend towards SiO_2. The overlying shales of the Bernesga Mb. pool towards illite, with a number of samples showing Fe_2O_3 enrichments.

6.4.4.5 Villanueva section

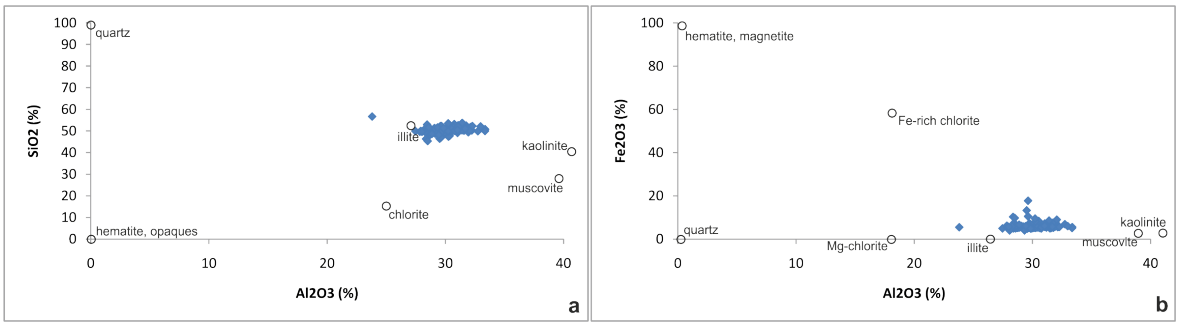

Figure 6.56 all data from the Villanueva section (111 samples). **a**) SiO_2 vs. Al_2O_3 of Cullers and Podkovyrov (2000), concentrations are plotted relative to the idealized composition of the observed minerals. Much of the variation in composition may be accounted for by variation in quartz and clay minerals-muscovite. The Bernesga Mb. shales are clustering around 'illite', with the bulk of the samples trending towards 'kaolinite'. **b**) Fe_2O_3 total vs. Al_2O_3 of Cullers and Podkovyrov (2000), concentrations plotted relative to the composition of the observed minerals, again much of the variation in composition may be accounted for by variation in quartz and clay minerals-muscovite. The Bernesga Mb. shales again cluster around the 'illite' trending towards an enrichment of 'kaolinite', a number of samples display slight enrichments of Fe_2O_3. The enrichments of Fe_2O_3 are interpreted to represent the presence of Fe-rich chlorite.

The sediments of the Villanueva section comprise the black shales of the Bernesga Mb. The shales mostly pool around the 'illite' zone (see **Figure 6.56**). A number of the shales show slight enrichment of Fe_2O_3 trending towards Fe-chlorite (**Figure 6.56 a** and **b**). The lack of Fe_2O_3

enriched horizons at this locality again suggests that the Fe_2O_3 enrichments really are a result of localised mineralisation.

When plotting the shales of the Villanueva section in the SiO_2-Fe_2O_3-Al_2O_3 discrimination diagram (see **Figure 6.57**), they cluster around the illite zone, with a number of samples showing a slight enrichment of Fe_2O_3, trending towards a chamosite. However, The Fe_2O_3 enrichments at this location are not as significant as the previously described and interpreted sections.

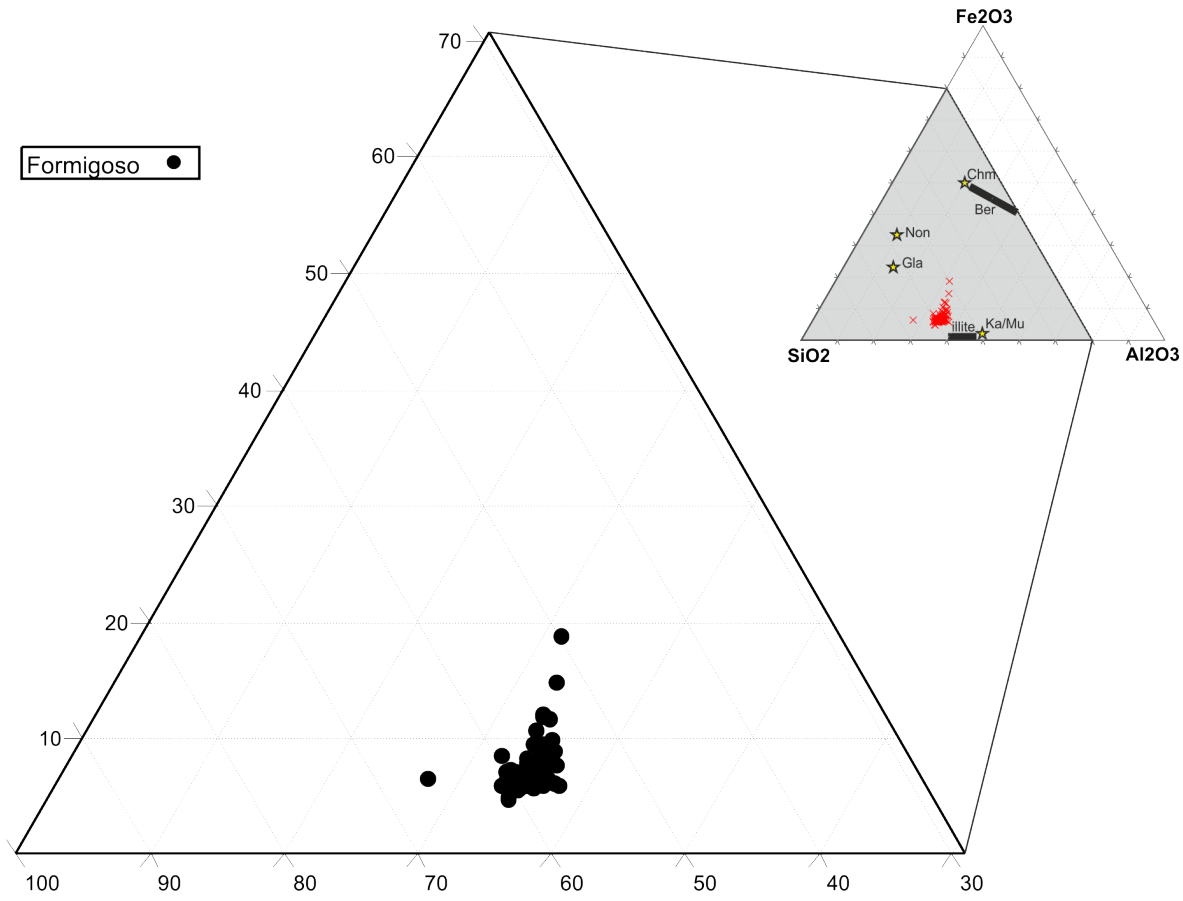

Figure 6.57 Distribution of the elements Fe, Al and Si within the Villanueva section (111 samples), compared with several ideal clay minerals, including chamosite (Chm), berthierine (Ber) thin/long rectangle to represent variable compositions, kaolin and muscovite (Ka/Mu), nontronite (Non), illite thick/long rectangle and glauconite (Gla) after Konhauser (1998), Konhauser and Urrutia (1999) and Eickmann *et al.* (2009). The shales of the Bernesga Mb. pool towards illite with a number of samples trending towards an enrichment of chamosite.

6.4.5 The Index of Compositional Variation (ICV) and weathering indices

The principles and usage of the index of compositional variation (ICV) are described in detail in **Chapter 3.1.13** 'Sediment recycling: Index of compositional variation (ICV)', whereas the chemical index of alteration (CIA) and chemical index of weathering (CIW) are described in **Chapter 3.1.14** 'Weathering indices: CIA, PIA and CIW'. The ICV, CIA and CIW values were calculated for all the analysed sections. However, the values calculated for each of the above were that similar for the individual localities that only the Aralla section is used as an example. The remaining sections are documented within **Results appendix B** (part 1).

The K_2O/Al_2O_3 ratio of Cox (1995) was applied to the geochemical results of the analysed sediments belonging to the Aralla section (see **Figure 6.58 a**). The Barrios Fm. and Getino Beds fall within the uppermost limits of the 'range of clay minerals'. The shales of the Bernesga Mb. are located well within the 'range of clay minerals'. The overlying sand- and siltstones of the Villasimpliz Mb. display elevated K_2O/Al_2O_3 ratios, towards the upper limts of the 'range of clay minerals'. The ICV calculation (see **Figure 6.58 c**) shows that the the Barrios Fm. and Getino Beds exhibit values > 1. The shales of the Bernesga Mb. plot within the 'clay window', within the proximity of the plagioclase catagory between the muscovite/illite values, the sands/silts of the Villasimpliz Mb. plot within/above the plagioclase catagory with values greater than the illite region. The ICV values are lower at the base of the Bernesga Mb. and increase gradually towards the top of the Mb.. The average ICV value of the Bernesga Mb. is **0.45**. ICV values greater than one are interpreted to indicate the presence of immature shales. Whereas values below one indicate the presence of compostionally mature shales. In this instance the Bernesga Mb. shales are classified as 'highly mature shales'. The average ICV value of the Villasimpliz Mb. is **0.69**, this value suggests that the Mb. is significantly less compositionally mature than the underlying Bernesga Mb. shales. The maturity trend decreases from the base to the top of the Formigoso Fm. with the introduction of detrital material from the hinterland.

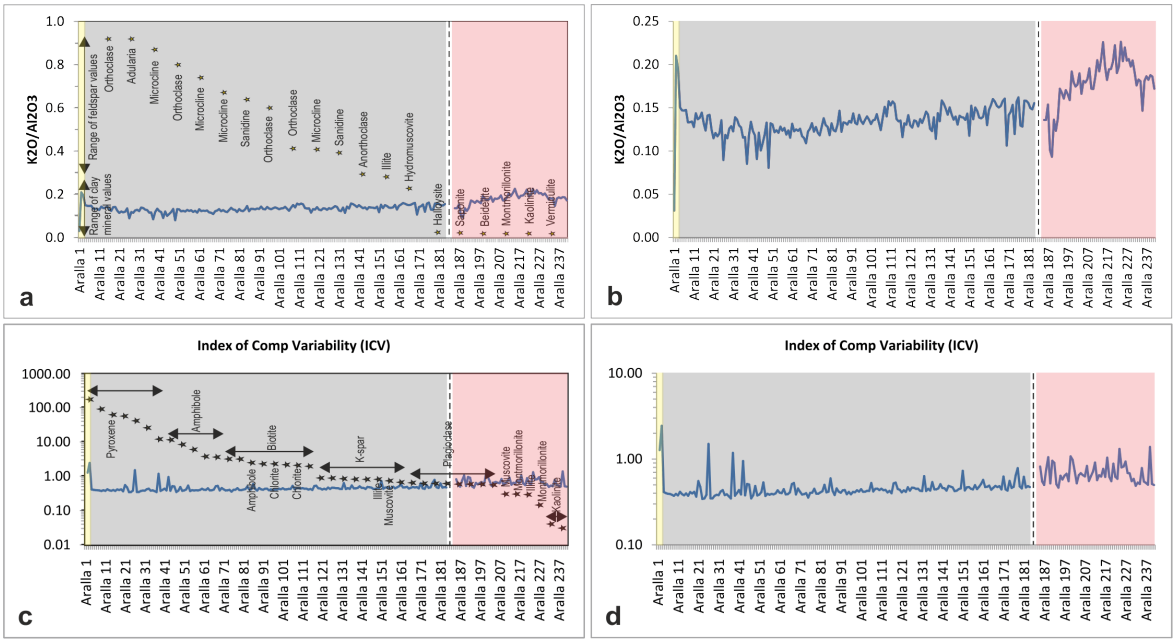

Figure 6.58 a) K_2O/Al_2O_3 ratio for the Aralla section (in order to discriminate the K-feldspars from the clay minerals). The stars represent values for specific minerals, data from Deer and Howie (1966), overlay after Cox *et al.* (1995). **b)** expanded plot of **(a)** to illustrate the variability of K_2O/Al_2O_3 ratios. **c)** Index of Compositional Variation (ICV): $(Fe_2O_3 + K_2O + Na_2O + CaO + MgO + MnO + TiO_2)/Al_2O_3$, the stars represent values for specific minerals, the arrows show the range of values for the particular mineral group, data from Deer and Howie (1966), after Cox *et al.* (1995). **d)** Expanded plot of **c)**. K_2O/Al_2O_3 - range of Bernesga Mb.: 0.0804-0.1620, K_2O/Al_2O_3 - range of Villasimpliz Mb.: 0.0933-0.2259, K_2O/Al_2O_3 - average of Bernesga Mb.: 0.1333, K_2O/Al_2O_3 - average of Villasimpliz Mb.: 0.1791, ICV - range of Bernesga Mb.: 0.3423-0.7831 (1.5004 including Fe peak), ICV - range of Villasimpliz Mb.: 0.4635-1.3832, ICV - average of Bernesga Mb.: 0.4519 and ICV - average of Villasimpliz Mb.: 0.6989. The ICV values increase gradually from the base of the Formigoso Fm. to the top, indicating a decreasing maturity trend with the increased influx of terrigenous material.

The Chemical Index of Alteration (CIA) is a well-established parameter for determining the degree of weathering and is the most accepted of the available weathering indices (Bahlburg and Dobrzinski, 2011). During the degradation of feldspars, Ca, Na, and K are removed and clay minerals with a higher fraction of Al formed. The CIA is estimated from the proportion of Al_2O_3 vs. the weathering-prone oxides (Hetzel *et al*., 2006). This index measures the degree of feldspar decomposition to secondary clay products, where CIA values of ~50 indicate fresh bedrock (no chemical weathering), and values of 75-100 indicate complete conversion of feldspars to aluminous clay minerals under intense chemical weathering (see Fedo *et al*., 1995).

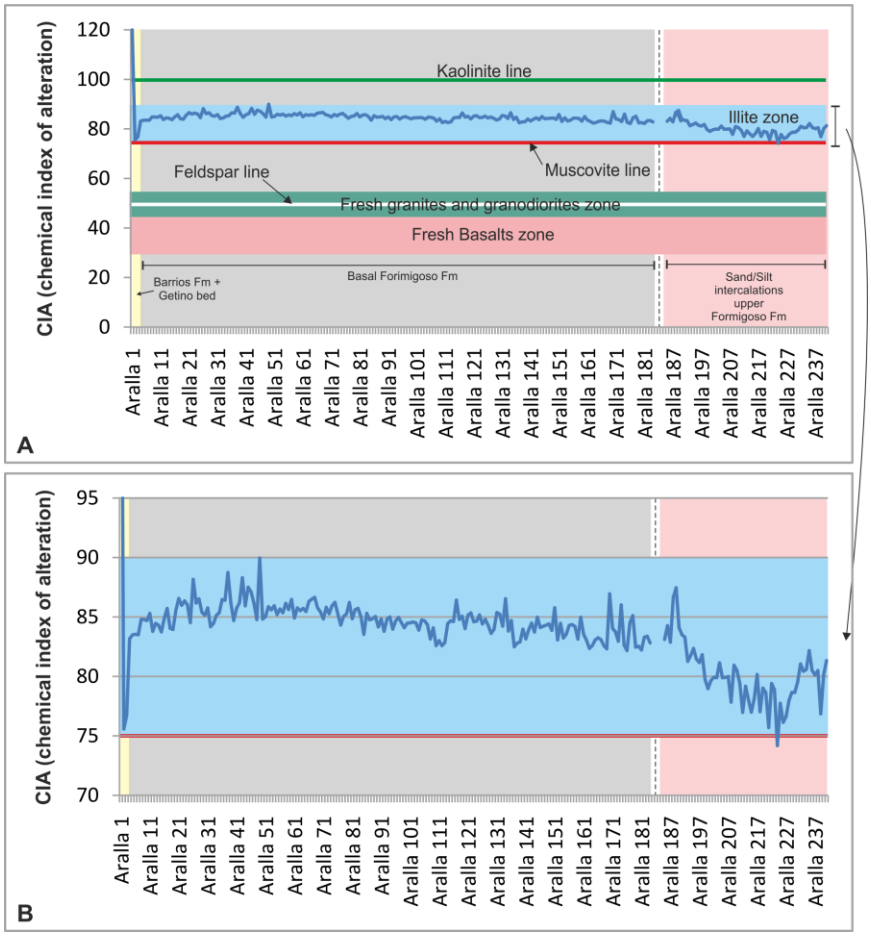

Figure 6.59 'Chemical Index of Alteration' (CIA); CIA = $[Al_2O_3/(Al_2O_3 + CaO + Na_2O + K_2O)] \times 100$, after Nesbitt and Young 1982 and Taylor and McLennan 1985. Kaolinite has a CIA value of 100 and represents the highest degree of weathering. Illite ranges between 75 and c. 90, muscovite at 75, the feldspars at 50. Fresh basalts have values between 30 and 45, fresh granites and granodiorites of 45 to 55 (Nesbitt and Young, 1982; Fedo *et al*., 1995). **a)** Representing data from the Aralla section (all 241 samples), the CIA values are relatively uniform throughout the Bernesga Mb. displaying slightly elevated values at the base. The Villasimpliz Mb. has CIA values that are lower relative to the underlying Bernesga Mb. **b)** Expanded plot, focusing on the Illite Zone, the muscovite line is included for reference.

The Barrios Fm. is showing an extreme high CIA value, most likely as a result of the depletion in trace elements. The average CIA value for the Bernesga Mb. at the Aralla section is: **84.73** (well within the illite range), suggesting a high degree of chemical weathering of the source material (see Hetzel *et al*., 2006 p.6). The CIA values for the shales of the Bernesga Mb. are higher at the base (see **Figure 6.59**), suggesting a higher degree of weathering and increased maturity of the shales relative to the upper extremes of the Mb. The sand- and siltstones of the upper Villasimpliz Mb. have lower CIA values, interpreted to indicate a lower intensity of chemical weathering of the source material, and consequently a lower maturity. **Figure 6.60** illustrates the CIA values of the Bernesga Mb. ranging between 75 and 90. The bulk of the Bernesga Mb. shales cluster towards the illite region yet the mature basal shales trend towards the kaolinite/chlorite. The international standard 'upper continental crust' is also included for comparison. The sediments of the Aralla section are significantly enriched in Al_2O_3 relative to the upper continental crust.

The CIA values for the Aralla section work in conjunction with the previously described Aralla ICV values. The CIA variations could be interpreted as a function of climate oscillations between glacial and warm-humid interglacial conditions (Rieu *et al*., 2007). The CIA values also correspond closely to the previously described humidity and clay typing proxies (see **Chapters 6.4.3** and **6.4.4**).

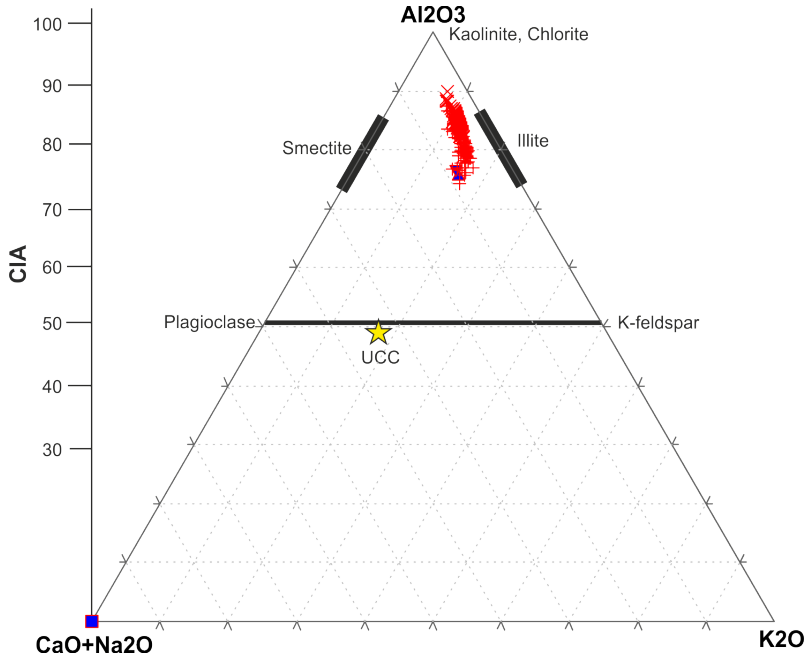

Figure 6.60 CIA - Al_2O_3–(CaO+Na_2O)–K_2O diagram, after Nesbitt and Young (1982). The blue square represents the Barrios Fm. whereas the blue triangles (plotting near the lower part of the shale data) represent the Getino Beds. The diagonal crosses represent the basal Bernega Mb. and the upright crosses the sands/silts of the Villasimpliz Mb. The majority of the sediments from the Aralla section, have high CIA values and show a significant enrichment in Al_2O_3 relative to the internation standard 'upper continental crust' of Taylor and McLennon (1985).

The Chemical Index of Weathering **(CIW)** increases with the degree of depletion of the soil or sediment in Na and Ca, relative to Al. The value of this index increases together with the degree of weathering (Harnois, 1988).

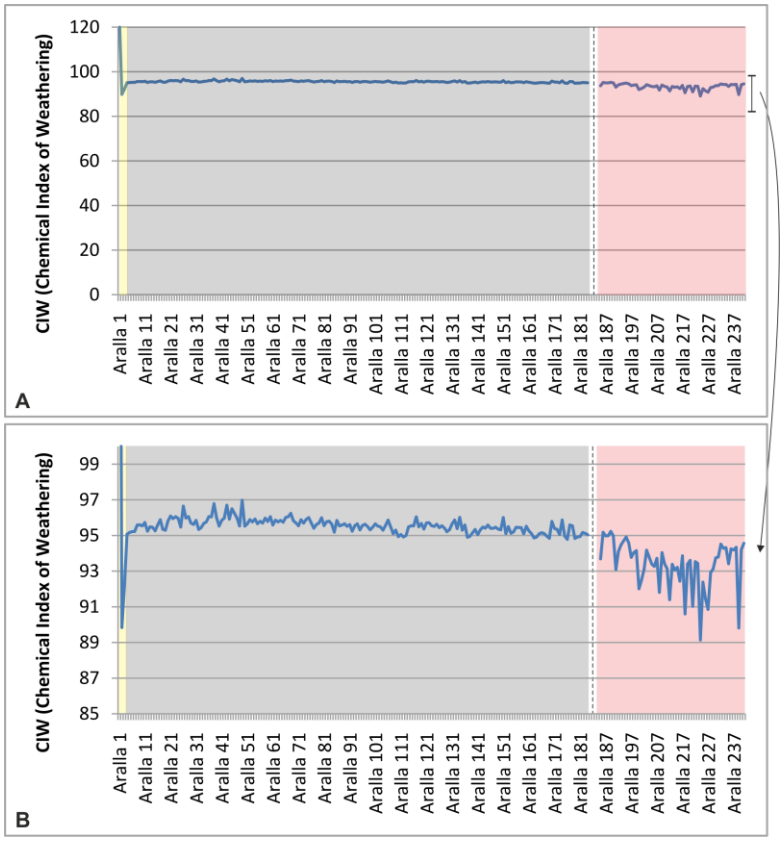

Figure 6.61 Representing all data from the Aralla section (241 samples), the 'Chemical Index of Weathering' (CIW), **CIW = $[Al_2O_3/(Al_2O_3 + CaO + Na_2O)]*100$** after Harnois (1988). **a)** CIW values for the Aralla section, **b)** expanded plot of the CIW values in **(a)**, the values are elevated at the base of the Bernesga Mb. relative to the overlying Villasimpliz Mb.

The average CIW value for the Bernesga Mb. (black shales) at Aralla is **95.5**. This value again suggests that the shales are significantly weathered. The CIW values are higher at the base of the Bernesga Mb. relative to the top and are hence directly comparable to the previously interpreted CIA values (see **Figure 6.61 b**). The CIW values deplete as the sand- and siltstones of the overlying Villasimpliz Mb. are introduced. These sediments are interpreted to be less compositionally mature than the underlying Bernesga Mb. shales. The oxygenated sediments of the Villasimpliz Mb. are interpreted to have been deposited in the predominantly anoxic black shale regime by prograding deltaic systems.

To summarise, the degree of chemical weathering of the source material increases significantly with the onset of black shale deposition. The calculated weathering indices peak at the base of the Bernesga Mb. before gradually decreasing towards the overlying sand- and siltstones of the Villasimpliz Mb. caused by the introduction of detrital material from the hinterland.

6.4.6 3D model reconstructions: Synthesis of the environmental factors

This section combines a selection of the previously interpreted environmental proxies. The factors were introduced into 3D plots in order to establish any potential relationship between the controlling environmental parameters. The factors combined were **[1]** the Rb/K salinity proxy of Campbell and Williams (1965), **[2]** the redox proxies, V/(V+Ni) of Hatch and Leventhal (1992) and Th/U of Fertl (1979) and **[3]** the grain-size proxies, Zr/Rb and Si/Al. The data-set of the Aralla section will be used to exemplify these potential relationships. The reconstructions for the other examined localities have been documented in **Results appendix B** (part 1).

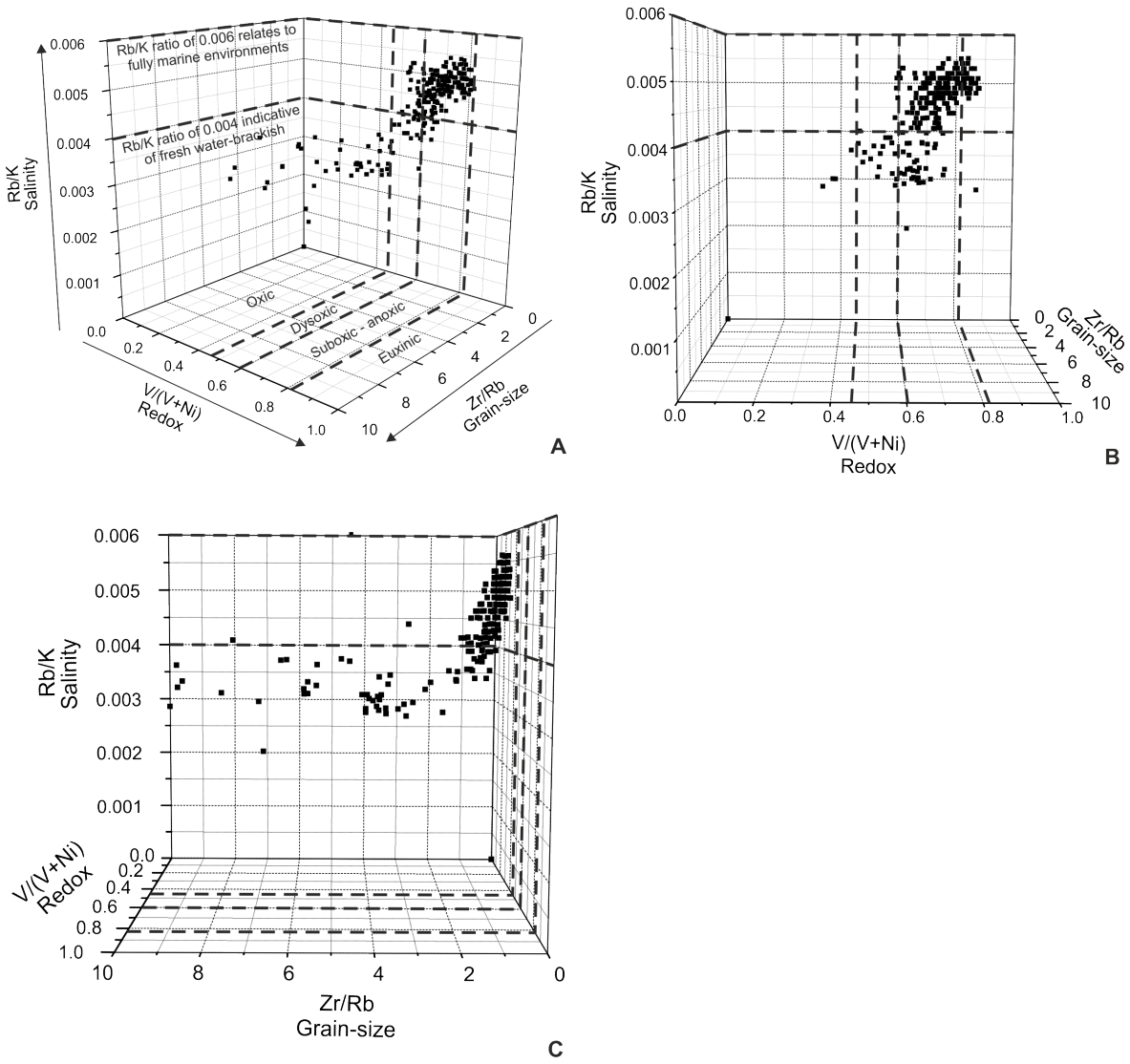

Figure 6.63 Geochemical environmental reconstruction, using the elemental ratios of Rb/K, V/(V+Ni) and Zr/Rb, displaying data from the Aralla section (all 241 samples). The Rb/K ratio is used as a palaeosalinity proxy, a value of ≤0.004 represents fresh water, values >0.004 to ≤0.006 indicate brackish waters and values >0.006 suggest a fully marine developed environment (Campbell and Williams, 1965). The V/(V+Ni) is a redox indicator, the values <0.46 'oxic', 0.46-0.60 'dysoxic', 0.54-0.82 'suboxic-anoxic' and >0.82 'euxinic' after Hatch and Leventhal (1992). The Zr/Rb ratio is used as a grain size indicator (Zr associated with quartz grains, Rb associated with Al_2O_3, TiO_2, and K_2O in the clay fraction) high values reflect course grained units, lower values in clay stones and shales.

The 3D plot (see **Figure 6.63**) combines a salinity proxy (Rb/K), a redox state proxy (V/(V + Ni)) and a grain-size indicator (Zr/Rb). The shales of the Bernesga Mb. have high Rb/K ratios indicating elevated levels of salinity relative to the sand- and siltstones of the Villasimpliz Mb. (see **Figure 6.63 c**). The Bernesga Mb. shales display a higher redox state relative the Villasimpliz Mb. (see **Figure 6.63 b**). The sand- and siltstones of the Villasimpliz Mb. display a wide range of grain-sizes, significantly higher that the underlying Bernesga Mb. (see see **Figure 6.63 c**). The relation between these parameters can be used to infer a direct link between a reducing environment, higher salinity levels and diminished siliciclastic (detrital) input. From this interpretation, the rising sea-level combined with basin subsidence seems to be the main driving force for the establishment of the starved basin conditions and elevated reducing environmental conditions. This scenario is well suited for the development of the organically enriched black shales deposits. Furthermore, this interpretation is well in line with the different environmental proxies (e.g. the salinity proxy Rb/K, the redox proxy Th/U and the grain-size indicator Si/Al, see **Figure 6.64**).

The 3D plots prove to be powerful instruments, as they discriminate effective the sediments of the Bernesga Mb. and the overlying Villasimpliz Mb.

The interpretation of the 3D plots for all the analysed sections offers a straight explanation for the existence of small-sized benthic fauna, consisting predominantly of small sized representatives of the brachiopod genus *Lingula* (Aramburu *et al*., 2002). As the shales were forming under starved basin, reducing conditions, the small-sized benthic fauna may have also been affected by a severe lack of nutrients, which was at times with elevated detrital influx provided by the terrigenous sediment supply of the hinterland. The overall low-biodiversity graptolite assemblages documented from the Bernesga Mb. (Aramburu *et al*., 2002) may reinforce the interpretation of temporarily reduced salinity conditions. During seasonal phases with normal marine salinity (winter), the graptolites were able to invade the shelfal areas and to thrive, whereas during the summer, the increased freshwater influx caused by melting ice-caps and glaciers would reduce the salinity levels leading to brackish water conditions and the establishment of a stratified water column. Both, the small-sized benthic fauna and the low-biodiversity graptolite fauna point towards highly stressed environmental conditions.

The sand/silts horizons fall within the less reducing zones, most likely related to prograding deltas providing oxygen rich sediments into the predominantly anoxic black shale regime. The salinity levels and redox states are much lower within the sand- and siltstone intercalations, which is in line

with the high abundance of trace fossils (e.g. *Cruziana* sp. and *Planolites* sp.) of organisms thriving in the oxygen and nutrient rich sediments.

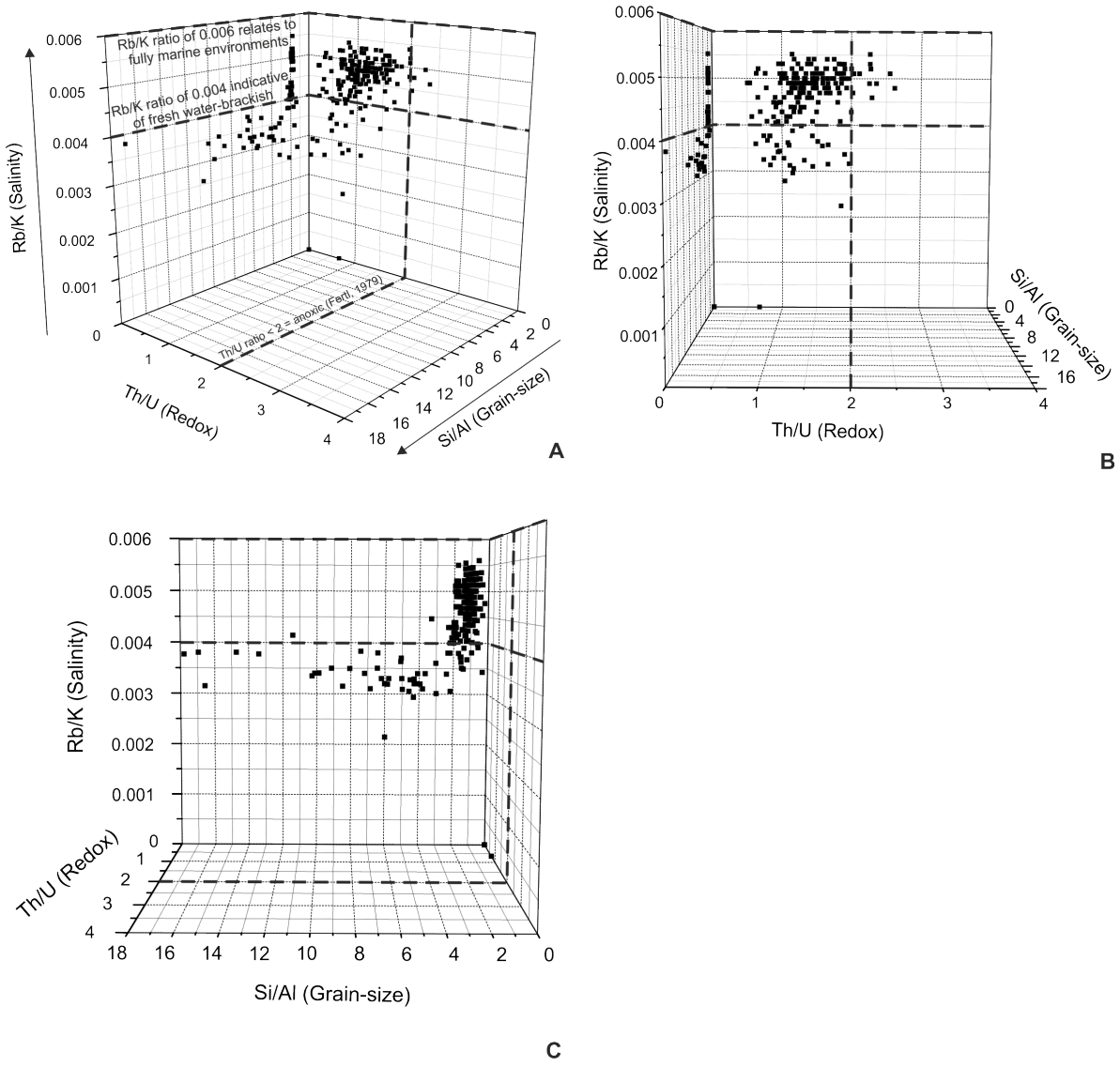

Figure 6.64 Geochemical environmental reconstruction, using the ratios Rb/K, Th/U and Si/Al (contrasting grain size proxy to the previous figure Zr/Rb), displaying data from the Aralla section (all 241 samples). The Rb/K ratio is used as a palaeosalinity proxy, a value of ≤0.004 represents fresh water, values >0.004 to ≤0.006 indicate brackish waters and values >0.006 suggest a fully marine developed environment (Campbell and Williams, 1965). Th/U is used as a redox indicator, the dashed black line = Th/U ratio of 2, less than 2 indicates anoxic after Fertl (1979). There is no U within the sandstones (oxic); explaining they fall into the anoxic zone (0 values for ratio). The Si/Al ratio is used as a grain size indicator (Si associated with quartz grains, Al associated with Al_2O_3, TiO_2, and K_2O in the clay fraction) high values reflect course grained units, lower values in clay stones and shales.

6.4.7 Hydrothermal overprint

The hydrothermal indicator of Boström (1973) was applied to all geochemical samples of the analysed sections. The indictor uses the function Fe_2O_3/TiO_2 vs. $Al_2O_3/(Al_2O_3+Fe_2O_3+MnO)$ to determine whether sediments have been affected by hydrothermal activity. Two end members are plotted to indicate either no alteration (terrigenous, argillite (T)) or significant alteration

(hydrothermal (H)). The $Al_2O_3/(Al_2O_3+Fe_2O_3+MnO)$ ratio is based on the assumption of metal-enrichment derived from hydrothermal fluids relative to Al_2O_3. Al_2O_3 is considered to be relatively immobile in hydrothermal systems. The Fe_2O_3/TiO_2 component is used to determine the degree of mixing between hydrothermal overprinted sediments and non-altered matter.

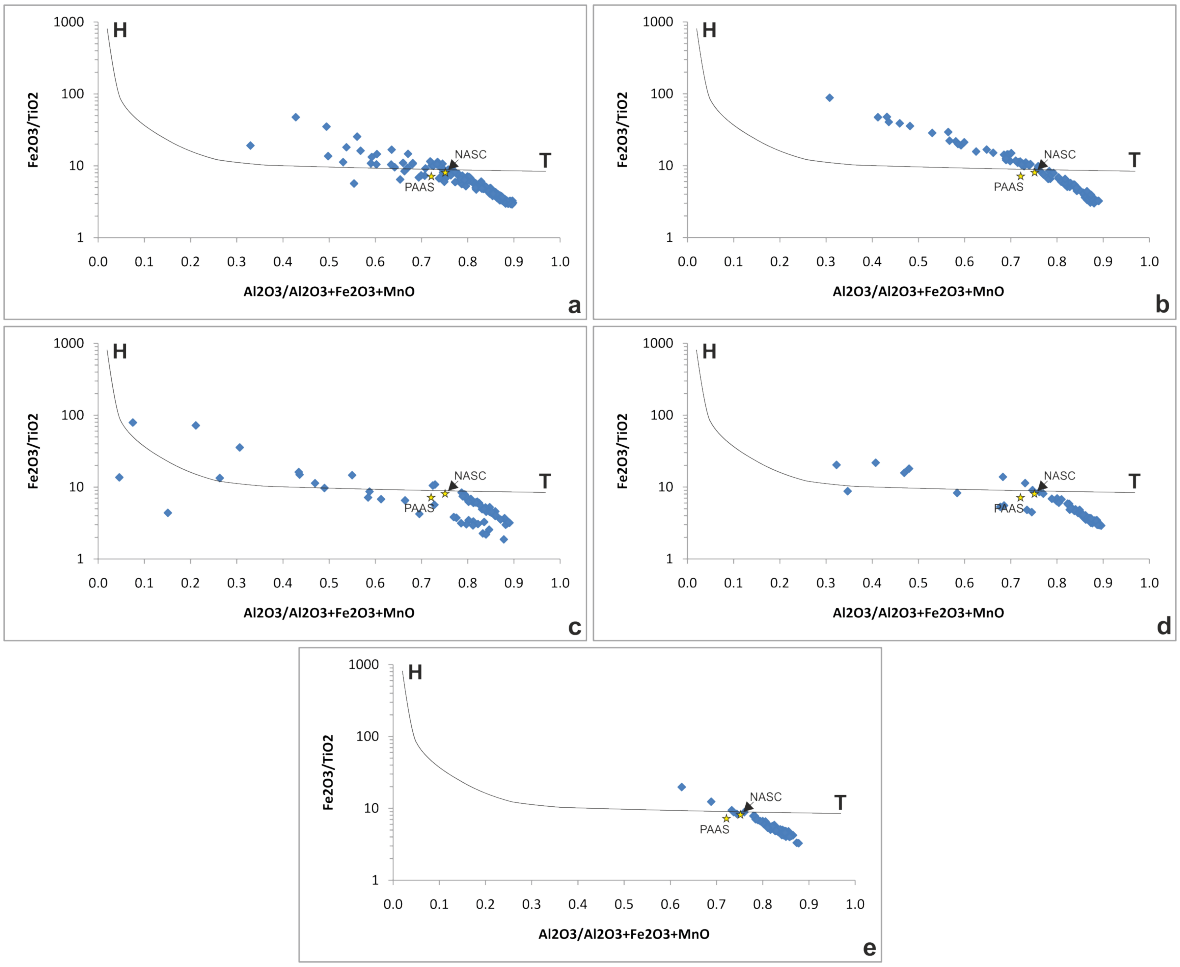

Figure 6.65 Boström (1973) diagrams, the analysed sediments are compared to the terrigenous argillite (T) and hydrothermal (H) end members whose mixing is modelled by the H-T curve. The international standards of PAAS and NASC (data from Gromet *et al*., 1984) are reported for comparison (Barbera *et al*., 2006). **a**) Aralla section, the shales of the Bernesga Mb. are trending towards the argillite (T) end member, with higher $Al_2O_3/(Al_2O_3+Fe_2O_3+MnO)$ and lower Fe_2O_3/TiO_2 values than the international standards, the sand- and silts of the Villasimpliz Mb. trend towards the hydrothermal end member, **b**) Caldas de Luna section, the shales of the Bernesga Mb. display a wide range of values trending from the argillite (T) to the hydrothermal end member, **c**) La Majua section, the shales of the Bernesga Mb. are clearly discriminated from the sand- and siltstones of the Getino Beds. The Bernesga Mb. remains at the argillite (T) end member, whereas the sediments of the Getino trend towards the hydrothermal end member, **d**) Sena de Luna section, again the shales of the Bernesga Mb. are clearly discriminated from the sand- and siltstones of the Getino Beds. The Bernesga Mb. is plotting at the argillite (T) end member, whereas the sand- and siltstones of the Getino Beds trend towards the hydrothermal end member, to a lesser extent than the previously described La Majua section, and **e**) Villanueva section, displaying the Bernesga Mb. clearly plotting towards the argillite (T) end member in the proximity of the international standards.

The sediments analysed from the Aralla section indicate no significant hydrothermal overprint. The **[1]** shales of the Bernesga Mb. (see **Figure 6.65 a**) pool towards the argillite (T) end member. Whereas the **[2]** sand- and siltstones of the overlying Villasimpliz Mb. trend towards the hydrothermal end member. The international standards PAAS and NASC are reported for comparison. The Bernesga Mb. shales of the Caldas de Luna section (see **Figure 6.65 b**) pool

around the argillite end member. The Getino Beds of the La Majua section (see **Figure 6.65 c**) plot towards the hydrothermal end member, whereas the Bernesga Mb. groups at the argillite (T) end member. For the Sena de Luna section, the analysed sediments of the Getino Beds trend towards the hydrothermal end member on a separate trend line compared to the overlying Bernesga Mb. The shales of the overlying Bernesga Mb. plot towards the argillite end member. Finally, the Bernesga Mb. shales of the Villanueva section (see **Figure 6.65 e**) plot within the proximity of the international standards and trend towards the argillite end member.

To summarise, the shales of the Bernesga Mb. have not been subject to hydrothermal alteration. The sand- and siltstones of the underlying Getino Beds and overlying Villasimpliz Mb. have been partly overprinted. This partial overprint is interpreted to be a result of increased pore space available, in contrast to the impermeable shales of the Bernesga Mb. Other plots were introduced for the hydrothermal testing, for example the **[1]** (Cu+Co+Ni)*10 – Fe – Mn – (Si+Al) quaternary diagram and the **[2]** Th – As – U ternary diagram. Both of these diagrams showed, that the Bernesga Mb. shales have not been affected by any significant hydrothermal overprinting. However, the Getino Beds and Villasimpliz Mb. have been partially affected by slight hydrothermal activity. These plots are documented in **Appendix B** (Part 1).

6.4.8 Palaeobioproductivity reconstructions

The use of Ba as a palaeoproductivity proxy has its limitations. The Ba concentrations within sediments can be altered by hydrothermal overprinting, leading to false interpretations of the palaeobioproductivity reconstructions. However, as previously stated the shales of the Bernesga Mb. were not affected by any hydrothermal overprint. In this instance, the application of Ba as a palaeobioproductivity indicator was viable. The association of Ba to the organic fraction of the sediment was supported by the SEM and SEM-based ED-XRF analysis of a sample representative for the basal shales of the Bernesga Mb. from the Aralla section (see **Figure 6.66**).

Sedimentary Al concentrations can be effected by biogenic processes, leading to Ba/Al ratios of no particular value. The plot of Al_2O_3 vs. TiO_2 (r^2 = 0.87) clearly indicates that the Al_2O_3 was derived from the detrital clay fraction, suggesting that biogenic processes did not affect the relative Al_2O_3 concentrations (see **Appendix B** (Part 1) 'Bioproductivity reconstruction').

However, the Al_2O_3 concentrations are enriched relative to the international shale standards. The following ratios were implemented to determine the source of the enrichment. The Al_2O3/TiO_2

ratios, when compared to those of Murray and Leinen (1996) and Gordon *et al*. (1996 in: Murray and Leinen (1996) p.6), indicated that the shales of the Bernesga Mb. are derived from a predominantly granitic source. This interpretation is enforced by the Fe_2O_3/Al2O3 ratios also suggesting a granitic source for the sediments. These ratios indicate, that the chemical weathering of the predominantly granitic hinterland led to the elevated Al_2O_3 concentrations. These ratios are documented in **Appendix B** (Part 1).

For the calculation of the palaeobioproductivity data the following Ba/Al ratios were used: **[1] 0.002913** (the average Ba/Al ratio value representative of all black shale samples of the Bernesga Mb.) and **[2] 0.0037** the average global Ba/Al crustal ratio from Reitz *et al*. (2004 in: Bernárdez *et al.,* 2008 p.6). The later was used for comparison. The Ba/Al average Bernesga Mb. ratio (**0.002913**) is much lower than that of the average shale **0.0073** of Wedepohl (1971 in: Prakash Babu *et al.,* 2002 p.9). This effect is interpreted to relate to grain-size, where the lowest Ba/Al values belong to the smallest grain-size fraction of the Bernesga Mb. The highest Ba/Al values are apparent in the sand- and siltstones of the Villasimpliz Mb. The application of the high Ba/Al ratios results in negative biogenic Ba (Ba_{bio}) concentrations. As the Ba_{bio} values cannot be negative the following method of Prakash Babu *et al.* (2002) is applied. The minimum Ba/Al ratio (Ba/Al_{min}) present at each of the analysed section was used. It is assumed that the lowest Ba/Al value represents the regional detrital Ba background value. The minimum Ba/Al ratios for the analysed sections were: **[1]** Aralla 0.001204, **[2]** Caldas de Luna 0.001481, **[3]** La Majua 0.002169, **[4]** Sena de Luna 0.001019 and **[5]** Villanueva 0.001105. Ti concentrations were also used to calculate Ba_{bio} values. The $Ba/Ti_{aluminosilicate}$ values used were **[1] 0.068156** (the average value for the Bernesga Mb.) and **[2] 0.126** the global Ba/Ti average from Turekian & Wedephol (1961 in: Bonn *et al.*, 1998). The lowest Ba/Ti ratios (Ba/Ti_{min}) for the analysed sections area were used, under the assumption that the lowest Ba/Ti value represents the regional detrital Ba background value. The lowest Ba/Ti ratios for the analysed sections were: **[1]** Aralla 0.01488309, **[2]** Caldas de Luna 0.022215, **[3]** La Majua 0.047084, **[4]** Sena de Luna 0.022544 and **[5]** Villanueva 0.0232729. The calculated values for Ba_{bio} and $Ba_{bio(min)}$ using Ba/Al, $Ba/Al_{(min)}$ and Ba/Ti, $Ba/Ti_{(min)}$ ratios are all documented in the palaeobioproductivity reconstructions for comparison.

The following section documents and discusses only the calculated palaeobioproductivity (PP) values for the analysed sections. The other plots and calculations necessary for the approximation of PP including Ba_{bio}, $Ba_{bio(min)}$, AR Ba_{bio}, AR $Ba_{bio(min)}$, F_{ba}, $F_{ba(min)}$, P_{new}, and $P_{new(min)}$ can be found in

the palaeoproductivity sections of **Appendix B** (part 1). The methodology utilised for the calculation of the PP can be found in the **Chapter 4.10.5** 'Palaeobioproductivity calculations using barium'.

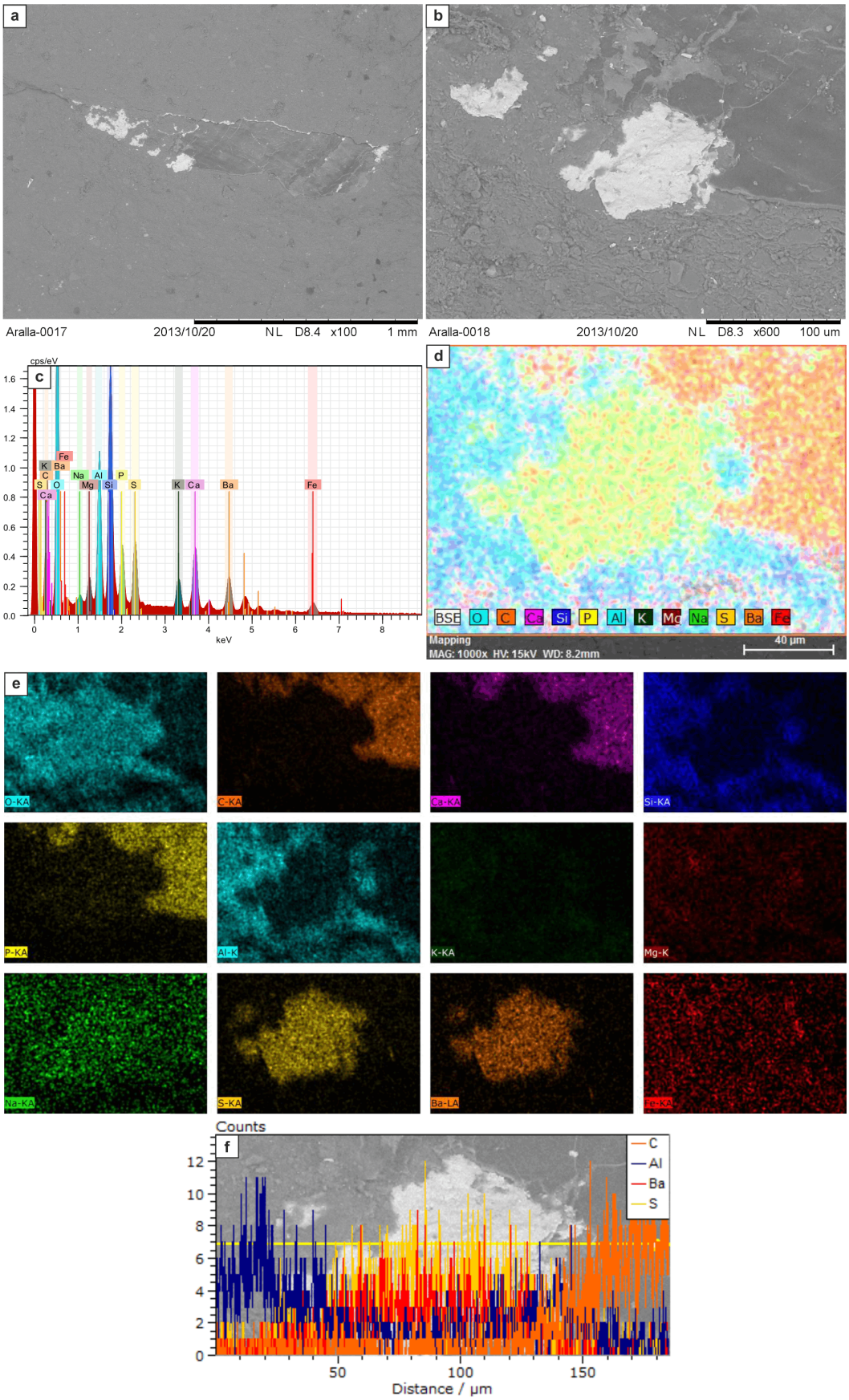

Figure 6.66 The relation of baryte ($BaSO_4$) to organic content, in this case a graptolite fragment within the lower Bernesga Mb. at the Aralla section. **a** & **b)** SEM micrographs of the organic content in relation to the baryte formation. **c)** SEM ED-XRF Spectrum of the analysed specimen **d** & **e)** SEM ED-XRF element distribution maps for the specimen presented in **a** & **b)**, illustrating the enrichments in Ba and S within the baryte crystal and the enrichments in C, Ca and P within the organic content. **f)** Line-scan and the variation in the detected elemental concentrations of C, Al, Ba and S within the analysed specimen.

6.4.8.1 Aralla section

The analysis of the calculated palaeobioproductivity (PP) values led to the interpretation of elevated primary palaeobioproductivity rates for the lower parts of the Bernesga Mb. (see **Figure 6.67**). Ba/Al and Ba/Ti ratios of the Bernesga Mb. (see Figure **6.67 a** and **b**, respectively) were used to calculate the concentrations of Ba_{bio}. The results were compared to calculations performed using the global Ba/Al ratio (see Figure **6.67 c**). When using the global average Ba/Ti the PP values diminish from the base to the top of the Formigoso Fm. including the Villasimpliz Mb. (see **Figure 6.67 d**). The elevated PP values calculated for the basal section of the Bernesga Mb. coincides with the high abundance of monograptid graptolites observed at the base of the section.

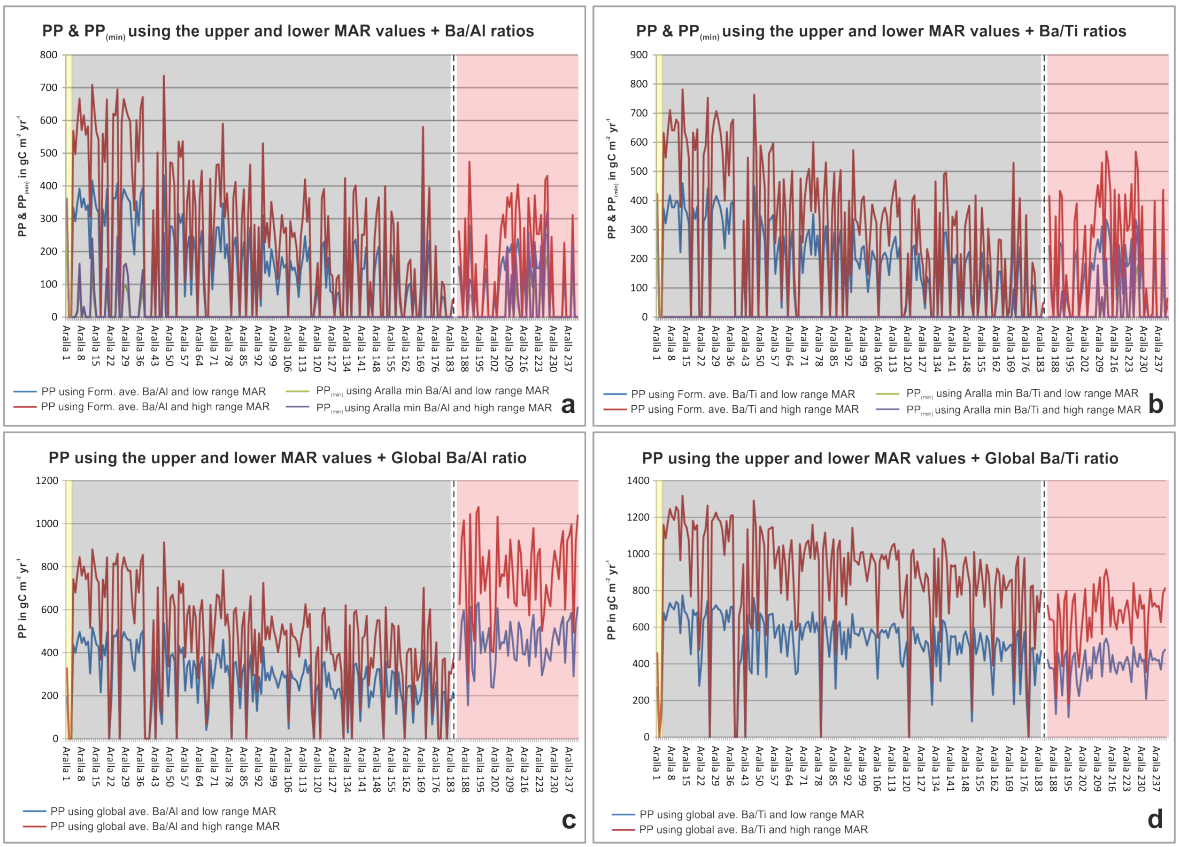

Figure 6.67 Palaeobioproductivity (PP) for the Aralla section using the following formula of Pfeifer *et al.* (2001) and Bonn *et al.* (1998): **PP = 20 (P_{new}) 0.5** expressed in gC m^{-2} yr^{-1}. **a)** Reconstructed PP values using the average Ba/Al ratio from the Bernesga Mb. The productivity levels are significantly elevated at the base of the Bernesga Mb. relative to the top. **b)** Approximated PP values for the average Ba/Ti ratio of the Bernesga Mb. The productivity values are elevated for the basal shales. **c)** PP values using the global Ba/Al ratio. In this instance the Villasimpliz Mb. displays higher productivity values relative to the underlying Bernesga Mb. **d)** The calculated PP values using the global Ba/Ti ratio. The PP values gradually fall throughout the Formigoso Fm. including the sand- and siltstones of the Villasimpliz Mb.

6.4.8.2 Caldas de Luna section

The combined average Bernesga Mb. Ba/Al and Ba/Ti PP values for the Caldas de Luna section are erratic (see **Figure 6.68 a** and **b**). More importantly, the elevated values observed at the base of the previously described Aralla section are not apparent. This may be related to the hiatus

covering the lowermost parts of the Bernesga Mb. When calculating the PP values using the average global Ba/Al and Ba/Ti ratios (see **Figure 6.68 c** and **d**) the productivity rates are still erratic. However, the rates of productivity rise towards the top of the Bernesga Mb. shales.

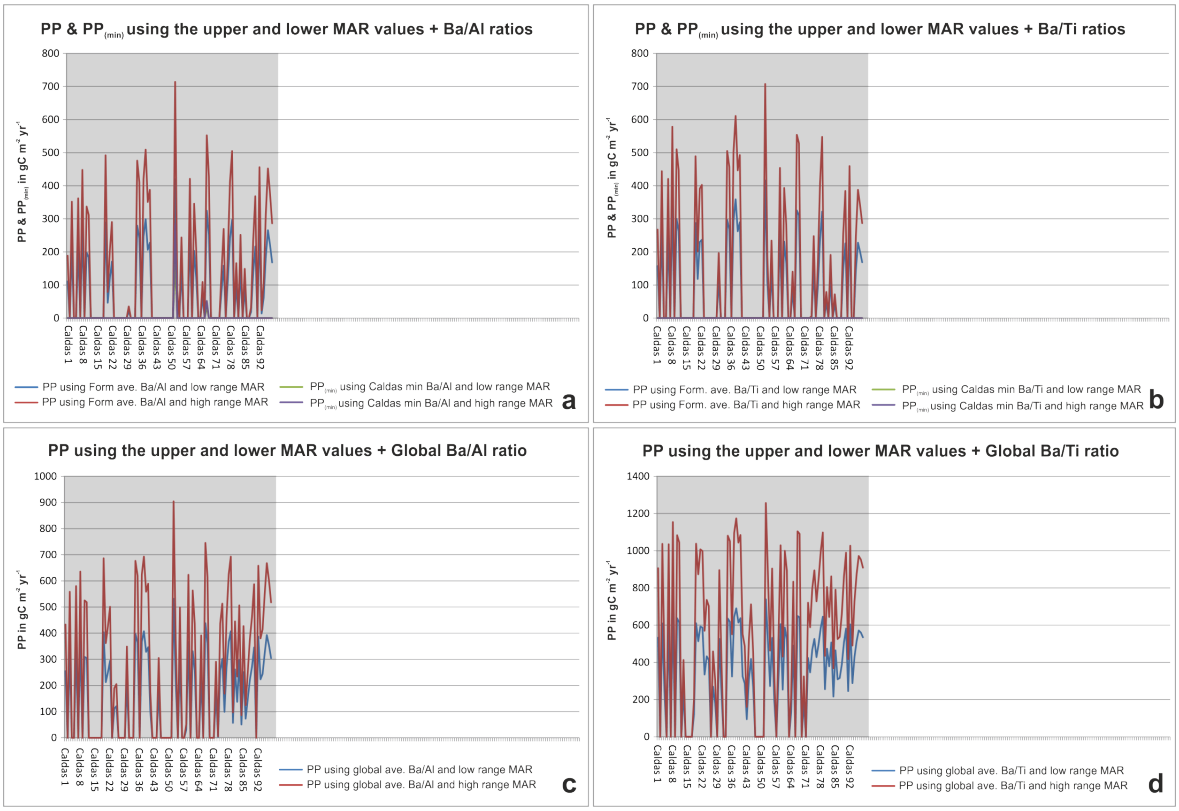

Figure 6.68 Palaeobioproductivity (PP) for the Caldas de Luna section **a)** The reconstructed PP values by applying the average Ba/Al ratio from the Bernesga Mb. The productivity levels are erratic. **b)** PP values using the average Ba/Ti ratio of the Bernesga Mb. the productivity values are irregular. **c)** PP values using the global Ba/Al ratio. The productivity values rise towards the top of the Bernesga Mb. **d)** Calculated PP values using the global Ba/Ti ratio. The productivity values are erratic ate the base becoming more consistent towards the top of the Mb.

6.4.8.3 La Majua section

The average Ba/Al and Ba/Ti ratios from the Bernesga Mb. were used to calculate the PP fluctuations for the La Majua section. The sand- and siltstones of the Getino Beds display higher PP values relative to the overlying Bernesga Mb. shales (see **Figure 6.69 a** and **b**). The high PP values of the basal shales of the Bernesga Mb. observed at the Aralla section and Caldas de Luna sections are not present at the La Majua section. The La Majua area is interpreted to be located near a palaeo-high during the deposition of the lower Bernesga Mb. shales. Thus, explaining the absence of the organically enriched shales at the base of the Bernesga Mb. This interpretation is supported by the lack of redox sensitive element cycles at the base of the La Majua section. When using the average global Ba/Al and Ba/Ti ratios (see **Figure 6.69 c** and **d**), the Bernesga Mb. shales display elevated and relatively consistent PP values. The sands and silts of the Getino Beds

display lower PP values than the basal Bernesga Mb. when the global average Ba/Al ratio is used, and the opposite relationship when using the average global Ba/Ti ratio.

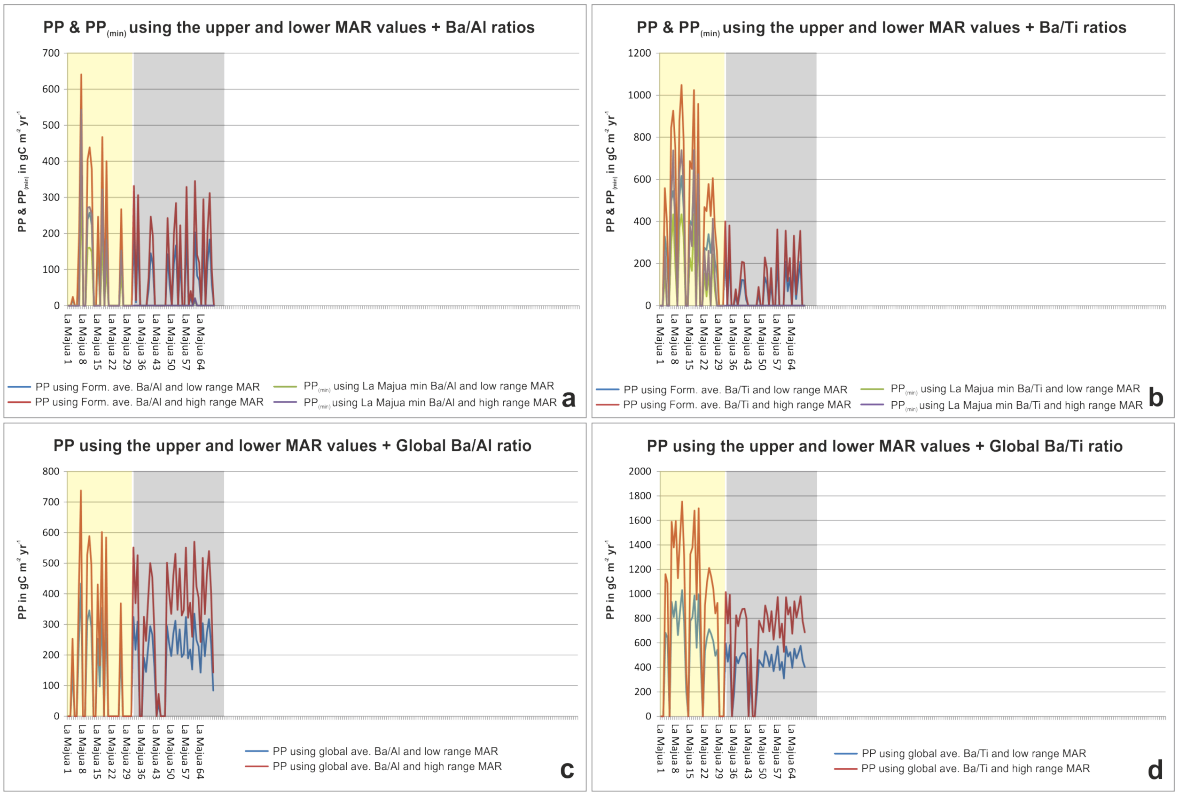

Figure 6.69 a) reconstructed PP using the average Ba/Al of the Bernesga Mb. The estimated productivity levels are significantly elevated for the Getino Beds relative to the base of the Bernesga Mb. **b)** Approximated PP values for the average Ba/Ti ratio of the Bernesga Mb. The productivity values are high for the Getino Beds relative to the basal shales of the Bernesga Mb. **c)** reconstructed PP values using the global Ba/Al ratio. The Getino Beds displays higher yet erratic values relative to the overlying Bernesga Mb. **d)** The calculated PP values using the global Ba/Ti ratio. The PP values fall significantly throughout the Getino Beds, within the overlying Bernesga Mb. the PP values remain relatively consistent.

6.4.8.4 Sena de Luna section

The reconstructed PP values when using the average Bernesga Mb. Ba/Al and Ba/Ti ratios increase from the onset of black shale deposition (see **Figure 6.70 a** and **b**). The PP values drop significantly towards the top of the Bernesga Mb. This interpretation is supported by the abundance of monograptid graptolites at the base of the section. The graptolites diminish throughout the Bernesga Mb. along with the PP values. When utilising the average global Ba/Al and Ba/Ti ratios (see **Figure 6.70 c** and **d**) the high PP rates are calculated for the base of the section, these values fall towards the top of the section.

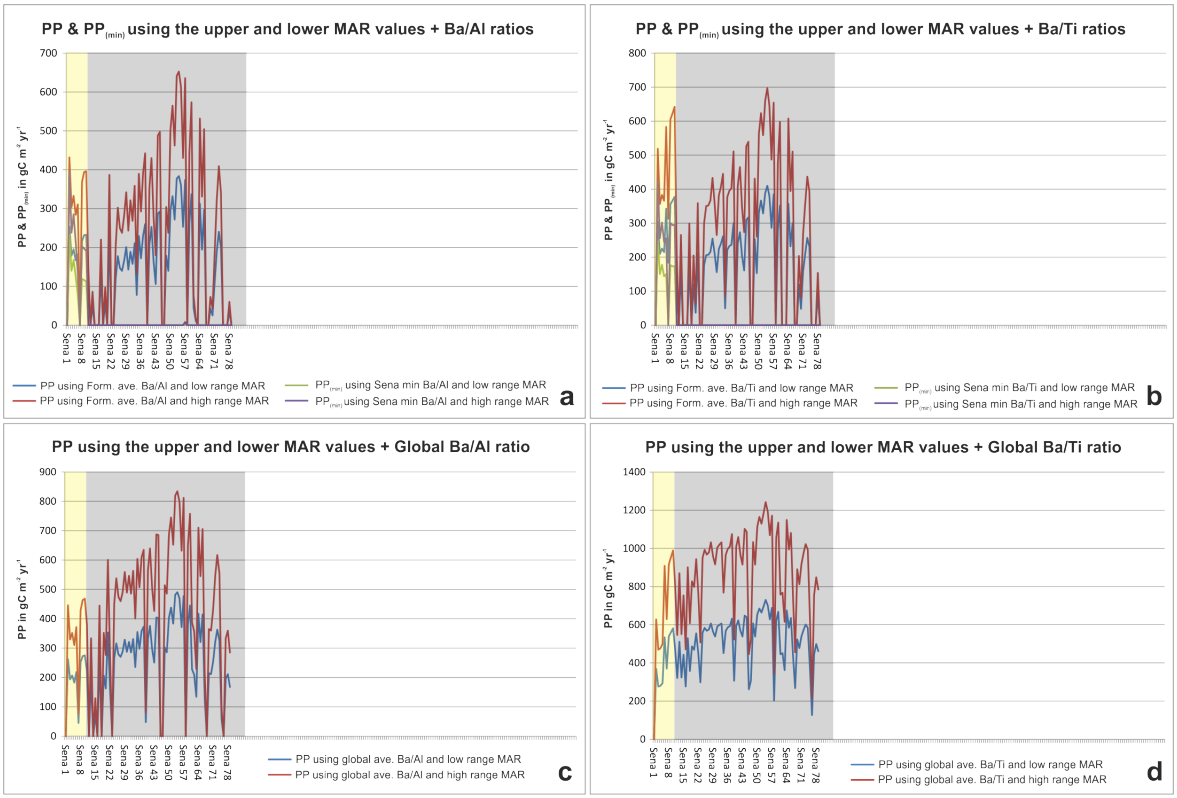

Figure 6.70 a) Reconstructed PP values using the average Ba/Al ratio from the Bernesga Mb. The productivity levels rise significantly from the base of the Bernesga Mb. before dropping towards the top of the Mb. **b)** Approximated PP values for the average Ba/Ti ratio of the Bernesga Mb. The productivity values are elevated for the basal shales, the values fall before rising towards the top of the Mb. where they reduce again. **c)** PP values using the global Ba/Al ratio. The PP values rise from the base of the Bernesga Mb. before falling at the top. **d)** The calculated PP values using the global Ba/Ti ratio. The PP values gradually rise throughout the Bernesga Mb. before falling at the top.

6.4.8.5 Villanueva section

When applying the average Bernesga Ba/Al and Ba/Ti values (see **Figure 6.71 a** and **b**), the PP values are erratic at the base of the Bernesga Mb. before rising towards the top of the Mb. The average global Ba/Al and Ba/Ti ratios (see **Figure 6.71 c** and **d**) are used for comparison, the reconstructed PP values are relatively consistent throughout if not slightly elevated towards the top of the Mb.

To summarise, the generally elevated productivity rates at the base of the Bernesga Mb. shales coincide with the upwelling model of Moore *et al*. (1993). The vast upwelling zone, located off the northern margin of Gondwana during the late early Silurian, was introducing nutrient rich bottom waters into the photic zone. The increase of available nutrients led to a boom in overall primary productivity rates within the surface waters, leading to a high flux of organic carbon to the sea-floor. This interpretation is supported by the presence of the organically enriched sediments of the basal Bernesga Mb., and for that matter the Silurian 'hot' shales spanning the northern margins of Gondwana.

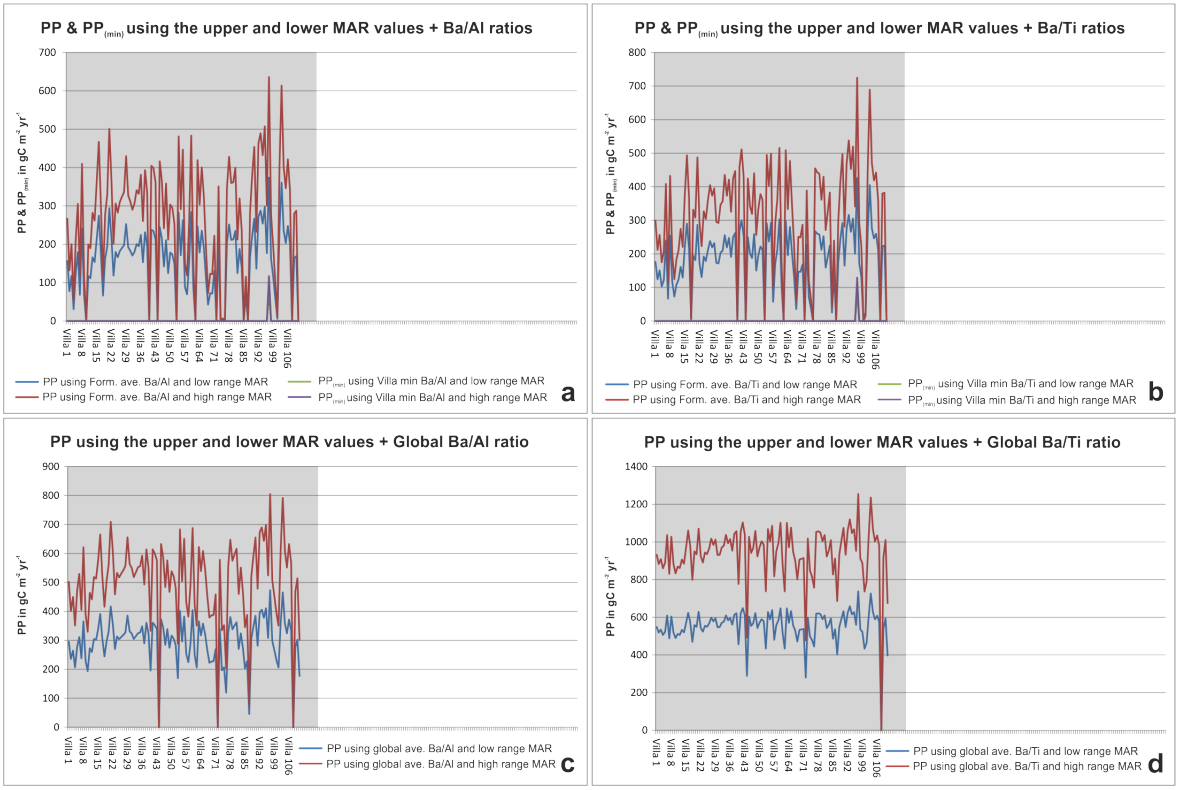

Figure 6.71 a) Reconstructed PP values using the average Ba/Al ratio from the Bernesga Mb. The productivity levels rise from the base of the Bernesga Mb., before decreasing towards the top. **b)** Approximated PP values for the average Ba/Ti ratio of the Bernesga Mb. The productivity values rise from the base to the top. **c)** PP values using the global Ba/Al ratio. The productivity rates increase from the base to the top. **d)** Approximated PP values using the global Ba/Ti ratio. The PP values are relatively consistent before rising towards the top of the Mb.

6.4.9 Gamma-ray signatures

Gamma-ray logs were generated by converting the K_2O, Th and U concentrations into API units following the steps detailed in **Chapter 3.1.11** 'Gamma ray signals and API units'. The TOC values were approximated using the absolute U values following the methods documented in **Chapter 4.10.2** 'Total Organic Carbon (TOC) proxy'. The sections are described and interpreted in the following order: **[1]** Aralla, **[2]** Caldas, **[3]** La Majua, **[4]** Sena de Luna and, **[5]** Villanueva. The figures relating to this section document: **[I]** the spectral curves of K_2O, Th and U in wt% and ppm respectively **[II]** gamma-ray log in API units, **[III]** computed gamma-ray log in API units and **[IV]** total organic carbon (TOC) content in wt%.

6.4.9.1 Aralla section

From interpreting the parameters illustrated in **Figure 6.72**, it is important to note the behaviour of the U ppm concentrations throughout the Bernesga Mb., with a particular emphasis on the basal 60 samples. The U ppm concentrations show three prominent cycles within the first 60 samples, these cycles are tentatively interpreted to reflect the dynamic sedimentological response to changes in the earth's orbital cycle. The gamma-ray values also indicate the presence of the basal 'hot' shales (>300 API). According to Lüning *et al.* (2000), the shales are termed 'hot' when they exceed the gamma-ray threshold of 200 API. The middle and upper parts of the Bernesga Mb. display significantly lower API values than the basal shales, fluctuating at the 'lean' shale boundary of API ≤120 API. The TOC values follow the same cyclic behaviour of the U ppm concentrations as the TOC values were reconstructed using the relationship between U and TOC of Fertl and Chilingar (1988). The approximated TOC values also fall into this 'hot' shale category with TOC values exceeding the 3 wt% threshold.

It is important to note the significant shift in the dataset after the 3rd cycle. This shift is also traceable throughout the other analysed sections and is interpreted to be a tectonically induced event. The sand- and siltstones of the overlying Villasimpliz Mb. are easily identifiable by their erratic signal towards the top of the K_2O, Th and U spectral curves, gamma-ray curve and TOC reconstructions.

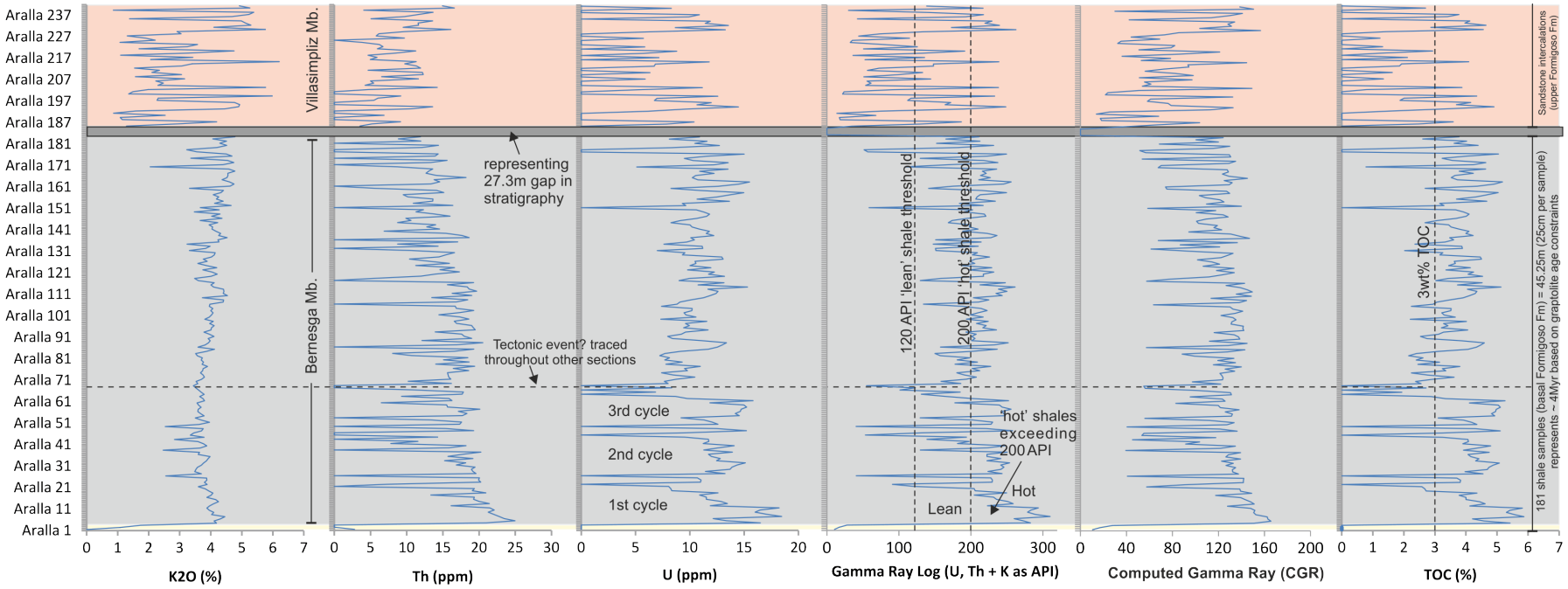

Figure 6.72 K_2O, Th and U concentrations for the Aralla section from the Barrios Fm. (Aralla 1), Getino Beds (Aralla 2+ 3), the Bernesga Mb. (Aralla 4-184) there is then gap in the section of 27.3m represented by the grey shaded line. This gap is followed by the Villasimpliz Mb. (Aralla 185 – 241). The figure also documents the calculated gamma-ray (GR), computed gamma-ray (CGR) and total organic carbon (TOC) values for the Aralla section. Note the cyclic behaviour of the GR and TOC values, in particular the prominent 3 cycles within the first 60 samples. GR values were calculated by converting K_2O, Th and U concentrations to API (American Petroleum Institute), using the conventional $8U + 4Th + 16K_2O$. CGR was formulated in the same way yet the U API values were excluded. The TOC curve was generated by using the analysed U ppm concentrations and the following function: **TOC =3.9637*LN(Uranium Values)-5.6873**. This formula was calculated from the relationship between TOC and U observed by Fertl and Chilingar (1988). The dashed line '200 API' for the GR values and '3 wt% TOC' represent the Silurian 'hot' shale thresholds, the dashed line '120 API' is the lower limit characterising the 'lean' shales of Lüning *et al.* (2000).

6.4.9.2 Caldas de Luna section

The sediments analysed for the Caldas de Luna section consist only of the Bernesga Mb. The concentrations of K_2O, Th and in particular U are elevated at the base of the Bernesga Mb. (see **Figure 6.73**). The combined elevated concentrations of these elements results in API values exceeding the 'hot' shale threshold of Lüning *et al.* (2000) previously mentioned. There is evidently a basal 'hot' shale (> 340 API), a second 'hot' shale level lies above this (~300 API). From analysing the first 50 samples, the U concentrations display two prominent cycles. From this it is interpreted that the first 'hot' shale horizon observed at the Aralla section is here absent.

It is also important to note the significant shift in the dataset after the 2nd cycle. The Bernesga shales are here affected drastically in terms of their Th and U concentrations, before recovering into the mid-upper parts of the Mb.

The mid-upper shales of the Bernesga Mb. are characterised as 'lean' shales. These shales exceed the 120 API 'lean' shale threshold yet fall below the 'hot' shale 200 API confinement. The reconstructed TOC concentrations exceed the 3 wt%. 'hot' shale category at the base, before falling dramatically towards the mid-section and gradually recovering towards the top.

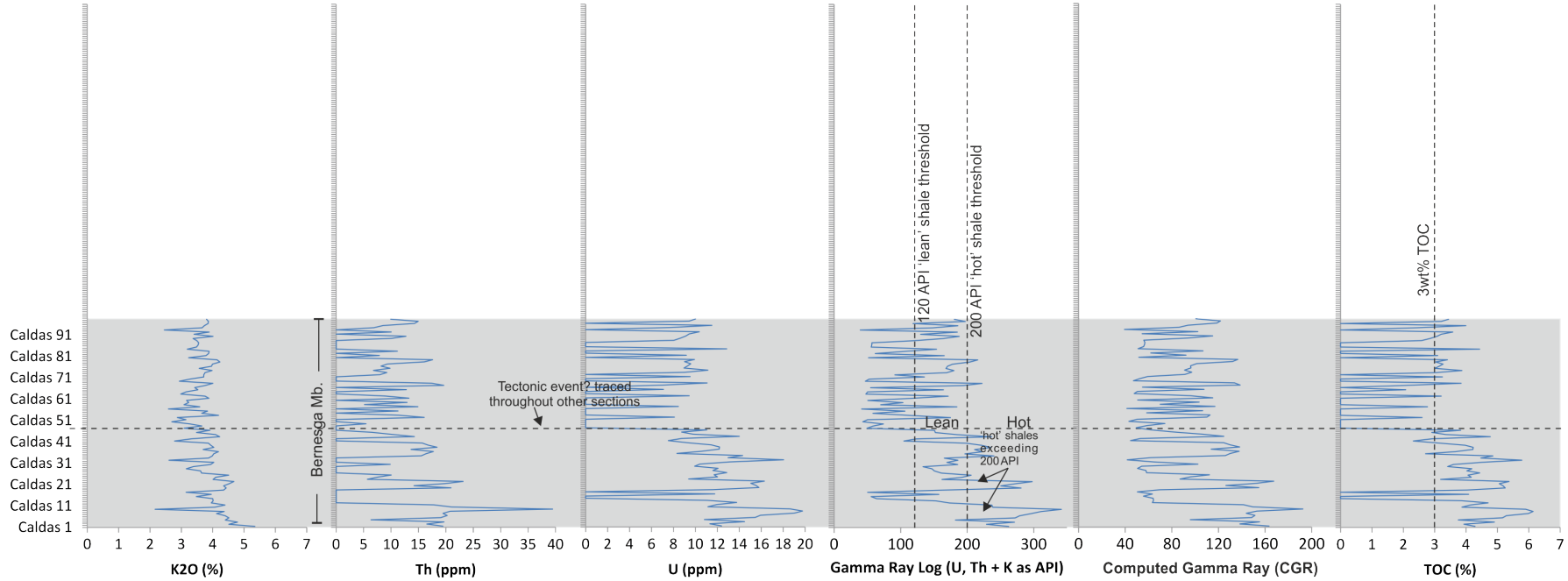

Figure 6.73 K_2O, Th and U concentrations for the Caldas de Luna section. Only the Bernesga Mb. shales were analysed at this location. The figure documents the calculated gamma-ray (GR), computed gamma-ray (CGR) and total organic carbon (TOC) values. Note the cyclic behaviour of the GR and TOC values (prominent 2 cycles within the first 50 samples). The dashed line '200 API' for the GR values and the '3 wt% TOC' for the TOC values represent the 'hot shale' threshold, the dashed line '120 API' is the lower threshold for the 'lean' shales of Lüning *et al.* (2000).

6.4.9.3 La Majua section

The analysed sediments of the Getino Beds at the La Majua locality, display depleted K_2O, Th and U concentrations relative to the overlying Bernesga Mb. When calculating the API values these combined depletions are observable at the base of the gamma-ray log (see **Figure 6.74**). The overlying sediments of the Bernesga Mb. have elevated K_2O, Th and in particular U concentrations. When paying particular attention to the basal 30 samples (La Majua 31 – 70), cyclicity is not as prominent. It could be tentatively interpreted that there are two cycles present. However, it is important to note the absence of the dominant basal 'hot' shales seen in the previous two localities 'Aralla' and 'Caldas de Luna'. This is interpreted to be the result of a palaeo-high present at the time of deposition. Thus, explaining the absence of the organically enriched shales at the base of the Bernesga Mb. The Aralla and Caldas de Luna sections were located within palaeodepressions allowing the very onset of black shale deposition to form these 'hot' shales.

The majority of the Bernesga Mb. at La Majua falls into the 'lean' shale category exceeding 120 API yet falling below the 'hot' shale 200 API confinement. However, there is one horizon that displays values slightly exceeding the 'hot' shale threshold. In contrast, the TOC values do exceed the 3 wt%. 'hot' shale threshold throughout the entirety of the Bernesga Mb.

The inferred 'tectonically induced event' is not traceable within the La Majua section.

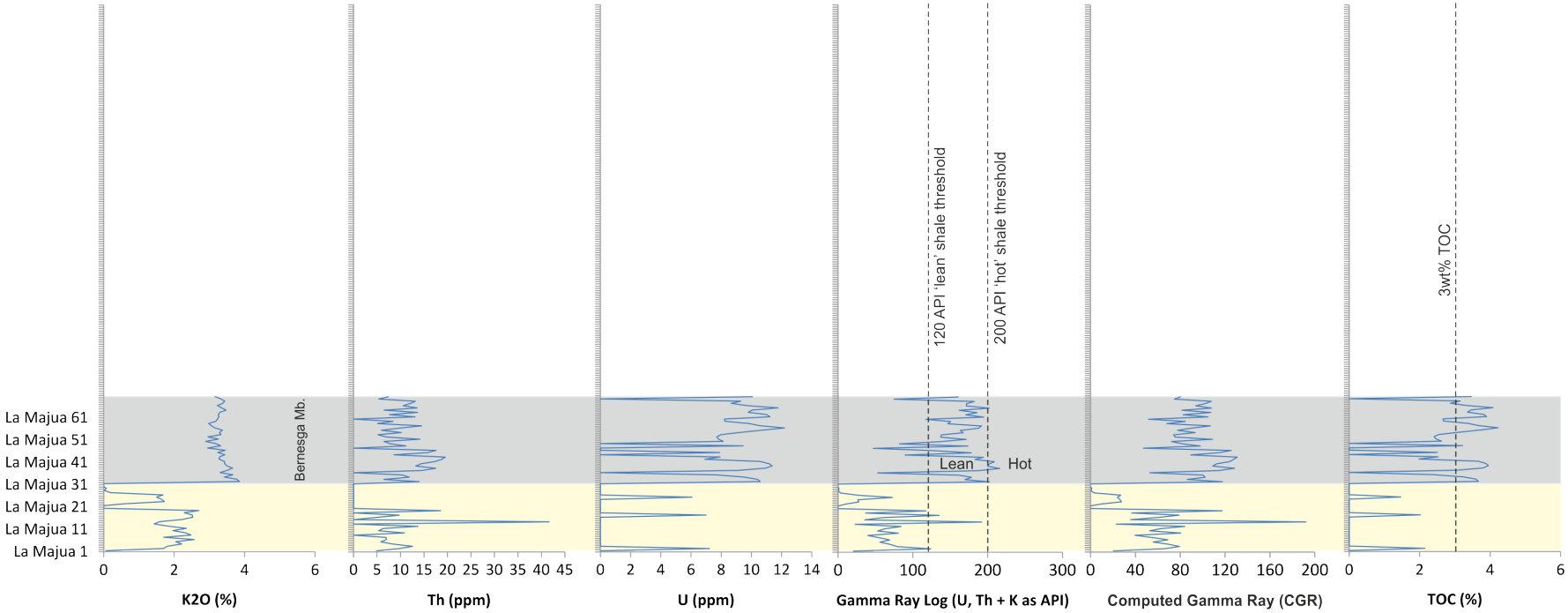

Figure 6.74 K_2O, Th and U concentrations for the La Majua section. La Majua 1 represents the Barrios Fm, La Majua 2-31 the Getino beds, La Majua 32-70 the Bernesga Mb. The figure illustrates the gamma-ray (GR), computed gamma-ray (CGR) and total organic carbon (TOC) values. Importantly the Bernesga Mb. does not display the prominent 'hot' shale horizons evident at the Aralla and Caldas de Luna sections. The dashed line '200 API' for the GR values and the '3 wt% TOC' for the TOC values represent the 'hot shale' threshold, the dashed line '120 API' is the lower threshold of the 'lean' shales of Lüning *et al.* (2000).

6.4.9.4 Sena de Luna section

The sand- and siltstones of the Getino Beds are easily identifiable by their erratic depleted signals (K_2O, Th and U concentrations) relative to the overlying Bernesga Mb. (see **Figure 6.75**). The Th and U concentrations of the Bernesga Mb. increase from the base to the middle parts, where they are comparatively stable. The K_2O concentrations decrease from the base of the Bernesga Mb. becoming relatively uniform towards the top. The combination of the K_2O, Th and U concentrations lead to API values >200 API. This indicates that the 'hot' shales are present, possibly the 2nd and 3rd cycles when relating to the Aralla section. The basal hot shale > 300 API at the Aralla section is not apparent at the Sena de Luna section. It is interpreted that the Sena de Luna section was also situated above a palaeo-high. This palaeo-high was not as large as the La Majua high, as the 2nd and 3rd cycles of the Aralla section are present with the Sena de Luna sediments.

The 'tectonically induced event' is apparent towards the top of the Bernesga Mb. with a significant shift in the various parameters documented.

The TOC concentrations indicate that the Bernesga Mb. shales are borderline 'hot' shales at the base, these values increase towards the top (>3 wt%.) of the Mb. clearly indicating the presence of the 'hot' shales.

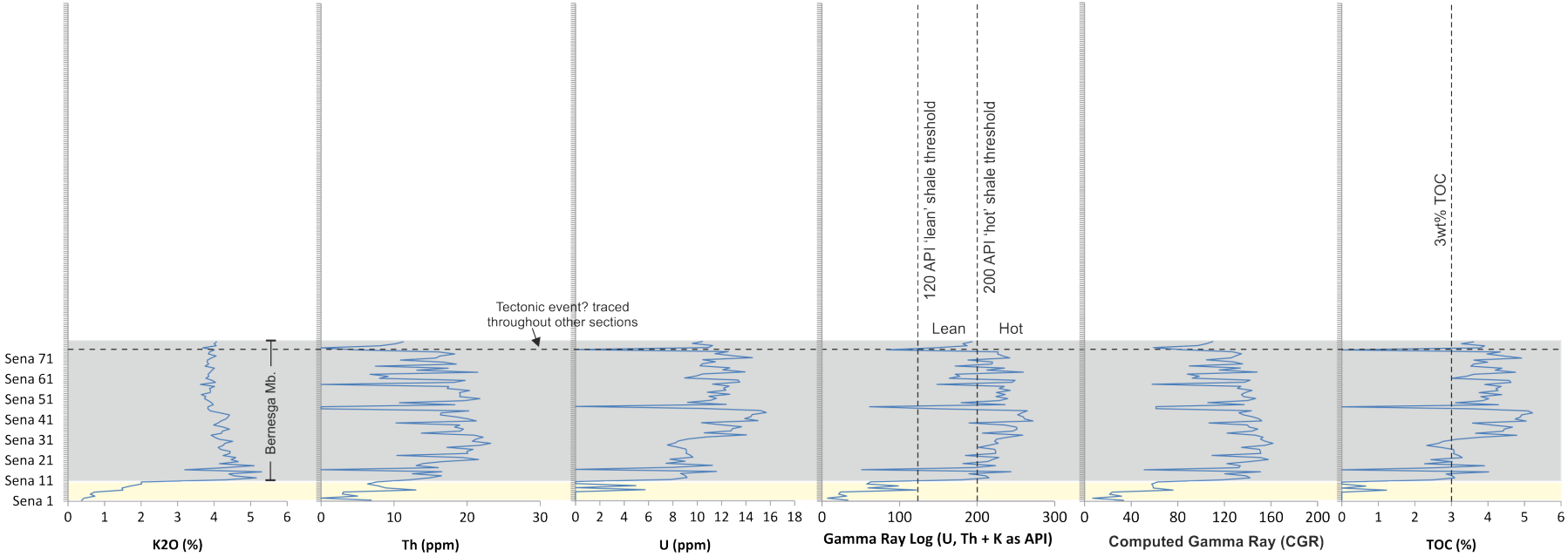

Figure 6.75 K_2O, Th and U concentrations for the Sena de Luna section. Sena 1 represents the Barrios Fm, Sena 2-10 the Getino Beds, Sena 11-79 the Bernesga Mb. There is a significant shift in the data 'dotted line' towards the top of the section, this is noted to be a possible tectonically induced event. The figure also documents the calculated gamma-ray (GR), computed gamma-ray (CGR) and total organic carbon (TOC) values. Note the cyclic behaviour of the U, GR and TOC values (prominent 2 cycles from sample 11). The dashed line '200 API' for the GR values and the '3 wt% TOC' for the TOC values represent the 'hot shale' threshold, the dashed line '120 API' is the lower threshold for the 'lean' shales of Lüning *et al.* (2000).

6.4.9.5 Villanueva section

From analysing the presented parameters in **Figure 6.76** is observable that the 'hot' shales are present (> 200 API) within the basal shales of the Villanueva locality. However, the punctuated elevated 'hot' shale cycles (> 300 API) apparent for the basal Aralla and Caldas de Luna sections are not present. This can again be interpreted as a result of the undulating palaeo-relief present at the time of deposition.

The inferred 'tectonically induced event' is present at the Villanueva section. This event significantly effects the concentrations of K_2O, Th and U towards the middle of the Bernesga Mb., the values recover towards the top, mostly within the limits of the 'lean' shale confinements.

The majority of the basal Bernesga Mb. exceeds the 200 API 'hot' shale threshold as do the concentrations of TOC (> 3 wt%.).

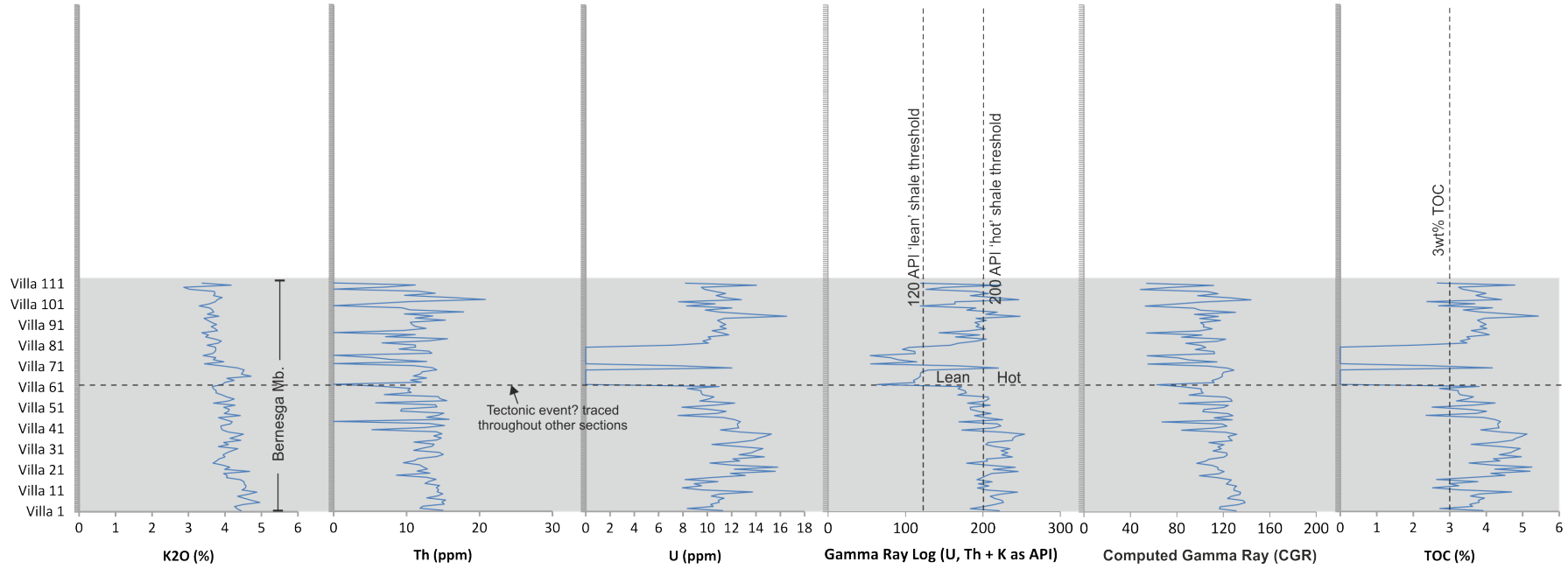

Figure 6.76 K_2O, Th and U concentrations for the Villanueva section. All samples are representative of the Bernesga Mb. The figure also illustrates the gamma-ray (GR), computed gamma-ray (CGR) and total organic carbon (TOC) values. The dashed line '200 API' for the GR values and the '3 wt% TOC' for the TOC values represent the 'hot shale' threshold, the dashed line (120 API) is lower threshold for the 'lean' shales of Lüning *et al.* (2000).

6.4.10 Cyclicity and high order sea-level oscillations

When referring to the previous **Chapter 6.4.9** 'Gamma-ray signatures', cyclicity is evident within the U concentrations of the basal shales belonging to the Bernesga Mb., particularly for the Aralla and Caldas de Luna sections. As a result, other redox sensitive elements patterns were analysed to determine similar cyclic patterns during the initial onset of black shale deposition. It was observed that the V concentrations expressed the same cyclic patterns as that of U (for e.g. see **Chapter 5.1.2** 'Trace element variations', **Figure 5.2 c** and **Figure 5.3 g**). For this reason, the U and V concentrations of the Bernesga Mb. shales were analysed applying a Fourier spectral analysis. This spectral analysis was used to determine whether these cyclic redox element patterns were significant signals that could be interpreted, and importantly, to what frequency the cycles occurred. The Fourier analysis was applied by utilising the PAST software of Hammer *et al.* (2001) as detailed in **Chapter 4.10.6** 'Cyclicity (Fourier analysis)'. The sampling interval was consistent (25 cm) for the Bernesga Mb. The time interval represented by each sample was calculated to be ~22099.44 yr. For the Aralla high resolution log, the Bernesga Mb. was analysed every 1cm, a time interval of ~883.97 yr was calculated (see **Chapter 4.10.5.1** 'Calculation of biogenic barium and its accumulation rates').

6.4.10.1 Aralla section

Firstly the absolute U ppm concentrations were introduced into a matrix plot (see **Figure 6.77 b**). The Matrix plot showed that a cyclic nature of the U values was present at the base of the Bernesga Mb. When applying the spectral analysis to the absolute U ppm concentrations a clear cyclic frequency is determined (see **Figure 6.77 c**). By using the time interval of ~22099.44 yr previously calculated, the periodicity of the cycles can be determined. The most prominent frequency was **0.038194** giving a calculated cyclicity of **578.59 Kyr**. A short-term Fourier analysis (see **Figure 6.77 d**) also reveals the frequency of these cycles at the base of the Bernesga Mb. and what point these cycles cease (~ Aralla 80).

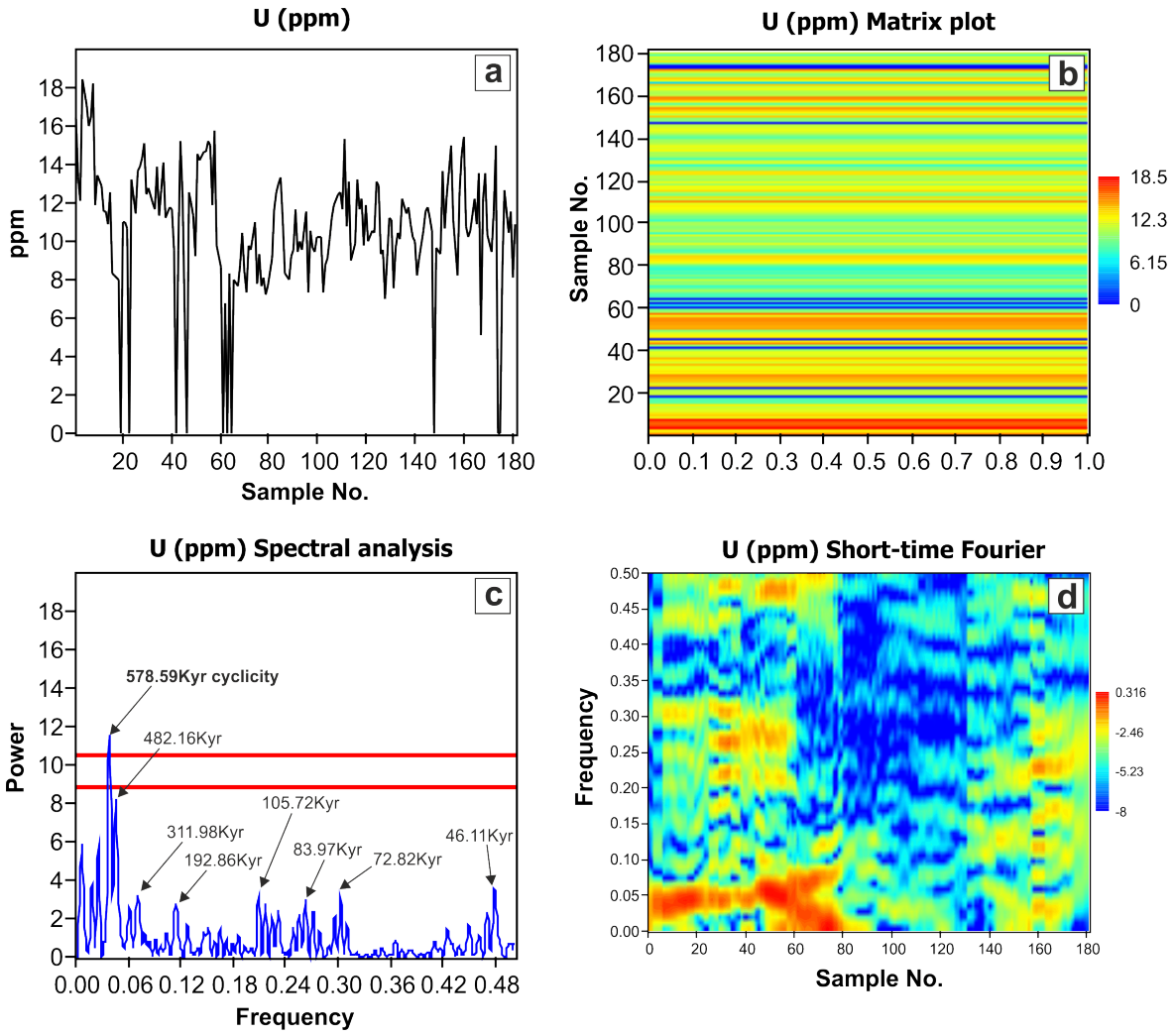

Figure 6.77 Analysed U ppm concentrations from the Bernesga Mb. of the Aralla section (181 samples, Aralla 4 – Aralla 184). **a)** Illustrates the absolute U ppm concentrations from the base (sample No. 1) to the top (sample No. 181) of the Bernesga Mb. **b)** Matrix plot of the U ppm values with the sample numbers on the Y-axis and the intensity of the U ppm values expressed as colours (values to the right of plot), this plot emphasises the cyclicity at the base. **c)** Spectral analysis of the U ppm values, the red lines signify the lower ($p<0.05$) and upper limits ($p<0.01$) of the significance levels with respect to white, uncorrelated noise and **d)** Short-time Fourier analysis highlighting the cyclic frequency (Y-axis) at the base and at which point they cease, the sample numbers are shown on the X-axis.

Frequencies (plots c and d, above)	Calculations of periodicity	Cyclicity values
0.0069444	= 1/(0.0069444/22099 yrs)	3.18 Myr
0.01875	= 1/(0.01875/22099 yrs)	1.17 Myr
0.025694	= 1/(0.025694/22099 yrs)	860.08 Kyr
0.038194 **(highest intensity)**	**= 1/(0.038194/22099 yrs)**	**578.59 Kyr**
0.045833	= 1/(0.045833/22099 yrs)	482.16 Kyr
0.070833	= 1/(0.070833/22099 yrs)	311.98 Kyr
0.11458	= 1/(0.11458/22099 yrs)	192.86 Kyr
0.20903	= 1/(0.20903/22099 yrs)	105.72 Kyr
0.26317	= 1/(0.26317/22099 yrs)	83.97 Kyr
0.30347	= 1/(0.30347/22099 yrs)	72.82 Kyr
0.47917	= 1/(0.47917/22099 yrs)	46.11 Kyr

Table documenting the prominent frequencies determined by spectral analysis (plot **c** above). The cyclicity periodicity was calculated by dividing the frequencies by the sampling interval.

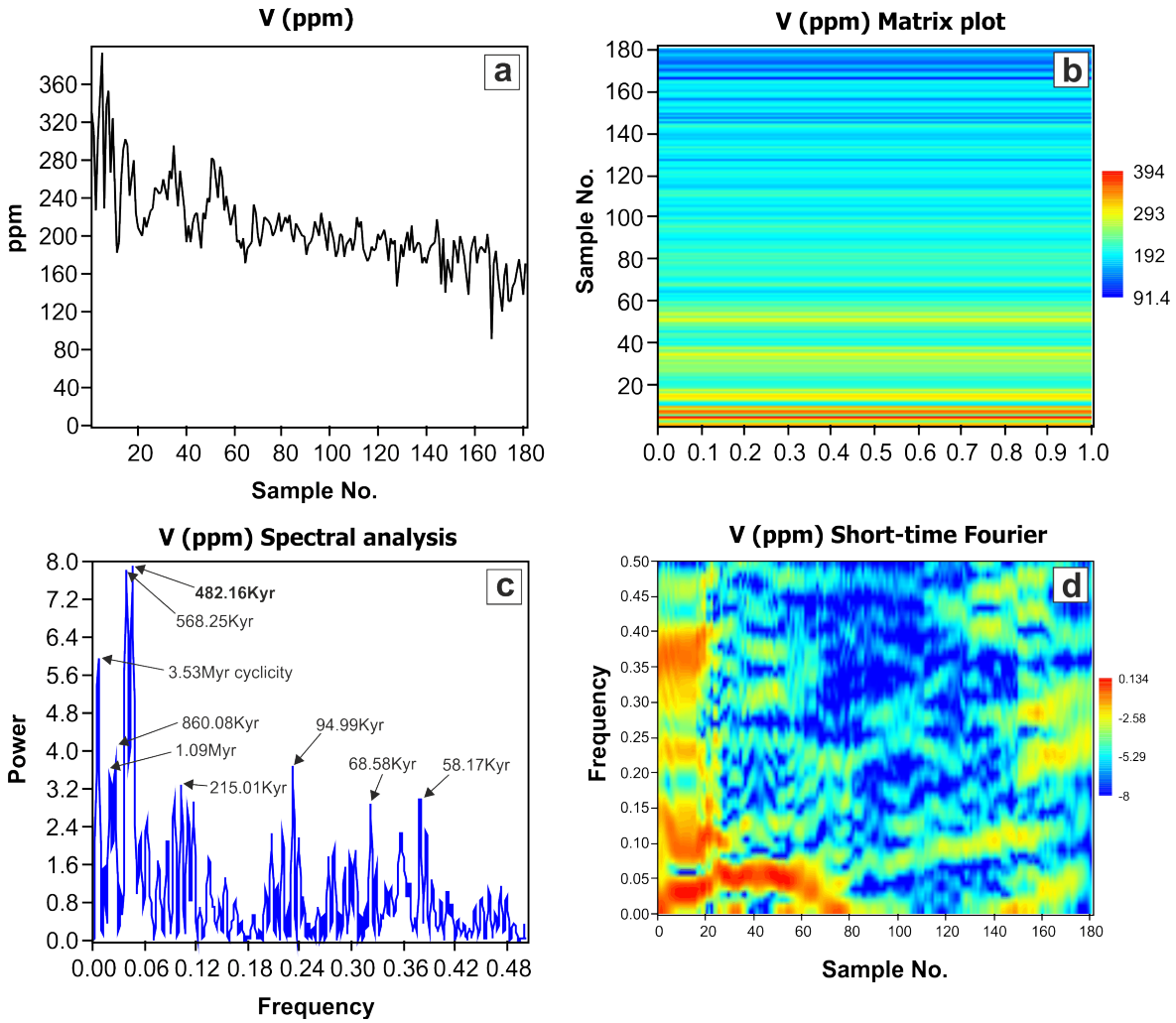

Figure 6.78 Analysed V ppm concentrations from the Bernesga Mb. of the Aralla section (181 samples, Aralla 4 – Aralla 184). **a)** Illustrating the absolute V concentrations from the base (sample No. 1) to the top (sample No. 181) of the Bernesga Mb. **b)** Matrix plot of the V ppm values with the sample numbers on the Y-axis and the intensity of the V ppm values expressed as colours (values to the right of plot), this plot emphasises the cyclicity at the base. **c)** Spectral analysis applied to the V concentrations, and **d)** Short-time Fourier analysis highlighting the cyclic frequency (Y-axis) at the base and at which point they cease, the sample numbers are shown on the X-axis.

Frequencies (plots c and d, above)	Calculations of periodicity	Cyclicity values
0.00625	= 1/(0.00625/22099 yrs)	3.53 Myr
0.020139	= 1/(0.020139/22099 yrs)	1.09 Myr
0.025694	= 1/(0.025694/22099 yrs)	860.08 Kyr
0.038889	= 1/(0.038889/22099 yrs)	568.25 Kyr
0.045833 **(highest intensity)**	**= 1/(0.045833/22099 yrs)**	**482.16 Kyr**
0.10278	= 1/(0.10278/22099 yrs)	215.01 Kyr
0.23264	= 1/(0.23264/22099 yrs)	94.99 Kyr
0.32222	= 1/(0.32222/22099 yrs)	68.58 Kyr
0.35764	= 1/(0.35764/22099 yrs)	61.79 Kyr
0.37986	= 1/(0.37986/22099 yrs)	58.17 Kyr

Table documenting the prominent frequencies determined by spectral analysis (plot **c** above).

The absolute V concentrations are documented in **Figure 6.78 a**, cycles are observable at the base of the Bernesga Mb. When interpreting the matrix plot of the absolute V values the cycles are evident at the base of the analysed section (see **Figure 6.78 b**). The Fourier analysis of the V values resulted in a dominant frequency of **0.045833**, and a calculated **482.16 Kyr** cyclicity (see **Figure 6.78 c**). The short-time Fourier plot illustrates the frequencies present at the base of the Bernesga Mb., these cycles cease at sample No. 80 (see **Figure 6.78 d**).

In order to eliminate the background noise apparent within the middle to upper parts of the Bernesga Mb. a spectral analysis was performed for the first 3 cycles (basal 66 samples), relating to the absolute U and V concentrations of the Aralla section. The result of the spectral analysis led to a calculated **514.3 Kyr** cyclicity for both the U and V ppm values. For these plots see **Results Appendix B** (Part 1).

6.4.10.1.1 Aralla high resolution section

Based on the laboratory results, it was decided to analyse the first prominent cycle (~ 3 m in the field), at high resolution utilising a handheld Niton XL3t XRF analyser in the field. The resolution increased from the consistent 25 cm equidistant sampling interval to 1 cm analysed *in-situ*. The objective of this higher resolution analysis was to determine if there was a higher order cyclicity superimposed on the previously discovered **514.3 Kyr** cyclicity. The 1 cm analysis interval gave an approximate sample interval of **~883.97 yrs** as previously calculated.

The absolute U ppm concentrations were just above the detection limit for *in-situ* analysis. This resulted in a partial U ppm curve for the high resolution field data (see **Figure 6.79 a**). However, even with the partial curve the remnants of the **513.3 Kyr** cyclicity are still apparent (first cycle). The Matrix plot of the U concentrations illustrates a possible cyclic nature at the base of the analysed section (see **Figure 6.79 b**). The highest frequencies apparent after applying the Fourier analysis were: 0.0044788, 0.03298 and **0.1816** (highest intensity). These gave calculated periodicities (respectively) of [1] **197.3 Kyr**, [2] **26.8 Kyr** and [3] **4.8 Kyr**, the latter having the highest intensity (see **Figure 6.79 c**). These calculated cyclicity values must however be viewed with caution, due to the extent of U ppm data below detection limit. The extent of background noise present for the spectral analysis is highlighted with the application of the short-time Fourier analysis (see **Figure 6.79 d**).

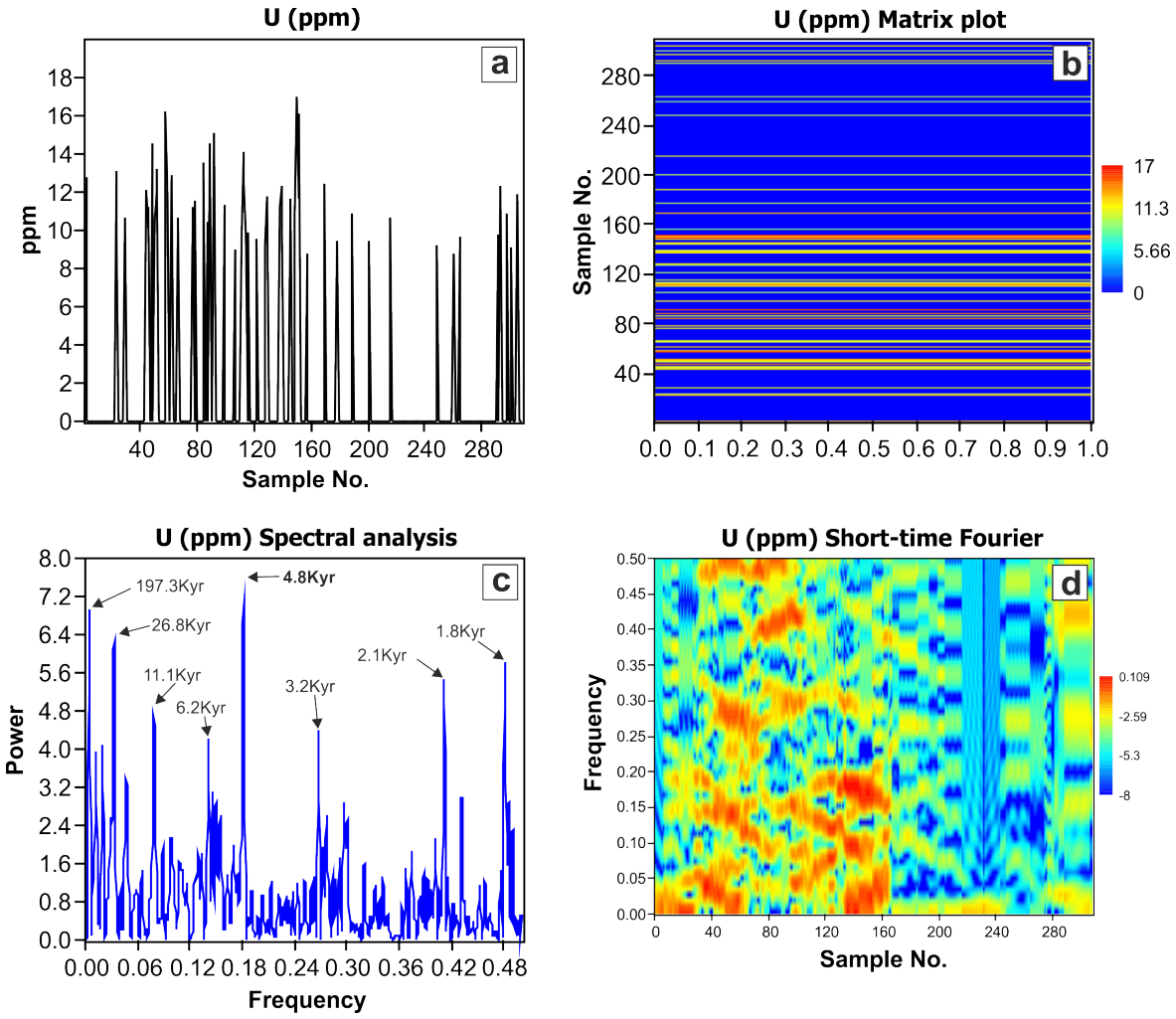

Figure 6.79 High resolution U concentrations of the first cycle (lowermost Bernesga Mb.) of the Aralla section, 309 *in-situ* analysis points (HR 32 – HR 339). **a)** U ppm concentrations values from the base (sample No. 1) to the top (sample No. 309). **b)** Matrix plot of the U ppm values with the sample numbers on the Y-axis and the intensity of the U ppm values expressed as colours (values to the right of plot), this plot emphasises possible cyclicity. **c)** Spectral analysis of the U ppm values, and **d)** Short-time Fourier analysis, highlighting the extent of background noise. The sample numbers are shown on the X-axis.

Frequencies (plots c and d, above)	Calculations of periodicity	Cyclicity values
0.0044788	= 1/(0.0044788/883.97 yrs)	197.36 Kyr
0.03298	= 1/(0.03298/883.97 yrs)	26.8 Kyr
0.07899	= 1/(0.07899/883.97 yrs)	11.1 Kyr
0.14129	= 1/(0.14129/883.97 yrs)	6.2 Kyr
0.1816 **(highest intensity)**	**= 1/(0.1816/883.97 yrs)**	**4.8 Kyr**
0.26792	= 1/(0.26792/883.97 yrs)	3.2 Kyr
0.41205	= 1/(0.41205/883.97 yrs)	2.1 Kyr
0.48168	= 1/(0.48168/883.97 yrs)	1.8 Kyr

Table documenting the prominent frequencies determined by spectral analysis (plot **c** above). The cyclicity periodicity was calculated by dividing the frequencies by the sampling interval.

Cyclicity is evident within absolute V concentrations of the analysed in-situ section (see **Figure 6.80 a**). When the absolute V concentrations were introduced into the matrix plot (see **Figure 6.80 b**) the cyclic nature of the V values is evident. The spectral analysis determined that there is clearly a higher-order cyclicity superimposed on the previously calculated **513.3 Kyr** cyclicity (see **Figure 6.80 c**). The most prominent frequencies apparent were: [1] **0.0040717** (highest intensity), [2] 0.023208 and [3] 0.029316. These frequencies gave calculated periodicities of (respectively): [1]

217.1 Kyr (highest intensity), [2] **38 Kyr** and [3] **30.1 Kyr**. These calculated values must however be interpreted with caution, due to the extent of background noise (see **Figure 6.80 d**).

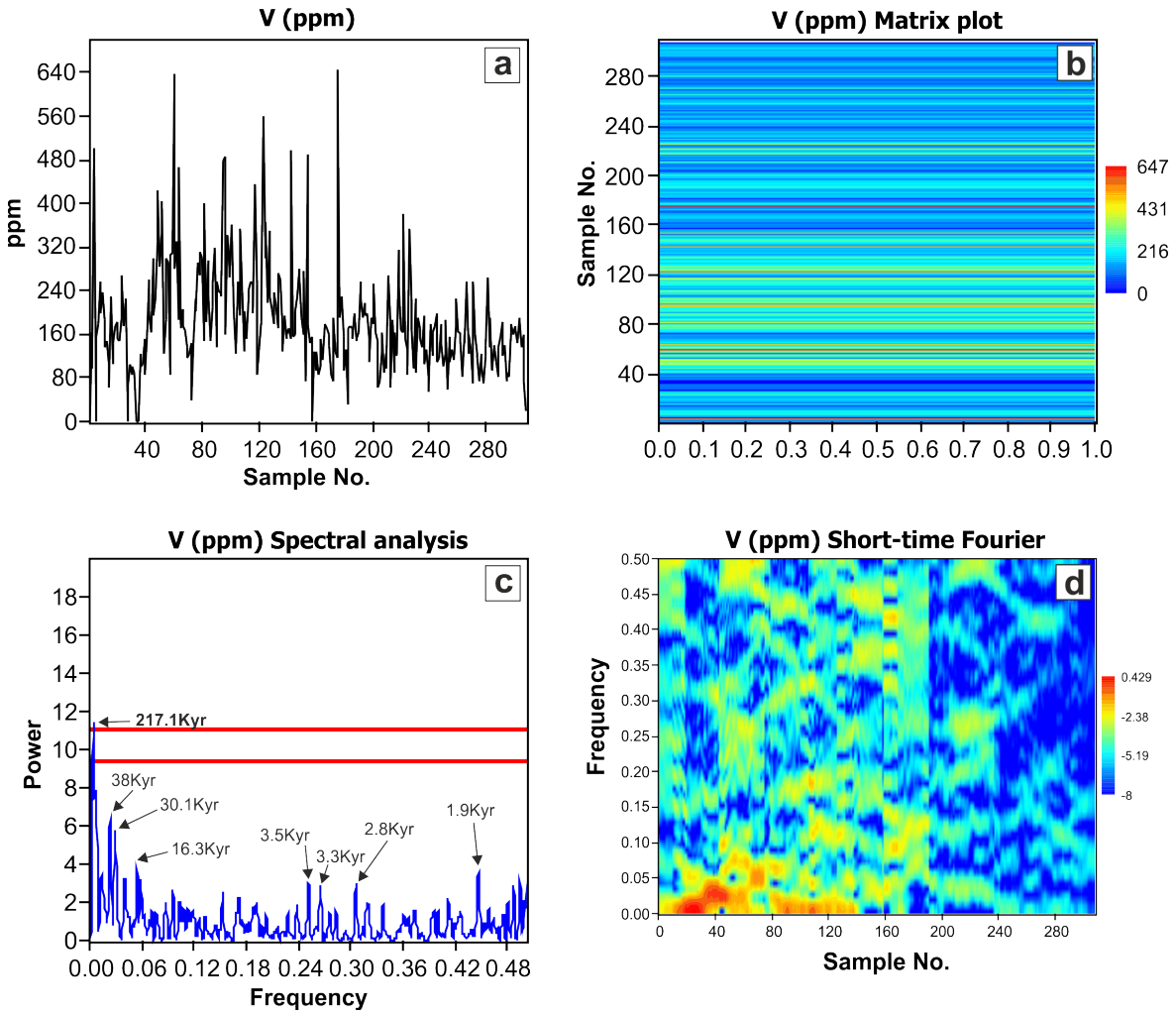

Figure 6.80 High resolution data of V concentrations for the first cycle (lower Bernesga Mb.) of the Aralla section, 309 *in-situ* analysis points (HR 32 – HR 339). **a)** Absolute V ppm values from the base (sample No. 1) to the top (sample No. 309), cyclicity is apparent. **b)** Matrix plot of the V ppm values with the sample numbers on the Y-axis and the intensity of the V ppm values expressed as colours (values to the right of plot), this plot emphasises the cyclicity at the base. **c)** Represents the spectral analysis of the V ppm values, the red lines signify the lower ($p<0.05$) and upper limits ($p<0.01$) of the significance levels with respect to white, uncorrelated noise and **d)** Short-time Fourier analysis, pinpointing the elevated frequencies, note there is a significant amount of background noise, the sample numbers are shown on the X-axis.

Frequencies (plots c and d, above)	Calculations of periodicity	Cyclicity values
0.0040717 **(highest intensity)**	**= 1/(0.0040717/883.97 yrs)**	**217.1 Kyr**
0.023208	= 1/(0.023208/883.97 yrs)	38 Kyr
0.029316	= 1/(0.029316/883.97 yrs)	30.1 Kyr
0.054153	= 1/(0.054153/883.97 yrs)	16.3 Kyr
0.25163	= 1/(0.25163/883.97 yrs)	3.5 Kyr
0.26547	= 1/(0.26547/883.97 yrs)	3.3 Kyr
0.30619	= 1/(0.30619/883.97 yrs)	2.8 Kyr
0.44707	= 1/(0.44707/883.97 yrs)	1.9 Kyr

Table documenting the prominent frequencies determined by spectral analysis (plot **c** above). The periodicity was calculated by dividing the frequencies by the sampling intervals.

6.4.10.1.2 A new high-resolution sea-level curve for the lower-mid Telychian

The previously published sea-level curves were analysed with a special emphasis on the mid Early Silurian (see **Figure 6.81**). The global sea-level curve of Loydell (1998), displays a similar cyclic pattern to that observed within the redox sensitive elements of the Bernesga Mb. at Aralla (see **Figure 6.82**). The redox sensitive elements U and V were plotted against stratigraphy. These redox sensitive elements are fluctuating in response to changing sea-levels, correlating directly with the transgressions and regressions of the early to mid-Telychian sea-level (see **Figure 6.82**). The periods of elevated reducing conditions (high U and V concentrations), correspond to sea-level highs. Whereas, the lower reducing conditions (low U and V concentrations), correspond to sea-level lows. The previous Fourier analyses isolated two major frequencies in the high resolution V ppm concentrations, **217.1 Kyr** and **38 Kyr**. This higher order **38 Kyr** cyclicity is superimposed upon the **513.3 Kyr**. When the 513.3 Kyr and 38 Kyr cycles are combined, a new high-resolution relative sea-level curve for the lower Silurian (early to mid Telychian) of the Cantabrian region can be inferred.

The sea-level highs are related to the retreating Hirnantian ice masses, whereas the lows are periods of glacial advance.

The fluctuations in sea-level may be coherent with the earth's eccentricity. The earth's eccentricity fluctuates in a cyclic 413Kyr fashion. Thus the cyclicity found in the redox sensitive elements V and U (**513.3 Kyr**) could be a dynamic response to the changing orbital patterns. In times of low eccentricity (close to concentric, very low eccentricity–values) the Earth remains during the summer in closer proximity to the sun (thereby triggering glacial retreat and a relative eustatic sea-level rise). In periods of high eccentricity (elliptical closer to 1) the Earth is orbiting the sun in greater distance, hence promoting temperature drops leading to the increase of ice masses and a consequent relative eustatic sea-level drop.

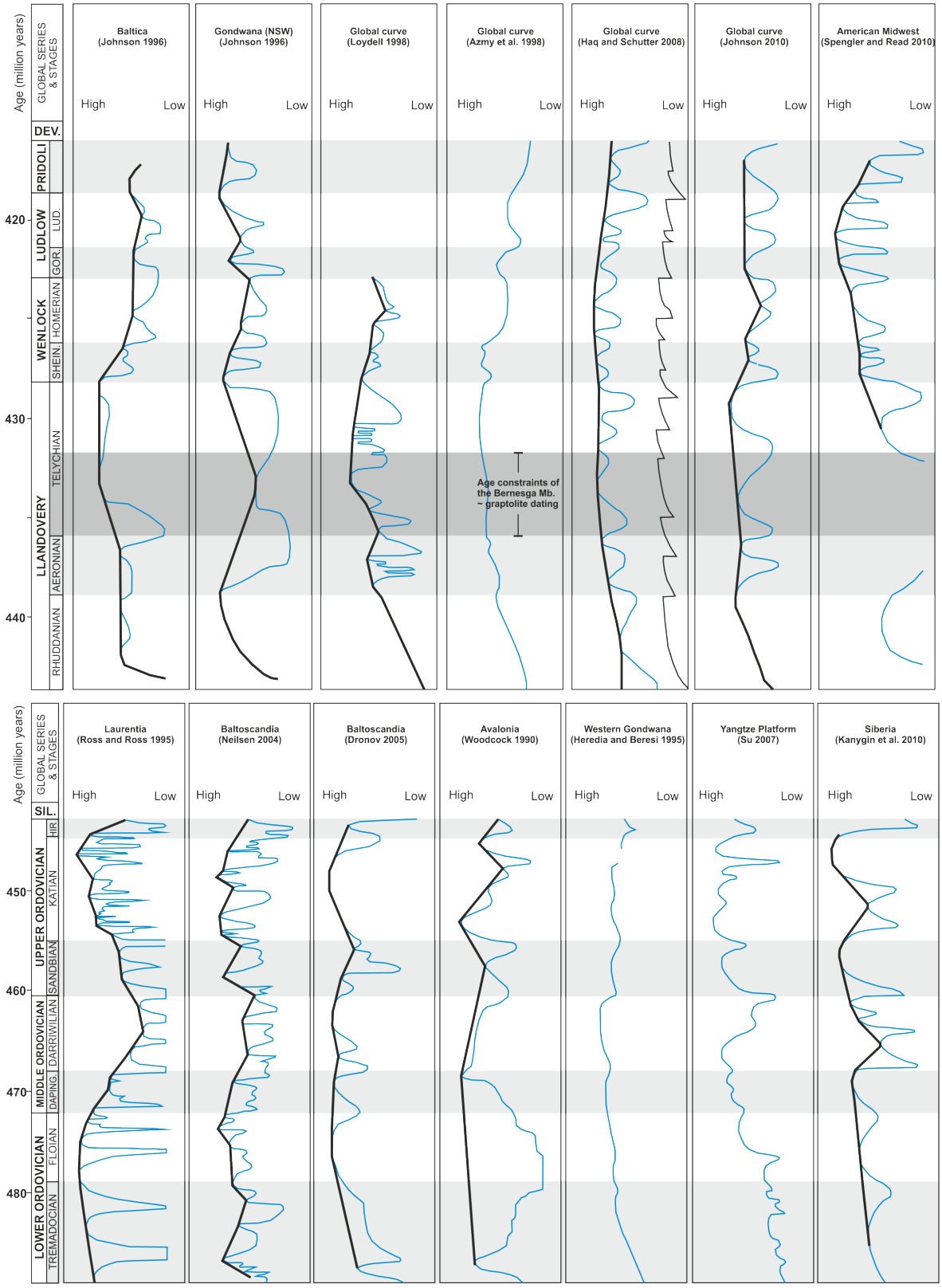

Figure 6.81 Ordovician and Silurian relative sea-level curves modified after Munnecke *et al*. (2010). The area of interest is highlighted within the Silurian curves, using the age constraints for the Bernesga Mb. spanning ~ 4Myr from base to top.

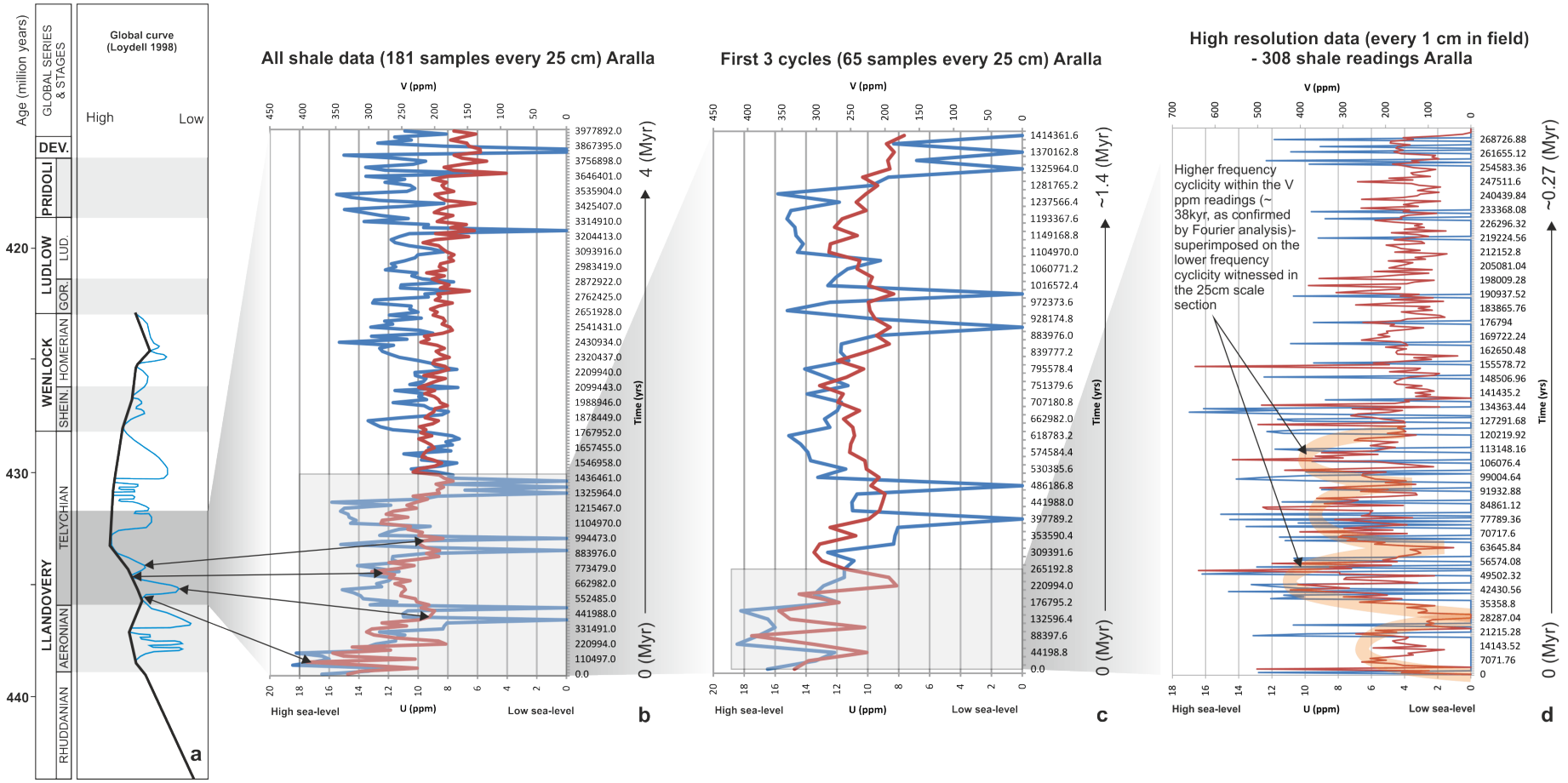

Figure 6.82 Documenting the high resolution whole rock geochemistry, specifically the redox sensitive elements U + V. These elements are used to reconstruct a part of the early Silurian sea-level curve. (**a**) The global sea-level curve of Loydell (1998), the area highlighted in grey spanning from the Aeronian/Telychian boundary (436Ma) to the mid-Telychian *Monoclimacis* Graptolite Zone (~432Ma). These are the approximate age constraints for the Bernesga Mb. of the Formigoso Fm. (**b**) Displaying the absolute concentrations of U (blue) and V (red) for the Aralla section (181 samples of the Bernesga Mb.). The redox element cyclicity is comparable to global sea-level curve of Loydell (1998), (**c**) The first 3 cycles from (**b**), and finally (**d**) The high resolution *in-situ* data. The redox element cyclicity is superimposed upon the 513.3 Kyr cyclicity (**b**). The high-resolution cyclicity can be used to infer a new high resolution relative sea-level curve for the lower Silurian (lower to middle Telychian) of the Cantabrian region.

6.4.10.2 Caldas de Luna section

The absolute U values for the Caldas de Luna section are presented in **Figure 6.83 a**. The data was used in a matrix plot, which clearly documents the two cycles evident within the basal Bernesga Mb. shales (see **Figure 6.83 b**). The spectral analysis performed indicated the presence of two prominent frequencies **0.014175** and **0.05799**, resulting in calculated periodicities of **1.55 Myr** and **381.08 Kyr** respectively (see Figure **6.83 c**). The short-time Fourier analysis discriminates the frequencies present (see Figure **6.83 d**).

The V concentrations were also introduced into the matrix diagram, clearly indicating the two basal cycles of the Caldas section (see **Figure 6.84 b**). The spectral analysis of the V values, resulted in the following significant frequencies: **0.012887** and **0.056701,** giving calculated cyclicities of **1.71 Myr** and **389.74 Kyr** respectively (see **Figure 6.84 b)**. The short-time Fourier function documents the intensity of these basal cycles and at which point they cease.

In order to eliminate the background noise when applying the spectral analysis, a Fourier analysis was performed upon the first two cycles within the U and V concentrations of the Caldas de Luna section. In this instance the spectral analysis indicated the presence of a dominant **365.36 Kyr** periodicity for both the U and V ppm concentrations. These plots are documented in **Results Appendix B** (Part 1). The lower calculated cyclicity of **365.36 Kyr** compared to the previous **513.3 Kyr** of the Aralla section, may be a result of condensed horizons at Caldas de Luna, again fitting with the changing underlying topography at the time of deposition.

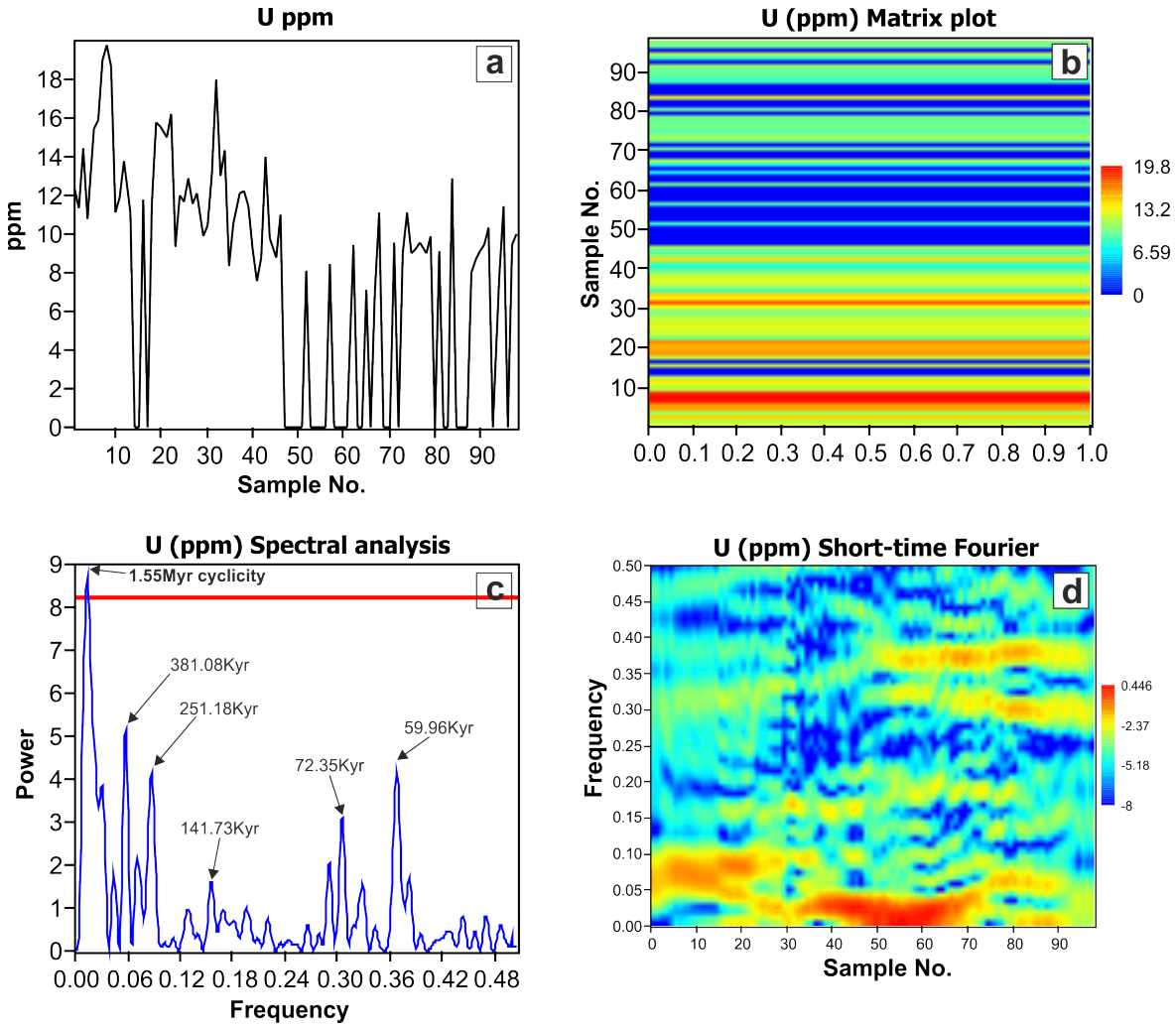

Figure 6.83 Spectral analysis of the absolute U concentrations for the Caldas de Luna section (Caldas 1 – Caldas 98). **a)** Absolute U ppm values from the base (sample No. 1) to the top (sample No. 98). **b)** Matrix plot of the U ppm values with the sample numbers on the Y-axis and the intensity of the U ppm values expressed as colours (values to the right of plot), this plot emphasises the basal cyclicity. **c)** Spectral analysis of the U ppm values, the red line signifies the lower p<0.05 significance level with respect to white, uncorrelated noise and **d)** Short-time Fourier analysis pin-pointing the elevated frequencies present, and the extent of the background noise, the sample numbers are shown on the X-axis.

Frequencies (plots c and d, above)	Calculations of periodicity	Cyclicity values
0.014175 **(highest intensity)**	**= 1/(0.014175/22099 yrs)**	**1.55 Myr**
0.05799	= 1/(0.05799/22099 yrs)	381.08 Kyr
0.087629	= 1/(0.087629/22099 yrs)	251.18 Kyr
0.15593	= 1/(0.15593/22099 yrs)	141.73 Kyr
0.30541	= 1/(0.30541/22099 yrs)	72.35 Kyr
0.36856	= 1/(0.36856/22099 yrs)	59.96 Kyr

Table documenting the prominent frequencies determined by spectral analysis (plot **c** above). The periodicity was calculated by dividing the frequencies by the sampling interval.

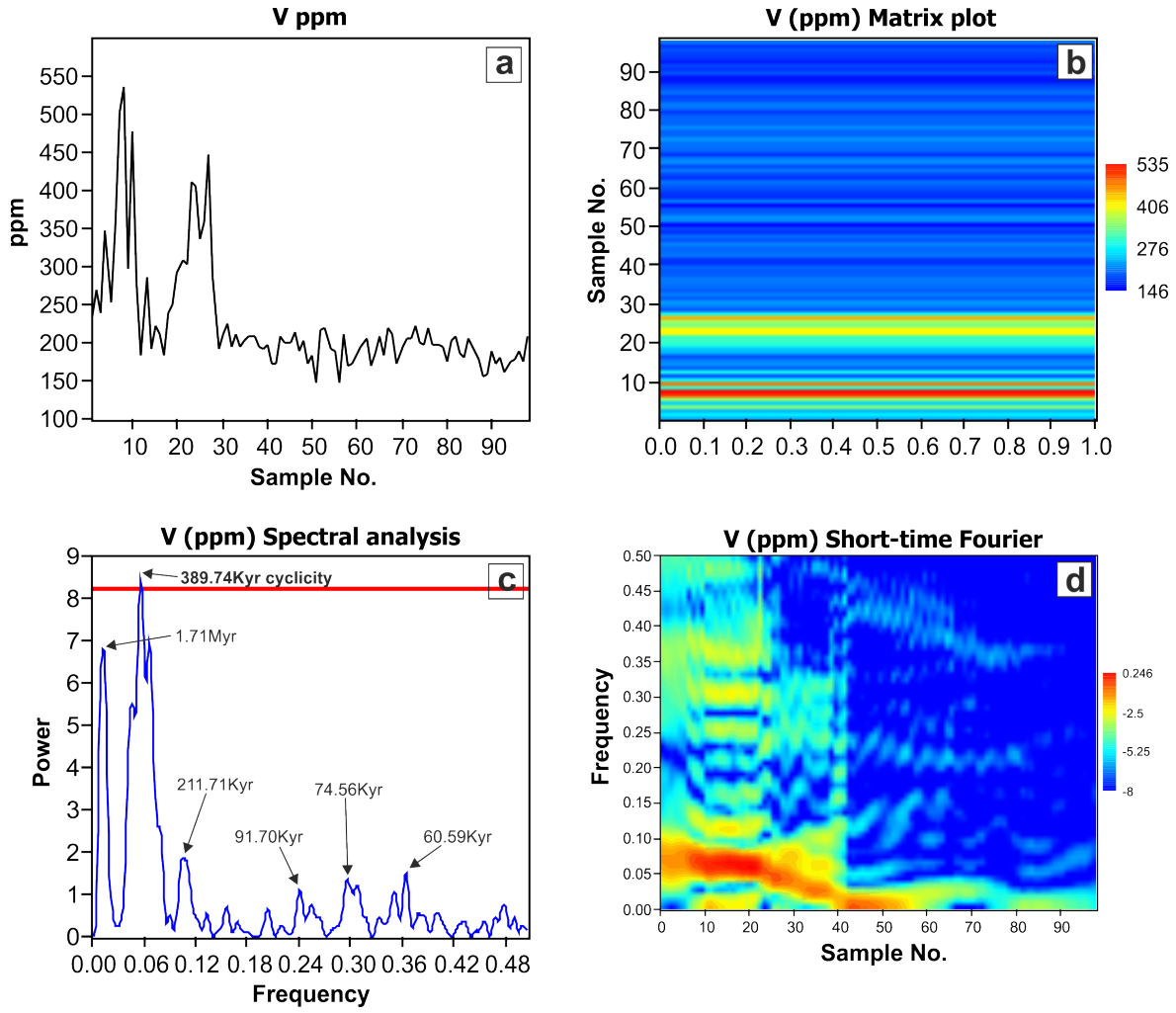

Figure 6.84 Fourier analysis of the Caldas de Luna section (Caldas 1 – Caldas 98). **a)** V ppm values from the base (sample No. 1) to the top (sample No. 98) of the Bernesga Mb., cyclicity is apparent in the V values. **b)** Matrix plot of the V ppm values with the sample numbers on the Y-axis and the intensity of the V ppm values expressed as colours (values to the right of plot), this plot emphasises the basal cyclicity. **c)** Application of a spectral analysis performed on the V ppm values, the red line signifies the lower p<0.05 significance level with respect to white, uncorrelated noise and **d)** Short-time Fourier analysis, the prominent frequencies are evident, the sample numbers are shown on the X-axis.

Frequencies (plots c and d, above)	Calculations of periodicity	Cyclicity values
0.012887	= 1/(0.012887/22099 yrs)	1.71 Myr
0.056701 **(highest intensity)**	**= 1/(0.056701/22099 yrs)**	**389.74 Kyr**
0.10438	= 1/(0.10438/22099 yrs)	211.71 Kyr
0.24098	= 1/(0.24098/22099 yrs)	91.704 Kyr
0.29639	= 1/(0.29639/22099 yrs)	74.56 Kyr
0.36469	= 1/(0.36469/22099 yrs)	60.59 Kyr

Table presenting the prominent frequencies determined by spectral analysis (plot **c** above). The periodicity was calculated by dividing the frequencies by the sampling interval.

6.4.10.3 La Majua section

The cyclic nature of the absolute U concentrations are presented in **Figure 6.85 a**. The matrix plot highlights cycles present. The fourier analysis of the U concentrations determined that there was one dominant frequency apparent, **0.039474** giving a calculated periodicity of **559.83 Kyr**. However, the short-term Fourier analysis displays the elevated background noise. The interpretation of the spectral analysis of U is hereby viewed with caution (see **Figure 6.85**).

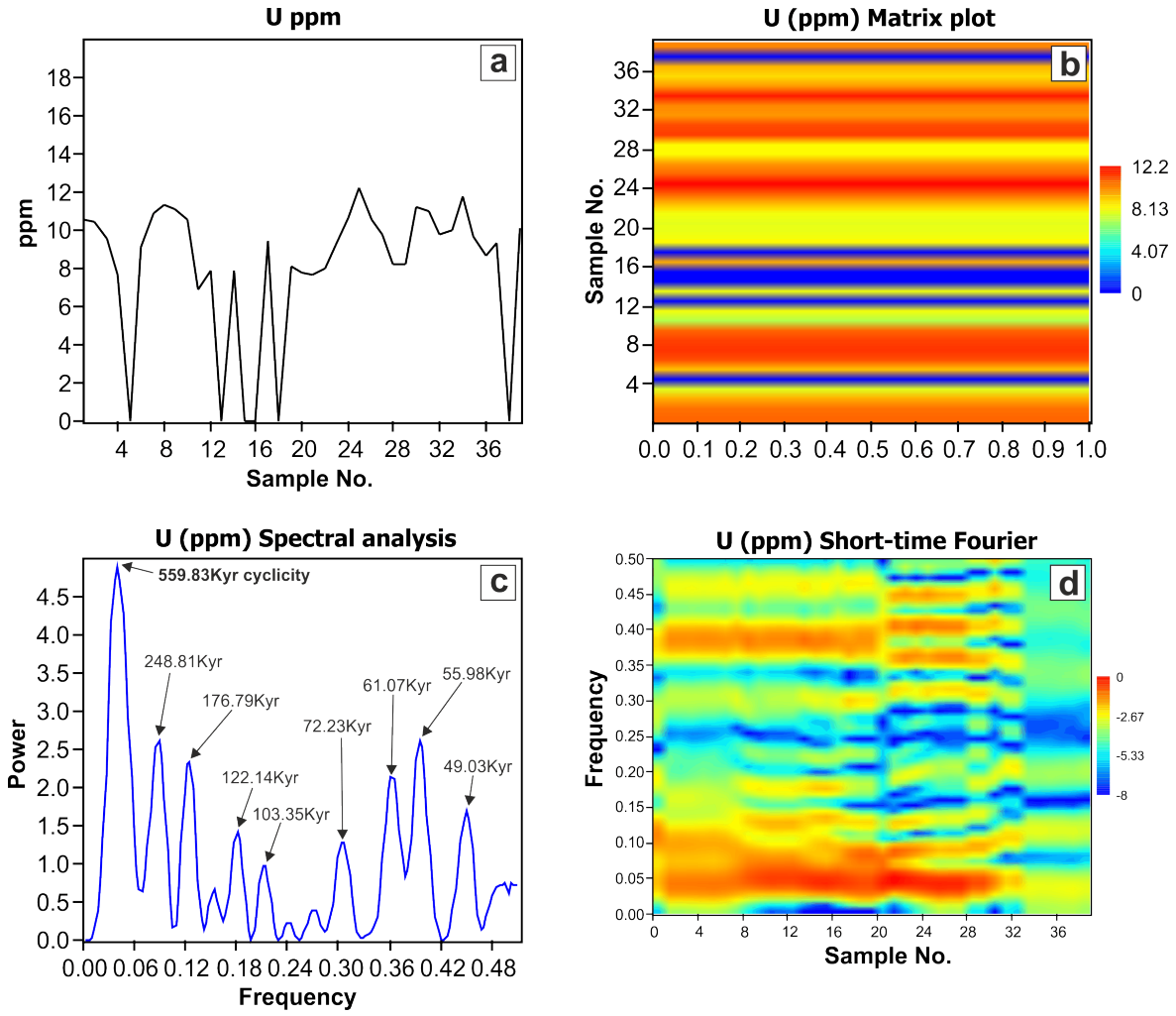

Figure 6.85 U concentrations from the Bernesga Mb. of the La Majua section (La Majua 32 – La Majua 70). **a)** Absolute U ppm values from the base (sample No. 1) to the middle (sample No. 39) of the Bernesga Mb., cyclicity is evident. **b)** Matrix plot of the U ppm values with the sample numbers on the Y-axis and the intensity of the U ppm values expressed as colours (values to the right of plot), this plot emphasises the cyclicity present. **c)** Spectral analysis of the U ppm values **d)** Short-time Fourier analysis highlighting the frequencies present, the sample numbers are shown on the X-axis.

Frequencies (plots c and d, above)	Calculations of periodicity	Cyclicity values
0.039474 **(highest intensity)**	**= 1/(0.039474/22099 yrs)**	**559.83 Kyr**
0.088816	= 1/(0.088816/22099 yrs)	248.81 Kyr
0.125	= 1/(0.125/22099 yrs)	176.79 Kyr
0.18092	= 1/(0.18092/22099 yrs)	122.14 Kyr
0.21382	= 1/(0.21382/22099 yrs)	103.35 Kyr
0.30592	= 1/(0.30592/22099 yrs)	72.23 Kyr
0.36184	= 1/(0.36184/22099 yrs)	61.07 Kyr
0.39474	= 1/(0.39474/22099 yrs)	55.98 Kyr
0.45066	= 1/(0.45066/22099 yrs)	49.03 Kyr

Table presenting the prominent frequencies determined by spectral analysis (plot **c** above). The periodicity was calculated by dividing the frequencies by the sampling interval.

The V absolute concentrations display lower order cyclicity than that of the U concentrations within the Bernesga Mb. shales of the La Majua section (see **Figure 6.86 a**). The spectral analysis of the V concentrations revealed that the dominant frequency present was **0.026316**, giving a calculated periodicity of **839.75 Kyr**. The short-time Fourier analysis illustrates the high amounts of the background noise when analysing the spectrum. Hence, the V cyclicity is again viewed with caution (see **Figure 6.86**).

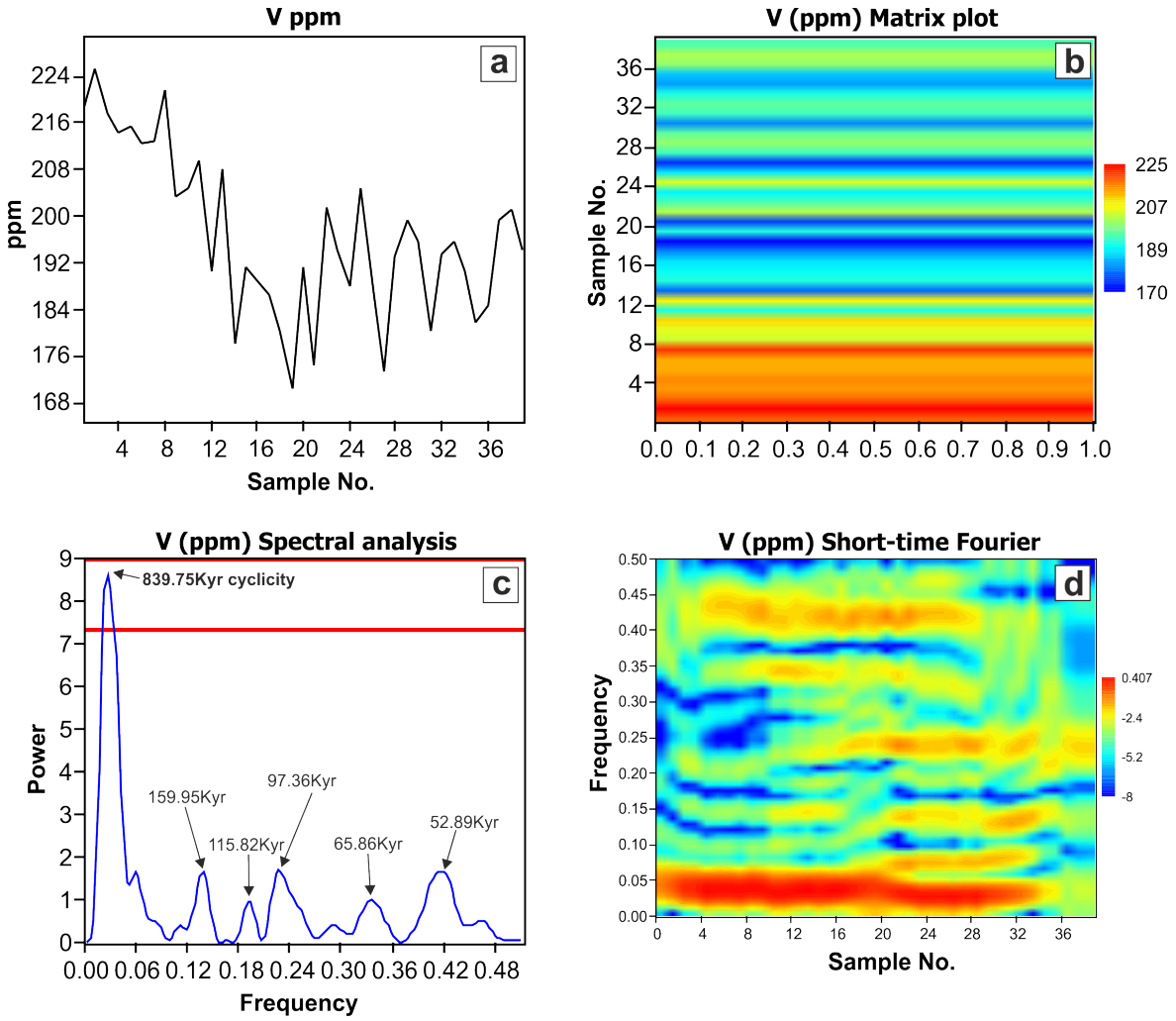

Figure 6.86 a) Absolute V ppm values from the base (sample No. 1) to the middle (sample No. 39) of the Bernesga Mb. **b)** Matrix plot of the V ppm values with the sample numbers on the Y-axis and the intensity of the V ppm values expressed as colours (values to the right of plot). **c)** Fourier analysis of the V ppm values, the red lines signify the lower ($p<0.05$) and upper ($p<0.01$) limits of the significance levels with respect to white, uncorrelated noise, and **d)** Short-time Fourier analysis making the presenting the dominant frequencies, the sample numbers are shown on the X-axis.

Frequencies (plots c and d, above)	Calculations of periodicity	Cyclicity values
0.026316 **(highest intensity)**	**= 1/(0.026316/22099 yrs)**	**839.75 Kyr**
0.13816	= 1/(0.13816/22099 yrs)	159.95 Kyr
0.19079	= 1/(0.19079/22099 yrs)	115.82 Kyr
0.22697	= 1/(0.22697/22099 yrs)	97.36 Kyr
0.33553	= 1/(0.33553/22099 yrs)	65.86 Kyr
0.41776	= 1/(0.41776/22099 yrs)	52.89 Kyr

Table documenting the elevated frequencies determined by spectral analysis (plot **c** above). Periodicity was calculated by dividing the frequencies by the sampling interval.

6.4.10.4 Sena de Luna section

Within the absolute U concentrations of the Bernesga Mb. the cyclic nature previously described is not as observable (see **Figure 6.87 a**). However, the matrix plot illustrates, that cyclicity is present to a lesser extent in the upper part of the Mb. A spectral analysis revealed that there were three dominant frequencies, **0.014706**, **0.036765** and **0.38971** giving periodicities of **1.5 Myr**, **601 Kyr**

and **56.7 Kyr** respectively (see **Figure 6.87 c**). The short-time Fourier analysis illustrates the significant background noise present.

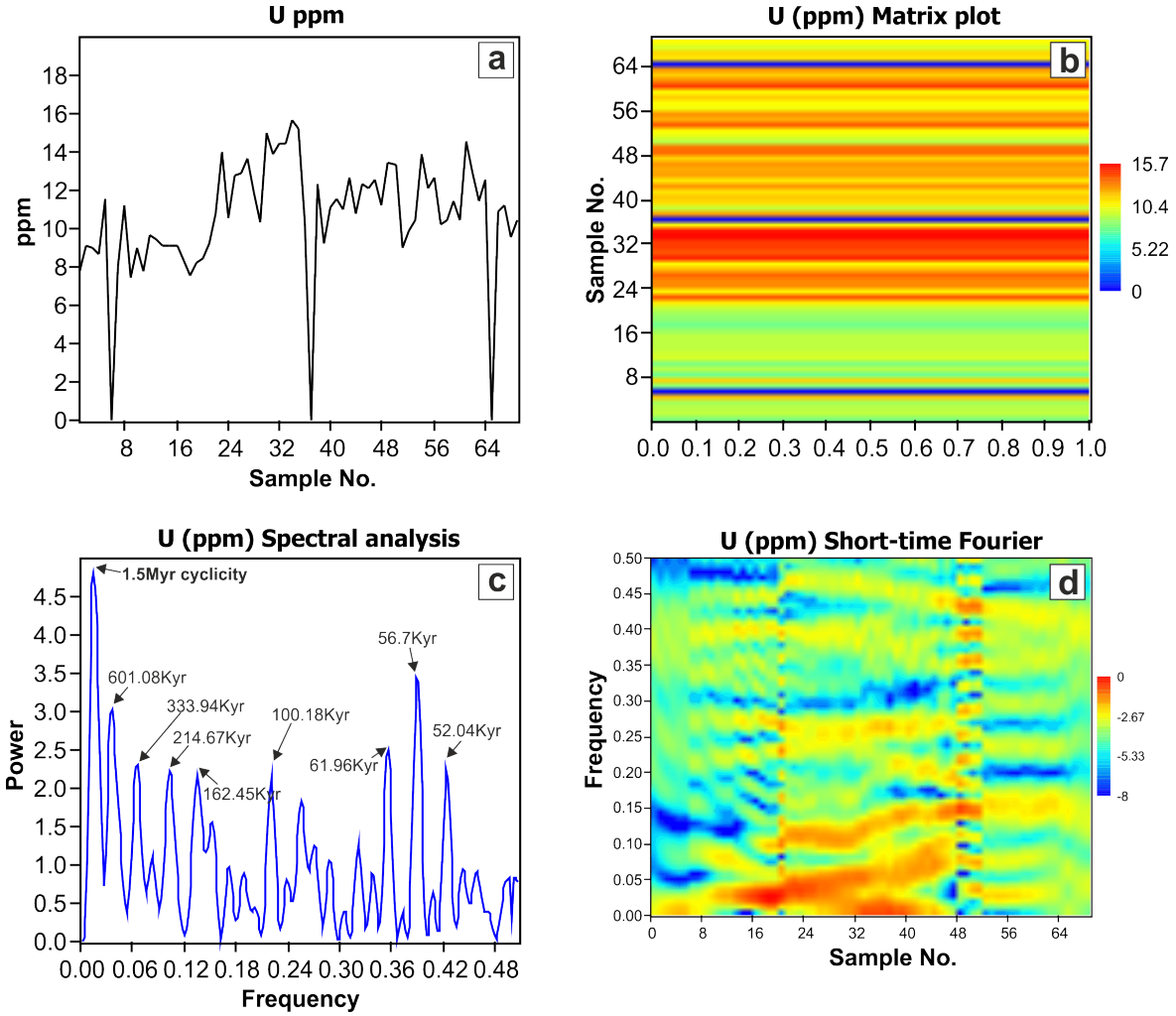

Figure 6.87 Spectral analysis of the Bernesga Mb., for the Sena de Luna section (Sena 11 – Sena 79). **a)** Absolute U concentrations from the base (sample No. 1) to the top (sample No. 69) of the Bernesga Mb. **b)** Matrix plot of the U ppm values with the sample numbers on the Y-axis and the intensity of the U ppm values expressed as colours (values to the right of plot). **c)** Fourier analysis of the U ppm values, and **d)** Short-time Fourier analysis, illustrating the dominant frequencies present and extent of background noise, the sample numbers are shown on the X-axis.

Frequencies (plots c and d, above)	Calculations of periodicity	Cyclicity values
0.014706 (highest intensity)	**= 1/(0.014706/22099 yrs)**	**1.5 Myr**
0.036765	= 1/(0.036765/22099 yrs)	601.08 Kyr
0.066176	= 1/(0.066176/22099 yrs)	333.94 Kyr
0.10294	= 1/(0.10294/22099 yrs)	214.67 Kyr
0.13603	= 1/(0.13603/22099 yrs)	162.45 Kyr
0.22059	= 1/(0.22059/22099 yrs)	100.18 Kyr
0.35662	= 1/(0.35662/22099 yrs)	61.96 Kyr
0.38971	= 1/(0.38971/22099 yrs)	56.7 Kyr
0.42463	= 1/(0.42463/22099 yrs)	52.04 Kyr

Table presenting the prominent frequencies determined by spectral analysis (plot **c** above). The periodicity was calculated by dividing the frequencies by the sampling interval.

A spectral analysis of the absolute V concentrations determined that the prominent cyclic frequencies present were **0.018382** and **0.060662**, and calculated periodicities of **1.2 Myr** and **364.29 Kyr** respectively (see **Figure 6.88 c**). The short-time Fourier analysis documents the extent of background noise present. The basal cyclic signals of the Aralla and Caldas de Luna sections

are not apparent at the Sena de Luna section. Thus, enforcing the interpretation of the presence of an undulating topography during the onset of black shale deposition.

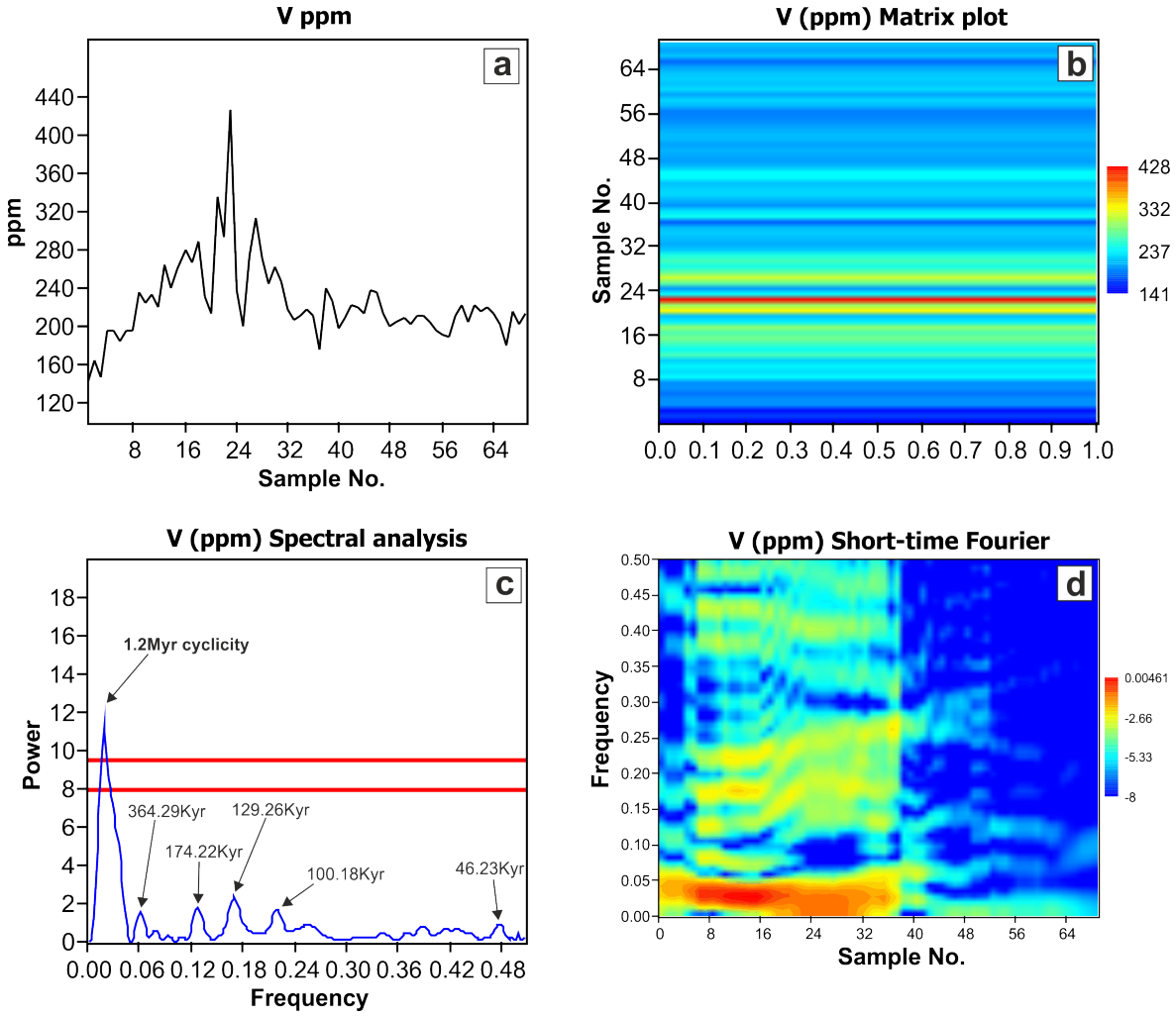

Figure 6.88 Spectral analysis of the Bernesga Mb. shales belonging to the Sena de Luna section (Sena 11 – Sena 79). **a)** V ppm concentrations from the base (sample No. 1) to the top (sample No. 69) of the Bernesga Mb. **b)** Matrix plot of the V ppm values with the sample numbers on the Y-axis and the intensity of the V ppm values expressed as colours (values to the right of plot). **c)** Fourier analysis of the V concentrations, the red lines signify the lower ($p<0.05$) and upper limits ($p<0.01$) of the significance levels with respect to white, uncorrelated noise, and **d)** Short-time Fourier analysis illustrating the dominant frequencies present, and the high intensity of background noise, the sample numbers are shown on the X-axis.

Frequencies (plots c and d, above)	Calculations of periodicity	Cyclicity values
0.018382 **(highest intensity)**	**= 1/(0.018382/22099 yrs)**	**1.2 Myr**
0.060662	= 1/(0.060662/22099 yrs)	364.29 Kyr
0.12684	= 1/(0.12684/22099 yrs)	174.22 Kyr
0.17096	= 1/(0.17096/22099 yrs)	129.26 Kyr
0.22059	= 1/(0.22059/22099 yrs)	100.18 Kyr
0.47794	= 1/(0.47794/22099 yrs)	46.23 Kyr

Table documenting the prominent frequencies determined by spectral analysis (plot **c** above). The periodicity was calculated by dividing the frequencies by the sampling interval.

6.4.10.5 Villanueva section

Cyclicity within the absolute U concentrations of the Villanueva sections is mostly absent. However, a spectral analysis did determine that one particular frequency dominated the section, **0.013636** a

periodicity of **1.62 Myr**. The matrix plot function illustrates the lack of redox element cyclicity. The short-time Fourier analysis documents the dominant frequency present and the relatively low extent of background noise observed at other sections analysed (see **Figure 6.89**).

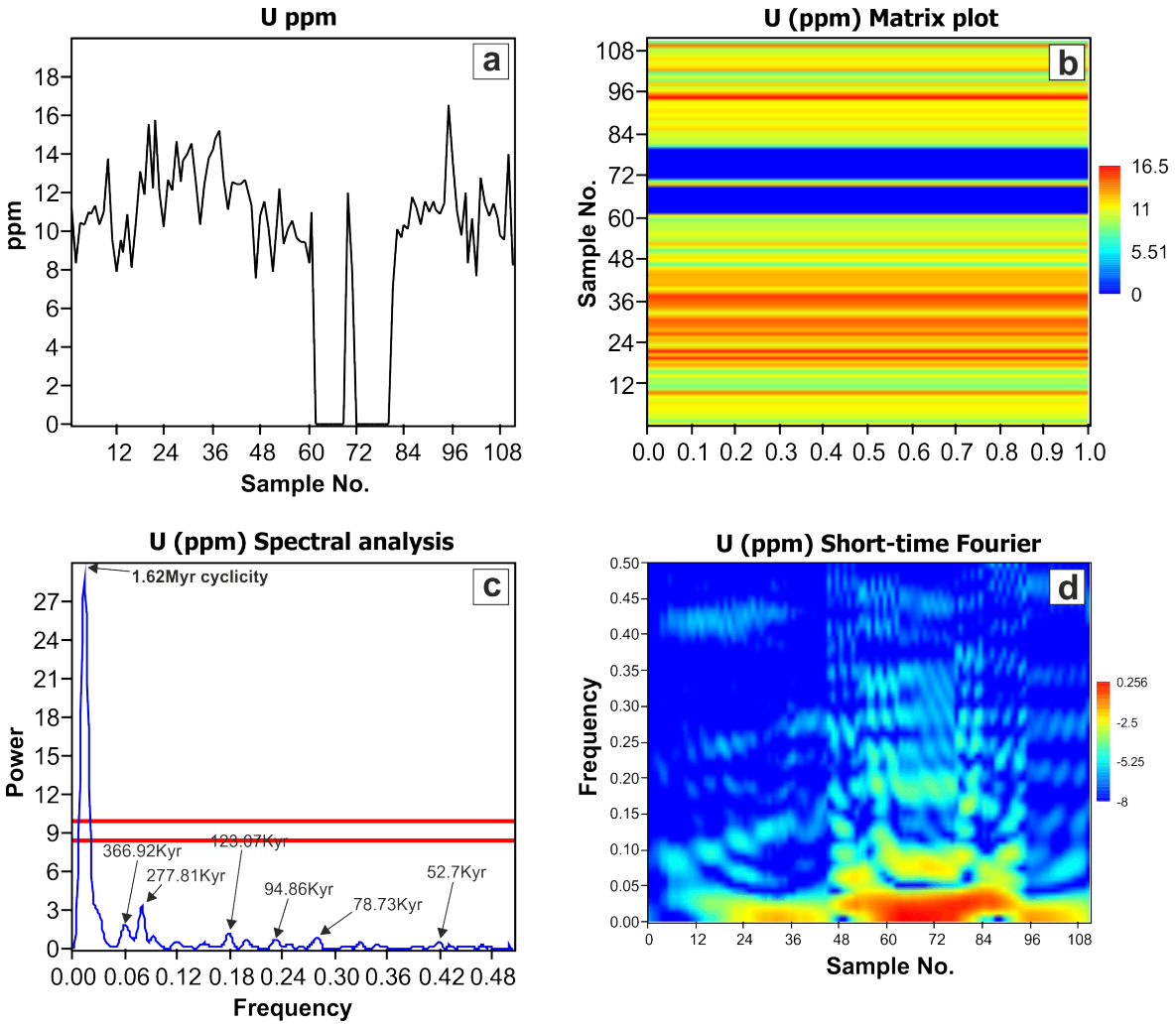

Figure 6.89 Spectral analysis of the Bernesga Mb. of the Villanueva section (Villa 1 – Villa 111). **a)** Illustrating the absolute U concentrations from the base (sample No. 1) to the top (sample No. 111). **b)** Matrix plot of the U ppm values with the sample numbers on the Y-axis and the intensity of the U ppm values expressed as colours (values to the right of plot). **c)** Fourier analysis of the U ppm values, the red lines signify the lower ($p<0.05$) and upper limits ($p<0.01$) of the significance levels with respect to white, uncorrelated noise, and **d)** Short-time Fourier analysis illustrating the dominant frequency calculated with a lower extent of the background noise, the sample numbers are shown on the X-axis.

Frequencies (plots c and d, above)	Calculations of periodicity	Cyclicity values
0.013636 **(highest intensity)**	**= 1/(0.013636/22099 yrs)**	**1.62 Myr**
0.060227	= 1/(0.060227/22099 yrs)	366.92 Kyr
0.079545	= 1/(0.079545/22099 yrs)	277.81 Kyr
0.17955	= 1/(0.17955/22099 yrs)	123.07 Kyr
0.23295	= 1/(0.23295/22099 yrs)	94.86 Kyr
0.28068	= 1/(0.28068/22099 yrs)	78.73 Kyr
0.41932	= 1/(0.41932/22099 yrs)	52.7 Kyr

Table documenting the prominent frequencies present, determined by spectral analysis (plot **c** above). The periodicity was calculated by dividing the frequencies by the sampling interval.

The absolute V concentrations express lower order cyclicity (see **Figure 6.90 a**). The matrix plot indicates that there are possibly two significant fluctuations in the V values at the base of the Bernesga Mb. However, when the spectral analysis was performed, only one prominent frequency was apparent, **0.011364** giving a calculated cyclicity of **1.94 Myr**. This value is far higher that the

previously documented cyclic values for the other analysed sections. This again enforces the interpretation of the undulating topography at the time of black shale deposition.

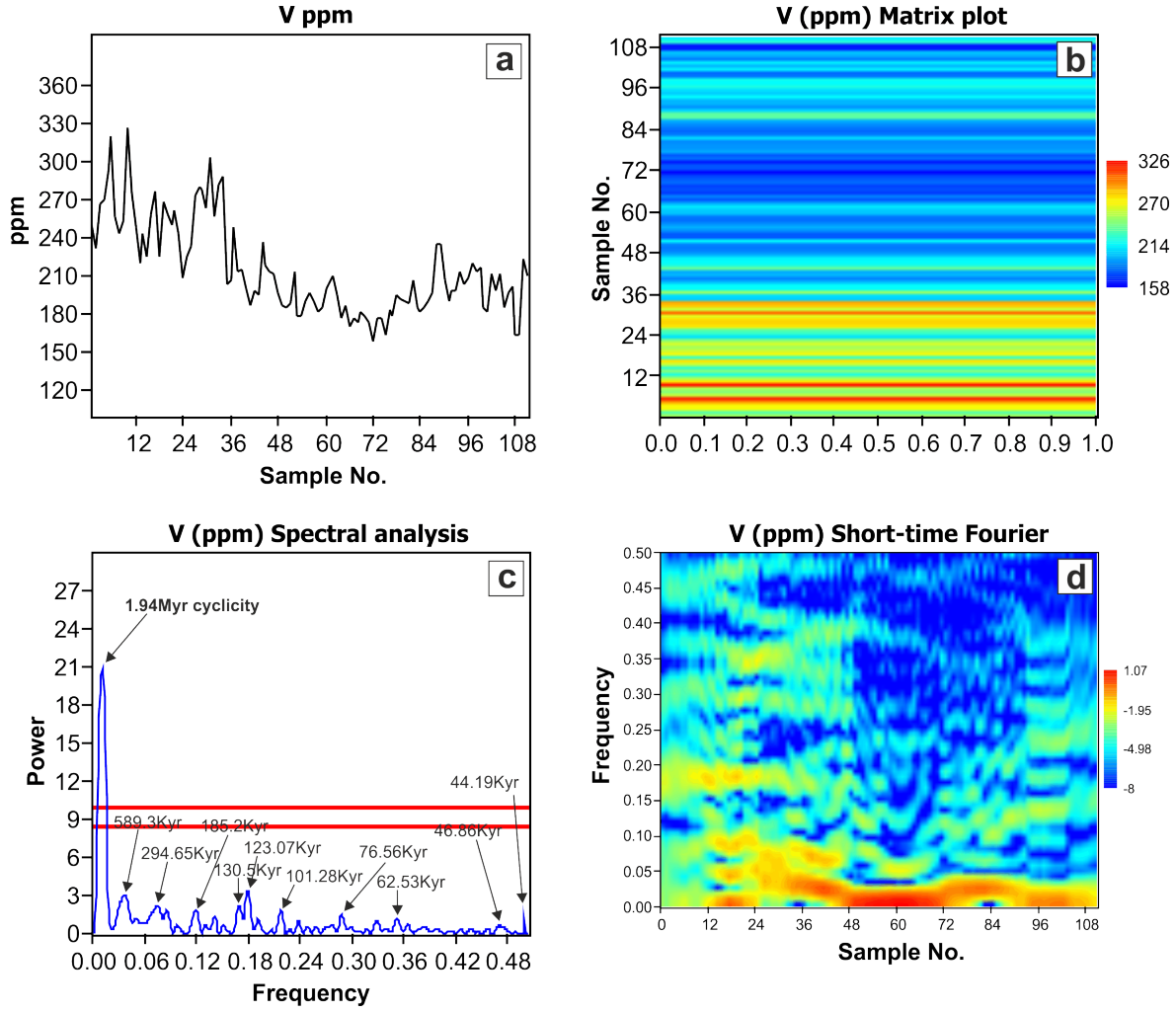

Figure 6.90 Spectral analysis of the shales belonging to the Bernesga Mb. at the Villanueva section (Villa 1 – Villa 111). **a)** The analysed V ppm concentrations from the base (sample No. 1) to the top (sample No. 111) of the Bernesga Mb. **b)** Matrix plot of the V ppm values with the sample numbers on the Y-axis and the intensity of the V ppm values expressed as colours (values to the right of plot). **c)** Fourier analysis of the V concentrations, the red lines signify the lower ($p<0.05$) and upper limits ($p<0.01$) of the significance levels with respect to white, uncorrelated noise, and **d)** Short-time Fourier analysis making illustrating the dominant frequency present and high extent of background noise. The sample numbers are present on the X-axis.

Frequencies (plots c and d, above)	Calculations of periodicity	Cyclicity values
0.011364 **(highest intensity)**	**= 1/(0.011364/22099 yrs)**	**1.94 Myr**
0.0375	= 1/(0.0375/22099 yrs)	589.3 Kyr
0.075	= 1/(0.075/22099 yrs)	294.65 Kyr
0.11932	= 1/(0.11932/22099 yrs)	185.2 Kyr
0.16932	= 1/(0.16932/22099 yrs)	130.51 Kyr
0.17955	= 1/(0.17955/22099 yrs)	123.07 Kyr
0.21818	= 1/(0.21818/22099 yrs)	101.28 Kyr
0.28864	= 1/(0.28864/22099 yrs)	76.56 Kyr
0.35341	= 1/(0.35341/22099 yrs)	62.53 Kyr
0.47159	= 1/(0.47159/22099 yrs)	46.86 Kyr
0.5	= 1/(0.5/22099 yrs)	44.19 Kyr

Table documenting the prominent frequencies determined by spectral analysis (plot **c** above). The periodicity was calculated by dividing the frequencies by the sampling interval.

Chapter 7
Discussions and conclusions

Contents

7.1 Geochemical signatures in direct correlation to sedimentological logs

The purpose of this section is to document the changes in a select few of the key major and trace elements analysed relative to the sedimentological logs detailed in **Chapter 5** (Geochemical Results). The gamma-ray (GR) signal, total organic carbon (TOC) and the redox proxy V/(V+Ni) are also included for comparison. For the major and trace elements not included (near detection limits) in this section, please refer to **Chapter 5** (Geochemical Results).

From analysing the Aralla section (see **Figure 7.1**) the first observation is the significant changes in the geochemical signatures and patterns relative to the differing lithological units present within the sedimentary log section. At the base of the section the Barrios Fm. (yellow unit) is present. The formation is represented by little if none of the redox sensitive elements (V and U), a very low GR signal and abundance of SiO_2. Overlying the Barrios Fm. are the Getino Beds (green unit) containing a slightly elevated redox signature, an increase in the GR signal and a substantial fall in the available SiO_2. The boundary to the shales of the Bernesga Mb. (dark blue unit) is easily identifiable with the significant increase in the clay related major and trace elements and the substantial increase in the redox sensitive trace elements including a dramatic increase in the overall GR signal. This basal Bernesga Mb. has for the first time been further sub divided based on the geochemical signatures presented. The figure highlights the first three prominent cycles (labelled 1^{st}, 2^{nd} and 3^{rd} cycle) within the redox sensitive elements previously described in the **Chapter 6.4.10**. After the third cycle (~ sample 68) there is a notable change to the chemostratigraphical signatures. This change in the overall geochemical signature has been previously interpreted to represent a tectonic event (or pulse represented by the lowermost horizontal red line). The geochemical signatures from this point forth remain relatively stable and hence this unit has been assigned the lower Bernesga unit of the Bernesga Mb. (grey unit). From ~ sample 132 there is again a change to the overall geochemical pattern, the signals become more erratic with the increase in detrital material into the predominantly black shale regime. The increase in detrital material is recorded within the elevated SiO_2 and Zr concentrations, the increased terrestrial influx results in the introduction of fine silt grade intercalations. This horizon has led to a further subdivision of the Bernesga Mb. into the upper Bernesga unit (yellowish unit) coupled with a slightly more erratic GR signal. The boundary to the overlying sands and siltstones of the Villasimpliz Mb. (orange unit) is clearly apparent from sample 184 with the erratic nature of the major and trace element signatures and GR signature.

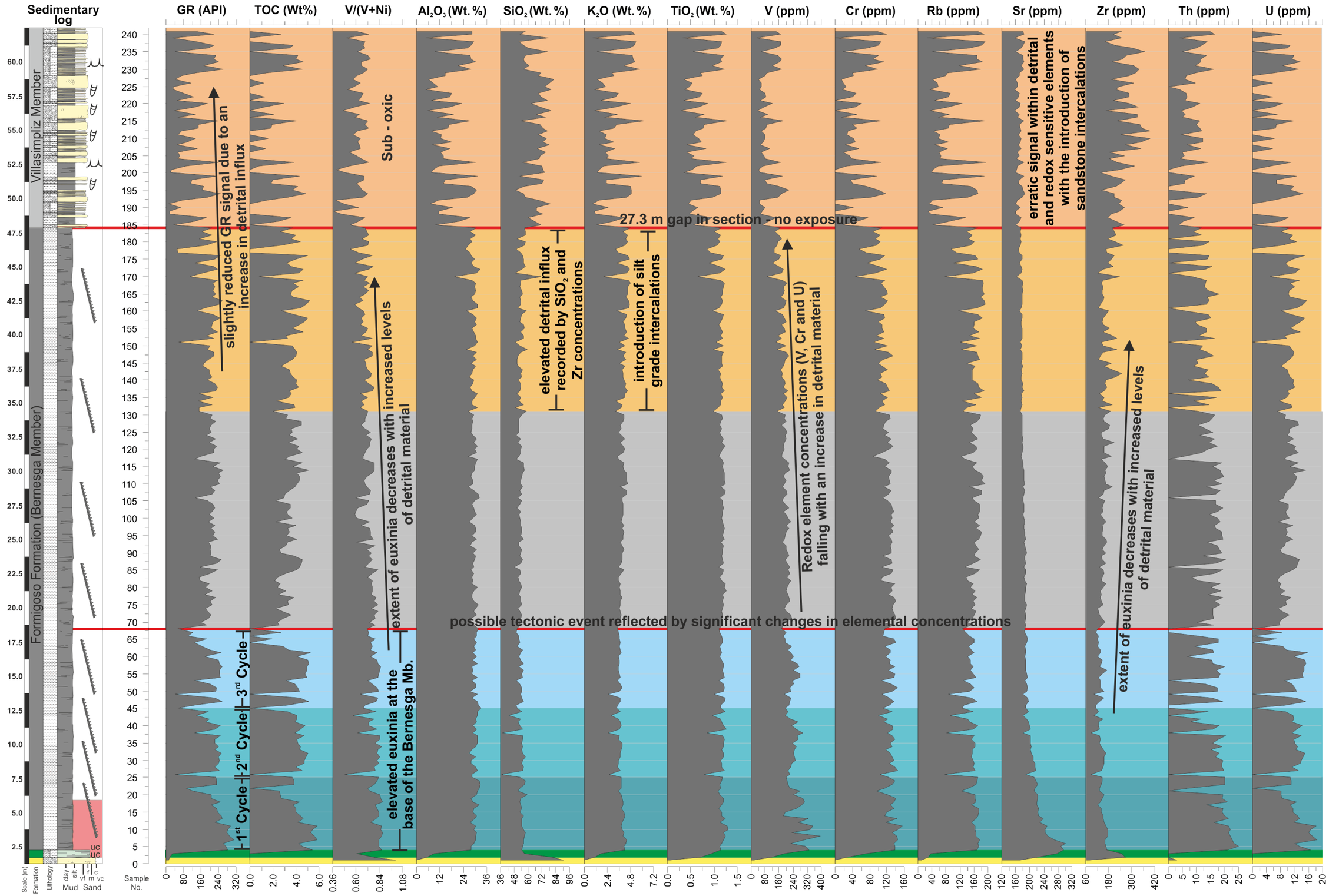

Figure 7.1: The key geochemical elements and parameters of the Aralla section directly correlated to the sedimentary log. To the left of the figure the sedimentary log is found with an appropriate scale. The chemostratigraphy has been directly correlated to this sedimentary lo section. Please refer to the text for a detailed description of the figure.

The elevated concentrations of the redox sensitive elements (V and U) and the redox proxy V/(V+Ni) within the Bernesga Mb. are clearly related to the abundance of organic material depicted by the graptolite symbols on the sedimentary log section. The redox sensitive elements are seen to decrease in concentration toward the top of the Bernesga Mb. with the introduction of an increasing siliciclastic influx represented by the SiO_2 and Zr concentrations.

The dramatic increase of the redox sensitive elements at the base of the Bernesga Mb. is coupled with a logarithmic decrease in the Sr signal. The increase in the redox sensitive elements relates to the overall deepening (transgression) effecting the Cantabrian Basin during the lowermost Silurian and subsequent shut down of the oceanic circulation. The transgression ultimately triggers starved basin conditions and black shale genesis, effectively pushing all terrestrial material far inland. This scenario may also be supported by the systematic decrease in the Sr signal as the Sr has been previously related to celestine formation most probably associated to the coarser detrital fraction.

The analysed portion of the Caldas de Luna section (see **Figure 7.2a**) did not include the underlying Barrios Fm. and the Getino Beds were not apparent at outcrop. Therefore, the distinct changes in lithology in comparison with the changes in the geochemical patterns are not evident for this locality. However, the Bernesga Mb. can once again be clearly subdivided into a number of sub units when taking into account the overall chemostratigraphy. The redox sensitive elements V and U and the GR signal together display two clear cycles (blue and light blue, corresponding to the colours of the Aralla section) at the base of the Bernesga Mb. It has been previously interpreted that these two cycles represent the 2nd and 3rd cycles apparent at the adjacent Aralla section. The first cycle is not evident at the base of the Caldas de Luna section. There is once again a significant shift in the geochemical patterns at ~ sample 31, which is thought to be related to the notable shift in the dataset evident at the Aralla section. From this point forth the major and trace element behaviour is relatively consistent in contrast to the basal cycles of the Bernesga Mb. and has been assigned to the lower unit of the Bernesga Mb. (grey unit) correlating to the lower unit of the Aralla section. The analysed section at Caldas de Luna does not display the increasing detrital element trends towards the top, therefore, we have not quite reached the boundary to the upper Bernesga unit evident at the Aralla section.

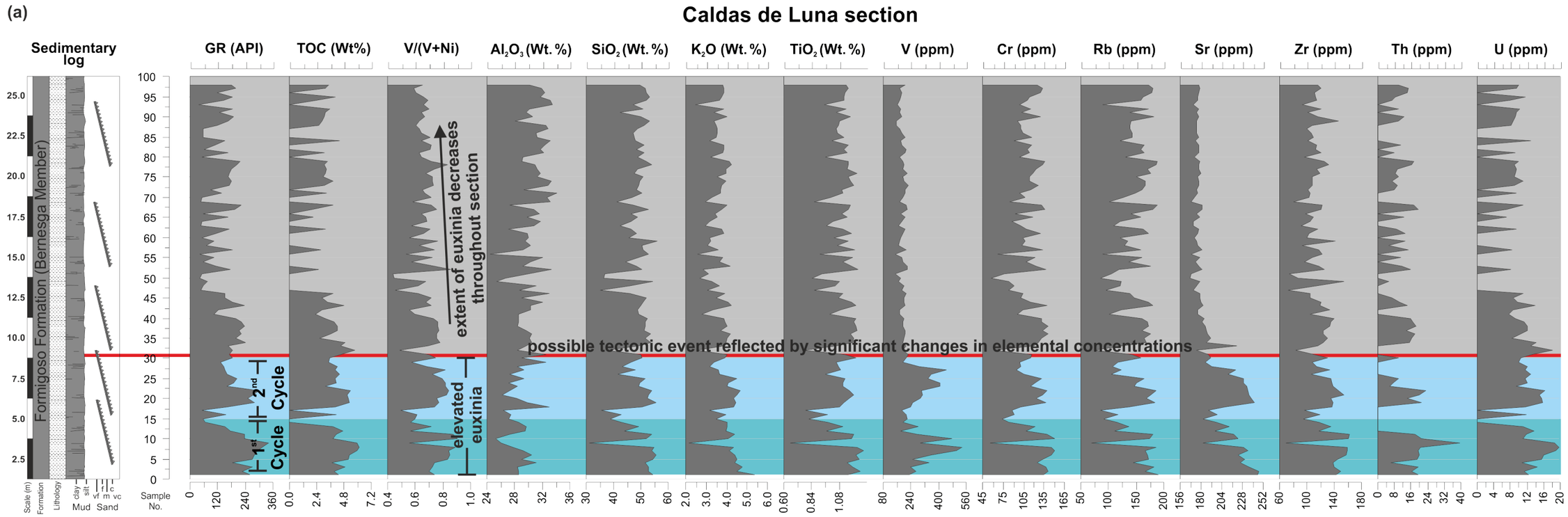

Figure 7.2: (a) The key geochemical elements and parameters of the Caldas de Luna section directly correlated to the sedimentary log. **(b)** Again documenting the major and trace element variations against the sedimentary log of the La Majua section. Please refer to the text for detailed discussions of the figure.

The higher redox element concentrations at the base of the Caldas de Luna section are again related to the abundance of organic material present, here represented by the graptolites on the sedimentary log section. The extent of euxinia is seen to be much higher at the base of the Bernesga Mb. and falls pretty consistently towards the top when observing the changes in the V/(V+Ni) redox proxy and the U concentrations. The pattern evident at the Aralla section relating to the enrichments of redox sensitive elements and the depletion of Sr at the base of the section is also clearly apparent for the basal part of the Caldas de Luna section.

The sedimentary log section and the related chemostratigraphy for the La Majua section (see **Figure 7.2b**) clearly distinguishes between the differing formations present. The colour scheme remains comparable to the previously described sections. The geochemical signature of the Barrios Fm. (yellow unit) is comparable to that of the Aralla section previously discussed. The boundary to the overlying Getino Beds (green unit) is marked by an increase in the GR signal and erratic behaviour of the major and trace elements. The erratic behaviour of the chemostratigraphy within the Getino Beds is a result of mixed lithologies present, consisting of intercalated fine-coarse sandstones, mudstones and siltstones. The boundary to the overlying Bernesga Mb. (grey unit) is again clearly apparent when observing the changes in the overall chemostratigraphy. The GR signal at this point effectively doubles in its overall strength and remains relatively constant throughout the unit. The major and trace elements related to the presence of the clay minerals (Al_2O_3, K_2O, Rb, Th and U) clearly increase at the boundary to the Bernesga Mb. and remain again consistent throughout. The cycles related to the enrichments of the redox sensitive elements and GR signal at the Aralla and Caldas de Luna section are not present at the La Majua section. it is therefore considered that the lowermost section of the lower Bernesga unit is missing from the La Majua section.

The redox sensitive elements along with the V/(V+Ni) redox proxy do display slight enrichments towards the base of the Bernesga Mb. and fall very gradually towards the top. There is no significant increase in the elements belonging to the terrestrial detrital fraction (i.e. the Zr and SiO_2 concentrations) so it can therefore be insinuated that only the lower unit of the Bernesga Mb. is present at the La Majua section, correlating with the previously discussed Aralla and Caldas de Luna sections.

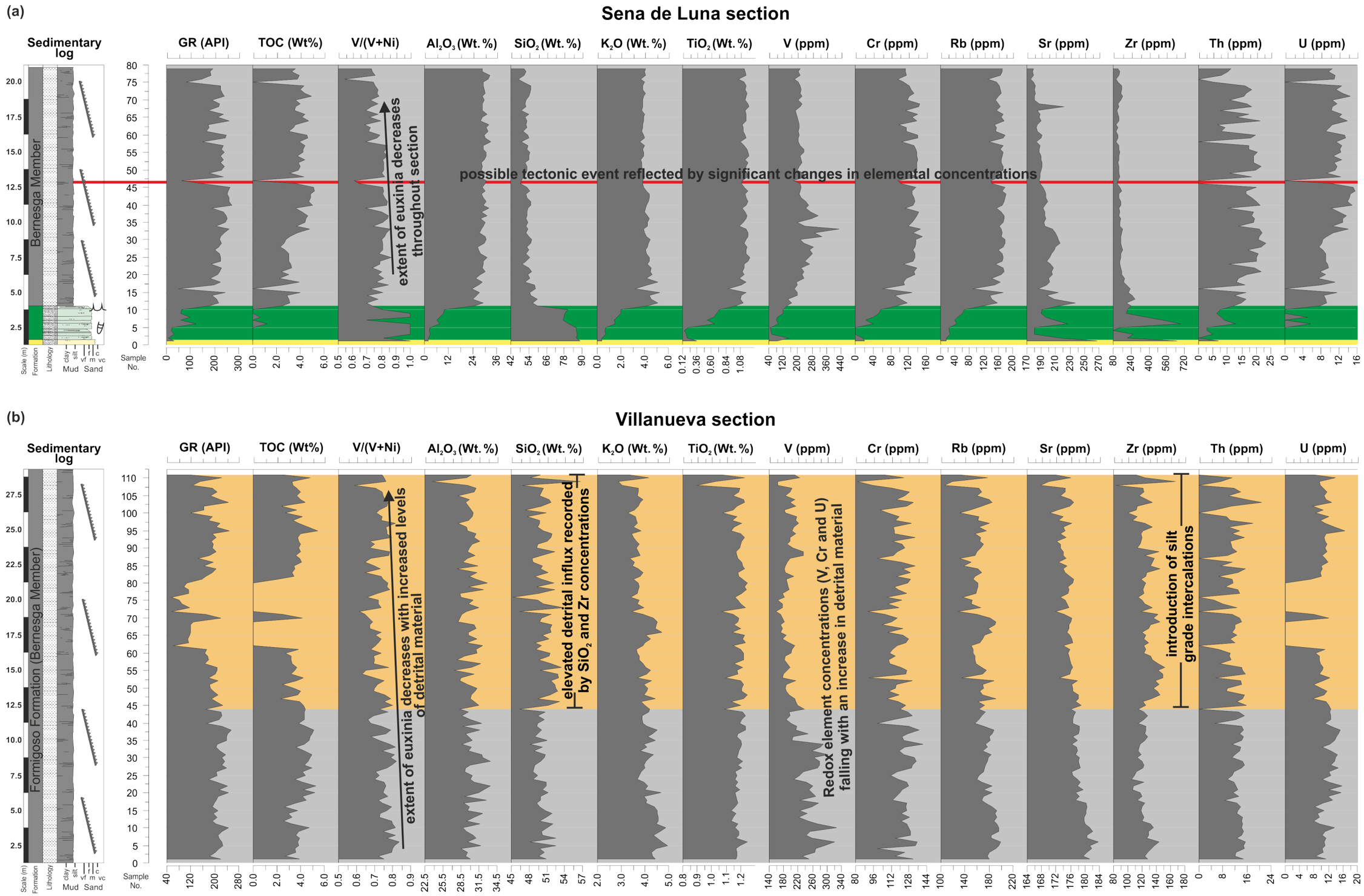

Figure 7.3: (a) The key geochemical elements and parameters of the Sena de Luna section directly correlated to the sedimentary log. **(b)** Again documenting the major and trace element variations against the sedimentary log of the Villanueva section. Please refer to the text for a detailed description of the figure.

From observing the chemostratigraphy of the Sena de Luna section (see **Figure 7.3a**) it is once again easy to distinguish the boundaries to the formations present. At the base of the analysed section the Barrios Fm. (yellow unit) is present, again displaying comparable geochemical signatures to the previously discussed Aralla and La Majua sections. At the boundary to the overlying Getino Beds (green unit) the GR signal is seen to increase, including the concentrations of Al_2O_3, TiO_2, V, Cr, Rb, Th and U related to the presence of clay minerals within the intercalated mud/siltstones. The boundary to the Bernesga Mb. (grey unit) is clearly observable, with the significant increase in GR signal and considerable rise in the concentrations of the redox sensitive elements. As with the previously discussed La Majua section, the cycles of the Aralla and Caldas de Luna sections are clearly not present within the lower most region of the Bernesga Mb. Therefore, it is again considered that the lowermost section of the lower Bernesga unit is missing from the Sena de Luna section. It is also notable that the increased siliciclastic influx (increase in the SiO_2 and Zr contents) of the upper Bernesga unit apparent at the Aralla section is not evident here, indicating that once again only the lower unit of the Bernesga Mb. is present at the Sena de Luna section. There is also the presence of a distinct horizon within the chemostratigraphy (indicated by horizontal red line) that could represent the tectonic event observed at the previous Aralla and Caldas de Luna sections.

The levels of euxinia for the Sena de Luna section are seen to decrease from the base of the Bernesga Mb. as seen in the previously discussed sections. This scenario is clearly displayed by the V/(V+Ni) redox proxy and the concentrations of the redox element U.

The relationship between the redox sensitive elements and Sr previously discussed for the other analysed sections is again present for the Sena de Luna section.

Finally the Villanueva section (see **Figure 7.3b**), the analysed part of the section only consists of the Bernesga Mb. From reviewing the correlation of the elements and the parameters displayed in the figure it is again clear that the member can be sub-divided. The lowermost section of the lower Bernesga unit is not evident at the Villanueva section, as the cycles of the Aralla and Caldas de Luna section are not present. However, there is a clear change in the chemostratigraphy from sample 45. From this point forth the GR signal and the other elemental patterns become more erratic as the influx of detrital material increases (an increase in SiO_2 and Zr concentrations). This

upper section of the Bernesga Mb. has been assigned to the upper unit of the Bernesga Mb. correlating with the upper unit present at the Aralla section.

As with the previously discussed sections the extent of the euxinic conditions decreases from the base of the analysed section. The level of euxinia is represented by the V/(V+Ni) redox proxy and the concentrations of U.

7.2 Geochemical classification

Various geochemical classification schemes were applied on the data set generated for this research. The geochemical discrimination system log(Fe_2O_3/K_2O) *vs*. log(SiO_2/Al_2O_3) of Herron (1988) characterises the vast majority of the sediments of the Bernesga Mb. as 'shales'. A number of samples from the Bernesga Mb. showed 'Fe-shale' properties, which is here interpreted to be the effects of localised, postdepositional Fe_2O_3 mineralisation. The majority of the sand- and siltstones of the Villasimpliz Mb. plot within the 'wacke' category. The bivariate plot of TiO_2 *vs*. Ni (Floyd *et al.,* 1989) discriminated well between the shales of the Bernesga Mb. and the overlying sand- and siltstones of the Villasimpliz Mb., with the latter clustering at the 'Acidic' provenance field. This is in good agreement with previous provenance studies, which concluded a bulk granitic composition of the hinterland. Other provenance discrimination diagrams applied did successfully discriminate between the Bernesga Mb. from the overlying Villasimpliz Mb., however, compared to each other, they proved to be inconclusive and did not allow any certain reconstructions of the provenance area.

The classification scheme of Pearce *et al.* (2010) also successfully discriminated between the basal Bernesga Mb. sediments and the deposits of the middle to upper Bernesga Mb. The basal Bernesga Mb. discriminated here as fully marine developed mudstones, whereas the middle to upper parts were characterised as marginal marine deposits. This geochemical discrimination corresponds well to initial field-based sedimentological observations, which were tentatively interpreted to indicate an overall shallowing-upward sequence with an increased terrestrial influx towards the top of the Formigoso Fm. Only at one investigated locality ('La Majua'), were the fully marine developed basal sediments of the Bernesga Mb. absent. This gap in stratigraphy is interpreted to be a hiatus caused by palaeotopographical factors.

The analysis of the Cantabrian Formigoso data using the ternary systems of Mongelli *et al.* (2006) and Ross and Bustin (2009) revealed a pronounced Al_2O_3 enrichment of the Bernesga Mb. relative to international average shale standards ('average shale' of Wedepohl (1971) and PAAS, Taylor and McLennan, 1985). The Al_2O_3 enrichment is interpreted to reflect intense chemical weathering of the original source material. The TOC–TS10–Fe diagram (Dean and Arthur, 1989; Arthur and Sageman, 1994) enabled to distinguish for the first time different shale groups within the otherwise rather homogenous sediments of the basal parts of the Bernesga Mb.: [1] Basal organic-rich 'hot' shales (with a high content of U) are conformably overlain by [2] organic Carbon depleted 'lean' shales (with diminished U values) and these are followed by organic-poor 'cold' shales (exhibiting low U concentrations).

7.3 Anoxia

Various ratios of redox sensitive elements (V/Cr, V/Sc, V/(V+Ni), U/Th and Th/U, after Jones and Manning (1994), Kimura and Watanabe (2001), Hatch and Leventhal (1992), Jones and Manning (1994) and Fertl (1979), respectively) were used to estimate and reconstruct the extents of potential anoxia that prevailed during the time of deposition of the Formigoso Fm. The onset of the black shale deposition is identified by highly anoxic 'euxinic' conditions as indicated by all of the applied redox proxies. The V/(V+Ni) ratio of Hatch and Leventhal (1992) in combination with the DOP of Wignall (1994) appeared to be the most effective redox proxies for the black shales of the Bernesga Mb. However, the informative value of the V/(V+Ni) ratio was seen to be limited for the sand- and siltstones of the underlying Getino Beds and overlying Villasimpliz Mb., due to the comparable low Ni concentrations within this slightly coarser grained sediments.

During the time of black shale deposition, the initial prevailing euxinic conditions were discontinuous across large parts of the southern Cantabrian Basin. The sections containing the basal euxinic black shales were Aralla, Caldas de Luna and Sena de Luna, with the latter being just within the euxinic range. At the La Majua section these basal euxinic marine shales are not developed at all, and at the Villanueva section marine shales are present, but they lack the distinct 'euxinic' signature. This indicates, that both, the onset of the sedimentation of the basal marine shales as well as the development of the euxinic conditions were diachronous over the Cantabrian Basin. The marine euxinic black shales of the Formigoso Fm. are hence laterally not persistent, as it was previously postulated, but have a patchy distribution.

The main factor controlling the irregular lateral distribution and variation in thickness of the basal euxinic marine shales is interpreted to be the complex and differentiated palaeotopography of the Lower Silurian Cantabrian Basin. This palaeotopographic relief is regarded to have formed from a combination of tectonic and climatic processes: the extensional tectonic regime related to the opening of the Rheic ocean led to the formation of extensive horst (palaeotopographic highs) and graben (palaeotopographic lows) structures, which were then exacerbated by the following intense erosion caused by the sea-level drop during the Hirnantian glaciation. During the initial stages of the Silurian transgression the palaeo-lows were the first to be flooded, whereas the palaeo-highs became submerged later. Furthermore, the palaeo-highs within the shelfal terrain may have acted as flow-barriers restricting the circulation and the exchange of the overlying water masses with the open ocean, hence promoting and accelerating the development of euxinic conditions within the palaeo-depressions. As the relative sea-level continued to rise throughout the Lower Silurian, the palaeo-highs became submerged and lost subsequently their ability to act as barriers, leading the black shale deposition to become laterally uniform and the conditions less reducing.

7.4 Palaeosalinity

The salinity levels were reconstructed using the Rb/K ratio of Campbell and Williams (1965). This salinity proxy suggests, that the Bernesga Mb. shales were deposited under brackish water conditions, thus contradicting the previously interpreted ‘fully marine developed’ environment based on the classification scheme of Pearce *et al*. (2010). However, the sand- and siltstones of the Getino Beds at the Aralla and La Majua sections, discriminate clearly as brackish water deposits using the Rb/K proxy, which is supported by field observations. The glauconitic Getino Beds exhibit a high degree of bioturbation and have previously already been interpreted to represent very shallow marine, well oxygenated deposits. The assumption of a sporadic fresh-water input leading to brackish water conditions as indicated by the used proxy is clearly not far-fetched.

7.5 Palaeohumidity

The humidity proxies of Akul'shina (1976) and Suttner and Dutta (1986) indicate, that the sand- and siltstones of the Getino Beds were most likely derived from a hinterland subjected to ‘arid’ to ‘humid’ environmental conditions. The sudden changes in palaeo-humidity from ‘arid’ to ‘humid’ could be interpreted to represent glacial - interglacial periods, causing the ‘waxing’ and ‘waning’ of

the Hirnantian ice masses. According to the proxy applied, the Bernesga Mb. shales are interpreted to have been sourced from areas under 'arid' conditions. The interpretation of an 'arid' hinterland is in good agreement with current palaeogeographic reconstructions, which place the Iberian Peninsula in a polar setting for the time of the Early/Mid Silurian (Scotese *et al.* 1999). The sand- and siltstones of the overlying Villasimpliz Mb. display a trend towards semiarid/humid. This interpretation is supported by the northwards drift of Iberia during the Mid/Late Silurian towards lower latitudes and the palaeo-equator (Scotese *et al.* 1999), and a consequent elevation of temperature and humidity.

7.6 Clay typing

The Schlumberger (2009) K_2O *vs.* Th system, commonly used for the identification of different clay types shows, that the majority of the Bernesga Mb. shales grouped across the 'illite' and 'mixed-layer clays' discrimination fields. However, at the Villanueva locality the predominant clay mineral present is illite, mixed-layer clays are absent. It can be interpreted, that the Bernesga shales at the Villanueva section are less mature and that the source sediment had been subjected to a lower degree of chemical weathering.

The SiO_2 *vs*. Al_2O_3 and Fe_2O_3 *vs*. Al_2O_3 plots of Cullers and Podkovyrov (2000) illustrate the predominant nature of the clay minerals within the Bernesga Mb. to be illite, only a small number of samples however trend towards kaolinite. The sand- and siltstones of the underlying Getino Beds exhibit a trend towards the SiO_2 end member as do the overlying sand- and siltstones of the Villasimpliz Mb. The Fe_2O_3 *vs.* Al_2O_3 diagram revealed, that a select few samples of the Bernesga Mb. from the Aralla and Caldas de Luna sections trend towards Fe-rich chlorite. This is interpreted to be the result of localised Fe_2O_3 mineralisation.

In the SiO_2-Al_2O_3-Fe_2O_3 ternary plot of Konhauser (1998), Konhauser and Urrutia (1999) and Eickmann *et al.* (2009) the Bernesga Mb. shales pool near to the illite zone. The sands- and siltstones of the underlying Getino Beds trend towards the SiO_2 component, with a number of samples from the Aralla and La Majua sections indicating the presence of glauconite. The sand- and siltstones of the overlying Villasimpliz Mb. display a compositional maturity trend towards the SiO_2 component. A number of shale samples from the Aralla and Caldas de Luna sections exhibit a trend towards chamosite. This is again interpreted to be an effect of the minor, localised Fe_2O_3 mineralisation.

In the past, the presence of illite in shales was used to indicate humid-temperate climates for the source area (Einsele 2000). However, Chamley (1989) and Weaver (1989 in: Diester-Haass *et al.* 1998) suggest chlorite and illite to be derived from areas subject to intense uplift (leading to elevated active mechanical erosion) and cold/desert climate conditions. The later assumption is in good agreement with the presence of illite within the Bernesga Mb. shales, and finds a coherent explanation by the previously discussed palaeohumidity reconstruction. The presence of 'mixed-layer clays' within the Bernesga shales could be used to suggest an only weak development of chemical weathering (Chamley 1989) in; (Diester-Haass *et al.* 1998). However, this contradicts the high chemical weathering rates interpreted from the various weathering indices applied (see below). Illite is the predominant clay mineral in marine shales as it is more stable than kaolinite, with the later dominating freshwater sediments (Weaver 1989).

In retrospect, it may have been beneficial to compare the obtained XRF signatures to XRD data. The XRD data may have been more precise, however the XRF data generated and the discrimination diagrams applied proved to be sufficient.

7.7 Weathering indices

The K_2O/Al_2O_3 ratio and index of compositional variation (ICV) of Cox *et al.*(1995) allow for the interpretation, that the basal shales of the Bernesga Mb. are of a higher compositional maturity than that of the middle and upper parts of the Bernesga Mb., which are diluted by an increased influx of terrestrial material. Additionally, the ICV values again indicate illite to be the predominant clay mineral within the Bernesga Mb. shales, reiterating the result derived from the clay-typing discrimination diagrams (see above).

The chemical index of alteration (CIA) of Nesbitt and Young (1982) and Taylor and McLennan (1985) and the chemical index of weathering (CIW) of Harnois (1988) led to calculation of significantly high chemical weathering values for the shales of the Bernesga Mb. The sand- and siltstones of the Getino Beds belonging to the La Majua and Sena de Luna sections have low CIA values relative to the overlying Bernesga Mb. These Getino Beds are shallow marine deposits, composed of sediment affected by a lower rate of chemical weathering. The shales of the Bernesga Mb. plot within the range of the illite zone of the CIA diagram. The Bernesga Mb. shales of the Aralla section have an average CIA value of **84.73**, at the Caldas section **85.28**, La Majua **87.2**, Sena de Luna **84.07** and the Villanueva section **84.85**. In conclusion, the shales of the

Bernesga Mb. are comprised of source sediments that have undergone elevated chemical weathering rates. The chemical weathering has resulted in a complete conversion of the feldspars to aluminous clay minerals.

The sand- and siltstones of the Villasimpliz Mb. at the Aralla section have lower CIA values (lower degree of feldspar degradation) relative to the shales of the Bernesga Mb. The Villasimpliz Mb. is interpreted to represent a prograding deltaic front, responsible for the incorporation of elevated amounts of detrital material from the hinterland. This prograding delta is also considered to have introduced oxygenated sediments into a predominantly anoxic mature black shale environment.

7.8 3D environmental reconstruction models

The 3D environmental reconstructions combine three of the previously discussed parameters. **[1]** The redox state using the V/(V+Ni) proxy of Hatch and Leventhal (1992) and Th/U ratio of Fertl (1979), **[2]** the palaeosalinity indicator Rb/K of Campbell and Williams (1965), and **[3]** the detrital influx proxies Zr/Rb and Si/Al. The relation between these parameters can be used to infer a direct link between a reducing environment, higher salinity levels and diminished siliciclastic (detrital) input.

7.9 Hydrothermal activity

The diagram of Boström (1973) was utilised to determine any potential hydrothermal overprint of the sediments analysed. The shales of the Bernesga Mb. do not show any consistent and significant hydrothermal alterations. Additionally, the shales analysed plot in very close proximity to the international shale standards NASC and PAAS, indicating that no major elemental changes relative to these standards have taken place. This is most likely as a result of the low permeability of the shales.

However, the sands and silts of the underlying Getino Beds and overlying Villasimpliz Mb. may have been affected slightly (not significantly) by hydrothermal activity. A number of samples from these Members are trending towards the hydrothermal end member. This is interpreted to reflect the higher permeability of the sandstone intercalations, allowing the percolation of hydrothermal fluid.

7.10 Bioproductivity

As previously described, the shales of the Bernesga Mb. have not been affected by any significant hydrothermal alteration process. This permitted the application of barium-based geochemical proxies (Peterson 1979, Bonn *et al.* 1998, Dymond *et al.* 1992, Francois *et al.* 1995, Pfeifer *et al.* 2001, Prakash Babu *et al.* 2002, Bernárdez *et al.* 2008) to estimate the palaeo-productivity.

The calculated palaeo-productivity estimates vary only slightly between the analysed localities. The highest productivity rates coincide in general with the onset of the black shale deposition (when developed). This is in particular well documented by the productivity values of the Aralla section. There, the productivity rates are elevated within the basal, graptolite rich parts of the Bernesga Mb. and decrease systematically towards the top. Overall the high productivity rates for the Bernesga Mb. at the Aralla section vary between 570 gC m^2yr^{-1} to 800gC m^2yr^{-1}, which is in good agreement with previously published productivity rates for upwelling-related ancient black shales (400 – 1200 gC m^2yr^{-1}, Einsele, 2000; Kuypers *et al*., 2002) and modern day analogues (≥ 600 gC m^2yr^{-1}, Handoh *et al*., 2003).

It is interpreted, that the Aralla section was situated within a palaeo-depression leading to the development of a complete black shale sequence contrary to the Caldas de Luna, La Majua, Sena de Luna and Villanueva localities, which are regarded to have been situated on relative palaeo-highs. As a consequence, the localities positioned on the palaeo-highs were only later reached by the Lower Silurian relative sea-level rise and the high-productivity black shale sequence developed either incomplete (Caldas de Luna, Sena de Luna, Villanueva) or not at all (La Majua).

The elevated productivity values during the onset of black shale deposition across the Cantabrian Basin correspond well to the Early Silurian upwelling model of Moore *et al.* (1993), which implies the introduction of nutrient rich waters to the shelfal environments of northern Gondwana. This upwelling triggered a significant increase in primary productivity, which in turn is regarded to be one of the key-factors responsible for the development of the widely distributed Silurian ‘hot’ shales, not only within the Cantabrian Basin but throughout large parts of the northern Gondwanan margin.

7.11 Gamma-ray logs

The calculated gamma-ray signatures derived from the XRF analysis of the Aralla section provide important insights into the development and the nature of the lower Bernesga Mb. shales. At the base of the member, the shales exceed with approximately 310 API clearly the defined threshold of 200 API (Lüning *et al.,* 2000) for 'hot' shales. Additionally, the approximated TOC values (~ 6 Wt%) also indicate the presence of 'hot' shales by exceeding the threshold of 3 Wt% TOC (Lüning *et al.,* 2000). An abrupt decrease of the gamma-ray signal, which is traceable in all but the La Majua section, is interpreted to reflect the sedimentological response to a significant tectonic event. The Caldas de Luna section again shows the basal shales of the Bernesga Mb. exceeding the 200 API and 3 wt% TOC 'hot' shale thresholds. However, it appears that the first cycle expressed at the Aralla section is here missing. The basal 'hot' shale horizons together with the distinctive calculated gamma ray signal evident at Aralla and Caldas de Luna is absent from the La Majua section. The basal 'hot' shales are not present within the Sena de Luna and Villanueva sections, although the gamma ray signal of the interpreted tectonic event documented at the Aralla and Caldas de Luna sections is developed.

7.12 Cyclicity and high order sea-level reconstructions

One of the most prominent features of the XRF data for the Bernesga Mb. shales is the presence of a cyclic signal within the redox sensitive elements U and V, particularly apparent at the Aralla and Caldas de Luna sections. The data were subjected to spectral analysis (Tanner, 2010), in order to examine and discuss these cyclic patterns in detail.

The cyclicity is most prominently developed within the basal parts of the Bernesga Mb. at the Aralla and Caldas de Luna sections. A Fourier analysis of these sections resulted in a calculated cyclicity of **514.3 kyr** (first three cycles observed in the U and V concentrations) for the Aralla section and **365.3 kyr** (first two cycles in the U and V concentrations) for the Caldas de Luna section. The Caldas de Luna section displays higher order cyclicity than that of the Aralla section. This higher order cyclicity is most likely the result of condensed horizons and hiatuses within the basal Bernesga Mb., these condensed horizons are represented by the mass accumulations of monograptids, suggesting starved basin conditions.

The first cycle of the Aralla section (~3m) was analysed at a higher resolution in the field to determine whether or not there was a higher order cyclicity superimposed on the calculated **514.3 kyr**. The *in-situ* field analysis determined that there was indeed a higher order cyclicity of **38 kyr** present within the V concentrations.

The Sena de Luna, La Majua and Villanueva sections are missing a significant part of the organically enriched basal shales. This interpretation is supported by the lack of redox element cyclicity apparent within the Aralla and Caldas de Luna sections.

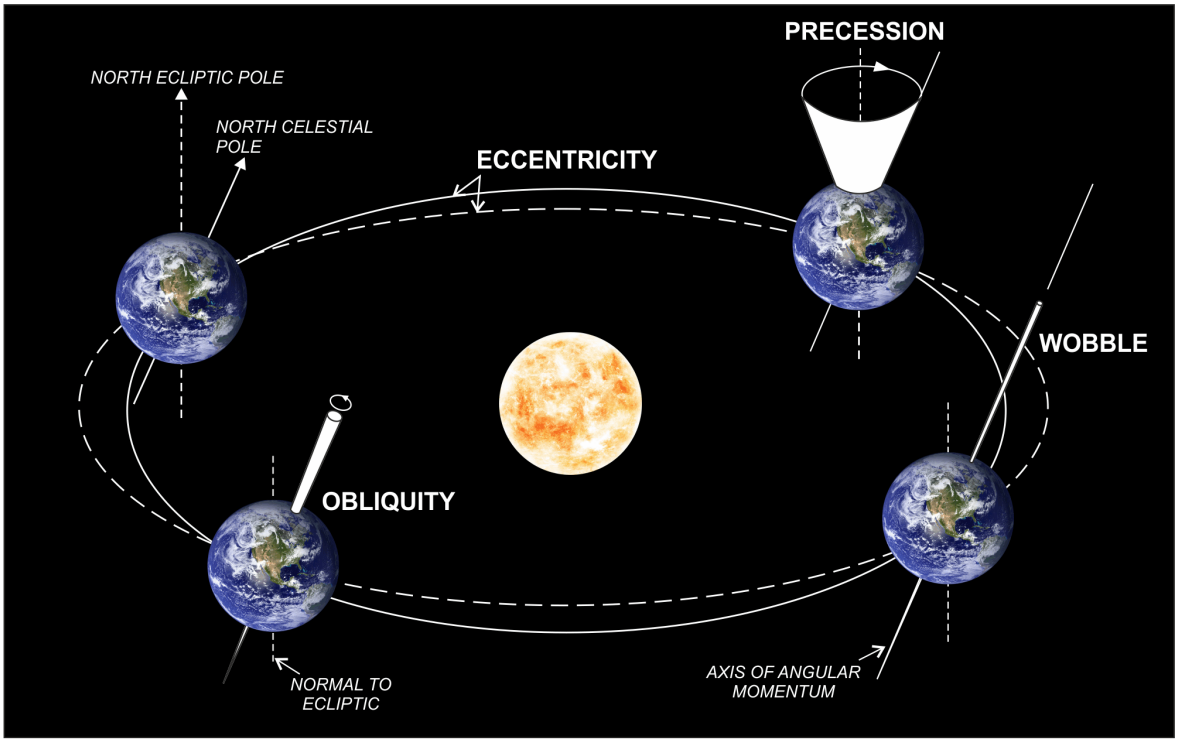

Figure 7.4: Illustrating the Earth-Moon-Sun system and the oscillations which effect rates of insolation and energy flux on the Earth's outer atmosphere. Thus leading to orbitally forced signatures in the sedimentary record. Modified after House (1995) p.10.

Several orbital parameters can have large effects on the rates of insolation and therefore on sedimentological processes (Imbrie and Imbrie, 1980; Schwarzacher, 1993a; House, 1995; Valdes *et al.*, 1995; Yang and Baumfalk, 1997; Marshall, 2000; Tanner, 2010; Ellwood *et al.,* 2012; see **Figure 7.1**). The highest order cyclicity is related to precession (19-23 kyr). Precession (or 6th order cyclicity according to Vail, 1977 in: Yang and Baumfalk, 1997) refers to the movement of the axial projection of Earth's rotation axis (or axial wobble) in relation to the stars (House, 1995).

The second orbital factor is the obliquity or tilt of the Earth's axis (5th order cyclicity Vail, 1977 in: Yang and Baumfalk, 1997). The celestial equator of the Earth lies presently at 23.5^{o} in relation to the plane of orbit. This angle fluctuates between 21.5^{o} to 24.4^{o} at a periodicity of 41 kyr (or between

41 and 54 kyr Berger *et al.,* 1989b). A low obliquity implies a relatively small difference between summer and winter, yet it has profound effects on insolation in equatorial and high latitude polar regions (Schwarzacher, 1993b).

Precession and obliquity cycles are dependent on the Earth-Moon system. The lunar day and month has changed significantly throughout Earth's geological history, having a direct effect on both precession and obliquity. For the last 590 Ma the mean retreat rate of the moon has been calculated to be ~3.16cm/yr, prior to this, the retreat rate was significantly lower ~1.36cm/yr (Berger and Loutre, 1994). Berger *et al.* (1989b) developed an algorithm to correct for these changes within the precession and obliquity cycles (quasi-periodic) for the past several million years to present. For earlier times, the calculation becomes progressively uncertain. Obliquity cycles have shown the largest change according to Berger *et al.* (1989b) with an increase of ~10'000 years since the Cambrian (Schwarzacher, 1993b). Thus, it is nearly impossible to distinguish between the obliquity and precession cycles of the Precambrian. With the lengthening of the Earth – Moon distance throughout Earth's geological history, Berger and Loutre (1994) calculated changes in precession and obliquity. For the Silurian the precession cycles of 19 and 23 kyr are re-calculated into 16.4 and 19.3 kyr and the obliquity cycles 41 and 54 kyr calculate into 30.5 and 37.2 kyr respectively (see **Table 7.1**).

P1	**P2**	**O1**	**O2**	**E1**	**E2**		
16.40	19.30	30.50	37.20	106.00	410.00		
					1.00	410.00	**E2**
				1.00	3.87	106.00	**E1**
			1.00	2.85	11.02	37.20	**O2**
		1.00	1.22	3.48	13.44	30.50	**O1**
	1.00	1.58	1.93	5.49	21.24	19.30	**P2**
1.00	1.18	1.86	2.27	6.46	25.00	16.40	**P1**

Table 7.1 Table representing the Silurian Milankovitch Band periodicities as time durations in thousands of years (Kyr). The durations for P1 and P2 precession, O1 and O2 obliquity and E1 and E2 for eccentricity after Berger *et al.*(1989a) and Berger *et al.* (1989b in: Marshall, 2000).

Eccentricity (4^{th} order cyclicity according to Vail, 1977 in: Yang and Baumfalk, 1997) is considered to control the largest of the Earth's Milankovitch cycles. The Earth's orbit varies from near-circular (0 eccentricity values) to a partial ellipse (eccentricity values approaching 0.06, Tanner, 2010), which has significant effects on the insolation caused by solar radiation. When the Earth's orbit is circular the insolation effects are minimal. During the elliptical extremes, insolation can vary by as much as 30% of the total flux (House, 1995). However, Tanner (2010) concluded, that the

eccentricity has only a minimal effect on the total insolation, but that it does control the amplitude of the precession effect (with average periods of 19 and 23 kyr). The most powerful of the eccentricity signals are caused by the 106 and 410 kyr cycles (95 and 413 kyr, according to Imbrie and Imbrie, 1980; Berger *et al.,* 1989b). The total magnitude of these signals is periodically reduced by the interference with a higher frequency 54 kyr and a lower frequency 2.35 Myr eccentricity cycle (Van Vugt *et al.,* 2001). The eccentricity cycles are not affected by changes in the Earth-Moon system and have stayed relatively constant through time (they are considered to have varied by only ~1.5% over the last 200 Ma, Berger and Loutre, 1994). The combination of the above orbital parameters, precession, obliquity and eccentricity lead to regular changes in the Earth's climate systems as a direct response to the changing insolation.

Most of the cyclicity signals analysed since the mid-1980's in Triassic sediments turned out to be modulations of the basic cycle. The eccentricity cycle is superimposed on the precession cycles (Tiwari *et al.,* 1997; Tanner, 2010). Heckel (1986 in: House, 1995) recognised a substantial series of cycles within Pennsylvanian aged sediments which were estimated at 0.5 Ma each. These cycles were related to transgressive pulses caused by the melting of ice masses and have been interpreted in the past to represent the sedimentological response to the Earth's 410 kyr cycles (House, 1995).

Orbital forcing may be well the factor controlling the cyclic signals observable within the basal part of the Bernesga Mb. The **513 kyr** cyclicity reconstructed for the Aralla section, can tentatively be interpreted to be the sedimentological response to the periodic waxing and waning of the Hirnantian ice-age related ice masses, moderated by the Earth's 413 kyr eccentricity cycle or 'deep time' interval (Marshall, 2000). The high resolution *in-situ* data, spanning the first cycle of the Aralla section, displayed a cyclicity of **38 kyr**. This cyclicity is interpreted to be a product of the Earth's obliquity (37.2 kyr, see **Table 7.1**), which affects the insolation and consequently changes the intensity of the seasons, hereby controlling the magnitude of the melting of the ice masses generated during the Hirnantian ice age. The periodic influxes of glacial melt-waters combined with periods of glacial advance resulted in high-order sea-level changes and consequent redox state fluctuations. The **365.3 kyr** cycles of the Caldas de Luna section are tentatively linked to the Earth's 413 Kyr eccentricity cycle.

The cyclicity apparent within the basal shales of the Bernesga Mb. is interpreted to be the product of ice-sheet advances and retreats, related to changes in isolation as a product of the combined

eccentricity and obliquity orbital factors. Le Heron *et al.* (2013) suggest that the lingering ice sheets of the Hirnantian glaciation played an important role for the localised and patchy development of the 'hot' shale deposits.

It is important to note, that not all signals apparent within the sediments may be related to orbital forcing. The 'pure' cyclic signal caused by orbital forcing may be altered, transformed and sometimes even completely masked by tectonic pulses that affected the basin, by drastically changing important parameters like the sedimentation rate or the availability of accommodation space. Álvaro *et al.* (2000b) described and discussed precisely this complex interplay between orbital forcing and tectonic pulses for Cambrian successions of the Iberian chains, concluding that the deciphering of original signals under these circumstances may be extremely difficult and sometimes even impossible.

7.13 A generic model for the Silurian Cantabrian Basin

Combining and summarising all of the factors analysed, described and discussed within this thesis, the following generic model for the black shale deposits of the Lower Silurian Formigoso Fm. of the Southern Cantabrian Basin is suggested.

7.13.1 Correlation across the southern Cantabrian region using the GR signature's and the Rb/Zr grain-size proxy

From taking into account the subunits identified earlier (see **Chapter 7.1**) within the lowermost Bernesga Mb. of the Formigoso Fm., the following correlation panel has been constructed (see **Figure 7.5**). The correlation panel utilises a number of parameters in order correlate laterally between the sections spanning the southern Cantabrian margin, the inset map towards the top left of the figure displays the orientation of the correlation line. The parameters selected were [1] the GR signatures, with the gamma signal incorporating the variations of K_2O, Th and U for each of the analysed sections, and [2] the Rb/Zr grain size proxy, an ideal proxy for indicating the presence of terrestrial detrital material. In this instance the Rb represents the fine grade clay fraction of the sediment analysed and the Zr belongs to the coarser grained terrestrial detrital material. The lower the Rb/Zr ratio, the higher the influx of coarser terrestrial material, the higher the ratio the higher the clay content of the sediment analysed.

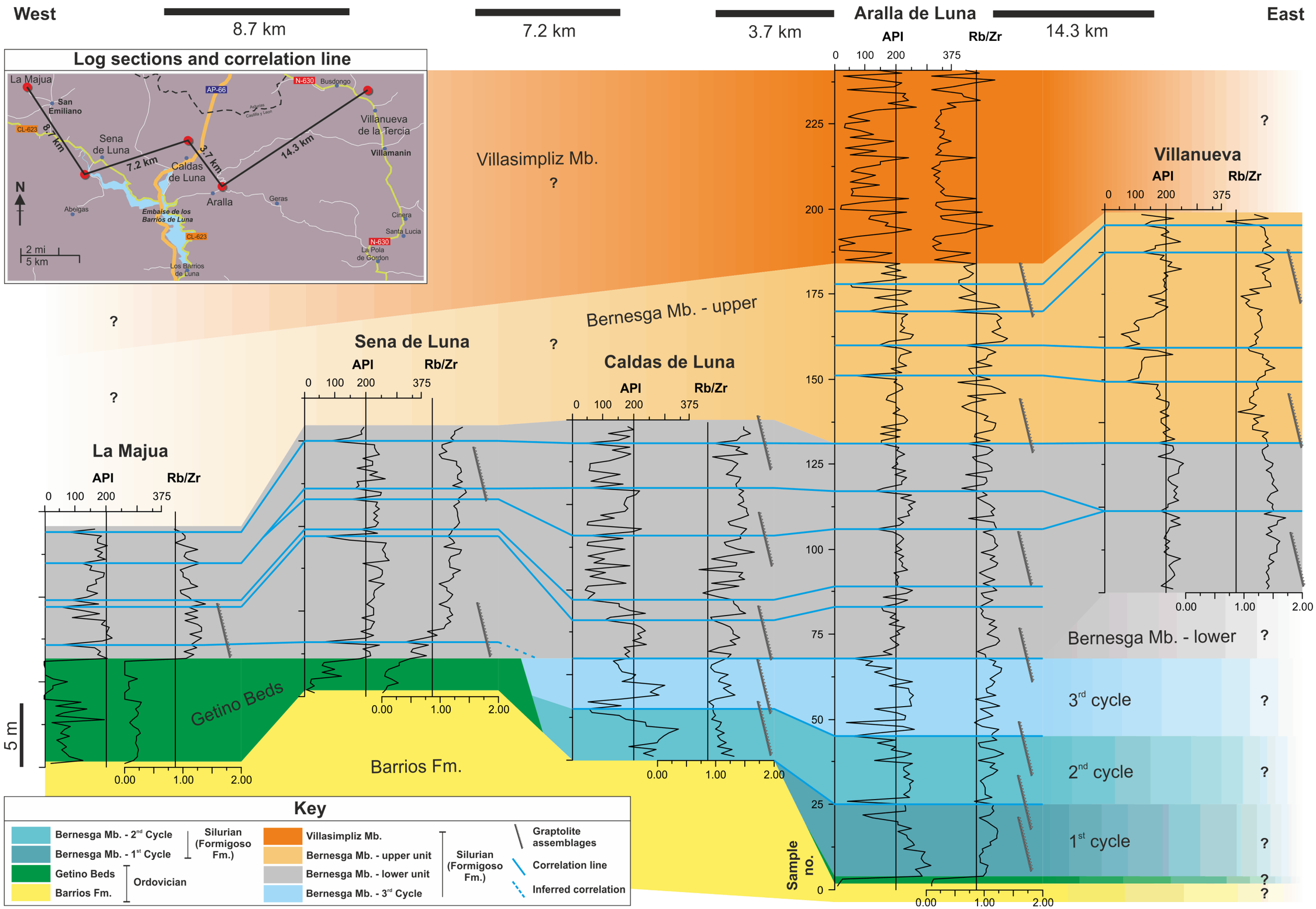

Figure 7.5: Correlation of the analysed sections spanning from west to east across the southern Cantabrian Basin. The correlation utilises the gamma ray (GR) and the grain-size indicator Rb/Zr for each location. See text for detailed discussion.

From reviewing the previously documented correlation panel (see **Figure 7.5**) it is clear that the relief of the underlying Barrios Fm. is ultimately controlling the accommodation space available for the overlying Getino Beds and Formigoso Fm. Areas where there are palaeotopographical lows or grabens within the Barrios Fm. such as the Aralla section, are where the Silurian Formigoso Fm. is at its most complete. The complete Formigoso Fm. at the Aralla section consists of the 1st, 2nd and 3rd cycles within the redox sensitive elements at the base of the lower Bernesga unit. Areas located above palaeotopographical highs or horst structures such as the Sena de Luna section are missing in their entirety the cycles of the redox elements found at the basal parts of the lower Bernesga unit. The correlation panel also leads to the conclusion that the presence and absence of the Getino Beds is also controlled by the palaeorelief of the underlying Barrios Fm.

The other significant point to note from the correlation is that key horizons within the lower unit of the Bernesga Mb. can be correlated based on the signature of the GR signal and combined Rb/Zr ratio. These horizons when correlated also re-enforce the effects of the undulating palaeorelief on the overall accommodation space available for the sedimentation of the overlying black shales. The localities towards the west (La Majua and Sena de Luna) display condensed horizons within the lower unit of the Bernesga Mb. when taking into account the correlated horizons as they are situated above a palaeo-high.

For the Aralla and Villanueva sections the upper unit of the Bernesga Mb. is present, which is signified by an increased siliciclastic influx (lower Rb/Zr ratios) and a slightly more erratic GR signal (see **Chapter 7.1**). It is also notable that certain horizons within this upper unit of the Bernesga Mb. can also be correlated laterally, as is the case with the Aralla and Villanueva sections documented (see **Figure 7.5**).

7.13.2 Systematic development of the Cantabrian 'hot' shales

From taking into account all of the previously discussed factors within this thesis and the correlation panel discussed and documented in **Chapter 7.13.1**, the following generic model has been postulated for the formation of the Cantabrian 'hot' shales.

It is assumed, that prior to the deposition of the Lower Silurian black shales of the Formigoso Fm. a palaeo-topographical-relief developed that affected the thickness of the pre-Silurian lithostratigraphic units. This relief is interpreted to be the result of a combination of the extensional

tectonic regime, related to the opening of the Rheic Ocean towards the north (Weil *et al.,* 2001; Crowley *et al.,* 2002; Gutiérrez-Alonso *et al.,* 2008; Linnemann *et al.,* 2008; von Raumer and Stampfli, 2008; Keller *et al.,* 2008; Ballèvre *et al.,* 2009; Díez Fernández and Martínez Catalán, 2009; Martínez Catalán *et al.,* 2009; Romer and Hahne, 2010; Barba *et al.,* 2011) and glacial processes during the Hirnantian, such as the formation of incised valleys and the deposition of glaciogenic sediments (Bernárdez Rodríguez *et al.,* 2006; Gutiérrez-Marco *et al.,* 2010).

During the initial transgression at the lowermost Silurian, the Getino Beds (or 'transitional beds' of Bosch Van den, 1969) were deposited upon the glaciogenic deposits. The sedimentation of the Getino Beds occurred under shallow marine conditions, as indicated by the abundance of bioturbation and presence of glauconite, presumably during an interglacial period. The Getino Beds show a considerable lateral variation in thickness across the southern Cantabrian Basin, in some cases, for example at Caldas de Luna, they are not developed at all. It is assumed, that the palaeo-topography significantly controlled the distribution and thickness of the Getino Beds.

Starved basin conditions prevailed during the onset of the black shale deposition as a consequence of melting ice-masses and combined rise in relative sea-level. The rise in sea-level effectively led to the deposition of the coarser-clastic terrigenous material far inland, only reduced amounts of fine-grained sediments were able to reach the shelf areas. This relative sea-level rise in combination with upwelling flooded large parts of the northern Gondwanan shelf with nutrient rich bottom waters (Moore *et al.,* 1993; Armstrong, 1996). The elevated levels in available nutrients within the upper-parts of the water column led to a boom amongst the primary producers and consequently to a strongly increased net primary production for the time of the lowermost Silurian (Paris and Robardet, 1990; Cramer and Saltzman, 2007). This significant rise in palaeo-bioproductivity and the starved basin conditions are most likely the fundamental triggering factors leading to the formation of the organic rich 'hot' shale deposits.

The basal 'hot' shales of the Bernesga Mb. are discontinuous in distribution across the southern Cantabrian Basin. The 'patchy' nature of the 'hot' shales was strongly controlled by the presence of palaeo-topographical features, such as palaeo-highs and palaeo-depressions. The formation of 'hot' shales was confined to palaeo-lows during the initial transgression and the palaeo-highs acted as flow barriers, effectively reducing the exchange of water between the shelf areas and the open ocean, thereby exacerbating the prevailing anoxic conditions. The redox state reached in some instances euxinic levels, leading to the precipitation and enrichment of authigenic U^{+4}, which was

largely adsorbed to the organic content. The absence of bioturbation and presence of framboidal pyrite is in support of the anoxic/euxinic bottom water hypothesis (e.g. Droser and Bottjer, 1986 in: Armstrong *et al.,* 2009; Wignall, 1994). This palaeo-topographical background together with the presence of a fresh water cap (which is assumed to have only developed during brief inter-glacial periods) prevented the mixing of the water column, and consequently forced the development of a stratified water column. At times of glacial retreat, the resulting fresh-water influx moderated the salinity levels, which were possibly lowered to even brackish conditions. The low taxonomic diversity of the graptolites present in combination with a small-sized (?'Lilliput'-) benthic fauna (Harris and Knorr, 2009), may reflect these harsh environmental conditions. The humidity proxies suggest that during the deposition of the basal 'hot' shales, arid climatic conditions prevailed. This environmental interpretation is supported by the clay typing proxies and weathering indices. The high-latitude polar setting of the Iberian Peninsula during the Early and Mid Silurian conforms to this interpretation. The overlying Villasimpliz Mb. developed under elevated palaeo-humidity levels, coinciding with the northward drift of Iberia towards the palaeo-equator during the Late Silurian.

The basal Bernesga shales were affected by a combination of orbital parameters (obliquity 37.2 Kyr and eccentricity 413 Kyr) and tectonic pulses, which ultimately controlled the intensity of the prevailing redox conditions. Relative sea-level may have been moderated by the advances and retreats ('waxing' and 'waning') of polar ice masses, in response to changes in the insolation caused by orbital parameters such as obliquity and eccentricity. However, the relative sea-level may have also been additionally regulated by a series of tectonic pulses, effectively changing the available accommodation space and/or the sedimentation rates.

High palaeo-bioproductivity rates are assumed to have been persistent throughout the deposition of the Bernesga Mb., as predicted by the upwelling model of Moore *et al.* (1993). However, the Ba palaeo-productivity reconstructions indicate, that the net primary production reduced at the same time as the cyclic signal of the redox elements U and V disappears. This is seen to indicate the onset of the oxygenation of the entire water column: The relative sea-level at this point may have risen above the palaeo-highs, enabling the re-establishment of water-exchange and circulation, which consequently led to the ventilation of the water column.

The 'hot' basal Bernesga Mb. - shales are within the Cantabrian Basin conformably overlain by the 'lean' shale deposits of the upper Bernesga Mb. These 'lean' shales are less enriched in organic matter and contain an increased amount of detrital siliciclastic material. The increase in detrital

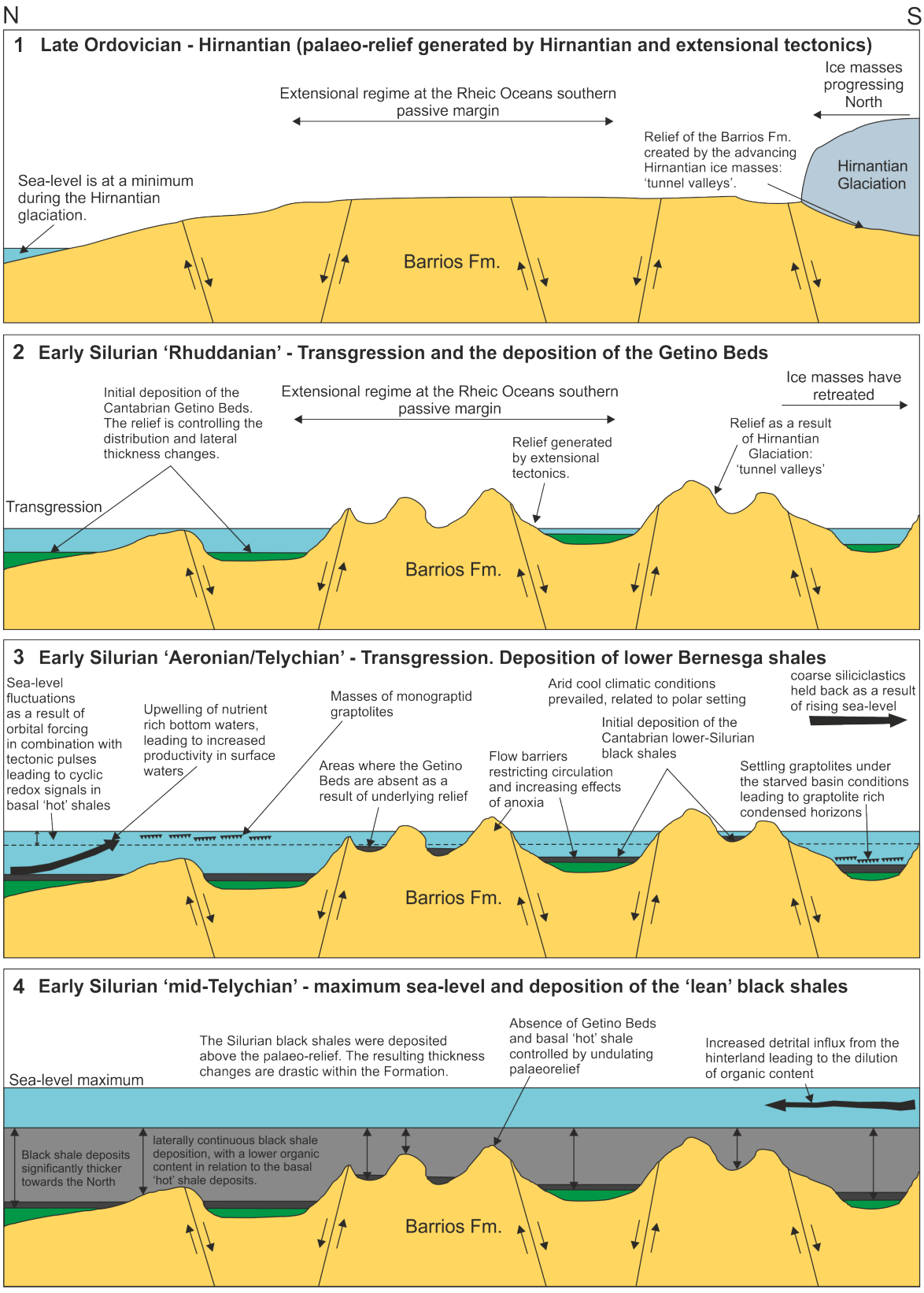

Figure 7.6(a): Generic model for the formation of the lower Silurian black shales within the southern Cantabrian Basin. **(1)** During the late-Ordovician the Hirnantian ice masses reach their widest distribution, consequently the relative sea-level is at a minimum. The extensional tectonic regime in combination with the glaciogenic processes leads to the development of a palaeorelief. **(2)** During the earliest Silurian the relative sea-level begins to rise with the demise of the Hirnantian ice masses. The rise in relative sea-level results in the laterally discontinuous distribution of the Getino Beds (deposited within palaeo-depressions). **(3)** The marine transgression continues to develop, leading to the formation of 'patchy' 'hot' shales of the basal Bernesga Mb. The cyclic nature of the 'hot' shale horizons were modulated by the fluctuations in relative sea-level, related to the 'waxing' and waning' of the ice masses. **(4)** The transgression reached its maximum (breaching of the palaeo-highs), resulting in the deposition of laterally continuous 'lean' shales of the upper Bernesga Mb. The organic content of the 'lean' shales is effectively diluted by the increased presence of terriginous material.

material is interpreted to relate to a relative sea-level fall and the subsequent introduction of terrigenous material from the hinterland. The lean shales do not express the redox sensitive cyclic properties of the underlying 'hot' shales. This is seen to indicate, that the periodic fresh-water input resulting from the fluctuating Hirnantian ice masses, may have ceased by this point.

The overlying sand- and siltstones of the Villasimpliz Mb. were deposited during relative sea-level fall. The detrital material from the hinterland was introduced into the now consequently shallowing basin by progradational deltaic fronts. The sandstones are highly bioturbated throughout, thus indicating that benthic and endo-benthic organisms were able to thrive within a well oxygenated environment.

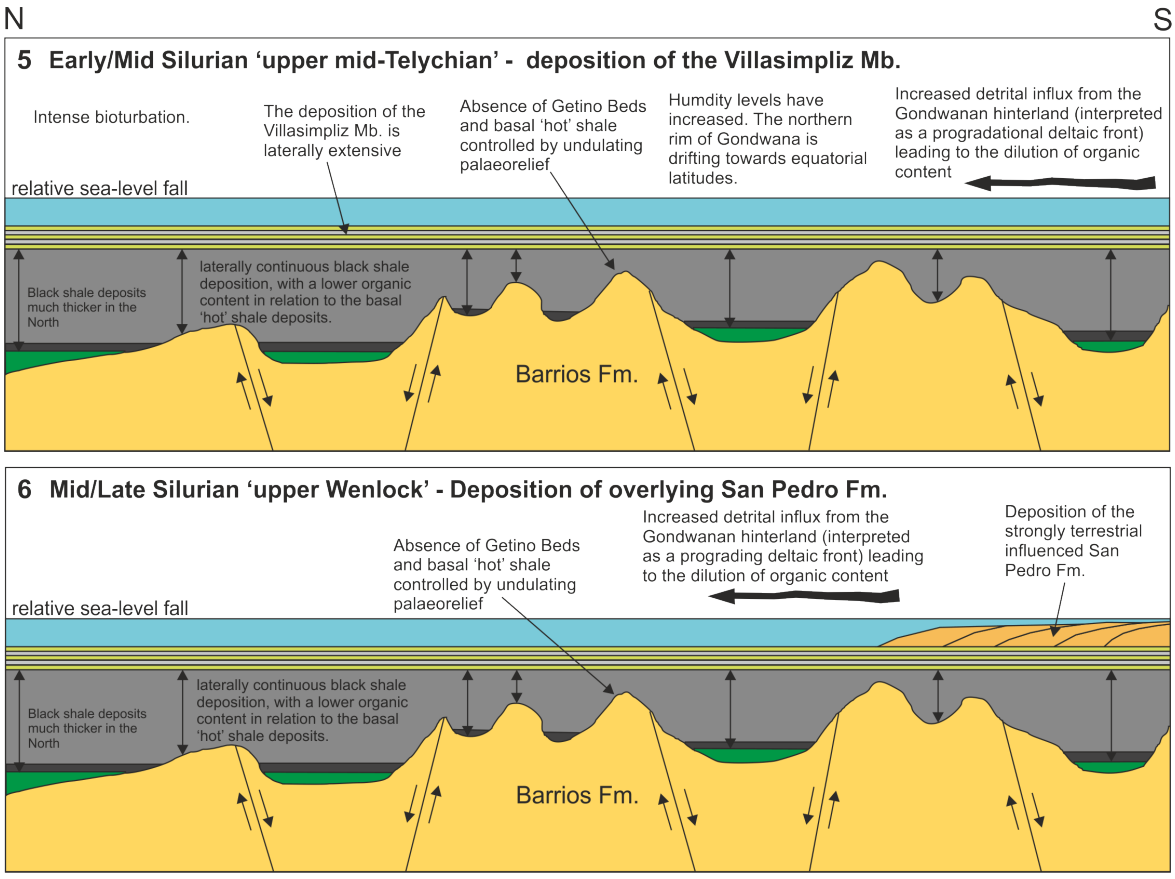

Figure 7.6(b): Generic model, continued. **(5)** With the fall of the relative sea-level the laterally continuous sand- and siltstones of the Villasimpliz Mb. are deposited, interpreted to be the product of progradational deltaic fronts. **(6)** With the continued fall of the relative sea-level, the strongly terrestrial sediments of the San Pedro Fm. are deposited.

7.13.3 Comparison of the Cantabrian black shale model to previously published studies

The postulated model for the formation of the Cantabrian black shales is inspired by and in large agreement with the basal transgressive 'puddle model' of Wignall (1994). The generic model displayed in **Figures 7.6(a&b)** is backed by all previously discussed parameters and the correlation panel found in **Chapter 7.13.1**.

The ‘puddle model’ readily explains the patchy distribution of the basal black shales of the Bernesga Mb. Lüning *et al.* (2000) developed a depositional Silurian ‘hot’ shale model that is also based on Wignall’s ‘puddle model’, but introduce additionally a combination of other controlling factors, such as a basal transgression, upwelling, flow barriers and minimum dilution of organic matter by coarse detritus. The intensity of the palaeo-topography is in this model considered to be the fundamental controlling factor for the distribution of the laterally discontinuous ‘hot’ shale deposits and the laterally continuous ‘lean’ shales of northern Africa (Lüning *et al.,* 2000; Craig *et al.,* 2002; Lüning *et al.,* 2003a; Lüning *et al.,* 2005; Varol *et al.,* 2006; Le Heron *et al.,* 2008; Butcher, 2009; Le Heron *et al.,* 2009; Loydell *et al.,* 2009. However, Armstrong *et al.* (2005) suggest that the palaeo-relief was not the dominating factor for the development and distribution of the ‘hot’ shales, as an older Hirnantian ‘lean’ shale has been found underlying the Silurian ‘hot’ shales, in areas with a high amount of potential accommodation space (palaeo-depressions). Armstrong *et al.* (2005) and Armstrong *et al.* (2009) suggest that, beside the palaeo-relief, other important factors, such as the development of a halocline (fresh water cap) controlled the formation of the Silurian ‘hot’ shales.

The ‘lean’ Hirnantian shale of Armstrong *et al.* (2005) is absent throughout the entire Cantabrian Basin, only the basal Silurian ‘hot’ shales are developed. This observation is supporting the palaeo-relief based model of Lüning *et al.* (2000, 2006). Le Heron *et al.* (2009) and Le Heron *et al.* (2013) suggest that the early Silurian black shale sedimentation and the extents of anoxia were modulated by the presence of localised ice-sheets, which persisted well into the Llandovery, despite the demise of the Hirnantian ice-cap. The ‘waxing’ and waning’ of this ice masses were controlled by orbital parameters such as eccentricity, obliquity and precession (Sutcliffe *et al.,* 2000; and Armstrong, 2007 in: Le Heron *et al.,* 2009), an interpretation that is also favoured for the cyclic signals observed within the lower Bernesga Mb. black shales of the Cantabrian Basin.

7.14 Conclusions

Firstly, the generic model put forth in this thesis for the formation of the early Silurian black shales of the Cantabrian basin is in large agreement with the ‘puddle’ model of Wignall (1994) and Lüning *et al.* (2000) as discussed in the previous **Chapter 7.13.3**. The main difference with the black shale model developed for the Cantabrian black shales is the influence of orbital parameters, specifically eccentricity and obliquity and how these orbital factors effected/mitigated the extent/presence of

the cyclic ‘hot’ shales found at the base of the Formigoso Fm. at a select few locations throughout the southernmost Cantabrian basin.

The generic model for the black shales of this research and the parameters for which it was built upon will aid future researchers into the understanding of the genesis of these economically important black shale deposits. The model and black shale formation as a whole is dependent on the delicate intertwining of the numerous environmental parameters explored, which in turn are backed by a substantial high-resolution geochemical database.

Secondly, the modern day advancement of portable XRF spectrometry has enabled the detailed and reproducible analysis of the black shales related to this research. In particular, under laboratory controlled conditions the Niton XL3t (ED-XRF) produced results easily comparable to conventional lab based XRF analysers (WD-XRF). The high resolution *in-situ* field analysis and the absolute elemental concentrations were affected by factors such as, grain-size, homogeneity, surface topography (uneven), temperature and moisture content. However, the overall signals (signatures) analysed for the various major and trace elements were comparable to the lab based readings.

This thesis aids future researchers into the understanding of black shale development by:

1) Fundamentally advancing our current knowledge and understanding of orbitally induced cyclicity and the depositional/environmental processes effecting the development of black shale deposits, which are in turn economically important hydrocarbon source rocks.
2) Providing a highly detailed account of variations in sedimentary geochemistry in a Silurian black shale deposit. Using as a case study the elemental variations of the early Silurian black shales belonging to the Bernesga Mb. of the Formigoso Fm. located within the southern margins of the Cantabrian Basin. The chemostratigraphy is backed by a substantial dataset of numerous major and trace element concentrations.
3) It provides a detailed review of the application of modern day ED-XRF portable analysers in particular the Niton XL3t in analysing and interpreting black shale elemental signatures. This thesis includes importantly the development of appropriate measurement, calibration, sampling and analysis methodologies for the Niton XL3t portable XRF analyser (pXRF) in compiling a high resolution geochemical dataset for early Silurian black shales or more specifically hydrocarbon source rock deposits.

References

Abalos, B., Carreras, J., Druguet, E., Viruete, J.E., Pugnaire, M.T.G., Alvarez, S.L., Quesada, C., Fernandez, L.R.R. and Gil-Ibarguchi, J.I., 2002. Variscan and Pre-Variscan Tectonics. In: Gibbons, W., and Moreno, T., (eds), *The Geology of Spain*. London: Geological Society, pp.155-183.

Abanda, P.A. and Hannigan, R.E., 2006. Effect of diagenesis on trace element partitioning in shales. *Chemical Geology*, Vol.**230**(1–2), pp.42-59.

Abbey, S. and Geological Survey of Canada, 1983. Studies in "standard Samples" of Silicate Rocks and Minerals, 1969-1982, *Canadian Geological Survey Paper* 83-15, p.114.

Abbey, S., 1981. The Search for “Best Values” - A Study Of Three Canadian Rocks. *Geostandards Newsletter*, Vol.**5**(1), pp.13-26.

Abdou, A. and Shehata, M., 2007. Geochemical Study of the Shales of Gebel Ghorabi Member, Bahariya Oasis, Western Deser, Egypt. *Australian Journal of Basic and Applied Sciences*, Vol.**1**(4), pp.553-560.

Adams, J.A.S. and Weaver, C.E., 1958. Thorium-to-Uranium Ratios as Indicators of Sedimentary Processes: Example of Concept of Geochemical Facies. *Bulletin of the American Association of Petroleum Geologists*, Vol.**42**(2). pp.387-430.

Akul'shina, E., 1976. Methods for determining weathering conditions, sedimentation and post-sedimentary transformations according to clay minerals. Clay minerals as indicators of rock forming conditions: *Novosibirsk Nauka*, pp.9-37.

Albani, R., Bagnoli, G., Bernárdez, E., Gutíerrez-Marco, J.C. and Ribecai, C., 2006. Late Cambrian acritarchs from the “Túnel Ordovícico del Fabar”, Cantabrian Zone, N Spain. *Review of Palaeobotany and Palynology*, Vol.**139**(1–4), pp.41-52.

Aldridge, R.J., Jeppsson, L. and Dorning, K.J., 1993. Early Silurian oceanic episodes and events. *Journal of the Geological Society*, Vol.**150**(3), pp.501-513.

Algeo, T.J. and Maynard, J.B., 2004. Trace-element behavior and redox facies in core shales of Upper Pennsylvanian Kansas-type cyclothems. *Chemical Geology*, Vol.**206**(3–4), pp.289-318.

Algeo, T.J., Schwark, L. and Hower, J.C., 2004. High-resolution geochemistry and sequence stratigraphy of the Hushpuckney Shale (Swope Formation, eastern Kansas): implications for climato-environmental dynamics of the Late Pennsylvanian Midcontinent Seaway. *Chemical Geology*, Vol.**206**(3–4), pp.259-288.

Aller, J., Valín, M.L., García-López, S., Brime, C. and Bastida, F., 2005. Superposition of tectono-thermal episodes in the southern Cantabrian Zone (foreland thrust and fold belt of the Iberian Variscides, NW Spain). *Bulletin de la Societe Geologique de France*, Vol.**176**(6), pp.487-497.

Álvaro, J., Vennin, E., Muñoz, A., Sánchez-Valverde, B. and Ojeda, J., 2000b. Interplay of orbital forcing and tectonic pulses in the Cambrian Iberian platform, NE Spain. *International Journal of Earth Sciences*, Vol.**89**(2), pp.366-376.

Álvaro, J.J., Rouchy, J.M., Bechstädt, T., Boucot, A., Boyer, F., Debrenne, F., Moreno-Eiris, E., Perejón, A., Vennin, E. 2000a. Evaporitic constraints on the southwards drifting of the western Gondwana Margin during Early Cambrian times. *Palaeogeography, Palaeoclimatology, Palaeoecology*. Vol.**160**, pp.105-122.

Álvaro, J.J., Van Vliet-Lanoë, B., Vennin, E. and Blanc-Valleron, M., 2003. Lower Cambrian paleosols from the Cantabrian Mountains (northern Spain): a comparison with Neogene–Quaternary estuarine analogues. *Sedimentary Geology*, Vol.**163**(1–2), pp.67-84.

Álvaro, J.J., Vennin, E., Moreno-Eiris, E., Perejón, A., Bechstädt, T., 2000a. Sedimentary patterns across the Lower-Middle Cambrian transtition in the Esla Nappe (Cantabrian Mountains, Northern Spain). *Sedimentary Geology*, Vol.**137**, pp.43-61.

Anderson, R.F. and Winckler, G., 2005. Problems with paleoproductivity proxies. *Paleoceanography*, **20**(3), PA3012.

Aramburu, C., 1989. El Cambro-Ordovicico de la Zona Cantabrica (No de Espana). *PhD Thesis*, University of Oviedo.

Aramburu, C., Méndez-Bedia, I., and Arbizu, M., 2002. The Lower Palaeozoic in the Cantabrian Zone (Cantabrian Mountains, NW Spain). in: Garciá-López, S. and Bastida, F., (eds) 2002. Palaeozoic conodonts from northern Spain. Insituto Geológico y Minero de Españia, *Serie Cuadernos del Museo Geominero*, Vol. **1**, pp.35-50 (Madrid).

Aramburu, C., Truyols, J., Arbizu, M., Méndez-Bedía, I., Zamarreño, I., García-Ramos, J.C., Suarez de Centi, C. and Valenzuela, M., 1992. El Paleozoico Inferior de la Zona Cantábrica. In: Gutiérrez Marco, J.C., Saavedra, J., and Rábano, I., (eds), *Paleozoico Inferior de Ibero-America*. Badajoz: Univ. of Extremadura, pp.397-421.

Aramburu-Zabala Higuera, C. and García Ramos, J., 1993. La sedimentación cambroordovícica en la Zona Cantábrica (NO de España). *Trabajos de Geología*, Vol.**19**, pp.45-73.

Armstrong, H.A, 2007. On the cause of the Ordovician glaciation. In: Williams, M., Haywood, A.M., Gregory, F.J., and Schmidt, D.N., (eds). Deep Time Perspectives on Climate Change: Marrying the Signal from Computer Models and Biological Proxies. *Micropalaeontological Society, Special Publications*. pp.101-121. The Geological Society (London).

Armstrong, H.A., 1996. Biotic recovery after mass extinction: the role of climate and ocean-state in the post-glacial (Late Ordovician-Early Silurian) recovery of the conodonts. Geological Society, London, *Special Publications*, Vol.**102**(1), pp.105-117.

Armstrong, H.A., Abbott, G.D., Turner, B.R., Makhlouf, I.M., Muhammad, A.B., Pedentchouk, N. and Peters, H., 2009. Black shale deposition in an Upper Ordovician–Silurian permanently stratified, peri-glacial basin, southern Jordan. *Palaeogeography, Palaeoclimatology, Palaeoecology*, Vol.**273**(3–4), pp.368-377.

Armstrong, H.A., Turner, B.R., Makhlouf, I.M., Weedon, G.P., Williams, M., Al Smadi, A. and Abu Salah, A., 2005. Origin, sequence stratigraphy and depositional environment of an upper Ordovician (Hirnantian) deglacial black shale, Jordan. *Palaeogeography, Palaeoclimatology, Palaeoecology*, Vol.**220**(3–4), pp.273-289.

Armstrong-Altrin, J.S., and Verma, S.P., 2005. Critical evaluation of six tectonic setting discrimination diagrams using geochemical data of Neogene sediments from known tectonic settings. *Sedimentary Geology*, Vol.**177**, pp.115-129.

Arnaboldi, M. and Meyers, P.A., 2006. 10. Data Report: Multiproxy Geochemical Characterization of OAE-Related Black Shales at Site 1276, Newfoundland Basin. In: Tucholke, J., Sibuet, J., and Klaus, A., (eds), 210 edn. *Proceedings of the Ocean Drilling Program, Scientific Results*, Vol.**210**, pp.1-16.

Arribas, J., Critelli, S., and Johnnson, M.J., 2007. Sedimentary Provenance and Petrogenesis: Perspectives from Petrography and Geochemistry. *Geological Society of America Special Paper* 420. pp.396. The Geological Society of America (Boulder, Colorado).

Arthur, M.A. and Sageman, B.B., 1994. Marine Black Shales: Depositional Mechanisms and Environments of Ancient Deposits. *Annual Review of Earth and Planetary Sciences*, Vol.**22**(1), pp.499-551.

Arthur, M.A., 1979. 36. North Atlantic Cretaceous Black Shales: The Record at Site 398 and a Brief Comparison with other occurances. In: Sibuet, J.C., et al. (eds). *Initial Reports of the Deep Sea Drilling Project,* Vol.**47**(2), pp.719-751.

Bahamonde, J.R., Colmenero, J.R., Vera, C., 1997. Growth and demise of Late Carboniferous carbonate platforms in the eastern Cantabrian Zone, Asturias, northwestern Spain. *Sedimentary Geology,* Vol.**110**, pp.99-122.

Bahlburg, H. and Dobrzinski, N., 2011. A review of the Chemical Index of Alteration (CIA) and its application to the study of Neoproterozoic glacial deposits and climate transitions. *Geological Society, London, Memoirs*, Vol.**36**(1), pp.81-92.

Ballèvre, M., Bosse, V., Ducassou, C. and Pitra, P., 2009. Palaeozoic history of the Armorican Massif: Models for the tectonic evolution of the suture zones. *Comptes Rendus Geoscience*, Vol.**341**(2–3), pp.174-201.

Barba, P. and Fernández, L.P., 1991. Estratigrafía. In: Memoria del mapa geologico de España, Escala 1:50.000, No.103 (La Pola de Gordón), 2. Seria (MAGNA) edn. Madrid: ITGE.

Barba, P., Ugidos, J.M., Gonzalez-Clavijo, E. and Valladares, M.I., 2011. Geochemical features of the Ordovician succession in the Central Iberian Zone (Spain). In: Gutiérrez Marco, J.C., Rábano, I., and Garcia-Bellido, D., (eds), Ordovician of the World. Madrid: Instituto Geológico y Minero de España, pp. 49.

Barbera, G., Mazzoleni, P., Critelli, S., Pappalardo, A., Giudice, A.L. and Cirrincione, R., 2006. Provenance of shales and sedimentary history of the Monte Soro Unit, Sicily. *Periodico di Mineralogia*, Vol.**75**(2-3), pp.313-330.

Barrois, C.E., 1882. Recherches sur les terrains anciens des Asturies et de la Galice. *Mémoires de la Société Géologique du Nord*, Vol.**2**(1). pp.1-630.

Bassett, M.G., (ed.) 2009. Early Palaeozoic Peri-Gondwana Terranes: New Insights from Tectonics and Biogeography. *Geological Society, London, Special Publications*, Vol.**325**, pp.1-2.

Berger, A. and Loutre, M., 1994. Astronomical forcing through geological time. In: Boer, P.L. and Smith, D.G. (eds), Orbital forcing and cyclic sequences. *IAS Special Publication*, Vol.**19**, pp.15-24.

Berger, A., Loutre, M. and Dehant, V., 1989a. Influence of the changing lunar orbit on the astronomical frequencies of pre-Quaternary insolation patterns. *Paleoceanography*, Vol.**4**(5), pp.555-564.

Berger, A., Loutre, M. and Dehant, V., 1989b. Pre-quaternary Milankovitch frequencies. *Nature*, Vol.**342**, p.133.

Bernárdez Rodríguez, E., Marco, G., Carlos, J. and Hacar, M., 2006. Sedimentos glaciomarinos de Ordovícico terminal en el Zona Cantábrica (NO de España). *Geogaceta*, Vol.**40**, pp.239-242.

Bernárdez, P., González-Álvarez, R., Francés, G., Prego, R., Bárcena, M. and Romero, O., 2008. Palaeoproductivity changes and upwelling variability in the Galicia Mud Patch during the last 5000 years: geochemical and microfloral evidence. *The Holocene*, Vol.**18**(8), pp.1207-1218.

Berry, W., Gutiérrez-Marco, J. and Rábano, I., 1998. The Arabian Sea: a modern analogue for North African–Southern European Silurian organic-rich graptolites-bearing shales, Proceedings of the 6 th International Graptolite Conference (GWG-IPA) and 1998 Field Meeting. In: Gutiérrez-Marco, JC, and Rabano, I.(eds.), IUGS Subcommission on Silurian Stratigraphy. *Temas Geologico-Mineros ITGE*, pp.57-59.

Berry, W.B. and Wilde, P., 1978. Progressive ventilation of the oceans; an explanation for the distribution of the lower Paleozoic black shales. *American Journal of Science*, Vol.**278**(3), pp.257-275.

Bhatia, M.R., 1983. Plate Tectonics and Geochemical Composition of Sandstones. *Journal of Geology*, Vol.**91**(6), pp611-627.

Bloch, J.D., Schroder-Adams, C. and Leckie, D., 1999. Sedimentology, micropaleontology, geochemistry, and hydrocarbon potential of shale from the Cretaceous Lower Colorado Group in Western Canada. *Bulletin of the Canadan Geological Survey*, Vol.**531**, pp.185.

Boggs, S., 1995. Principles of Sedimentology and Stratigraphy. pp.784. Prentice Hall Englewood Cliffs. Columbus (Ohio).

Boggs, S., 2009. Petrology of Sedimentary rocks. pp.600. Cambridge University Press. (Cambridge).

Bohacs, K.M., Grabowski Jr, G.J., Carroll, A.R., Mankiewicz, P.J., Miskell-Gerhardt, K.J., Schwalbach, J.R., Wegner, M.B. and Simo, J.T., 2005. Production, destruction, and dilution—the many paths to source-rock development. in: Harris, N.B., *Deposition of Organic-Carbon-Rich Sediments: Models, Mechanisms, and Consequences*. pp.61-101

Bonn, W.J., Gingele, F.X., Grobe, H., Mackensen, A. and Fütterer, D.K., 1998. Palaeoproductivity at the Antarctic continental margin: opal and barium records for the last 400 ka. *Palaeogeography, Palaeoclimatology, Palaeoecology*, Vol.**139**(3), pp.195-211.

Bosch, van den W.J., 1969. Geology of the Luna-Sil region, Cantabrian Mountains (NW Spain). *Leidse Geologische Mededelingen*, Vol.**44**, pp.137-225.

Boström, K., 1973. The origin and fate of ferromanganoan active ridge sediments. *Stockholm Contributions to Geology, Vol.**27**, pp.149-243.*

Bowman, M., 1982. The stratigraphy of the San Emiliano formation and its relationship to other Namurian/Westphalian A sequences in the Cantabrian Mts., NW Spain. *Trabajos de Geología*, Vol.**12**(12), pp.23-37.

Brenchley, P., Carden, G., Hints, L., Kaljo, D., Marshall, J., Martma, T., Meidla, T. and Nõlvak, J., 2003. High-resolution stable isotope stratigraphy of Upper Ordovician sequences: Constraints on the timing of bioevents and environmental changes associated with mass extinction and glaciation. *Geological Society of America Bulletin*, Vol.**115**(1), pp.89-104.

Brouwer, A. 1967. Devonian of the Cantabrian Mountains, northwestern Spain. *International Symposium of the Devonian System: Papers*. Vol.**2**, pp.37-45.

Brouwer, P., (2003). Theory of XRF. pp.62. Panalytical Publishing. (Almelo).

Brumsack, H., 1981. Geochemistry of Cretaceous black shales from the Atlantic Pcean (DSDP Legs 11, 14, 36 and 41). *Chemical Geology*, Vol.**31**, pp.1-25.

Brumsack, H.J., 1986. The inorganic geochemistry of Cretaceous black shales (DSDP Leg 41) in comparison to modern upwelling sediments from the Gulf of California. *Geological Society, London, Special Publications*, Vol.**21**(1), pp.447-462.

Burgan, A.M., Ali, C.A. and Tahir, S.H., 2008. Chemical composition of the Tertiary black shales of West Sabah, East Malaysia. *Chinese Journal of Geochemistry*, Vol.**27**(1), pp.28-35.

Butcher, A., 2009. Early Llandovery chitinozoans from Jordan. *Palaeontology*, Vol.**52**(3), pp.593-629.

Calvert, S. and Fontugne, M., 2001. On the late Pleistocene-Holocene sapropel record of climatic and oceanographic variability in the eastern Mediterranean. *Paleoceanography*, Vol.**16**(1), pp.78-94.

Calvert, S.E. and Pedersen, T.F., 1993. Geochemistry of Recent oxic and anoxic marine sediments: Implications for the geological record. *Marine Geology*, Vol.**113**(1–2), pp.67-88.

Calvert, S.E. and Pedersen, T.F., 2007. Elemental Proxies for Palaeoclimatic and Palaeoceanographic Variability in Marine Sediments: Interpretation and Application. In: Hillaire-Marcel, C., and De Vernal, A., (eds), *Proxies in Late Cenozoic Paleoceanography*. Elsevier Science, pp. 518.

Campbell, F. and Williams, G., 1965. Chemical Composition of Shales of Mannville Group (Lower Cretaceous) of Central Alberta, Canada. *AAPG Bulletin*, Vol.**49**(1), pp.81-87.

Campos Alvarez, N.O. and Roser, B.P., 2007. Geochemistry of black shales from the Lower Cretaceous Paja Formation, Eastern Cordillera, Colombia: Source weathering, provenance, and tectonic setting. *Journal of South American Earth Sciences*, Vol.**23**(4), pp.271-289.

Carballo, N.H., 1984. La estructura de la escama de Villar de Vildas (Manto de Somiedo, Zona Cantábrica). *Trabajos de Geología*, Vol.**14**(14-15), p.65.

Challands, T.J., Armstrong, H.A., Maloney, D.P., Davies, J.R., Wilson, D. and Owen, A.W., 2009. Organic-carbon deposition and coastal upwelling at mid-latitude during the Upper Ordovician (Late Katian): A case study from the Welsh Basin, UK. *Palaeogeography, Palaeoclimatology, Palaeoecology*, Vol.**273**(3–4), pp.395-410.

Chamley, H., 1989. Clay Sedimentology. pp.623. Springer-Verlag New York.

Chang, C.W., Iizuka, Y., Tzeng, W.N., 2004. Migratory environmental history of the grey mullet Mugil cephalus as revealed by autolith Sr:Ca ratios. *Marine Ecology Progress Series*, Vol.**269**. pp.277-288.

Charriau, A., Lesven, L., Gao, Y., Leermakers, M., Baeyens, W., Ouddane, B. and Billon, G., 2011. Trace metal behaviour in riverine sediments: Role of organic matter and 320ulphides. *Applied Geochemistry*, Vol.**26**(1), pp.80-90.

Chester, R., 1990. Marine Geochemistry. pp.698, Wiley-Blackwell. London.

Chun, C.O. and Delaney, M.L., 2006. 8. Phosphorus, Barium, Manganese, and Uranium Concentrations and Geochemistry, Nazca Ridge Site 1237 Sediments. *Proceedings of the Ocean Drilling Program*, Vol.**202**, pp.1-19.

Ciglenečki, I., Pichler, S., Prohić, E. and Ćosović, B., 2006. Distribution of redox-sensitive elements in bottom waters, porewaters and sediments of Rogoznica Lake (Croatia) in both oxic and anoxic conditions. *Water, Air and Soil Pollution*, Vol.**6**, pp.173-181.

Clifford, A.C., 1986. African oil - past, present, and future. In: Halbouty, M.T., (ed), Future Petroleum Provinces of the world. *AAPG Memoire*, pp.339-372.

Cocks, L.R.M., 2007. Blowing hot and cold in the Palaeozoic. *Proceeding of the Geologists' Association*, Vol.**118**. pp.225-237.

Cocks, L.R.M., and Torsvik, T.H., 2002. Earth geography from 500-400 million years ago: a faunal and palaeomagnetic review. *Journal of the Geological Society*, Vol.**159**, pp.631-644.

Cocks, L.R.M., and Torsvik, T.H., 2006. European Geography in a global context from the Vendian to the end of the Palaeozoic. In: Gee, D.G. and Stephenson, R.A. (eds). European Lithosphere Dynamics. *Geological Society, London, Memoirs*, Vol.**32**. pp.83-95.

Colmenero, J.R., Fernandez, L.P., Moreno, C., Bahamonde, J.R., Barba, P., Heredia, N. and Gonzalez, F., 2002. Carboniferous. In: Gibbons, W., and Moreno, T., (eds), *The Geology of Spain*. London: Geological Society, pp. 93-116.

Combaz, A., 1967. Leiosphaeridaceae Eisenack, 1954, et Protoleiosphaeridae Timofeev, 1959 — leurs affinités, leur rôle sédimentologique et géologique. *Review of Palaeobotany and Palynology*, Vol.**1**(1-4), pp.309-321.

Combaz, A., 1986. Les "Zones Gamma" du Silurian des region Sahariennes; Contenu organique et conditions de depot. In: Breheret, J.G. (ed), Les couches riches en matierés organiques et leur conditions de depot. *Documents du BRGM*, Vol.**110**, pp.239-258.

Comte, P., 1936. Le Dévonien inférieur du León. *Comptes Rendus de l'Académie des Sciences*, Paris, Vol.**202**, pp.771-773.

Comte, P., 1937. La Serie cambrienne et silurienne du Leon. *Comptes Rendus de l'Academie des Sciences*, Paris, Vol.**202**, pp.337-341.

Comte, P., 1959. Recherches sur les terrains anciens de la Cordillére Cantabrique. *Memorias, IGME*, Vol.**60**, pp. 1-440.

Cox, R. and Lowe, D.R., 1995. A conceptual review of regional-scale controls on the composition of clastic sediment and the co-evolution of continental blocks and their sedimentary cover. *Journal of Sedimentary Research*, Vol.**65**(1).

Cox, R., Lowe, D.R. and Cullers, R.L., 1995. The influence of sediment recycling and basement composition on evolution of mudrock chemistry in the southwestern United States. *Geochimica et Cosmochimica Acta*, Vol.**59**(14), pp.2919-2940.

Craig, J., Sutcliffe, O.E., Lüning, S., Le Heron, D.P. and Whittington, R.J., 2002. Ice Sheets and Hot Rocks: Unravelling the glacial signature in the Late Ordovician reservoirs of North Africa. *Petroleum Exploration Society of Great Britain Newsletter*, (Dec), pp.6-11.

Cramer, B.D. and Saltzman, M.R., 2007. Fluctuations in epeiric sea carbonate production during Silurian positive carbon isotope excursions: A review of proposed paleoceanographic models. *Palaeogeography, Palaeoclimatology, Palaeoecology*, Vol.**245**(1–2), pp.37-45.

Cramer, F. and Diez, M., 1978. Iberian Chitinozoans I. Introduction and Summary of Pre-Devonian Data. *Palinologia, número extraordinaire*, Vol.**1**, pp.149-201.

Cramer, F.H., 1967. Chitinozoans of a composite section of Upper Llandovery to basal Lower Gedinnian sediments in northern León, Spain. *Bulletin de la Societe belge Geologique*, Vol.**75**, pp.69-129.

Crimes, T. and Marcos, A., 1976. Trilobite traces and the age of the lowest part of the Ordovician reference section for NW Spain. *Geological Magazine*, Vol.**113**(04), pp.349-356.

Crimes, T., Legg, I., Marcos, A., Arboleya, M., Crimes, T. and Harper, J., 1977. Late precambrian-low Lower Cambrian trace fossils from Spain. *Trace Fossils*, Vol.**2**, pp.91-138.

Crowley, Q.G., Floyd, P.A., Štědrá, V., Winchester, J.A., Kachlík, V. and Holland, J.G., 2002. The Mariánské-Lázně Complex, NW Bohemian Massif: development and destruction of an early Palaeozoic seaway. *Geological Society, London, Special Publications*, Vol.**201**(1), pp.177-195.

Cullen, J.T., Lane, T.W., Morel, F.M.M, Sherrell, R.M., 1999. Modulation of cadmium uptake in phytoplankton by sea-water CO_2 concentration. *Nature*, Vol.**402**, pp.165-167.

Cullers, R.L. and Podkovyrov, V.N., 2000. Geochemistry of the Mesoproterozoic Lakhanda shales in southeastern Yakutia, Russia: implications for mineralogical and provenance control, and recycling. *Precambrian Research*, Vol.**104**(1–2), pp.77-93.

De Barry Barnett, E. and Wilson, C.L., 1960. Inorganic chemistry: a text-book for advanced students. pp. 599. Wiley. (London).

De la Roche, H. and Govindaraju, K., 1976. Nouveaux étalons géochimiques granite GS. N et feldspath FK. N. *Analusis*, Vol.**4**(8), pp.347-372.

De Vos, W., Tarvainen, T., Salminen, R., Reeder, S., De Vivob,. Demetriadds, A., Pircs., Batista, M.J., Marsina, K., Ottesen, R.T., O'Connor, P.J., Bidovec, M., Lima, A., Siewers, U., Smith, B., Taylor, H., Shaw, R., Salpeteur, I., Gregorauskiene, V., Halamic, J., Slaninka, I., Lax, K., Gravesen, P., Birke, M., Breward, N., Ander, E.L., Jorden, G., Duris, M., Klein, P., Locutura, J., Bellan, A., Pasieczna, A., Lis, J., Mazreku, A., Gilucis, A., Heitzmann, P., Klaver, J. and Petersell, V., 2006. Geochemical Atlas of Europe. Part II – Interpretation of Geochemical Maps, Additional Tables, Figures, Maps, and Related Publications. *Association of Geological Surveys of the European Union and IUGS/IAGC 'Global Geochemical Base Lines' Project*. Vol. **2**, pp. 692 (Espoo, Geological Survey of Finland).

Dean, W., Arthur, M. and Stow, D., 1984. Origin and geochemistry of Cretaceous deep-sea black shales and multicolored claystones, with emphasis on Deep Sea Drilling Project Site 530, southern Angola Basin. *Initial Reports of the Deep Sea Drilling Project*, Vol.**75**, pp.819-844.

Dean, W.E. and Arthur, M.A., 1989. Iron-sulfur-carbon relationships in organic-carbon-rich sequences; I, Cretaceous Western Interior Seaway. *American Journal of Science*, Vol.**289**(6), pp.708-743.

Dean, W.E. and Arthur, M.A., 1998. Geochemical expressions of cyclicity in Cretaceous pelagic limestone sequences: Niobrara Formation, Western Interior Seaway. Stratigraphy and Paleoenvironments of the Cretaceous Western Interior Seaway, USA: SEPM, *Concepts in Sedimentology and Paleontology*, Vol.**6**, pp.227-255.

Deer, W.A., Howie, R.A., and Zussman, J., 1966. An introduction to the rock-forming minerals. pp.528. John Wiley and Sons (New York).

Delaney, M., 1998. Phosphorus accumulation in marine sediments and the oceanic phosphorus cycle. *Global Biogeochemical Cycles*, Vol.**12**(4), pp.563-572.

Dellwig, O., Hinrichs, J., Hild, A. and Brumsack, H., 2000. Changing sedimentation in tidal flat sediments of the southern North Sea from the Holocene to the present: a geochemical approach. *Journal of Sea Research*, Vol.**44**(3–4), pp.195-208.

Demaison, G., 1993. Contributions of geochemistry to exploration strategy. *Applied Petroleum Geochemistry*, Éditions Technip, Paris, pp.489-503.

Demaison, G.J. and Moore, G.T., 1980. Anoxic environments and oil source bed genesis. *AAPG Bulletin*, Vol.**64**(8), pp.1179-1209.

Descourvieres, C., Douglas, G., Leyland, L., Hartog, N. and Prommer, H., 2011. Geochemical reconstruction of the provenance, weathering and deposition of detrital-dominated sediments in the Perth Basin: The Cretaceous Leederville Formation, south-west Australia. *Sedimentary Geology*, Vol.**236**(1–2), pp.62-76.

Dias, R. and Ribeiro, A., 1995. The Ibero-Armorican Arc: A collision effect against an irregular continent? *Tectonophysics*, Vol.**246**(1–3), pp.113-128.

Díaz Rodríguez, L., 1989. Procesos de dolomitización-dedolomitización de la formación Láncara (Cámbrico inferior-medio) en la región de pliegues y mantos de la zona Cantábrica, NW de España. *Estudios Geológicos*, Vol.**45**(1-2), pp.61-70.

Didyk, B.M., Simoneit, B.R.T., Brassell, S.C. and and Eglinton, G., 1978. Organic geochemical indicators of paleoenvironmental conditions of sedimentation. *Nature*, Vol.**272**, pp.216-222.

Diester-Haass, L., Robert, C. and Chamley, H., 1998. Paleoproductivity and climate variations during sapropel deposition in the eastern Mediterranean Sea, *Proceedings of the Ocean Drilling Program. Scientific Results*, 1998, Ocean Drilling Program, pp.227-248.

Díez Fernández, R. and Martínez Catalán, J.R., 2009. 3D Analysis of an Ordovician igneous ensemble: A complex magmatic structure hidden in a polydeformed allochthonous Variscan unit. *Journal of Structural Geology*, Vol.**31**(3), pp.222-236.

Dill, H., 1986. Metallogenesis of early Paleozoic graptolite shales from the Graefenthal Horst (northern Bavaria-Federal Republic of Germany). *Economic Geology*, Vol.**81**(4), pp.889-903.

Djarnia, M.R. and Fekirine, B., 1998. Sedimentological and diagenetic controls on Cambro-Ordovician reservoir quality in the southern Hassi Messaoud area (Saharan Platform, Algeria). *Geological Society, London, Special Publications*, Vol.**132**(1), pp.167-174.

Dodd, J.R. and Crisp, E.L., 1982. Non-linear variation with salinity of Sr/Ca and Mg/Ca ratios in water and aragonitic bivalve shells and implications for paleosalinity studies. *Palaeogeography, Palaeoclimatology, Palaeoecology*. Vol.**38**(1-2). pp.45-56.

Doveton, J.H. and Merriam, D.F., 2004. Borehole petrophysical chemostratigraphy of Pennsylvanian black shales in the Kansas subsurface. *Chemical Geology*, Vol.**206**(3–4), pp.249-258.

Droser, M.L. and Bottjer, D.J., 1986. A semiquantitative field classification of ichnofabric. *Journal of Sedimentary Research*, Vol.**56**(4), pp.558-559.

Drost, K., Linnemann, U., Wemmer, K., Budil, P., Kraft, P., Fatka, O. and Marek, J., 2003. Provenance and early diagenetic processes of the Ordovician Šárka Formation at Praha–Červený vrch Hill (Barrandian, Czech Republic). *Bulletin of Geosciences*, Vol.**78**(2), pp.147-156.

Dymond, J., Suess, E. and Lyle, M., 1992. Barium in deep-sea sediment: A geochemical proxy for paleoproductivity. *Paleoceanography*, Vol.**7**(2), pp.163-181.

Dypvik, H. and Harris, N.B., 2001. Geochemical facies analysis of fine-grained siliciclastics using Th/U, Zr/Rb and (Zr+Rb)/Sr ratios. *Chemical Geology*, Vol.**181**(1–4), pp.131-146.

Dypvik, H., 1984. Geochemical compositions and depositional conditions of Upper Jurassic and Lower Cretaceous Yorkshire clays, England. *Geological Magazine*, Vol.**121**(5), pp.489.

Eichmüller, K. and Seibert, P., 1984. Faziesentwicklung zwischen Tournai und Westfal D im Kantabrischen Gebirge (NW-Spanien). In: Meiburg, P., and Schumann, D., (eds), Das Iberia. *Symposium der Deutschen Geologischen Gesellschaft*. Enke, pp.163-191.

Eickmann, B., Bach, W., Kiel, S., Reitner, J. and Peckmann, J., 2009. Evidence for cryptoendolithic life in Devonian pillow basalts of Variscan orogens, Germany. *Palaeogeography, Palaeoclimatology, Palaeoecology*, Vol.**283**(3–4), pp.120-125.

Einsele, G., 2000. Sedimentary basins: evolution, facies, and sediment budget. pp.792. Springer-Verlag. (Berlin, Heidelberg, New York).

Elbaz-Poulicheet, F., Nagy, A. and Cserny, T., 1997. The distribution of redox sensitive elements (U, As, Sb, V and Mo) along a river-wetland-lake system (Balaton Region, Hungary). *Aquatic Geochemistry*, Vol.**3**(3), pp.267-282.

Elbaz-Poulichet, F., Seidel, J.L., Jézéquel, D., Metzger, E., Prévot, F., Simonucci, C., Sarazin, G., Viollier, E., Etcheber, H., Jouanneau, J., Weber, O. and Radakovitch, O., 2005. Sedimentary record of redox-sensitive elements (U, Mn, Mo) in a transitory anoxic basin (the Thau lagoon, France). *Marine Chemistry*, Vol.**95**(3–4), pp.271-281.

Ellwood, B.B., Brett, C.E., Tomkin, J.H. and Macdonald, W.D., 2012. Visual identification and quantification of Milankovitch climate cycles in outcrop: an example from the Upper Ordovician Kope Formation, Northern Kentucky. *Geological Society, London, Special Publications*, Vol.**373**. pp.341-353.

Erbacher, J., Foreerich, O., Wilson, P.A., Birch, H., Mutterlose, J., 2005. Stable organic carbon isotope stratigraphy across Oceanic Anoxic Event 2 of Demerara Rise, western tropical Atlantic. *Geochemistry, Geophysics, Geosystems*, Vol.**6**(6). Pp:Q06010,DOI:10.1029/2004GC00850.

Erbacher, J., Mosher, D.C., Malone, M.J., Berti, D., Bice, K.L., Bostock, H., Brumsack, H., Danelian, T., Forster, A., Glatz, C., Heidersdorf, F., Henderiks, J., Janecek, T.R., Junium, C., Le Callonnec, L., MacLeod, K., Meyers, P.A., Mutterlose, H.J., Nishi, H., Norris, R.D., Ogg, J.G., O'Regan, A.M., Rea, B., Sexton, P., Sturt, H., Suganuma, Y., Thurow, J.W., Wilson, P.A., Wise, S.W., 2004. Demerara Rise: Equatorial Cretateous and Paleogene Paleoceanographic Transect, Western Atlantic. *Proceedings of the Ocean Drilling Program. Initial Reports*, Vol.**207**, doi:10.2973/odp.proc.ir.207.2004 College Station. Texas.

Evers, H.J., 1967. Geology of the Leonides between the Bernesga and Porma rivers, Cantabrian mountains (NW Spain). *Leidse Geologische Mededelingen*, Vol.**41**, pp.83-151.

Fagel, N., 2007. Clay Minerals, Deep Circulation and Climate. In: Hillaire-Marcel, C., and De Vernal, A., (eds), Proxies in Late Cenozoic Paleoceanography. *Developments in Marine Geology*, p.139-184, Elsevier (Amsterdam).

Fedo, C.M., Nesbitt, H.W. and Young, G.M., 1995. Unraveling the effects of potassium metasomatism in sedimentary rocks and paleosols, with implications for paleoweathering conditions and provenance. *Geology*, Vol.**23**(10), pp.921-924.

Fedo, C.M., Young, G.M., Nesbitt, H.W. and Hanchar, J.M., 1997. Potassic and sodic metasomatism in the Southern Province of the Canadian Shield: Evidence from the Paleoproterozoic Serpent Formation, Huronian Supergroup, Canada. *Precambrian Research*, Vol.**84**(1–2), pp.17-36.

Fekirine, B. and Abdallah, H., 1998. Palaeozoic lithofacies correlatives and sequence stratigraphy of the Saharan Platform, Algeria. *Geological Society, London, Special Publications*, Vol.**132**(1), pp.97-108.

Fello, N., Luning, S., Storch, P. and Redfern, J., 2006. Identification of early Llandovery (Silurian) anoxic palaeo-depressions at the western margin of the Murzuq Basin,(southwest-Libya) based on gamma-ray spectrometry in surface exposures. *Geoarabia-Manama*, Vol.**11**(3), p.101.

Fernández, L.P., 1993. La Formación San Emiliano (Carbonífero de la Zona Cantábrica, no. de España): Estratigrafía y extensión lateral. Algunas implicaciones paleogeográficas. *Trabajos de Geología*, Vol.**19**, pp.97-122.

Fernández-Suárez, J., Dunning, G.R., Jenner, G.A., and Gutiérrez-Alonso, G., 2000. Variscan collisional magmatism and deformation in NW Iberia: constraints from U–Pb geochronology of granitoids. *Journal of the Geological Society*, Vol.**157**(3), pp.565-576.

Ferriday, T. and Montenari, M., 2012. Chemostratigraphical Characterisation of the Lower Silurian Formigoso Formation: A Case Study from Aralla (Cantabrian Mountains, Province Leon, NW Spain), *EGU General Assembly Conference Abstracts*, 2012, pp.290.

Fertl, W. and Chilingar, G., 1988. Total organic carbon content determined from well logs. *SPE Formation Evaluation*, Vol.**3**(2), pp.407-419.

Fertl, W.H., 1979. Gamma ray spectral data assists in complex formation evaluation. The Log Analyst, Vol.**20**(5), pp.3-37.

Fisher, Q.J. and Wignall, P.B., 2001. Palaeoenvironmental controls on the uranium distribution in an Upper Carboniferous black shale (Gastrioceras listeri Marine Band) and associated strata; England. *Chemical Geology*, Vol.**175**(3–4), pp.605-621.

Flanagan, F., 1976. Description and analyses of eight new USGS rock standards. *US Geological Survey, Professional Papers*, Vol.**840**, pp.131-183.

Flanagan, F.J. and Geological Survey (US), 1984. Three USGS mafic rock reference samples, W-2, DNC-1, and BIR-1. *US Government Printing Office*. pp.54.

Floyd, P., Winchester, J. and Park, R., 1989. Geochemistry and tectonic setting of Lewisian clastic metasediments from the early Proterozoic Loch Maree Group of Gairloch, NW Scotland. *Precambrian Research*, Vol.**45**(1), pp.203-214.

Floyd, P.A. and Winchester, J.A., 1978. Identification and discrimination of altered and metamorphosed volcanic rocks using immobile elements. *Chemical Geology*, Vol.**21**(3-4). pp.291-306.

Fombella, M., 1978. Acritarcos de la Formación Oville, edad Cámbrico Medio-Tremadoc, Provincia de León, España. *Palinología*, Vol.**1**, pp.245-261.

Fortey, R.A., and Cocks, L.R.M., 2003. Palaeontological evidence bearing on global Ordovician-Silurian continental reconstructions. *Earth-Science Reviews*, Vol.**61**. pp.245-307.

Francois, R., Honjo, S., Manganini, S.J. and Ravizza, G.E., 1995. Biogenic barium fluxes to the deep sea: Implications for paleoproductivity reconstruction. *Global Biogeochemical Cycles*, Vol.**9**(2), pp.289-303.

Froelich, P., Klinkhammer, G., Bender, M.a.a., Luedtke, N., Heath, G.R., Cullen, D., Dauphin, P., Hammond, D., Hartman, B. and Maynard, V., 1979. Early oxidation of organic matter in pelagic sediments of the eastern equatorial Atlantic: suboxic diagenesis. *Geochimica et Cosmochimica Acta*, Vol.**43**(7), pp.1075-1090.

Galindo, C., Mougin, L., Fakhi, S., Nourreddine, A., Lamghari, A. and Hannache, H., 2007. Distribution of naturally occurring radionuclides (U, Th) in Timahdit black shale (Morocco). *Journal of Environmental Radioactivity*, Vol.**92**(1), pp.41-54.

Garcia-Alcalde, J., Carls, P., Alonso, M.V.P., Lopez, J.S., Soto, F., Truyols-Massoni, M. and Valenzuela-Rios, J.I., 2002a. Devonian. In: Gibbons, W., and Moreno, T., (eds), *The Geology of Spain*. London: Geological Society, pp.67-91.

Garcia-Alcalde, J.L., Carls, P., Pardo Alonso, M.V., Lopez, J.S., Soto, F., Truyols-Massoni, M. and Valenzuela-Rios, J.I., 2002b. 6. Devonian. In: Gibbons, W., and Moreno, T., (eds), *The Geology of Spain*. London: Geological Society, pp.67-91.

Garciá-López, S. and Bastida, F., (eds) 2002. Palaeozoic conodonts from northern Spain. Insituto Geológico y Minero de Españia, *Serie Cuadernos del Museo Geominero*, Vol.**1**, pp.438, Madrid.

García-López, S., Brime, C., Valín, M.L., Sanz-López, J., Bastida, F., Aller, J. and Blanco-Ferrera, S., 2007. Tectonothermal evolution of a foreland fold and thrust belt: the Cantabrian Zone (Iberian Variscan belt, NW Spain). *Terra Nova*, Vol.**19**(6), pp.469-475.

García-Ramos, J., Valenzuela, M. and Suárez De Centi, C., 1989. Estructuras de deformación asociadas a tempestivas: ejemplos en series siliciclásticas y carbonatadas someras del Paleozoico y Jurásico de Asturias. *Trabajos de Geología*, Vol.**18**(18), pp.65-77.

Garnier, V., Giuliani, G., Ohnenstetter, D., Fallick, A.E., Dubessy, J., Banks, D., Vinh, H.Q., Lhomme, T., Maluski, H., Pêcher, A., Bakhsh, K.A., Long, P.V., Trinh, P.T. and Schwarz, D., 2008. Marble-hosted ruby deposits from Central and Southeast Asia: Towards a new genetic model. *Ore Geology Reviews*, Vol.**34**(1–2), pp.169-191.

Gladney, E.S. and Roelandts, I., 1988. 1987 Compilation of Elemental Concentration Data for USGS BHVO - 1, MAG - 1, QLO - 1, RGM - 1, SCo - 1, SDC - 1, SGR - 1 and STM - 1. *Geostandards Newsletter*, Vol.**12**(2), pp.253-362.

González Lastra, J., 1978. Facies salinas en la Caliza de Montaña (Cordillera Cantábrica). *Trabajos de Geología*, Vol.**10**, pp.249-265.

González, R.M.R., 1983. *Palinología de las formaciones del Silúrico Superior-Devónico Inferior de la Cordillera Cantábrica*. Institución Fray Bernardino de Sahagún de la Excelentísima Diputación Provincial de León y del Servicio de Publicaciones de la Universidad de León, pp.231, (Universidad de León).

Gordon, R.M., Coale, K.H. and Johnson, K.S., 1997. Iron distributions in the equatorial Pacific: Implications for new production. *Limnology and Oceanography*, Vol.**42**(3), pp.419-431.

Govindaraju, K., 1980. Report (1980) on Three GIT - IWG Rock Reference Samples: Anorthosite from Greenland, AN - G; Basalte d'Essey - la - Côte, BE - N; Granite de Beauvoir, MA - N. *Geostandards Newsletter*, Vol.**4**(1), pp.49-138.

Govindaraju, K., 1984. Report (1984) on Two GIT - IWG Geochemical Reference Samples: Albite from Italy, AL - I and Iron Formation Sample from Greenland, IF - G. *Geostandards Newsletter*, Vol.**8**(1), pp.63-113.

Govindaraju, K., 1989. 1989 compilation of working values and sample description for 272 geostandards. *Geostandards Newsletter*, Vol.**13**(s1), pp.1-113.

Govindaraju, K., 1994. 1994 compilation of working values and sample description for 383 geostandards. *Geostandards Newsletter*, Vol.**18**(S1), pp.1-158.

Gradstein, F.M., Ogg, J.G., Schmitz, M.D. and Ogg, G.M., (eds). 2012. The Geological Time Scale 2012. Vol. **1** & **2**, pp.1144. Elsevier (Amsterdam).

Gromet, L.P., Haskin, L.A., Korotev, R.L. and Dymek, R.F., 1984. The “North American shale composite”: Its compilation, major and trace element characteristics. *Geochimica et Cosmochimica Acta*, Vol.**48**(12), pp.2469-2482.

Gutiérrez-Alonso, G., Fernández-Suárez, J., Gutiérrez-Marco, J.C., Corfu, F., Murphy, J.B., Suárez, M. 2007. U-Pb depositional age for the upper Barrios Formation (Armorican Quartzite facies) in the Cantabrian Zone of Iberia: Implications for stratigraphic correlation and paleogeography. Linnemann

Unancerd Karftp Zulaufg. Eds. evolution of the Rheic Ocean: from Avalonian-Cadomian active margin to Alleghenian-Variscan collision. *Geological Society of America Special Paper* No.423. pp 287-296.

Gutiérrez-Alonso, G., Fernández-Suárez, J., Jeffries, T.E., Jenner, G.A., Tubrett, M.N., Cox, R. and Jackson, S.E., 2003. Terrane accretion and dispersal in the northern Gondwana margin. An Early Paleozoic analogue of a long-lived active margin. *Tectonophysics*, Vol.**365**(1–4), pp.221-232.

Gutiérrez-Alonso, G., Johnston, S., Weil, A., Pastor-Galán, D., Fernández-Suárez, J., Autin, W.J. and Holbrook, J.M., 2012. Buckling an orogen: The Cantabrian Orocline. *GSA Today*, Vol.**22**(7), pp.4-9.

Gutiérrez-Alonso, G., Murphy, J.B., Fernández-Suárez, J. and Hamilton, M.A., 2008. Rifting along the northern Gondwana margin and the evolution of the Rheic Ocean: A Devonian age for the El Castillo volcanic rocks (Salamanca, Central Iberian Zone). *Tectonophysics*, Vol.**461**(1–4), 157-165.

Gutiérrez-Marco, J., Aramburu, C., Arbizu, M., Méndez-Bedia, I., Rábano, I. and Villas, E., 1996b. Rasgos estratigráficos de la sucesión del Ordovícico Superior en Portilla de Luna (Zona Cantábrica, noroeste de España). *Geogaceta*, Vol.**20**(1), pp.11-14.

Gutierrez-Marco, J., Robardet, M., Rabano, I., Sarmiento, G.N., Lancha, M.A.S.J., Araujo, P.H. and Pidal, A.P.P., 2002. Ordovician. In: Gibbons, W., and Moreno, T., (eds), *The Geology of Spain*. London: Geological Society, pp.31-49.

Gutiérrez-Marco, J.C, and Rábano, I.,(eds), 1998. Proceedings of the Sixth International Graptolite Conference of the GWG (IPA) and the SW Iberia Field Meeting 1998 of the International Subcommission on Silurian Stratigraphy (ICS-IUGS). Insituto Technological Geominero de Epspania, *Temas Geológico-Mineros*, Vol.**23**, pp337. (Madrid).

Gutierrez-Marco, J.C. and Štorch, P., 1998. Graptolite biostratigraphy of the lower Silurian (Llandovery) shelf deposits of the Western Iberian Cordillera, Spain. *Geological Magazine*, Vol.**135**(1), pp.71-92.

Gutiérrez-Marco, J.C., Aramburu, C., Arbizu, M., Mendez-Bedia, I., Rabano, I. and Villas, E., 1996a. Rasgos estratigraficos de la sucesion del Ordovicico Superior en Portilla de Luna (Zona Cantabrica, noroeste de Espana). *Geogaceta*, Vol.**20**(1), pp.11-14.

Gutiérrez-Marco, J.C., Ghienne, J., Bernárdez, E. and Hacar, M.P., 2010. Did the Late Ordovician African ice sheet reach Europe? *Geology*, Vol.**38**(3), pp.279-282.

Hallberg, R.O., 1976. A Geochemical Method for Investigation of Paleoredox Conditions in Sediments. *Ambio Special Report*, Vol.**4**, pp.139-147.

Hammann, W., 1992. The Ordovician trilobites from the Iberian chains in the province of Aragon, NE-Spain. 1. The trilobites of the Cystoid Limestone (Ashgill series). *Beringeria*, Vol.**6**, pp1-219.

Hammer, Ø. and Harper, D.A.T., 2006. Paleontological Data Analysis. pp.351. Wiley-Blackwell.

Hammer, Ø., Harper, D.A.T. and Ryan, P.D., 2001. PAST: paleontological statistics software package for education and data analysis. *Palaeontologia Electronica*, Vol.**4**(1), pp. 1-9.

Handoh, I.C., Bigg, G.R., and Jones, E.J.W., 2003. Evolution of upwelling in the Atlantic Ocean basin. *Palaeogeography, Palaeoclimatology, Palaeoecology*, Vol.**202**(1-2), pp.31-58.

Hans Wedepohl, K., 1995. The composition of the continental crust. *Geochimica et Cosmochimica Acta*, Vol.**59**(7), pp.1217-1232.

Harland, W.B., 1972. The Ordovician Ice Age. *Geological Magazine*, Vol.**109**(5), pp.451-456.

Harnois, L., 1988. The CIW index: A new chemical index of weathering. *Sedimentary Geology*, Vol.**55**(3–4), pp.319-322.

Harris, N.B., Freeman, K.H., Pancost, R.D., White, T.S. and Mitchell, G.D., 2004. The character and origin of lacustrine source rocks in the Lower Cretaceous synrift section, Congo Basin, west Africa. *AAPG Bulletin*, Vol.**88**(8), pp.1163-1184.

Harris, P.J., and Knorr, P.O., 2009. What does the 'lilliput effect' mean?. *Palaeogeography, Palaeoclimatology, Palaeoecology*, Vol.**284**(1-2), pp.4-10.

Hatch, J. and Leventhal, J., 1992. Relationship between inferred redox potential of the depositional environment and geochemistry of the Upper Pennsylvanian (Missourian) Stark Shale Member of the Dennis Limestone, Wabaunsee County, Kansas, USA. *Chemical Geology*, Vol.**99**(1), pp.65-82.

Heckel, P.H., 1986. Sea-level curve for Pennsylvanian eustatic marine transgressive-regressive depositional cycles along midcontinent outcrop belt, North America. *Geology*, Vol.**14**(4), pp.330-334.

Hedges, J.I. and Keil, R.G., 1995. Sedimentary organic matter preservation: an assessment and speculative synthesis. *Marine Chemistry*, Vol.**49**(2–3), pp.81-115.

Heinz, W., Loeschke, J., Vavra, J., 1985. Phreatomagmatic volcanism during the Ordovician of the Cantabrian Mountains (NW Spain). *Geologische Rundschau*, Vol.**74**(3), pp.623-639.

Herron, M.M., 1988. Geochemical classification of terrigenous sands and shales from core or log data. *Journal of Sedimentary Research*, Vol.**58**(5), pp.820-829.

Herut, B. and Sandler, A., 2006. Normalization methods for pollutants in marine sediments: review and recommendations for the Mediterranean. *Israel Oceanographic & Limnological Research and Geological Survey of Israel IOLR Report* H, pp. 1-18.

Hetzel, A., Brumsack, H., Schnetger, B. and Böttcher, M.E., 2006. Chapter 8. Inorganic geochemical characterization of lithologic units recovered during ODP Leg 207 (Demerara Rise). In: Mosher, D.C., Erbacher, J. and Malone, M.J. (eds), *Proceeding of the Ocean Drilling Program, Scientific Results*, Vol.**207**, pp.1-37.

Hetzel, A., März, C., Vogt, C. and Brumsack, H., 2011. Geochemical environment of Cenomanian - Turonian black shale deposition at Wunstorf (northern Germany). *Cretaceous Research*, Vol.**32**(4), pp.480-494.

Higgins, A.C., 1971. Conodont biostratigraphy of the Late Devonian-Early Carboniferous rocks of the south central Cantabrian Cordillera. *Trabajos de Geologia*. Vol.**3**, pp.179-192.

Hild, E., Brumsack,H.J., 1998. Major and minor element geochemistry of Lower Aptian sediments from the NW German Basin (core Hohenegglesen KB 40). *Cretaceous Research*, Vol.**19**, pp.615-633.

Hillaire-Marcel, C. and De Vernal, A., 2007. Methods in Late Cenozoic Paleoceanography: Introduction. In: Hillaire-Marcel, C., and De Vernal, A., (eds), *Proxies in Late Cenozoic Paleoceanography*. pp.1-15. Elsevier Science.

Hillebrand, W.F., 1907. The Vanadium Sulphide, Patronite, and its mineral associates from Minasragra, Peru. *Journal of the American Chemical Society*, Vol.**29**(7), pp.1019-1029.

Hofmann, M. H. and Keller, M., 2006. Sequence stratigraphy and carbonate platform organisation of the Devonian Santa Lucia Formation, Cantabrian Mountains, N-W Spain. *Facies*, Vol.**52**, pp.149-167.

House, M.R., 1995. Orbital forcing timescales: an introduction. *Geological Society, London, Special Publications*, Vol.**85**(1), pp.1-18.

Huntsman-Mapila, P., Ringrose, S., Mackay, A.W., Downey, W.S., Modisi, M., Coetzee, S.H., Tiercelin, J.-., Kampunzu, A.B. and Vanderpost, C., 2006. Use of the geochemical and biological sedimentary record in establishing palaeo-environments and climate change in the Lake Ngami basin, NW Botswana. *Quaternary International*, Vol.**148**(1), pp.51-64.

Imbrie, J. and Imbrie, J.Z., 1980. Modeling the climatic response to orbital variations. *Science*, Vol.**207**(4434), pp.943-953.

Instituto Tecnológico GeoMinero de España, 2002, Mapa Geologico de España. Escala 1:50000, No.10,11,12,13,14,15, 25, 26, 27, 28, 29, 30, 31, 32, 49, 50, 51, 52, 53, 54, 55, 56, 74, 75, 76, 77, 78, 79, 80, 81, 99, 100, 101, 102, 103, 104, 105. Instituto Geológico y Minero de España. Ministerio de Economía y Competitividad (Madrid).

Janoušek, V., Farrow, C.M. and Erban, V., 2006. Interpretation of whole-rock geochemical data in igneous geochemistry: introducing Geochemical Data Toolkit (GCDkit). *Journal of Petrology*, Vol.**47**(6), pp.1255-1259.

Janoušek, V., Farrow, C.M., Erban, V. and Trubač, J., 2011. Brand new Geochemical Data Toolkit (GCDkit 3.0) - is it worth upgrading and browsing documentation? (Yes!). *Geologické výzkumy na Moravě a ve Slezsku*, Vol.**18**, pp.26-30.

Jeppsson, L., 1990. An oceanic model for lithological and faunal changes tested on the Silurian record. *Journal of the Geological Society*, Vol.**147**(4), pp.663-674.

Jochum, K.P., Wang, X., Nohl, U., Schmidt, S., Schwager, B., Stoll, B., Yang, Q., and Weis, U., 2011. Geostandards and Geoanalytical research-Bibliographic review 2010. *Geostandards and Geoanalytical Research,* Vol.**35**. pp.485-488.

Johnson, M.E., 2006. Relationship of Silurian sea-level fluctuations to oceanic episodes and events. *GFF*, Vol.**128**(2), pp.115-121.

Johnson, M.E., 2010. Tracking Silurian eustasy: Alignment of empirical evidence or pursuit of deductive reasoning? *Palaeogeography, Palaeoclimatology, Palaeoecology*, Vol.**296**(3), pp.276-284.

Johnsson, M.J., and Basu, A., 1993. Processes Controlling the Composition of Clastic Sediments. *Geological Society of America* Special Paper 284, pp.352., The Geological Society of America, Boulder (Colorado).

Jones, B. and Manning, D.A.C., 1994. Comparison of geochemical indices used for the interpretation of paleoredox conditions in ancient mudstones. *Chemical Geology*, Vol.**111**, pp.111-129.

Jorissen, F.J., Fontanier, C. and Thomas, E., 2007. Paleoceanographical Proxies Based on Deep-Sea Benthic Foraminiferal Assemblage Characteristics. In: Hillarie-Marcel, C., and De Vernal, A, (eds), *Proxies in Late Cenozoic Paleoceanography*, pp.263-325. Elsevier Science.

Julivert, M. and Marcos, A., 1973. Superimposed folding under flexural conditions in the Cantabrian Zone (Hercynian Cordillera, northwest Spain). *American Journal of Science*, Vol.**273**(5), pp.353-375.

Julivert, M., 1971. Decollement tectonics in the Hercynian Cordillera of Northwest Spain. *American Journal of Science*, Vol.**270**(1), pp.1-29.

Julivert, M., 1978. Hercynian orogeny and Carboniferous paleogeography in Northwestern Spain: A model of deformation-sedimentation relationships. *Zeitschrift der Deutschen Geologischen Gesellschaft*, Vol.**129**, pp.565-592.

Julivert, M., Fontboté, J., Ribeiro, A. and Conde, L., 1972. Mapa Tectonico de la Penınsula Iberica Y Baleares, Escala 1⁄1 000 000. Instituto Geológico y Minero de Espana, Madrid.

Kampunzu, A.B., Cailteux, J.L.H., Moine, B. and Loris, H.N.B.T., 2005. Geochemical characterisation, provenance, source and depositional environment of 'Roches Argilo-Talqueuses' (RAT) and Mines Subgroups sedimentary rocks in the Neoproterozoic Katangan Belt (Congo): Lithostratigraphic implications. *Journal of African Earth Sciences*, Vol.**42**(1–5), pp.119-133.

Kato, Y., Nakao, K. and Isozaki, Y., 2002. Geochemistry of Late Permian to Early Triassic pelagic cherts from southwest Japan: implications for an oceanic redox change. *Chemical Geology*, Vol.**182**(1), pp.15-34.

Kegel, W., 1929. Das Gotlandium in den kantabrischen Ketten Nordspaniens. *Zeitschrift der Deutschen Geologischen Gesellschaft*, Vol.**81**, pp.35-62.

Keller, M. 1997. Evolution and sequence stratigraphy of an Early Devonian carbonate ramp, Cantabrian Mountains, northern Spain. *Journal of Sedimentary Research*, Vol.**67**(4), pp.638-652.

Keller, M., Bahlburg, H. and Reuther, C., 2008. The transition from passive to active margin sedimentation in the Cantabrian Mountains, Northern Spain: Devonian or Carboniferous? *Tectonophysics*, Vol.**461**(1–4), pp.414-427.

Ketris, M.P. and Yudovich, Y.E., 2009. Estimations of Clarkes for Carbonaceous biolithes: World averages for trace element contents in black shales and coals. *International Journal of Coal Geology*, Vol.**78**(2), pp.135-148.

Kiipli, E., Kiipli, T. and Kallaste, T., 2004. Bioproductivity rise in the East Baltic epicontinental sea in the Aeronian (Early Silurian). *Palaeogeography, Palaeoclimatology, Palaeoecology*, Vol.**205**(3–4), pp.255-272.

Kiipli, E., Kiipli, T., Kallaste, T. and Siir, S., 2012. Al2O3/TiO2 ratio of the clay fraction of Late Ordovician–Silurian carbonate rocks as an indicator of paleoclimate of the Fennoscandian Shield. *Palaeogeography, Palaeoclimatology, Palaeoecology*, Vol.**365**, p.312-320.

Killops, S.D. and Killops, V.J., 2009. An introduction to organic geochemistry. Wiley-Blackwell.

Kimura, H. and Watanabe, Y., 2001. Oceanic anoxia at the Precambrian-Cambrian boundary. *Geology*, Vol.**29**(11), pp.995-998.

King, C., 2004. The Black Sea: A History. pp.296. Oxford University Press.

Konhauser, K.O. and Urrutia, M.M., 1999. Bacterial clay authigenesis: a common biogeochemical process. *Chemical Geology*, Vol.**161**(4), pp.399-413.

Konhauser, K.O., 1998. Diversity of bacterial iron mineralization. *Earth-Science Reviews*, Vol.**43**(3-4), pp.91-121.

Krauskopf, K.B. and Burg, D.K. 1995. Introduction to Geochemistry. 3rd Ed. pp. 647, McGraw-Hill Inc.

Kupers, M.M., Pancost, R.D., Nejenhuis, I.A., and Damsté, J.S.S., 2002. Enhanced productivity led to increased organic carbon burial in the euxinic North Atlantic basin during the late Cenomanian oceanic anoxic event. *Paleoceanography*. Vol.**17**(4), pp.3-13.

Kuroda, J., Ohkouchi, N., Ishii, T., Tokuyama, H. and Taira, A., 2005. Lamina-scale analysis of sedimentary components in Cretaceous black shales by chemical compositional mapping: Implications for paleoenvironmental changes during the Oceanic Anoxic Events. *Geochimica et Cosmochimica Acta*, Vol.**69**(6), pp.1479-1494.

La Roche, H., a. et Govindaraju K.(1968). Rapport sur deux roches, Diorite DR-N et Serpentine UB-N, proposées comme étalons analytiques par un groupe de laboratoires français. Bulletin de la Société française de Céramique, Vol.**85**, pp.35-50.

La Roche, H., b. et Govindaraju K.(1971).—Rapport sur un minerai d'aluminium Bauxite BX-N et sur un réfractaire silico-alumineux Disthène DT-N proposés comme étalons analytiques. Bulletin de la Société française de Céramique, Vol.**90**, pp.3-19.

Lane, T.W., Saito, M.A., George, G.N., Pickering, I.J., Prince, R.C., Morel, F.M.M., 2005. Biochemistry: A Cadmium Enzyme From a Marine Diatom. *Nature*, Vol.**435**. p.42.

LaPorte, D.F., Holnden, C., Patterson, W.P., Loxton, J.D., Melchin, M.J., Mitchell, C.E., Finney, S.C., and Sheets, H.D., 2009. Local and global perspectives on carbon and nitrogen cycling during the Hirnantian glaciation. *Paleogeography, Paleoclimatology, Paleoecology*, Vol.**276**, pp.182-195.

Lavergren, U., 2005. Black shale as a metal contamination source. *ESS Bulletin*, Vol.**3**(1), pp.18-31.

Le Heron, D., Sutcliffe, O., Bourgig, K., Craig, J., Visentin, C. and Whittington, R., 2004. Sedimentary architecture of Upper Ordovician tunnel valleys, Gargaf Arch, Libya: Implications for the genesis of a hydrocarbon reservoir. *Geoarabia-Manama*, Vol.**9**, pp.137-160.

Le Heron, D., Sutcliffe, O., Whittington, R. and Craig, J., 2005. The origins of glacially related soft-sediment deformation structures in Upper Ordovician glaciogenic rocks: implication for ice-sheet dynamics. *Palaeogeography, Palaeoclimatology, Palaeoecology*, Vol.**218**(1), pp.75-103.

Le Heron, D.P. and Craig, J., 2008. First-order reconstructions of a Late Ordovician Saharan ice sheet. *Journal of the Geological Society*, London, Vol.**165**(1), pp.19-29.

Le Heron, D.P., Craig, J. and Etienne, J.L., 2009. Ancient glaciations and hydrocarbon accumulations in North Africa and the Middle East. *Earth-Science Reviews*, Vol.**93**(3–4), pp.47-76.

Le Heron, D.P., Ghienne, J., El Houicha, M., Khoukhi, Y. and Rubino, J., 2007. Maximum extent of ice sheets in Morocco during the Late Ordovician glaciation. *Palaeogeography, Palaeoclimatology, Palaeoecology*, Vol.**245**(1–2), pp.200-226.

Le Heron, D.P., Khoukhi, Y., Paris, F., Ghienne, J. and Le Herissé, A., 2008. Black shale, grey shale, fossils and glaciers: Anatomy of the Upper Ordovician–Silurian succession in the Tazzeka Massif of eastern Morocco. *Gondwana Research*, Vol.**14**(3), pp.483-496.

Le Heron, D.P., Meinhold, G., Page, A. and Whitham, A., 2013. Did lingering ice sheets moderate anoxia in the Early Palaeozoic of Libya? *Journal of the Geological Society*, Vol.**170**(2), pp.327-339.

Lee, Y.I., 2009. Geochemistry of shales of the Upper Cretaceous Hayang Group, SE Korea: Implications for provenance and source weathering at an active continental margin. *Sedimentary Geology*, Vol.**215**(1–4), pp.1-12.

Leton, T.M., Crouch, M., Johnson, M., Pires, N. and Dolan, L., 2012. First plants cooled the Ordovician*. Nature Geoscience*, Vol.**5**, pp.86-89.

Lev, S.M. and Filer, J.K., 2004. Assessing the impact of black shale processes on REE and the U–Pb isotope system in the southern Appalachian Basin. *Chemical Geology*, Vol.**206**(3–4), pp.393-406.

Lewis, S.E., Henderson, R.A., Dickens, G.R., Shields, G.A. and Coxhell, S., 2010. The geochemistry of primary and weathered oil shale and coquina across the Julia Creek vanadium deposit (Queensland, Australia). *Mineralium Deposita*, Vol.**45**(6), pp.599-620.

Limburg, K.E., 1995. Otolith strontium traces environmental history of subyearling American shad Alosa sapidissima. *Marine Ecology Progress Series*, Vol.**119**, pp.25-35.

Linan, E., Gozalo, R., Palacios, T., Vintaned, J.A.G., Ugidos, J.M. and Mayoral, E., 2002. Cambrian. In: Gibbons, W., and Moreno, T. (eds), *The Geology of Spain*. London: Geological Society, pp.17-29.

Liñán, E., Perejón, A. and Sdzuy, K., 1993. The Lower-Middle Cambrian stages and stratotypes from the Iberian Peninsula: a revision. *Geological Magazine*, Vol.**130**, pp.817-833.

Linnemann, U., Pereira, F., Jeffries, T.E., Drost, K. and Gerdes, A., 2008. The Cadomian Orogeny and the opening of the Rheic Ocean: The diacrony of geotectonic processes constrained by LA-ICP-MS U–Pb zircon dating (Ossa-Morena and Saxo-Thuringian Zones, Iberian and Bohemian Massifs). *Tectonophysics*, Vol.**461**(1–4), pp.21-43.

Lipinski, M., Warning, B. and Brumsack, H., 2003. Trace metal signatures of Jurassic/Cretaceous black shales from the Norwegian Shelf and the Barents Sea. *Palaeogeography, Palaeoclimatology, Palaeoecology*, Vol.**190**(0), pp.459-475.

López de Luchi, M., Cerredo, M., Siegesmund, S., Steenken, A. and Wemmer, K., 2003. Provenance and tectonic setting of the protoliths of the metamorphic complexes of Sierra de San Luis. *Revista de la Asociación Geológia Argentina*, Vol.**58**, pp.525-540.

Lotze, F., 1945. Zur Gliederung der Varisziden der Iberischen Meseta. *Geotektonische Forschungen*, Vol.**6**, pp.78-92.

Lotze, F., 1956. Das Präkambrium Spaniens. *Neues Jb. Geol. Paläont. Mh.*, Vol.**8**, pp.373-380.

Lotze, F., 1961. Das Kambrium Spaniens. Teil I: Staratigraphie. *Akademie der Wissenschaften und der Literatur, Abhandlungen der mathematisch-naturwissenschaftlichen Klasse*, pp.1-216.

Loydell, D., Butcher, A., Frýda, J., Lüning, S. and Fowler, M., 2009. Lower Silurian “hot shales” in Jordan: a new depositional model. *Journal of Petroleum Geology*, Vol.**32**(3), pp.261-270.

Loydell, D.K., 1998. Early Silurian sea-level changes. *Geological Magazine*, Vol.**135**(4), pp.447-471.

Lüning, S. and Kolonic, S., 2003. Uranium spectral gamma-ray response as a proxy for organic richness in black shales: applicability and limitations. *Journal of Petroleum Geology*, pp.153-174.

Lüning, S. and Kolonic, S., 2006. Uranium as a proxy for organic richness in black shales: applicability and limitations. *Journal of Petroleum Geology*, Vol.**26**(2), pp.153-174.

Lüning, S., Archer, R., Craig, J. and Loydell, D., 2003a. The Lower Silurian ‘Hot Shales’ and ‘Double Hot Shales’ in North Africa and Arabia. The geology of northwest Libya (Ghadamis, Jifarah, Tarabulus and Sabratah basins): Tripoli, *Earth Science Society of Libya*, Vol.**3**, pp.91-105.

Lüning, S., Craig, J., Loydell, D.K., Štorch, P. and Fitches, B., 2000. Lower Silurian `hot shales' in North Africa and Arabia: regional distribution and depositional model. *Earth-Science Reviews*, Vol.**49**(1–4), pp.121-200.

Lüning, S., Kolonic, S., Loydell, D.K. and Craig, J., 2003b. Reconstruction of the original organic richness in weathered Silurian shale outcrops (Murzuq and Kufra basins, southern Libya). *GeoArabia*, Vol.**8**(3). pp.299-308.

Lüning, S., Loydell, D.K., Štorch, P., Shahin, Y. and Craig, J., 2006. Origin, sequence stratigraphy and depositional environment of an Upper Ordovician (Hirnantian) deglacial black shale, Jordan—Discussion. *Palaeogeography, Palaeoclimatology, Palaeoecology*, Vol.**230**(3-4), pp.352-355.

Lüning, S., Shahin, Y., Loydell, D.K., Al-Rabi, H.T., Masri, A., Tarawneh, B. and Kolonic, S., 2005. Anatomy of a world-class source rock: Distribution and depositional model of Silurian organic rich shales in Jordan and implications for hydrocarbon potential. *AAPG Bulletin*, Vol.**89**(10), pp.1397-1427.

Lyons, T.W., Werne, J.P., Hollander, D.J. and Murray, R.W., 2003. Contrasting sulfur geochemistry and Fe/Al and Mo/Al ratios across the last oxic-to-anoxic transition in the Cariaco Basin, Venezuela. *Chemical Geology*, Vol.**195**(1–4), pp.131-157.

Maas, K., 1974. The geology of Liebana, Cantabrian Mountains, Spain: deposition and deformation in a flysch area. *Leidse Geologische Mededelingen*, Vol.**49**. pp.379-465.

Mac Niocaill, C.M., Van der Pluijm, B.A., and Van der Voo, R., 1997. Ordovician Palegeography and the evolution of the Iapetus Ocean. *Geology*, Vol.**25**(2), pp.159-162.

Mackenzie, F.T., 2005. Sediments, Diagenesis, and Sedimentary Rocks. *Treatise on Geochemistry,* Vol.**7**, pp.425. Elsevier-Pergamon. (Oxford).

Małkowski, K. and Racki, G., 2009. A global biogeochemical perturbation across the Silurian-Devonian boundary: ocean-continent-biosphere feedbacks. *Paleogeography, Paleoclimatology, Paleoecology,* Vol.**276**(1-4), pp.244-254.

Marcos, A. and Pulgar, J.A., 1982. An approach to the tectonostratigraphic evolution of the Cantabrian foreland thrust and fold belt, Hercynian Cordillera of NW Spain. *Neues Jahrbuch Geol. Paläont. Abhandlungen*, Vol.**163**, pp.256-260.

Marcos, A., 1973. Las series del Paleozoico Inferior y la estructura herciniana del Occidente de Asturias (NW. de España). *Trabajos de Geología*, Vol.**6**(6), pp.3-113.

Marshall, J.E.A., 2000. Palynofacies and orbital cyclicity: an example from the Silurian of Saudi Arabia. In: Al-Hajri, S., and Owens, B., (eds), Stratigraphic palynology of the Palaeozoic of Saudi Arabia. Bahrain, *Gulf PetroLink*, pp.216-231.

Martens, C.S., Haddad, R.I. and Chanton, J.P., 1992. Organic matter accumulation, remineralization, and burial in an anoxic coastal sediment. In: Whelan, J. and Farrington, J.W. (eds), *Organic Matter - Productivity, Accumulation, and Preservation in Recent and Ancient Sediments*, pp.82-98, Columbia University Press.

Martínez Catalán, J.R., Aller, J., Alonso, J.L. and Bastida, F., 2009a. The Iberian Variscan Orogen. In: Cortes, A.G., Villar, J.A., Suarez-Valgrande, J.P., and Gonzalez, C.L.S., (eds), *Spanish geological frameworks and geosites: an approach to Spanish geological heritage of international relevance*. pp.13-30, Instituto Geológico y Minero de España (Madrid).

Martínez Catalán, J.R., Arenas, R., Abati, J., Martínez, S.S., García, F.D., Suárez, J.F., Cuadra, P.G., Castiñeiras, P., Barreiro, J.G., Montes, A.D., Clavijo, E.G., Pascual, F.J.R., Andonaegui, P., Jeffries, T.E., Alcock, J.E., Fernández, R.D. and Carmona, A.L., 2009b. A rootless suture and the loss of the roots of a mountain chain: The Variscan belt of NW Iberia. *Comptes Rendus Geoscience*, Vol.**341**(2–3), pp.114-126.

Martínez García, E., 1981. El Paleozoico de la Zona Cantábrica Orienta (Noroeste de España). *Trabajos de Geología*, Vol.**11**(11), pp.94-129.

Marynowski, L., Zatoń, M., Rakociński, M., Filipiak, P., Kurkiewicz, S. and Pearce, T.J., 2012. Deciphering the upper Famennian Hangenberg Black Shale depositional environments based on multi-proxy record. *Palaeogeography, Palaeoclimatology, Palaeoecology*, Vol.**346**, pp.66-86.

März, C., Beckmann, B., Franke, C., Vogt, C., Wagner, T. and Kasten, S., 2009. Geochemical environment of the Coniacian–Santonian western tropical Atlantic at Demerara Rise. *Palaeogeography, Palaeoclimatology, Palaeoecology*, Vol.**273**(3–4), pp.286-301.

März, C., Poulton, S.W., Beckmann, B., Küster, K., Wagner, T., Kasten, S., 2008. Redox sensitivity of P cycling during marine black shale formation: dynamics of sulphidic and anoxic, non-sulphidic bottom waters. *Geochimica et Cosmochimica Acta*, Vol.**72**, pp.3703-3717.

Maurer, F., Martini, R., Rettori, R., Hillgärtner, H. and Cirilli, S., 2009. The geology of Khuff outcrop analogues in the Musandam Peninsula, United Arab Emirates and Oman. *GeoArabia*, Vol.**14**(3), pp.125-158.

McLennan, S.M., 1993. Weathering and global denudation. *The Journal of Geology*, Vol. 101, pp.295-303.

McLennan, S. and Taylor, S., 1991. Sedimentary rocks and crustal evolution: tectonic setting and secular trends. *The Journal of Geology*, Vol. **99**(1), pp.1-21.

McManus, J., Berelson, W.M., Klinkhammer, G.P., Johnson, K.S., Coale, K.H., Anderson, R.F., Kumar, N., Burdige, D.J., Hammond, D.E., Brumsack, H.J., McCorkle, D.C. and Rushdi, A., 1998. Geochemistry of barium in marine sediments: implications for its use as a paleoproxy. *Geochimica et Cosmochimica Acta*, Vol.**62**(21–22), pp.3453-3473.

Meyers, P.A., 1997. Organic geochemical proxies of paleoceanographic, paleolimnologic, and paleoclimatic processes. *Organic Geochemistry*, Vol.**27**(5–6), pp.213-250.

Meyers, P.A., 2006. Paleoceanographic and paleoclimatic similarities between Mediterranean sapropels and Cretaceous black shales. *Palaeogeography, Palaeoclimatology, Palaeoecology*, Vol.**235**(1–3), pp.305-320.

Meyers, S.R., Sageman, B.B. and Lyons, T.W., 2005. Organic carbon burial rate and the molybdenum proxy: Theoretical framework and application to Cenomanian-Turonian oceanic anoxic event 2. *Paleoceanography*, Vol.**20**(2), PA2002.

Milankovitch, M., 1941. Kanon der Erdbestrahlung und seine Anwendung auf das Eiszeitenproblem. *Königlich Serbische Akademie Beograd*, Edition Special, Vol.**132**, pp. 1-33.

Mohanti, M. 1972. The Portilla Formation (Middle Devonian) of the Alba syncline, Cantabrian Mountains, Province Leon, Northwestern Spain: Carbonate facies and rhynchonellid palaeontology. *Leidse Geologische Mededelingen*, Vol.**48**, pp.1-70.

Mongelli, G., Critelli, S., Perri, F., Sonnino, M. and Perrone, V., 2006. Sedimentary recycling, provenance and paleoweathering from chemistry and mineralogy of Mesozoic continental redbed mudrocks, Peloritani mountains, southern Italy. *Geochemical Journal*, Vol.**40**(2), pp.197-209.

Monod, O., Kozlu, H., Ghienne, J.F., Dean, W.T., Günay, Y., Hérissé, A.L., Paris, F. and Robardet, M., 2003. Late Ordovician glaciation in southern Turkey. *Terra Nova*, Vol.**15**(4), pp.249-257.

Moore, G.T., Hayashida, D.N. and Ross, C.A., 1993. Late Early Silurian (Wenlockian) general circulation model-generated upwelling, graptolitic black shales, and organic-rich source rocks—An accident of plate tectonics? *Geology*, Vol.**21**(1), pp.17-20.

Moosavirad, S.M., Janardhana, M.R., Sethumadhav, M.S., Moghadam, M.R. and Shankara, M., 2011. Geochemistry of lower Jurassic shales of the Shemshak Formation, Kerman Province, Central Iran: Provenance, source weathering and tectonic setting. *Chemie der Erde - Geochemistry*, Vol.**71**(3), pp.279-288.

Müller, P.J. and Suess, E., 1979. Productivity, sedimentation rate, and sedimentary organic matter in the oceans—I. Organic carbon preservation. *Deep Sea Research Part A.Oceanographic Research Papers*, Vol.**26**(12), pp.1347-1362.

Munnecke, A., Calner, M., Harper, D.A.T. and Servais, T., 2010. Ordovician and Silurian sea–water chemistry, sea level, and climate: A synopsis. *Palaeogeography, Palaeoclimatology, Palaeoecology*, Vol.**296**(3–4), pp.389-413.

Murphy, A.E., Sageman, B.B., Hollander, D.J., Lyons, T.W. and Brett, C.E., 2000. Black shale deposition and faunal overturn in the Devonian Appalachian basin: Clastic starvation, seasonal water-column mixing, and efficient biolimiting nutrient recycling. *Paleoceanography*, Vol.**15**(3), pp.280-291.

Murray, R., Leinen, M. and Isern, A., 1993. Biogenic flux of Al to sediment in the central equatorial Pacific Ocean: Evidence for increased productivity during glacial periods. *Paleoceanography*, Vol.**8**(5), pp.651-670.

Murray, R.W. and Leinen, M., 1996. Scavenged excess aluminum and its relationship to bulk titanium in biogenic sediment from the central equatorial Pacific Ocean. *Geochimica et Cosmochimica Acta*, Vol.**60**(20), pp.3869-3878.

Nagarajan, R., Madhavaraju, J., Nagendra, R., Armstrong-Altrin, J.S. and Moutte, J., 2007. Geochemistry of Neoproterozoic shales of the Rabanpalli Formation, Bhima Basin, Northern Karnataka, southern India: implications for provenance and paleoredox conditions. *Revista Mexicana de Ciencias Geológicas*, Vol.**24**(2), pp.150-160.

Nance, R.D., Gutiérrez-Alonso, G., Keppie, J.D., Linnemann, U., Murphy, J.B., Quesada, C., Strachan, R.A. and Woodcock, N.H., 2010. Evolution of the Rheic Ocean. *Gondwana Research*, Vol.**17**(2–3), pp.194-222.

Nath, B.N., Kunzendorf, H. and Plüger, W., 2000. Influence of provenance, weathering, and sedimentary processes on the elemental ratios of the fine-grained fraction of the bedload sediments from the Vembanad Lake and the adjoining continental shelf, southwest coast of India. *Journal of Sedimentary Research*, Vol.**70**(5), pp.1081-1094.

Nesbitt, H. and Young, G., 1982. Early Proterozoic climates and plate motions inferred from major element chemistry of lutites. *Nature*, Vol.**299**(5885), pp.715-717.

Nielsen, A.T., 2004. Ordovician Sea Level Changes: A Baltoscandian Perspective. In: Webby, B.D., Paris, F., Droser, M.L., and Percival, I.G. (eds). *The Great Ordovician Biodiversification Event*, pp.84-93, Columbia University Press (New York).

Nijenhuis, I.A., Bosch, H.-., Sinninghe Damsté, J.S., Brumsack, H.-. and De Lange, G.J., 1999. Organic matter and trace element rich sapropels and black shales: a geochemical comparison. *Earth and Planetary Science Letters*, Vol.**169**(3–4), pp.277-290.

Nyakairu, G.W. and Koeberl, C., 2001. Mineralogical and chemical composition and distribution of rare earth elements in clay-rich sediments from central Uganda. *Geochemical Journal*, Vol.**35**(1), pp.13-28.

Okunlola, O., Adeigbe, O. and Oluwatoke, O., 2009. Compositional and Petrogenetic features of schistose rocks of Ibadan area, Southwestern Nigeria. *Earth Sciences Research Journal*, Vol.**13**(2), pp.119-133.

Osae, S., Asiedu, D.K., Banoeng-Yakubo, B., Koeberl, C. and Dampare, S.B., 2006. Provenance and tectonic setting of Late Proterozoic Buem sandstones of southeastern Ghana: Evidence from geochemistry and detrital modes. *Journal of African Earth Sciences*, Vol.**44**(1), pp.85-96.

Oschmann, W., 2000. Microbes and Black Shales. In: Riding, R., and Awramik, S.M., (eds), *Microbial Sediments*. pp.137-148, Springer (Berlin).

Page, A., Zalasiewicz, J.A., Williams, M. and Popov, L.E., 2007. Were transgressive black shales a negative feedback modulating glacioeustasy in the Early Palaeozoic Icehouse? In: Williams, M., Haywood, A.M., Gregory, F.J. and Schmidt, D.N. (eds*), Deep-Time Perspectives on Climate Change: Marrying the Signal from Computer Models and Biological Proxies*. The Micropalaeontological Society, Special Publications, pp. 123-156.

Parés, J.M. and Van Der Voo, R., 1992. Paleozoic paleomagnetism of Almaden, Spain - A cautionary note. *Journal of Geophysical Research*, Vol.**97**, pp.9353-9356.

Paris, F. and Robardet, M., 1990. Early Palaeozoic palaeobiogeography of the Variscan regions. *Tectonophysics*, Vol.**177**(1–3), pp.193-213.

Paris, F., Elaouad-Debbaj, Z., Jaglin, J., Massa, D. and Oulebsir, L., 1995. Chitinozoans and Late Ordovician glacial events on Gondwana. In: Cooper, J.C., Droser, M.L., Finney, S. (eds). *Ordovician Oddessey: Short papers for the 7th ISOS, Las Vegas*, Society for Sedimentary Geology, Pacific Section, Vol.**77**. pp171-176.

Paris, F., Thusu, B., Rasul, S., Meinhold, G., Strogen, D., Howard, J.P., Abutarruma, Y., Elgadry, M., and Whitham, A.G., 2012. Palynological and palynofacies analysis of early Silurian shales from borehole CDEG-2a in Dor el Gussa, eastern Murzuq Basin, Libya. *Review of Palaeobotany and Palynology*, Vol.**174**, pp.1-26.

Parkinson, D., 1996. Gamma-ray spectrometry as a tool for stratigraphical interpretation: examples from the western European Lower Jurassic. *Geological Society, London, Special Publications*, Vol.**103**(1), pp.231-255.

Parrish, J.T., 1982. Upwelling and petroleum source beds, with reference to Paleozoic. *AAPG Bulletin*, Vol.**66**(6), pp.750-774.

Passey, Q., Creaney, S., Kulla, J., Moretti, F. and Stroud, J., 1990. A practical model for organic richness from porosity and resistivity logs. *AAPG Bulletin*, Vol.**74**(12), pp.1777-1794.

Pastor-Galán, D., Gutiérrez-Alonso, G., Murphy, J.B., Fernández-Suárez, J., Hofmann, M. and Linnemann, U., 2013. Provenance analysis of the Paleozoic sequences of the northern Gondwana margin in NW Iberia: Passive margin to Variscan collision and orocline development. *Gondwana Research*, Vol.**23**(3), pp.1089-1103.

Paytan, A. and Gornitz, V., 2008. Ocean paleoproductivity. *Encyclopedia of Paleoclimatology and Ancient Environments*: pp.644-650, Springer (New York).

Pearce, R., Clayton, T. and Kemp, A.E., 1991. Illitization and organic maturity in Silurian sediments from the Southern Uplands of Scotland. *Clay Minerals*, Vol.**26**(2), pp.199-210.

Pearce, T., McLean, D., Martin, J.H., Ratcliffe, K. and Wray, D., 2010. A whole-rock geochemical approach to the recognition and correlation of" marine bands". Application of Modern Stratigraphic Techniques: Theory and Case Histories. *SEPM Special Publication* **94**, p.221-238.

Pedersen, T.F. and Calvert, S.E., 1990. Anoxia vs productivity; what controls the formation of organic-carbon-rich sediments and sedimentary rocks? *AAPG Bulletin*, Vol.**74**(4), pp.454-466.

Pérez-Estaún, A., 1973. Datos sobre la sucesion estratigrafica del precambrico y la estructura del extreme sur del Antiforme del Narcea (NW de Espania). *Breviora Geologica Asturica*, Vol.**17**, pp.5-16.

Pérez-Estaún, A., 1978. Estratigrafía y estructura de la rama sur de la Zona Asturoccidental-Leonesa. *Mem. Inst. Geol. Min. España*, Vol.**92**, pp.1-151.

Pérez-Estaún, A., Bastida, F., Alonso, J.L., Marquínez, J., Aller, J., Alvarez-Marrón, J., Marcos, A. and Pulgar, J.A., 1988. A thin-skinned tectonics model for an arcuate fold and thrust belt: The Cantabrian Zone (Variscan Ibero-Armorican Arc). *Tectonics*, Vol.**7**(3), pp.517-537.

Perroud, H. and Bonhommet, N., 2007. A Devonian palaeomagnetic pole for Armorica. Geophysical *Journal of the Royal Astronomical Society*, Vol.**77**(3), pp.839-845.

Perroud, H., Calza, F. and Khattach, D., 1991. Paleomagnetism of the Silurian volcanism at Almaden, southern Spain. *Journal of Geophysical Research*, Vol.**96**(B2), pp.1949-1962.

Peterson, B.J., 1979. Particulate organic matter flux and planktonic new production in the deep ocean. *Nature*, Vol.**282**, pp.677-680.

Pettijohn, F. J., 1975. Sedimentary Rocks (3rd Ed.): pp.628. Harper and Row (New York).

Pettijohn, F.J., Potter, P.E. and Siever, R., 1987. Sand and Sandstone. pp.553. Springer (New York).

Pfeifer, K., Kasten, S., Hensen, C. and Schulz, H.D., 2001. Reconstruction of primary productivity from the barium contents in surface sediments of the South Atlantic Ocean. *Marine Geology*, Vol.**177**(1–2), pp.13-24.

Pi, D., Liu, C., Shields-Zhou, G.A. and Jiang, S., 2013. Trace and rare earth element geochemistry of black shale and kerogen in the early Cambrian Niutitang Formation in Guizhou province, South China: Constraints for redox environments and origin of metal enrichments. *Precambrian Research*, Vol.**225**(0), pp.218-229.

Piper, D.Z. and Calvert, S.E., 2009. A marine biogeochemical perspective on black shale deposition. *Earth-Science Reviews*, Vol.**95**(1–2), pp.63-96.

Poll, K., 1970. Stratigraphie und Tektonik an der Wende Silurium/Devon im westlichen Kantabrischen Gebirge (Nordspanien). Sitzungsberichte der Physikalisch-Medizinischen Gesellschaft, Erlangen, Vol.**83**(84), pp.32-176.

Potts, P. and Holbrook, J., 1987. Ailsa Craig - The History of a Reference Material. *Geostandards Newsletter*, Vol.**11**(2), pp.257-260.

Prakash Babu, C., Brumsack, H., Schnetger, B. and Böttcher, M.E., 2002. Barium as a productivity proxy in continental margin sediments: a study from the eastern Arabian Sea. *Marine Geology*, Vol.**184**(3–4), pp.189-206.

Price, J.R. and Velbel, M.A., 2003. Chemical weathering indices applied to weathering profiles developed on heterogeneous felsic metamorphic parent rocks. *Chemical Geology*, Vol.**202**(3–4), pp.397-416.

Priewalder, H., 2010. Chitinozoan Type Specimens in the F.H. Cramer Collection at the Geological Survey of Austria. *Jahrbuch der Geologischen Bundesanstalt*, Vol.**150**(1-2), pp.231-243.

Rahman, M.J.J. and Suzuki, S., 2007. Geochemistry of sandstones from the Miocene Surma Group, Bengal Basin, Bangladesh: Implications for Provenance, tectonic setting and wealthering. *Geochemical Journal*, Vol.**41**(6), pp.415-428.

Raiswell, R. and Berner, R.A., 1985. Pyrite formation in euxinic and semi-euxinic sediments*. American Journal of Science*, Vol.**285**(8), pp.710-724.

Raiswell, R., Buckley, F., Berner, R.A. and Anderson, T., 1988. Degree of pyritization of iron as a paleoenvironmental indicator of bottom-water oxygenation. *Journal of Sedimentary Research*, Vol.**58**(5), pp.812-819.

Raven, J.G.M.,1983. Conodont biostratigraphy and depostional history of the Middle Devonian to lower Carboniferous in the Cantabrian Zone (Cantabrian Mountains Spain). *Leidse Geologische Mededelingen*, Vol.**52**(2), pp.265-339.

Reitz, A., Pfeifer, K., De Lange, G. and Klump, J., 2004. Biogenic barium and the detrital Ba/Al ratio: a comparison of their direct and indirect determination. *Marine Geology*, Vol.**204**(3), pp.289-300.

Reolid, M. and Martínez-Ruiz, F., 2012. Comparison of benthic foraminifera and geochemical proxies in shelf deposits from the Upper Jurassic of the Prebetic (southern Spain). *Journal of Iberian Geology*, Vol.**38**(2), pp.449-465.

Richardson, J., Rodriguez, R. and Sutherland, S., 2001. Palynological zonation of Mid-Palaeozoic sequences from the Cantabrian Mountains, NW Spain: implications for inter-regional and interfacies correlation of the Ludford/Prídolí and Silurian/Devonian boundaries, and plant dispersal patterns. *Bulletin-Natural History Museum Geology Series*, Vol.**57**(2), pp.115-162.

Rider, M. and Kennedy, M., 2011. The Geological Interpretation of Well Logs. 3rd Eds. pp.432. Rider-French Consulting Ltd.

Riding, R.E. and Awramik, S.M., 2000. Microbial Sediments. pp.331. Springer (Heidelberg).

Rieke, H.H., and Chilingarian, G.V., 1974. Compaction of Argillaceous Sediments. pp.424. Elsevier (Amsterdam).

Rieu, R., Allen, P., Plotze, M. and Pettke, T., 2007. Compositional and mineralogical variations in a Neoproterozoic glacially influenced succession, Mirbat area, south Oman: Implications for paleoweathering conditions. *Precambrian Research*, Vol.**154**(3), pp.248-265.

Rimmer, S.M., 2004. Geochemical paleoredox indicators in Devonian–Mississippian black shales, Central Appalachian Basin (USA). *Chemical Geology*, Vol.**206**(3–4), pp.373-391.

Rinna, J., Warning, B., Meyers, P., Brumsack, H. and Rullkötter, J., 2002. Combined organic and inorganic geochemical reconstruction of paleodepositional conditions of a Pliocene sapropel from the eastern Mediterranean Sea. *Geochimica et Cosmochimica Acta*, Vol.**66**(11), pp.1969-1986.

Robardet, M. and Gutierrez-marco, J., 2002. Silurian. In: Gibbons, W., and Moreno, T., (eds), *The Geology of Spain*. London: Geological Society, pp.51-66.

Robardet, M., 2003. The Armorica 'microplate': fact or fiction? Critical review of the concept and contradictory palaeobiogeographical data. *Palaeogeography, Palaeoclimatology, Palaeoecology*. Vol.**195**(1-2), pp.125-148.

Rodrigues Sastre, M.A. and Gonzalez Menendez, L., 2011. Stratigraphy and structure of the uppermost of the Luarca Formation in Alto Bierzo, Leon (Ordovician, NW Spain). In: Gutierrez-Marco, J.C., Rabano, I., and Garcia-Bellido, D., (eds), *Ordovician of the World*. pp.473, Instituto Geológico y Minero de España (Madrid).

Rollinson, H.R. 1993. Using Geochemical Data: Evaluation, Presentation, Interpretation. pp. 352, Pearson Prentice Hall (Harlow).

Romer, R.L. and Hahne, K., 2010. Life of the Rheic Ocean: Scrolling through the shale record. *Gondwana Research*, Vol.**17**(2–3), pp.236-253.

Roser, B. and Korsch, R., 1988. Provenance signatures of sandstone-mudstone suites determined using discriminant function analysis of major-element data. *Chemical Geology*, Vol.**67**(1), pp.119-139.

Ross, D.J.K. and Bustin, R.M., 2009. Investigating the use of sedimentary geochemical proxies for paleoenvironment interpretation of thermally mature organic-rich strata: Examples from the Devonian–Mississippian shales, Western Canadian Sedimentary Basin. *Chemical Geology*, Vol.**260**(1–2), pp.1-19.

Roubault, M., de la Roche, H. and Govindaraju, K., 1970. Present status (1970) of the co-operative studies on the geochemical standards of the "Centre de Recherches Pétrographiques et Géochemiques". *Science de la Terre*, Vol.**15**, pp.351-393.

Rubino, J., Deynoux, M., Ghienne, J-F., Moreau, J., Blanpied, C., Lafont, F., Andres-Calatrava, R., Galeazzi, S., Mynth, T., and Sommer, F., 2003. Late Ordovician Glaciation in Northern Gondwana, Reappraisal and Petroleum Implications, in: *AAPG Search and Discovery Article* #90016, AAPG Hedberg Conference, 2003, Algiers, Algeria.

Rudnick, R. and Gao, S., 2003. Composition of the Continental Crust. *Treatise on Geochemistry*, Vol.**3**, pp.1-64.

Rule, J.H., 1986. Assessment of trace element geochemistry of Hampton Roads Harbor and lower Chesapeake Bay area sediments. *Environmental Geology*, Vol.**8**(4), pp.209-219.

Rupke, J., 1965. The Esla nappe, Cantabrian Mountains (Spain). *Leidse Geologische Mededelingen*, Vol.**32**, pp.1-74.

Sachanski, V., Göncüoglu, M.C. and Gedik, I., 2010. Late Telychian (early Silurian) graptolitic shales and the maximum Silurian highstand in the NW Anatolian Palaeozoic terranes. *Palaeogeography, Palaeoclimatology, Palaeoecology*, Vol.**291**(3–4), pp.419-428.

Sageman, B.B., Murphy, A.E., Werne, J.P., Ver Straeten, C.A., Hollander, D.J. and Lyons, T.W., 2003. A tale of shales: the relative roles of production, decomposition, and dilution in the accumulation of organic-rich strata, Middle–Upper Devonian, Appalachian basin. *Chemical Geology*, Vol.**195**(1–4), pp.229-273.

Sánchez de la Torre, S., Agueda Villar, J.A., Colmenero Navarro, J.R., García-Ramos, J.C. and Gonzales Lastra, J., 1983. Evolucion sedimentaria y paleogeografica del Carbonifero en la Cordillera Cantabrica. In: Martinez Diaz, C., (ed), *Carbonifero y Permico de Espana*. Madrid: IGME, pp.133-150.

Sánchez de Posada, L.C., Martínez Chacón, M.L., Méndez Fernández, C., Menéndez Alvarez, J.R., Truyols, J. and Villa, E., 1990. Carboniferous Pre-Stephanian rocks of the Asturian-Leonese Domain (Cantabrian Zone). In: Dallmeyer, R.D. and Martenez-Garcia, E., (eds), *Pre-Mesozoic Geology of Iberia*. pp.24-33. Springer Verlag (Berlin).

SARM Program., 2006. South African Reference Materials, Catalogue of reference materials produced by Mintek. **Catalogue** 1(November).

Sarmiento, G., Méndez-Bedia, I., Aramburu, C., Arbizu, M. and Truyols, J., 1994. Early Silurian conodonts from the Cantabrian Zone, NW Spain. *Geobios*, Vol.**27**(4), pp.507-522.

Scheffler, K., 2004. Reconstruction of sedimentary environment and climate conditions by multi-geochemical investigations of Late Palaeozoic glacial to postglacial sedimentary sequences from SW-Gondwana. *PhD thesis*, pp.243, Rheinischen Friedrich-Wilhelms-Universität Bonn.

Scheffler, K., Buehmann, D. and Schwark, L., 2006. Analysis of late Palaeozoic glacial to postglacial sedimentary successions in South Africa by geochemical proxies – Response to climate evolution and sedimentary environment. *Palaeogeography, Palaeoclimatology, Palaeoecology*, Vol.**240**(1–2), pp.184-203.

Schieber, J., 2003. Black Shales. In: Middleton, G.V., Church, M.J., Coniglio, M., Hardie, L.A., and Longstaffe, F.J., (eds), *Encyclopedia of Sediments and Sedimentary Rocks*. p.128-132. Springer (Heidelberg).

Schlumberger, 2009. Log Interpretation Charts. 2009 Edition. Schlumberger (Texas).

Schmitz, B., Charisi, S.D., Thompson, E.I. and Speijer, R.P., 1997. Barium, SiO2 (excess), and P2O5 as proxies of biological productivity in the Middle East during the Palaeocene and the latest Palaeocene benthic extinction event. *Terra Nova*, Vol.**9**(2), pp.95-99.

Schneider, J., de Wall, H., Kontny, A. and Bechstädt, T., 2004. Magnetic susceptibility variations in carbonates of the La Vid Group (Cantabrian Zone, NW-Spain) related to burial diagenesis. *Sedimentary Geology*, Vol.**166**(1–2), pp.73-88.

Schröder, S. and Grotzinger, J., 2007. Evidence for anoxia at the Ediacaran–Cambrian boundary: the record of redox-sensitive trace elements and rare earth elements in Oman. *Journal of the Geological Society*, Vol.**164**(1), pp.175-187.

Schultz, R.B., 2004. Geochemical relationships of Late Paleozoic carbon-rich shales of the Midcontinent, USA: a compendium of results advocating changeable geochemical conditions. *Chemical Geology*, Vol.**206**(3–4), pp.347-372.

Schwarzacher, W., 1993a. Cyclostratigraphy and the Milankovitch theory. Developments *in Sedimentology*. Vol.**52**, pp.225. Elsevier (Amsterdam).

Schwarzacher, W., 1993b. Milankovitch cycles in the pre-Pleistocene stratigraphic record: a review. *Geological Society, London, Special Publications*, Vol.**70**(1), pp.187-194.

Schweineberg, J., 1987. Silurische Chitinozoen aus der Provinz Palencia (Kantabrisches Gebirge, N-Spanien). *Göttinger Arbeiten zur Geologie und Paläontologie*, Vol.**33**, pp.1-94.

Scopelliti, G., Bellanca, A., Neri, R., Baudin, F. and Coccioni, R., 2006. Comparative high-resolution chemostratigraphy of the Bonarelli Level from the reference Bottaccione section (Umbria–Marche Apennines) and from an equivalent section in NW Sicily: Consistent and contrasting responses to the OAE2. *Chemical Geology*, Vol.**228**(4), pp.266-285.

Scotese, C.R., Boucot, A.J. and McKerrow, W.S., 1999. Gondwanan palaeogeography and paleoclimatology. *Journal of African Earth Sciences*, Vol.**28**(1), pp.99-114.

Sdzuy, K., 1968. Biostratigrafía de la griotte cambric de los Barrios de Luna (Léon) y de otras sucesiones comparables. *Trabajos de Geología*, Vol.**2**, pp.45-57.

Sdzuy, K., 1971. Acerca de la correlación del Cámbrico inferior en la Península Ibérica. *Geología*, Vol.**2**, pp.753-768.

Sdzuy, K., 1995. Acerca del conocimiento actual del Sistema Cámbrico y del límite Cámbrico Inferior-Cámbrico Medio. Memorias de las IV Jornadas Aragonesas de Paleontología: *La expansión de la vida en el Cámbrico*. Libro homenaje al Prof. Klaus Sdzuy. Zaragoza, Institución Fernando el Católico, pp.253-263.

Serra, O., 1984. Fundamentals of Well-log Interpretation: The acquisition of logging data. *Developments in Petrolium Science*. No.**15**A. pp.423. Elsevier (Amsterdam).

Servais, T. and Sintubin, M. Avalonia, Armorica, Perunica: terranes, microcontinents, microplates or palaeobiogeographical provinces? From: Bassett, M.G., (ed.) 2009. *Early Palaeozoic Peri-Gondwana Terranes: New Insights from Tectonics and Biogeography*. Geological Society, London, Special Publications, Vol.**325**, pp.103-115.

Sethi, P.S. and Schieber, J., 1998, Economic Aspects of Shales and Clays: An Overview. In: Schieber, J., Zimmerle, W., Sethi, P. (Eds). *Shales and Mudstones: Petrography, Petrophysics, Geochemistry and Economic Geology*. pp.237-253.

Shaw, D., 1968. A review of K-Rb fractionation trends by covariance analysis. *Geochimica et Cosmochimica Acta*, Vol.**32**(6), pp.573-601.

Shaw, D., Reilly, G., Muysson, J., Pattenden, G. and Campbell, F., 1967. An estimate of the chemical composition of the Canadian Precambrian Shield. *Canadian Journal of Earth Sciences*, Vol.**4**(5), pp.829-853.

Shaw, D.M., Dostal, J. and Keays, R.R., 1976. Additional estimates of continental surface Precambrian shield composition in Canada. *Geochimica et Cosmochimica Acta*, Vol.**40**(1), pp.73-83.

Shaw, J., Johnston, S.T., Gutiérrez-Alonso, G. and Weil, A.B., 2012. Oroclines of the Variscan orogen of Iberia: Paleocurrent analysis and paleogeographic implications. *Earth and Planetary Science Letters*, Vol.**329**, pp.60-70.

Sheehan, P.M., 2001. The late Ordovician mass extinction. *Annual Review of Earth and Planetary Sciences*, Vol.**29**(1), pp.331-364.

Stanley, D.J. and Blanpied, C., 1980. Late Quaternary water exchange between the eastern Mediterranean and the Black Sea. *Nature*, Vol.**285**, pp.537-541.

Stanley, S.M., 1988. Paleozoic mass extinctions: shared patterns suggest global cooling as a common cause. *American Journal of Science*, Vol.**288**, pp.334-352.

Steele, T., Wilson, A., Goudvis, R., Ellis, P. and Radford, A., 1978. Trace Element Data (1966 - 1977) for the Six “NIMROC” Reference Samples. *Geostandards Newsletter*, Vol.**2**(1), pp.71-106.

Stein, R., 1990. Organic Carbon Content/Sedimentation Rate Relationship and its Paleoenvironmental Significance for Marine Sediments. *Geo-Marine Letters*, Vol.**10**, pp.37-44.

Štorch, P. and Kraft, P., 2009. Graptolite assemblages and stratigraphy of the lower Silurian Mrákotín Formation, Hlinsko Zone, NE interior of the Bohemian Massif (Czech Republic). *Bulletin of Geosciences*, Vol.**84**(1), pp.51-74.

Štorch, P., 1998. Biostratigraphy, palaeobiogeographical links and environmental interpretation of the Llandovery and Wenlock graptolite faunas of peri-Gondwanan Europe. In: Gutiérrez-Marco, J.C. and Rábano, I., (eds). *Proceedings of the sixth international graptolite conference (GWG-IPA) and 1998 Field Meeting, IUGS Subcommison on Silurian stratigraphy*. Insitituto Tecnológico Geominero de Españia, Temas Geológico-Mineros. Vol.**23**, pp.126-129.

Stow, D.A.V., Huc, A.-. and Bertrand, P., 2001. Depositional processes of black shales in deep water. *Marine and Petroleum Geology*, Vol.**18**(4), pp.491-498.

Suarez de Centi, C., 1988. Estratigrafia, Sedimentologia y Paleogeografia de la Fm. Furada/San Pedro. Zona Cantabrica (NW de Espana), *PhD thesis*, pp.530, Departimento de Geología, Universidad de Oviedo.

Suárez de Centi, C., García-Ramos, J. and Valenzuela, M., 1989. Icnofósiles del Silúrico de la Zona Cantábrica (NO de España). *Boletín Geológico y Minero*, Vol.**100**(3), pp.339-394.

Sutcliffe, O.E., Dowdeswell, J.A., Whittington, R.J., Theron, J.N. and Craig, J., 2000. Calibrating the Late Ordovician glaciation and mass extinction by the eccentricity cycles of Earth's orbit. *Geology*, Vol.**28**(11), pp.967-970.

Suttner, L.J. and Dutta, P.K., 1986. Alluvial sandstone composition and paleoclimate, I. Framework mineralogy. *Journal of Sedimentary Research*, Vol.**56**(3), pp.329-345.

Svendsen, J.B. and Hartley, N.R., 2001. Comparison between outcrop-spectral gamma ray logging and whole rock geochemistry: implications for quantitative reservoir characterisation in continental sequences. *Marine and Petroleum Geology*, Vol.**18**(6), pp.657-670.

Swanson, V.E., 1961. Geology and geochemistry of uranium in marine black shales-a review. *U.S. Geolological Survey Profesional Papers*, Vol.**356**(C), pp.67-112.

Tait, J., Bachtadse, V., Franke, W. and Soffel, H., 1997. Geodynamic evolution of the European Variscan fold belt: palaeomagnetic and geological constraints. *Geologische Rundschau*, Vol.**86**(3), pp.585-598.

Tanner, L.H., 2010. Cyclostratigraphic record of the Triassic: a critical examination. *Geological Society, London, Special Publications*, Vol.**334**(1), pp.119-137.

Taylor, S.R. and McLennan, S.M., 1985. The Continental Crust: Its Composition and Evolution. pp.328. Blackwell Scientifc Publications.

Taylor, S.R. and McLennan, S.M., 1995. The geochemical evolution of the continental crust. *Reviews of Geophysics*, Vol.**33**(2), pp.241-265.

Taylor, S.R. McLennan, S.M and McCulloch, M.T., 1983. Geochemistry of Loess Continental Crust Composition and Crustal Model Ages. *Geochimica et Cosmochimica Acta*. Vol.**47**(11), pp.1897-1905.

Thompson, R.N., 1982. Magmatism of the British Tertiary province, *Scottish Journal of Geology*, Vol.**18**, pp.49-107.

Tiwari, R., Negi, J. and Rao, K., 1997. Detection of long term modulation orbital cycles in the sea level oscillations using clean algorithm of spectral analysis. *Geofizika*, Vol.**14**(1), pp.133-147.

Torsvik, T.H., and Van der Voo, R. 2002. Refining Gondwana and Pangea palaeogeography: Estimates of Phanerozoic non-depole (octupole) fields. *Geophysical Journal International*, Vol.**151**, pp.771-794.

Tourtelot, H.A., 1979. Black shale; its deposition and diagenesis. *Clays and Clay Minerals*, Vol.**27**(5), pp.313-321.

Tribovillard, N., Algeo, T.J., Lyons, T. and Riboulleau, A., 2006. Trace metals as paleoredox and paleoproductivity proxies: An update. *Chemical Geology*, Vol.**232**(1–2), pp.12-32.

Trotter, J. and Barnes, W.H., 1958. The Structure of Vanadinite. *The Canadian Mineralogist*, Vol.**6**(2), pp.161-173.

Truyols, J. and Julivert, M., 1983. El Silúrico en el Macizo Ibérico. Libro Jubilar JM Ríos, *Geología de España*, Vol.**1**, pp.246-265.

Truyols, J., Aramburu, C., Arbizu, M., García-Ramos, J.V., Gutiérrez-Marco, J., Méndez-Bedia, I., Rábano, I. and Villas, E., 1996. La Formación vulcanosedimentaria del Castro (Ordovícico-Silúrico) en el Cabo Peñas (Zona Cantábrica, NO España). *Geogaceta*, Vol.**20**(1), pp.15-18.

Truyols, J., Arbizu, M., García-Alcalde, J.L., García-López, S., Méndez Bedia, I., Soto, F. and Truyols-Massoni, M., 1990. Cantabrian and Palentian Zones; Stratigraphy: The Asturian-Leonese Domain (Cantabrian Zone). In: Dallmeyer, R.D., and Martínez-Garcia, E., (eds), *Pre-Mesozoic Geology of Iberia*. pp.10-19. Springer (Berlin).

Truyols, J., Philippot, A. and Julivert, M., 1974. Les formations siluriennes de la Zone Cantabrique et leurs faunes. *Bulletin de la Societé Géologique de France*, 7ème sèrie, Vol.**16**, pp.25-35.

Turekian, K.,1955. Paleoecological Significance of the Sr/Ca Ratio in Fossils and Sediments. *Bulletin of the Geological Society of America*, Vol.**66**, pp.155-158.

Turekian, K.K. and Kulp, J.L., 1956. The geochemistry of strontium. *Geochimica et Cosmochimica Acta*, Vol.**10**(5), pp.245-296.

Turekian, K.K. and Wedepohl, K.H., 1961. Distribution of the elements in some major units of the earth's crust. *Geological Society of America Bulletin*, Vol.**72**(2), pp.175-192.

Turekian, K.K., 1964. The marine geochemistry of strontium. *Geochimica et Cosmochimica Acta*, Vol.**28**, pp.1479-1496.

Turgeon, S. and Brumsack, H., 2006. Anoxic vs. dysoxic events reflected in sediment geochemistry during the Cenomanian–Turonian Boundary Event (Cretaceous) in the Umbria–Marche Basin of central Italy. *Chemical Geology*, Vol.**234**(3–4), pp.321-339.

Tyson, R., 1987. The genesis and palynofacies characteristics of marine petroleum source rocks. *Geological Society, London, Special Publications*, Vol.**26**(1), pp.47-67.

Tyson, R.V. and Pearson, T.H., 1991. The modern and ancient continental shelf anoxia: An overview. *Geological Society Special Publication*, Vol.**58**, pp.1-24.

Tyson, R.V., 1995. Sedimentary Organic Matter: Organic Facies and Palynofacies. pp.615. Chapman & Hall (London).

Vail, P., 1977. Seismic stratigraphy and global changes of sea level, Part 4: Global cycles of relative changes of sea level, Seismic stratigaphy-applications to hydrocarbon exploration. *AAPG Memoir*, Vol.**26**, pp.83-97.

Valdes, P., Sellwood, B. and Price, G., 1995. Modelling Late Jurassic Milankovitch climate variations. *Geological Society, London, Special Publications*, Vol.**85**(1), pp.115-132.

Valladares, M.I., Barba, P. and Ugidos, J.M., 2002. Precambrian. In: Gibbons, W., and Moreno, T., (eds), *The Geology of Spain*. pp.7-16, Geological Society (London)

Van der Meer Mohr, C.G., 1969. The stratigraphy of the Cambrian Láncara Formation between the Luna river and the Esla river in the Cantabrian Mountains, Spain. *Leidse Geologische Mededelingen,* Vol.**43**. pp.233-316.

Van der Voo, R., 2005. Paleomagnetism of the Atlantic, Tethys and Iapetus Oceans. Cambridge University Press.

Van der Weijden, C.H., 2002. Pitfalls of normalization of marine geochemical data using a common divisor. *Marine Geology*, Vol.**184**(3–4), pp.167-187.

Van Vugt, N., Langereis, C. and Hilgen, F., 2001. Orbital forcing in Pliocene–Pleistocene Mediterranean lacustrine deposits: dominant expression of eccentricity versus precession. *Palaeogeography, Palaeoclimatology, Palaeoecology*, Vol.**172**(3), pp.193-205.

Varol, Ö.N., Demirel, I.H., Rickards, R.B. and Günay, Y., 2006. Source rock characteristics and biostratigraphy of the Lower Silurian (Telychian) organic-rich shales at Akyaka, central Taurus region, Turkey. *Marine and Petroleum Geology*, Vol.**23**(9–10), pp.901-911.

Veizer, J., Demovič, R., 1974. Strontium as a tool in facies analysis. *Journal of Sedimentary Petrology*, Vol.**44**, pp.93-115.

Verniers, J., Nestor, V., Paris, F., Dufka, P., Sutherland, S. and Van Grootel, G., 1995. A global Chitinozoa biozonation for the Silurian. *Geological Magazine*, Vol.**132**(06), pp.651-666.

Veselovsky, Z., 2004. Integrated numerical modelling of a polyhistory basin, Southern Cantabrian Basin (Palaeozoic, NW-Spain). *PhD thesis*. Gaea heidelbergensis, Vol.**13**, pp.225.

Vidal, G., Palacios, T., Gámez-Vintaned, J.A., Balda, M.A.D. and Grant, S.W., 1994. Neoproterozoic-early Cambrian geology and palaeontology of Iberia. *Geological Magazine*, Vol.**131**(06), pp.729-765.

Vidal, G., Palacios, T., Moczydłowska, M. and Gubanov, A.P., 1999. Age constraints from small shelly fossils on the early Cambrian terminal Cadomian Phase in Iberia. *GFF*, Vol.**121**(2), pp.137-143.

Villas, E. and Cocks, L.R.M., 1996. The first Early Silurian brachiopod fauna from the Iberian Peninsula. *Journal of Paleontology*, Vol.**70**(4), pp.571-588.

Villiers, S., 1999. Seawater strontium and Sr/Ca variability in the Atlanitc and Pacific oceans. *Earth and Planetary Science Letters*. Vol.**171**, pp.623-634.

Vine, J.D. and Tourtelot, E.B., 1970. Geochemistry of black shale deposits; a summary report. *Economic Geology*, Vol.**65**(3), pp.253-272.

von Raumer, J.F. and Stampfli, G.M., 2008. The birth of the Rheic Ocean—Early Palaeozoic subsidence patterns and subsequent tectonic plate scenarios. *Tectonophysics*, Vol.**461**(1), pp.9-20.

Wahlberg, J.S, Baker, J.H, Vernon, R.W and Dewar, R.S., 1965. Exchange Adsorption of Strontium on Clay Minerals. *Geological Survey Bulletin*, Vol.**1140**-C, pp.1-26.

Walliser, O.H., 1996. Global events and event stratigraphy in the Phanerozoic. pp.341, Springer (Berlin and Heidelberg).

Walther, J.V., 2009. Essentials of Geochemistry. Jones & Bartlett Learning. Sudbury (Massachusetts).

Wang, Z., Yin, C., Gao, L., Tang, F., Liu, Y. and Liu, P., 2006. The character of the chemical Index of alteration and discussion of subdivision and correlation of the Nanhua System in Yichang Area. *Geological Review*, Vol.**52**(5), pp.577-585.

Warning, B., Brumsack, H.J., 2000. Trace metal signatures of eastern Mediterranean sapropels. *Palaeogeography Palaeoclimatology Palaeoecology,* Vol.**158**, pp.293-309.

Watson, J.S., 1996. Fast, simple method of powder pellet preparation for X - ray fluorescence analysis*. X - Ray Spectrometry*, Vol.**25**(4), pp.173-174.

Weaver, C.E., 1989. Clays, muds, and shales. *Developments in Sedimentology*, Vol.**44**. pp.819. Elsevier (Amsterdam).

Wedepohl, K., 1971. Environmental influences on the chemical composition of shales and clays. *Physics and Chemistry of the Earth*, Vol.**8**, pp.305-333.

Wedepohl, K., 1991. The composition of the upper earth's crust and the natural cycles of selected metals. In: Merrian, E. (ed): *Metals in natural raw materials. Metals and their compounds in the environment. Occurrence, analysis, and biological relevance*. pp. 3-18, Wiley-VCH (Weinheim).

Wei, G., Liu, Y., Li, X., Shao, L. and Liang, X., 2003. Climatic impact on Al, K, Sc and Ti in marine sediments: evidence from ODP site 1144, South China Sea. *Geochemical Journal-Japan*, Vol.**37**(5), pp.593-602.

Wei, H., Chen, D., Wang, J., Yu, H. and Tucker, M.E., 2012. Organic accumulation in the lower Chihsia Formation (Middle Permian) of South China: Constraints from pyrite morphology and multiple geochemical proxies. *Palaeogeography, Palaeoclimatology, Palaeoecology*, Vol.**353**, pp.73-86.

Weil, A., Gutiérrez-alonso, G. and Conan, J., 2010. New time constraints on lithospheric-scale oroclinal bending of the Ibero-Armorican Arc: a palaeomagnetic study of earliest Permian rocks from Iberia. *Journal of the Geological Society*, Vol.**167**(1), pp.127-143.

Weil, A.B., Van der Voo, R. and van der Pluijm, B.A., 2001. Oroclinal bending and evidence against the Pangea megashear: The Cantabria-Asturias arc (northern Spain). *Geology*, Vol.**29**(11), pp.991-994.

Weil, A.B., Van der Voo, R., van der Pluijm, B.A. and Parés, J.M., 2000. The formation of an orocline by multiphase deformation: a paleomagnetic investigation of the Cantabria–Asturias Arc (northern Spain). *Journal of Structural Geology*, Vol.**22**(6), pp.735-756.

Werne, J.P., Sageman, B.B., Lyons, T.W. and Hollander, D.J., 2002. An integrated assessment of a “type euxinic” deposit: evidence for multiple controls on black shale deposition in the Middle Devonian Oatka Creek Formation. *American Journal of Science*, Vol.**302**(2), pp.110-143.

White, W.M., 2013. Geochemistry. pp.672, John Wiley and Sons-Blackwell.

Wignall, P.B. and Hallam, A., 1991. Biofacies, stratigraphic distribution and depositional models of British onshore Jurassic black shales. Geological *Society, London, Special Publications*, Vol.**58**(1), pp.291-309.

Wignall, P.B. and Maynard, J.R., 1993. The sequence stratigraphy of transgressive black shales. Source rocks in a sequence stratigraphic framework: *American Association of Petroleum Geologists, Studies in Geology*, Vol.**37**, pp.35-47.

Wignall, P.B. and Myers, K.J., 1988. Interpreting benthic oxygen levels in mudrocks: A new approach. *Geology*, Vol.**16**(5), pp.452-455.

Wignall, P.B. and Newton, R., 2001. Black shales on the basin margin: a model based on examples from the Upper Jurassic of the Boulonnais, northern France. *Sedimentary Geology*, Vol.**144**(3–4), pp.335-356.

Wignall, P.B., 1994. Black shales. pp.127, Clarendon Press Oxford, UK.

Wilde, P., Berry, W. and Quinby-Hunt, M., 1991. Silurian oceanic and atmospheric circulation and chemistry. *Special Papers in Palaeontology*, Vol.**44**, pp.123-143.

Wilde, P., Lyons, T.W. and Quinby-Hunt, M.S., 2004. Organic carbon proxies in black shales: molybdenum. *Chemical Geology*, Vol.**206**(3-4), pp.167-176.

Wortmann, U.G., Hesse, R. and Zacher, W., 1999. Major-element analysis of cyclic black shales: Paleoceanographic implications for the Early Cretaceous deep western Tethys. *Paleoceanography*, Vol.**14**(4), pp.525-541.

Wright, J. and Colling, A., 1995. Seawater: its composition, properties, and behaviour. pp.168. Pergamon Press (in association with the Open University).

Xie, X., Ellis, A., Wang, Y., Xie, Z., Duan, M. and Su, C., 2009. Geochemistry of redox-sensitive elements and sulfur isotopes in the high arsenic groundwater system of Datong Basin, China. *Science of The Total Environment*, Vol.**407**(12), pp.3823-3835.

Xu, H., Liu, B. and Wu, F., 2010. Spatial and temporal variations of Rb/Sr ratios of the bulk surface sediments in Lake Qinghai. *Geochemical Transactions*, Vol.**11**, pp.3-3.

Xu, Y., Morel, F.M.M. 2013. Chapter 16 Cadmium in marine phytoplankton. In: Sigel, A., Sigel, H. and Sigel, R.K.O (eds). Cadmium: From Toxicity to Essentiality. *Metal Irons in Life Sciences*. Vol.**11**, pp.509-528.

Yang, C. and Baumfalk, Y., 1997. Application of high-frequency cycle analysis in high-resolution sequence stratigraphy. *Geological Society, London, Special Publications*, Vol.**123**(1), pp.181-203.

Zabel, M., Bickert, T. and Dittert, L., 1999. Significance of the sedimentary Al: Ti ratio as an indicator for variations in the circulation patterns. *Paleoceanography*, Vol.**14**(6), pp.789-799.

Zamarreño, I. and Julivert, M., 1967. Estratigrafía del Cámbrico del oriente de Asturias y estudio petrográfico de las facies carbonatadas. *Trabajos de Geología*, Vol.**1**, pp.135-168.

Zamarreño, I., 1972. Las litofacies carbonatadas del Cámbrico de la Zona Cantábrica (NW España) y su distribución geográfica. *Trabajos de Geología*, Vol.**5**, pp.3-118.

Zhang, S., Barnes, C.R. and Jowett, D.M.S., 2006. The paradox of the global standard Late Ordovician–Early Silurian sea level curve: Evidence from conodont community analysis from both Canadian Arctic and Appalachian margins. *Palaeogeography, Palaeoclimatology, Palaeoecology*, Vol.**236**(3–4), pp.246-271.

Zwicky, C.N. and Lienemann, P., 2004. Quantitative or semi - quantitative?–laboratory - based WD - XRF versus portable ED - XRF spectrometer: results obtained from measurements on nickel - base alloys. *X - Ray Spectrometry*, Vol.**33**(4), pp.294-300.